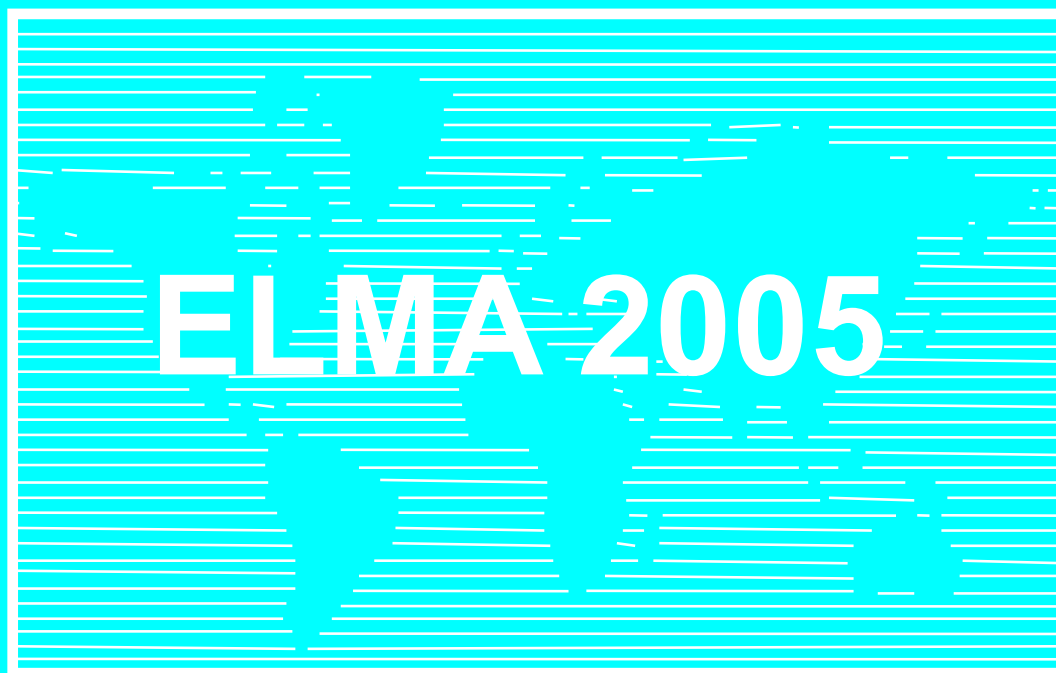


**ELEVENTH INTERNATIONAL CONFERENCE ON  
ELECTRICAL MACHINES, DRIVES AND POWER SYSTEMS**

Supported by  **IEEE** Bulgaria Section



**PROCEEDINGS**

**VOLUME 2**

**15-16 September 2005  
Sofia, BULGARIA**

ELEVENTH INTERNATIONAL CONFERENCE ON  
ELECTRICAL MACHINES, DRIVES AND POWER SYSTEMS

# ELMA 2005

15 – 16 September 2005, Sofia, BULGARIA

## PROCEEDINGS

### VOLUME 2

Supported by  **IEEE** Bulgaria Section

Organised by:

Union of Electronics, Electrical Engineering and Telecommunications (CEEC)  
Technical University of Sofia  
Technical University of Varna  
Technical University of Gabrovo

ELMA 2005 – XI International Conference on  
Electrical Machines, Drives and Power Systems  
15 – 16 September 2005, Sofia, BULGARIA

## Proceedings

Editorial board: Emil Sokolov, Pancho Dundarov, Gancho Bojilov,  
Vladimir Lazarov, George Todorov, Dimitar Sotirov,  
Zahari Zarkov

Printed by AVANGARD, Sofia, Bulgaria

Number of copies: 150

Printing of this edition has been financially supported by  
The Technical University of Sofia

ISBN 954-902-09-6-7

These Proceedings are reviewed by members of The Steering Committee.

**Disclaimer:** The authors are fully responsible for respecting the authors' rights, industrial and patent properties.

## ELMA 2005 is sponsored by:

- SIEMENS BG
- ABB Bulgaria
- ELPROM TRAF0 CH Kjustendil
- ELDOMINVEST Varna
- ELPROM Harmanli
- ELPROM – ZEM Sofia
- HYUNDAY HEAVY INDUSTRIES
- CERB Sofia
- SPARKY ELTOS Lovech
- ELMOT Veliko Tarnovo
- ABB-Avangard Sevlievo
- ZAVN Dobrich
- IEEE Bulgaria Section
- ELPROM - ILEP
- ELPROM – IEP
- ELMA Troyan
- UNITRAF Sokolovo
- DIT-M Sofia
- TROYAN MOTOR
- INOVATICS Sofia
- Rousse University "Angel Kunchev"
- ELISOT Sofia
- DENI-EN-K Sofia
- TO-NTS Varna
- EMNM – TU Sofia

## STEERING COMMITTEE

### INTERNATIONAL STEERING COMMITTEE MEMBERS

<b>Viktor BESPALOV</b>	Technical University of Moscow, Russia
<b>Gancho BOJILOV</b>	Technical University of Sofia, Bulgaria
<b>Stanislaw BOLKOWSKY</b>	SEP, Warsaw, Poland
<b>Milan CHUNDEV</b>	University "Sts. Cyril & Methodius", Skopje, Macedonia
<b>Manuel Perez DONSION</b>	Vigo University, Spain
<b>Gerhard DREGER</b>	VDE – Frankfurt, Germany
<b>Pancho DUNDAROV</b>	CEEC, Bulgaria
<b>Masato ENOKIZONO</b>	Oita University, Japan
<b>Bulent ERTAN</b>	Middle East Technical University, Ankara, Turkey
<b>Antonios KLADAS</b>	National Technical University of Athens, Greece
<b>Istvan KROMER</b>	VEIKI RT, Hungary
<b>Vladimir LAZAROV</b>	Technical University of Sofia, Bulgaria
<b>Afef LEBouc</b>	LEG – INPG, France
<b>Jiří LETTL</b>	CVUT – Prague, Czech Republic
<b>Gerard MEUNIER</b>	LEG – INPG, France
<b>Emil MITEV</b>	Polytechnic Radom, Poland
<b>Gilles NOTTON</b>	University of Corsica, France
<b>Viktor PETROUSHIN</b>	Odessa Polytechnic Institute, Ukraine
<b>Michel POLOUJADOFF</b>	University Pierre and Marie Curie, Paris, France
<b>Ioan POPA</b>	University of Craiova, Romania
<b>Viktor POPOV</b>	Technical University of St. Petersburg, Russia
<b>Mircea RADULESKU</b>	Technical University of Cluj-Napoca, Romania
<b>Saifur RAHMAN</b>	Virginia Tech, USA
<b>Christian SCHAEFFER</b>	LEG –INPG, France
<b>Wolfgang SCHROPPEL</b>	Technical University of Chemnitz, Germany
<b>Sergey SHIRINSKY</b>	Technical University of Moscow, Russia
<b>Emil SOKOLOV</b>	Technical University of Sofia, Bulgaria
<b>Dimitar SOTIROV</b>	Technical University of Sofia, Bulgaria
<b>Henryk SUPRONOWICZ</b>	Warsaw Polytechnic, Poland
<b>John TEGOPOULOS</b>	National Technical University of Athens, Greece
<b>George TODOROV</b>	Technical University of Sofia, Bulgaria
<b>Osami TSUKAMOTO</b>	Yokohama National University, Japan
<b>Christian VASSEUR</b>	University of Lille, France
<b>Ivan VASSILEV</b>	CEEC, Bulgaria

### CONFERENCE CHAIRMEN

<b>Emil SOKOLOV</b>	Technical University of Sofia
<b>Pancho DUNDAROV</b>	CEEC

### EXECUTIVE COMMITTEE

<b>Chairman:</b>	
<b>Vladimir LAZAROV</b>	Technical University of Sofia, Bulgaria
<b>Secretariat:</b>	
<b>George TODOROV</b>	Technical University of Sofia, Bulgaria
<b>Ivan VASSILEV</b>	CEEC, Bulgaria
<b>Yuli STAFUNSKI</b>	Technical University of Varna, Bulgaria
<b>Zahari ZARKOV</b>	Technical University of Sofia, Bulgaria

Conference Internet Site: <http://elma2005.tu-sofia.bg>

---

**NATIONAL ORGANIZING COMMITTEE MEMBERS**

---

<b>Kondyo ANDONOV</b>	Rousse University
<b>Rumen ATANASOV</b>	Bulgarian Chamber of Electrical Engineering
<b>Dimitar BAKARDJIEV</b>	Technical University of Sofia
<b>Dimitar DIMITROV</b>	Technical University of Varna
<b>Lyubomir DIMITROV</b>	Technical University of Varna
<b>Peter DINEFF</b>	Technical University of Sofia
<b>Krum GERASIMOV</b>	Technical University of Varna
<b>Petar GORANOV</b>	Technical University of Sofia
<b>Vasil GOSPODINOV</b>	Technical University of Sofia
<b>Nikola GRADINAROV</b>	Technical University of Sofia
<b>Marin HRISTOV</b>	Technical University of Sofia
<b>Kostadin ILIEV</b>	Technical University of Sofia, branch Plovdiv
<b>Todor IONKOV</b>	Technical University of Sofia
<b>Dimitar JETCHEV</b>	Technical University of Sofia
<b>Maria KANEVA</b>	Technical University of Sofia
<b>Milka KONSULOVA</b>	Technical University of Gabrovo
<b>Sava KONTROV</b>	Technical University of Varna
<b>Anastasia KRASTEVA</b>	Technical University of Sofia
<b>Rumen KUNCHEV</b>	Technical University of Sofia
<b>Iliana MARINOVA</b>	Technical University of Sofia
<b>Deshka MARKOVA</b>	Technical University of Gabrovo
<b>Nikolai MICHAILOV</b>	Rousse University
<b>Miho MIHOV</b>	Technical University of Sofia
<b>Mincho MINCHEV</b>	Technical University of Sofia
<b>Petar NAKOV</b>	Technical University of Sofia
<b>Petko NOTOV</b>	Technical University of Sofia
<b>Angel PACHAMANOV</b>	Technical University of Sofia
<b>Lazar PETKANICHIN</b>	Technical University of Sofia
<b>Vasil PIPEROV</b>	Technical University of Sofia
<b>Emil RATZ</b>	Technical University of Sofia
<b>Georgi RASHKOV</b>	Rousse University
<b>Plamen RIZOV</b>	Technical University of Sofia
<b>Nikola SHOYLEV</b>	University of Chemical Technology and Metallurgy, Sofia
<b>Yuli STAFUNSKI</b>	Technical University of Varna
<b>Rumiana STANCHEVA</b>	Technical University of Sofia
<b>Stefan TABAKOV</b>	Technical University of Sofia
<b>Raina TZENEVA</b>	Technical University of Sofia
<b>Hristo VASSILEV</b>	Technical University of Sofia
<b>Pencho VENKOV</b>	Technical University of Sofia
<b>Pencho VLADIMIROV</b>	Technical University of Gabrovo
<b>Ivan YATCHEV</b>	Technical University of Sofia
<b>Kiril ZAHARINOV</b>	Technical University of Sofia



# TABLE OF CONTENTS

## Volume 1

### INVITED PAPERS

<b>PL.1 Energy Strategies in a Liberalized Electricity Industry.....</b>	<b>P-I</b>
István Krómer <i>Institute for Electric Power Research, Budapest, Hungary</i>	
<b>PL.2 R&amp;D Status of HTS Power Applications in Japan.....</b>	<b>P-VI</b>
Osami Tsukamoto <i>Yokohama National University, Yokohama, Japan</i>	

### ELECTRICAL MACHINES I

<b>EM.1 The Nonlinear Model of a Switched Reluctance Motor.....</b>	<b>1</b>
Eleonora Darie and Emanuel Darie* <i>Technical University of Civil Engineering, Bucharest, Romania</i> <i>*Police Academy, Bucharest, Romania</i>	
<b>EM.2 The Control of Switched Reluctance Drives.....</b>	<b>5</b>
Eleonora Darie and Emanuel Darie* <i>Technical University of Civil Engineering, Bucharest, Romania</i> <i>*Police Academy, Bucharest, Romania</i>	
<b>EM.3 New Methods in Flux Measurement and Static Torque Calculation in a 7.5 kW SR Machine.....</b>	<b>8</b>
Feriha Erfan Kuyumcu, Kadir Yılmaz and Mevlut Karacor <i>Kocaeli University, Turkey</i>	
<b>EM.4 Computing Phase Resistance Value of Short Pitched and Fully Pitched Switched Reluctance Motors by using Parametric CAD Model.....</b>	<b>14</b>
Kadir Yılmaz and Abdulkadir Cengiz <i>Kocaeli University, Turkey</i>	
<b>EM.5 Dynamic Model and Steady-State Characteristics of the Induction Motor at Variable Frequenc.....</b>	<b>18</b>
Doru Adrian Nicola, Daniel Cristian Cismaru and Aida Cornelia Bulucea <i>University of Craiova, Romania</i>	
<b>EM.6 Optimum Design and Performance Analysis of Three-Phase Induction Motor.....</b>	<b>24</b>
A. Gökhan Yetgin, A. İhsan Çanakoglu*, K. Nur Bekiroglu** and Sibel Zorlu** <i>Sakarya University, Adapazarı, Turkey</i> <i>*Dumlupınar University, Kütahya, Turkey</i> <i>**Yildiz Technical University, Istanbul, Turkey</i>	
<b>EM.7 Influence of Equivalent Circuit Parameters of the Induction Machine on its Energy Characteristics.....</b>	<b>31</b>
Pencho Vladimirov, Deshka Markova and Dimitar Spirov <i>Technical University of Gabrovo, Bulgaria</i>	
<b>EM.8 Model of the Temperature Regime of a Three-Phase Induction Motor.....</b>	<b>38</b>
Ivan Evstaiev and Nicolay Mihailov <i>“Angel Kunchev” University of Rousse, Bulgaria</i>	
<b>EM.9 Applications of Infrared Thermography to Diagnose Electrical Machines.....</b>	<b>40</b>
Lyubormir Dimitrov and Velko Naumov <i>Technical University of Varna, Bulgaria</i>	
<b>EM.10 Vibration and Acoustic Noise of Switched Reluctance Motor .....</b>	<b>44</b>
Vladimir Kuzmichev <i>Moscow Power Engineering Institute (Technical University), Moscow, Russia</i>	
<b>EM.11 Information and Methodical Issues of Technologic Forecasting for Electrical Machines Reliability at the Design Stage.....</b>	<b>49</b>
Victor V. Popov and Igor A. Arseniev <i>St.Petersburg State Polytechnical University, StPetersburg, Russia</i>	
<b>EM.12 Complex Electronic Protection of the Low-Voltage Three-Phase Induction Motors .....</b>	<b>53</b>
Gabriel Nicolae Popa, Iosif Popa and Sorin Deaconu <i>„Politehnica” University of Timisoara, Hunedoara, Romania</i>	



## POWER SYSTEMS AND DISTRIBUTION SYSTEMS I

<b>PS.1 Voltage Stability - Essence, Methodology and Analysis.....</b>	<b>59</b>
Petko Notov and Rad Stanev <i>Technical University of Sofia, Bulgaria</i>	
<b>PS.2 Voltage Stability Static Analysis of Distribution Networks.....</b>	<b>63</b>
Petko Notov and Rad Stanev <i>Technical University of Sofia, Bulgaria</i>	
<b>PS.3 Usage of Graphic Systems for the Solution of Technological Problems of Control by Operational Modes both Availability Index of Product of Electric Equipment of Electrical Networks and Electrical Power Systems.....</b>	<b>69</b>
Youri Koubarkov and Valery Goldshtein <i>Samara State Technical University, Samara, Russia</i>	
<b>PS.4 Prony Analysis and its Application in Studies of Inter-Area Oscillations in the Former Second UCTE Synchronous Zone.....</b>	<b>72</b>
Chavdar Ivanov, Krum Gerasimov, Bozhidar Pavlov and Yulian Rangelov <i>Technical University of Varna, Bulgaria</i>	
<b>PS.5 Selection of PSS Gain Based on Impedance Matching... ..</b>	<b>76</b>
Chavdar Ivanov, Olof Samuelsson and Krum Gerasimov <i>Technical University of Varna, Bulgaria</i>	
<b>PS.6 Determination of the Optimal Repair Cost Limit Under Minimal Repair of the Electrical Equipment .....</b>	<b>81</b>
Svetlana Tzvetkova <i>Technical University of Sofia, Bulgaria</i>	
<b>PS.7 A New Approach to Modeling High Voltage Three-Phase Pipe Type Cable Using Conformal Mapping.....</b>	<b>84</b>
Jamal Moshtagh and Raj K. Aggarwal <i>University of Bath, U.K.</i>	
<b>PS.8 Calculation of the Safety Conditions from High Touch and Step Voltages in the Grounding System of REK Bitola – Suvodol .....</b>	<b>92</b>
Nikolce Acevski, Risto Ackovski* and Mile Spirovski <i>University St. Kliment Ohridski, Bitola, R.Macedonia</i> <i>* University Sts. Cyril and Methodius, Skopje, R. Macedonia</i>	
<b>PS.9 Dynamic Voltage Restorer with Zero Sequence Compensation.....</b>	<b>98</b>
Mehmet Tumay, K. Cagatay Bayindir, M. Ugras Cuma and C. Onur Tokunc <i>University of Cukurova, Adana, Turkey</i>	
<b>PS.10 Fuzzy Logic Control of Dynamic Voltage Restorer .....</b>	<b>103</b>
Mehmet Tumay, M. Ugras Cuma, Ahmet Teke and K. Cagatay Bayindir <i>University of Cukurova, Adana, Turkey</i>	

## ELECTRICAL DRIVES

<b>ED.1 Modelling and Simulation of an Electrical Drive with Induction Motor Controlled with Neuro-Fuzzy Regulator.....</b>	<b>109</b>
Cătălin Constantinescu <i>University of Craiova, Romania</i>	
<b>ED.2 A Half Bridge Converter for Motoring and Regenerating Operation of a DC Motor, Using a PWM Method Current Control.....</b>	<b>115</b>
Marian Pearsica <i>"Henri Coanda" Air Force Academy, Brasov, Romania</i>	
<b>ED.3 Plant Control using Digital Sensors that introduce a Delayed and Sampled Output.....</b>	<b>119</b>
Afzal Chamroo, Christian Vasseur and Haoping Wang <i>University of Science and Technology, Lille, France</i>	
<b>ED.4 SIMULINK Models of Direct Self Control Used in Electrical Traction with Induction Motors.....</b>	<b>125</b>
Daniel Cristian Cismaru, Doru Adrian Nicola and Aida Cornelia Bulucea <i>University of Craiova, Romania</i>	
<b>ED.5 The Intelligent Drive for Permanent Magnet AC Motors.....</b>	<b>131</b>
Eleonora Darie and Emanuel Darie* <i>Technical University of Civil Engineering, Bucharest, Romania</i> <i>Police Academy, Bucharest, Romania</i>	

<b>ED.6 Galvanomagnetic Antilock Braking System .....</b>	<b>134</b>
Nikola Draganov and Anatolij Alexandrov <i>Technical University of Gabrovo, Bulgaria</i>	
<b>ED.7 Modular Framework for Electrical Drives Analysis; a Petri Nets Approach.....</b>	<b>138</b>
Mircea Adrian Drighiciu <i>University of Craiova, Romania</i>	
<b>ED.8 Analysis, Designing, Modelling and Simulation of an Electric Driving System Equipped with Chopper Used in Electric Urban Traction.....</b>	<b>144</b>
Petre-Marian Nicolae, Ileana-Diana Nicolae, Ioana-Gabriela Sirbu and Viorel-Dumitru Vitan <i>University of Craiova, Romania</i>	
<b>ED.9 Realization of Different Methods for Defining the Speed in the Sensorless Systems for Orientation of the Magnetic Field.....</b>	<b>149</b>
Dimitar Spirov and Pencho Vladimirov <i>Technical University of Gabrovo, Bulgaria</i>	
<b>ED.10 An Improved Method for Frequency Control of an Induction Motor for Different Systems for Pulse Width Modulation.....</b>	<b>155</b>
Pencho Vladimirov and Dimitar Spirov <i>Technical University of Gabrovo, Bulgaria</i>	
<b>ED.11 Frequency Method for Obtaining Low Velocities.....</b>	<b>160</b>
Lubomir Genchev and Tsvetozar Petkov <i>Technical University of Gabrovo, Bulgaria</i>	

## TECHNOLOGIES, NEW MATERIALS AND COMPONENTS I

<b>TM.1 Magnetic Refrigeration at Room Temperature: From Materials to Applications.....</b>	<b>163</b>
Afef Kedous-Lebouc, Farid Allab, Jean Marc Fournier and Jean Paul Yonnet <i>Laboratoire d'Electrotechnique de Grenoble (LEG), INPG, ENSIEG, Saint Martin d'Hères Cedex, France</i>	
<b>TM.2 Micro Heat Pipe for Electronic Cooling.....</b>	<b>169</b>
Mariya Ivanova, Christian Schaeffer and Yvan Avenas <i>Laboratoire d'Electrotechnique de Grenoble (LEG), INPG, ENSIEG, Saint Martin d'Hères Cedex, France</i>	
<b>TM.3 Analysis of the Water Flow Behaviour in a Water Modification Device.....</b>	<b>174</b>
Yanko Slavtchev, Raina Tzeneva and Peter Dineff <i>Technical University of Sofia, Bulgaria</i>	
<b>TM.4 An Application of the Piezoelectric Effect for the Generation of Mechanical Shocks.....</b>	<b>180</b>
Marian Pearsica <i>"Henri Coanda" Air Force Academy, Brasov, Romania</i>	
<b>TM.5 Frequency Converter for Plasma Treatment with Step-up Transformer and Parallel Load Circuit.....</b>	<b>184</b>
Anastassia Krusteva, Plamen Avramov and Tsvetan Marinov <i>Technical University of Sofia, Bulgaria</i>	
<b>TM.6 Modeling of Starting Regimes of Tungsten Halogen Lamps.....</b>	<b>189</b>
Angel Pachamanov, Kamelia Nikolova, Neli Ratz and Nikolay Matanov <i>Technical University of Sofia, Bulgaria</i>	
<b>TM.7 Virtual Diagnosis of Cellular Manufacturing Systems.....</b>	<b>195</b>
Călin Ciufudean, Alexandru Bogdan Larionescu and Valentin Popa <i>„Ștefan cel Mare” University of Suceava, Romania</i>	
<b>TM.8 Energy Efficiency at Insurance Microclimatic Parameters in Livestock Building.....</b>	<b>201</b>
Nikolay Mihailov and Valentin Stoyanov <i>"Angel Kunchev" University of Rousse, Bulgaria</i>	
<b>TM.9 Three-Module Converter System for High Frequency Electrotechnological Applications .....</b>	<b>207</b>
Georgi Kunov, Marian Popov and Elissaveta Gadjeva <i>Technical University of Sofia, Bulgaria</i>	

## ELECTRICAL MACHINES II

<b>EM.13 Some Problems of Brushless Exciter for Synchronous Generator.....</b>	<b>211</b>
Emil Sokolov <i>Technical University of Sofia, Bulgaria</i>	

<b>EM.14 Static Characteristics of Brushless Switched Reluctance Motor, Calculated with Finite Element Analysis.....</b>	<b>215</b>
Dimitar Sotirov, Plamen Rizov and Anton Kalapish <i>Technical University of Sofia, Bulgaria</i>	
<b>EM.15 CAD System for Design and Teaching Distribution Transformers.....</b>	<b>220</b>
Radoslav Spasov and George Todorov <i>Technical University of Sofia, Bulgaria</i>	
<b>EM.16 About Designing an Average Model of RL Loaded Single-Phased Transformers in Periodical ac-Switching Regime.....</b>	<b>223</b>
Cristian-George Constantinescu, Constantin Strîmbu and Mihai Miron <i>"Henri Coandă" Air Force Academy of Brasov, Romania</i>	
<b>EM.17 A Comparative Study (Using Several Models) Of The RC Loaded, Single Phased Transformer In Periodical ac Switching Mode .....</b>	<b>227</b>
Constantin Strîmbu and Cristian-George Constantinescu <i>"Henri Coanda" Air Force Academy, Brasov, Romania</i>	
<b>EM.18 Numerical Approach for Defining Induction Motors Parameters by Catalogue Data and Data from No-Load and Short Circuit Tests.....</b>	<b>233</b>
Miho Mihov, Andrei Krumov, Emil Ratz and Petya Dimitrova <i>Technical University of Sofia, Bulgaria</i>	
<b>EM.19 An Analysis of Stator and Rotor Leakage Reactance in Induction Motors Based on Slot Dimensions.....</b>	<b>237</b>
A. Gökhan Yetgin and Nevra Akbilek <i>Sakarya University, Adapazarı, Turkey</i>	
<b>EM.20 A Dynamic Computer Model Investigation of Induction Motor by Loading with a Static Torque Dependent from the Rotor Speed.....</b>	<b>243</b>
Dinko Gospodinov and Pencho Georgiev <i>Technical University of Gabrovo, Bulgaria</i>	
<b>EM.21 A Software Method for Stator Current Values Processing during Induction Motor Rotor Faults Diagnosis .....</b>	<b>248</b>
Lyubomir Dimitrov and Georgi Getzov <i>Technical University of Varna, Bulgaria</i>	
<b>EM.22 Modelling of Heat Processes in Induction Motor and Determination of Thermal Life of Stator Winding Insulation by MATLAB 6.5.....</b>	<b>253</b>
Totyo Iliev and Vladislav Dimitrov <i>Technical University of Gabrovo, Bulgaria</i>	

<b>ELECTRICAL MACHINES III</b>
--------------------------------

<b>EM.23 A Comparison of the Main Classes of Brushless Motors by Analytical and Numerical Calculation.....</b>	<b>257</b>
Daniel Fodorean, Ioan-Adrian Viorel, Adesslem Djerdir* and Abdellatif Miraoui* <i>Technical University of Cluj-Napoca, Romania</i> <i>*University of Belfort-Montbéliard, Belfort, France</i>	
<b>EM.24 Brushless DC Motor with Unsymmetrical Magnetization and Combination Control .....</b>	<b>263</b>
Sameer H. Khader <i>College of Applied Professions, Palestine Polytechnic University, Palestine</i>	
<b>EM.25 Microstepping Control of 5-phase Hybrid Step Motor.....</b>	<b>272</b>
Zahari Zarkov <i>Technical University of Sofia, Bulgaria</i>	
<b>EM.26 Simulation and Measurement Study of Commutator DC Motor with Internal Asymmetries.....</b>	<b>278</b>
Zygfryd Głowacz and Antoni Zdrojewski <i>University of Science and Technology, Cracow, Poland</i>	
<b>EM.27 AC Commutator Motor: Calculation of Field, Parameter and Commutational Processes.....</b>	<b>283</b>
Victor Bepalov and Michail Panikhin <i>Moscow Power Engineering Institute (Technical University), Moscow, Russia</i>	
<b>EM.28 Active Resistance of Rotor Winding of Large Turbogenerators .....</b>	<b>286</b>
Natasa Mojsoska <i>University St. Kliment Ohridski, Bitola, R.Macedonia</i>	
<b>EM.29 Partial Discharges of Insulating System at Large Turbogenerators.....</b>	<b>289</b>
Natasa Mojsoska <i>University St. Kliment Ohridski, Bitola, R.Macedonia</i>	

<b>EM.30 Broken Part in Stator Core End Teeth Zone of AC Electrical Machine-Effects and Diagnosis.....</b>	<b>293</b>
Rumena Stancheva and Ilona Iatcheva <i>Technical University of Sofia, Bulgaria</i>	
<b>EM.31 Steady-State Performance Analysis of a Salient-Poles Synchronous Generator based on the Finite Element Method .....</b>	<b>298</b>
Zlatko Kolondzovski and Lidija Petkovska <i>University Sts. Cyril and Methodius, Skopje, R. Macedonia</i>	
<b>EM.32 Application of Hybrid Optimization Method on a Single Phase Shaded Pole Motor.....</b>	<b>303</b>
Vasilija Sarac, Lidija Petkovska and Goga Cvetkovski <i>University Sts. Cyril and Methodius, Skopje, R. Macedonia</i>	
<b>EM.33 A General Approach for Optimal Designing of Self-Starting Permanent Magnet Synchronous Micromotors.....</b>	<b>309</b>
Iliya Stanev <i>Technical University of Gabrovo, Bulgaria</i>	
<b>EM.34 The Asynchronous Machine for a Starter-Generating Unit (SGU).....</b>	<b>314</b>
Pavel Grachev, Vladimir Anisimov and Elena Ejova <i>Samara State Technical University, Samara, Russia</i>	

## Volume 2

<b>GENERAL PROBLEMS IN ELECTRICAL ENGINEERING</b>
---

<b>EE.1 Theoretical Considerations upon Electromagnets Energetics.....</b>	<b>317</b>
Aida Cornelia Bulucea, Doru Adrian Nicola, Nicolae Boteanu and Daniel Cristian Cismaru <i>University of Craiova, Romania</i>	
<b>EE.2 Magnetostatic Moments Method Dedicated to Electrotechnical Devices Modeling.....</b>	<b>321</b>
Olivier Chadebec, Jean-Louis Coulomb, Fleur Janet* and Gérard Meunier <i>Laboratoire d'Electrotechnique de Grenoble (LEG), INPG, ENSIEG, Saint Martin d'Hères Cedex, France</i> <i>* Schneider Electric, Corporate Research Division, Grenoble, France</i>	
<b>EE.3 Numerical Computation of the Induced Voltages in a Pipeline Using Special Interpolation Functions.....</b>	<b>327</b>
Dan Doru Micu, Emil Simion and Laura Cret <i>Technical University of Cluj-Napoca, Romania</i>	
<b>EE.4 Nondestructive Defect Determination by Field Visualization in Tubes.....</b>	<b>330</b>
Iliana Marinova and Valentin Mateev <i>Technical University of Sofia, Bulgaria</i>	
<b>EE.5 Diversity Systems Comparison in the Presence of Interference.....</b>	<b>336</b>
Milan Živković, Nenad Milošević, Bojan Dimitrijević and Zorica Nikolić <i>University of Niš, Serbia and Montenegro</i>	
<b>EE.6 3D Finite Element Modeling of Electromagnetic Devices by Using the Scalar Magnetic Potential.....</b>	<b>340</b>
Gérard Meunier <i>Laboratoire d'Electrotechnique de Grenoble (LEG), INPG, ENSIEG, Saint Martin d'Hères Cedex, France</i>	
<b>EE.7 Performance Improvement in Finite Element Analysis by Modifying Mesh Structure.....</b>	<b>346</b>
Kadir Yılmaz, Abdulkadir Cengiz, Murat Ayaz and Erkan Mese* <i>Kocaeli University, Turkey</i> <i>* Advanced Energy Conversion, LLC, Malta, NY, USA</i>	
<b>EE.8 Methods for Magnetic Field Calculation.....</b>	<b>350</b>
Ana N. Mladenović and Slavoljub R. Aleksić <i>University of Niš, Serbia and Montenegro</i>	
<b>EE.9 Maximum Energy Flow Problem Through Power Systems Under Interval Uncertainties.....</b>	<b>355</b>
Georgi Sapundjiev and Simona Petrakieva <i>Technical University of Sofia, Bulgaria</i>	
<b>EE.10 Electric Field Strength and Potential Determination in Dielectric Body with Cavity.....</b>	<b>361</b>
Slavoljub R. Aleksić, Zlata Ž. Cvetković, Mirjana T. Perić and Bojana Z. Nikolić <i>University of Niš, Serbia and Montenegro</i>	

## TECHNOLOGIES, NEW MATERIALS AND COMPONENTS II

<b>TM.10 Analysis of Electrothermal Regimes of High Temperature Heating Elements with Negative Coefficient of Resistance .....</b>	<b>367</b>
Nikolai Nikolov <i>Technical University of Varna, Bulgaria</i>	
<b>TM.11 Analysis of Electrothermal Regimens of High Temperature Heaters with Positive Temperature Coefficient of Resistance.....</b>	<b>371</b>
Nikolai Nikolov and Hristofor Tahrilov <i>Technical University of Varna, Bulgaria</i>	
<b>TM.12 About Using Dimming Devices in Tunnel Lighting .....</b>	<b>374</b>
Angel Pachamanov, Neli Ratz, Emil Ratz and Nikolay Matanov <i>Technical University of Sofia, Bulgaria</i>	
<b>TM.13 Composit Foamed Thermoplastics with Increased Electrostatic Safety.....</b>	<b>378</b>
Nikolay Piperov and Vasil-Mario Piperov* <i>Institute for Metal Science, Bulgarin Academy of Scinces, Sofia, Bulgaria</i> <i>*Technical University of Sofia, Bulgaria</i>	
<b>TM.14 Simulations and Measurements of Some Parameters from Plate-Type Electrostatic Precipitator.....</b>	<b>382</b>
Gabriel Nicolae Popa, Corina Diniş, Cristian Abrudean and Ovidiu Tirian <i>„Politehnica” University of Timisoara, Hunedoara, Romania</i>	
<b>TM.15 Invariability of Torques at Magnetization Modification Technology by Slowly Changed Fields .....</b>	<b>388</b>
Peter Dineff and Raina Tzeneva <i>Technical University of Sofia, Bulgaria</i>	
<b>TM.16 Electrolysis as Electromagnetic Phenomenon: Effect of Self-Magnetic Influence on Anodic Dissolution and Cathodic Corrosion of Aluminium in Solution of Sodium Chloride.....</b>	<b>394</b>
Peter Dineff <i>Technical University of Sofia, Bulgaria</i>	
<b>TM.17 Influence of High Frequency Welding Machines on Voltage Quality .....</b>	<b>400</b>
Vasil Gospodinov, Borislav Bojchev and Magdalina Kushleva <i>Technical University of Sofia, Bulgaria</i>	

## ENERGY GENERATION AND DISTRIBUTION

<b>EG.1 Variable Speed Induction Generators Connected to the Grid or in Island Mode Operation.....</b>	<b>403</b>
Sorin Deaconu, Gabriel Nicolae Popa and Iosif Popa <i>„Politehnica” University of Timisoara, Hunedoara, Romania</i>	
<b>EG.2 The Situation of Electricity Generation in Corsica Towards 40% Renewable Energy Sources Supply.....</b>	<b>405</b>
Gilles Notton, Philippe Poggi and Christian Cristofari <i>University of Corsica, Corte, France</i>	
<b>EG.3 The Data Handler of Weather Wind Observations, Calculation Wind Power Potential and Efficiency the Use of Wind Power Generators.....</b>	<b>411</b>
Petr Kountsevich, Michail Kostyrev* and Pavel Grachev* <i>Unified Electrical Power Complex, Moscow, Russia</i> <i>*Samara State Technical University, Samara, Russia</i>	
<b>EG.4 Modelisation and Performance of a Photovoltaic System Connected to the Electrical Grid.....</b>	<b>413</b>
Philippe Poggi, Marc Muselli, Gilles Notton, Nicolas Heraud and Stefka Nedeltcheva* <i>University of Corsica, Corte, France</i> <i>*Technical University of Sofia, Faculty of Sliven, Bulgaria</i>	
<b>EG.5 Solar Energy Resource Estimation for the Area of Rousse .....</b>	<b>418</b>
Nicolay Mihailov and Ivaylo Stoyanov <i>“Angel Kunchev” University of Rousse, Bulgaria</i>	
<b>EG.6 Impact of the Deregulation of the Electric Power System on its Optimal Operation.....</b>	<b>422</b>
Lazar Petkanchin and Maria Kaneva <i>Technical University of Sofia, Bulgaria</i>	
<b>EG.7 Simulation Study of DG Effect on Fault Location Methods in Distribution Networks.....</b>	<b>426</b>
D.Penkov, B. Raison, C. Andrieu, L. Stoyanov and J.-P. Rognon <i>Laboratoire d’Electrotechnique de Grenoble (LEG), INPG, ENSIEG, Grenoble, France</i>	
<b>EG.8 Models of Transient Processes During Operation and Faults in Autonomous Energy Systems .....</b>	<b>432</b>
Lyubomir Dimitrov and Stefka Kanturska <i>Technical University of Varna, Bulgaria</i>	

## ELECTRONICS

<b>EL.1 Development of Micro Heat Spreaders Integrated in 3-Dimensional Stacked Electronic Packages.....</b>	<b>435</b>
Nataliya Popova, Christian Schaeffer, Claude Sarno*, Serge Parbaud* and Georges Kapelski** <i>Laboratoire d'Electrotechnique de Grenoble (LEG), INPG, ENSIEG, Grenoble, France</i> <i>*Thales Avionics 25, Valence Cedex, France</i> <i>** Laboratoire de Génie Physique et Mécanique des Matériaux, INPG, ENSPG, Grenoble, France</i>	
<b>EL.2 Modeling and Analysis of Three-Phase Boost Rectifier Bidirectional Converters in Open Loop .....</b>	<b>440</b>
Jenica Ileana Corcau <i>University of Craiova, Romania</i>	
<b>EL.3 A Study About Power Transfer In Buck PWM AC Regulators.....</b>	<b>444</b>
Liliana Miron, Mihai Miron, Ioan Matlac* and Cristian Constantinescu <i>"Henri Coandă" Air Force Academy of Brasov, Romania</i> <i>**"Transilvania" University of Brasov, Romania</i>	
<b>EL.4 Active Power Sharing and Frequency Restoration in Parallel Operated Inverters.....</b>	<b>448</b>
Koray Şener Parlak, Mehmet Timur Aydemir* and Mehmet Özdemir <i>Firat University, Elazığ, Turkey</i> <i>*Gazi University, Maltepe, Ankara, Turkey</i>	
<b>EL.5 Uniform Approach for Analysis of Resonant Inverters with Reversed Diodes.....</b>	<b>453</b>
Nikola Gradinarov, Nikolay Hinov and Tsvetan Marinov <i>Technical University of Sofia, Bulgaria</i>	
<b>EL.6 Analysis of Parallel Resonant Inverter, Operating at Active Load.....</b>	<b>457</b>
Nikolay Hinov, Nikola Gradinarov, Tsvetan Marinov and Vasil Trenkov <i>Technical University of Sofia, Bulgaria</i>	
<b>EL.7 Design of a Modular DC/DC Converter for Fuel Cell Application .....</b>	<b>461</b>
Dang Bang Viet, Yves Lembeye, Jean Barbaroux and Jean Paul Ferrieux <i>Laboratoire d'Electrotechnique de Grenoble (LEG), INPG, ENSIEG, Grenoble, France</i>	

## ELECTRICAL MACHINES IV

<b>EM.35 Experimental determination of non-linear parameters of a single-phase commutator motor.....</b>	<b>465</b>
Gancho Bojilov, Adrian Ivanov and Nezabravka Ivanova <i>Technical University of Sofia, Bulgaria</i>	
<b>EM.36 Replacement of the Standard Graphic Concept of Synchronous Machines Potier's Diagram with Analytic Calculation .....</b>	<b>469</b>
Miho Mihov and Gancho Bojilov <i>Technical University of Sofia, Bulgaria</i>	
<b>EM.37 Diagnostic Laboratory Module for Coils of Electric Power Tools.....</b>	<b>475</b>
Milko Dochev <i>Technical College, Lovech, Bulgaria</i>	
<b>EM.38 Computer System for Research and Control of Electromechanical Objects.....</b>	<b>479</b>
Emil Marinov and Nikolai Nikolov* <i>Technical University of Varna, Bulgaria</i> <i>**"C&amp;C Technology" LTD Engineering, Varna, Bulgaria</i>	

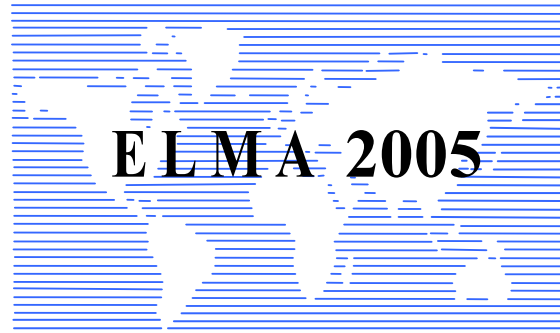
## POWER SYSTEMS AND DISTRIBUTION SYSTEMS II

<b>PS.11 On the Topological Observability of an Electrical System.....</b>	<b>483</b>
Nicolas Heraud, Olivier Wally, Oudie Bennouna and Philippe Poggi <i>University of Corsica, Corte, France</i>	
<b>PS.12 Mathematical Description of Complicated Power Supply Systems.....</b>	<b>487</b>
Vyacheslav Soloviov, Alexandr Kupov, Konstantin Khandoshko and Anastasia Kupova <i>Technical University of Komsomolsk-on-Amur, Russia</i>	
<b>PS.13 Computer Program for Setting of Earth Protection in Electric Power Networks of Average Voltage.....</b>	<b>491</b>
Mediha Mehmed-Hamza and Anton Filipov <i>Technical University of Varna, Bulgaria</i>	
<b>PS.14 Computer Graphic Processing of Discretely Registered Electrical Quantities in Electric Power Objects .....</b>	<b>497</b>
Anton Filipov, Mediha Mehmed-Hamza and St. Andreev <i>Technical University of Varna, Bulgaria</i>	

<b>PS.15 Fuzzy Logic PWM Current Controller based Shunt Active Power Filter for Power Quality Compensation.....</b>	<b>501</b>
K. Cagatay Bayindir, Mehmet Tumay and M. Ugras Cuma <i>University of Cukurova, Adana, Turkey</i>	
<b>PS.16 Assessment of the Influence of the Tower Grounding Resistance on the Lightning Overvoltages in the Substation.....</b>	<b>507</b>
Danail Dachev and Valentin Kolev <i>Technical University of Sofia, Bulgaria</i>	
<b>PS.17 Possibilities and Application of LOVATO Electric's Multimeter DMK32.....</b>	<b>512</b>
Vasil-Mario Piperov, Valery Assev and Georgie Stanchev <i>Technical University of Sofia, Bulgaria</i>	
<b>PS.18 Hybrid Power Systems with Renewable Energy Sources – Types, Structures, Trends for Research and Development .....</b>	<b>515</b>
Vladimir Lazarov, Gilles Notton*, Zahari Zarkov and Ivan Bochev <i>Technical University of Sofia, Bulgaria</i> <i>* University of Corsica, Corte, France</i>	
<b>PS.19 Commutation of Capacitor Circuits at Compensation of Power Factor.....</b>	<b>521</b>
Vasil-Mario Piperov and Galia Georgieva <i>Technical University of Sofia, Bulgaria</i>	

<b>TECHNOLOGIES, NEW MATERIALS AND COMPONENTS III</b>
---

<b>TM.18 Geometric Nonlinear Control of the Induction Motor .....</b>	<b>525</b>
Stanislav Enev <i>Technical University of Sofia, Bulgaria</i>	
<b>TM.19 Finite Element Analysis of Linear Actuator with Moving Permanent Magnet.....</b>	<b>531</b>
Ivan Yatchev, Krastyo Hinov, Georgi Dikov*, Stoiko Krastev and Dimitar Atanasov <i>Technical University of Sofia, Bulgaria</i> <i>*INCOMTECH Ltd., Sofia, Bulgaria</i>	
<b>TM.20 Influence of Some Constructive Parameters on the Electromagnetic Force of a Solenoid Actuator.....</b>	<b>535</b>
Dimitar Dimitrov, Kamen Yanev and Ivan Yatchev* <i>Technical University of Varna, Bulgaria</i> <i>*Technical University of Sofia, Bulgaria</i>	



---

---

**GENERAL PROBLEMS IN  
ELECTRICAL ENGINEERING**

---

---





## Theoretical Considerations upon Electromagnets Energetics

**Aida Cornelia BULUCEA, Doru Adrian NICOLA,  
Nicolae BOTEANU and Daniel Cristian CISMARU**

**Abstract.** In the paper have been approached in a unitary and original mode two essential aspects in the electromagnets theory: 1) the determination of the energy stored in the field of a electromagnet without elements in movement and the evaluation, on this basis of the static and dynamic inductances of the circuit, and 2) the establishment of the expression of the mechanical work done by the field forces when the electromagnet armature is in moving. The obtained results are a direct application of the theoretical electrotechnics in the electromagnets domain.

**Keywords:** electromagnet, energetics, inductance, magnetic field, mechanical work

### Introduction

The electromagnets are component elements of many control and protection electrical equipments, constituting the motor element in the construction of the electromagnetic contactors, relays, circuit-breakers and switchers [5]. Because of the importance of the electromagnets in the realization of the electric equipments, their study at a high level it is imposed. In this paper will be approach in a unitary mode two essential aspects in the electromagnets theory:

1) The determination of the energy stored in the field of a electromagnet without elements in movement (an electromagnet with the "immobilized" armature) and the evaluation, on this basis of the static and dynamic inductances of the circuit.

2) The establishment of the expression of the mechanical work done by the field forces when the electromagnet armature is in moving.

### Magnetic Field Energy in Case of Fixed Armature

It is considered an electromagnet [3] with a ferromagnetic core, the armature being "immobilized", like in the Fig.1. The excitation coil (made from copper Cu) has  $w$  turns, having the electric resistance  $r$  [ $\Omega$ ]. At the sudden connection (at the moment  $t = 0$ ) of the excitation winding to a constant voltage source  $U=ct.$ , it will appear the current "i", which will increase [2] (see Fig.1), from the value 0 to the steady-state regime value  $I_s=U/r$ , following a curve like that represented in Fig.1.

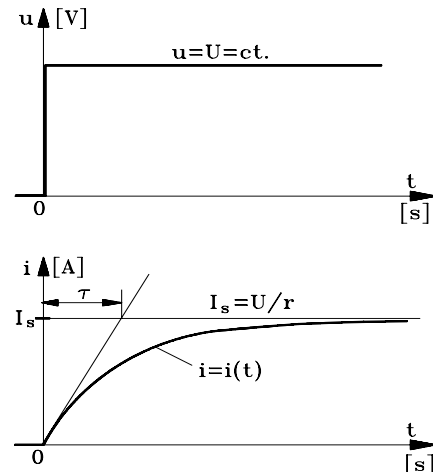


Fig.1. Electromagnet with fixed armature. Applied voltage  $u$  and current evolution with time  $i=i(t)$

In the current diagram  $i = i(t)$  from Fig.1., the quantity  $\tau = L/r$  represents the delay time electric constant of the circuit. Normally, the current  $i$  reaches the steady-state regime value  $I_s$  after  $(4 - 5)\tau$ .

From the analytically view point, during the transient regime, all electromagnetic processes of the circuit are governed [6] by the Electromagnetic Induction Law. Consequently, there have been obtained the following equations:

$$\begin{aligned}
 (1) \quad & -U + ri = e \\
 & e = - \frac{d\psi}{dt} \\
 & \psi = w\phi
 \end{aligned}$$

Therefore, it can be written:  $U = ri + d\Psi/dt$ , meaning that the applied voltage to the electromagnet winding terminals it is balanced (in the transient regime) by the drop voltage "ri" (on the coil resistance) and by the electromotive back force " $e=d\Psi/dt$ " induced in the coil (and caused by the total flux variation  $\Psi = w\Phi$ ).

As a result of the mathematical calculus, it will obtained the energetic balance equation during the transient regime of the electromagnet [4]:

$$(2) \quad \int_0^t U i dt = \int_0^t r i^2 dt + \int_0^\psi i d\psi$$

or:

$$(3) \quad W = W_J + W_m$$

where:  $W = \int_0^t U i dt$  represents the electric energy delivered by the supply source;

$W_J = \int_0^t r i^2 dt$  is the energy lost by Joule effect, and

$W_m = \int_0^\psi i d\psi$  represents the energy stored in the magnetic field.

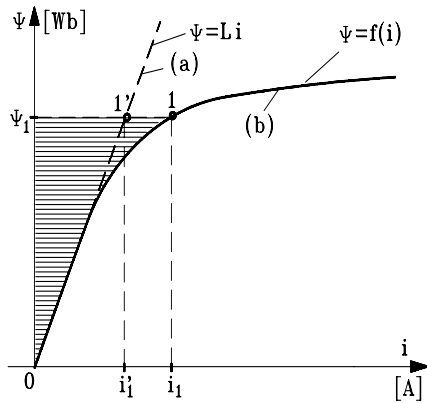


Fig.2. Electromagnet characteristic  $\psi=f(i)$ :  
(a)=coil "on the air";  
(b)=coil on the ferromagnetic core

Consequently, the magnetic field energy  $W_m$  it is obtained from the source energy  $W$  after the energy losses  $W_J$  (in the coil) are covered, meaning  $W_m=W-W_J$ .

When the transient regime it is "extinguished" (in the moment when winding current reaches the steady-state value  $I_s = U/r$ ) the magnetic flux also arrives to the constant value corresponding at the stationary regime  $\Psi=ct$ . After this moment (when  $d\Psi = 0$ ) the magnetic field energy remains constant and the whole energy taken from the source  $W$  will be spent entirely in covering the coil conductor losses  $W = W_J$ .

On the other hand, because the total magnetic flux (of the winding with  $w$  turns)  $\Psi=w\Phi$  depends on the fascicular magnetic flux  $\Phi = BS$  and because the induction curve  $B = f(H)$ , corresponding to the core magnetizing characteristic it is non-linear, as a result the total flux  $\Psi$  will depend by the current  $\Psi = f(i)$ , after a curve like that represented in Fig.2. The linear dependence figured at the position (a), meaning the straight line  $\Psi = Li$ , with  $L=ct$ . corresponds to the excitation coil without ferromagnetic core (coil "on the air"), while the non-linear curve  $\Psi=f(i)$  figured at the position (b) corresponds to the winding on a ferromagnetic core.

The shape of the curve (b) it is reproducing the non-linearity of the core magnetizing characteristic and it is depending both on the dimensions and the type of the core material, and on the total magnitude of the electromagnet air gap.

Corresponding to the non-linear curve  $\Psi=f(i)$  from the position (b), the magnetic field energy  $W_m$  (in the case of a constant air gap) has, like a graphical interpretation, the magnitude of the hatched surface, meaning:

$$(4) \quad W_{m1} = \int_0^{\psi_1} i d\psi = \text{surface}(01\psi_1)$$

For any point of the characteristic  $\Psi=f(i)$ , the positive ratio between the total magnetic flux  $\Psi$  and the current  $i$  it is defining the static own inductance  $L_s$  (see Fig.3.):

$$(5) \quad L_s = \frac{\Psi(i)}{i} > 0$$

$$L_s = L_s(i) = tg\alpha$$

The static inductance  $L_s$  is variable and depends on the current  $i$ , like in Fig.4 [1].

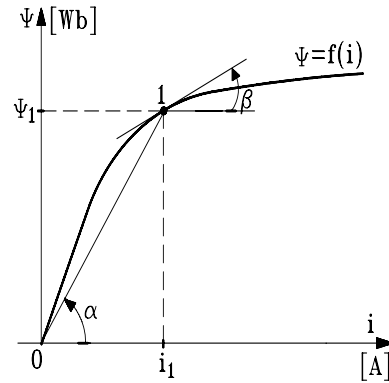


Fig.3. Defining static inductance  $L_s$  and dynamic inductance  $L_d$

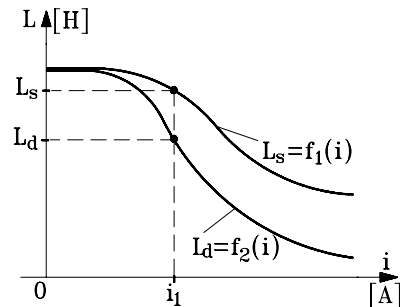


Fig.4. Curves of static  $L_s=f_1(i)$  and dynamic  $L_d=f_2(i)$  inductances

In the case of the ferromagnetic core windings it is defined (punctual) the dynamic inductance  $L_d$  (see Fig.3.) by the relations:

$$(6) \quad L_d = \left. \frac{d\psi}{di} \right|_{i=i_1}; \quad L_d = L_d(i) = tg\beta$$

For instance, if  $dL/dt=0$  (when  $L$  it is independent with time), then the inductance necessary in the Electromagnetic Induction Law is the dynamic inductance  $L_d$ :

$$e = -L \frac{di}{dt}$$

$$L = \frac{-e}{\frac{di}{dt}} = \frac{-(-\frac{d\psi}{dt})}{\frac{di}{dt}} = \frac{d\psi}{di} = L_d$$

The dynamic inductance  $L_d$  is variable and depends on the current  $i$  (see Fig.4.).

### Mechanical Work Done in Moving Armature

To any energized electromagnet, the electromagnetic forces will approach the armature to the core and will have as a result the air gap reduction.

For the evaluation of the mechanical work  $L_{12}$  done by the field forces (when the armature is in moving) it will be considered an electromagnet (see Fig.5.), characterized (in the initial state) by the air gap magnitude  $\delta_1$  and by the flux curve  $\Psi=f_1(I)$  on which, in the steady-state regime, the operation has been stabilized in the point 1, with the coordinates  $I_1$  and  $\Psi_1$  (see Fig.5.a).

After the attraction armature, the final state will describe by the air gap  $\delta_2$  (with  $\delta_2 < \delta_1$ ) and by the flux characteristic  $\Psi=f_2(I)$ , on which it is found the stabilized operation point 2, with the coordinates  $I_2$  and  $\Psi_2$ , like in Fig.5.b.

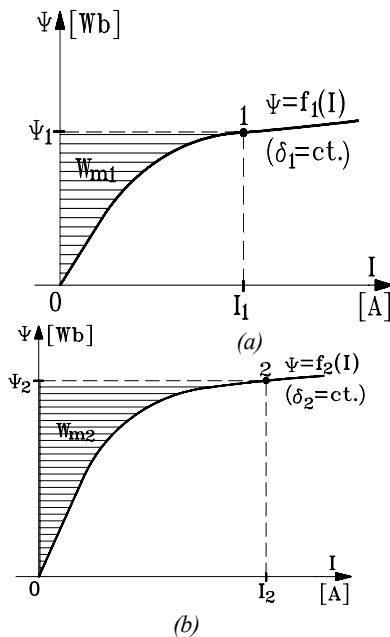


Fig.5. Characterization of initial (a) and final (b) states of electromagnet with armature in moving

On the basis of the relation (4), the magnetic field energy in the initial state  $W_{m1}$  and respectively, in the final state  $W_{m2}$  will be proportional with the hatched surfaces in Fig.5.:

$$(7a) \quad W_{m1} = \int_0^{\psi_1} i d\psi = \text{surface}(01\psi_1)$$

$$(7b) \quad W_{m2} = \int_0^{\psi_2} i d\psi = \text{surface}(02\psi_2)$$

Moreover, it is admitted that the phenomena evolution from the initial state 1 to the final state 2 has been produced very slowly, so that all intermediary states would be stationary. Therefore, in the plan  $(I, \Psi)$ , all intermediary balance points will be on the passing curve (between 1 and 2)  $\Psi = \Psi(I)$ , like in Fig.6.

In these conditions, during the armature moving (from  $\delta_1$  to  $\delta_2$ ) it is producing a double energy change between the source and the field: on one hand, the electromagnet takes from the source the energy  $\Delta W_m$  (proportional with the hatched surface corresponding to the flux variation from  $\Psi_1$  to  $\Psi_2$  on the evolution curve  $\Psi(I)$  in Fig.6.):

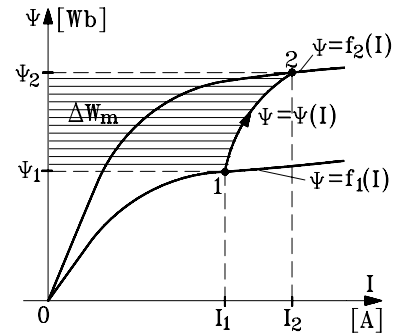


Fig.6. Evolution curve  $\psi = \psi(I)$  and magnetic energy  $\Delta W_m$  at armature moving

$$(8) \quad \Delta W_m = \int_{\psi_1}^{\psi_2} i d\psi = \text{surface}(\psi_1 12 \psi_2)$$

and, on the other hand, the magnetic field forces effect the mechanic work  $L_{12}$  (corresponding to the displacement  $\Delta\delta$  of the electromagnet armature).

Therefore, in the absence of the losses forces, the energetic balance of the electromagnet at the state - quantities variation due to the armature moving will be described by the equation:

$$(9) \quad W_{m1} + \Delta W_m = W_{m2} + L_{12}$$

Consequently, it results the done mechanic work:  $L_{12} = W_{m1} + \Delta W_m - W_{m2}$ , with the graphical interpretation corresponding to the relations (7) and (8):

$$(10) \quad L_{12} = \text{surface}(01\psi_1) + \text{surface}(\psi_1 12 \psi_2) - \text{surface}(02\psi_2) = \text{surface}(012)$$

The mechanic work  $L_{12}$  done by the magnetic field forces when the electromagnet armature is in moving will be equal with the surface (012), bounded by the curves  $\Psi=f_1(I)$ ,  $\Psi=f_2(I)$  and by the evolution curve  $\Psi=\Psi(I)$ . Graphical, the aria (012) it is the hatched surface in Fig.7.

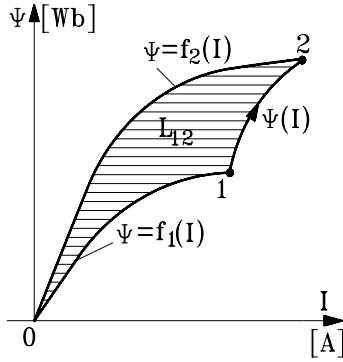


Fig. 7. Mechanical work  $L_{12}$  at armature moving

In the plan (IO $\Psi$ ), the most simple evolution curves  $\Psi(I)$  from the state 1 to the state 2 are parallel straight lines with the axes (see Fig.8.):

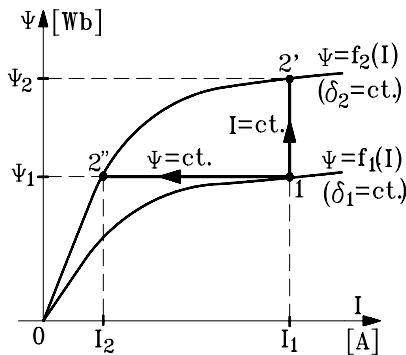


Fig. 8. Two particular evolutions  $\psi=\psi(I)$ : 1-2' (at  $I=ct.$ ) and 1-2'' (at  $\psi=ct.$ )

- at a constant current  $I=I_1=const.$ , when the evolution is produced by the straight line  $\overline{12'}$  or

- at a constant flux  $\Psi=\Psi_1=const.$ , when the evolution is following the straight line  $\overline{12''}$ .

In such cases, the mechanic work  $L_{12}$  (on the basis of the graphical interpretation as before) it is calculated, approximately, with the following relations:

a) At  $I = ct.$  (when the evolution it is made on the straight line  $\overline{12'}$ );  $L_{12} = L_{12'}$ , where:

$$(11) \quad \begin{aligned} L_{12'} &= \text{surface}(012') \approx \\ &\approx \frac{1}{2}(\psi_2 - \psi_1) I_1 = \frac{1}{2} \Delta \psi_{12} I_1 \end{aligned}$$

b) At  $\Psi = ct.$  (when the evolution it is made on the straight line  $\overline{12''}$ );  $L_{12} = L_{12''}$ , where:

$$(12) \quad \begin{aligned} L_{12''} &= \text{surface}(012'') \approx \frac{1}{2} \psi_1 (I_1 - I_2) = \\ &= -\frac{1}{2} \psi_1 (I_2 - I_1) = -\frac{1}{2} \psi_1 \Delta I_{12} \end{aligned}$$

## Conclusions

1. Due to the existence of the two inductances (the static one  $L_s$  and the dynamic one  $L_d$ ), the "danger" of the double interpretation appears many times, on the results always "gliding" the suspicion. Only if the coils are without ferromagnetic core (when  $\Psi = f(i)$  is a straight

line) the two inductances (static and dynamic) are the same  $L_s = L_d = L$  and  $\Psi = Li$ .

2. This particularity it is maintaining in the case of the magnetizing characteristic linearity (when  $\Psi=Li$ , with  $L=const.$ ) and the magnetic field energy  $W'_{m1}$  calculated with the relation (4) becomes  $W'_{m1} = \frac{\Psi_1^2}{2L}$ . Because  $\Psi_1 =$

$Li_1$  it will result  $W'_{m1} = \frac{1}{2} Li_1^2$ . On this basis it is evaluated the unique inductance  $L$  of a circuit, if there are known the magnetic energy  $W'_{m1}$  and the corresponding current value  $i_1$ :  $L = 2W'_{m1}/i_1^2$ .

3. From the theoretical developments there have been obtained graphical interpretations of the classic formulas for the calculation of the mechanical work, both at the constant current ( $I=ct.$ ) and at the constant flux ( $\Psi=ct.$ ). Thus, the approximation from the results (11) and (12) consists in the equivalence between the curved triangles surfaces 012' and 012'' with the surfaces of some fictive triangles, with the same basis and the same height, but with straight sides.

4. With the general expression  $W_m = \frac{1}{2} I \psi$  of the magnetic energy, the mechanic work  $L_{12'}$  (11) and  $L_{12''}$  (12) (done in moving the armature) can be expressed in a unitary mode by the formulas  $L_{12'} = \Delta W_{m12}|_{I=ct.}$  and

$$L_{12''} = - \Delta W_{m12}|_{\psi=ct.}$$

## References

- [1]. Bulucea, C.A., Nicola, D.A. Introducere în electrotehnica și echipamente electrice, Ed. SITECH Craiova, 2004.
- [2]. Coulon, I. Jufer, M. Introduction à l'électrotechnique, 5-ème édition, Piesses Politechniques Romandes, Laussane, 1989.
- [3]. Hortopan, Gh. Aparate electrice, E.D.P., Bucuresti, 1980.
- [4]. Nicola, D.A. Electrotehnica, transformatoare și masini electrice, Teoria Electrotehnicii, Ed. SITECH, Craiova, 1998.
- [5]. Rodstein, L. Electrical Control Equipment, MIR PUBLISHERS, 1974, English Translation.
- [6]. Timotin, A., Hortopan, V., Ifrim, A., Preda, M. Lectii de bazele electrotehnicii, E.D.P., Bucuresti, 1970.

**Aida Cornelia Bulucea** - Associate Professor, Dr., Electromechanical Faculty, University of Craiova, Bd. Decebal, Nr.5, Craiova, ROMANIA, e-mail: abulucea@em.ucv.ro.

**Doru Adrian Nicola** - Professor, Dr., Electromechanical Faculty, University of Craiova,, e-mail: dnicola@em.ucv.ro.

**Nicolae Boteanu** - Lecturer, Dr., Electromechanical Faculty, University of Craiova, @em.ucv.ro.

**Daniel Cristian Cismaru** - Lecturer, Dr., Electromechanical Faculty, University of Craiova, e-mail: dcismaru@em.ucv.ro

# Magnetostatic moments method dedicated to electrotechnical devices modeling

Olivier Chadebec, Jean-Louis Coulomb, Fleur Janet and Gérard Meunier

**Abstract:** This paper proposes a review of the magnetostatic moments method (MoM) applied to model electromagnetic devices. This method is now well-known for its "light weight" and its simplicity of implementation. Its main advantages are the non-requirement of an air region mesh and a coarse mesh of the ferromagnetic material. It leads to very fast resolution and very accurate field, force and moment computations. The paper proposes a state of the art of this approach and shows some efficient realizations.

**Keywords:** Magnetostatic, moment method, point-matching approach, simplified moment method,

## I. Introduction

Magnetostatic Moments method (Magnetostatic MoM) is now known as a powerful approach to model electrotechnical devices. Developed more than thirty year ago by Harrington [1], several academic codes like RADIA [2] or CALMAG3D [3] have already shown the reliability of the approach. Nowadays, it can be an interesting alternative to classical FEM methods in some situations.

In this method, only ferromagnetic material parts are divided into elementary elements with a constant magnetization affected on each of them. These elements are called moments and the distribution naturally respects Maxwell's equations. The main idea of the approach is that the magnetic field is created by the inductor sources and all the moments defined in the problem. With a point matching technique, which ensures the validity of the materials constitutive laws, a system is obtained. It remains to solve it to obtain the value of the moment and then to compute the magnetic field everywhere. Force or flux can thus be easily computed too.

The main advantage of the approach is that air (or equivalent) does not require any mesh. Only ferromagnetic materials and magnets are meshed and often with coarse subdivisions. It leads to very high speed resolutions and to high accuracies for stray field computations, in comparison with FEM. Most part of references found in the literature deals with this use of moment method. However, others interesting application can be found.

The method could be called a "light weight" approach because of its simplicity of implementation, its speed and above all its efficiency to solve complex problems with very few numbers of unknowns. It is why this method is

particularly well adapted for multi-static studies with motion or optimization strategy (no mesh of the air region is required at each step and the evaluation of a problem is very fast). Finally, the method can easily be inverted and so gives very good results for magnetization identification.

However, to apply moment method to all these applications is not without difficulties. The use of this approach needs a good knowledge of the physical phenomena and of the numerical method. In opposition to FEM, which is very general, the moment method requires a high level of how-to skill.

This paper proposes a review of this method based on significant applications. First, we will sum up the main concepts of the theory. Linear and non linear models will be considered. Different kind of element will be shown in order to reduce the computation times and increase the accuracy of the method. Moreover, we will show some numerical realizations.

## II. Basic theory

### A - Standard equation

Let us consider a magnetostatic problem composed by some ferromagnetic regions and coils in which currents flow. Equations governing the problem are:

$$\operatorname{div} \mathbf{B} = 0 \quad (1)$$

$$\operatorname{curl} \mathbf{H} = \mathbf{J} \quad (2)$$

We must add the classical following material law [4]:

$$\mathbf{M}_{\text{ind}} - \mathbf{M}_{\text{rem}} = f(\mathbf{H})\mathbf{H} \quad (3)$$

where  $\mathbf{M}_{\text{ind}}$  is called the induced magnetization of the material and  $\mathbf{M}_{\text{rem}}$  is the permanent one. It is usual to divide the magnetic field  $\mathbf{H}$  into the summation of two terms:  $\mathbf{H}_0$ , the source magnetic field created by currents and  $\mathbf{H}_{\text{red}}$ , the reduced magnetic field created by the ferromagnetic material. As we have,

$$\operatorname{curl} \mathbf{H}_0 = \mathbf{J} \quad (4)$$

we can conclude that the reduced magnetic field derives from a scalar potential:

$$\mathbf{H}(\mathbf{P}) = \mathbf{H}_0(\mathbf{P}) - \operatorname{grad} \varphi_{\text{red}}(\mathbf{P}) \quad (5)$$

where  $\mathbf{P}$  is a point located everywhere in the domain region. The reduced scalar potential is equal to [5]:

$$\varphi(\mathbf{P}) = \frac{1}{4\pi} \iiint_V \frac{(\mathbf{M}_{\text{ind}} + \mathbf{M}_{\text{rem}}) \cdot \mathbf{r}}{r^3} dV \quad (6)$$

where  $V$  is the volume of ferromagnetic material and  $\mathbf{r}$  the vector between the integration point and the point  $P$  where the field is expressed. Let us notice that the expression (6) ensures the validity of (1). By calculating the gradient of (6), we get thus an equation for the magnetic field.

$$\mathbf{H}(P) = \mathbf{H}_0(P) + \frac{1}{4\pi} \iiint_V \left( \frac{3(\mathbf{M}_{\text{ind}} \cdot \mathbf{r})}{r^5} \mathbf{r} - \frac{1}{r^3} \mathbf{M}_{\text{ind}} \right) dV + \frac{1}{4\pi} \iiint_{V_{\text{magnet}}} \left( \frac{3(\mathbf{M}_{\text{rem}} \cdot \mathbf{r})}{r^5} \mathbf{r} - \frac{1}{r^3} \mathbf{M}_{\text{rem}} \right) dV \quad (7)$$

In the integral terms, readers will recognize the standard expression of field created by a dipoles volume distribution.

### B - Mesh of the device

Let us consider a device composed of several magnets ( $V_{\text{magnet}}$ ) with a known magnetization  $\mathbf{M}_{\text{rem}}$ , inductors in which flows static currents  $I$  and ferromagnetic parts ( $V$ ) with unknown magnetization  $\mathbf{M}_{\text{ind}}$  (see Fig.1.).

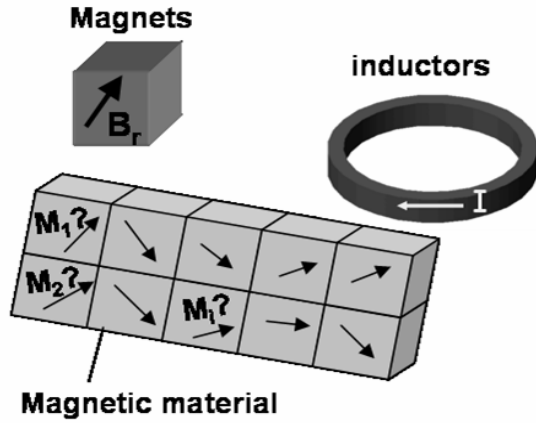


Fig.1. Device under study, with magnets, inductors and ferromagnetic parts meshed into volume elements

The ferromagnetic material is meshed into  $J$  volume elements and the magnets are divided into  $K$  volume elements too. Let us assume that magnetizations are uniform in each element of the ferromagnetic material and in the magnets. Equation (7) becomes:

$$\mathbf{H}(P) = \mathbf{H}_0(P) + \frac{1}{4\pi} \sum_{j=1}^J \iiint_{V_j} \left( \frac{3(\mathbf{M}_{\text{ind}_j} \cdot \mathbf{r})}{r^5} \mathbf{r} - \frac{1}{r^3} \mathbf{M}_{\text{ind}_j} \right) dV_j + \frac{1}{4\pi} \sum_{k=1}^K \iiint_{V_{\text{magnet}_k}} \left( \frac{3(\mathbf{M}_{\text{rem}_k} \cdot \mathbf{r})}{r^5} \mathbf{r} - \frac{1}{r^3} \mathbf{M}_{\text{rem}_k} \right) dV_k \quad (8)$$

Now, Let us define an orthogonal basis in each volume element for the magnetization. As equation (8) is linear, it can be rewritten as it follows:

$$\mathbf{H}(P) = \mathbf{H}_0(P) + \{\mathbf{g}\} [\mathbf{m}_{\text{rem}}] + \{\mathbf{f}\} [\mathbf{m}_{\text{ind}}] \quad (9)$$

where coefficients  $\mathbf{m}_{\text{ind}}$  and  $\mathbf{m}_{\text{rem}}$  define magnetizations in each local basis,  $\{\mathbf{g}\}$  is a  $(3 \times 3K)$  matrix,  $\{\mathbf{f}\}$  is a  $(3 \times 3J)$  matrix. Let us notice that  $[\mathbf{m}_{\text{rem}}]$  is a  $(3K \times 1)$  vector and  $[\mathbf{m}_{\text{ind}}]$  is a  $(3J \times 1)$  one.

### C - Point-matching method

A simple way to obtain an approximate solution of (7) is to ensure that this equation will be satisfied at discrete points in the region of interest. This procedure is called point matching approach. In our method, chosen points will be the barycenter of each element  $i$  of ferromagnetic regions. Equation (9) will be written at each barycenter of each element and projected in its local basis.

#### 1) Linear material law

In the case of a linear ferromagnetic material, the relation between the magnetization and the field is:

$$\mathbf{M}_{\text{ind}} = (\mu_r - 1)\mathbf{H} \quad (10)$$

By combining (9) and (10), we can write a linear system:

$$\{\{\mathbf{I}_d\} - \{\mathbf{F}\}\} [\mathbf{m}_{\text{ind}}] = [\mathbf{h}_0] + \{\mathbf{G}\} [\mathbf{m}_{\text{rem}}] \quad (11)$$

with  $3 \times J$  unknowns.  $\mathbf{I}_d$  is the identity matrix, and  $[\mathbf{h}_0]$  the source field at each barycenter projected in local basis. It can easily be computed by analytical or numerical computation of Biot and Savart's law. Let us notice that in this model, equations (1) and (2) are satisfied by construction. In fact, the moment method solves (10) (i.e. the material law) by a numerical approximation (i.e. a point matching approach).

The system obtained is square and full. This is the main drawback of the approach. In fact, for large meshes, the matrix of this system become too memory consuming and required too many time to be solved. It is the most important drawback of the method in comparison with the finite element one.

#### 2) Non-linear law

For a non-linear material, an iterative algorithm is required (relaxation) using the equation (3). In some cases, the convergence is difficult to reach, but some now well-known techniques can ensure and improve the convergence speed [6].

## III. Integration improvements

### A - Reduction of the singularity

The main difficulty in moment method is the computation of matrix  $\mathbf{F}$  coefficients (and/or  $\mathbf{G}$  matrix too). If we compute the influence of element  $j$  at the barycenter of element  $i$ , the coefficient have the following expression.

$$f_{ij} = \left\langle \left( \frac{1}{4\pi} \iiint_{V_j} \left( \frac{3(\mathbf{b}_j \cdot \mathbf{r}_{ij})}{r_{ij}^5} \mathbf{r}_{ij} - \frac{1}{r_{ij}^3} \mathbf{b}_j \right) dV_j \right), \mathbf{b}_i \right\rangle \quad (12)$$

where  $\langle \cdot, \cdot \rangle$  denotes the classical scalar product operator. Let us notice that (12) is a  $(3 \times 3)$  matrix for volume element. In particular, for  $i=j$  (computation of the influence of an element on itself), even if this integral is analytically convergent, the use of numerical integration can lead to artificial numerical singularity (i.e. Gauss integration points are too close from the matching point). Moreover for an unspecified element shapes, no analytical solution for (12) can be found.

A well-known solution is to consider that all the elements are spherical (or better ellipsoidal). Equation (12) has thus a very simple expression in all the cases [7]. However, if this technique can be acceptable to compute the field created by magnet in air, it can lead to important inaccuracies when ferromagnetic materials are taken into account.

The best solution is to use the well-known equivalent surface charge distribution. As we said, the magnetization  $\mathbf{M}_{ind}$  is constant on each element. Its divergence is equal to zero on the volume. On this assumption, the field created by the volume is exactly the same that the field created by a surface charge distribution  $\mathbf{M}_{ind} \cdot \mathbf{n}$  located on the surface delimiting the volume [5] (the vector  $\mathbf{n}$  is the external normal of  $V$ ). The advantage of this approach is to present a reduced singularity ( $\sim 1/r^2$ ) in comparison with (12) ( $\sim 1/r^3$ ). Equation (12) becomes thus:

$$f_{ij} = \left\langle \left( \frac{1}{4\pi} \iint_{S_i} \mathbf{b}_j \cdot \mathbf{n}_j \frac{\mathbf{r}_{ij}}{r_{ij}^3} dS_i \right), \mathbf{b}_i \right\rangle \quad (13)$$

The integral can be computed analytically [6] [8], so with a great accuracy. However, formulae are complex to implement and their evaluation can increase the computation time. It is thus possible to use numerical Gauss technique. It allows us to use a vectorized algorithm ("for" loops are replaced by matrix manipulations). Computation time decreases, but the accuracy decreases too.

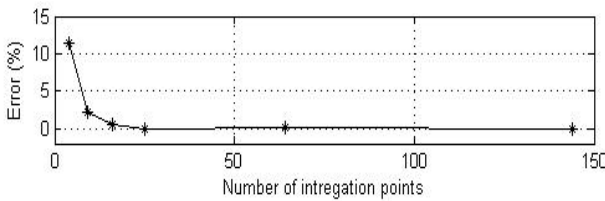


Fig 2. Computation of the influence of a cube volume element on itself (point-matching at the element barycenter). The magnetization is parallel to a face. Curve shows values of (13) obtain for different number of Gauss points and compared with analytical solution.

As it is shown on previous figure, an important number of integration points (16 for a square surface) is needed to ensure an error inferior to 0.5%. This number still leads to high computation time even if a vectorized algorithm is used. Our preferred solution is to use a limited number of integration points (4 per rectangular faces for example) and to recompute matrix terms which

represent the influence of an element on itself with an analytical integration. It allows us to increase the speed of the algorithm, the accuracy remaining very good.

### B - Other elements

For some particular geometries, the direction of magnetization in the device can be known. Equation (13) is thus simplified and number of unknowns is significantly reduced. In this section, we present two different kinds of elements: Surface one which allows to model shells and line ones dedicated to rods modelings.

#### 1) Surface elements

Let us consider a ferromagnetic shell. We consider that the permeability of the sheet is high and that the thickness  $e$  is small in comparison with other dimensions. The field in the sheet is mainly tangential and constant through the thickness of the shell [9]. Equation (13) becomes then:

$$f_{ij} = \left\langle \left( \frac{e}{4\pi} \iint_{S_i} \mathbf{b}_j \cdot \mathbf{n}_j \frac{\mathbf{r}_{ij}}{r_{ij}^3} dL_i \right), \mathbf{b}_i \right\rangle \quad (14)$$

The shell needs thus to be meshed only by surface elements (elements are not meshed in the thickness). Charges are then located on segments delimiting the surface elements. Surface integration becomes thus line ones and only two bases ( $\mathbf{b}_1, \mathbf{b}_2$ ) tangential to the surface element are used ( $\mathbf{n}$  is the external normal of the element and is tangential to it). It allows us to reduce significantly the number of unknowns. Analytical and numerical integrations can be provided. Reference [10] compares obtained results.

#### 2) Line elements

Let us now consider a device composed of ferromagnetic rods (small section  $s$  and high permeability). By applying the same approach that in previous section, we can model the rod by segments (line elements) with charges located at the extremity of each of them. Equation (13) becomes:

$$f_{ij} = \left\langle \left( \frac{s}{4\pi} \sum_{1,2} \mathbf{b}_j \cdot \mathbf{n}_j \frac{\mathbf{r}_{ij}}{r_{ij}^3} \right), \mathbf{b}_i \right\rangle \quad (15)$$

Only one basis is need ( $\mathbf{b}_1$  tangential to the line element). In some particular case, an high mesh density is necessary to take into account important variation of the magnetization along the rod. The length of elements may become so small that the section of the rod cannot be neglected any more. Special integration, taken into account the shape of the section can thus be provided [11].

## IV. Post-processing

### A - Stray field computation

The stray field created by the device can easily be



computed with (8). The main advantage of the method is that the air region is not meshed, so no numerical noise decreases the accuracy of the stray field computation. The method has already shown good results in shielding effects computation or magnetic signature of ferromagnetic hulls. A combination of FEM and moment method can lead also to interesting results [12]. This method seems easier to implement than the use of infinite modeling tools in FEM or coupling with BEM.

### B - Forces and moments computations

The computation of force acting on the ferromagnetic devices can be obtained with the following equation [5]:

$$\mathbf{F} = \sum_{i=1}^N \iint_{S_i} \mathbf{B}_{\text{ext}}(\mathbf{M}_i \cdot \mathbf{n}_i) dS \quad (24)$$

where  $\mathbf{B}_{\text{ext}}$  is the induction created by all the devices (inductor, magnets and ferromagnetic regions) except the ferromagnetic region considered. Moments can easily be computed too. The method leads to accurate and really fast computations for devices composed with magnets and with a high leakage field (Magnetic Micro-actuator for example), for which a high density of mesh is needed in FEM modelings. Let us notice that the use of Maxwell's tensor integration on a surface surrounding the region can reduce the computation time significantly.

## V - Some numerical example

### A - Modeling of an actuator

In this section, we present a classical application of magnetostatic moment method. Let us consider an actuator. It is composed by two ferromagnetic cylindrical columns carrying two inductor coils. Between these two columns, another one, with a rectangular section, is composed by a permanent magnet and ferromagnetic material. A bottom support and a top pallet channel the induction. The goal of this section is to compute the force acting on the pallet without any current in coils. Let us notice that the device has a symmetry plan. The problem is solved with the 3D commercial software Flux3D. The force obtained is 25.24N.

The actuator is now modeled by moment method. The first step is to mesh the active ferromagnetic parts and the magnet by volume elements. A standard FEM mesh generator is used. It is usual to use mapped elements (hexahedral and prism elements). In fact, in the magnetostatic moment method relevant elements must be used. Their shape must be chosen to ensure that the flux will be well-channeled. Indeed, tetrahedral elements often lead to numerical difficulties (bad condition number of the matrix obtained). With such a mapped mesh, the integration is made and the problem solved. The force is computed thanks to (24). It is equal to 22.88N. The method provides an error of 10%.

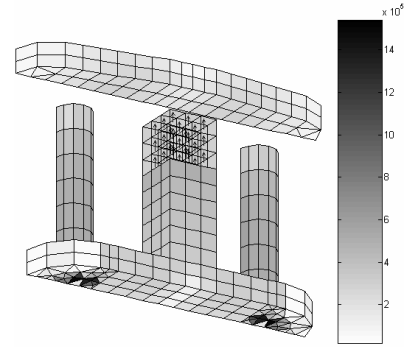


Fig. 4. Magnetization distribution (A/m) obtained with a standard mesh. Moments directions are not represented ( $\mu_r=2000$ ).

Even if the error provided by MoM is not so bad (less than 10% with few elements), the result cannot be considered as satisfying and must be improved. In fact, this result has mainly two causes. The first one deals with the mesh at the interface between cylindrical columns and the bottom support. As we can see on Fig.4., some prism elements have a very high magnetization in comparison with their neighbors. A numerical problem seems to occur there. In fact, in this area, the flux makes a strong direction change (90 degrees). As we have already said, the shape of elements must help the flux to have a good direction and prism element, in this device, does not. A simple solution consists in changing both cylindrical columns in equivalent ones with square same sections. In fact, the reluctance of the circuit will be not modified (nor the flux), and the force will be the same. This result has been verified with a FEM modeling. With this assumption, only hexahedral elements can be used. However, this numerical trick is not sufficient, because one another main problem occurs. Let us remember that the magnetic field (and so the force) is calculated thanks to equivalent charge distribution. In fact, charges are a representation of the flux (see (13)). A good way to apply moment method is to imagine where these charges are going to have the highest variation and then to refine the mesh in this area and not elsewhere. It allows to keep an acceptable number of elements. In our device, the permeability is high thus the ferromagnetic material well-channeled the induction flux. Charges on most part of interfaces between elements are going to cancel themselves (the eternal normal are in opposite directions) except where the flux goes through the columns to join the pallet (air gap of the actuator). It is thus a good solution to refine the mesh there (top of the two square equivalent columns and bottom of the pallet). Let us notice that the magnetization of magnet being known, no mesh refinement is needed in this region. The mesh and magnetizations obtained are presented in fig.5. Let us notice also that non-conformal mesh is used. This is one of the main advantages of the method in comparison with FEM where the use of non-conformal mesh is not obvious. The computed force is equal to 25.04N (less than 1% in comparison with FEM). This problem is a

good example of moment method use to model devices with complex magnetic circuit geometries.

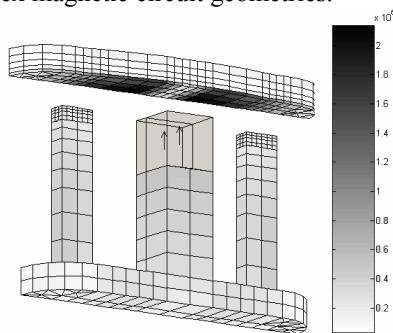


Fig. 5. Magnetization distribution (A/m) obtained with an adapted mesh.

### B - Simplified moment method

This section deals with the study of a current transformer which generates consequent magnetic leakage due to saturation. The goal is to found an electromagnetic model as light as possible (few unknowns so very fast resolution) to allow a global optimization strategy (coupling with electronic supply). The chosen method is the magnetostatic MoM used with very few elements, in which some directions for magnetizations are imposed (see Fig. 6.). This approach will be called “simplified moment method”.

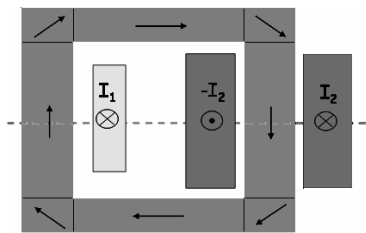


Fig.6. Mesh of a currents transformer with 8 volume elements. Only 7 unknowns are necessary to describe the problem (symmetries).

Simultaneous resolutions of (9) with a non-linear material law (see section II.C.2) make it possible for a couple of current currents ( $I_1, I_2$ ) to determine magnetic state of the device, for which can be deduced the flux under the secondary coil. A response surface of this flux can thus be built. Each time step,  $I_2$  is obtained reading  $I_2(I_1, \Phi_2)$ . Due to physical relation connecting current transformer variables,  $I_2$  can be deduced from  $I_1$ . Let us notice that the use of “light” moment method leads to an acceptable response surface time computation.

This approach is reliable and accurate while the magnetization can be considered as constant in each element (this is the case for high saturation level in the magnetic circuit). However, for low current values, magnetizations will be not uniform. According to our own experience, to refine the mesh in the current transformer could lead to accurate results but this solution is too time consuming to build the response surface.

To improve the results at low currents levels, the main idea is to combine moment method with reluctance network method, well-known for its accuracy in nonsaturated cases. This approach is equivalent to restore the Ampere’s law in the matrix and vector coefficient of (9) and is explained in [13]. The combination of two very simple models (a reluctance network and a MoM) for two different cases of operation modes (saturated and nonsaturated) can thus lead to accurate modeling of complex devices. Figure 7 shows results obtained with this approach and compares them with classical FEM and measurements.

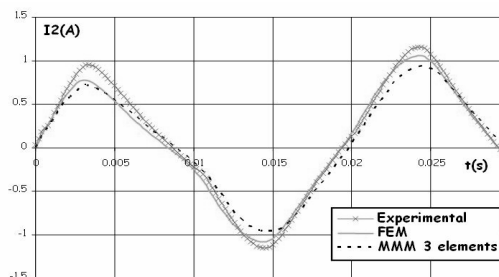


Fig.7. Comparison with the results obtained by MoM, FEM and measurements for the currents transformer. Computation times of MMM are divided per 10 in comparison of FEM.

## VI - Conclusions

In this paper, we have shown different potentialities of the magnetostatic moment method. Based on a point matching approach of the material law, this numerical method is easy to implement and lead to small matrix systems and therefore to fast resolutions. The approach has demonstrated its ability to solve accurately problems with consequent magnetic leakage (permanent magnets structure like microsystems, magnetic shieldings,...). However, for devices with complex magnetic circuit, a good knowledge of the numerical approach is needed to avoid high mesh density which leads to an unacceptable increase of the memory space.

Moreover, according to us, one of the main advantages of the method is to allow inverse modeling easier than with traditional FEM. The models being very light, optimization strategies and identifications can be advantageously provided.

All the numerical examples showed in this paper have been solved with a software package implementing the magnetic moment method and called LOCAPI.

## Acknowledgements

This work was supported in part by Schneider Electric and the French Navy

## References

- [1] R. F. Harrington, “Field computation by moment methods,” IEEE Press, 1993.
- [2] O. Chubar, P. Elleaume, J. Chavanne, “A three-dimensional magnetostatic computer code for insertion devices,” J. Synchrotron Rad. Vol. 5, pp 481-484, 1998

- [3] M. Souza, C. Vidigal, A. Momy, J. Taquin, M. Sauzade, "Non linear calculation of 3D static magnetic fields", IEEE Trans. Magn, Vol 33., No 4, July 1997, p2486-2491.
- [4] O.Chadebec, J.-L. Coulomb, G. Cauffet, J-P. Bongiraud, S. Guerin, "Magnetization Identification Problem - Illustration of an Effective Approach," COMPEL, Vol 23, Issue 2, 2004, pp 518-530
- [5] E. Durand, Magnétostatique, Masson et Cie, Paris, 1968
- [6] P. Elleaume, O. Chubar, J. Chavanne, "Computing 3D magnetic fields form insertion devices", Particle Accelerator Conference, 1997. Vol. 3, pp 3509 - 3511.
- [7] H. Zijlstra, "Experimental method in magnetism – 2. Measurement of magnetic quantity," Noth-Holland publishing company, Amsterdam 1967.
- [8] O.-M. Kwon,; C. Surussavadee; M.V.K. Chari, S. Salon, K. Sivasubramaniam K., "Analysis of the far field of permanent-magnet motors and effects of geometric asymmetries and unbalance in magnet design, " IEEE Trans. Magn, Vol. 40, No 2, March 2004 pp 435 – 442.
- [9] O. Chadebec, J.-L. Coulomb, J. P. Bongiraud, G. Cauffet, P. Le Thiec, "Recent improvement for solving inverse magnetostatic problem applied to thin shells," IEEE Trans. Magn, Vol 38, No 2, Mars 2002; pp 1005-1008
- [10] S. Guerin, J-L. Coulomb, G. Cauffet, L-L. Rouve "Analytic integration for closed-loop degaussing computation, " Proceedings of International Conference on Marine Electromagnetic, Marelec 2004, march 2004, London
- [11] O. Chadebec, L-L. Rouve, J.-L. Coulomb "New method for a fast and easy computation of stray fields created by wound rods," IEEE transactions on magnetics, Vol 38, No 2, Mars 2002, pp 517-520
- [12] B. Froidurot, L-L. Rouve, A. Foggia, J-P. Bongiraud, G. Meunier, "Magnetic discretion of naval propulsion machines," IEEE Trans. Magn, Vol 38 , No 2 , pp 1185 - 1188, March 2002.
- [13] F. Janet, J-L. Coulomb, C. Chillet, P. Mas "Simplified magnetic moment method applied to current transformer modeling" IEEE Trans. Magn, Vol. 40, No 2, March 2004, pp 818 - 821

---

**Olivier Chadebec** – CNRS Researcher, Dr., Laboratoire d'Electrotechnique de Grenoble, INPG / UJF / CNRS, LEG-ENSIEG, BP46, 38402 Saint Martin D'Hères, France. [chadebec@leg.ensieg.inpg.fr](mailto:chadebec@leg.ensieg.inpg.fr)

**Jean-Louis Coulomb**– Professor, Dr., Laboratoire d'Electrotechnique de Grenoble, INPG / UJF / CNRS, LEG-ENSIEG, BP46, 38402 Saint Martin D'Hères, France.

**Fleur Janet**– Reseach engineer, Dr., Schneider Electric, Corporate Research Division, 38050 Grenoble cedex, France.

**Gérard Meunier**– Senior CNRS Researcher, Dr., Laboratoire d'Electrotechnique de Grenoble, INPG / UJF / CNRS, LEG-ENSIEG, BP46, 38402 Saint Martin D'Hères, France. [meunier@leg.ensieg.inpg.fr](mailto:meunier@leg.ensieg.inpg.fr)

# Numerical computation of the induced voltages in a pipeline using special interpolation functions

Dan Doru Micu, Emil Simion and Laura Cret

**Abstract:** In the paper are evaluated the induced potential in pipeline based on the subdivision of the zone of influence AC Power Lines / pipeline in a relatively great number of sections in order to be able to determine voltages at many positions along the pipeline. Is presented a practical case of subdivision of the zone of influence in sections (a circuit model) and is calculated with special interpolation functions in Mathcad the values of the induced voltages in different points taking into account the measured data.

**Keywords:** induced voltage, electromagnetic interference, interpolation functions, power systems

## Introduction

There is some situations in which power lines, pipelines, communication lines, and similar services must coexist in a relatively narrow band of land. Pipelines located near power lines, may capture a portion of the energy encompassed by the conductors' paths, particularly under unfavorable circumstances such as long parallel exposures and power fault conditions [1], [2].

Interference calculations consist essentially of inductive and conductive interference calculations, which are performed independently; computation results can subsequently be combined together, see figure 1.

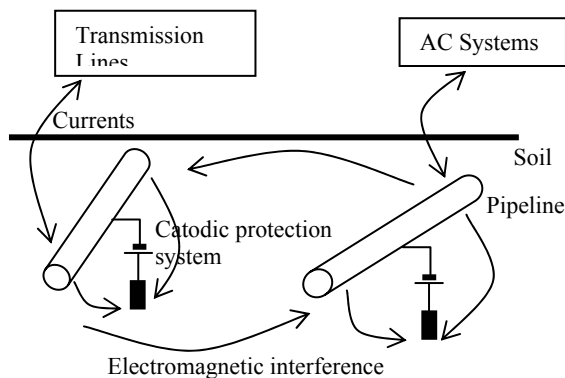


Fig. 1. Electromagnetic interference

Thus it is seen that inductive interference calculations are performed on a hybrid field theory/circuit theory model.

Conductive interference calculations deal with buried conductors exclusively. Conductors are first subdivided into segments of lengths small enough with respect to both wavelength and overall length of the ground network such that they will lead satisfactory to the desired engineering accuracy.

A finite elements field theory approach is then used to relate the currents and potentials in the segments in such a way that an equivalent circuit model can be created which involves the internal and external impedances of the segments. [2]

Hence circuit theory can be applied once again to obtained potentials at all segment end points, as well as longitudinal and leakage currents in every conductor segment in a quite straightforward manner.

## Evaluation of the induced voltages

Calculation of the voltages appearing on the pipelines is work out in two steps.

The first step is the determination of the electromotive forces (EMF) induced along the pipeline (EMF cause currents circulation in the pipeline and voltages between the pipeline and surrounding earth-is a longitudinal electromotive force induced by transmission line current) and the second step is to calculate the voltages to earth and the circulating current in response to the induced longitudinal electromotive forces. See in figure 2 the equivalent circuit formed by the pipeline and the earth [2].

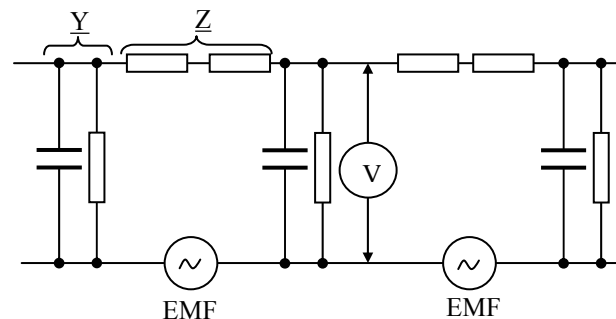


Fig.2. Equivalent circuit pipeline - earth

A clear distinction has to be made between EMF and voltages appearing on the pipeline.

EMF's are virtually electric generators inside the circuit pipeline/earth resulting from the influence of the magnetic coupling. These EMF's produce voltages on the pipeline, and only these voltages  $V$  represent the actual stresses on the pipeline and its equipment. The evaluation is based on the subdivision of the zone of influence in a relatively great number of sections [1], [2].

This is done in order to be able to determine voltages at many positions along the pipeline.

Each section is represented by a  $\pi$  cell submitted to the influence of the electromotive force calculated according the method developed for normal operation (steady state condition) and fault conditions [3].

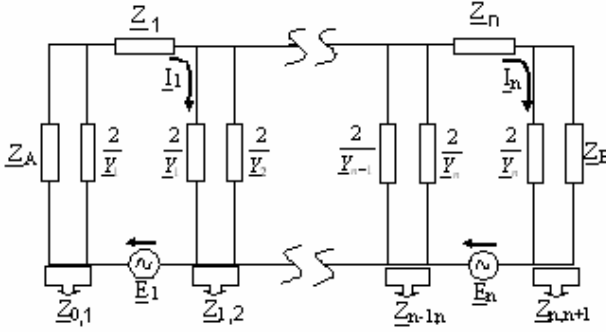


Fig. 3. Equivalent circuit -  $\pi$  cell

Each section is represented by a  $\pi$  cell submitted to the influence of the electromotive force calculated according the method developed for normal operation (steady state condition) and fault conditions. [3]

Except for the voltage source, figure 4 present an equivalent elemental pipeline circuit which is identical to the elemental circuit for the usual electrical transmission line with the same definitions of series impedance per unit length  $Z = R + j\omega L$ , and shunt admittance per unit length,  $Y = G + j\omega C$ .

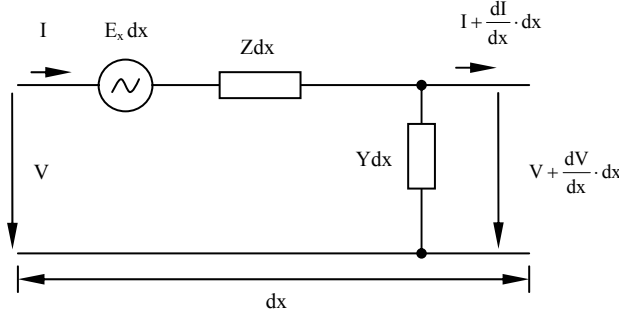


Fig.4. Equivalent elemental pipeline circuit

Using the electrical transmission line parameters is determined the induced potential in pipeline:

$$V(x) = Z_C \{ [K_1 + P(x)]e^{-\gamma x} - [K_2 + Q(x)]e^{\gamma x} \}$$

where:

$$P(x) = \frac{1}{2Z_C} \int_{x_A}^x e^{\gamma s} E_x(s) ds; Q(x) = \frac{1}{2Z_C} \int_x^{x_B} e^{-\gamma s} E_x(s) ds$$

and the coefficients resulting for the boundary conditions at ends:

$$K_1 = v_1 e^{\gamma x_A} \cdot \frac{v_2 P(x_B) e^{-\gamma x_B} - Q(x_A) e^{\gamma x_B}}{e^{\gamma(x_B - x_A)} - v_1 v_2 e^{-\gamma(x_B - x_A)}}$$

$$K_2 = v_2 e^{-\gamma x_B} \cdot \frac{v_1 Q(x_A) e^{\gamma x_A} - P(x_B) e^{-\gamma x_A}}{e^{\gamma(x_B - x_A)} - v_1 v_2 e^{-\gamma(x_B - x_A)}}$$

For the induced potential evaluation is used an approximation which consist in an uniform sollicitation on the length of the influence zone:

$$E_0 = \frac{\sum_{i=1}^n E_i \cdot L_i}{L_t} = \frac{\sum_{i=1}^n E_i \cdot L_i}{\sum_{i=1}^n L_i}$$

where  $E_i$  is the electromotive force on the tronson with length  $L_i$  and  $L_t$  is the length of the entire influence zone electric line-pipeline.

At the extremity  $L_1$ , the influence of the line is equivalent with a voltage source with a value equal to the value of the voltage obtained with the following formula:

$$\underline{V}(x) = \frac{E_0}{\gamma} \cdot \frac{\underline{Z}_A \underline{Z}_B \cdot [\text{ch}(\gamma x) - \text{ch}(\gamma(L_1 - x))] + \underline{Z}_C \cdot [\underline{Z}_B \cdot \text{sh}(\gamma x) + \underline{Z}_A \cdot \text{sh}(\gamma(L_1 - x))]}{(\underline{Z}_A \underline{Z}_B + \underline{Z}_C^2) \cdot \text{sh}(\gamma L_1) + \underline{Z}_C \cdot (\underline{Z}_A + \underline{Z}_B) \cdot \text{ch}(\gamma L_1)}$$

For  $\underline{Z}_B = \infty$  and  $\underline{Z}_A = \underline{Z}_0$  is obtained:

$$\underline{V}_B = E_1 \cdot \frac{\underline{Z}_A (\text{ch} \gamma L_1 - 1) + \underline{Z}_0 \text{sh} \gamma L_1}{\gamma \cdot (\underline{Z}_A \text{sh} \gamma L_1 + \underline{Z}_0 \text{ch} \gamma L_1)} = -\frac{E_1}{\gamma} (1 - e^{-\gamma L_1})$$

and the source impedance:

$$\underline{Z}_B = \frac{\underline{Z}_0 \text{sh}(\gamma L_1) + \underline{Z}_A \text{ch}(\gamma L_1)}{\underline{Z}_0 \text{ch}(\gamma L_1) + \underline{Z}_A \text{sh}(\gamma L_1)}$$

The  $\underline{Z}_A$  impedance is the circuit pipeline/soil impedance located at the left side of the A point.

At the extremity  $L_2$ , with an electromotive force  $E_2$ , the equivalent voltage source is the summ of the sources given by the influence of AB and BC tronson:

$$\underline{V}_C = \underline{V}_B \cdot e^{-\gamma L_2} + \underline{V}_C^*$$

$$\underline{V}_C^* = E_2 \cdot \frac{\underline{Z}_B (\text{ch} \gamma L_2 - 1) + \underline{Z}_0 \text{sh} \gamma L_2}{\gamma \cdot (\underline{Z}_B \text{sh} \gamma L_2 + \underline{Z}_0 \text{ch} \gamma L_2)} = -\frac{E_2}{\gamma} (1 - e^{-\gamma L_2})$$

with:  $\underline{Z}_B = \underline{Z}_0$ ;  $\underline{Z}_A = \underline{Z}_B = \underline{Z}_0$ , so:

$$\underline{V}_C = \frac{E_1}{\gamma} (1 - e^{\gamma L_1}) e^{-\gamma L_2} + \frac{E_2}{\gamma} (1 - e^{-\gamma L_2})$$

### Induced voltages for a practice case

Is made an evaluation af the induced voltages in a pipeline wich runs in the same right of way with a power line for a monophas short circuit on the line [4].

A phase to ground fault occurs on the transmission line at two location points. As a result fault currents start flowing in the phase conductors, skywires, transmission line structure grounds, earth and pipelines [1], [5].

The input data of this problem are: power line and pipelines geometrical configuration; conductor and pipeline physical characteristics (including insulating and coating characteristics); environmental parameters (air characteristics, soil structure and characteristics); power system terminal (or boundary) parameters (power source voltages, equivalent source impedances); fault parameters (fault location and type) [2], [6].

The results demonstrates that is possible to obtain a precise evaluation of the sollicitations if is known the resistance and the adduction current in the pipe.

After the determination in each point the potentials due to the right and left side of the line is applied the superposition method [6].

Is briefly presented in Mathcad a program using

some interpolation predefined functions for the induced voltage calculation in different points on the pipeline for the measured data. It is observed that the interpolation spline function with linear end conditions is more precise than the linear interpolation polynomial [3], [5].

It is made in Mathcad7 a program which uses the predefined interpolation function and in figure 5 is represented the measured values and the interpolation function for the induced voltages on the comune zone at various distances [3], [6].

$$d_i := \prod_j \text{if}(i = j, 1, x_i - x_j)$$

$$sl(z) := \text{interp}(\text{lspline}(x, V(x)), x, V(x), z)$$

$$l(z) := \text{linterp}(x, V(x), z)$$

$$\omega(z) := \prod_i (z - x_i) \quad l(i, z) := \text{if} \left[ z = x_i, 1, \frac{\omega(z)}{(z - x_i) \cdot d_i} \right]$$

$$sl_c(z) := \text{interp}(\text{lspline}(x, V_c(x)), x, V_c(x), z)$$

$$l_c(z) := \text{linterp}(x, V_c(x), z)$$

$$x := \begin{pmatrix} 58 \\ 68 \\ 73 \\ 83 \end{pmatrix} \quad V(x) := \begin{pmatrix} 220 \\ 150 \\ 255 \\ 220 \end{pmatrix} \quad V_c(x) := \begin{pmatrix} 205 \\ 144 \\ 240 \\ 215 \end{pmatrix}$$

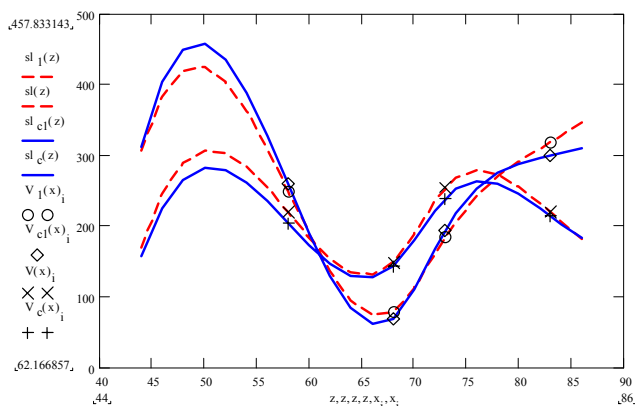
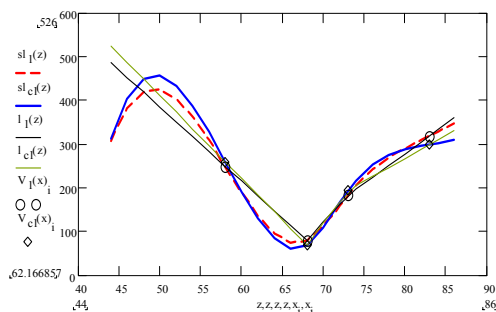


Fig. 5. Interpolation functions for the induced voltages in a pipeline

In the first figure are presented the results obtained with spline and linear interpolation of the measured data. The calculus and the program made in mathcad with the predefined functions help us to determine more precisely the values of the induced voltages on the entire influence zone.

### Conclusion

The evaluation of the induced voltage in pipeline is based on the subdivision of the zone of influence in a relatively great number of sections in order to be able to determine voltages at many positions along the pipeline using Thevenin equivalent circuits. It is presented a practical case of subdivision of the zone of influence in sections (a circuit model) and is made a precise evaluation of the induced voltages using some interpolation functions for the measured data. It is observed that the interpolation spline function with linear end conditions is more precise than the linear interpolation polynomial.

### References

- [1] Dawalibi, F. Analysis of electrical interference from power lines to gas pipelines-Part I-Computation method, PWRD-4, No3, July 1989, pp. 1840-1848.
- [2] \*\*\*, Guide Concerning Influence of High Voltage AC Power Systems on Metallic Pipelines, CIGRE Working Group 36.02, Canada, 1995.
- [3] Micu, D. D. Numerical model for the calculation of the induced voltage in an underground pipeline, ANCME Gent, 2003, pp. 179-191.
- [4] \*\*\*, Laborelec Brussel. *Resultats des mesures et interference sur la ligne Neufchateau/Villers-sur-Semois et la canalization de gaz distrigaz Ben-Ahin/Athus*. Brussel, Research Report 1990.
- [5] Micu, D. D. Numerical methods in electromagnetic interferences, Mediamira, Cluj-Napoca, Romania, 2004.
- [6] Micu D. D., Simion, E., Lingvay I. Influence of AC transmission lines on underground pipelines, 4<sup>th</sup> International Conference Study and control of corrosion in the perspective of sustainable development of urban distribution grids, ICPE Bucharest, Sibiu, June 2005, pp. 68-81.

**Dan Doru Micu** – Lecturer, Dr., Faculty of Electrical Engineering, Technical University of Cluj-Napoca, 15 Daicoviciu Str., Cluj-Napoca, ROMANIA. e-mail: Dan.Micu@et.utcluj.ro.

**Emil Simion** – Professor, Dr., Faculty of Electrical Engineering, Technical University of Cluj-Napoca, 15 Daicoviciu Str., Cluj-Napoca, ROMANIA. e-mail: Emil.Simion@et.utcluj.ro.

**Laura Cret** – Assistant, Ph.D. Student, Faculty of Electrical Engineering, Technical University of Cluj-Napoca, 15 Daicoviciu Str., Cluj-Napoca, ROMANIA. e-mail: Laura.Cret@et.utcluj.ro.

# Nondestructive Defect Determination by Field Visualization in Tubes

Iliana Marinova, Valentin Mateev

**Abstract:** In this paper we propose an approach for defect determination during nondestructive inspection of tubes. The developed approach combines the magnetic field analysis, high visualization technologies and data manipulation. The virtual magnetic microscope is design for analysis of field distributions in tubes. It is capable to explore and process the extremely large quantities of data required to represent a collection of slides as well as provides an access to archived digital slide images. The virtual microscope is successfully applied for nondestructive defect determination in tubes.

**Keywords:** nondestructive testing, magnetic field, visualization, virtual reality.

## Introduction

The magnetic field distributions are very important for the nondestructive defect determination solving various inverse electromagnetic problems during nondestructive testing, electromagnetic compatibility, identifications etc [1-5].

The present visualizing devices and high technology methodologies for visualization, image processing and data manipulations give possibilities for building the modern interactive systems for nondestructive testing. Visualization of the data obtained during inspection is extremely important in order to realize effective reliable nondestructive defect detection system [6-8].

The locally measured data of the electromagnetic field during inspection are visualized and used for 3D field reconstructions. The field distribution changes according to respective space locations, shapes, numbers and dimensions of existed defects. Development of computation model of electromagnetic field distributions that take into account all properties and characteristics of the object are very important in order to identify and to characterize the defects.

In this paper an approach for field and source 3D reconstruction visualizing the locally measured data is applied. Using the 2D images as slices of 3D image and based on the field theory and image processing techniques we build reconstruction approach for 3D visualization of magnetic field distribution.

The proposed 3D reconstruction approach is successfully applied for visualization and analysis of field distributions as well as field sources obtained during tubing inspection. Development of effective methods and tools for visualization of electromagnetic fields as well as field sources is extremely important in order to realize effective nondestructive evaluation, control and inspection. The virtual magnetic microscope is design for

analysis of field distributions in tubes. It is capable to explore and process the extremely large quantities of data required to represent a collection of slides as well as provides an access to archived digital slide images. The virtual microscope is successfully applied for nondestructive defect determination in tubes.

## Inspecting Tube System

The tube with defect(s) under consideration is shown in Fig.1. Different number and sized defects are placed in the scanning area.

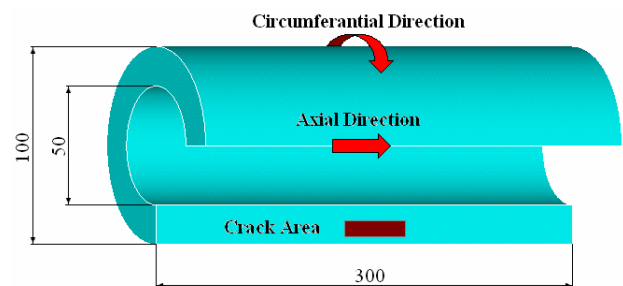


Fig.1. Tube system with defects

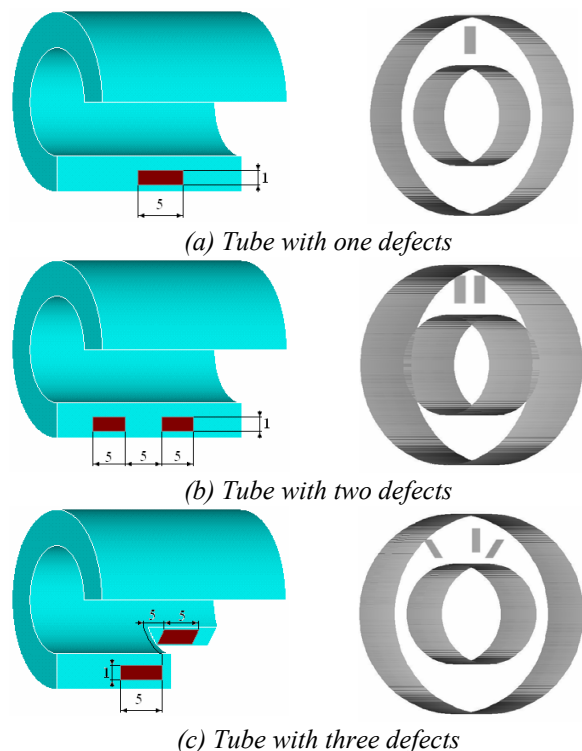


Fig. 2. Tube with defects

From the inspection tube the 2D parallel geometry slices are obtained and 3-D stacked image models, shown in Fig.2, are visualized from the 2-D tube slices.

### Governing Equations for Electromagnetic Field

For modeling of electromagnetic fields in tube with cracks let consider the domains  $\Omega$ ,  $\Omega_a$ ,  $\Omega_j$  to be the whole domain, the air domain and current source domain, respectively. The defects are supposed to exist inside the nonmagnetic conductive domain  $\Omega_m^1$ , but the domain  $\Omega_m^2$  is defect free domain. The magnetic vector potential  $A^u$  is if the domain  $\Omega_m^1$  is not cracked. The governing equations are as following

$$(1) \quad \begin{aligned} \nabla \times \frac{1}{\mu_0} \nabla \times A^f + \sigma^u \frac{\partial A^f}{\partial t} &= \\ &= (\sigma^u - \sigma^f) \frac{\partial (A^u + A^f)}{\partial t} \end{aligned} \quad \text{in } \Omega_m^1$$

$$(2) \quad \nabla \times \frac{1}{\mu} \nabla \times A^f + \sigma \frac{\partial A^f}{\partial t} = 0 \quad \text{in } \Omega_m^2$$

$$(3) \quad \nabla \times \frac{1}{\mu_0} \nabla \times A^f = 0 \quad \text{in } \Omega_a + \Omega_s$$

where  $\sigma^u$  and  $\sigma^f$  are conductivity when  $\Omega_m^1$  is defected and defected free;  $\mu$  and  $\sigma$  are magnetic permeability and electric conductivity in  $\Omega_m^2$ ;  $(\sigma^u - \sigma^f)$  is not zero only in the defect domain.

A magnetic vector potential  $A^f$  is expressed by

$$(4) \quad A^f = A - A^u,$$

if the defects exist in the domain  $\Omega_m^1$ .

The right side of (1) can be considered as the effect of the dipole current, which appear in the defect domain only.

Based on the governing equations the Finite Element Method (FEM) solver is developed for electromagnetic field calculation in the tube using magnetic vector potential formulation. Various simulations have been made changing the number, sizes, space location and shapes of the cracks in tube.

Formulating the inverse color problem over the image of 2D magnetic field distribution at parallel surfaces of the inspecting tube it is possible to determine the color source distribution that correspond to the field source distribution [6-8]. The color source distribution is obtained using the image color model where the image colors are considered as components of the field potentials. Then the image color distribution is imposed

to satisfy the field equations. Using the vector potential expressed by (5) and Green Function (6) over the image we determined the color source distributions - J.

$$(5) \quad A = \frac{1}{4\pi\mu_0} \int_{\Omega} JG(r, r') d\Omega$$

$$(6) \quad G(r, \omega) = \frac{1}{4\pi(r)} \exp j \frac{\omega}{c}(r)$$

The color source distribution corresponds to the field source distribution. Thus, visualizing the color source distribution it is possible to reconstruct and visualize the field source distribution.

### 3D Reconstruction of Magnetic Fields in Tube with Defects

In nondestructive testing of tubes the inspection sensor system generates dataset with locally measured field data. In order to determine the tube defects the magnetic field distributions are analyzed. The inverse electromagnetic problem is formulated and solved for determine the electromagnetic field distributions in the inspection domain of the tube from locally measured and visualized field distribution [6-8]. The magnetic field is visualized producing 2D field distribution images.

A 3D volume of data for visualization of magnetic field was created from the 2D slices of locally determined and visualized magnetic field distribution at parallel surfaces by transforming each pixel in the 2D slice to its corresponding 3D location using the position, orientation and Green's function. If the 2D slices are arbitrary oriented and positioned in space, some of the voxels in the volume data set are not assigned intensity values. These voxels were identified and assigned an intensity value based on the weighted average of its neighboring voxels. The resulting volume of data resembled 3D magnetic field data set that is visualized.

### Implementation

The proposed approach was successfully applied for 3D field reconstruction and visualization. The field distribution of the tube with defects has been considered. The different number, sizes and space location of the defects are investigated.

The locally field data were measured during tube inspection. Using these data and solving the inverse color problem over the images visualizing the measured data we determine and visualize the color source distribution in the region of interest in the axial – Fig. 3(a) and in radial Fig. 3(b) direction of the tube with one defect. The 3D reconstruction of the obtained color source distributions in both directions are realized in Fig. 4. The color source distributions correspond to the field source distributions. The high intensity colors outline the shape of the defect which is considered as a field source. Using the images of the color source distributions the magnetic field distribution in tube is determined and visualized at different parallel surfaces of the tube with single defect as



shown in Fig. 5. Using the 2D field distributions and reconstruction approach described above we visualized the 3D field distribution in Fig. 6(b). In order to compare the results obtained by 3D reconstruction approach we calculate and visualize the magnetic field distribution of the tube with one defect using FEM – Fig. 6(a). It was found the good coincidence of the results obtained using the 3D reconstruction approach and those obtained by FEM simulator.

In Fig. 7(a) and 7(b) are given magnetic field distributions in tube with one defect and different defect depth - 45% and 92%, respectively.

The field data at parallel surfaces are determined and shown in Fig. 8 and Fig.10 for the tube with two and three cracks with different sizing and space locations.

The electromagnetic field is calculated and reconstructed by FEM and 3D reconstruction approach - Fig. 9 and Fig. 11, respectively. Using the proposed approach it is possible to extract geometrical information for defects and cracks.

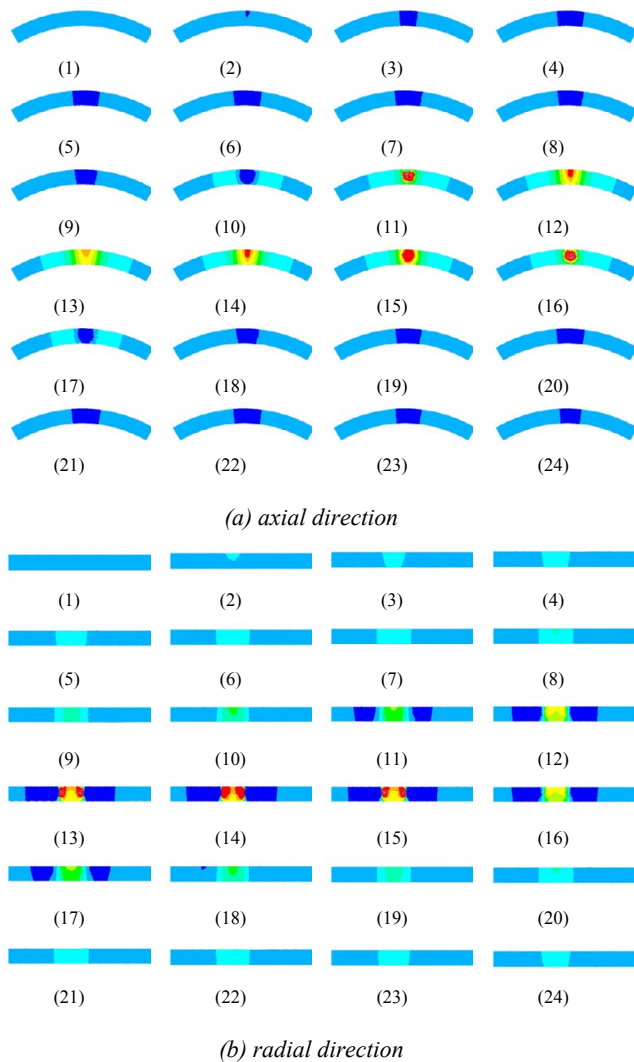


Fig. 3 2D Field source distributions in the tube with one defect

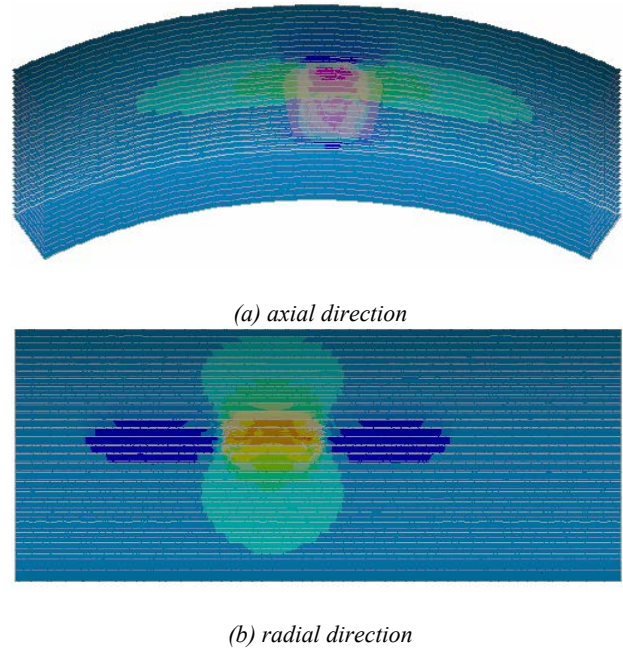


Fig. 4 3D Reconstruction of field sources distributions of the tube with one crack

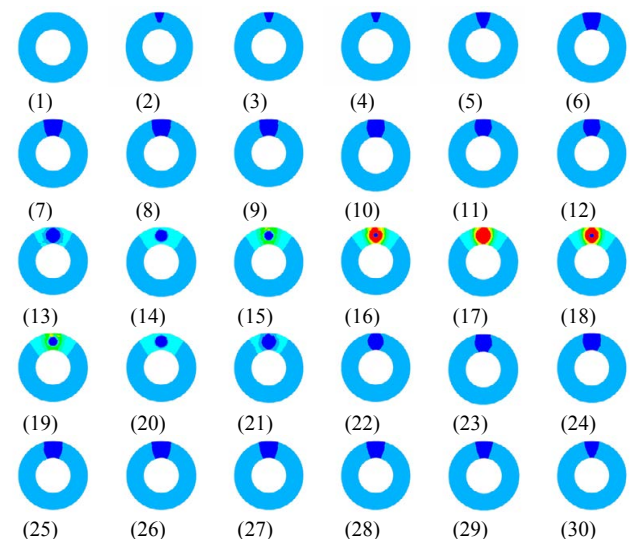


Fig.5 2D Field distributions in the tube with one defect

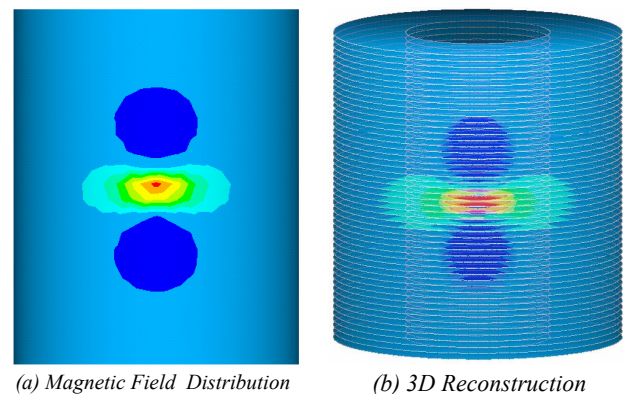


Fig. 6. Magnetic field of tube with one crack and its 3D reconstruction

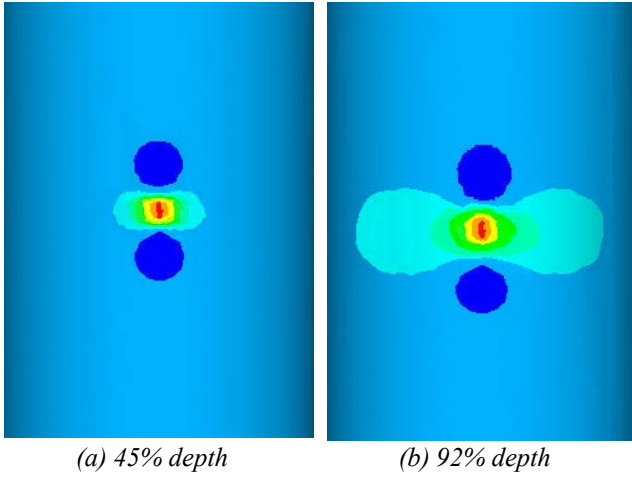


Fig. 7. Magnetic field distributions in tube with 45% and 92% defect depth

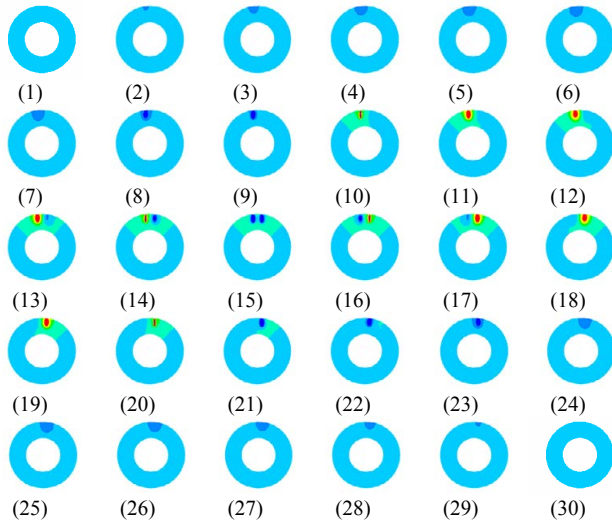


Fig. 8. 2D Magnetic field distributions in tube with three defects

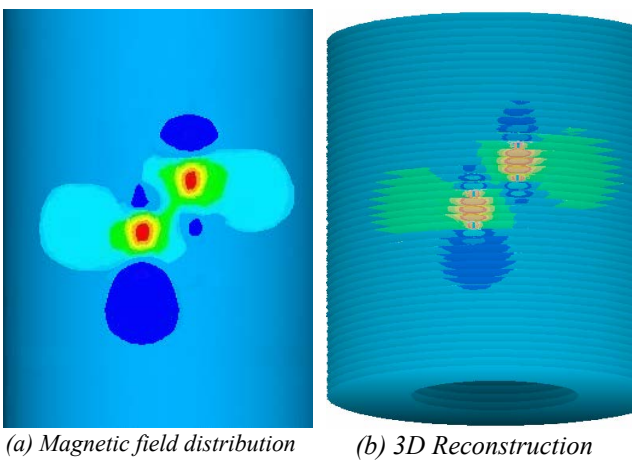


Fig. 9. Magnetic field of tube with two defects and its 3D reconstruction

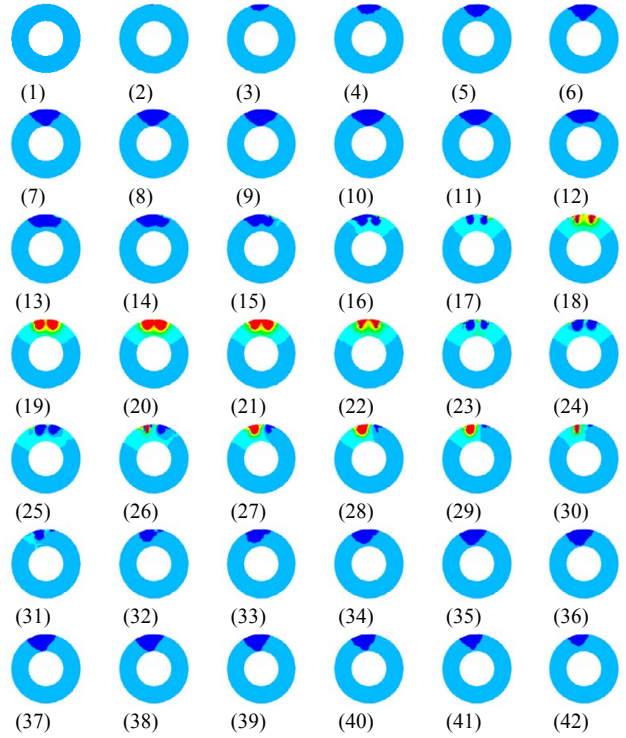


Fig. 10. 2D Magnetic field distributions in tube with three defects

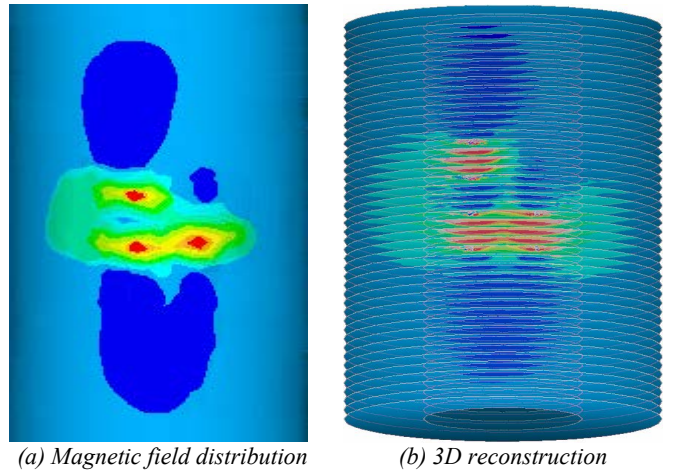


Fig.11. Magnetic field of tube with three cracks and its 3D reconstruction

### Virtual Microscope

For precise analyses of the field distribution in tubes for defect determination during nondestructive inspections we design and implement a virtual microscope.

### Virtual Microscopy Architecture

The Virtual Microscope is a client-server system designed to provide a realistic digital emulation of a high power light microscope. The architecture of the

developed virtual microscope is shown in Fig. 12. The client/user interface allows viewing slides over a network and runs on a user's PC or workstation. The server is responsible for storing, retrieving, image processing, and serving the datasets and runs on a high performance machine.

The modularity of the system allows developing each part somewhat independently and focusing on the unique requirements of each piece. So, while the client interface must be user-friendly, web-friendly and portable, the server can be finely tuned for a fast data control.

The server primary responsibility is to connect the client, running on a PC or workstation, to the data stored on server. The client must communicate with the server over a standard network protocol. For performance reasons, that functionality may eventually migrate into the client so that the client can receive parts of the output image as they are produced by the data server, without waiting for the entire image to be produced.

The client is a Java program that can be run on any PC or workstation that has the Java virtual machine available [9]. The client connects, across a local network or the Internet, to a network server program running as the front end to a data server that accesses the slide image data stored.

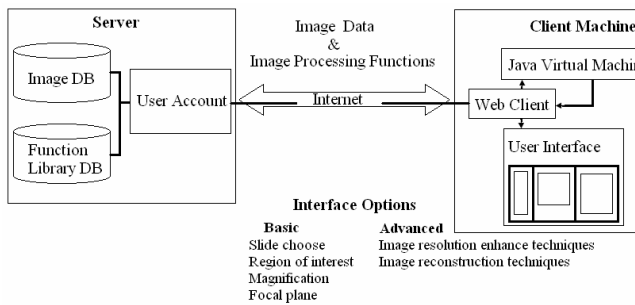


Fig. 12 Basic architecture of the virtual microscope

**Basic Functions of the Virtual Microscope**

The functionality of the developed virtual microscope is realised by a number of basic operations as a Fast browsing through the slide to locate an area of interest; Local browsing to observe the region surrounding the current view; Changing magnification; Changing the image characteristics-contrast, brightness, colour intensity. The system design of the Virtual Microscope aims to support these operations efficiently.

The Java computer software shown in Fig. 13 provides a graphical user 2D and 3D interface so that users can control browsing and zooming by dragging and clicking the mouse.

The 2D Virtual Microscope interface shown in Fig. 13 consists of 2D display window of electromagnetic structure, the 2D field distribution window and control window.

The display window of the electromagnetic structure shows the selected slide of the object under consideration

and selected magnification (controlled by zoom scroll). By moving the mouse in this window we can choose the four directions (i.e., up, down, left, right) by clicking the corresponding directional button and using the current mouse position for centre of the newer zoomed region.

The 2D magnetic field distribution window shows the field distribution of the selected slide and selected magnification (controlled by zoom scroll). We can operate in this window with mouse and keyboard as in the display window.

The Main control window provides the operations supported by the Virtual Microscope – Fig. 14.

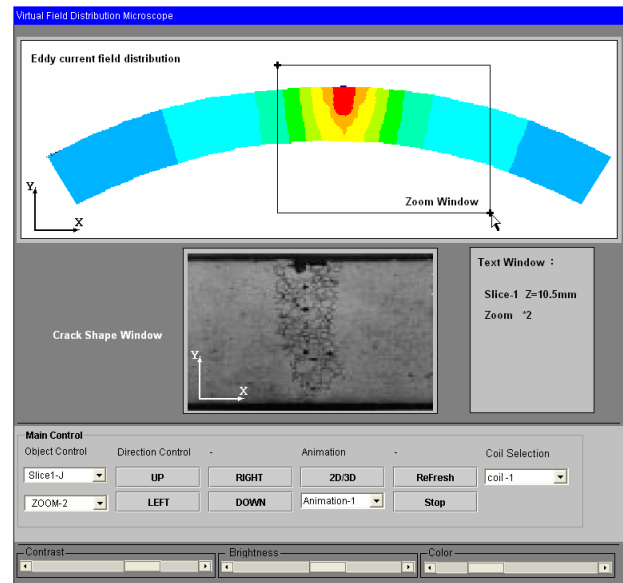
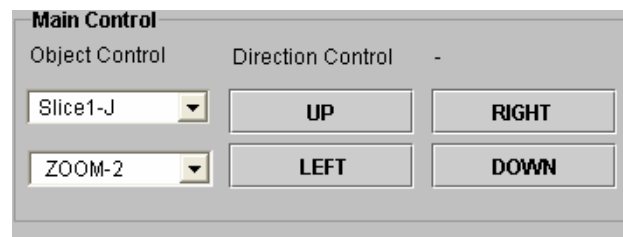


Fig. 13. Display window



(a)



(b)

Fig.14 The Main Control Window

The control panel has the following sub-components: a sample selection box, a magnification selection box, a contrast, brightness, colour intensity box, and four directional buttons.

Also the user could choose between magnetic field distributions or current distribution. Zoom menu is capable to change the zooming coefficient which will be applied over the image. Directional control window contains the four directional buttons (Up, Down, Left, Right). The Animation Controls are active only in 3D mode. The picture properties scrollbar window contains usual functions for picture manipulations as Contrast, Brightness and Colour controls.

Both the control window and the display window are resizable. When the user resizes the display window, the size of the slice window also changes accordingly. The display window is continuously updated while the user is panning through the image, either using actual image data cached at the client from previous queries or from the lower resolution thumbnail image. Once the user stops dragging and releases the mouse button, a query is generated and is satisfied either from the client cache or from the server, with the display area updated from the full image data at the desired resolution.

The 3D Virtual Microscope interface consists of 3D display window of the electromagnetic structure, the 3D field distribution window and control window.

The 3D display window of the electromagnetic structure shows the 3D reconstruction of the available 2D field slices of the object under consideration. The 3D Field Distribution window presents the corresponding 3D field distribution of the object obtained by reconstruction of 2D field distribution shown using 2D virtual magnetic microscope interface.

### **Advanced Image Processing Functions**

The image quality depends on the image resolution and the color distribution. To obtain higher resolution parameters the Virtual Microscope uses its own function library, which allows the image data to be processed in client/user machine and also allows minimization of data flow between server and client machine. The available functions are resolution enhancement and changing of the color intensity, contrast and brightness of the image. The field theory is successfully applied over the image in order to change and improve the image characteristics. Using the image color model and solving the inverse problem over the image it is possible to improve the quality and to change the characteristics of the image [6-8].

### **Conclusion**

The inverse approach using field visualization is developed for nondestructive defect determination in tubes. The locally measured field data at parallel cross-sections of the tube are visualized. The 3D field visualization is realized by the 3D reconstruction approach using images of 2D field distribution. The 3D reconstruction approach combines new technologies of 3D visualizations and characterizes with flexibility, simplicity and portability. The proposed approach was successfully applied for 3D reconstruction and

visualization of magnetic field of the tubes defect determination during NDT.

Computational model using Finite Element Method has been developed and used to investigate the electromagnetic field distributions in tubes with defects.

The virtual magnetic microscopy is design and implement for analysis of field distributions in tubes during NDT.

In practical aspect this study can be used to build the effective methodologies for modeling and investigation of the fields, processes and phenomena during nondestructive testing, control and inspection as well as for design of electromagnetic devices for NDT.

### **References**

- [1] Doi T., S. Hayano, I. Marinova, Y. Saito, "Defect recognition in conductive materials by local magnetic field measurement", *Journal of Applied Physics*, Vol. 75, No. 10, May, 1994, pp. 5907-5909.
- [2] Rubinacci G., A. Tamburrino, S. Ventre, F. Villone, Shape identification in conductive materials by electrical resistance tomography, in E'NDE, *Electromagnetic Non-destructive Evaluation (VI)*, F. Kojima et al. (Eds.), IOS Press, 2002, pp. 13-20.
- [3] Huang H., T. Takagi and H. Fukutomi, Fast Signal Predictions of Noised Signals in Eddy Current Testing, *IEEE Trans. Magn.* vol. 36, No. 4, July 2000, pp. 1719-1723.
- [4] Kojima F. and K. Ito, "Reconstruction of Magnetic Charge Densities using Regularization of Bounded Variations under Noisy Observations, *International Journal of Applied Electromagnetics and Mechanics*, Vol. 19, 2004, pp. 309-313.
- [5] Marinova I., S. Hayano, Y. Saito, "Inverse approach for shape design of magnetic core," *IEEE Trans on Magnetics*, Vol. 31, No. 3, May, 1995, pp. 1992-1995.
- [6] Marinova I., H. Endo, S. Hayano, Y. Saito, "Image Reconstruction for Electromagnetic Field Visualization by an Inverse Problem Solution", *Int. Journal of Applied Electromagnetics and Mechanics*, 15 (2001/2002) IOS Press, pp. 403-408
- [7] Marinova I., H. Endo, S. Hayano, Y. Saito, "Inverse Electromagnetic Problems by Field Visualization", *IEEE Trans. Magn.* Vol. 40, No. 2, 2004, pp. 1088-1093
- [8] Endo H., Y. Saito, "Smart Visualization and Computer Vision in Electromagnetism," *Int. Journal of Applied Electromagnetics and Mechanics*. 15 (2001/2002) IOS Press, pp. 337-342.
- [9] Arnold K., J. Gosling. *The Java Programming Language. The Java Series.* Addison-Wesley, 1996.

---

*Iliana Marinova* – Associate Professor, Ph.D., Faculty of Electrical Engineering, Technical University of Sofia, 8 Kl. Ohridski Str., 1000 Sofia, BULGARIA. e-mail: [iliana@tu-sofia.bg](mailto:iliana@tu-sofia.bg)

*Valentin Mateev* – Ph.D. Student, Faculty of Electrical Engineering, Technical University of Sofia, 8 Kl. Ohridski Str., 1000 Sofia, BULGARIA e-mail: [vmateev@tu-sofia.bg](mailto:vmateev@tu-sofia.bg)

## Diversity Systems Comparison in the Presence of Interference

Milan Živković, Nenad Milošević, Bojan Dimitrijević, Zorica Nikolić

**Abstract:** In this paper we consider performances of diversity receivers in the microcellular environment affected by multipath fading and multiple cochannel interferers, where the fading amplitudes of desired and interfering signals are modeled as random variables with Nakagami  $m$  distribution. The dependence of the BER of the average SINR and SIR per branch is used as the measure of performances.

**Keywords:** BPSK signaling, diversity combining, Nakagami fading, cochannel interference.

### Introduction

A major source of performance impairment in a mobile environment is multipath fading that results in rapid fluctuations in the amplitude of the received radio signal over a short period of time caused due to the interference between two or more versions of the transmitted signals which arrive at the receiver at slightly different times. The resultant received signal can vary widely in amplitude and phase, depending on various factors such as the intensity, relative propagation time of the waves, or the bandwidth of the transmitted signal. Also, due to frequency reuse needed for spectrum efficiency increasing, there is another degrading effect known as cochannel interference. To characterize urban and microcellular mobile radio environment in the presence of multipath fading and multiple interfering signals we use Nakagami channel model where the fading amplitudes of desired and interfering signals are modeled as random variables with Nakagami  $m$  distribution [5]. Furthermore, Nakagami channel model is derived in agreement with experimental data, and present general model for fading channel, so Rayleigh and Rice distribution present special cases of Nakagami distribution, depending of Nakagami parameter  $m$ . So, we model considered system as Nakagami-Nakagami flat channel model with additive white Gaussian noise (AWGN) assuming that the changes of fading amplitudes of desired and interfering signals are sufficiently slow during one bit interval. A powerful communication receiver technique that provides wireless channel improvement at relatively low cost is a well-known as diversity reception. Diversity techniques are based on the notion that errors occur in reception when the channel attenuation is large (when channel is in a deep fade). Supplying to the receiver several replicas of the same information signal transmitted over independently fading channels, the probability that all the signal components will fade simultaneously is reduced considerably [1] and therefore, instant and mean SNR can be increased. Also, diversity signals can reduce the effect

of multiple interferers at the receiver. This paper presents some simulation results that show improvement attained by implementing various types of diversity receivers including Selection Combining (SC), S + N Selection [3], AR Selection [4], Equal Gain Combining (EGC), Maximal Ratio Combining (MRC) and Optimum Combining (OC). As measure of performances we consider Bit Error Rate (BER) dependency of average signal-to-interference-plus-noise ratio (SINR) per branch, and average signal-to-interference ratio (SIR) per branch, which is useful in determining the cochannel reduction factor in systems with frequency reuse.

### System Model

Consider BPSK signaling in flat Nakagami fading channel with AWGN and additional multiple cochannel interferers modeled with Nakagami distribution implying corresponding diversity receiver. Let  $L$  be the number of diversity branches which is assumed to be independent and  $M$  is the number of independent interference signals. The received signal in matrix notation may be written as [2]

$$(1) \quad \mathbf{r} = \mathbf{u}_s \cdot x_s + \sum_{j=1}^M \mathbf{u}_j \cdot x_j + \boldsymbol{\eta}$$

where

$\mathbf{u}_s = [\alpha_{s,1}(t), \alpha_{s,2}(t), \dots, \alpha_{s,L}(t)]^T$  -  $L$ -dimensional vector of fading amplitudes of desired signal,

$\mathbf{u}_j = [\alpha_{j,1}(t) \cdot \cos(\phi_{j,1}), \dots, \alpha_{j,L}(t) \cdot \cos(\phi_{j,L})]^T$  -  $L$ -dimensional vector of fading amplitudes of  $j$ th interfering signal,

$x_s$  - desired signal equals  $\sqrt{E_b}$  or  $-\sqrt{E_b}$  with a priori probability  $\frac{1}{2}$ .

$x_j$  -  $j$ th interfering signal equals  $\sqrt{E_b}$  or  $-\sqrt{E_b}$  with a priori probability  $\frac{1}{2}$ .

$\boldsymbol{\eta} = [\eta_1(t), \eta_2(t), \dots, \eta_L(t)]^T$  -  $L$ -dimensional vector of additive complex Gaussian noises.

$E_b$  - energy per bit.

$\phi_{j,l}$  - random phase of  $j$ th interfering signal in  $l$ th diversity branch, assumed to be uniformly distributed over the interval  $[0, 2\pi)$ .

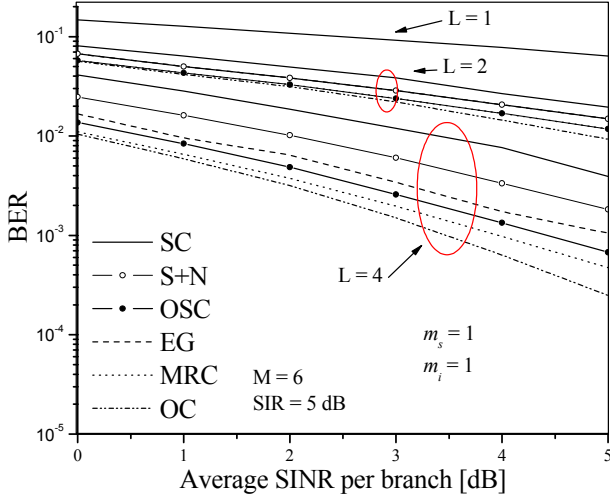


Fig. 1. BER dependency of average SINR per branch for  $M = 6$ ,  $SIR_{per\ branch} = 5$  [dB],  $m_s = 1$  and  $m_i = 1$

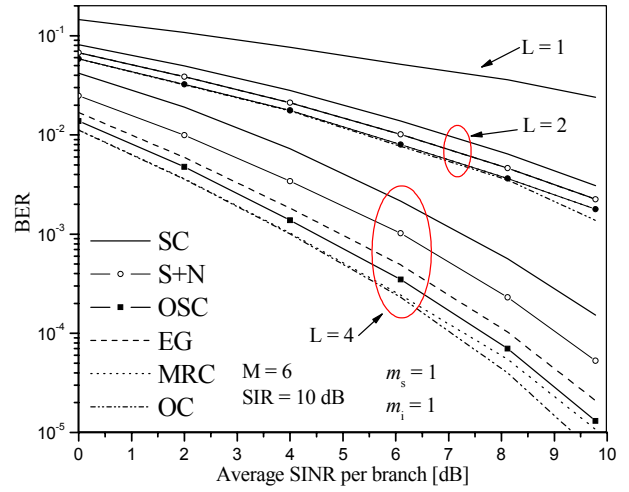


Fig. 3. BER dependency of average SINR per branch for  $M = 6$ ,  $SIR_{per\ branch} = 10$  [dB],  $m_s = 1$  and  $m_i = 1$

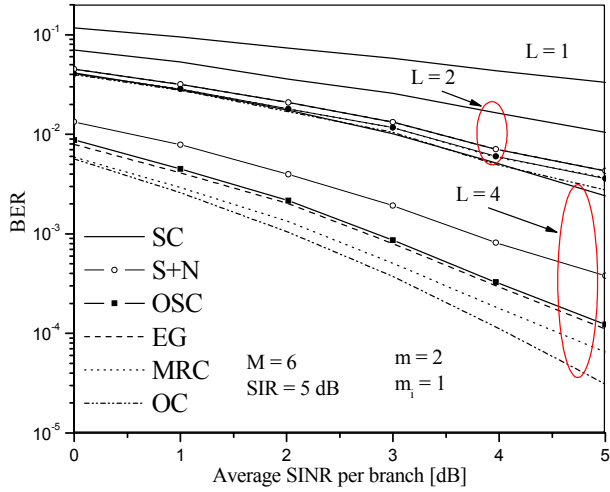


Fig. 2. BER dependency of average SINR per branch for  $M = 6$ ,  $SIR_{per\ branch} = 5$  [dB],  $m_s = 2$  and  $m_i = 1$

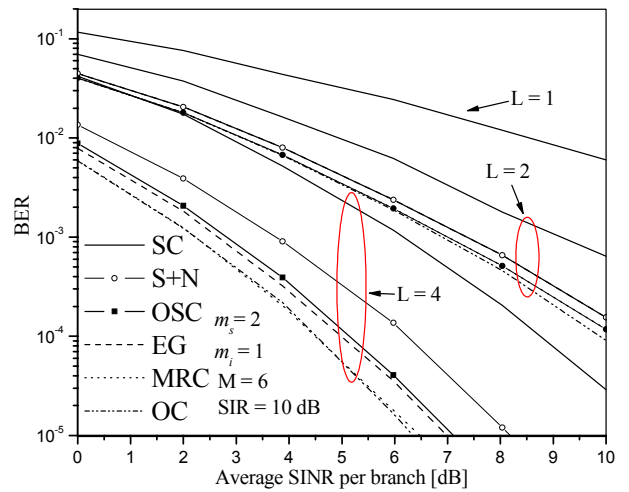


Fig. 4. BER dependency of average SINR per branch for  $M = 6$ ,  $SIR_{per\ branch} = 10$  [dB],  $m_s = 2$  and  $m_i = 1$

As we consider model where changes of fading amplitudes is sufficiently slow during one bit interval, we assume that they are constant during one bit interval, so time dependences will be omitted in further analysis.

As we consider Nakagami-Nakagami channels, fading amplitudes of desired and interference signals are modelled using Nakagami distribution

$$(2) \quad p_{\alpha_s}(\alpha_s) = \frac{2m^m}{\Gamma(m)\Omega_s^m} \alpha_s^{2m-1} \exp\left(\frac{-m\alpha_s^2}{\Omega_s}\right), \quad \alpha_s \geq 0$$

and

$$(3) \quad p_{\alpha_j}(\alpha_j) = \frac{2m_j^{m_j}}{\Gamma(m)\Omega_j^{m_j}} \alpha_j^{2m_j-1} \exp\left(\frac{-m_j\alpha_j^2}{\Omega_j}\right),$$

$$\alpha_j \geq 0, j = 1, \dots, M$$

where  $\Omega_s = E[\alpha_s^2]$  and  $\Omega_j = E[\alpha_j^2]$ ,  $j = 1, \dots, M$  denote the average power of desired and interference signal, respectively. Parameters  $m_s$  and  $m_j$ ,  $j = 1, \dots, M$  denote Nakagami  $m$  parameter of desired and interference signal, respectively. In our analysis we assume that all interfering signals signals are identically distributed with equal average power so  $\Omega_j = \Omega_i$ ,  $m_j = m_i$ , for  $j = 1, \dots, M$ .

The value of  $m$  defines the of fading (deep of fade) present in considering environment. Furthermore, Nakagami channel model present general model for fading channel that is derived in agreement with experimental data. For example, for  $m = 1$ , (2) and (3) simplify to the Rayleigh pdf, while for  $m = \infty$ , they simplify to the Rice pdf.

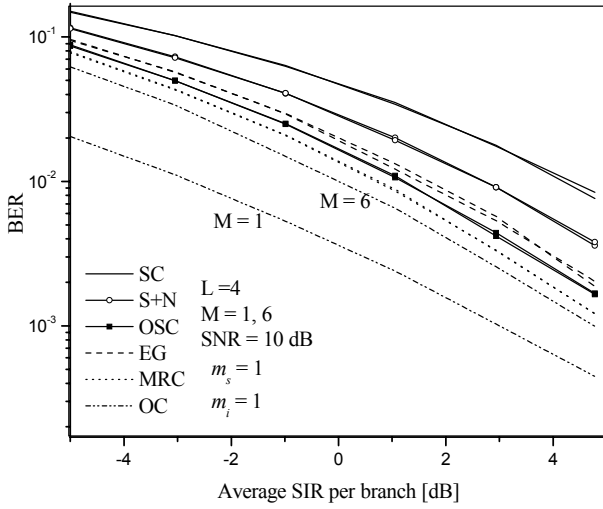


Fig. 5. BER dependency of average SIR per branch for  $M=1, 6$ ,  $SNR_{per\ branch} = 10$  [dB],  $m_s = 1$  and  $m_i = 1$

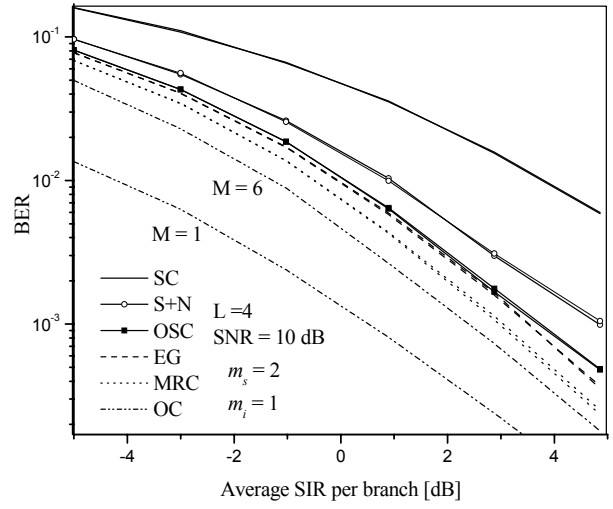


Fig. 6. BER dependency of average SIR per branch for  $M=1, 6$ ,  $SNR_{per\ branch} = 10$  [dB],  $m_s = 2$  and  $m_i = 1$

### System Performance

In order to improve performances of considered system, diversity techniques may be employed. We do simulation analysis of different diversity selection and combining methods, including SC, S+N, AR, EG, MRC and OC, and comparing their influences on system performances.

For selection methods, including SC and its modifications S+N [3] and AR [4], receiver selects one branch, and that selection is based on some criterion. SC selects, among the  $L$  diversity branches, the branch providing the largest SNR ratio (or largest fading amplitude). S+N is modification of previous method and it selects the signal from diversity branch where the largest signal-plus-interference-plus-noise sample is present (no need to power measurement). AR also present modification of SC and selection criterion is based on weighting the received signals in diversity branches with corresponding fading amplitude and selection the largest product.

Combining methods involve linear combining of signals from diversity branches with some processing over them. In MRC the signals from all the branches are co-phased and individually weighed by fading amplitude,  $\alpha_{s,l}$ ,  $l=1, \dots, L$ , of desired signal and then added.

Weighting MRC vector is

$$(4) \quad \mathbf{w} = \mathbf{u}_s$$

so the signal at the output of combiner is

$$(5) \quad y = \mathbf{w}^H \mathbf{r} = |\mathbf{u}_s|^2 \cdot x_s + \sum_{j=1}^M \mathbf{u}_s^H \mathbf{u}_j \cdot x_j + \mathbf{u}_s^H \boldsymbol{\eta}$$

EGC is practical simplification of MRC, involving only co-phasing and adding without weighting, at cost of performances.

While MRC is optimal diversity technique in environments without interference in sense of maximizing SNR and combating fading effect at the output of receiver, but it ignores the effect of cochannel interference [6]. OC addresses both effects of fading of desired signal and the presence of cochannel interference and optimize the signal-to-interference-plus-noise ratio (SINR) at the output of receiver [8]. Weighting OC vector is [7]

$$(6) \quad \mathbf{w} = \mathbf{R}^{-1} \mathbf{u}_s$$

where  $\mathbf{R}$  is the interference-plus-noise covariance matrix across the array's elements

$$(7) \quad \mathbf{R} = E \left[ \left( \sum_{j=1}^M \mathbf{u}_j \cdot x_j + \boldsymbol{\eta} \right) \left( \sum_{j=1}^M \mathbf{u}_j \cdot x_j + \boldsymbol{\eta} \right)^H \right]$$

Note that OC weight vector is conditioned on desired signal fading amplitudes vector  $\mathbf{u}_s$ , interference signals fading amplitudes vectors  $\mathbf{u}_j$ ,  $j=1, \dots, M$  and AWGN vector  $\boldsymbol{\eta}$ , while MRC weight vector is conditioned only on desired signal fading amplitudes vector  $\mathbf{u}_s$ .

As parameters in our analysis we use average signal-to-interference-plus-noise ratio SINR per branch defined as

$$(8) \quad SINR_{per\ branch} = \frac{E[\alpha_s^2]}{M \cdot E[\alpha_j^2] + N_0} = \frac{\Omega_s}{M \cdot \Omega_i + N_0},$$

average signal-to-interference ratio SIR per branch defined as

$$(9) \quad SIR_{per\ branch} = \frac{E[\alpha_s^2]}{M \cdot E[\alpha_j^2]} = \frac{\Omega_s}{M \cdot \Omega_i},$$

and signal-to-noise ratio SNR per branch defined as

$$(10) \quad \text{SNR}_{\text{per branch}} = \frac{E[\alpha_s^2]}{N_0} = \frac{\Omega_s}{N_0},$$

where  $N_0$  is AWGN noise power.

Fig. 1 and Fig. 2 we can see BER dependency of average SINR per branch for  $M = 6$ ,  $\text{SIR}_{\text{per branch}} = 5$  [dB],  $m_i = 1$ , and 2 different values  $m_s = 1$  and  $m_s = 2$ . In first case, both the desired signals and interferers are in the same fade which corresponds to Rayleigh fading model, while in second case it is reasonable to assume that the cochannel interferers experience much deeper fading than the desired signal ( $m_s > m_i$ ) which is characteristic for microcellular environment. It is shown that AR selection method has better performance than AR combining method in case where the fade statistic is the same ( $m_s = m_i = 1$ ), while in second case ( $m_s = 2, m_i = 1$ ) the situation is reverse. It can be explained with the fact that AR selection criterion exploits information about desired signal fading amplitude which is more critical in the situation when desired signal experiences deeper fading. Fig. 3 and Fig. 4 depict the same characteristics of considered systems, with the different parameter  $\text{SIR}_{\text{per branch}} = 10$  [dB]. It can be noticed that difference between MRC and OC is less evident in the case when  $\text{SIR}_{\text{per branch}}$  has bigger value (interference has the less power).

Fig. 5 and Fig. 6 depict the BER dependency of average SIR per branch for  $\text{SNR}_{\text{per branch}} = 10$  [dB],  $M=1$  and  $M=6$  number of interferers, and 2 different values of  $m_s = 1$  and  $m_s = 2$ . We can see that the increasing the number of interferers changes only the performance of OC combining technique in both cases. Also, it can be noticed that performance differences between various combining/selection methods become more evident in case when interferers experience much deeper fading than the desired signal ( $m_s > m_i$ ).

## Conclusion

We present performances comparison of diversity receivers with distinct combining/selection techniques in the microcellular environment affected by multipath fading and multiple independent cochannel interferers, where the fading amplitudes of desired and interfering signals are modeled as random variables with Nakagami  $m$  distribution. It is shown that AR selection method has better performance than AR combining method in case where the fade statistic is the same ( $m_s = m_i = 1$ ), while in second case ( $m_s = 2, m_i = 1$ ). Also, it can be noticed that the number of interferers changes only the performance

of OC combining technique in both cases. Also, it can be noticed that performance differences between various combining/selection methods become more evident in case when interferers experience much deeper fading than the desired signal ( $m_s > m_i$ ).

## References

- [1] J.G. Proakis, Digital Communications, 3<sup>rd</sup> ed. New York: McGraw-Hill, 1995.
- [2] M. G., Simon, M.-S., Alouini, Digital Communication over Fading Channels: A Unified Approach to Performance Analysis, New York: Wiley, 2000
- [3] E.A. Naesmith, N. C. Beaulieu "New Results on Selection Diversity", IEEE Trans. Commun., vol. 46, pp. 695-704, May 1998.
- [4] Y.G. Kim and S.W. Kim, "Optimum Selection Diversity for BPSK Signals in Rayleigh Fading Channels", IEEE Trans. Commun., vol. 49, pp. 1715-1718, October 2001.
- [5] V. A. Aalo and J. Zhang, "On the Effect of Cochannel Interference on Average Error Rates in Nakagami-Fading Channels", IEEE Comm. Letters., vol. 3, pp. 136-138, May 1999.
- [6] A., Shah, A. M., Haimovich, "Performance Analysis of Maximal Ratio Combining and Comparison with Optimum Combining for Mobile Radio Communications with Cochannel Interference", IEEE Trans. Veh. Technol., vol. 49, pp. 1454-1463, July 2000.
- [7] R. K., Mallik, M. Z. Win, M. Chiani, A. Zanella "Bit Error probability for Optimum Combining of Binary Signals in The Presence of Interference and Noise", IEEE Trans. Wirel. Technol., vol. 3, pp. 395-407, June 2004.

---

**Milan Živković** – M.Sc. Student, Faculty of Electronic Engineering, University of Niš, Aleksandra Medvedeva 14, Niš, SERBIA AND MONTENEGRO.  
e-mail: mikaz@elfak.ni.ac.yu.

**Nenad Milošević** – Ph.D. Student, Faculty of Electronic Engineering, University of Niš, Aleksandra Medvedeva 14, Niš, SERBIA AND MONTENEGRO.  
e-mail: nemilose@elfak.ni.ac.yu.

**Bojan Dimitrijević** – Ph.D. Student, Faculty of Electronic Engineering, University of Niš, Aleksandra Medvedeva 14, Niš, SERBIA AND MONTENEGRO.  
e-mail: dbojan@elfak.ni.ac.yu.

**Zorica Nikolić** – Professor, Ph.D., Faculty of Electronic Engineering, University of Niš, Aleksandra Medvedeva 14, Niš, SERBIA AND MONTENEGRO.  
e-mail: zora@elfak.ni.ac.yu.



# 3D Finite Element Modelling of electromagnetic devices by using the scalar magnetic potential

Gérard Meunier

**Abstract:** This paper present a formulation to realize simulations of multiply connected magnetic circuit surrounded by stranded coils or solid conductors. This formulation, which needs cuts, is a powerful and economical alternative to the vector potential formulation.

**Keywords:** finite element formulation electromagnetism 3D

### Introduction

The use of the magnetic vector potential allow a very general solution for solving electromagnetic field equations with the finite element method and allow, in 2D as in 3D, a natural coupling with circuit equation without problem of connexity. Nevertheless this formulation remains expensive places memory and time calculation.

Recently, it was shown that the use of the magnetic scalar potential allows the setting of very powerful solutions compatible with complex simulations (movement, coupling circuits, massive conductors) proving to be an economic and powerful alternative to the magnetic vector potential [2]. Moreover the formulations containing magnetic scalar potentials proved particularly powerful for the treatment of thin regions [7]. Generally these formulations are based on the reduction of the total field  $\mathbf{H}$  by a  $\mathbf{T}_0$  source field [4] created by the conductors (coils or massive conductors). However this reduction can lead to inaccuracies and problems of convergence in the presence of ferromagnetic regions.

Let us examine figure 1: a closed magnetic circuit is surrounded by a coil and a massive conductor (with induced eddy currents). We will show in this paper how to solve this problem by using a magnetic scalar potential, allowing the coupling with the circuit equations and ensuring a good precision in the ferromagnetic regions. To achieve this goal, we will present our work along three points:

- the choice of the field  $\mathbf{T}_0$  source expressed with a nodal interpolation, whereas this one is generally expressed with an edge interpolation [6],
- the adaptation of the previous formulation to the case of closed magnetic circuits, to allow to calculate the magnetic field with a good precision in these regions,
- the taking into account of conducting massive regions when those are surrounded by a closed magnetic circuit.

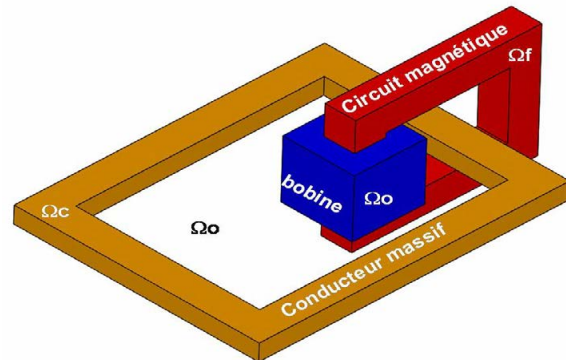


Fig.1. Multiply connected problem

### Modelling with coils

#### Coupling with circuit equations

Let us consider first a domain composed of air, simply connected magnetic regions and coils with average current density  $\mathbf{J}$ . The use of a scalar potential in the air and magnetic regions is possible since  $\text{curl } \mathbf{H} = 0$ , so we can write  $\mathbf{H}$  as  $\mathbf{H} = -\text{grad } \Phi$ . However some precautions must be taken in presence of a coil since, according to the Ampere theorem, the integral of the magnetic field  $\mathbf{H}$  along a closed contour surrounding the coil is equal to  $nI$  ( $nI$  is the sum of the currents crossing the coil) whereas the integral of a gradient is equal to 0. The solution consists in defining a region  $\Omega_0$  including the coil. We can express  $\mathbf{H}$  as :

- (1)  $\mathbf{H} = \mathbf{T}_0 - \text{grad } \Phi$  in  $\Omega_0$
- (2)  $\mathbf{H} = -\text{grad } \Phi$  in  $\Omega - \Omega_0$

$\mathbf{T}_0$  is a source field which verify  $\text{rot } \mathbf{T}_0 = \mathbf{J}$  in  $\Omega_0$  et  $\mathbf{T}_0 \times \mathbf{n} = \mathbf{0}$  on the interface  $\delta\Omega_0$ , for insuring the continuity of the tangential component of  $\mathbf{H}$  on  $\partial\Omega_0$ . So the magnetic field  $\mathbf{H}$  is « reduced » in  $\Omega_0$  and « total » in  $\Omega - \Omega_0$ . With this definition the Ampere theorem is well verified. Different choices of  $\mathbf{T}_0$  domain are possible like the classical solution which consist to choice  $\Omega_0 = \Omega$  with a  $\mathbf{T}_0$  field equal to the Biot-et-Savart field or like the solution which consist to define  $\Omega_0$  by a box surrounding the coil and allowing, for simple geometries, an analytical solution for  $\mathbf{T}_0$  [11].

Let us consider the case of devices including open magnetic circuits: we can choose the air and the coils as domain  $\Omega_0$ . This approach presents two advantages:

- The calculation of the magnetic field in the ferromagnetic regions is made with a total potential ( $\mathbf{H} = -\mathbf{grad} \Phi$ ). The magnetic field, very small in the regions with a high permeability, can be obtained by a better precision compared with the difference between  $\mathbf{T}_0$  and  $\mathbf{grad} \Phi$ . This is particularly important in the case of non linear ferromagnetic regions : indeed in the case of the use of a reduced magnetic field in these region, the inaccuracies of calculation can lead to important difficulties of convergence for the non linear system

- It is not necessary to describe the geometry of the domain  $\Omega_0$ , this one is a part of the initial geometry (ferromagnetic regions).

In the general case of a coupling with the circuit equations we express  $\mathbf{T}_0$  as  $\mathbf{T}_0 = \sum \mathbf{tok}.I_k$  where  $I_k$  is the current flowing the coil k (unknown) et  $\mathbf{tok}$  the  $\mathbf{T}_0$  field created by the coil k with a current of 1A. For the  $\mathbf{tok}$  calculations different approaches exist, in particular by using a edge interpolation, which is interesting for insuring the condition  $\mathbf{T}_0 \times \mathbf{n} = \mathbf{0}$  on the interface  $\partial\Omega_0$ . We propose an originality approach which consists to express  $\mathbf{tok}$  as:

$$(3) \quad \mathbf{tok} = \mathbf{hok} - \mathbf{grad} \delta\phi_k$$

where  $\mathbf{hok}$  is the Biot et Savart field create by the coil k for a current of 1A ;  $\delta\phi_k$  is calculated on  $\partial\Omega_0$  for insure  $\mathbf{tok} \times \mathbf{n} = \mathbf{0}$ . We solve :

$$(4) \quad \mathbf{grad} \delta\phi_k \times \mathbf{n} = \mathbf{hok} \times \mathbf{n} \text{ on } \partial\Omega_0$$

In practice values of  $\mathbf{hok}$  and  $\delta\phi_k$  are often computed by a finite element minimisation respectively  $\Omega_0$  and  $\partial\Omega_0$ . We can notice that electrical circuits can be represented like meshed regions or like inductors independent of the finite element. The obtained values are stored on the nodes of the mesh, which allows making this relatively expensive calculation only one time in the case of a step by step procedure. In the case of a coupling with circuit equations, the presence of supplementary unknowns  $I_k$  needs to write relations between current and voltage to be coupling with field equations. These relations, which need integration in the domain  $\Omega_0$ , are expressed as [2]:

$$(5) \quad R_k I_k + \int_{\Omega_0} \mathbf{t}_{0k} \cdot \frac{\partial \mathbf{B}}{\partial t} d\Omega = U_k$$

where  $R_k$  represent the electric resistance of the coil k et B the magnetic induction obtained by the constitutive relation  $\mathbf{B}(\mathbf{H})$ . The coupling resolution of field equations and circuit equations is expressed as a symmetric matrix system where the unknowns are the nodal potentials  $\Phi$

and the currents  $I_k$  of the coils. An detailed example of the construction of the system of equation is presented in [2].

### Closed magnetic circuits

In the case of closed magnetic circuits crossed by coils, the use of the total magnetic field for insure a good precision in magnetic regions, needs some precautions. Indeed, the integral of  $\mathbf{H} = -\mathbf{grad} \Phi$  along a path inside the magnetic circuit gives  $\mathbf{0}$  whereas the value should be equal to the total current crossing the magnetic circuit. For solving this problem we introduce a cut in the closed magnetic circuit  $\Omega_f$  such as a jump of the magnetic scalar potential take into account the total current crossing the magnetic region. In practice we express the field  $\mathbf{H}$  as:

$$(6) \quad \mathbf{H} = \mathbf{hok}.I_k - \mathbf{grad} \Phi \text{ in } \Omega_0$$

$$(7) \quad \mathbf{H} = \mathbf{grad} \delta\phi_k.I_k - \mathbf{grad} \Phi \text{ in } \Omega_f$$

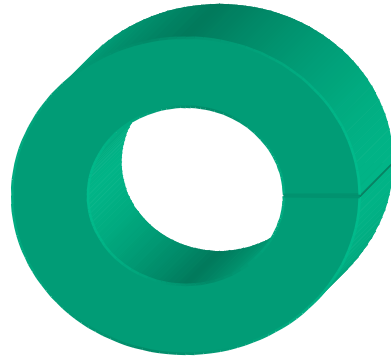


Fig.2. Magnetic circuit with a cut

The computation of the increments  $\delta\phi_k$  is leaded as previously (4) by considering the cut impassable. So we have two values for  $\delta\phi_k$  on each side of the cut. By taking  $\Phi$  continuous, we verify, as previously, the continuity of the tangential component of the magnetic field on the interface air-magnetic region.

We can notice that the magnetic field  $\mathbf{H}$  is partially reduced in  $\Omega_f$  since  $\mathbf{grad} \delta\phi_k$  is not equal to zero in the first layer of elements of the magnetic region. In practice, it is better to compute  $\delta\phi_k$  inside magnetic regions so we can express  $\mathbf{H}$  as continuous gradient in  $\Omega_f$ . In this case, the increments  $\delta\phi_k$  are computed in all the volume such as:

$$(8) \quad \mathbf{grad} \delta\phi_k = \mathbf{hok} \text{ in } \Omega_f$$

With the definition given in (4) or in (8), a integration on a path inside  $\Omega_f$  we have, by considering that  $\mathbf{hok}$  is the Biot-et-Savart field created by the coil k make with n turns flowing by a current of 1A :

$$(9) \quad \int_C \mathbf{grad} \delta\phi_k dC = \int_C \mathbf{hok} dC = n$$

So the jump  $\Delta(\delta\phi_k)$  on this cut is equal to “n” which allow to verify the Ampere theorem with the field expression given in (7), since  $\Phi$  has the same value on each side of the cut.

In a domain which contains several coils and magnetic regions, simply connected or not, the above formulations can be generalized without difficulty. The two approaches can be combined with respect the relative position of coils and magnetic circuits. Moreover, the definition domain for  $\mathbf{tok}$  can be adapted and limited for each coil.

Finally, the relation between current and voltage must be adapted for the coil crossing closed magnetic circuit if we wish keep a symmetrical matrix. For this we have to transform the equation (5) such below [3]:

$$(10) \quad R_k I_k + \int_{\Omega_0} \mathbf{h}_{0k} \cdot \frac{\partial \mathbf{B}}{\partial t} d\Omega + \int_{\Omega - \Omega_0} \mathbf{grad} \delta \Phi_k \cdot \frac{\partial \mathbf{B}}{\partial t} d\Omega = U_k$$

**Modelling of a current transformer**

We can apply the two previous formulations for the simulation of a current transformer (figure 3 – collaboration between Cedrat and Schneider Electric) [5]. Because we have a closed magnetic circuit, we have to use the formulation with cut. Finally, we compare our solution with the solution obtained with a very little air-gap whose reluctance is negligible compared with the reluctance of the magnetic circuit.

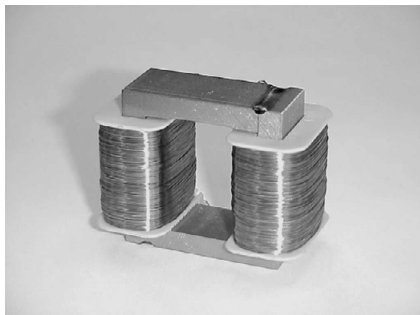


Fig.2. A current transformer (Schneider Electric)

The figure 4 represents the electric circuits and the geometry part which is treated by the finite element method (1/8 for symmetry reasons). We can notice that all the conductors are not meshed. For the simulation we impose a sinusoidal current in the copper bar and the induced currents are determined in the coils. Results of simulations are compared with experimental results given by Schneider Electric.

The figure 5 represents the finite element mesh for the modelling with a air-gap. Since the air-gap is very small, it needs a very fine mesh around it, which is very constraining for memory place and computation time.

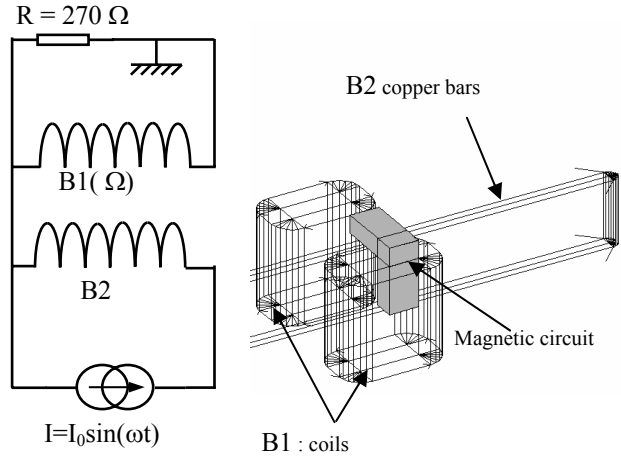


Fig.4. Current transformer description

Due to the non linearity of the magnetic material the simulations are made in a step by step procedure. At each time step, the Newton-Raphson algorithm is used for insure the convergence of the non linear system of equation.

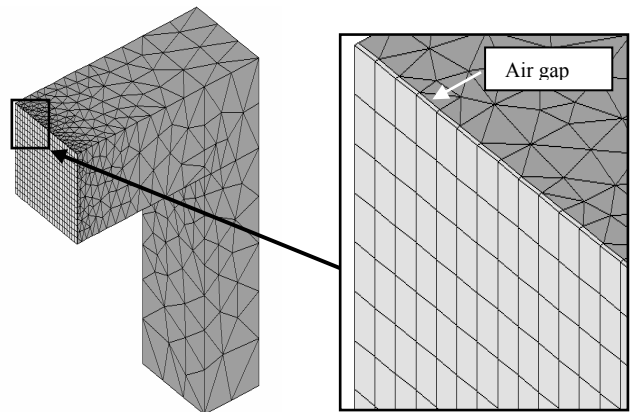


Fig.5 Finite element mesh

Figure (6) show a comparison between the two simulations and the experimental results. We can notice that the two finite element solutions are very closed

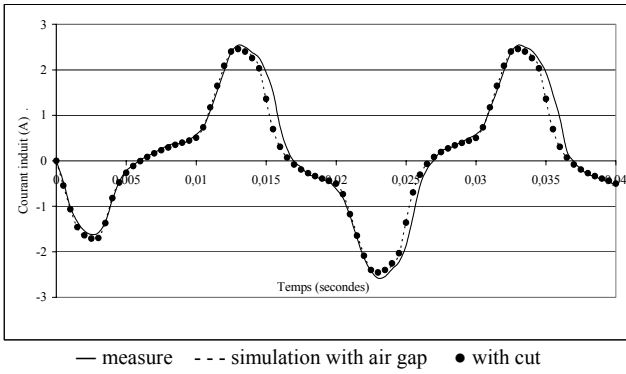


Fig 6. Eddy current in the secondary

Nevertheless the solution obtained with the cut is easier to mesh and more interesting in terms of computation time. (Cf Table 1).

Method	Nb of unknown	CPU time
Air gap	9884	1h 17min
Cut	799	28 min

Table 1. CPU time comparison

### Modelling of a moving motor

The formulation is very useful for the modelling of moving motors. It needs a coupling with circuit equations and to take into account the movement. A great interest of the scalar formulation is the possibility to make easily a mesh interpolation during the rotation.

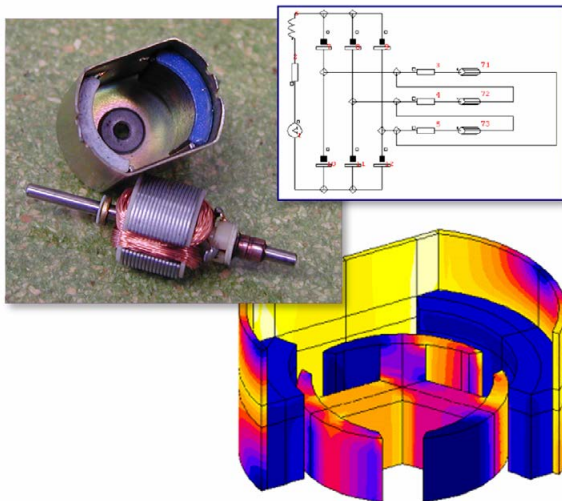


Fig.7 Moving motor

In this example and generally in the case of electrical machines, it is interesting to consider (at least) two domains  $\Omega_0$  : one for the stator and one for the rotor. So,

the  $\mathbf{to}$  computations will be made only one time if the mesh is remained during the rotation.

### Massive conductors

#### Multiply connected massive conductors

In the case of massive conductors (region  $\Omega_c$ ), some recent works have proposed a general formulation allowing the coupling with circuit equations and the taking into account of massive multiply connected conductors (with holes) [2].

The formulation one is base on a  $\mathbf{T}-\mathbf{To}-\phi$  formulation where  $\mathbf{To}$  represents a source field used for solve the connexity problem and  $\mathbf{T}$  a vector electric potential due to the presence of eddy currents. If we consider a massive conductor with a hole in air we can solve the connexity problem due to eddy currents flowing the conductor by defining a current  $\mathbf{j}_{0c}$  such as the total current around the hole is equal to 1A. The repartition of this current density  $\mathbf{j}_{0c}$  must be whatever and we can choose for instance the electrokinetic solution. Like for coils, we define a field  $\mathbf{to}_c$  which verify:

$$(11) \quad \mathbf{to}_c = \mathbf{ho}_c - \text{grad } \delta\phi_c$$

where  $\text{curl } \mathbf{ho}_c = \mathbf{j}_{0c}$  and  $\delta\phi_c$  is computed on  $\partial\Omega_{0c}$  (domain for  $\mathbf{to}_c$ ). As previously  $\Omega_{0c}$  can be choose equal to  $\Omega - \Omega_f$ .

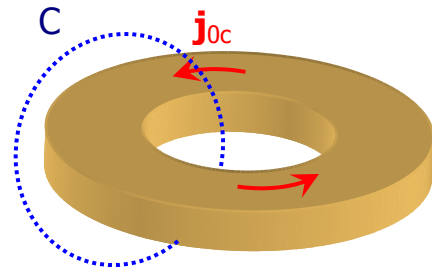


Fig.8 Multiply connected massive region

The magnetic field  $\mathbf{H}$  and the current density  $\mathbf{J}$  in the massive conductor are written such as:

$$(12) \quad \mathbf{H} = \mathbf{T} + \mathbf{to}_c \cdot I_c - \text{grad } \Phi \quad \mathbf{J} = \text{rot } \mathbf{T} + \mathbf{j}_{0c} \cdot I_c$$

In air, if we have only this conductor, the magnetic field is written :

$$(13) \quad \mathbf{H} = \mathbf{to}_c \cdot I_c - \text{grad } \Phi$$

With this representation, Ampere theorem is satisfied when the field  $\mathbf{H}$  is integrated along a path surrounding the conductor. The supplementary unknown  $I_c$  needs a supplementary relation which express that the voltage is equal to zero [2] :

$$(14) \int_{\Omega_0} \mathbf{j}_{0c} \cdot \mathbf{E} d\Omega + \int_{\Omega_0} \mathbf{t}_{0k} \cdot \frac{\partial \mathbf{B}}{\partial t} d\Omega = U_c = 0$$

$\mathbf{E}$  represent the electric field which can be obtained through the constitutive relation  $\mathbf{E}(\mathbf{J})$ . We can notice that the relation (14) doesn't make hypothesis on linearity of the electric and magnetic materials. For the case of massive conductors supply by several entries, this approach can be generalized as explained in [2].

### **Multiply connected massive conductors with closed magnetic circuit**

In the case of a closed magnetic circuit crossed by a massive conductor (figure 9), we can apply the method proposed for the coils. By introducing a cut in the magnetic circuit, with a partial reduction of the magnetic field  $\mathbf{H}$  in the magnetic circuit allow to solve the problem of connexity, with respect a field which derive from a gradient.

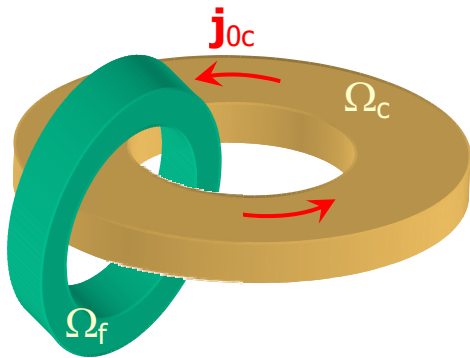


*Fig.9 Multiply connected massive conductors with closed magnetic circuit*

With the example of the figure (8) we can write  $\mathbf{H}$  as:

$$(15) \quad \mathbf{H} = \mathbf{T} + \mathbf{h}_{0c} \cdot I_c - \mathbf{grad} \Phi \text{ in massive conductor}$$

$$(16) \quad \mathbf{H} = \mathbf{h}_{0c} \cdot I_c - \mathbf{grad} \Phi \text{ in air}$$

$$(17) \quad \mathbf{H} = -\mathbf{grad} \Phi + \mathbf{grad} \delta\phi_c I_c \text{ in magnetic circuit}$$

The relations between the current and the voltage have to be adapted for insure the symmetry of the system of equations. Equation (14) can be transformed in equation (18) :

$$\int_{\Omega_c} \mathbf{j}_{0c} \cdot \mathbf{E} d\Omega + \int_{\Omega_0} \mathbf{h}_{0k} \cdot \frac{\partial \mathbf{B}}{\partial t} d\Omega + \int_{\Omega - \Omega_0} \mathbf{grad} \delta\phi_k \cdot \frac{\partial \mathbf{B}}{\partial t} d\Omega = U_c = 0$$

### **General case**

Previous formulations can be combined, by computing a  $\mathbf{t}_0$  field for each conductor (coil or massive) on a domain  $\Omega_0$  which can be choose identical and equal to  $\Omega - \Omega_f$  where  $\Omega_f$  represents the ferromagnetic regions. In practice, the domain of definition  $\Omega_0$  of each coil can be adapted and limited, which can be interesting for reduce the computation time of  $\mathbf{t}_0$  field

The final system of equations, after the finite element meshing, leads to the resolution of a symmetric matrix system where the unknowns are  $\Phi$ ,  $\mathbf{T}$ ,  $I_c$  et  $I_k$ . All the formulations have been implemented in FLUX3D<sup>®</sup> software.

### **Modelling of a multiply connected problem**

In the case of the figure 1, where we have a coil and a massive conductor crossed by a closed magnetic circuit, we can write the magnetic field  $\mathbf{H}$  such as :

$$(19) \quad \mathbf{H} = \mathbf{h}_{0k} \cdot I_k + \mathbf{h}_{0c} \cdot I_c - \mathbf{grad} \Phi \text{ dans } \Omega_0 - \Omega_c$$

$$(20) \quad \mathbf{H} = \mathbf{grad} \delta\phi_k \cdot I_k + \mathbf{grad} \delta\phi_c \cdot I_c - \mathbf{grad} \Phi \text{ dans } \Omega_f$$

$$(21) \quad \mathbf{H} = \mathbf{T} + \mathbf{h}_{0k} \cdot I_k + \mathbf{h}_{0c} \cdot I_c - \mathbf{grad} \Phi \text{ dans } \Omega_c$$

A sinusoidal current ( $I_c = 20\text{kA}$ ,  $f = 50\text{Hz}$ ) is imposed in the massive conductor (in copper), and the simulation compute the value of the induced current in the coil (5000 turns). The magnetic circuit is non linear. A cut must be defined in the magnetic circuit. Figure (10) present the results obtained which are compared with a solution using a little air-gap. The two simulations give results very closed.

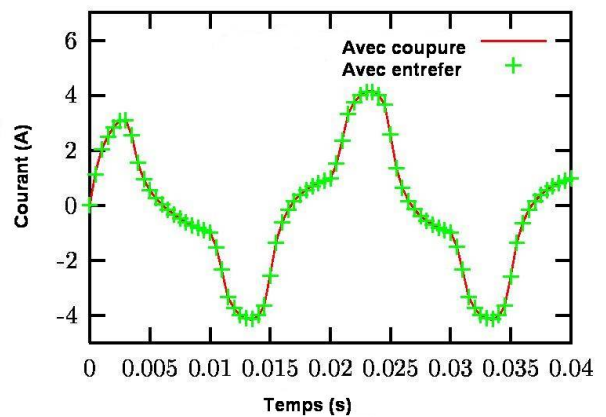


*Fig.10 Current in the coil: comparison of solutions obtained with a cut and with an air-gap*

## Modelling of a electromagnetic launcher

As a complex and real example we present the simulation of an electromagnetic launcher where different effects are modeled (Simulation made by Cedrat in collaboration with Institut Saint Louis):

- Capacitance discharge
- Eddy current effects in the coil
- Eddy current in the projectile
- Kinematics coupling to consider the linear motion

At each time step, the air is re-meshed.

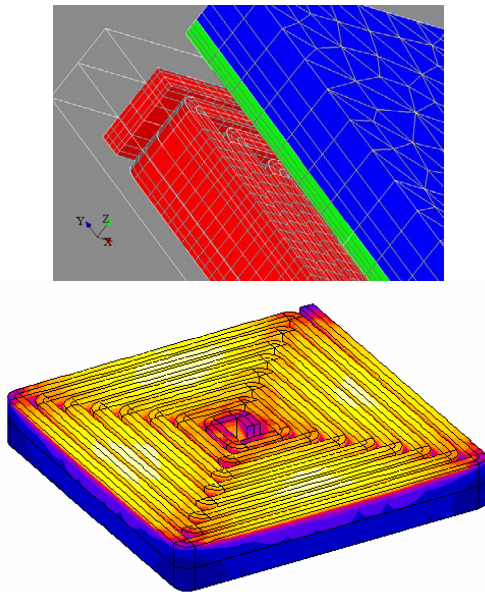


Fig.11 Electromagnetic launcher

The results obtained fit the measurement: 0.2 % gap between the 3D model and the measurement on the maximum current (reduced values).

	Measurement	Modelling
<b>I<sub>max</sub></b>	1	0.998
<b>T for I<sub>max</sub></b>	0.24	0.30
<b>Speed max</b>	1	1.145

## Conclusions and perspectives

The solution proposed which is based on the use of magnetic scalar potential and vector electric potential, is powerful as attests the results obtained. It proves to be a interesting alternative to the vector magnetic potential, presenting a great character of generality in particularly for the coupling with circuit equations for coils and massive conductors. Moreover, the formulation is well adapted for problems with moving parts. Its relative low cost, in place memory and time calculation confers to it an additional interest.

Recently, some works on automatic determination of cuts of close magnetic circuits have been developed [8]. It is an important point for a comfortable use of this method. It will be interesting to extend this for the case of closed massive conductors to determine automatically (without user intervention) the electrokinetic current  $\mathbf{j}_0$ .

It will be also interesting to limit the domain of computation of the  $\mathbf{t}_{0k}$ , by defining  $\Omega_0$  as near as possible of each conductor. A deflating technique of mesh [9] coupled with an automatic determination of cut of the closed magnetic circuits seems to be an interesting solution.

## Bibliography

- [1] Buisson S., Piriou F., "A numerical simulation of power transformer using 3D finite element method coupled to circuit equation", *IEEE Trans. Mag*, vol. 30, N° 5, pp. 3224-3227, September 1994.
- [2] Meunier G., Le Floch Y., Guérin C., "A non linear circuit coupled T-To- $\phi$  formulation for solid conductors", *IEEE Trans. MAG*, vol. 39, N°3, pp. 1729-1734, May 2003.
- [3] Le Floch Y., Meunier G., Guérin C., Labie P., Brunotte X., Boudaud D., "Coupled problem computation of 3D multiplyconnected magnetic circuits and electric circuits", *IEEE Trans. MAG*, vol. 39, N°3, pp. 1725-1728, May 2003.
- [4] Mayergoyz I. D., Chari M. V. K., D'Angelo J., "A new scalar potential formulation for threee-dimensional magnetostatic problem", *IEEE trans-Mag*, vol. 23, n° 6, pp. 3889-3894, 1987.
- [5] Le Floch Y., Guérin C., Boudaud D., Meunier G., Brunotte X., "A current transformer modeling", *COMPEL*, Vol. 21, n° 4, pp 505-511, 2002.
- [6] Le Menach Y., Clenet S., Piriou F., "Determination and utilization of the source field in 3D magnetostatic problem", *IEEE Trans-Mag*, Vol. 29, n° 2, pp 1368-1371, March 2005.
- [7] Guérin C., Tanneau G., Meunier G., Labie P., Ngnegueu T., Sacotte M., "A shell element for computing eddy currents in 3D. Application to transformers", *IEEE Trans-Mag*, Vol. 31, n° 3, Mai 1995.
- [8] Phung A. T., Chadebec O., Labie P., Le Floch Y. and Meunier G., "Automatic cuts for magnetic scalar potential formulations", *IEEE Trans-Mag*, Vol. 41, n° 5, pp 1668,1671, May 2005.
- [9] Leonard P.J., Lai H.C., Hill-Cottingham and Rodger D., "Automatic implementation of cuts in multiply connected magnetic scalar region for 3-D eddy current model", *IEEE Trans-Mag*, Vol. 29, n° 2, pp 1368-1371, March 2005.
- [11] Kladas A., Tegopoulos J.A., "A new scalar potential formulation for 3D magnetostatics, neccsating no source field calculation", *IEEE Trans-Mag*, Vol. 28, n° 2, pp 1103-1106, March 1992.

**G rard Meunier** – CNRS Researcher, Dr., *Laboratoire d'Electrotechnique de Grenoble, INPG / UJF / CNRS, LEG-ENSIEG, BP46, 38402 Saint Martin D'H res, France. Gerard.Meunier@inpg.fr*

# Performance Improvement in Finite Element Analysis by Modifying Mesh Structure

Kadir Yılmaz, Abdulkadir Cengiz, Murat Ayaz, Erkan Mese

**Abstract:** Computer aided solutions which are proposed to solve the problems encountered during electric machine modelling requires engineering work. The structure of the model should be known very well such that potential errors can be foreseen ahead of prototype construction. This paper investigates the effect of mesh structure on the modelling performance, which plays an important role in the finite element analysis (FEA) of electric machines. FEA of a switched reluctance motor (SRM) with 6 stator and 4 rotor poles are given as an example. FEA is performed with Maxwell 2D software. Flux linkage characteristics, current versus torque characteristics are presented with different mesh structures for comparison purposes.

**Keywords:** Electromagnetic Analysis, Mesh structure, SRM, FEM.

## Introduction

Numerical solution of magnetic field problems, is an important engineering tool for performance prediction of many electric machines. Usage of this technique in magnetic design has been increasing recently. Among these methods, finite element method (FEM) is the most popular tool. In electrical engineering FEM is used in calculating the electrical and magnetic fields. Using these field data, model's parameters such as current, moment, magnetic flux, power loss can be predicted. Maxwell 2D is a popular software in the industry which utilizes FEM.

In this paper, effects of element selection and mesh structure, which are very significant in FEM modelling performance, are being examined.

## II. Finite Element Method and Element Selection

FEM is a numerical procedure in structural solution. Because it's quite complex to solve the problem analytically, generally FEM is being used as an alternative. FEM's aim is to determine the system's finite unknowns in terms of system's known parameters. By using FEM, a 2nd order Poisson equation is solved numerically. In order the FEM to be used, area of interest needs to be divided into sub-areas, which are called finite elements. This subdividing and discretization have to be done such that no element should cover 2 different media at the same time.

Another important concept in FEM is the behaviour of the elements in the model. Groups of elements are called mesh. A model with well-chosen element structure

gives better results compared to the ones with randomly selected elements. Fig.1 shows the schematics of different types of element structures.

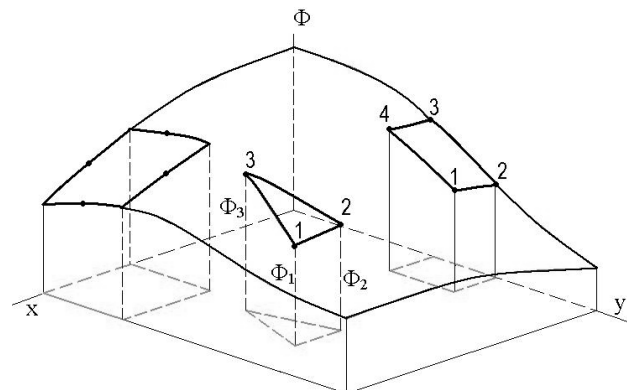


**Fig.1** – Schematics of different types of element structures.

In forming the mesh, geometry of the structure model has to be taken into account. Triangular shaped elements have to be preferred in curved geometries, while square shaped elements can fit better for non-curved shapes. In a mesh formed by triangular shaped elements, each node on the element contains the same information and the results are multiples of each other. On the other hand, in a mesh formed by square elements, information on the nodes is not equal and may vary.

## III. Determining the Mesh Structure and Building Parametric Model

As an example application, 6/4 SR motor has been chosen. In Fig 2, geometry of 6/4 SR motor is shown.

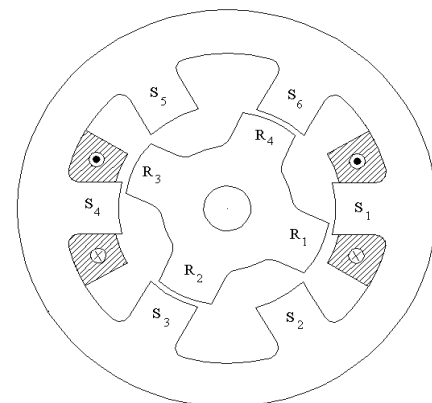
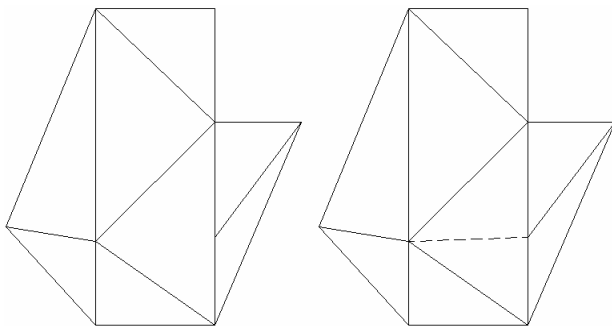


**Fig.2.** Geometry of a conventional SRM.

Triangular shaped mesh structure is preferred in this application since it fits to the motor's geometry very well. In Fig. 3, triangular mesh elements can be seen.



False True  
Fig. 3. Triangular elements

In selection of the triangular elements, it has to be made sure that all nodes have to coincide with the vertices of the triangles. This makes the computational cost feasible. Since SR motors produce the torque by the change of air-gap reluctance with respect to rotor position [1,2], it is quite important to model this gap carefully, as far as the mesh structure of the gap is concerned. Therefore this thin air-gap between rotor and the stator needs to be rotated with every incremental rotation of the rotor [3,4]. This can be seen in Fig 4.

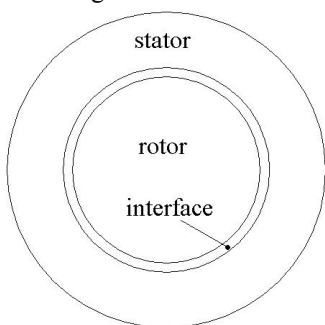


Fig.4. Airgap interface between stator and rotor

In order to solve the problem, parametric model is formed. In Figure 5, parametric model of 6/4 SR motor application model can be seen as an example.

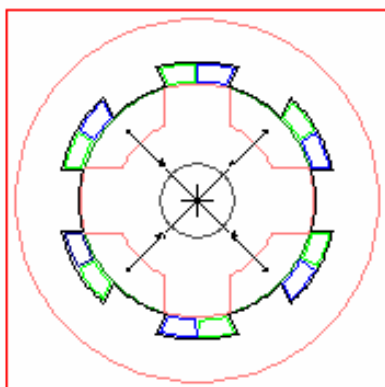


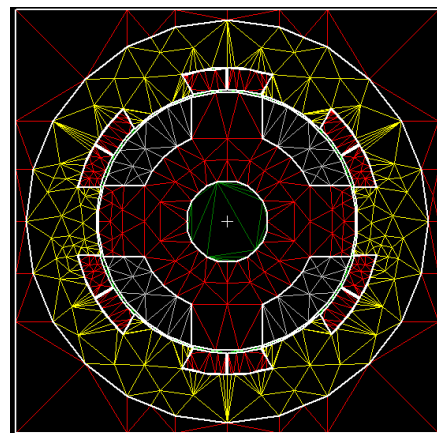
Fig.5 Parametric SR motor model

To be able to keep the mesh structure unchanged in the model, parametric constraints are introduced. These constraints for 6/4 example SR motor can be seen in Table 1.

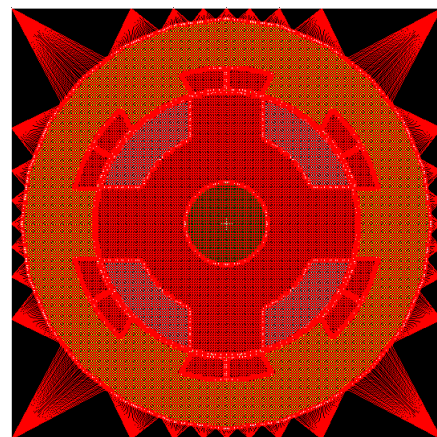
Table 1. Constraint variables

Name	Value	Expression
h1	45	45+r
h2	135	135+r
h3	225	225+r
h4	315	315+r
rotor	0	0

Two different models that have been built in accordance with fitting the model's geometry can be seen in Fig 6.



Coarse mesh pattern



Fine mesh pattern

Fig.6 Two different mesh pattern model of SR motor.

Properties of two different mesh structures can be seen below.

**COARSE MESH:**

12000 triangles elements (total) 2799 triangles elements (in the airgap)  
Computation time is approximately 53sn. (1.30 hours)



**FINE MESH:**

55139 triangles elements (total)  
 11760 triangles elements (in the airgap)  
 Computation time is approximately 1.68sn. (4.76 hours)

In order to get the operational characteristics of these two SRMs, 10 incremental rotational positions of the rotor between zero and 45 electrical degrees, 17 incremental current values between 15A and 255A are analysed for 170 different computational scenario in total. The results of these analyses are then used to form flux and torque profile for different position and current values. Program performs 2D computation and can calculate the windings flux. There are a few methods to calculate the flux linkage in 2D software packages. The one used throughout this investigation is given in Figure 7.

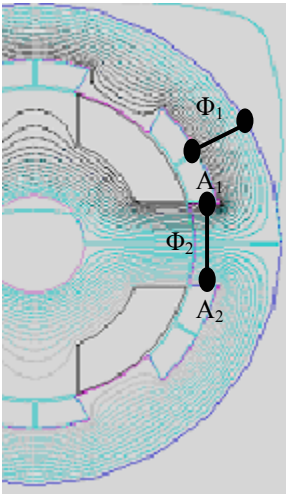


Fig.7 Flux linkage calculation.

In this work, magnetic potentials of the nodes, which are calculated by the program, have been used. According to the Figure.7, flux value normal to the surface between two nodes are calculated as in eqn.1 and eqn.2.

$$\phi = \int \vec{A} \cdot d\vec{l} \tag{1}$$

$$\phi = (A_1 - A_2) \tag{2}$$

Where,

A<sub>1</sub> is the magnetic vector potential of node 1 in Fig. 7  
 A<sub>2</sub> is the magnetic vector potential of node 2 in Fig. 7  
 Φ<sub>2</sub> is flux per pole per turn

Flux linkage per phase is then calculated as in eqn.3

$$\Psi = (2 \cdot N) \cdot \phi_2 \cdot L \tag{3}$$

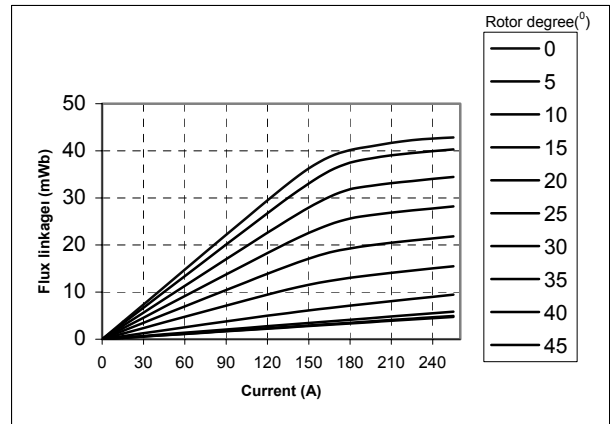
Where,

L: Stack length  
 N: Number of turns

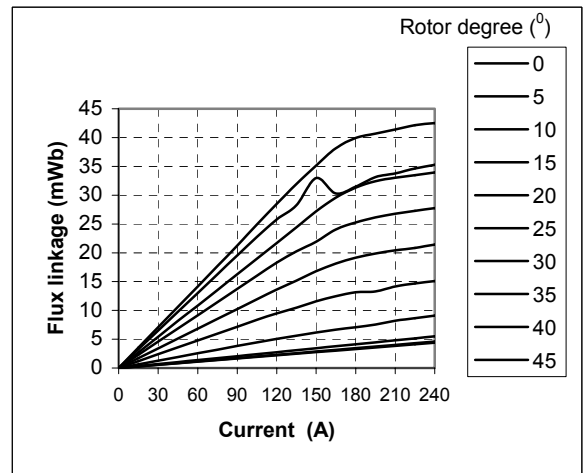
Flux leakage is calculated as in eqn.4.

$$\text{Leakage flux} = 2\phi_1 - \phi_2 \tag{4}$$

Fig. 7 and Fig.8 show flux linkage ψ (i,θ) and torque T (i,θ) profiles of 6/4 SR motor for different mesh structure, respectively.



Fine mesh pattern

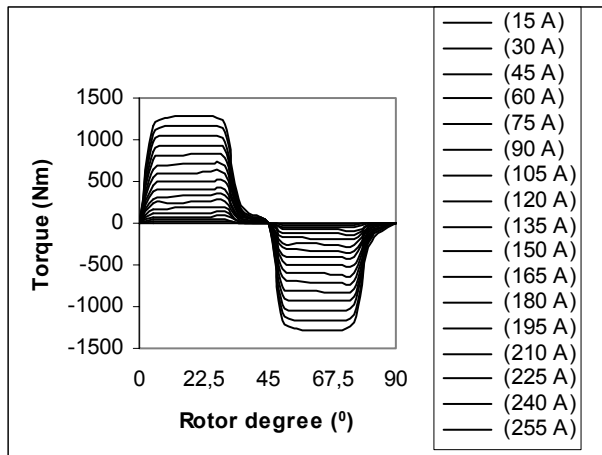


Coarse mesh pattern

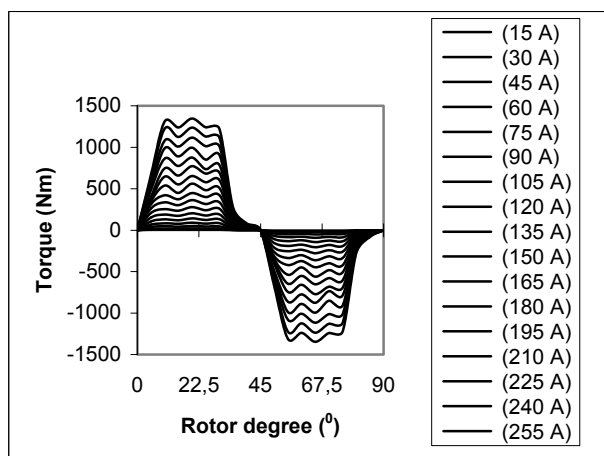
Fig.7 Flux linkage profiles of SRM

Fig.7 clearly shows the effect of the selected mesh structure on the working characteristics. In the solution with the randomly and automatically generated mesh structure, some defects appear at certain angle and current values of the solution. On the contrary, the mesh structure built according to the machine structure and geometry gives better results.

Static moment curves plotted using the data out of magnetic analysis can be seen in Fig. 8. In coarse mesh solution, significant ripples can be seen in the torque output. They are not because of the motor's nature; in fact they are simply due to the wrong selection of meshing structure.



Fine mesh pattern



Coarse mesh pattern

Fig.8 Torque profiles of SRM

In the solution with careful meshing structure, more smooth plots are obtained compared to the coarse meshing structure.

Two mesh structures are compared for 60A phase current, and rotor positions between 0 and 45 degrees. The comparison can be seen in Table 2. and Table 3..

Table 2. Torque for SRM at various positions at 60 A.

Rotor pos.	Torque (Nm) Maxwell 2D Coarse Mesh	Torque (Nm) Maxwell 2D Fine Mesh
0	0	0
5	20,4	22,02
10	25,13	23,35
15	22,91	24,05
20	27,11	24,41
25	23,52	24,51
30	25,32	25,03
35	4,51	4,57
40	1,35	1,43
45	0	0

Table 3. Flux linkage for SRM for 60 A.

Rotor pos.	Flux (mWb) Maxwell 2D Coarse Mesh	Flux (mWb) Maxwell 2D Fine Mesh
0	14,15	14,75
5	13,01	13,37
10	10,82	11,30
15	9,15	9,16
20	6,81	6,97
25	4,78	4,76
30	2,55	2,53
35	1,37	1,37
40	1,14	1,16
45	1,09	1,11

#### IV. CONCLUSION

In this study, a method regarding the improvement of prediction performance of a FEM software, Maxwell 2D, is presented. The importance of element selection and mesh structure in a FEM application is given with SR motor example. In the 6/4 SR motor, flux linkage and torque profiles are obtained and a comparative study is given for different mesh structure. The study aims to increase the awareness of the FEM software users regarding the trade off between mesh structures vs. prediction performance vs. computational cost.

#### V. REFERENCES

- [1] W.,F., Ray, P.,J., Lawrenson, R.,M.,Davis, J.,M., Stephenson, N.,N.,Fulton, R.,J.,Blake, "High-Performance Switched Reluctance Brushless Drives", IEEE Transactions on Industry Applications, Vol. IA-22, No.4, July/August 1986.
- [2] J.,M., Stephenson, J.,Corda, "Computation of torque and current in doubly salient reluctance motors from nonlinear magnetisation data", Proc. IEE, Vol.126, No.5, pp.393-396, 1979.
- [3] T.,J.,E., Miller, M.,McGilp, "Nonlinear theory of the switched reluctance motor for rapid computer-aided design", IEE Proceedings, Vol.137, Pt.B, No.6, pp.337-347, November 1990.
- [4] J.,V., Byrne, J.,B., O'Dwyer, "Saturable variable reluctance machine simulation using exponential functions", Proc. Int. Conf. on Stepping Motors & Systems, pp.11-16, 1976.

**Kadir Yilmaz** – Dr., Technical Education Faculty, Department of Electrical Education, Kocaeli University, 41380., Kocaeli, TURKEY

e-mail: kayel@kou.edu.tr

**Abdulkadir Cengiz** – Ph.D. Student, Faculty of Mechanical Education, Kocaeli University, 41380., Kocaeli, TURKEY

e-mail: akcengiz@kou.edu.tr

**Murat Ayaz** – Student, Faculty of Electrical Education, Kocaeli University, 41380., Kocaeli, TURKEY

e-mail: mayaz@hotmail.com

**Erkan Mese** – Dr., Advanced Energy Conversion, LLC, Malta, NY, 12020, USA

e-mail: emese@alum.rpi.edu

## Methods for magnetic field calculation

Ana N. Mladenović, Slavoljub R. Aleksić

**Abstract:** This paper presents methods for magnetic field calculation. The first method that is presented is based on a system of equivalent magnetic dipoles and it is applied for determining magnetic field components of toroidal shaped permanent magnet with air gap. The second method is based on determining distribution of microscopic Ampere's current and it is used for magnetic field calculation of rod shaped permanent magnet. The distributions of magnetic field of both permanent magnets are also shown in the paper.

**Keywords:** Magnetic field, Permanent magnet, Magnetic dipole, Amper's currents.

### Introduction

For determination the magnetic field components in surroundings of permanent magnets, it starts from supposition that magnetization of permanent magnet is known,  $\mathbf{M}$ . The following methods are useful in practical calculation:

- a) Method based on determining distribution of microscopic Ampere's current;
- b) Method based on Poisson's and Laplace's equations, determining magnetic scalar potential; and
- c) Method based on system of equivalent magnetic dipoles.

Magnetic field inside and outside the permanent magnet, if magnetization of permanent magnet is known, can be calculated using equivalent system of volume and surface microscopic Ampere's currents, which are determined as

$$(1) \quad \mathbf{J}_a(\mathbf{r}') = \text{rot } \mathbf{M}(\mathbf{r}'), \text{ and}$$

$$(2) \quad \mathbf{J}_{sa}(\mathbf{r}') = \mathbf{M}(\mathbf{r}') \times \hat{\mathbf{n}},$$

where  $\hat{\mathbf{n}}$  is unit vector of outgoing normal (Fig.1.).

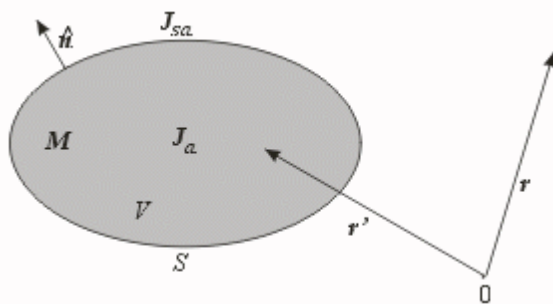


Fig.1. Permanent magnet

These currents produce magnetic vector potential

$$(3) \quad \mathbf{A}(\mathbf{r}) = \frac{\mu_0}{4\pi} \int_V \mathbf{J}_a(\mathbf{r}') \frac{dV'}{R} + \frac{\mu_0}{4\pi} \oint_S \mathbf{J}_{sa}(\mathbf{r}') \frac{dS'}{R},$$

where  $R = |\mathbf{r} - \mathbf{r}'|$ .

Magnetic flux density is

$$(4) \quad \mathbf{B}(\mathbf{r}) = \text{rot } \mathbf{A}(\mathbf{r}).$$

Inside a permanent magnet, magnetic field can be determined using relation

$$(5) \quad \mathbf{H} = \mathbf{B}/\mu_0 - \mathbf{M}.$$

Outside a permanent magnet, magnetic field can be determined using relation

$$(6) \quad \mathbf{H} = \mathbf{B}/\mu_0.$$

The second method is based on determining magnetic scalar potential  $\phi_m$ . Inside a permanent magnet magnetic scalar potential satisfies Poisson's equation

$$(7) \quad \Delta \phi_m = \text{div } \mathbf{M}.$$

Magnetic field vector can be presented as

$$(8) \quad \mathbf{H} = -\text{grad } \phi_m.$$

Outside a permanent magnet  $\mathbf{M} = 0$ , because of that magnetic scalar potential satisfies Laplace's equation,

$$(9) \quad \Delta \phi_{m0} = 0,$$

and magnetic field vector is

$$(10) \quad \mathbf{H}_0 = -\text{grad } \phi_{m0}.$$

The third method, that is mentioned in the paper for magnetic field calculation is based on superposition of elementary results obtained for elementary magnetic dipoles.

Elementary magnetic dipole (Fig.2.) has magnetic moment

$$(11) \quad d\mathbf{m} = \mathbf{M} dV'.$$

This magnetic moment produces, at field point  $P$ , elementary magnetic scalar potential

$$(12) \quad d\phi_m = \frac{1}{4\pi} \frac{\mathbf{R} d\mathbf{m}}{R^3} = \frac{1}{4\pi} \frac{\mathbf{R}\mathbf{M}}{R^3} dV',$$

where  $\mathbf{R} = \mathbf{r} - \mathbf{r}'$  and

$R = |\mathbf{r} - \mathbf{r}'|$  is distance from the point where the magnetic field is being calculated to elementary source.

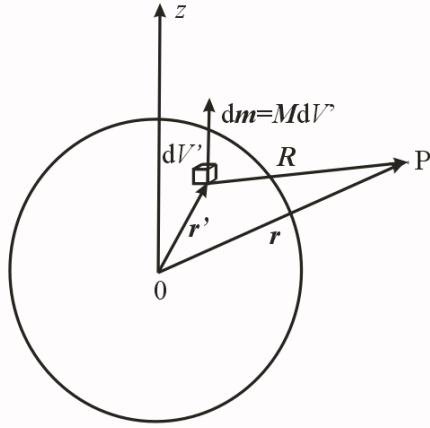


Fig.2. Elementary magnetic dipole

After integration magnetic scalar potential is obtained as

$$(13) \quad \varphi_m = \frac{1}{4\pi} \int_V \frac{\mathbf{R} \cdot d\mathbf{m}}{R^3} = \frac{1}{4\pi} \int_V \frac{\mathbf{R}\mathbf{M}}{R^3} dV'.$$

### Toroidal shaped permanent magnet with air gap

Toroidal shaped permanent magnet of rectangular cross section with air gap is considered. It is homogeneously magnetized in direction of angular component  $\theta$ ,

$$(14) \quad \mathbf{M} = M\hat{\theta},$$

where  $\theta$ ,  $r$  and  $z$  are cylindrical coordinates (Fig.3).

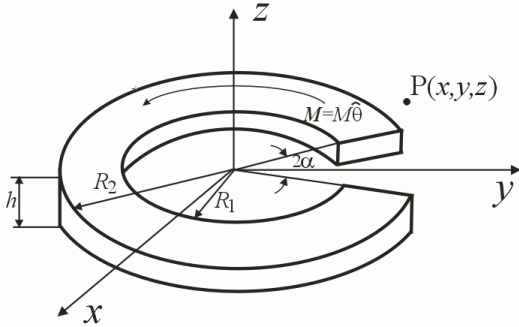


Fig.3. - Toroidal shaped permanent magnet

Dimensions of permanent magnet are  $h$ ,  $R_1$  and  $R_2$ .

Outside the permanent magnet, magnetic scalar potential, at field point  $P(x, y, z)$ , can be determined using superposition of results obtained for elementary magnetic dipoles, and it is presented in expression (13), where

$$(15) \quad R = |\mathbf{r} - \mathbf{r}'| = \sqrt{(x - x')^2 + (y - y')^2 + (z - z')^2},$$

$$(16) \quad \mathbf{R} = \mathbf{r} - \mathbf{r}' = (x - x')\hat{x} + (y - y')\hat{y} + (z - z')\hat{z}.$$

Relations between coordinates  $x$ ,  $y$ ,  $z$  and cylindrical coordinates are

$$(17) \quad x = r \cos \theta, \quad y = r \sin \theta, \quad \text{and} \quad z = z.$$

Using these relations, distance from the point where the magnetic field is being calculated to elementary source, can be presented as

$$(18) \quad R = \sqrt{r^2 + r'^2 - 2rr' \cos(\theta - \theta') + (z - z')^2}.$$

As magnetization has only angular component  $\theta$ , scalar product  $\mathbf{R}\mathbf{M}$  is obtained as

$$(19) \quad \mathbf{R}\mathbf{M} = [(x - x')\hat{x} + (y - y')\hat{y} + (z - z')\hat{z}]M\hat{\theta}.$$

Relation between unit vectors  $\hat{x}$ ,  $\hat{y}$ ,  $\hat{z}$  and  $\hat{\theta}$  is

$$(20) \quad \hat{\theta} = \frac{1}{r} \left( \frac{\partial x}{\partial \theta} \hat{x} + \frac{\partial y}{\partial \theta} \hat{y} + \frac{\partial z}{\partial \theta} \hat{z} \right),$$

and the following expressions are also satisfied

$$(21) \quad \hat{\theta}\hat{x} = \frac{1}{r} \frac{\partial x}{\partial \theta}, \quad \hat{\theta}\hat{y} = \frac{1}{r} \frac{\partial y}{\partial \theta}, \quad \hat{\theta}\hat{z} = \frac{1}{r} \frac{\partial z}{\partial \theta}.$$

Using relations (17) and (21), the following relations are obtained

$$(22) \quad \hat{\theta}\hat{x} = -\sin \theta, \quad \hat{\theta}\hat{y} = \cos \theta, \quad \hat{\theta}\hat{z} = 0,$$

and scalar product (19) can be presented as

$$(23) \quad \mathbf{R}\mathbf{M} = Mr' \sin(\theta - \theta').$$

Substituting expressions (18) and (23) in (13), magnetic scalar potential is obtained as

$$(24) \quad \varphi_m = \frac{1}{4\pi} \int_{R_1}^{R_2} \int_{\frac{h}{2}}^{\frac{h}{2} + 2\pi - \alpha} \int_{\alpha}^{2\pi - \alpha} \frac{Mr' \sin(\theta - \theta') dr' dz' d\theta'}{\left[ r^2 + r'^2 - 2rr' \cos(\theta - \theta') + (z - z')^2 \right]^{3/2}}$$

Solution of this integral is

$$(25) \quad \varphi_m = \frac{M}{4\pi r} \left[ R_2 \ln \frac{P_1 + C_1}{P_2 + C_2} \frac{P_2 + C_6}{P_1 + C_5} + R_1 \ln \frac{P_2 + C_4}{P_1 + C_3} \frac{P_1 + C_7}{P_2 + C_8} + P_3 \ln \frac{P_1 + C_1}{P_1 + C_3} \frac{P_2 + C_2}{P_2 + C_4} + P_1 \ln \frac{R_2 - P_3 + C_1}{R_1 - P_3 + C_3} \frac{R_1 - P_4 + C_7}{R_2 - P_4 + C_5} + P_4 \ln \frac{P_1 + C_5}{P_1 + C_7} \frac{P_2 + C_8}{P_2 + C_6} + P_2 \ln \frac{R_1 - P_3 + C_4}{R_2 - P_3 + C_2} \frac{R_2 - P_4 + C_6}{R_1 - P_4 + C_8} + 2|P_5| \left( \text{Arctg} \frac{R_1 - P_3 + C_3 + P_1}{|P_5|} - \text{Arctg} \frac{R_2 - P_3 + C_1 + P_1}{|P_5|} + \text{Arctg} \frac{R_2 - P_3 + C_2 + P_2}{|P_5|} \right) \right]$$

$$\begin{aligned}
& - \operatorname{Arctg} \frac{R_1 - P_3 + C_4 + P_2}{|P_5|} \Big) - \\
& 2|P_6| \left( \operatorname{Arctg} \frac{R_1 - P_4 + C_7 + P_1}{|P_6|} - \right. \\
& \operatorname{Arctg} \frac{R_2 - P_4 + C_5 + P_1}{|P_6|} - \operatorname{Arctg} \frac{R_1 - P_4 + C_8 + P_2}{|P_6|} \\
& \left. + \operatorname{Arctg} \frac{R_2 - P_4 + C_6 + P_2}{|P_6|} \right) \Big]
\end{aligned}$$

where  $P_1 = z + \frac{h}{2}$ ,  $P_2 = z - \frac{h}{2}$ ,

$$P_3 = r \cos(\theta + \alpha), P_4 = r \cos(\theta - \alpha),$$

$$P_5 = r \sin(\theta + \alpha), P_6 = r \sin(\theta - \alpha),$$

$$C_1 = \sqrt{r^2 + R_2^2 - 2rR_2 \cos(\theta + \alpha) + \left(z + \frac{h}{2}\right)^2}$$

$$C_2 = \sqrt{r^2 + R_2^2 - 2rR_2 \cos(\theta + \alpha) + \left(z - \frac{h}{2}\right)^2}$$

$$C_3 = \sqrt{r^2 + R_1^2 - 2rR_1 \cos(\theta + \alpha) + \left(z + \frac{h}{2}\right)^2}$$

$$C_4 = \sqrt{r^2 + R_1^2 - 2rR_1 \cos(\theta + \alpha) + \left(z - \frac{h}{2}\right)^2}$$

$$C_5 = \sqrt{r^2 + R_2^2 - 2rR_2 \cos(\theta - \alpha) + \left(z + \frac{h}{2}\right)^2}$$

$$C_6 = \sqrt{r^2 + R_2^2 - 2rR_2 \cos(\theta - \alpha) + \left(z - \frac{h}{2}\right)^2}$$

$$C_7 = \sqrt{r^2 + R_1^2 - 2rR_1 \cos(\theta - \alpha) + \left(z + \frac{h}{2}\right)^2}$$

$$C_8 = \sqrt{r^2 + R_1^2 - 2rR_1 \cos(\theta - \alpha) + \left(z - \frac{h}{2}\right)^2}$$

Components of magnetic field vector  $\mathbf{H}$ , in  $z=0$  plane, are

$$(26) \quad H_r = -\frac{\partial \varphi_m(r, \theta)}{\partial r} \quad \text{and} \quad H_\theta = -\frac{\partial \varphi_m(r, \theta)}{r \partial \theta}.$$

Magnetic field lines in the air gap, for dimension of torus,  $\alpha = \pi/36$ ,  $R_1/h=7$  and  $R_2/h=8$ , are shown in the Fig.4.

Distribution of magnetic field in the air gap, when it is very thin, for the following dimension of the torus,

$\alpha = \pi/90$ ,  $R_1/h=7$  and  $R_2/h=15/2$ , are presented in the Fig.5.

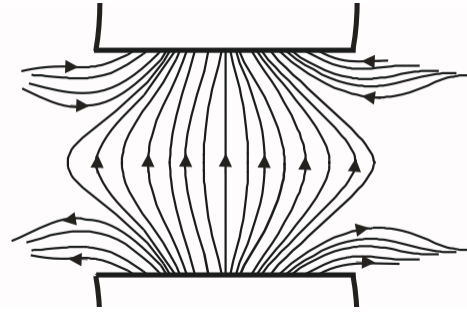


Fig.4. – Distribution of magnetic field in air gap

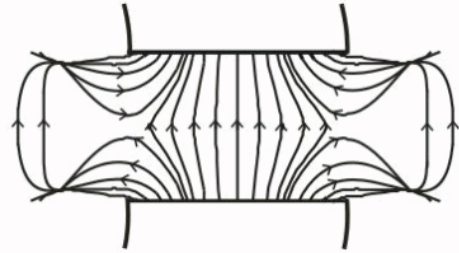


Fig.5. – Distribution of magnetic field in air gap

### Rod shaped permanent magnet

For calculation the magnetic field of rod shaped permanent magnet the method based on determining distribution of microscopic Ampere's current is used.

Parallelepiped shaped permanent magnet of length  $l$  and dimensions of cross-section  $a$  and  $b$  is considered (Fig.6.). It is homogeneously magnetised in direction of  $z$  axis,

$$(27) \quad \mathbf{M} = M\hat{\mathbf{z}}.$$

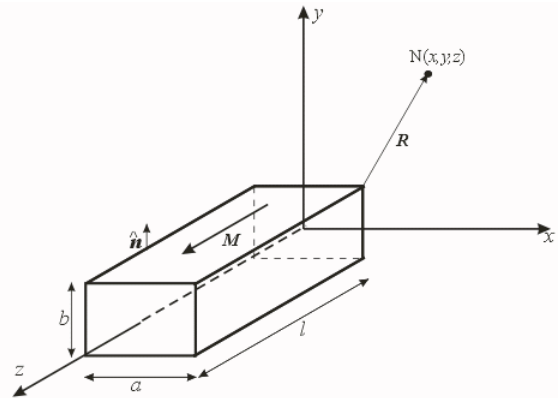


Fig.6. Parallelepiped shaped permanent magnet

Magnetization is uniform, so  $\mathbf{J}_a = \operatorname{rot} \mathbf{M} = 0$ , and only surface microscopic current of intensity  $\mathbf{J}_{sa} = \mathbf{M}$  exists on the rod cover, following in angular direction. Because of this, permanent magnet behaves as a thin, one layer uniformly wound solenoid coil.

This current produces magnetic vector potential

$$(28) \quad \mathbf{A}(\mathbf{r}) = \frac{\mu_0}{4\pi} \oint \frac{\mathbf{M} \times \hat{\mathbf{n}}}{R} dS',$$

where the distance from the point where the magnetic field is being calculated to elementary source has the form that is shown in expression (15).

Magnetic vector potential has the following form

(29)

$$\mathbf{A} = \frac{\mu_0}{4\pi} M \left[ \int_{-\frac{a}{2}}^{\frac{a}{2}} \int_0^l \frac{dx' dz'}{\sqrt{(x-x')^2 + \left(y + \frac{b}{2}\right)^2 + (z-z')^2}} - \int_{-\frac{a}{2}}^{\frac{a}{2}} \int_0^l \frac{dx' dz'}{\sqrt{(x-x')^2 + \left(y - \frac{b}{2}\right)^2 + (z-z')^2}} \right] \hat{\mathbf{x}} + \frac{\mu_0}{4\pi} M \left[ \int_{-\frac{b}{2}}^{\frac{b}{2}} \int_0^l \frac{dy' dz'}{\sqrt{\left(x - \frac{a}{2}\right)^2 + (y-y')^2 + (z-z')^2}} - \int_{-\frac{b}{2}}^{\frac{b}{2}} \int_0^l \frac{dy' dz'}{\sqrt{\left(x + \frac{a}{2}\right)^2 + (y-y')^2 + (z-z')^2}} \right] \hat{\mathbf{y}},$$

so,

$$(30) \quad \mathbf{A}(x, y, z) = A_x \hat{\mathbf{x}} + A_y \hat{\mathbf{y}},$$

where components of magnetic vector potential have the following form

$$(31) \quad A_x(x, y, z) = \frac{\mu_0}{4\pi} M (P(y+g, x+d, x-d, z, z-l) - P(y-g, x+d, x-d, z, z-l)), \text{ and}$$

$$(32) \quad A_y(x, y, z) = \frac{\mu_0}{4\pi} M (P(x-d, z, z-l, y+g, y-g) - P(x+d, z, z-l, y+g, y-g)),$$

where  $d = \frac{a}{2}$  and  $g = \frac{b}{2}$ .

These components can be presented using integral

$$(33) \quad P(a, x_1, x_2, y_1, y_2) = \int_{x_1}^{x_2} \int_{y_1}^{y_2} \frac{dx dy}{\sqrt{a^2 + x^2 + y^2}}.$$

Solution of this integral is

(34)

$$P(a, x_1, x_2, y_1, y_2) = x_2 \ln \frac{y_2 + R_1}{y_1 + R_3} + x_1 \ln \frac{y_1 + R_2}{y_2 + R_4} + y_1 \ln \frac{x_1 + R_2}{x_2 + R_3} + y_2 \ln \frac{x_2 + R_1}{x_1 + R_4} - 2|a| \text{Arctg} \frac{|a|(x_2 - x_1 + R_3 - R_2)}{\left((x_1 + R_2)(x_2 + R_3) + a^2 + y_1^2\right) + y_1 C_1} + 2|a| \text{Arctg} \frac{|a|(x_2 - x_1 + R_1 - R_4)}{\left((x_1 + R_4)(x_2 + R_1) + a^2 + y_2^2\right) + y_2 C_2},$$

where

$$R_1 = \sqrt{a^2 + x_2^2 + y_2^2}, \quad R_2 = \sqrt{a^2 + x_1^2 + y_1^2},$$

$$R_3 = \sqrt{a^2 + x_2^2 + y_1^2}, \quad R_4 = \sqrt{a^2 + x_1^2 + y_2^2}$$

$$C_1 = x_1 + x_2 + R_2 + R_3, \quad C_2 = x_1 + x_2 + R_1 + R_4.$$

When the magnetic vector potential is calculated, magnetic flux density can be determined as

$$(35) \quad \mathbf{B} = B_x \hat{\mathbf{x}} + B_y \hat{\mathbf{y}} + B_z \hat{\mathbf{z}},$$

where

$$(36) \quad B_x(x, y, z) = -\frac{\partial A_y(x, y, z)}{\partial z},$$

$$B_y(x, y, z) = \frac{\partial A_x(x, y, z)}{\partial z},$$

$$B_z(x, y, z) = \frac{\partial A_y(x, y, z)}{\partial x} - \frac{\partial A_x(x, y, z)}{\partial y}.$$

Magnetic field inside and outside the permanent magnet can be determined using expressions (5) and (6).

Parallelepiped shaped permanent magnet which cross-section dimensions are  $a$  and  $b = 2a$  and length  $l = 4a$  is considered.

The distribution of magnetic field is presented in  $xOz$  plane (Fig.7.) and in  $yOz$  plane (Fig.8.)

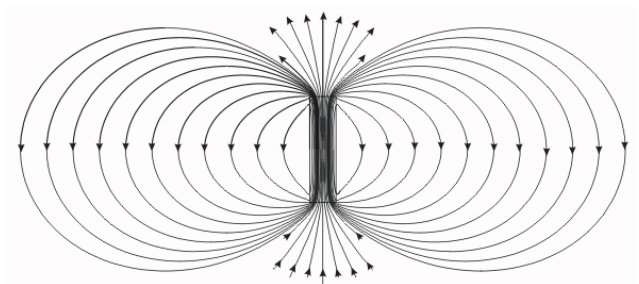


Fig.7. Distribution of magnetic field in  $xOz$  plane

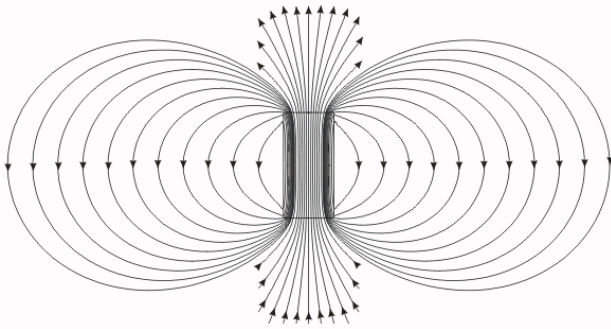


Fig.8. Distribution of magnetic field in  $y_0z$  plane

Enlarged figure of magnetic field lines inside the magnet is shown in the Fig.9.

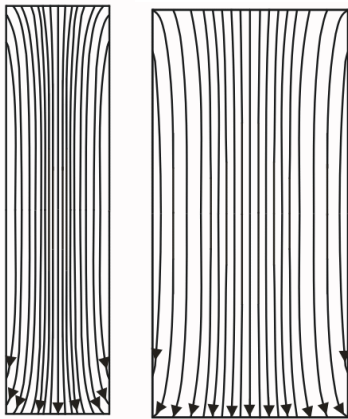


Fig.9. Distribution of the magnetic field inside the rod in the  $x_0z$  and  $y_0z$  plane

Magnetic flux density lines have the same direction as magnetization lines and the opposite direction of magnetic field lines inside the magnet and the same direction as magnetic field lines outside the magnet.

### Conclusion

The paper presents two different methods for determination the magnetic field in surroundings of permanent magnets. It contains calculation the magnetic field of the toroidal shaped permanent magnet with air gap, homogeneously magnetised in direction of angular component.

Method that is used for this determination is based on a system of equivalent magnetic dipoles. The second method that is explained is based on determining distribution of microscopic Ampere's current and on calculation the magnetic vector potential. It is applied for determination the magnetic field of the rod shaped permanent magnet which is homogeneously magnetised in axial direction. The distribution of magnetic field of both permanent magnets are also shown in the paper.

### References

- [1] Textbook of Electromagnetics, Edited by Hermann Uhlmann (Veličković D. M., Chapter 3.2: Magnetostatic field), Technische Universitaet Ilmenau/De (To be published).
- [2] A. N. Mladenović, S. R. Aleksić: Stalni magnet oblika štapa, 48. Konferencija ETRAN 2004, Čačak, 6-11 jun, Zbornik radova, pp. 233-236.
- [3] A. N. Mladenović: Toroidal shaped permanent magnet, International PhD-Seminar, Budva, September 23-28<sup>th</sup> 2004, Proceedings of Full Papers, pp.125-130.
- [4] A. N. Mladenović: Proračun polja stalnog magneta oblika torusa, 49. Konferencija ETRAN 2005, 5-10. jun.
- [5] A. N. Mladenović, Slavoljub R. Aleksić: Toroidal shaped permanent magnet with air gap, International Conference on Applied Electromagnetics PES2005, Niš 23<sup>rd</sup>-25<sup>th</sup> May 2005, Proceedings of Extended Abstracts, pp. 23-24.
- [6] D. M. Veličković: Elektromagnetika-prva sveska, II izdanje, 1999.

*Ana N. Mladenović* – M.Sc. Student, University of Niš, Faculty of Electronic Engineering, Aleksandra Medvedeva 14, 18000 Niš, Serbia&Montenegro

e-mail: [anam@elfak.ni.ac.yu](mailto:anam@elfak.ni.ac.yu)

*Slavoljub R. Aleksić* – Associate Professor, Dr., University of Niš, Faculty of Electronic Engineering, Aleksandra Medvedeva 14, 18000 Niš,

Serbia&Montenegro, e-mail: [as@elfak.ni.ac.yu](mailto:as@elfak.ni.ac.yu)

# Maximum energy flow problem through power systems under interval uncertainties

Georgi Sapundjiev, Simona Petrakieva

**Abstract:** The present paper addresses the maximum energy flow problem through power systems under interval uncertainties. The main problem, which arises in the two basic models of control power systems: single source – multiple recipients and multiple sources – multiple recipients, consists of obtaining the maximum energy flow through the system considered. It can be solved using the graph theory and transforming the original models to the basic graph model with single source – single recipient. A new interval technique for obtaining the maximum energy flow in arbitrary system using interval channel capacities is suggested. The associated procedures have simple realization and take a small volume of computation and time resources. Numerical example of power system with single source and multiple recipients is solved.

**Keywords:** maximum flow problem under interval uncertainties, graph theory

## 1. Introduction

The models, based on the graph theory [1], can be successfully used about flows control in the power systems.

The vertexes and the arcs of the graph model  $G = \langle V, L \rangle$  correspond to the elements  $V_i$  and the connection channels  $L_{ij} = (V_i \rightarrow V_j)$  of the power system considered, respectively. The energy interaction between the elements  $V_i$  and  $V_j$  of the system has exactly direction (“from  $\rightarrow$  to” or “to  $\leftarrow$  from” (fig. 1).

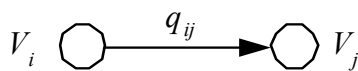


Fig. 1

Let the capacity and the flow, passed through the connection channel  $L_{ij} = (V_i \rightarrow V_j)$  are  $q_{ij}$  and  $f_{ij} = f(V_i, V_j)$ , respectively [2]. The topological analysis of the energy flows  $f_{ij}$  based on the following three assumptions, defined in [3]:

- energy balance condition;
- condition for sequencing the flow  $f_{ij} = f(V_i, V_j)$  to the capacity  $q_{ij}$  of the channel;

- condition for the invariability of the flow  $f_{ij}$  through the connection channel.

## 2. Problem statement

In analysis and optimization of the power systems the final graph model can be presented in the following two types:

- $G_1 = G [1 \rightarrow N_r]$  one source – multiple recipients ( $N_r$ );
- $G_2 = G [N_s \rightarrow N_r]$  multiple sources ( $N_s$ ) – multiple recipients.

In this paper, the basic aims are following:

- 1) to suggest an approach for transforming the graph model of type  $G_1$  or type  $G_2$  in model of type  $G = G [1 \rightarrow 1]$ ;
- 2) to suggest an algorithm for obtaining the maximum energy flow when the graph model is of type one source – multiple recipients (the most often case in practice). Thus the following two problems arise:
  - **Problem 1:** Find the maximum flow passed through the system considered when the capacities  $q_{ij}$  of the connection channels are exactly determinate;
  - **Problem 2:** Find the maximum flow passed through the system considered when the capacities of the connection channels are independent intervals  $q_{ij} = [q_{ij}^-, q_{ij}^+]$ .

Note: Throughout the paper, bold face letters will be used to denote interval quantities while ordinary letters will stand for their non-interval counterparts.

## 3. Solving the maximum flow problem in power systems

### 3.1. Transforming the graph model of type $G_1$ (resp. $G_2$ ) to model of type $G$

The solution of the Problem 1 can be determined in the following way.

1. We introduce *unreal* recipient  $\mathbf{V}_{rec}$ .
2. We assume that  $\mathbf{V}_{rec}$  is connected to all *real* recipients  $V_{rec} = \{V_{i,rec}\}, i = \overline{1, N_r}$  with unreal channels  $\mathbf{L}_{i,rec} (i = \overline{1, N_r})$  (фиг.2).



3. We assume that all channels  $\forall \mathbf{L}_{i,rec}$  ( $i = \overline{1, N_r}$ ) have the capacities  $q_{i,rec} = \infty$ .

Thus, the model of type  $G_1$  transforms to model of type  $G$ .

*Note: The transformation of the model  $G_2$  is analogous. Then we introduce an unreal source  $\mathbf{V}_{src}$ , which is connected to all of  $N_s$  real sources with unreal channels  $\mathbf{L}_{src,j}$  ( $j = \overline{1, N_s}$ ) with infinite capacities.*

In the present paper, a new approach for transformation the graph model  $G_1$  (resp.  $G_2$ ) to model of type  $G$  is suggested. It consists of obtaining the channel capacities  $q_{i,rec}$ , because using the condition  $q_{i,rec} = \infty$ , we have a lot of difficulties in solving the maximum flow problem in power systems.

It supposed that the capacities of the unreal channels obtain from the following condition:

$$(1) \quad \mathbf{q}_{i,rec} = \sum_{\mathbf{L}(rec)} q_{ki},$$

where -  $\mathbf{L}(rec)$  is the input arcs set to the vertexes, which are beginnings of the unreal channels  $\mathbf{L}_{i,rec}$  ( $i = \overline{1, N_r}$ ).

Throughout the paper, we will consider the model of type  $G$ , which is transformation of the model of type  $G_1$  (фиг. 2).

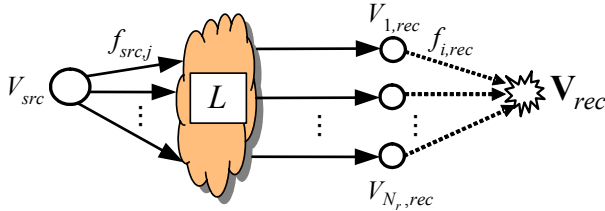


Fig. 2

The input energy flow  $f_{in} = f(V_{src})$  can be considered as flow generated from the vertex  $V_{src}$ , while the output flow  $-f_{out} = f(\mathbf{V}_{rec})$ , can be examined as flow absorbed in the vertex  $\mathbf{V}_{rec}$ . It is assumed that the flow is not changing passing through the intermediate vertexes.

*Note: For notational simplicity, we will use the terms graph arcs and vertexes instead of connection channels and system components.*

### 3.2. Determinate algorithm solving the Problem 1

It considers the case when the capacities of graph arcs take exact values.

The algorithm consists of the following 3 procedures.

1. We determine the graph model  $G_1 = G [1 \rightarrow N_r]$  of the energy system considered.

2. The model  $G_1$  transforms to the model of type  $G = G [1 \rightarrow 1]$ .

3. Based on the algorithm, proposed in [4], we find the maximum flow  $f_{\Sigma}^{\max}$

$$f_{\Sigma}^{\max} = \max_{V_i \in V'} \sum f(V_{src}, V_i) = \max_{V_s \in V'} \sum f(V_s, \mathbf{V}_{rec}),$$

as follows:

3.1. We obtain the marks  $M(V_i) = \{M_1(V_i), M_2(V_i)\}$ , corresponding the graph vertexes (passing the graph from source vertex to recipient vertex), as follows:

$$(2) \quad M_1(V_i) = \pm V_k,$$

( $V_k$  is the vertex, which transmits the energy to the vertex  $V_i$  through the arc  $\langle V_k, V_i \rangle$ , while the symbols “+” and “-” are fixed with respect to the possibility of increasing (+) or decreasing (-) of the flow through the arc  $\langle V_k, V_i \rangle$ )

$$(3) \quad M_2(V_i) = f_{add}(V_i),$$

where  $f_{add}(V_i)$  is the value of the additional flow from source vertex  $V_{src}$  to the vertex  $V_i$  through the set of arcs, where the flow increase as follows:

$$(4) \quad \begin{cases} f_{add}(V_i) = \min\{f_{add}(V_k), q_{ki} - f(V_k, V_i)\}, & \text{if } f(V_k, V_i) < q_{ki} \\ f_{add}(V_i) = \min\{f_{add}(V_k), f(V_k, V_i)\}, & \text{if } f(V_k, V_i) \geq q_{ki} \end{cases}$$

3.2. We correct the flow, passing through the graph arcs from recipient vertex  $\mathbf{V}_{rec}$  to source vertex  $V_{src}$ .

### 3.3. Interval algorithm solving the Problem 2

In real energy systems the channel parameters cannot be exactly determined. Therefore the capacities  $q_{ij}$  of the channels cannot be considered as certain quantities and each parameter take on his exact value  $q_{ij}$  within prescribed interval  $q_{ij}$ . Thus, in the paper we will consider the case when the capacities of graph arcs are independent intervals.

The algorithm for determining the maximum flow  $f_{\Sigma}^{\max}$  consists of three procedures – one initial and two iterative procedures.

Procedure 1 Determining the system graph model

1.1. We determine the transformed graph model  $G = \langle V, L \rangle$  and the interval capacities  $\mathbf{q}_{ij}$  of the channels, which are presented in the following way:

$$(5) \quad \mathbf{q}_{ij} = [q_{ij}^-, q_{ij}^+] = \{q_{ij} : q_{ij} \in q_{ij}^- \leq x \leq q_{ij}^+\},$$

where:  $q_{ij}^-$  is the left bound of the intervals  $\mathbf{q}_{ij}$ ;  
 $q_{ij}^+$  is the right bound of the intervals  $\mathbf{q}_{ij}$ .

1.2. We find the capacities of the unreal channels using (1) which modify as follows:

$$\mathbf{q}_{i,rec} = \left[ \sum_{L(rec)} q_{ij}^-, \sum_{L(rec)} q_{ij}^+ \right].$$

1.3. We assume the all energy flows are zero, i.e.  $f_{is} = f(V_i, V_s) = 0$ .

Procedure 2 Marks of the vertexes

2.1. We set a zero initial marks to all of graph vertexes, i.e.  $M(V_i) = \{0, 0\}$ .

2.2. The source vertex  $V_{src}$  gets an initial mark  $M(V_{src}) = \{V_{src}, \infty\}$ , which is constant until we find the problem solution. Its mark coefficient is  $M_2(V_{src}) = \infty$ , because, in general, the quality of generalized energy from  $V_{src}$  is infinitely.

2.3. We determine the type of each of graph vertex  $V_i$ :

- $V_i$  is not marked;
- $V_i$  is marked, but it is not verified, i.e. the vertexes connected to  $V_i$  with unique arc are not determined and not marked;
- $V_i$  is marked and verified, i.e. the mark coefficients  $M_1(V_i)$  and  $M_2(V_i)$  are found.

2.4. We obtain the vertexes mark coefficient from (4) and consider (5), as follows:

$$(6) \quad \begin{cases} f_{add}(V_i) = \min \{f_{add}(V_r), q_{ri}^- - f(V_r, V_i)\}, \\ \text{if } f(V_r, V_i) < q_{ri}^- \\ f_{add}(V_i) = \min \{f_{add}(V_r), f(V_r, V_i)\}, \\ \text{if } f(V_r, V_i) \geq q_{ri}^+ \end{cases}$$

and observe the following conditions:

- we pass from  $V_i$  to  $V_{i+1}$  only if  $V_i$  is marked;

- we assume that the vertexes  $V_i$  and  $V_s$  are not connected, if their respective arc  $L_{is} = \langle V_i, V_s \rangle$  satisfies the condition

$$(7) \quad f(V_i, V_s) = q^-(V_i, V_s) = q_{is}^-,$$

i.e. this arc is *saturated*.

2.5. We determine the vertexes marks based on the following conditions:

- if for  $V_\alpha$  and  $V_\beta$  is satisfied  $M_2(V_\alpha) = M_2(V_\beta)$ ,

then we choose:

$$(8) \quad \begin{cases} \text{the arc } L_{i\alpha}, \text{ if } q_{i\alpha} \leq q_{j\beta}; \\ \text{the arc } L_{j\beta}, \text{ if } q_{i\alpha} > q_{j\beta}; \\ \text{the vertex } V_i, \text{ if } q_{i\alpha} = q_{j\beta} \text{ and } i < j. \end{cases}$$

• if we can reach the vertex  $V_\gamma$  from the both vertexes  $V_\alpha$  and  $V_\beta$ , then we choose:

$$(9) \quad \begin{cases} \text{the arc } L_{\alpha\gamma}, \text{ if } M_2(V_\alpha) \leq M_2(V_\beta); \\ \text{the arc } L_{\beta\gamma}, \text{ if } M_2(V_\alpha) > M_2(V_\beta). \end{cases}$$

2.6. Then, all graph vertexes are marked and we go to the Procedure 3.

Procedure 3 Energy flow correction

3.1. We choose the recipient vertex  $V_{rec}$  as a *basis*.

3.2. We determine the value  $f_{add}(V_{rec})$ , which is the correction of the energy flow:

$$(10) \quad f_{add}(V_{rec}) = M_2(V_{rec}).$$

3.3. We obtain the set of arcs  $\langle V_{rec}, V_s \rangle \rightarrow \langle V_s, V_j \rangle \rightarrow \dots \rightarrow \langle V_i, V_{src} \rangle$ , connecting in series all marked vertexes from  $V_{rec}$  to  $V_{src}$ .

3.4. We correct the flows through these arcs by the condition:

$$(11) \quad \begin{cases} f^{cor}(V_i, V_s) = f(V_i, V_s) + f_{add}(V_{rec}), \\ \text{if } M(V_s) = \{+V_i, f_{add}(V_s)\} \\ f^{cor}(V_i, V_s) = f(V_i, V_s) - f_{add}(V_{rec}), \\ \text{if } M(V_s) = \{-V_i, f_{add}(V_s)\} \end{cases}$$

3.5. If we reach the source vertex  $V_{src}$  all marks take zero values, i.e.  $\forall M(V_i) = \{0, 0\}$  and save the energy flow values determined by (11).

*Note: The saturated arcs are not considered in the next iterations and the associated energy flow values are constant until the maximum flow  $f_\Sigma^{\max}$  is obtained.*

3.6. If all arcs inputting to the vertex  $V_{rec}$  are saturated, the maximum flow  $f_{\Sigma}^{\max}$  is found. Otherwise, we go to Procedure 2.

#### 4. Numerical example

The applicability of the method suggested will be illustrated by the following example of energy system with one real source  $V_{src}$  and two real recipients -  $V_6$  and  $V_7$ . The graph model is shown on fig. 3a. The intervals of the channels capacities  $q_{is} = [q_{is}^-, q_{is}^+]$  are noted under the arcs, while the associated current flow passed through the arcs is written above the arcs and it is underlined. The vertexes marks are noted in square brackets near the associated vertexes for the current iteration. They are calculated by (2) and (3) taking in mind conditions (8) and (9).

The initial vertexes marks and zero values of the energy flows  $f(V_i, V_s) = 0, \forall \langle V_i, V_s \rangle \in L$  are given in fig. 3b.

*Note: We will discuss only one iteration (fig. 3b), because it is not necessary to describe the same operations repeatedly.*

##### Iteration 1 (fig. 3b)

##### ➤ vertexes mark:

We mark the source vertex  $V_{src}$  with

$$M(V_{src}) = \{V_{src}, \infty\}.$$

The direct connection vertexes with  $V_{src}$  are  $V_1$  and  $V_2$ . They get the following marks:

$$\begin{cases} V_1 \rightarrow M = \{+V_{src}, 14\}, \text{ because } M_2 = \min\{\infty, 14-0\} = 14; \\ V_2 \rightarrow M = \{+V_{src}, 12\}, \text{ because } M_2 = \min\{\infty, 12-0\} = 12. \end{cases}$$

Therefore the vertex  $V_{src}$  is marked and verified.

Then we go to the next number marked, but unverified, vertex  $V_1$ . We determine the marks of the vertexes  $V_2, V_3$  and  $V_4$ , which are direct connected with  $V_1$ :

$$\begin{cases} V_2 \rightarrow M = \{+V_1, 8\}, \text{ because } M_2 = \min\{14, 9-0\} = 9 \\ V_3 \rightarrow M = \{+V_1, 7\}, \text{ because } M_2 = \min\{14, 7-0\} = 7 \\ V_4 \rightarrow M = \{+V_1, 12\}, \text{ because } M_2 = \min\{14, 12-0\} = 12 \end{cases}.$$

We correct the mark of the vertex  $V_2 \rightarrow M \{+V_{src}, 12\}$  based on (9) and it gets the following mark  $M \{+V_1, 8\}$ . Then we correct the marks

of the other vertexes ( $V_4$  and etc.) following the same way. Thus, the vertex  $V_1$  is marked and verified. The final vertexes marks in this stage of Iteration 1 are:

$$\begin{cases} V_{src} \rightarrow M = \{+V_{src}, \infty\} \\ V_1 \rightarrow M = \{+V_{src}, 14\} \\ V_2 \rightarrow M = \{+V_1, 9\} \\ V_3 \rightarrow M = \{+V_1, 7\} \\ V_4 \rightarrow M = \{+V_3, 6\} \\ V_5 \rightarrow M = \{+V_3, 4\} \\ V_6 \rightarrow M = \{+V_5, 4\} \\ V_7 \rightarrow M = \{+V_5, 4\} \\ V_{rec} \rightarrow M = \{+V_7, 4\} \end{cases}$$

Hence, all vertexes are marked and verified.

##### ➤ flows correction:

The vertex  $V_{rec}$  is basic.

First, we find the additional flow, using (4)

$$f_{add}(V_{rec}) = M_2(V_{rec}) = 4.$$

Second, we obtain the arcs set

$$\begin{aligned} \langle V_{rec}, V_7 \rangle \rightarrow \langle V_7, V_5 \rangle \rightarrow \langle V_5, V_3 \rangle \rightarrow \\ \rightarrow \langle V_3, V_1 \rangle \rightarrow \langle V_1, V_{src} \rangle \end{aligned}$$

based on the first mark coefficients  $M_1(V_i)$  of the associated vertexes.

Third, we determine the correction values of the energy flows through the arcs from the above set by (11), as follows:

$$\begin{aligned} f(V_7, V_{rec}) = f(V_5, V_7) = f(V_3, V_5) = f(V_1, V_3) = \\ = f(V_{src}, V_1) = 0 + f_{add}(V_{rec}) = 4 \end{aligned}$$

It is obvious that the condition  $f(V_3, V_5) = q_{35}^- = 4$  is satisfied for the arc  $\langle V_3, V_5 \rangle$ . Hence, it is saturated and it marks with bold arrow.

We go to the next iteration, because the arcs are not saturated.

After the last iteration (fig. 3c) the maximum flow is obtained as follows:

- from  $V_{src}$  to  $V_6$   $f_{\Sigma(V_{src} \rightarrow V_6)}^{\max} = 10$ ;
- from  $V_{src}$  to  $V_7$   $f_{\Sigma(V_{src} \rightarrow V_7)}^{\max} = 13$ .

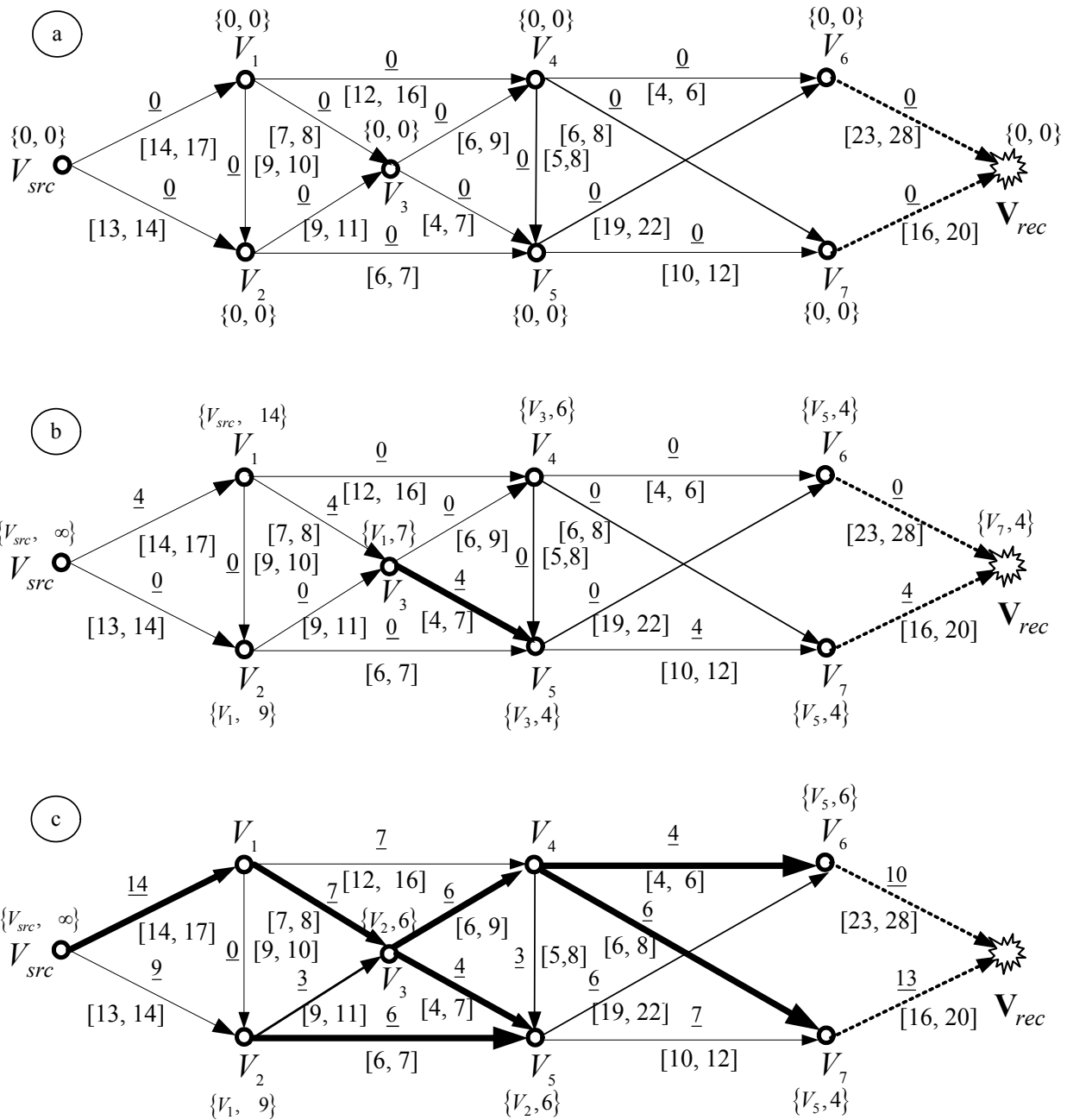


Fig. 3

#### 4. Conclusion

The interval algorithm suggested is universal. It can be applied for analysis of the power systems with two types models -  $G_1 = G [1 \rightarrow N_r]$  or  $G_2 = G [N_s \rightarrow N_r]$ , because these models transformed to the basic model of type *one source – one recipient*.

Obtaining of the maximum flow  $f_{\Sigma}^{\max}$ , based on the topology of the power system considered and the flows

distributing in it, is very important for optimal control of energy resources. Consider the interval uncertainties in the capacities of the connection channels in the power system the analysis is more precise and the energy losses are reduced to minimum.

The interval algorithm suggested can be expanded and applied for analysis of information and industrial systems, described by the graph theory models and interval uncertainties in the system parameters, which will be reported in future publications.

## References

- [1] Зыков, А., Основы теории графов, Москва, Наука, 1997.
- [2] Burch, J. , Grudnitski. Information system. Theory and Practice. N.Y., J.Wiley & Sohn, 1997.
- [3] Сапунджиев, Г., Топологичен анализ на информационни потоци – Сборник XIII Национален научен симпозиум с международно участие “Метрология и метрологично осигуряване - 2003 ” Созопол, 2003, стр.280-284.
- [4] Сапунджиев, Г., Оптимизация на потоци в промишлени системи. Сборник с доклади от VII Научна конференция с международно участие ЕМФ 2002 , Варна 2002, стр. 85-88.

---

**Georgi Sapundjiev** – Associate Professor, Dr., Faculty of Automatica, Technical University of Sofia, 8 Kl. Ohridski Str., 1000 Sofia, BULGARIA.  
e-mail: gensap@tu-sofia.bg.

**Simona Petrakieva** – Assistant Professor, Dr., Faculty of Automatica, Technical University of Sofia, 8 Kl. Ohridski Str., 1000 Sofia, BULGARIA.  
e-mail: petrakievas-te@tu-sofia.bg.

## Electric Field Strength and Potential Determination in Dielectric Body with Cavity

Slavoljub R. Aleksić, Zlata Ž. Cvetković, Mirjana T. Perić and Bojana Z. Nikolić

**Abstract:** In this paper the calculation of electric field strength and potential in cylindrical dielectric body with cavity is presented. The cross-section of dielectric body can have an arbitrary, but known shape. The whole system is in the homogeneous transverse electrical field. These results, obtained by the program's package FEMM 4.0, are compared to the results obtained by method of fictitious sources.

**Keywords:** FEMM4.0, Method of fictitious sources.

### Introduction

In last few years there has been developed a large number of program's packages for solving problems in Electromagnetics. They make calculations easier and it is also a good way to confirm the results obtained by some analytical or numerical method. Some of those packages can be found on the Internet so they are available to a large number of users. First of all, these are student versions of the programs such as Quickfield and Maxwell, which have limited number of nodes (use the finite element method) so often they are not precise enough. On the other hand, there are full versions of more precise programs such as FEMM (version 4.0) developed by David Meeker.

In this paper program's package FEMM [1] is used in obtaining potential and electric field distribution in the cavity of dielectric body placed in homogeneous electrostatic field (Fig.1).

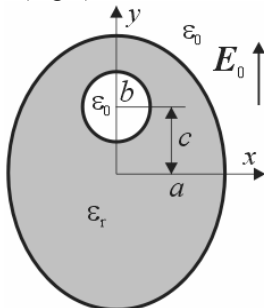


Fig.1. Dielectric body with cavity.

The cross-section of dielectric body can have an arbitrary, but known shape. Results shown in this paper are only part of research, which had been done at Technical University of Ilmenau, Germany [2]. These results are compared to the results obtained by method of fictitious sources. The problem of the calculation of potential distribution and electric field strength in the dielectric bodies with cavities is considered also before, at previous conferences [3], international meetings [4, 5] and magazine [6].

### Program package FEMM

Program's package FEMM (Finite Element Method Magnetics) has had many versions since 1998. The last one, version 4.0, comes up with combination of versions intended for solving electrostatic (BELA) and magnetostatic (FEMM) problems. It can be used for low-frequency 2D electromagnetic problems, axisymmetric problems, linear and non-linear electrostatic and magnetostatic problems, as well as for magnetic problems in time domain. This program's package is based on the finite element method.

### Method of fictitious sources

One of the mostly used methods for numerical electrostatic problems solving is Charge Simulation Method (CSM) or Method of fictitious sources (MFS) [6]. Basic idea of this method is replacing the existing electrodes by fictitious sources (FS), chosen in certain order and placed inside the electrodes volumes. The unknown intensities of FS are determined to satisfy boundary conditions on the electrode's surfaces. In that way, system of linear equations with FS as unknown values is formed,

$$(1) \quad \varphi(r) = \sum_j p_j(r) q_j,$$

where  $q_j$  represents the magnitude of the charge on the  $j^{\text{th}}$  distribution, and  $p_j(r)$  is a coefficient that depends only on the type of the distribution and the position of the point  $r$ . After solving this system, the unknown charges of the FS can be determined. Using standard electrostatic formulas the potential and the electric field strength can be calculated.

The correct choice of the type and the form of the FS is very important, especially with respect to the realized accuracy and convergence with the number of the FS [7]. Point charges (for three-dimensional systems), line charges with constant density per unit length (for plan-parallel systems) and linear circular loops (for systems with axial symmetry), can be mostly used for FS. Also, a very different and complex FS can be used depending on the problem geometry and on the experience of the investigator.

### Numerical results

#### Example 1

Dielectric body with circular cross-section and eccentric circular cavity is placed in vertical external electrostatic field,  $E_0 = E_0 \hat{y}$ . Intensity of the electric field is

$E_0 = 100 \text{ V/m}$ . Radius of the cavity is  $b = 25 \text{ mm}$ . Radius of the cross-section is  $a = 100 \text{ mm}$ . Eccentricity is  $c = 45 \text{ mm}$ . Centre of cylinder and centre of the cavity lie on  $y$ -axis, which makes an angle of  $90^\circ$  with axis of the system. Value of the permittivity of dielectric body is  $\epsilon_r = 3$ .

This system is symmetric, so only one half of the problem is considered. As the program's package FEMM can solve only the problems in closed system, it is necessary to define boundaries, which are far enough from the cylinder so they don't disturb the system. Mesh, which is applied, has 5729 nodes. A working surrounding with defined boundaries is presented in Fig.2. Mesh size in the cavity is 1, and in the dielectric body it is 2.

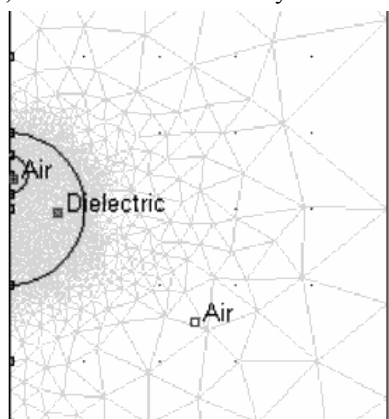


Fig.2. Circular cross-section of the dielectric body with eccentric circular cavity.

It is also necessary to define the boundary conditions. FEMM offers usage of Dirichlet's and Neumann's boundary conditions.

In Dirichlet's boundary conditions the magnetic or electric scalar potential is explicitly defined on the boundary. In this particular case on the vertical boundaries of the selected area, the condition  $dV/dn = 0$  is used. On the horizontal boundary in the bottom, the condition  $V = 0 \text{ V}$  is used, and on the top, it is  $V = -100 \text{ V}$ . Unit normal vector to the interface is marked as  $n$  and the potential is marked as  $V$ .

Neumann's boundary conditions refer to normal derivative of potential on the boundary area. In this particular case on the vertical boundaries, the condition  $dV/dn = 0$  is used. On the horizontal boundary in the bottom, the condition  $dV/dn = E_0 = 100 \text{ V/m}$  is used. The condition  $dV/dn = -E_0 = -100 \text{ V/m}$  is applied on the horizontal boundary on the top.

In Fig.3 a potential distribution with equipotential lines for case of dielectric cylinder with circle cross-section and Dirichlet's boundary conditions is presented.

Fig.4 and Fig.5 show electric field distribution with electric field intensity vector for case of dielectric cylinder with circle cross-section and Dirichlet's boundary conditions.

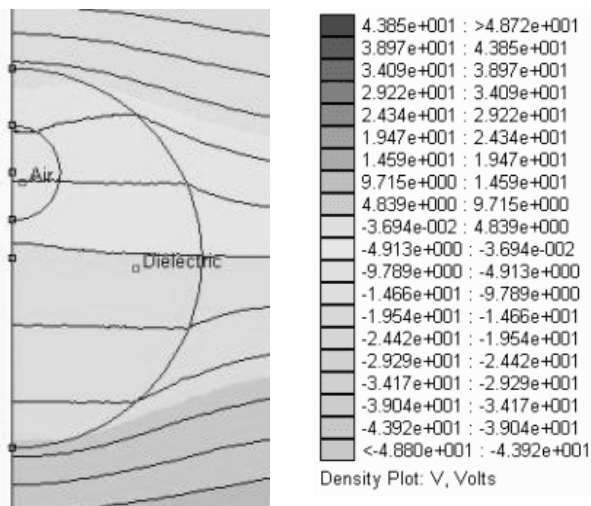


Fig.3. Potential distribution and equipotential lines (Dirichlet's boundary condition).

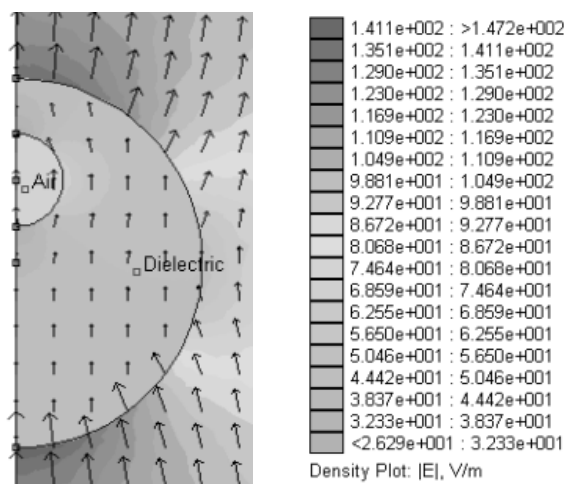


Fig.4. Electric field distribution and intensity vector (Dirichlet's boundary condition).

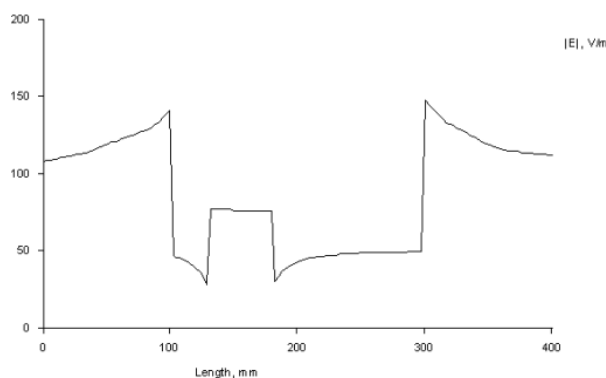


Fig.5. Magnitude of electric field intensity between points  $(0, -200 \text{ mm})$  and  $(0, 200 \text{ mm})$ .

Normalized values of the intensity of electric field in points  $(0, 0)$  and  $(0, -45 \text{ mm})$  are 0.4388 and 0.7829. These points are presented in Fig.5 as  $(0, 200 \text{ mm})$  and  $(0, 150 \text{ mm})$ , in the same order.

Normalization constant is value of homogeneous electric field 100V/m.

Usage of Neumann's boundary conditions gives similar values. Because of limited space, here will be presented only the potential distribution (Fig.6).

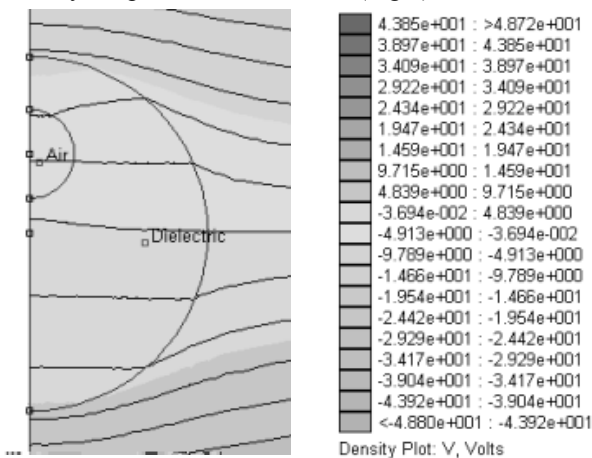


Fig.6. Potential distribution and equipotential lines (Neumann's boundary condition).

When the problem is considered as axisymmetric, obtained results are shown in Figs.7-9. In this case, Dirichlet's conditions are used on the boundaries of the selected area.

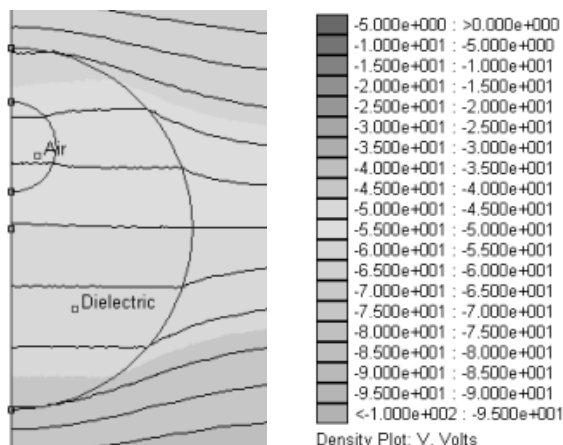


Fig.7. Potential distribution and equipotential lines (Dirichlet's boundary condition).

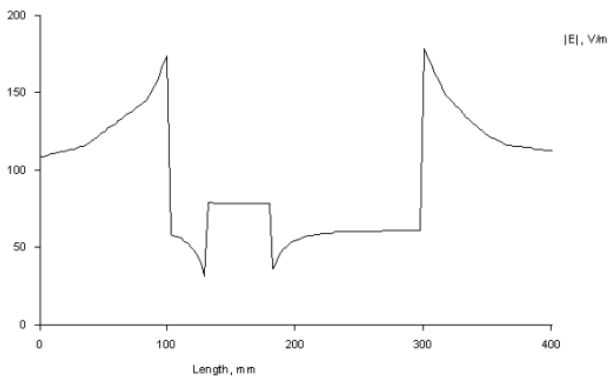


Fig.8. Magnitude of electric field intensity between points (0,-200mm) and (0,200mm).

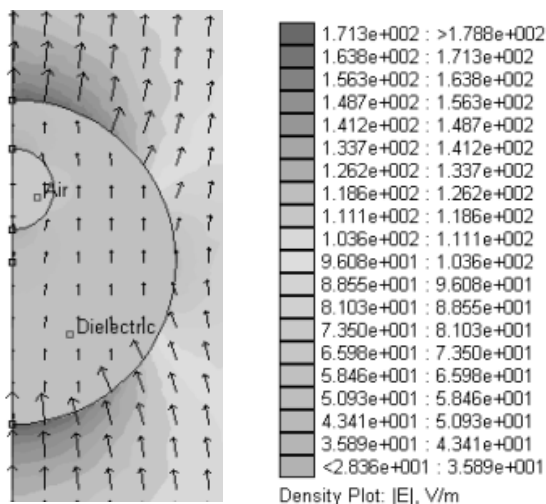


Fig.9. Electric field distribution and intensity vector (Dirichlet's boundary condition).

In Fig.10 the electric field strength distribution, with applied Neumann's boundary condition, is presented.

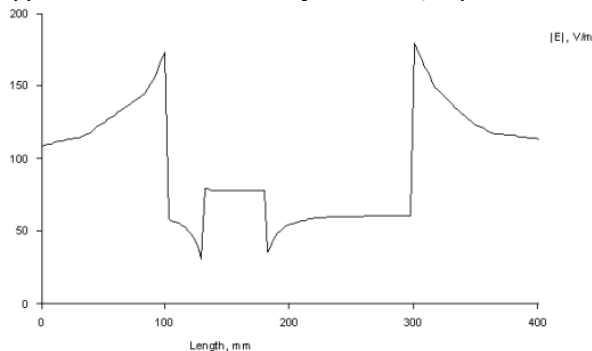


Fig.10. Electric field intensity (Neumann's boundary condition).

Usage of method of fictitious sources for solving this particular problem is described in detail in papers [4-6].

In this paper the distribution of the electric field strength (Fig.11) and the potential distribution (Fig.12) for different number of fictitious sources and given values of "inserting" factor  $f$  will be presented.

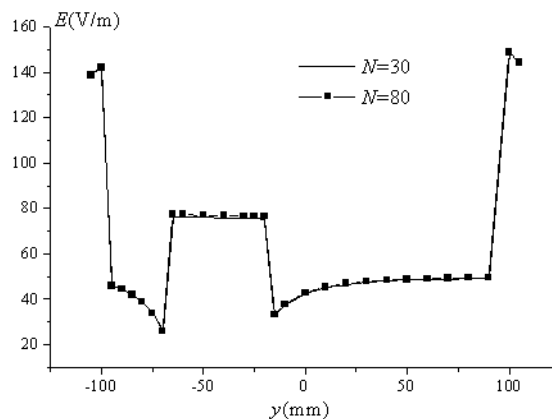


Fig.11. Electric field strength distribution along  $y$ -axis (method of fictitious sources).



Input data are:  $f_1 = 0.8$ ,  $f_2 = 1.2$ ,  $f_3 = 0.8$ ,  
 $f_4 = 1.2$ ,  $b/a = 0.25$ ,  $c/a = 0.45$  and  $\epsilon_r = 3$ .

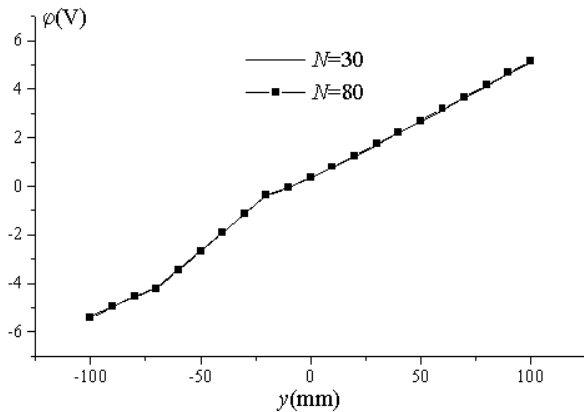


Fig.12. Potential distribution along  $y$ -axis (method of fictitious sources).

**Example 2**

Dielectric body with square cross-section of side  $a = 100$  mm, with eccentric circular cavity of radius  $b = 25$  mm and eccentricity  $c = 45$  mm is placed in transverse electric field,  $E_0 = E_0 \hat{y}$ . Intensity of the electric field is  $E_0 = 100$  V/m.

The working surrounding in the program's package FEMM4.0 is presented in the Fig.13.

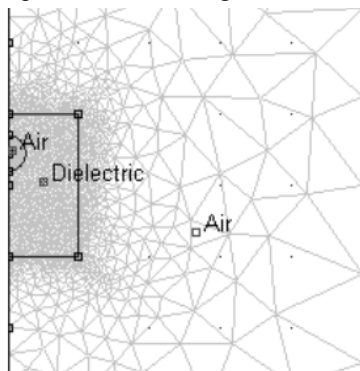


Fig.13. Square cross-section of the dielectric body with eccentric circular cavity.

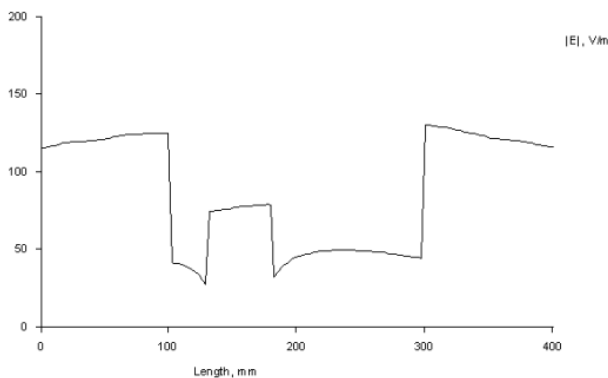


Fig.14. Electric field intensity (Dirichlet's boundary condition).

Figs.14-16 show the potential and electric field strength distribution. Also, the equipotential curves and electric field intensity vector are shown. These results are obtained using Dirichlet's boundary condition, for planar problem. Mesh which is applied has 7086 nodes.

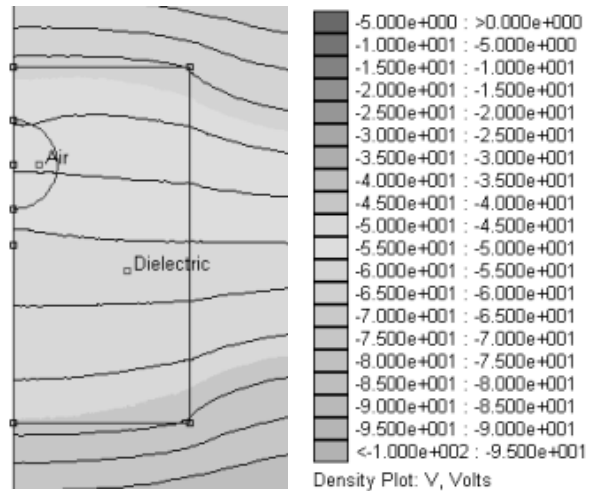


Fig.15. Potential distribution and equipotential lines (Dirichlet's boundary condition).

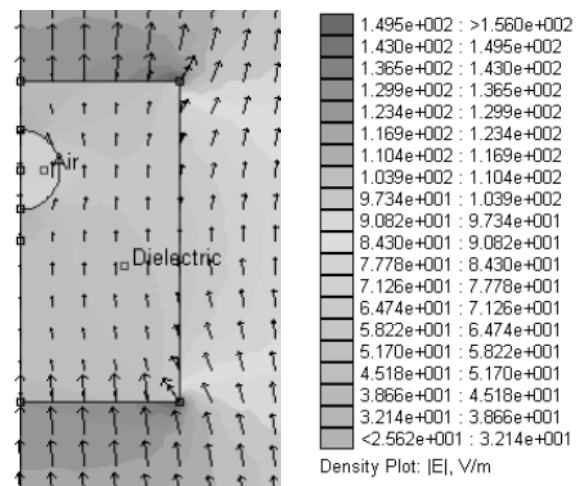


Fig.16. Electric field distribution and intensity vector (Dirichlet's boundary condition).

When the Neumann's boundary condition is applied, the electric field distribution is shown in Fig.17.

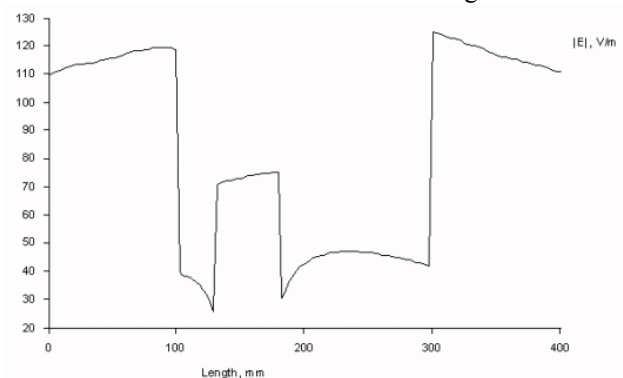


Fig.17. Electric field intensity (Neumann's boundary condition).

When the problem is considered as axisymmetric and Neumann's boundary condition is applied, the electric field and potential distributions along the  $y$ -axis are shown in Figs.18-20.

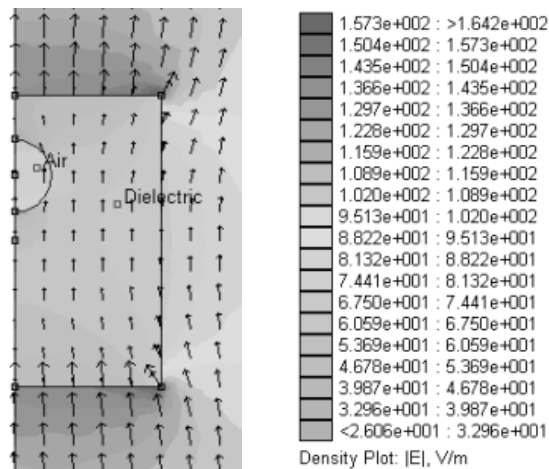


Fig.18. Electric field distribution and intensity vector (Neumann's boundary condition).

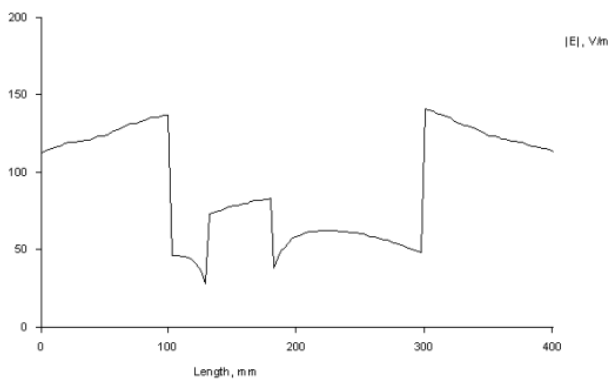


Fig.19. Electric field intensity (Neumann's boundary condition).

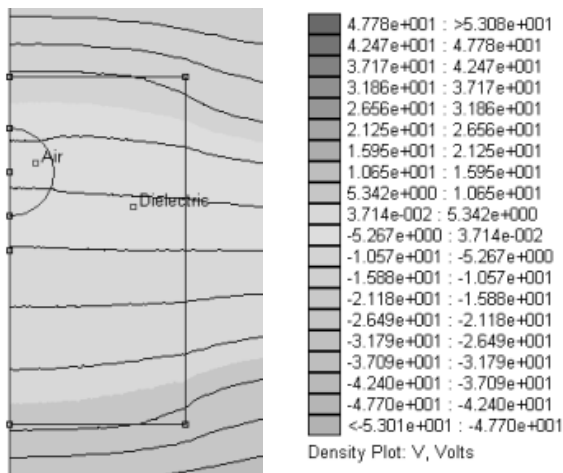


Fig.20. Potential distribution and equipotential curves (Neumann's boundary condition).

Because of limited space, the electric field strength distribution obtained using the Dirichlet's boundary condition won't be presented here.

Here will be presented only the potential distribution for this case (Fig.21).

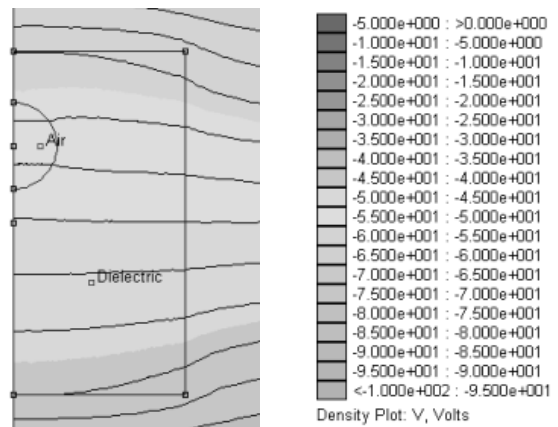


Fig.21. Potential distribution and equipotential curves (Dirichlet's boundary condition).

The potential and electric field distribution along the  $y$ -axis, for different number of fictitious sources, and for the same input data, as in the previous example, are shown in the Fig.22 and Fig.23.

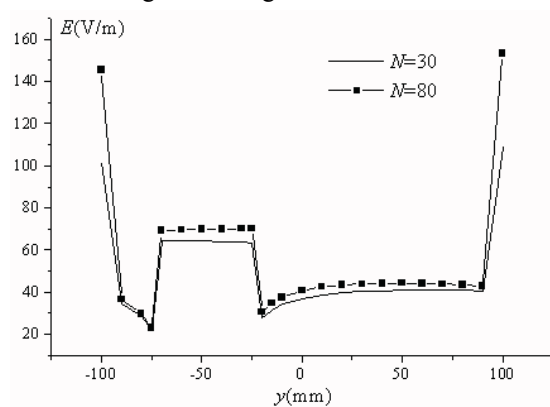


Fig.22. Electric field strength distribution along  $y$ -axis (method of fictitious sources).

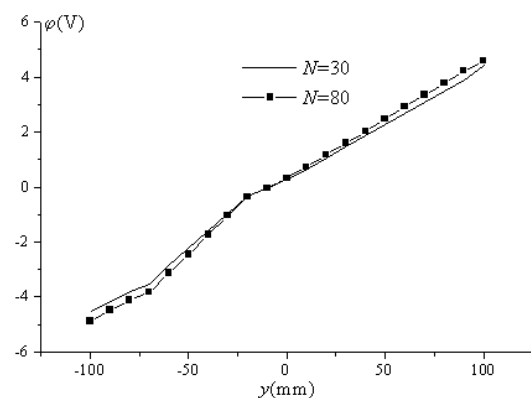


Fig.23. Potential distribution along  $y$ -axis (method of fictitious sources).

In Table 1, the electric field strength values in two points:  $(0, 0)$  i  $(0, -45 \text{ mm})$ , for all considered cases, are shown.

**Table 1**  
*Electric field strength in points (0, 0) and (0, -45 mm).*

Problem type/ bound. condition (BC)	<i>E</i> (V/m) in points	
	(0, 0)	(0, -45 mm)
FEMM, planar, circle/ Dirichlet's BC	43.87	78.29
FEMM, planar, circle/ Neumann's BC	42.45	75.83
Method of fictitious sources, circle	42.91	76.89
FEMM, axisymm., circle/ Dirichlet BC	54.76	78.07
FEMM, axisymm., circle/ Neumann BC	54.62	77.89
FEMM, planar, square/ Dirichlet BC	44.89	76.77
FEMM, planar, square/ Neumann BC	43.06	73.63
Method of fictitious sources, square	39.75	70.34
FEMM, axisymm., square/ Dirichlet BC	59.18	79.24
FEMM, axisymm., square/ Neumann BC	58.75	78.69

### Conclusion

The electric field strength and potential distribution in dielectric body with eccentric cavity using the program's package FEMM4.0 are determined. The obtained results are compared with the method of fictitious sources results. Theoretically, the precision of the solution depends on the number and position of the fictitious points, i.e. a higher precision can be realized by increasing the number of FS. If they are very close or too far from the surfaces the obtained error is higher. We have found very good agreement with the results obtained by the program's package FEMM4.0, in the planar problem case.

Three-dimensional problems cannot be solved using this program's package.

### References

[1] Program package: FEMM4.0, David Meeker, 2003, <http://femm.berlios.de>

[2] B. Z. Nikolić: "Calculation of the electric field strength and the potential in the arbitrary shaped cavity of the dielectric body", research during study staying on TU Ilmenau, Germany, 2004.

[3] S. R. Aleksić, Z. Ž. Cvetković, M. T. Perić, B. Z. Nikolić: "Određivanje jačine električnog polja i potencijala u šupljem dielektričnom telu", XLIX Konferencija ETRAN, 05-10. jun 2005, Budva, Srbija i Crna Gora.

[4] M. T. Perić: "Dielectric arbitrary shaped cylinder with arbitrary shaped and positioned cavity in homogeneous transverse electrical field", 6<sup>th</sup> International Conference on Applied Electromagnetics ПЕС2003, 01-03 June 2003, Niš, Serbia and Montenegro, pp. 209-212.

[5] M. T. Perić: "Calculation of electric field strength in hollow body using Charge Simulation Method", International PhD-Seminar "Computation of Electromagnetic Field", Budva, Serbia and Montenegro, 23-28 September 2004, pp.137-142.

[6] M. T. Perić: "Dielectric Body with Arbitrary Shaped and Positioned Cavity in Homogeneous Transversal Electric Field", Serbian Journal of Electrical Engineering, Technical faculty of Čačak, Serbia and Montenegro, Volume 1, No. 2, June 2004, pp. 175-186.

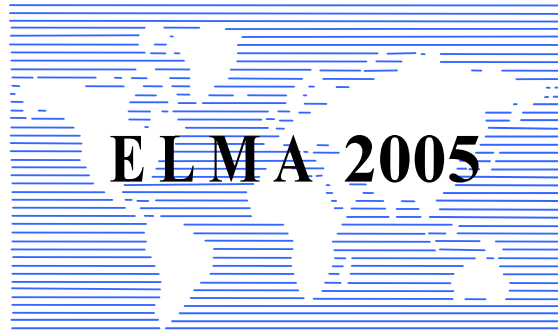
[7] D. M. Veličković: "Charge Simulation Method in Electromagnetic Field Computations", Summer School "Modern Aspects of Theoretical Electrical Engineering" SOZOPOL 2002, 29 September – 3 October 2002, Sozopol, Bulgaria, pp. 23-30.

**Slavoljub R. Aleksić** – Associate Professor, Dr., Faculty of Electronic Engineering, Aleksandra Medvedeva 14, 18000 Niš, SERBIA AND MONTENEGRO.  
e-mail: [as@elfak.ni.ac.yu](mailto:as@elfak.ni.ac.yu).

**Zlata Ž. Cvetković** – Assistant Professor, Dr., Faculty of Electronic Engineering, Aleksandra Medvedeva 14, 18000 Niš, SERBIA AND MONTENEGRO.  
e-mail: [zlata@elfak.ni.ac.yu](mailto:zlata@elfak.ni.ac.yu).

**Mirjana T. Perić** – M.Sc. Student, Faculty of Electronic Engineering, Aleksandra Medvedeva 14, 18000 Niš, SERBIA AND MONTENEGRO.  
e-mail: [mika@elfak.ni.ac.yu](mailto:mika@elfak.ni.ac.yu).

**Bojana Z. Nikolić** – B.Sc. Student, Faculty of Electronic Engineering, Aleksandra Medvedeva 14, 18000 Niš, SERBIA AND MONTENEGRO.  
e-mail: [zora@elfak.ni.ac.yu](mailto:zora@elfak.ni.ac.yu).



---

---

**TECHNOLOGIES, NEW MATERIALS  
AND COMPONENTS II**

---

---



# Analysis of Electrothermal Regimes of High Temperature Heating Elements with Negative Coefficient of Resistance

Nikolai Nikolov

**Abstract:** This work studies the regimes of operation of silicon carbide heating elements with negative temperature coefficient of resistance (TCR) while controlling their voltage, current and power. The obtained results may be used while choosing power supply source (regulator) for realization of specific processes.

**Key words:** ceramic, heaters

## Introduction

Heating elements of silicon carbide (SiC) are distinguished by the strong temperature dependence of their electrical resistance, which falls while heating up to 1000°C and then slowly rises. After a time, because of irreversible chemical reactions electrical resistance of the heater increases and the power dissipated by the heating element drops down. In some researches [2] is established that most favorable is the continuous work of the heating elements. Step control causes significant temperature fluctuations that destroy protective surface layer and the result is faster aging of the heaters [2] [3]. That imposes control of the parameters of the electrical power supply.

The aim of this research is to study the heating of SiC heating element while controlling one of the parameters of the power supply – current, voltage, power, considering the maximum allowed temperature and power of the element. The results may be used as a recommendation for power supply design.

## Research

Theoretic analysis is carried out when supplying the heater from:

- constant power source;
- step power regulator source;
- constant voltage source;
- constant current source;
- source with temperature dependent current.

All the calculations are made for particular heating element with following parameters (conformable to the maximum surface loading -  $w = 5 \text{ W/cm}^2$ ): maximum dissipated power – 2000 W; diameter of active zone – 6 mm; length of active zone – 1050 mm [1],[4].

### 1. Work at constant power

The work of the heater at constant power corresponds to first stage of the heating process when heat energy is accumulated in furnace walls. Working temperature and heating rate are different according to the value of the power supplied to the heater. The calculations of current

and voltage values as a function of temperature are made at nominal power by using resistance versus temperature dependence known from literature [1],[2],[4]. The obtained value for the voltage varies widely (table1, fig.1).

**Table 1**

T,°C	20	100	200	300	400	500	600
I,A	2.97	3.23	3.67	4.13	4.62	5.33	5.94
U,V	640	588	518	460	412	356	320
P,W	1900	1900	1900	1900	1900	1900	1900
R,Ω	215.4	182	141.1	111.4	89.1	67	54
T,°C	700	800	900	1000	1100	1200	1300
I,A	6.82	7.54	7.76	8.00	7.76	7.54	7.15
U,V	279	252	245	238	245	252	266
P,W	1900	1900	1900	1900	1900	1900	1900
R,Ω	40.85	33.42	31.57	29.71	31.57	33.42	37.14

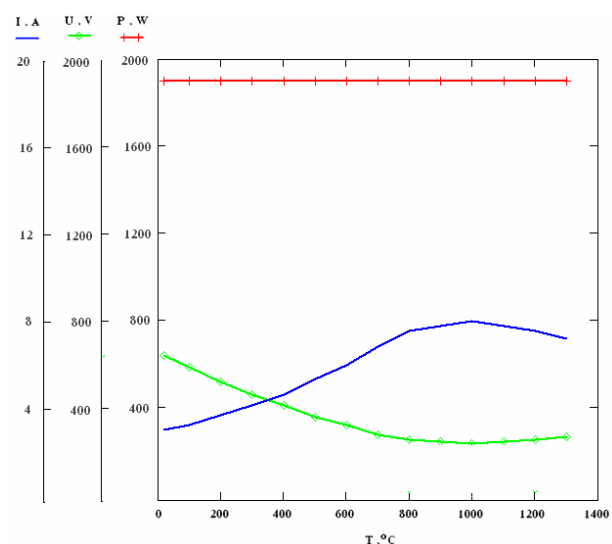


*Fig.1*

Connecting the heater to a power network with stable voltage (220 or 380 V) imposes the use of step-up and step-down regulators for the corresponding temperature ranges.

Using power step regulator eliminates this inconvenience (table 2, fig. 2). By suitable choice of number of steps, voltage variation is limited. Switching of power causes temperature fluctuations which must be concerned and restricted to a safer range.

**Table 2**

T, °C	20	100	200	300	400	500	600
I, A	0.96	1.05	2.06	2.32	2.60	3.00	4.31
U, V	208	191	290	259	231	200	232
P, W	200	200	600	600	600	600	1000
R, Ω	215.4	182	141.1	111.4	89.1	67	54
T, °C	700	800	900	1000	1100	1200	1300
I, A	4.95	5.47	6.42	6.62	7.76	7.54	7.15
U, V	202	183	203	197	245	252	201
P, W	1000	1000	1300	1300	1900	1900	1900
R, Ω	40.85	33.42	31.57	29.71	31.57	33.42	37.14

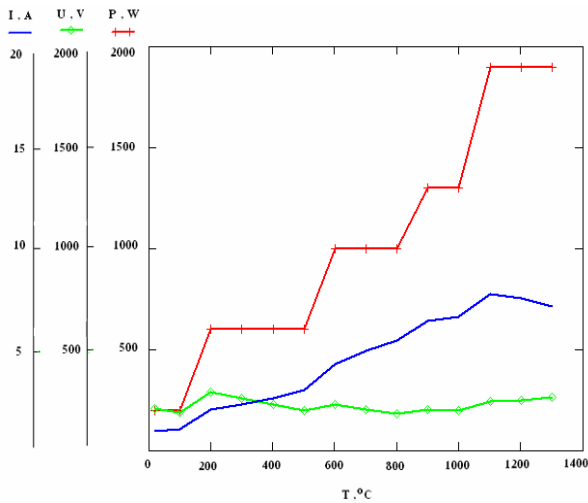


*Fig.2*

**2. Work at constant voltage**

Powering the heating element by a constant voltage network requires conforming with the particular types of heaters because of the different initial value of their electrical resistance.

Output voltage of the transformer (which is a buffering device) is chosen according to :

$$(1) \quad U^2/R_{\min} \leq P_{\text{nom}} \quad U = \sqrt{P_{\text{nom}} \cdot R_{\min}}$$

where  $R_{\min}$  is the minimum electrical resistance corresponding to temperature – 1000°C,  $P_{\text{nom}}$  is the nominal power of the heater .

The results are presented in table 3 and on fig. 3.

**Table3**

T, °C	20	100	200	300	400	500	600
I, A	1.1	1.30	1.68	2.13	2.66	3.55	4.40
U, V	237	237	237	237	237	237	237
P, W	261	309	398	504	630	840	1043
R, Ω	215.4	181.97	141.1	111.4	89.1	66.9	53.9
T, °C	700	800	900	1000	1100	1200	1300
I, A	5.80	7.09	7.51	7.98	7.51	7.09	6.38
U, V	237	237	237	237	237	237	237
P, W	1375	1681	1779	1891	1779	1681	1510
R, Ω	40.85	33.42	31.57	29.71	31.57	33.42	37.14

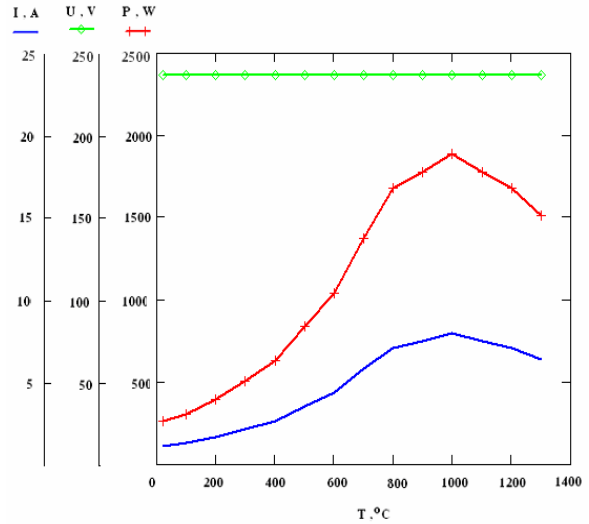


*Fig.3*

At 1000°C the temperature coefficient of resistance changes and the resistance rises slowly with temperature. That causes the power to drop down and that is inadmissible during the exploitation. To maintain constant value of the power at high temperatures increase of the input voltage is needed (table 4, fig. 4).

**Table4**

T, °C	20	100	200	300	400	500	600
I, A	1.1	1.30	1.68	2.13	2.66	3.55	4.40
U, V	237	237	237	237	237	237	237
P, W	261	309	398	504	630	840	1043
R, Ω	215.4	181.97	141.1	111.4	89.1	66.9	53.9
T, °C	700	800	900	1000	1100	1200	1300
I, A	5.80	7.09	7.76	8.25	7.98	7.75	7.35
U, V	237	237	245	245	252	259	273
P, W	1375	1681	1902	2021	2012	2007	2007
R, Ω	40.85	33.42	31.57	29.71	31.57	33.42	37.14

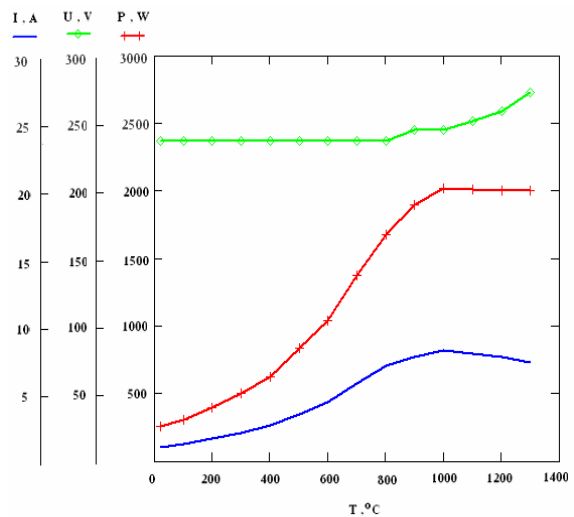


*Fig.4*

The voltage regulator must ensure fluent change of the power and current. That makes the heating process

slower and reduces the probability of mechanical strains to occur. The possibility to control the value of the voltage makes the regulator suitable to work with different heater types (with different resistance and nominal power) and also eliminates the agging problem.

### 3. Work at constant current

Electrical parameters of the heating element at constant current are determined by the following expressions:  $P = I^2 \cdot R$  and  $U = I \cdot R$ . The value of the current is chosen in condition with:

$$(2) \quad I^2 \cdot R_{\max} \leq P_{\text{nom}} \quad I = \sqrt{P_{\text{nom}} / R_{\max}}$$

where  $R_{\max}$  - is maximum value of the electrical resistance ( at the beginning of heating process)  $\Omega$ ;  $P_{\text{nom}}$  - is the nominal power of the element, W.

Table5

T,°C	20	100	200	300	400	500	600
I,A	3.05	3.05	3.05	3.05	3.05	3.05	3.05
U,V	657	555	430	340	272	204	164
P,W	2004	1693	1313	1.036	829	622	501
R,Ω	215.4	181.9	141.1	111.4	89.1	66.9	53.9
T,°C	700	800	900	1000	1100	1200	1300
I,A	3.05	3.05	3.05	3.05	3.05	3.05	3.05
U,V	125	102	96	91	96	102	113
P,W	380	311	294	276	294	311	345
R,Ω	40.85	33.42	31.57	29.71	31.57	33.42	37.14

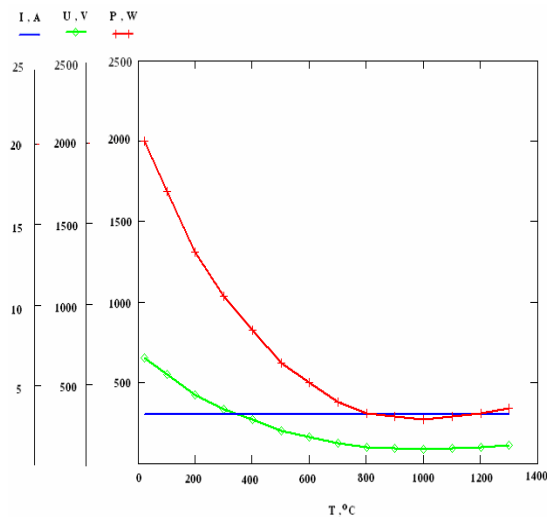


Fig.5

The work of the heater at constant current is characterized with decrease of the power in the temperature range 20-1000°C. The heating element may be considered as self-regulating device: any change of temperature caused by external factors results in a reciprocal change of the power. By suitable choice of current variation above 1000°C is possible to extend the zone of self-regulation. This regime may be used throughout the second stage of the heating process (after

reaching the working temperature). Disadvantage of this method is the wide range of voltage change.

### 4. Work at temperature dependent current source

Another possibility is powering the heating element by temperature controlled current source. The current value is determined after following formula:  $I = f(\tau) = a + b \cdot T$  and the coefficients  $a$  and  $b$ , are chosen so that the flowing current provides power less or equal to the nominal power of the heater.

Table6

T,°C	20	100	200	300	400	500	600
I,A	0.52	1.04	1.56	2.08	2.6	3.12	3.64
U,V	112	189	220	232	232	209	196
P,W	58	197	343	482	602	651	713
R,Ω	215.4	181.9	141.1	111.4	89.1	66.9	53.9
T,°C	700	800	900	1000	1100	1200	1300
I,A	4.16	4.68	5.2	5.72	6.24	6.76	7.28
U,V	170	156	164	170	197	226	270
P,W	707	732	854	972	1229	1527	1968
R,Ω	40.85	33.42	31.57	29.71	31.57	33.42	37.14

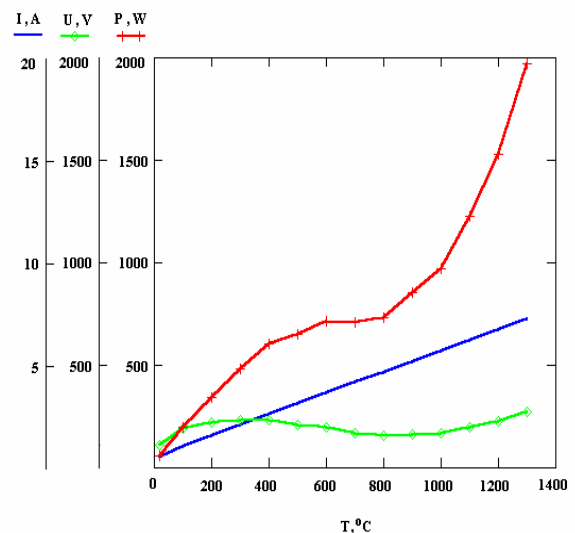


Fig.6

Using the power vs temperature graphic the process may be divided in two periods with different heating rates. If two equal temperature ranges are chosen: 100 °C to 700 °C and 700 °C to 1300 °C, then relative times and heating rates may be calculated after:

$$(3) \quad t_1 = K \cdot \frac{\Delta T_1}{\Delta P_1} = K \cdot \frac{700 - 100}{849 - 236} = K \cdot 0,98$$

$$(4) \quad t_2 = K \cdot \frac{\Delta T_2}{\Delta P_2} = K \cdot \frac{1300 - 700}{2365 - 880} = K \cdot 0,4$$

where :  $K$  - constant;  $\Delta T_1$ ,  $\Delta T_2$  - temperature ranges;  $\Delta P_1$ ,  $\Delta P_2$  - changes in power for the temperature ranges;  $t_1$ ,  $t_2$  - times of the two periods.



Considering that  $\Delta T_1 = \Delta T_2 = 600^\circ\text{C}$ , heating rates are  $V_1 = \frac{\Delta T_1}{t_1}$ ,  $V_2 = \frac{\Delta T_2}{t_2}$ , and their ratio is:

$$(5) \quad \frac{V_2}{V_1} = \frac{\frac{\Delta T_1}{t_1}}{\frac{\Delta T_2}{t_2}} = \frac{t_1}{t_2} = \frac{0,98}{0,4} = 2,45$$

This regimen should be used in consideration with maximum allowed heating rates for the detail and furnace insulation

### Conclusion:

The analysis of working regimen of SiC heaters with negative TCR reveals the following special features:

- constant power of the heating element is maintained using complicated dependence of voltage vs temperature;
- at constant voltage (in consideration of the maximum dissipated power) initial proportional increase of the power is observed. After reaching  $1000^\circ\text{C}$  a change of voltage value is needed to sustain constant power (otherwise it begins to fall down);

- at constant current the power is proportional to the electric resistance. As a result during the exploitation the furnace may not reach the initially set temperature.

The study of SiC heating elements with negative coefficient of resistance confirms the need of specialized power supply with regulated parameters in accordance with the effectuated process.

### Literature:

- [1]. T. Burakovskii, E. Guizinskii, A. Salia "Infrared radiators", "Energy", Leningrad, 1978.
- [2]. L. Rubinchuk, "Electric furnace with silicon carbide heaters", Energia, 1975.
- [3]. N. V. Bolshakova, K. S. Borissanova, V. I. Burtsev, "Materials for electrothermal devices", Moscow, Energoatomizdat, 1987
- [4]. [www.kanthal.com](http://www.kanthal.com).

---

*Nikolai Nikolov – Ph.D. Student, Faculty of Electrical Engineering, Technical University of Varna, 1 Studentska Str., 9000 Varna, BULGARIA, e-mail:n\_gn@abv.bg*

# Analysis of Electrothermal Regimens of High Temperature Heaters with Positive Temperature Coefficient of Resistance

Nikolai Nikolov, Hristofor Tahrilov

**Abstract:** High temperature metaloceramic heating elements are characterized with strong temperature dependence of their electrical resistance and require the use of regulated power supply. This research presents results from theoretic analysis of heating process when the heating element is powered by source with constant voltage, power or current. The obtained results may be used while choosing power supply source (regulator) for realization of specific process.

**Key words:** Kanthal Super, heaters.

## Introduction

The work of high temperature electrical resistance furnaces is characterized by some specific features as a result of the metaloceramic heaters that are used. They are distinguished by strong temperature dependence of their electrical resistance and that requires control of power supply voltage. The work of MoSi<sub>2</sub> heaters without regulator is impossible due to the low electrical resistance at the beginning of heating process that causes great currents to flow. Recommendations for their operating regimes are given in manufacturer's literature [1],[2],[3].

The aim of the following research is to study the work of MoSi<sub>2</sub> heaters while controlling one of the parameters of the power supply: current, voltage, power and in accordance with maximum operating temperature and maximum allowed current.

## Research

Theoretic analysis is carried out supplying the heater from:

- step power regulator source
- constant power source
- step voltage regulator source
- constant voltage source
- constant current source

The actual process of heating must be conformable to maximum heating rate, which is determined by thermal and mechanical parameters of heater and thermal insulation.

All the calculations are made for particular heating element with following parameters: maximum dissipated power – 2000W; diameter of active zone – 6 mm; length of active zone – 315 mm; maximum allowed current – 150A.

### 1. Work at step power regulator

Temperature dependence of the specific electrical resistance is given by:

$$(1) \quad \rho = \rho_{20}(1 + \alpha \cdot \theta)$$

After Kanthal's design handbook the heating process is accomplished by switching the power according to:

- to  $\tau = 200^\circ\text{C}$   $P = (1/3)P_{inst}$  W;
- to  $\tau = 600^\circ\text{C}$   $P = (2/3)P_{inst}$  W;
- to  $\tau = 1400^\circ\text{C}$   $P = P_{inst}$  W.

Results from calculations are presented in table 1 and graphically on fig.1.

**Table 1**

T,°C	20	100	200	300	400	500	600	700
P,W	666	666	666	1332	1332	1332	1332	1998
I,A	282	233	198	244	219	200	226	212
U,V	2.36	2.86	3.37	5.45	6.09	6.67	8.82	9.44
T,°C	800	900	1000	1100	1200	1300	1400	
P,W	1998	1998	1998	1998	1998	1998	1998	
I,A	199	188	179	171	164	157	151	
U,V	10.03	10.63	11.16	11.68	12.21	12.73	13.27	

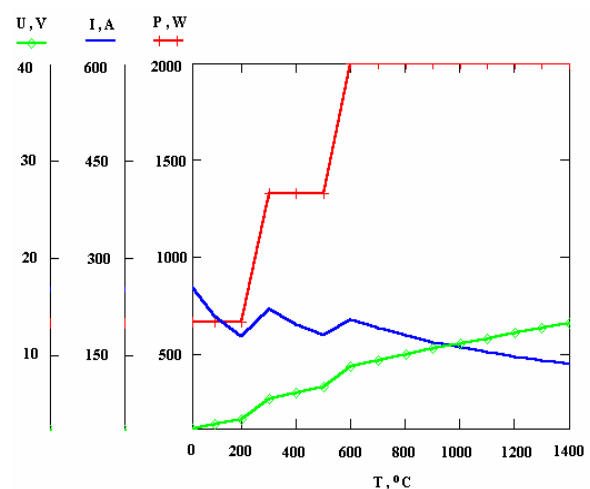


Fig. 1

That mode of operation determines variable values of current and voltage. Throughout the heating process current value is greater than maximum allowed so the heater is overloaded and that imposes to choose another solution either for interconnection of the heaters or for the step controller (to change number of steps and initial value of the switched power).

### 2. Work at constant power

Maintenance of constant power is achieved by regulating the voltage according to:

$$(2) \quad U = \sqrt{P \cdot R}$$

Results from calculations are presented in table 2 and on fig. 2. Likewise the above regimen the initial value of the current is greater than maximum allowed:  $I_{beg} / I_{nom} = 3,26$  - where  $I_{beg}$  - is current at the beginning of heating process;  $I_{nom}$  - is maximum allowed current for the specified heater type. That causes stronger electrodynamic forces to occur, which is highly undesirable.

**Table 2**

T, °C	20	100	200	300	400	500	600	700
P, W	2000	2000	2000	2000	2000	2000	2000	2000
I, A	489	403	343	299	268	245	226	212
U, V	4.08	4.95	5.83	6.67	7.46	8.17	8.82	9.44
T, °C	800	900	1000	1100	1200	1300	1400	
P, W	2000	2000	2000	2000	2000	2000	2000	
I, A	199	188	179	171	164	157	151	
U, V	10.04	10.63	11.16	11.68	12.21	12.73	13.28	

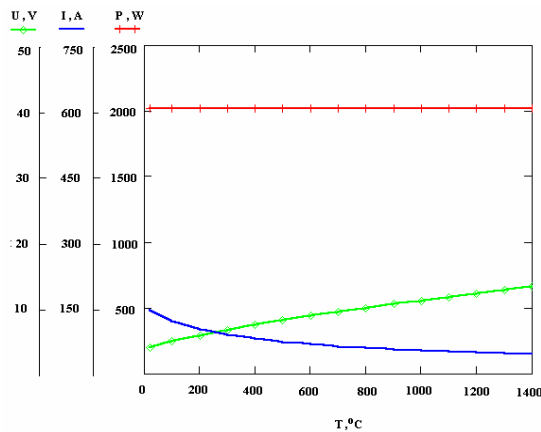


**Fig. 2**

As a result work at constant power equal to nominal is not recommended. Maximum power of the heater is reached at 1500°C and that corresponds to determined value of the electrical resistance, which is fifteen times greater than the value at room temperature:  $R_{end} / R_{start} \approx 15$ .

### 3. Work at step voltage regulator

Supplying the heater from step voltage regulator causes sharp changes of power and current at moment of switching. That has unfavorable effect on both heater and thermal processing. Improvement of working conditions is achieved by increasing number of steps. Results from calculations are presented in table 3 and on fig. 3.

**Table 3**

T, °C	20	100	200	300	400	500	600	700
P, W	1078	732	2116	1615	1291	1078	2078	1817
I, A	359.4	244.2	352.7	269.2	215.2	179.7	230.9	201.9
U, V	3	3	6	6	6	6	9	9
T, °C	800	900	1000	1100	1200	1300	1400	
P, W	1607	1433	1299	1186	1085	998	918	
I, A	178.6	159.2	144.3	131.8	120.6	111.0	102.0	
U, V	9	9	9	9	9	9	9	

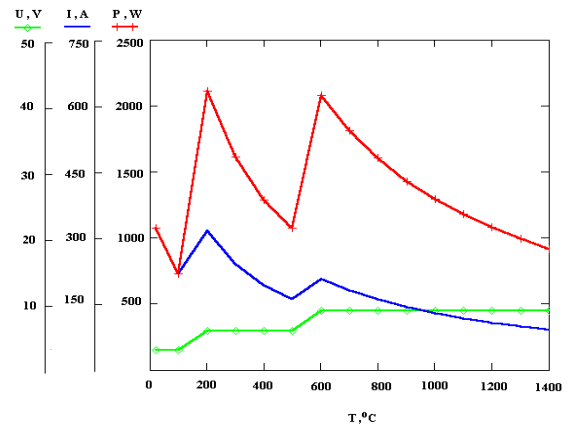


**Fig. 3**

### 4. Work at constant voltage

When the heating element is working at constant voltage source the value of that voltage is chosen so that the current is less than maximum allowed for the specified type of heater:  $U/R_{min} \leq I_{max} \leq 150$  A - where  $R_{min}$  - is the resistance of the heater at the beginning of heating process. Results from calculations are presented in table 4 and on fig. 4.

**Table 4**

T, °C	20	100	200	300	400	500	600	700
P, W	187	127	92	70	56	47	40	35
I, A	149.7	101.8	73.5	56.1	44.84	37.44	32.07	28.04
U, V	1.25	1.25	1.25	1.25	1.25	1.25	1.25	1.25
T, °C	800	900	1000	1100	1200	1300	1400	
P, W	31	28	25	23	21	19	18	
I, A	24.8	22.11	20.04	18.31	16.74	15.41	14.17	
U, V	1.25	1.25	1.25	1.25	1.25	1.25	1.25	

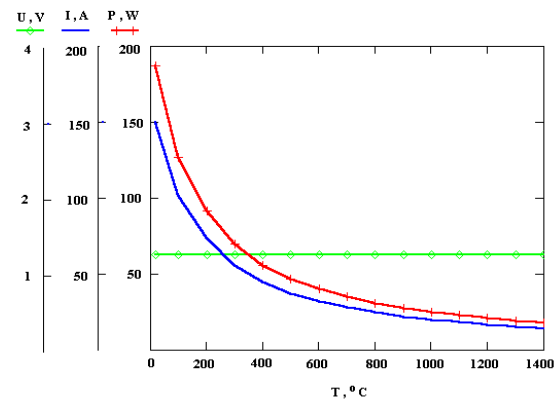


**Fig. 4**

Because of the positive temperature coefficient of resistance, power and current are falling down while temperature rises. The maximum power is attained at the beginning of heating process and is ten times smaller than nominal power of the heater. That results in establishment of much lower working temperature so this regimen becomes unusable for high temperature heating.

### 5. Work at constant current

Using source with constant current allows sustaining the maximum current throughout the heating process. The obtained temperature dependences for power and voltage are almost linear. Results from calculations are presented in table 5 and on fig. 5.

Table 5

T,°C	20	100	200	300	400	500	600	700
P,W	175	258	357	468	586	702	819	937
I,A	145	145	145	145	145	145	145	145
U,V	1.21	1.78	2.47	3.23	4.04	4.84	5.65	6.46
T,°C	800	900	1000	1100	1200	1300	1400	
P,W	1060	1189	1311	1436	1570	1705	1854	
I,A	145	145	145	145	145	145	145	
U,V	7.31	8.20	9.04	9.90	10.83	11.76	12.79	

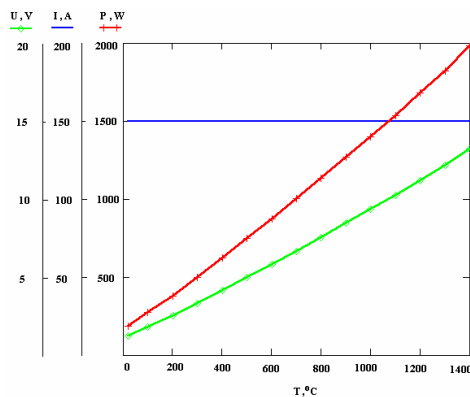


Fig. 5

### Conclusion:

The analysis of working regimens of MoSi<sub>2</sub> heaters with positive temperature coefficient of resistance reveals the following special features:

- Working at constant power equal to the nominal is impossible in view of the high current that flows at the beginning of the process.
- Great fluctuations of power and current while connected to a step voltage regulator. That requires increase of number of switching steps.
- At constant voltage in accordance with maximum allowed current is impossible to reach maximum power of the heating element.
- Work at constant current is most favorable because of linear increase of the power and maximum current loading of the element. The results show that this regimen may be realized by regulating the voltage.
- The study of self-dependent work of the heating elements must be extended with complex analysis of the whole system: heater – furnace – load.

### Litterature:

- [1] T. Burakovskii, E. Guizinskii, A. Salia “Infrared radiators”, “Energy”, Leningrad, 1978
- [2]. N. V. Bolshakova, K. S. Borissanova, V. I. Burtsev, “Materials for electrothermal devices”, Moscow, Energoatomizdat, 1987
- [3] [www.kanthal.com](http://www.kanthal.com)

**Hristofor Tahrilov** - Associate Professor, Dr., Faculty of Electrical Engineering, Technical University of Varna, 1 Studentska Str., 9000 Varna, BULGARIA.

**Nikolai Nikolov** – Ph.D. Student, Faculty of Electrical Engineering, Technical University of Varna, 1 Studentska Str., 9000 Varna, BULGARIA, e-mail:n\_gn@abv.bg

# About Using Dimming Devices in Tunnel Lighting

Angel Pachamanov, Neli Ratz, Emil Ratz, Nikolay Matanov

**Abstract:** The report describes the peculiarities when applying electronic devices for group dimming for adapting lighting for road tunnels. The harmonics of the electric current in the supplying lines, made by the non-linear character of the electrical load and the non-sinusoidal character of the supplying tension are evaluated.

**Keywords:** tunnel lighting, dimming of high pressure sodium lamps (HPSL)

## 1. Introduction

It is well known, that the artificial lighting in the entrance zone of road tunnels is regulated at the level of the adaptation luminance  $L_{20}$  for the car driver before entering the tunnel [1]. The luminance  $L_{20}$  depends on the entrance surround, position of the Sun and the atmospheric conditions. It is advisable the smooth change of the luminous flux (the so called dimming) of the high pressure sodium lamps (HPSL) to be used with a view to minimum expenditure of electric energy when controlling the tunnel lighting. Normally the lamps in one of the supplying lines are dimmed, i.e. 25-33% from the adaptation lighting. The rest of the lamps work at two-position regime (switched on – switched off) because of the higher efficiency of the lamps at nominal regime.

The group dimming could be achieved through several approaches:

- Through decrease the amplitude of the supplying tension;
- Through phase control of the efficient value of the supplying tension (Urms);
- Through changing the shape and the frequency of the supplying tension.

Results of researches done with devices, realizing the first two ways of dimming are given in [2]. The present report describes the peculiarities of the third way. The possible regimes for work of invertors with frequency from 50 to 125 Hz are examined, permitting dimming of tunnel luminaries of the entrance and transition zone without changing the traditional control gears in them [3]. In order not to enlarge the losses of energy in the inverter, which directly influences the real lighting yield of the lamps, the form of the tension, generated for one of the regimes is non-sinusoidal. That leads to additional increasing the level of the higher harmonics of the current towards the luminaries and loss of tension in the lines respectively, different from that at sinusoidal current [4].

## 2. Main part

### 2.1. Devices for frequency dimming

The module rectifier–inverter is the basic structure for every frequency transformer (Fig.1). They are produced at broad scale of electric power because of their large-scale application in electric motion with asynchronous motors. When these modules are used for group dimming of high pressure sodium lamps in street and tunnel lighting, the algorithm for control of the key elements of the inverter ensures pseudo-sinusoidal (Fig.2) or six-pulsed tension (Fig.3) towards the load. One priority of the first method is the lower level of the high harmonics of the current in the lines. From the other side this way of control is connected with higher losses of energy, dispersed in the transistors of the inverter, because using of PWM with frequency, several times higher than the basic one.

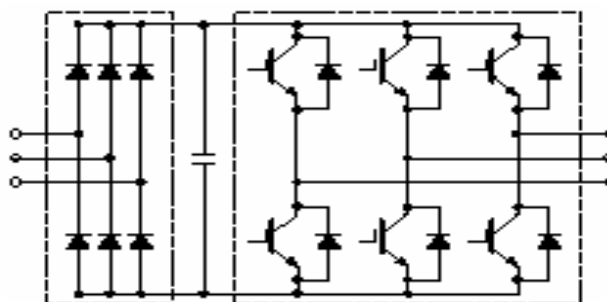


Fig.1. Module for AC-DC-AC conversion of supplying tension

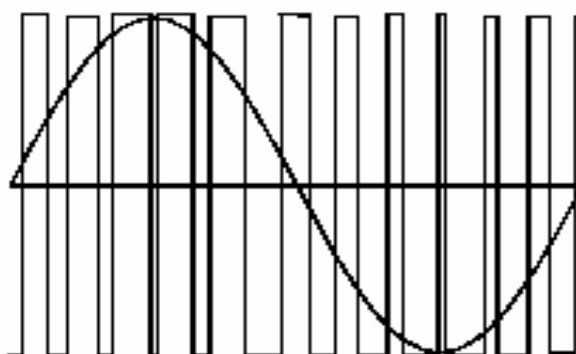


Fig.2. Pseudo-sinusoidal tension at the exit of an inverter with PWM

The inconvenience of the direct usage of this type of modules for dimming of high pressure sodium lamps is that the supply of the inverter is one-phased and the exit of the inverter is without neutral - the lamps are connected to two line tension. In that case the power of

the modules is not fully used (Fig.4). A variant with three phase supply is also possible, when the inverter is supplied with double polar tension. The exit tension of the inverter in that case has rectangular shape instead of six-pulse (Fig.5).

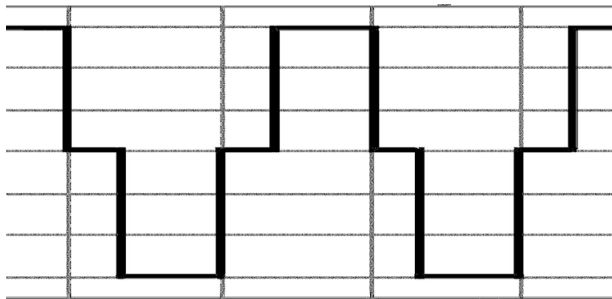


Fig.3. Six-pulse tension at the exit of an inverter

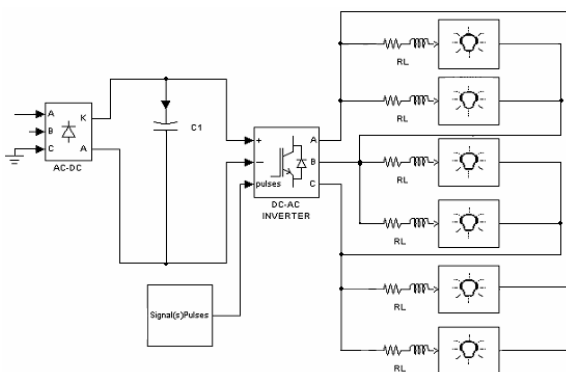


Fig.4. One-phase supply of the rectifier (one-polar supply of the inverter) and connection of the luminaries to the two line tension

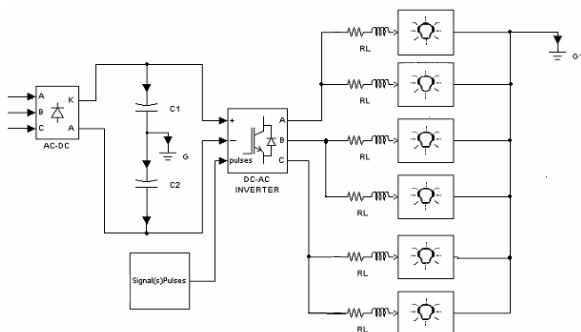


Fig.5. Three-phase supply of the rectifier (two-polar supply of the inverter) and connecting the luminaries to the line-neutral tension

## 2.2. Current harmonics at one-polar supply tension of the inverter

The measured current harmonics in the three lines of an inverter with one-polar supply tension (Fig.4) are shown in tables 1 and 2. It can be seen that at the two types of modulation (with PWM 1kHz and six-pulsed) in the three lines there is zero harmonic which is result by the non-symmetric wearing out of the lamp electrodes.

Table 1  
Current harmonics at the exit of an inverter with PWM 1kHz

№	$i_a, \%$	$i_b, \%$	$i_c, \%$
0	1,3	8,3	16,6
1	100,0	100,0	100,0
3	0,5	0,6	0,5
5	2,9	2,2	2,4
7	1,0	1,0	0,8
9	0,2	0,1	0,1

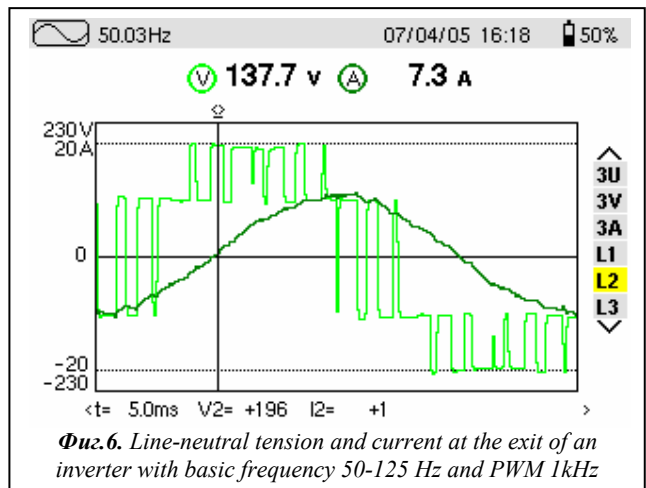


Fig.6. Line-neutral tension and current at the exit of an inverter with basic frequency 50-125 Hz and PWM 1kHz

Table 2  
Current harmonics at the exit of an inverter with six-pulsed modulation

№	$i_a, \%$	$i_b, \%$	$i_c, \%$
0	1,2	7,6	10,5
1	100,0	100,0	100,0
3	0,4	0,6	0,6
5	6,4	6,1	6,2
7	4,3	4,3	3,7
9	0,2	0,1	0,1

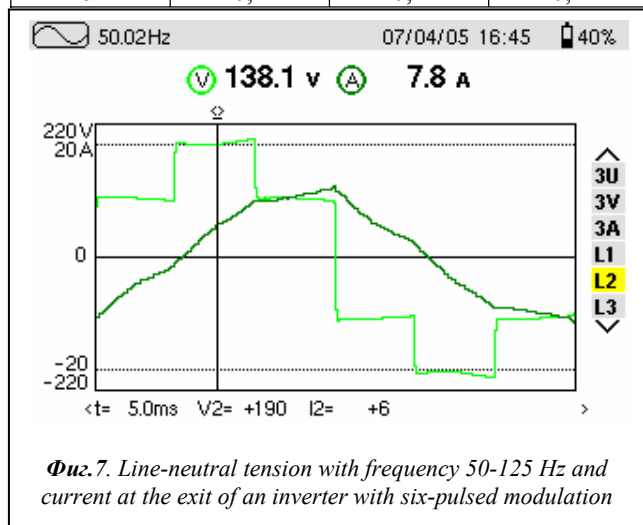
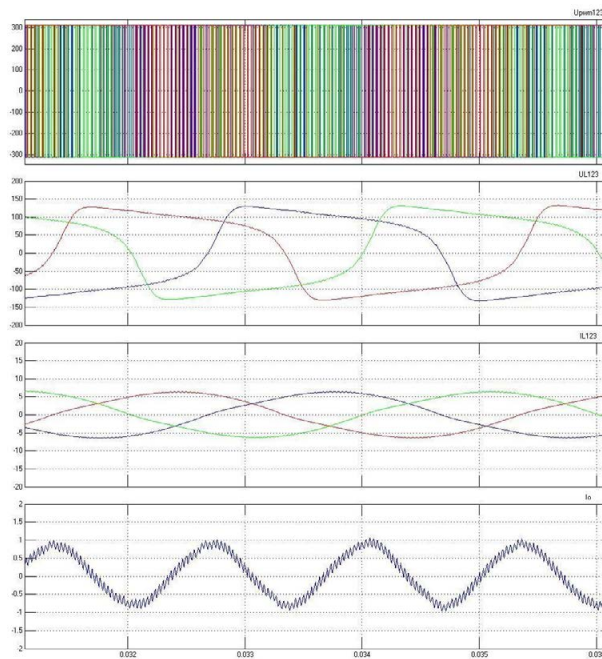


Fig.7. Line-neutral tension with frequency 50-125 Hz and current at the exit of an inverter with six-pulsed modulation

### 2.3. Inverter with two-polar supply tension and extended basic frequency

When devices for group dimming of HPSL are developed, it is more convenient the inverter to be supplied with a two-polar tension and the lamps to be connected to line-neutral tension (Fig.5). In that case the inverter can provide different according to the shape and magnitude of the lines tension and so – low levels of the zero current harmonic. Thus the life of the lamps is prolonged and before the end of their resource they are changed in groups (a normal practice for the tunnel lighting).

Aiming at decreasing the weight of the inductive ballast and avoiding pulsations of the luminous flux it is advisable the frequency of the supply tension to be enlarged. Frequencies from 250 up to 700 Hz are suitable, in which range the pulsations of the luminous flux are smaller, which influences favourably the functions of the human eye and no resonance phenomena are noticed in the work of the lamp.



**Fig.8.** Simulation of supply tension with bipolar PWM, tension and current through HPSL and current through the neutral wire

The Fig.8 shows the simulation of the work of the supply device with a group of HPSL. A three-phase source of PWM tension with bipolar modulation has been used. The model designed supposes [5] that the frequency transformer works of the basic harmonic 250 Hz. The parameters of the ballasts to the lamp are  $L=0.026\text{H}$  and  $R=1\ \text{ohm}$  and the simulation is implemented for three HPSL EWZ 400W. The enlarging of the number of the lighting sources is connected only with the enlarging the time for the calculation at simulation. At the end one can see the current through the zero wire. Obviously, its frequency is three times bigger than that of the basic harmonic of the supply tension, and its amplitude is about

15% from the amplitude of the phase (line) current. The frequency of the high-frequency pulsations corresponds to the frequency of PWM.

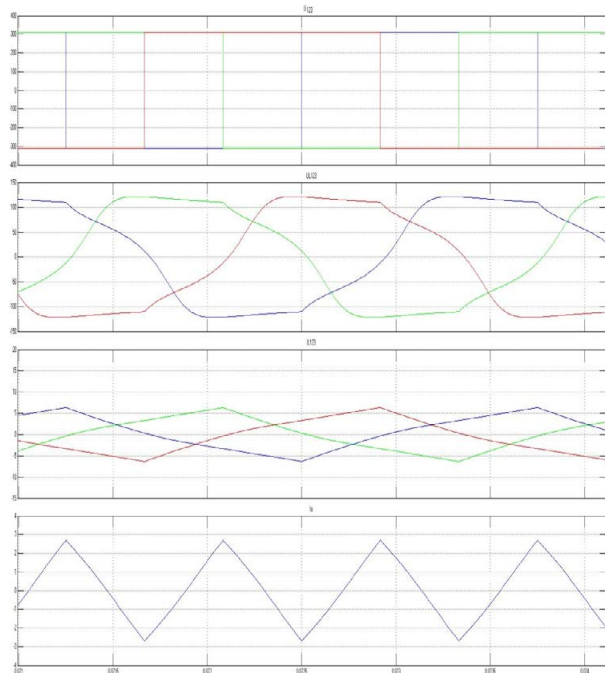


**Fig.9.** Simulation of rectangular supply tension, tension and current through HPSL and current through the neutral wire

The Fig.9 shows the simulation of group dimming of HPSL. A three-phase source with rectangular form of tension (without PWM) with bipolar modulation has been used. Obviously, the triangular form of the current is defined by the rectangular form of the supply tension and the inductive character of the load. At this variant of supply, the current through the neutral (zero) wire is about 43 % of the phase current.

### 3. Conclusions

It is most convenient at group dimming of HPSL the converter to be supplied with two-polar tension and the lamps to be connected in the classic style – between a phase and the neutral. This decision permits during the process of growing old of the lighting sources the inverter to realize a suitable change of the coefficient of filling in the supply tension aiming at neutralizing the results of the ventil effect – overheating of the ballasts and decreasing the life of the lamp-ballast set.

It is advisable the frequency of the supply tension to be changed from 250 to 700 Hz when dimming for decreasing the weight of the inductive ballast and leaving the zone of unfavourable influence of the pulsations of the luminous flux. For the short distances at which it is normal to work in the tunnel lighting, these frequencies permit becoming lighter the construction of the tunnel luminaries, without increasing the losses in the control gears of the luminaries in the supplying lines as well.

## References

- [1] **CIE Publication 88**, Guide for the Lighting of Tunnels and Underpasses. International Commission on Illumination (CIE), 1990
- [2] **Ratz N., A. Pachamanov**. Research of possibilities for dimming of high pressure discharge lamps. Proceedings of XII National Conference Light'2004, 15-17 June 2004, Varna, Bulgaria
- [3] **www.tunnellighting.com**
- [4] **Pachamanov A., N. Ratz**. Voltage losses in lines of lighting system supplied by inverter. Izvestia na TU-Sofia, 2005
- [5] **Ratz N.** Modeling of high pressure discharge lamps by dimming. Dissertation for Ph.D. Technical University-Sofia, 2005

---

*Angel Pachamanov* - Dr. Eng., Assoc. Professor, Electric Power Supply and Equipment Department, Technical University - Sofia, , E-mail: [pach@tu-sofia.bg](mailto:pach@tu-sofia.bg)

*Neli Ratz* - Mag. Eng., Assistant Profesor, OTK - Technical University – Sofia, E-mail: [neliratz@yahoo.com](mailto:neliratz@yahoo.com)

*Emil Ratz* - Dr. Eng., Assoc. Professor, Electric Machines Department, Technical University – Sofia, E-mail: [emil\\_ratz@yahoo.com](mailto:emil_ratz@yahoo.com)

*Nikolay Matanov* - Mag. Eng., Assistant Profesor, Electric Power Supply and Equipment Department, Technical University – Sofia



# Composit Foamed Thermoplastics with Increased Electrostatic Safety

Nikolay Piperov and Vasil-Mario Piperov

**Abstract:** *The conventionally obtained polymer and plastic products possess high surface ( $\rho_s$ ) and volume ( $\rho_v$ ) electrical resistance. By friction or contact with other hard objects they are easily electrified and the electrostatic charges, accumulated on their surface create conditions for the formation of discharges. By determined energy or inflammation of explosion – risk products materials or gas blends these discharges are too dangerous and could induce disastrous after-effects when conventionally polymer products are used in the explosion – risk production, electrical industry and special machine – building. Such disadvantages could be overcome with the help of a purposeful structure forming in the composed foamed thermoplastic melt, obtained in the conditions of the method of injection – moulding with gas counter – pressure (MIMGSP) by suitable filling with nano-sized or complex fillers and formation of the characteristic for this high technological eco – method, “bone-structure” of the products from composed foamed thermoplastics with constructional use and increased electrostatic safety.*

**Keywords:** *moulding under gas counter pressure, structure-forming, structural model, electrostatic properties, morphological peculiarities, physical-mechanical indices; foamed recycled thermoplastics.*

## Introduction

The utilization of polymer materials as well as of composit foamed thermoplastics (CFT) on the base of nano-sized (anorganic and organic) fillers in various technical branches recently requires development of new constructional products with increased stability towards the accumulation and the effect of electrostatic charges. It is known that conventionally obtained polymer and plastic products possess high surface ( $\rho_s$ ) and volume ( $\rho_v$ ) electrical resistances. By friction and contact with other hard objects they are easily electricized and the electrical charged accumulated on their surface create conditions for formation of discharges, which by a determined ignition energy of explosion – risk products, materials and gas-blends are rather dangerous and could provoke katastrophical aftereffects when used in electrical industry, special machine-building and in explosion-risk production [1-3].

## Method

Introducing special fillers to increase conductivity of thermoplastical matrix it is possible to decrease significantly  $\rho_v$  and  $\rho_s$ . Very often by such experiments the polymer composites decrease their cofigurational stability, functional designation and some physical-

mechanical indices in a determined temperature – performance range. It is possible to overcome these disadvantages with the help of purposeful structure – forming in composit foaming thermoplastic melt in the terms of the method of injection – moulding with gas counter – pressure (MIMGSP) by suitable filling with nano – sized filler as to obtain the characteristic for this high – technological eco – method “bone” structure of the CFT – products with constructional designation and enhanced electrostatic safety. Our analysis of literature and experimental data of the potential of the combination from homogenically foamed melt – core and presence of precisely dosed filler, distributed in the bound interphase zones of the structural model system “thermoplastic matrix – nano – sized filler gas – phase” showed that it comes to changes in the whole spectrum of physical – chemical, structural and physical – chemical. Structural and physical properties of the multiphase thermoplastic matrix: dielectrical constant, conductivity, crystallinity, refraction index, oxidation potential and other.

Without pretending to exhaust, we shall mention those utilization domains of the examined composites, some of which realized and some in realization process; casings and covers for heavy starter batteries, “monoblock” type; gas exchange materials and gas – and fluid – separating membranes, heterostructures protection from static electricity and other of the casings and surface elements of electric devices, containers for works in the explosion – risk production, computer and cosmic technique and other.

The different theories of initiating of electrostatic charges are based on the so called “twofold electro – layer”, formed at the position of contact of two surfaces. In our model structural systems on Fig.1 the bound phase surfaces are between the stiff thermoplastic matrix and the stiff phase of the filling particle (Fig.2), inbetween the gas-phase and the stiff thermoplastic matrix as well as between the gas-phase (Fig.3) and the surface of the stiff filler-particle.

By a given concentration of fillers – particles we observe contact also between stiff filler-particles, which are able to form even conductive small bridges in the dielectric thermoplastic matrix (Fig. 4b) as the gas phase is in the form of closed gas-bubbles, when contacting with the other phases, an electrical twofold layer is also formed but only at the side of the stiff surface.

Depending of the volume part of the filler, the conductivity of the composit will change from  $\sigma_2$  by  $C < C_n$ , i. e. when the filler’s particles are isolated one from other (Fig.4a) until  $\sigma_1$  by  $C > C_n$ , i. e. when a continuous medium of contacting particles is formed (Fig. 4b), where  $\sigma_1$  – conductivity of nano-sized particles,  $\sigma_2$  –

conductivity of thermoplastic matrix,  $C$  – volume part of the filler with conductivity  $\sigma_1$ ,  $C_n$ - bound (threshold) volume of current – passing, at which for the first time in the thermoplastic matrix a continuous conductive circuit with microscopic length is occurring. When introduced some theoretical assumptions are harmonized with experimentally obtained dependences of conductivity of the composition compound and structural particularities of test samples.

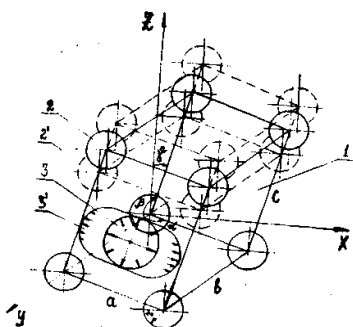


Fig.1. Model structural multi-phase system “thermoplastic matrix” (1); spherical particle – nanosized filler (2); gas-phase (spherical bubble) (3); triclinic crystallographic system – space grate, determined by three periods  $a, b, c$  and three angles  $\alpha, \beta$  and  $\gamma$ .

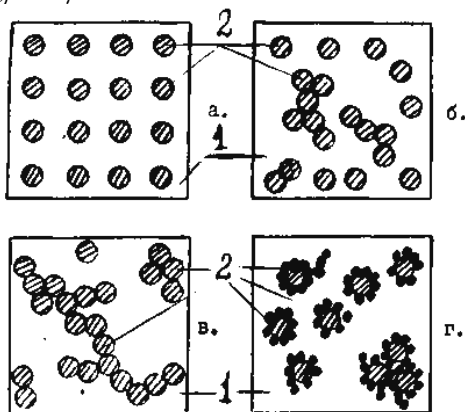


Fig.2. Bound phase surfaces in model composition structures: 1 – thermoplastic matrix, 2 – model filler – particles; a - matrix system, b - statistical system, v - structured (stitched together) flat system, z – structured volume system.

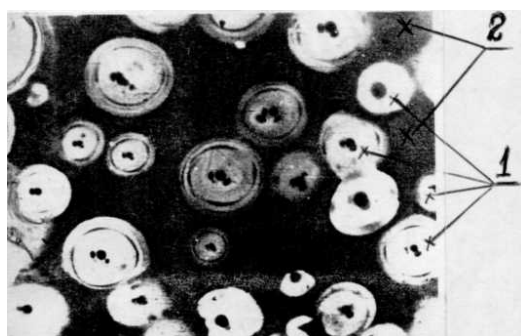


Fig.3. Bound Phase surfaces between gas-bubbles – 1 and hard thermoplastic matrix with nanosized fillers particles – 2.



Fig.4.a. Microphoto of structure of filled test bodies – the filler’s particles are isolated in a thermoplastic matrix.



Fig.4.b. Microphoto of structure of filled test bodies – the filler’s particles are contacting and form circuit electrical conductive formations

Hence, a generalized conductivity ( $\sigma_m$ ) of composit system matrix type (Fig. 2a) with model cubic-ordered grate and parallel walls of ordering would have following form [4];

$$(1) \quad \sigma_m = \sigma_2 + \sigma_2 \left( \frac{1-C_1}{3} + \frac{\sigma_2}{\sigma_1 - \sigma_2} \right) + C_1$$

$$(2) \quad \sigma_m = \sigma_1 \left( \frac{C}{f} - 2z \right)$$

by  $C > C_n$ ,

where  $z$  is the quantity of neighbouring nozzles – conductors in the grate, i.e. the conductivity is increasing linearly with concentration enhancement of the introduced filler at the account of the increased number of the infinite structural formations conductive character. By  $C < C_n$  the expression of the generalized elconductivity will be :

$$(3) \quad \sigma_m \approx \frac{\sigma_2}{1 - \frac{zC}{2f}}$$

where  $f$  is factor of filling (correlation of filler’s particles volume to the full volume of composit) in a model, whose particles have the form of sphere with radius equal to the half of the distance until the closest neighbouring particle, hence, these are structures, at which the elconductive filler doesn’t form current – conducting circuits, and it’s particles are more or less unevenly distributed in the volume of the thermoplastic matrix by samples with dence structure. In such a case a filling ranging from 65 – 70 mass% is necessary as to achieve some elconductivity, but this leads to an abrupt reduction

of physical-mechanical properties of the ready made products.

## Results

In accordance with [4] the fluctuation-diffusion mechanism by vacancies ("potential pits") in the structural grate and the experimental achievement of the optimum from the combination of these properties with the elconductivity through composition compound, filler's type and technological potential of the MIMGSP are the obtained results as well.

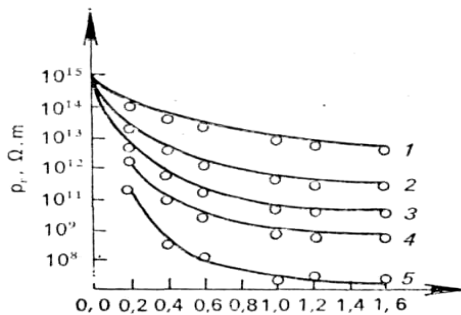


Fig.5. Dependences for  $\rho_v$  from the quantity, type and characteristics of the introduced in CFT composit fillers; 1-kaolin, 2 – graphite ( $C_1$  modification), 3 – metal disperse filler, 4 – binary filler (kaolin – graphite disperse filler) 5 – acetylen smuts (modification  $C_2$ ).

From Fig 5-7 is to be seen that  $\rho_v$  depends to a big degree not only on the the type , properties and quantity of introduced fillers, but also on the degree of gas counter-pressure and quantities of gasformers as well as morphology of the foamed structure, predetermined to a significant degree from moulding terms.

When changing size, type, anyzotrophie and other of the gas-bubbles in the foamed core of the mouldings, increase the chaotic state of structural elements, the wall's size separating one from the other bubble or from the filler's particles, or the anyzotrophic ordering of the structural elements in the volume of the thermoplastic matrix.

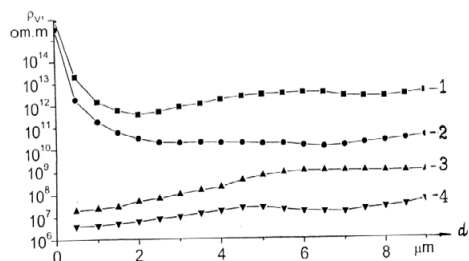


Fig.6. Dependences for the volume, electrical resistance ( $\rho_v$ ) from particles size  $d$  of complex filler (aerosol + boron carbide) and from moulding terms of CFT PP – test samples: 1 – conventionally moulded under pressure (with dense structure), 2 – conventionally moulded with foamed structure, 3 – moulded according MIMGSP ( $\Delta P = 15 \text{ kg/cm}^2$ ) with foamed structure (heterogene), foaming degree:  $0,85 \text{ g/cm}^3$ ; 4 – moulded according MIMGSP ( $\Delta P = 15 \text{ kg/cm}^2$ ) with foamed structure (homogene), foaming degree:  $0,75 \text{ g/cm}^3$

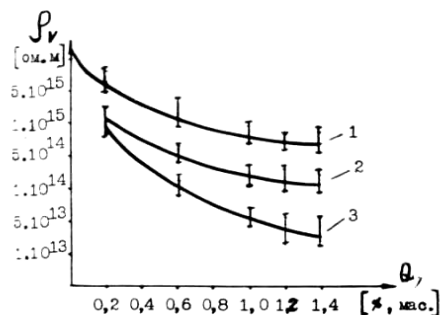


Fig.7. Dependences for ( $\rho_v$ ) from the degree of gas counter-pressure  $\Delta P$  and from the quantity gasformer: 1 – conventionally moulded test bodies; 2 – moulded according MIMGSP test bodies ( $\Delta P=10 \text{ g/cm}^2$ ), 3 – moulded according MIMGSP test bodies ( $\Delta P=20 \text{ kg/cm}^2$ ).

All this enables the so called pit electrical conductivity through polymer walls, fencing particles-filler of gas bubbles in investigated composit. In the bound zones of the system "thermoplastic matrix – filler – gas bubble" except for direct contacts also significant concentrations of free carriers of charges under the action of external electric field can occur. This creates conditions for electric field formation around structural switchings on and at the presence of "overlapping" it comes to injection of elcharges and current flow in such a way, i. e. in the foamed and moulded according. MIMGSP – samples certain elconductivity even at lower concentrations of the fillers (but after given values for  $C_n$ ).

The dependences of  $\rho_v$  from testing temperature for test samples determined in two ranges : low temperature – from  $-60^\circ\text{C}$  to  $+20^\circ\text{C}$  and high temperature from  $+20^\circ\text{C}$  to  $100^\circ\text{C}$ . This is subject of discussion of our following publication.

## Conclusion

The composit foamed thermoplastics moulded in MIMGSP – terms with well developed fine – cell and homogene structure have with about 1,5 - 2,5 orders lower values for  $\rho_v$  and when filled with nanosized (complex on the base of aerosol and boron carbide + titanium diboride) filler – from 4 to 5,5 orders lower values for  $\rho_v$  in comparison to the same samples, moulded under pressure with dense structure.

## Acknowledgements

This papers is in accordance with grant № NT -2-02/2004 of Fund "Scientific Invest." of Ministry of Education and Science"

## References

- [1] "Nanoscience & Nanotechnology", "Heron press science ser.", 1984, 318;
- [2] Шeverдяев, О. Н. Антистатические полимерные материалы. "Химия", М., 1983, 176;

- [3] Пиперов, Н. Л. Изследване на някои електростатични свойства на пластмасови контейнери от частично разпенени термопласти, получени по метода за леене с газово противоналягане. Техническа мисъл, № 4, 1987, 99÷104;
- [4] Сажин, Б. И. И др. Электрические свойства полимеров, “Химия”, 1977, 192;
- [5] Йоффе, А. Ф. Физика кристаллов. М., “Госсиздат”, 1929;

---

**Nikolay Piperov** – Assoc. Professor, Dr., Institute for Metal Science – Bulgarian Academy of Sciences, Sofia, Bul. “Shipchenski Prohod” 67, 1567 Sofia, Bulgaria  
e-mail: [inpiperov@abv.bg](mailto:inpiperov@abv.bg).

**Vasil – Mario Piperov** – Associate Professor, Dr., Faculty of Electrical Engineering, Technical University of Sofia, 8 Kl. Ohridski Str., 1000 Sofia, BULGARIA.  
e-mail: [pipi@tu-sofia.bg](mailto:pipi@tu-sofia.bg).

## Simulations and Measurements of Some Parameters from Plate-Type Electrostatic Precipitators

**Gabriel Nicolae Popa, Corina Diniş, Cristian Abrudean and Ovidiu Tirian**

**Abstract:** *The plate-type electrostatic precipitators have long been used by industry applications as the preferred method for controlling pollution with dust particles. The paper analyze the collection efficiency when are used different voltage supplies of electrostatic precipitators sections, the gas particles masses distributions, the inlet and the outlet dust concentration. The simulations compare with real parameters will show that is a good agreement between the ESPVI 4.0.a model and plate-type electrostatic precipitators parameters.*

**Keywords:** *pollution, electrostatic, precipitators, model*

### Introduction

The globalization of the environmental pollution problems caused by the increase of industrial production will lead in the cleaning of the waste gases. The basic idea of electrostatic precipitators is to give the particles an electrostatic charge when are place them into an electrostatic field that drives the particles to a collecting plates (electrodes) connected to earth.

This type of electrostatic precipitator is used to remove pollutants from large flow gas (hundreds of thousand m<sup>3</sup>/h). The efficiency of electrostatic precipitators depends by voltages shape and amplitude, by types of power supply, by current control, by geometry of electrostatic precipitators, by types of discharge wires, by gas composition, by particles distribution, by gas flow, by temperature, by gas pressure and particles velocities distribution [1].

One of software that compute the plate-type electrostatic precipitators performances is ESPVI 4.0.a. The model predictions show good agreement with experimental measurements taken at plate-type

electrostatic precipitators from U.S.A. under several operation conditions. For the modelling with ESPVI 4.0.a software are used parameters from thermal power station plate-type electrostatic precipitators (from Romania).

The dry plate-type electrostatic precipitators is used in industry applicaton to controlling pollution with dust particles.

The model predictions of ESPVI 4.0.a software shows good agreement with experimental measurements taken at plate-type electrostatic precipitators (ESP) from U.S.A. under several operation conditions. The ESPVI 4.0.a software is the latest in a long series of ESP models sponsored by the United States Environmental Agency. This software has a lot of plate-type electrostatic precipitators parameters:

- the tehnological electrostatic precipitator parameters;
- the electrical electrostatic precipitator parameters for every sections;
- the gas parameters;
- the dust parameters.

It is analyzed the work of plate-type electrostatic precipitators from thermal power stations (from) Romania with three sections [2,4].

With this software and the tehnological and electrical parameters from industry may be compare the performance of plate-type electrostatic precipitators for understanding how does it work.

### The Plate-Type Electrostatic Precipitators Performances

For the modelling with ESPVI 4.0.a software it is used electrostatic precipitators, with three sections (no. 4, 5, 6) from Thermal Power Station Mintia-Deva from Romania (1200 MW) [5,6,7].

**Table 1**

*The main electrical characteristics for plate-type electrostatic precipitators supplies from Thermal Power Station Mintia-Deva*

The main electrical characteristics	ESP no.5	ESP no.6	ESP no.7
The supply number [-]	6	6	6
The low voltage supply	2x380 V ±10% 50 Hz	2x380 V ±10% 50 Hz	2x380 V ±10% 50 Hz
The nominal supply current [A]	607	595	595
The ESP peak high voltage [kV]	111	111	111
The ESP nominal high voltage [kV]	65	65	65
The ESP maximal current [mA]	2800	2800	2800
The ESP nominal current [mA]	2000	2000	2000
The apparent power [kVA]	237.2	238	238

**Table 2**

*The main technological characteristics for plate-type electrostatic precipitators (ESP) from Thermal Power Station Mintia-Deva from Romania*

The main technological characteristics	ESP no.5	ESP no.6	ESP no.7
The number sections	3	3	3
The height of collecting plates (electrodes)	12	12	12
The distance between the collecting plates and the discharge wires [m]	0.3	0.3	0.3
The duct number from sections	54	55	56
The nominal gas stream flow [m <sup>3</sup> /h]	728900	728900	675000
The inlet dust concentration (from design) [mg/m <sup>3</sup> ]	85.69	93.61	93.61
The outlet dust concentration (from design) [mg/m <sup>3</sup> ]	0.75	0.889	0.889
The collecting efficiency [%]	99.12	99.05	99.05
The nominal temperature of inlet gases [°C]	148	148	148
The maximal temperature of inlet gases [°C]	163	163	163
The nominal ashes flow, evacuate from ESP [t/h]	44.5	44.5	44.5
The unburn combustible from ashes [%]	0.3-1.2	0.3-1.2	0.3-1.2
The gas viscovity [kg/(m·s)]	(1-5)·10 <sup>-5</sup>	(1-5)·10 <sup>-5</sup>	(1-5)·10 <sup>-5</sup>
The inferior calorific power of coal [kcal/kg]	2750	2450	2450
The dust resistivity [Ω·cm]	10 <sup>9</sup> -10 <sup>13</sup>	10 <sup>9</sup> -10 <sup>13</sup>	10 <sup>9</sup> -10 <sup>13</sup>

Because the electrostatic precipitators treat large gas flow, its are dived in three sections and every sections are divided in two fields for reliability, every sections has own electrical supply.

The discharge wires are dispose in the ducts and are equidistances.

**Simulations and Measurements of Tehnological and Electrical Parameters Using ESPVI 4.0.a Software**

The ESPVI 4.0.a (Electrostatic Precipitators U-I Curves and Performance Model) software is from 1992.

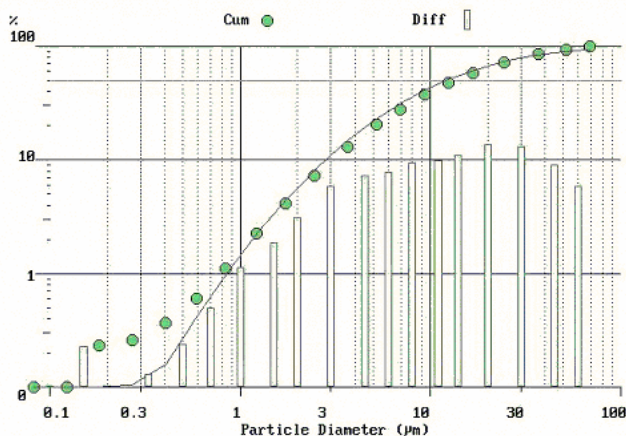


Fig.1.

The cumulative and differential mass distributions at inlet of precipitators are shown in fig.1.

The model predictions shows good agreement with experimental measurements taken at plate – type electrostatic precipitators from U.S.A. under several

conditions, including high resistivity ashes, the use of rectified current and intermittent energization of ESP sections, different size of dust particles (up to 1000µm), detects the onset of back Corona, peak to average ratio of voltages, different shapes of discharge wires.

The number and the mass as function of size dust particles are shown in fig.2.

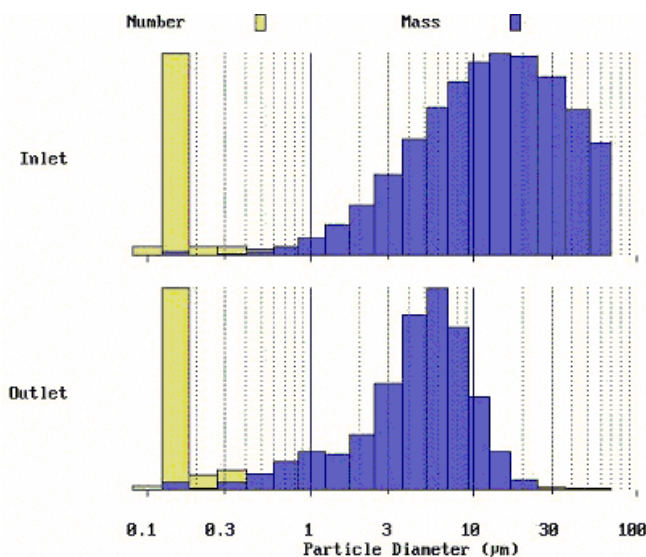


Fig.2.

When the ESP sections are supplies with full wave (1:01 with high voltage bridge, with negative polarity at discharge wires) the operation point (the onset Corona and spark discharge) are present in fig.3. for sections 1, 2, 3 for ESP [2,3].

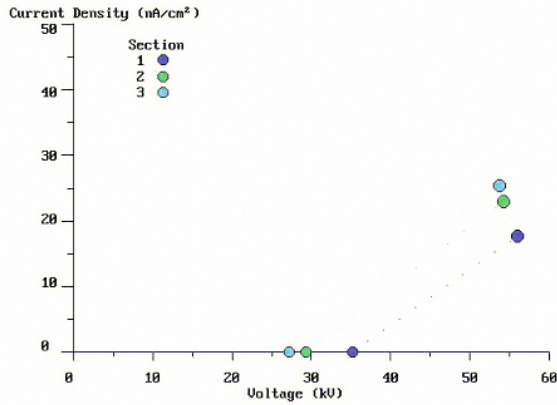


Fig.3.

The ESP voltage waveforms with high voltage bridge are present in fig.4.

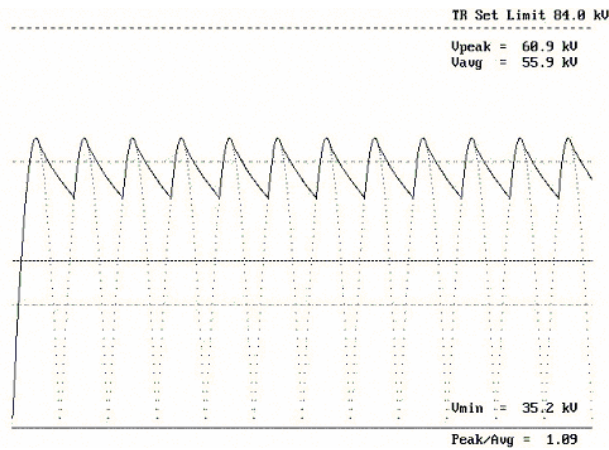


Fig.4.

The intermittent energization of sections with different degree of energization (3, 5 and 7) are present in fig. 5, 6, 7.

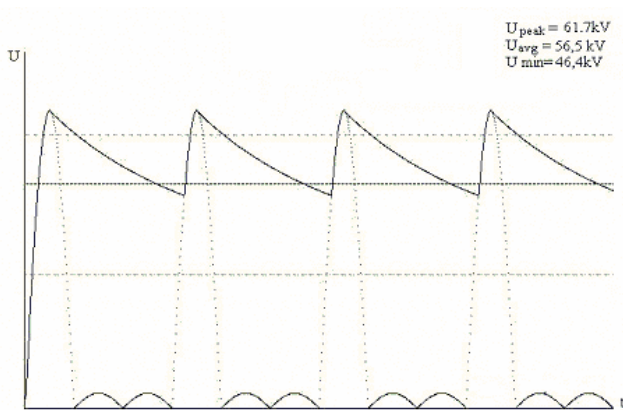


Fig.5.

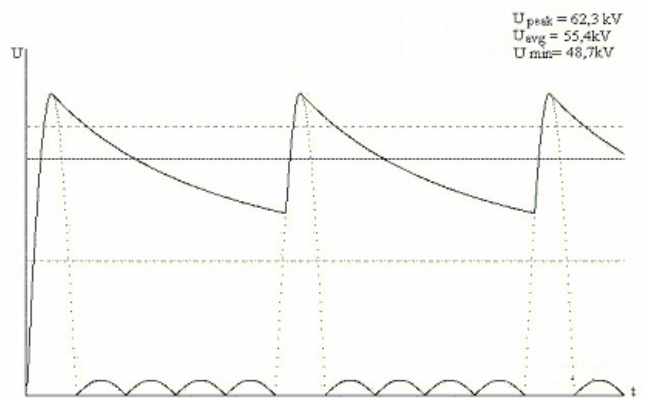


Fig.6.

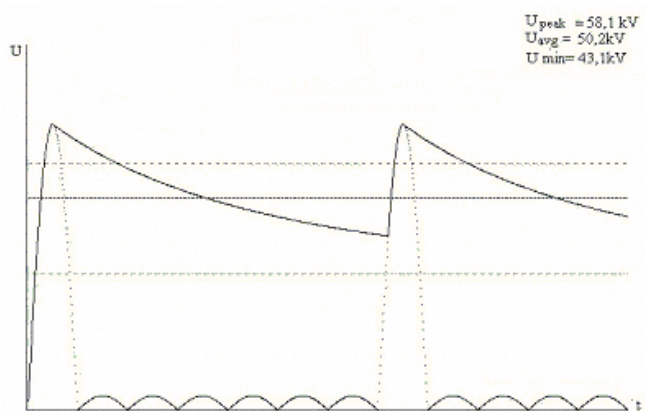


Fig.7.

An intermittent energization is one ESP current pulse are present and a number of current pulses are suppressed.

In fig.8, 9, 10 was simulated the main current-voltage characteristics (the onset Corona voltage, the spark discharge voltage and the spark current) in the case of DC energization, full wave energization and intermittent energization (1:03, 1:05, 1:07, 1:09).

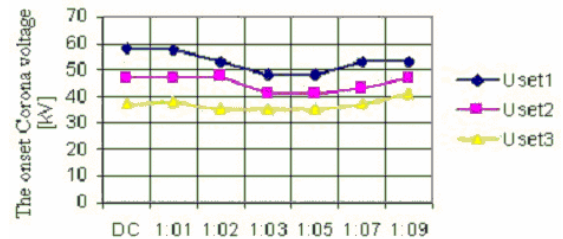


Fig.8. The onset Corona voltage for every section (1, 2, 3) when the ESP sections are supplies with the same voltage.

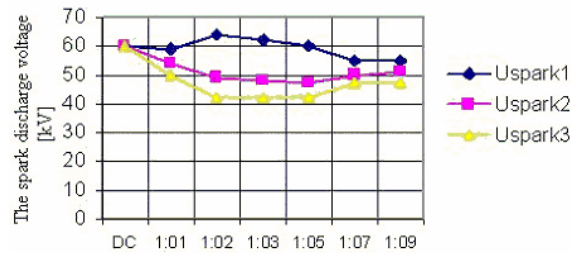


Fig.9. The spark discharge voltage for every section (1, 2, 3) when the ESP sections are supplies with the same voltage.

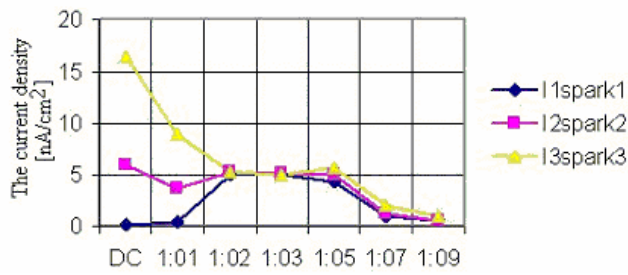


Fig.10. The current density when is spark discharge for every section (1, 2, 3) when the ESP sections are supplies with the same voltage.

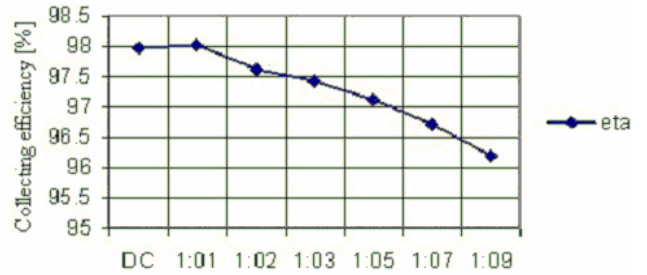


Fig.11. The collecting efficiency depending on the voltage supply.

The collecting efficiency depending on the voltage supply are present in fig.11.

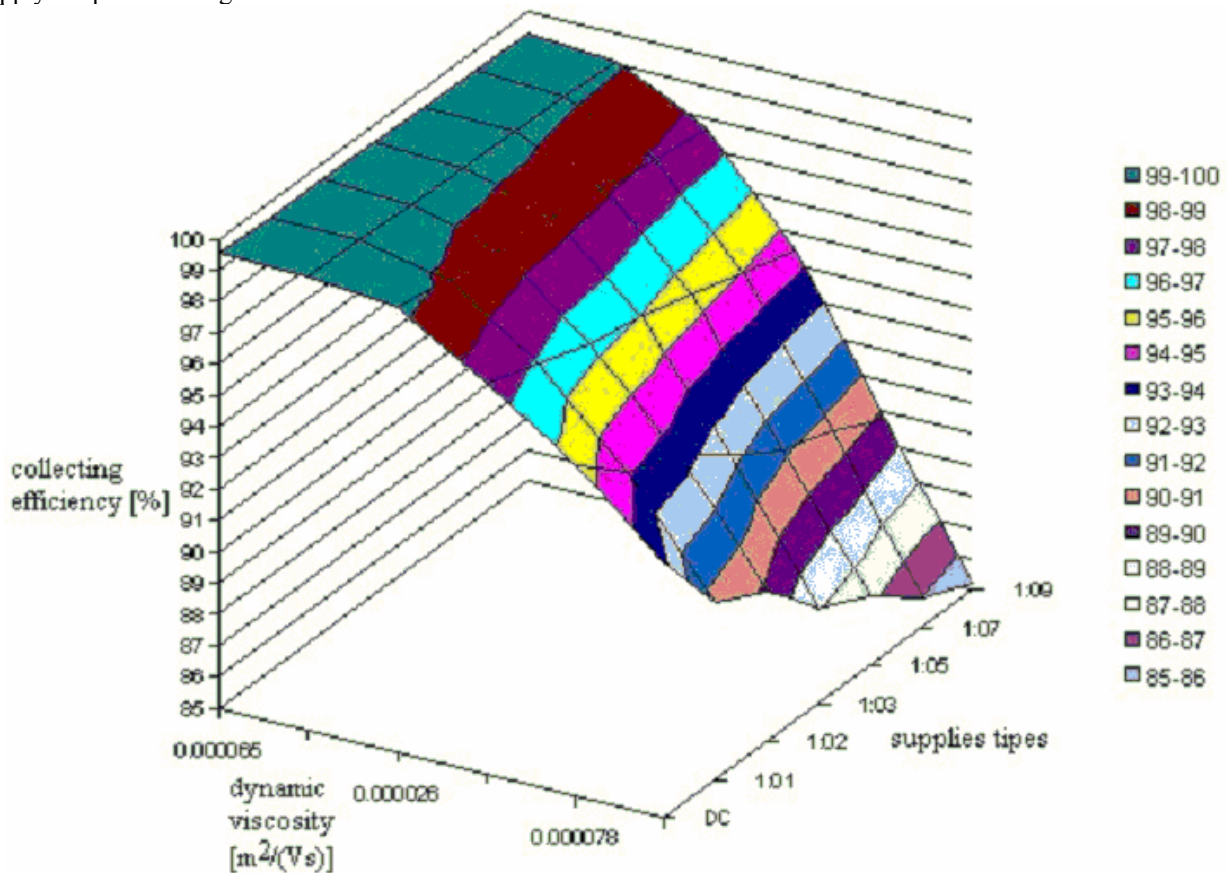


Fig.12. The collecting efficiency depending on the voltage waveforms and gas dynamic viscosity

The onset Corona voltage it is the same for every sections, indifferently by the voltage waveforms. The onset Corona voltage for sections 1 is bigger than the onset Corona for section 3 (fig.10). This observation are available for spark discharge voltage (fig.11). The current density, for intermitent energization 1:03,..., 1:09 are smaller for section 1 and bigger for section 3 [1,4].

The best collecting efficiency is when are supplies every sections with DC voltage (ideal) and full wave

voltage (98%) and the worst collecting efficiency when is use intermitent energization 1:09 (96.15%).

In fig.12 is present an analyze of collecting efficiency depending on dynamic viscosity and the waveforms voltage. The collecting efficiency are diminish when the dynamic viscosity and intermitent degree energization are lower.



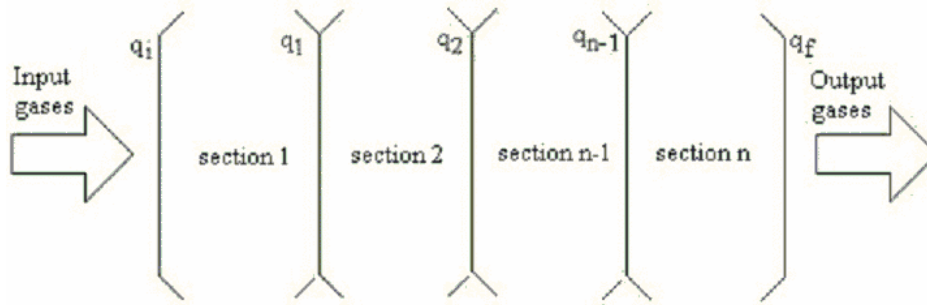


Fig.13.The electrostatic precipitators with n sections

It is note with  $q_i$ [g/m<sup>3</sup>] the inlet dust concentration and with  $q_f$ [g/m<sup>3</sup>] the outlet dust concentration for electrostatic precipitators. The plate-type electrostatic precipitator collection efficiency  $\eta$ [-] is:

$$(1) \quad \eta_1 = 1 - \frac{q_f}{q_i},$$

Let consider an plate-type electrostatic precipitators with n sections (fig.13). Practically, the maximum number of sections is 10. At the outlet of n-1 sections, the dust concentration is  $q_{n-1}$  [g/m<sup>3</sup>].

The collection efficiency  $\eta_1$ [-] of section 1 is:

$$(2) \quad \eta_1 = 1 - \frac{q_1}{q_i},$$

The collection efficiency  $\eta_2$ [-] of section 2 is:

$$(3) \quad \eta_2 = 1 - \frac{q_2}{q_1},$$

The collection efficiency  $\eta_n$ [-] of section n is:

$$(4) \quad \eta_n = 1 - \frac{q_f}{q_{n-1}},$$

From relations (1), (2), (3), (4) results the total collection efficiency:

$$(5) \quad \eta = 1 - (1 - \eta_1) \cdot (1 - \eta_2) \cdot \dots \cdot (1 - \eta_n),$$

The total collection efficiency depends by every sections collection efficiency.

Table 3

The measurement and simulate collection efficiency for different ESP with three sections

	No.	$q_i$ [g/m <sup>3</sup> ]	$q_f$ [g/m <sup>3</sup> ]	Collection efficiency			Relative error $\frac{ \eta_m - \eta_s }{\eta_m} 100$ [%]
				Measured [5,6,7] $\eta_m$ [%]	Average $\eta_{avg}$ [%]	Simulated $\eta_s$ [%]	
ESP 4	1	24.908	0.147	99.408	99.41	98	1.41
	2	25.528	0.138	99.459			
	3	24.127	0.154	99.362			
ESP 5	1	20.746	0.187	99.098	99.055	98	1.06
	2	20.061	0.198	99.013			
ESP 6	1	20.593	0.167	99.189	99.381	98	1.39
	2	26.464	0.113	99.573			

Table 4

The average diameter of dust collecting in ESP sections

	$d_{avg1}$ [μm] section 1	$d_{avg2}$ [μm] section 2	$d_{avg3}$ [μm] section 3
ESP 4	79.7	45.15	50.68
ESP 5	73.4	45.5	56.3
ESP 6	74.6	38.7	38.6

From table 3 results that the simulated collection efficiency is close by measured collection efficiency (the relative error is between 1.06-1.41 %). That demonstrated the performance of prediction model from ESPVI 4.0.a software. From table 4 results that the average diameter of dust particles are smaller to the outlet sections.

## Conclusions

The collection efficiency electrostatic precipitator depends on voltage waveforms, among other factors. Is necessary to supply with different shapes voltage from section to section to obtain a high collection efficiency. The dust resistivity rise up to outlet section. The inlet section may be supply with DC voltage (ideal) or full wave voltage with bridge diodes) for well charge of dust particle with normal resistivity. The outlet section may be supply with intermitent voltage (with different degree of intermitance) to collect dust particle with high resistivity.

## Acknowledgements

This work was supported by CNCSIS no.73 Grant AT no.27688/2005.

## References:

- [1] Popa G.N. Contribuții privind îmbunătățirea performanțelor unor electrofiltre industriale pentru sisteme bifazice gaz-particule solide, doctoral thesis, Universitatea "Politehnica" Timișoara, Facultatea de Electrotehnică și Electroenergetică, Timișoara, Romania, 2004.
- [2] Popa G.N., Popa I. Simulations of Same Parameters from Plate-Type Electrostatic Precipitators Using ESPVI 4.0.a software, pp.613-616, 6<sup>th</sup> International Conference on Accomplishments of Electrical and Mechanical Industries, DEMI 2003, Banja Luka, 2003.
- [3] Popa G.N., Popa I., Deaconu S. Soluții de alimentare cu energie electrică și de automatizare ale electrofiltrelor cu plăci industriale, Revista de Automatizări și Instrumentație, nr.1, București, 2005.
- [4] Vaida V., Șora I., Popa G.N. The Improving of Plate-Type Electrostatic Precipitators Performances, Conferința Națională a Energiei, CNE 2004, cod S3p-25, Neptun, Romania, 2004.
- [5] \*\*\* Instalația de desprăfuire electrică F.E.Deva – grup 4. Măsurători de performanță pentru stabilirea gradului de epurare, 2131 CPPM, ICPET – S.A. București, Divizia Protecția Mediului, 1995.

[6] \*\*\* Instalația de desprăfuire electrică F.E.Deva – grup 6. Măsurători de performanță pentru stabilirea gradului de epurare, 2130 CPPM, ICPET – S.A. București, Divizia Protecția Mediului, 1995.

[7] \*\*\* Măsurători de performanță pentru stabilirea gradului de epurare la instalația de desprăfuire electrică de la al 5-lea grup, 2161-CPPM, ICPET – S.A., București, Divizia Protecția Mediului, 1996.

---

**Gabriel Nicolae Popa** – Lecturer, Ph.D., Faculty of Engineering Hunedoara, „Politehnica” University of Timisoara, Revolutiei str. no 5, Hunedoara, ROMANIA, e-mail: gnpopa@fih.utt.ro

**Corina Diniș** – Lecturer, Faculty of Engineering Hunedoara, „Politehnica” University of Timisoara, Revolutiei str. no 5, Hunedoara, ROMANIA, e-mail: corina-dinis@fih.utt.ro

**Cristian Abrudean** – Assistant, Faculty of Engineering Hunedoara, „Politehnica” University of Timisoara, Revolutiei str. no 5, Hunedoara, ROMANIA, e-mail: cristi\_a@rdslink.ro

**Ovidiu Tirian** – Assistant, Faculty of Engineering Hunedoara, „Politehnica” University of Timisoara, Revolutiei str. no 5, Hunedoara, ROMANIA, e-mail: ovitir@fih.utt.ro

# Invariability of Torques at Magnetization Modification Technology by Slowly Changed Fields

Peter Dineff and Raina Tzeneva

**Abstract:** The magnetization modification technology involves a set of modern technologies for obtaining materials with physico-chemical properties modified by changing their structural organization. From electromagnetic point of view it is substantiated the invariability of the magnetic force action upon the magnetic turning moments at the transition from a uniform magnetic field to a non-uniform one. The magnetic turning moments acting upon the magnetic kinetic structure elements is evaluated.

**Keywords:** adiabatic invariability, magnetical dipole moment, magnetical kinetic structure element, magnetic torque, slowly changing uniform and non-uniform magnetic fields.

## Introduction

The magnetic or magnetization modification is in the basis of created magnetic technologies for modification of materials - polymers and polymeric materials, rubbers, metals and alloys, bio-materials, cement and polymer-cement concrete ware, water and water solutions, Fig. 1 [1, 2].

The magnetization polarization technology of physical modification of materials (diamagnetics, paramagnetics and ferromagnetics) is based on the concepts for the orientational (polarizing) behavior of so-called magnetic kinetic structural elements (KSE) during their motion in external magnetic field [1, 2, and 3].

The own screening investigations of the authors for creating magnetic technological devices (MTD) directed with time the attention to using non-uniform magnetic

Even in the case of magnetization modification in uniform magnetic field ( $dH/dx = 0$ ), the material treated passes through a non-uniform magnetic field with a gradient of changing the field  $H$  having different signs - positive ( $dH/dx > 0$ ) at entering, and negative ( $dH/dx < 0$ ) at going out from the device, Fig. 1.

It is posed the justified question for the contribution of additional orientating magnetic moments, caused by the non-uniformity of the magnetic field, to orientational modification of materials.

In the same time, it is well known that in many practical cases the magnetic field changes weakly at distances commensurable with the trajectory of motion of KSE, which defines on one hand the so-called invariability of their magnetic moment, and on the other hand – the insignificant effect of the additional orientating magnetic moments on polarization [2].

field technologies, ensuring greater technological effect in treating materials of various nature, polymeric materials included as well [4, 5, and 6].

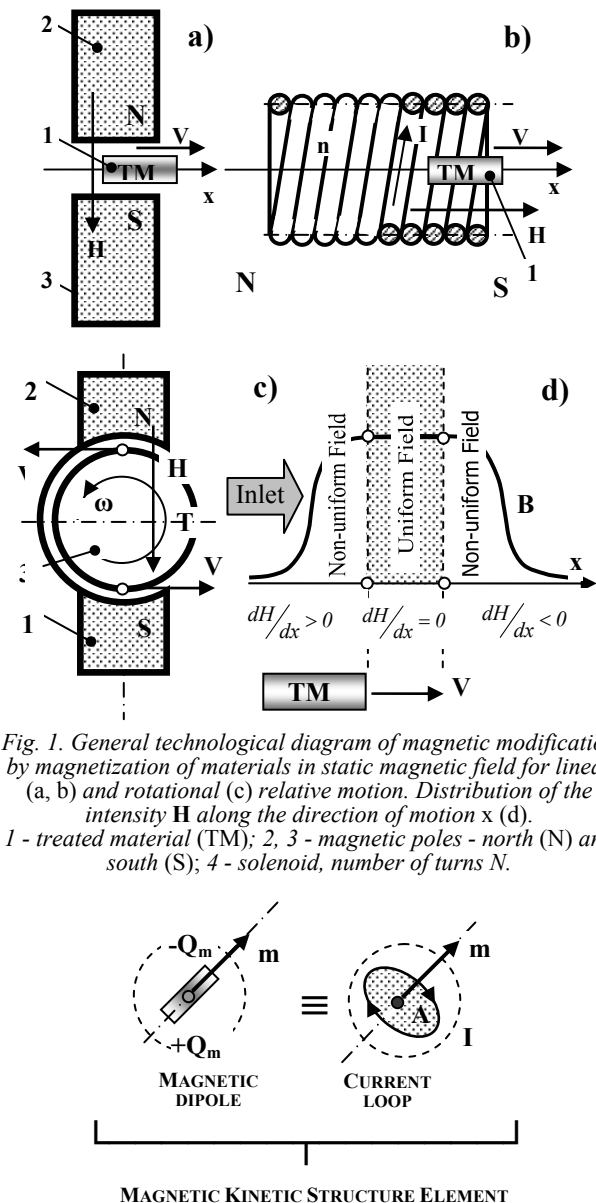


Fig. 1. General technological diagram of magnetic modification by magnetization of materials in static magnetic field for linear (a, b) and rotational (c) relative motion. Distribution of the intensity  $H$  along the direction of motion  $x$  (d). 1 - treated material (TM); 2, 3 - magnetic poles - north (N) and south (S); 4 - solenoid, number of turns  $N$ .

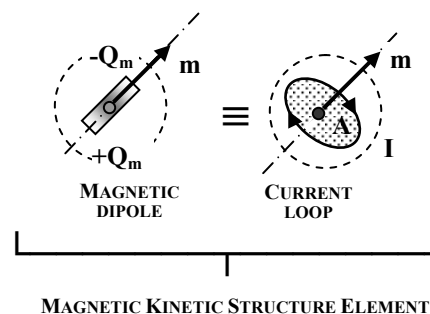


Fig. 2. Magnetic kinetic structural element (MKSE) – equivalent presentation of MKSE as a magnetic dipole and as a current loop.

THE PURPOSE of the present work is to propose defining expressions for torques acting upon kinetic structural elements in the magnetization modification technol-

ogy and to evaluate the degree of change in the magnetic field acting upon *kinetic structural elements*.

### Physical models of magnetization modification

The modification of every material in a magnetic field may be represented through the interaction of the kinetic structure elements (*KSE*) constituting it with the external magnetic field, these elements acquiring for various causes the possibility to perform motions – first of all rotational ones, at a higher energetic state, or at thermal and/or acoustic activation of the material [1 and 2].

It is assumed that these interactions remain linear for changing the intensity  $\mathbf{H}$  of the magnetic field and the temperature, i. e. it remains in force the *principle of superposition*.

Kinetic structure elements (*KSE*) may be represented in their interaction with the magnetic field through a magnetic dipole with magnetic pole strength  $Q_m$  and length  $l$ , i. e. as a magnetic structure kinetic element (*MKSE*), Fig.2.

It is well known that the magnetic dipole and the current loop are equivalent [7]:

$$(1) \quad m = Q_m l = I A .$$

### Magnetic kinetic structural element in static uniform magnetic field - magnetic torques

Let assume that *MKSE* is situated in a static uniform magnetic field  $\mathbf{H}$ , as suggested in Fig. 3 [7].

The north (+) pole experiences a force  $F$  to the right and the south (-) pole an equal force  $F$  to the left. The torque  $T$ , or turning moment (force x distance), on the dipole is:

$$(2) \quad T_0 = F l \sin \theta = Q_m l H \sin \theta = m H \sin \theta ,$$

where  $F = Q_m H$ ;  $l$  - length of dipole;  $\theta$  - angle between dipole axis and  $H$ ;  $m = Q_m l$  - magnetic dipole moment,  $A \cdot m^2$  [7].

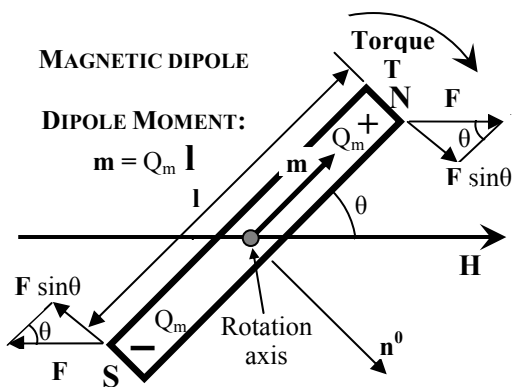


Fig. 3. Magnetic dipole in a uniform field  $H$  - in this case the torque is clockwise and tends to align ( $m > 0$ ) the unit vector  $\mathbf{n}^0$  with  $\mathbf{H}$ .

The magnetic moment of the *paramagnetic* materials as a vector  $\mathbf{m}$  has the direction of positive sense of the unit vector  $\mathbf{n}^0$  - from the negative to positive poles, when  $m = + |\mathbf{m}|$ , or  $m > 0$ .

The magnetic moment of the *diamagnetic* materials as a vector  $\mathbf{m}$  has the direction of negative sense of the unit vector  $\mathbf{n}^0$  - from the positive to negative poles, when  $m = - |\mathbf{m}|$ , or  $m < 0$ .

Then the magnetic dipole will turn around its axis till the magnetic torque reduces its magnitude to  $T_0 = 0$  or vector  $\mathbf{m}$  becomes collinear to vector  $\mathbf{H}$ :

at  $m > 0$ :

$$(3) \quad T_0 = + m H \sin \theta = 0 : \sin \theta = 0 \Rightarrow \theta = 0 .$$

at  $m < 0$ :

$$(4) \quad T_0 = - m H \sin \theta = m H \sin (\pi + \theta) \quad \text{or}$$

$$(5) \quad T_0 = m H \cos (\pi/2 + \theta) :$$

$$\cos (\pi/2 + \theta) = \sin (\pi + \theta) = 0 \Rightarrow \theta = \pi .$$

The polarization or arrangement of *MKSE* in one direction is a relaxation process as it is carried out against the counteracting thermal chaotic motion of *MKSE*. It becomes possible only at low internal friction (resistance), i. e. at thermal or acoustic (phonon) actuation of the material. In such a way, as a result of the magnetization, *MKSE* form an oriented structure along the direction of the external magnetic field.

The magnetic dipole moment  $m$  of *MKSE* with volume  $\mathcal{V}$ , containing elementary magnetic dipoles with dipole moment  $\Delta m$  of number  $N$ , may be represented through the magnetic dipole moment  $M$  per unit volume, called magnetization [7]:

$$(6) \quad m = \int_{\mathcal{V}} M d\mathcal{V} = \frac{N}{\mathcal{V}} \Delta m = N' \Delta m , \quad A \cdot m^2 .$$

The magnetization  $M$  of *MKSE* depends only on the magnetic susceptibility  $\chi_m$  of the structure element and the magnetic field intensity  $H$ :

$$(7) \quad M = \chi_m H = (\mu_r - 1) H$$

where  $\chi_m = \mu_r - 1$ ;  $\mu_r = B/(\mu_0 H)$  - relative permeability, dimensionless ratio;  $\mu_0 = 400 \pi$  - permeability of vacuum,  $nH \cdot m^{-1}$  [7].

The magnetic susceptibility  $\chi_m$  does not depend on the field – on the intensity  $H$ , on the degree of non-uniformity of the magnetic field, and on the temperature  $T$ . It is a characteristic of the material and of *MKSE*.

For the existence of only one type of elementary magnetic dipoles -  $M = const$ , i. e. for a mono-relaxation process of magnetization and the same number  $N$  of the

elementary dipoles per unit volume, according to Equation 6, the magnetic dipole moment  $m$  is given by:

$$(8) \quad m = M \vartheta .$$

Then, the magnitude of the magnetic torque is determined by Equations 2 and 8:

$$(9) \quad T_0 = m H \sin \theta = M H \vartheta \sin \theta , \text{ or}$$

$$(10) \quad T_0 = \chi_m \vartheta H^2 \sin \theta ,$$

$$(11) \quad T_0 = (\mu_r - 1) \vartheta H^2 \sin \theta .$$

The magnetization has the character of a polarization process, as the magnetic torque  $T_0$  depends on the square of the magnetic flux density  $H^2$ .

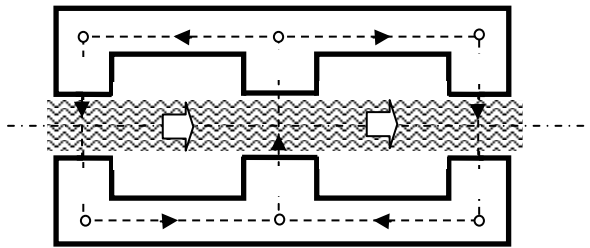


Fig. 4. Technological diagram of a device with closed magnetic circuit. The device has three polar groups alternating along the direction of motion - NS-SN-NS with periodic change in the direction of magnetic field  $H$ . A section of the device is shown.

The magnetic technological devices with linear motion of the material treated are constituted as a sequence of alternating polar groups NS, as that shown in Fig. 1a. Changing the direction of magnetic field  $H$  does not affect the direction and sense of the torque. This, from its part, allows building closed magnetic systems of minimal dispersion of the magnetic flux, Fig. 4.

Magnetic technological devices with rotational motion are also built with closed magnetic circuit, Fig. 1c.

### Magnetic kinetic structural element in static non-uniform magnetic field - magnetic torques

The interaction picture becomes more complex in a non-uniform magnetic field, as in the general case the gradient of the magnetic field  $\text{grad } H$  may have all possible directions with respect to the field  $H$ .

However, the general formulation of the issue requires that the MKSE motion direction shall be connected firmly with the direction of increasing and decreasing of the magnetic field. This assumption already poses the question of the existence of two interaction models – **model 1**, in which the motion is directed along the direction of the magnetic field, and **model 2**, in which the motion is directed transversally to the magnetic field.

The physical model of behavior of MKSE in these two characteristic cases is created under the condition that the magnetic moment  $m$  of MKSE remains invariable during

its motion in the magnetic field. It is assumed a priori the so-called adiabatic magnetic moment invariability that simplifies the consideration of the problem [7].

### Model 1

Let assume that MKSE is situated in a non-uniform magnetic field, where the direction of changing the magnetic field  $\text{grad}_x H = \partial H / \partial x$  is along the motion direction  $x - x$  of MKSE, and is parallel to the direction of the intensity  $H$  of the magnetic field, as suggested in Fig. 5.

The intensity of magnetic field  $H$  has already got different values in items 1 and 2 -  $H_1 \neq H_2$ , so that the two forces are of different magnitudes  $F_1 \neq F_2$  ( $F_1 = Q_m H_1$ ;  $F_2 = Q_m H_2$ ), Fig. 5.

The magnetic torque  $T$  acquires the form:

$$(12) \quad T = F_1 \frac{l}{2} + F_2 \frac{l}{2} = m \frac{(H_1 + H_2)}{2} \sin \theta .$$

After appropriate transformation of Equation 12:

$$(13) \quad T = \frac{m}{2} [2 H_1 + (H_2 - H_1)] \sin \theta ,$$

the following expression for the torque is obtained:

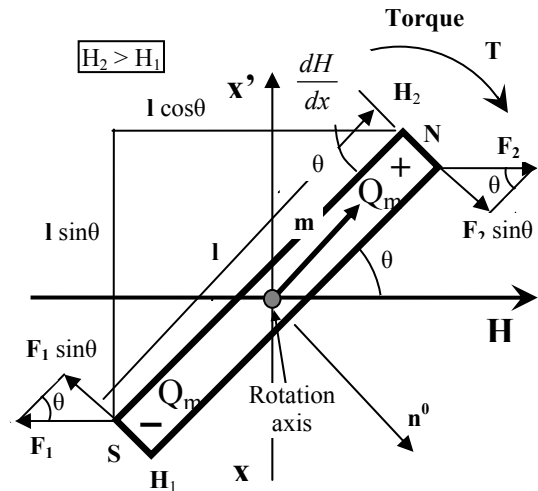


Fig. 5. Occurrence of magnetic torque  $T$  for MKSE motion in a non-uniform magnetic field. The increase of the field  $\text{grad}_x H$  ( $H_2 > H_1$ ) is transversal to the intensity of the field  $H$  – along the motion direction  $x - x$  of MKSE.

$$(14) \quad T = m H_1 \sin \theta + \frac{m}{2} (H_2 - H_1) \sin \theta , \text{ i. e.}$$

$$T = T_0 + T_G ,$$

where the first term  $T_0$  represents the torque at uniform magnetic field with intensity  $H = H_1$ , and the second term

$T_G$  – additional torque from the non-uniformity of the field  $H_2 - H_1$ .

The additional torque  $T_G$  depends strongly on the size of the magnetic dipole  $l$  and the field gradient -  $grad_x H = dH/dx = \text{const}$ :

$$(15) \quad T_G = \frac{m l}{4} \frac{dH}{dx} \sin 2\theta.$$

By using Eqs. 8 and 9, the additional torque may be represented in the form:

$$(16) \quad T_G = \frac{\chi_m \vartheta l}{8} \frac{dH^2}{dx} \sin 2\theta.$$

Then the general equation describing the *MKSE* behavior for motion in the magnetic field will be:

$$(17) \quad T = m H \sin \theta + \frac{m l}{2} \frac{dH}{dx} \sin 2\theta.$$

### Model 2

Let assume that *MKSE* is situated in a non-uniform magnetic field, where the direction of changing the magnetic field and the *MKSE* motion direction are oriented transversally to the direction of the magnetic field intensity  $H$ , as suggested in Fig. 6.

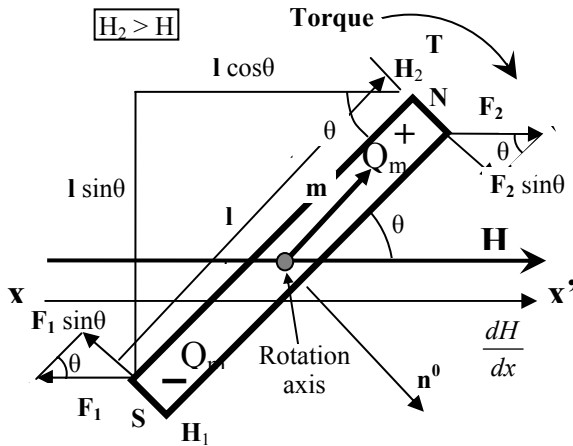


Fig. 6. Occurrence of magnetic torque  $T$  at *MKSE* motion in a non-uniform magnetic field. The increase of the field  $grad_x H$  ( $H_2 > H_1$ ) is transversal to the field intensity  $H$  – along the *MKSE* motion direction  $x - x'$ .

In this case the magnetic torque is also described by Equation 14, the additional torque acquiring a new expression:

$$(18) \quad T_G = \frac{m l}{2} \frac{dH}{dx} \sin^2 \theta \text{ or}$$

$$(19) \quad T_G = \frac{\chi_m \vartheta l}{2} H \frac{dH}{dx} \sin^2 \theta.$$

Then the general equation describing the change in the torque will be of the form:

$$(20) \quad T = m H \sin \theta + \frac{m l}{2} \frac{dH}{dx} \sin^2 \theta.$$

### Adiabatic invariability of the magnetic kinetic structural magnetic moment and of the force action

The analysis of Eqs. 17 and 20 shows the relatively weak influence of the additional torque  $T_G$  in the magnetic devices used in practice.

Structure kinetic elements of the largest size are observed in polymeric materials – groups and segments at molecular level and supermolecular structural formations as spherulites, packs, nodules, at supermolecular level of structural organization.

The characteristic size of magnetic dipoles  $l$  of the molecular and supermolecular *MKSE* remains rather small – from  $10^{-8}$  to  $10^{-5}$  m, which for field intensity  $H$  about  $60 \div 120$  kA/m and  $grad_x H$  about  $10^4$  kA/m<sup>2</sup> determines negligibly small values of the additional torque  $T_G$ , Eq. 20.

Let assume  $\sin \theta = 1$ : then the magnitude of the additional torque  $T_G$  will be commensurable with the magnitude of the magnetic torque  $T_0$  at observing the condition  $l > 10^{-2}$ , i. e. for *MKSE* dimensions of the order of centimeters.

The picture may become substantially different for rapidly changing magnetic fields, for which  $grad_x H$  exceeds  $10^6 \div 10^8$  kA/m<sup>2</sup>. However, the modern *MTD* devices belong to the group of devices with a slowly changing magnetic field.

In such a case it will be justified to introduce the following **action invariability principle** for *MKSE* motion in constant magnetic fields: *the local non-uniformity of a slowly changing magnetic field within the limits of the dimension  $l$ , characteristic for the really existing *MKSE*, does not affect substantially the magnetic torque  $T$ , as the component  $T_G$  remains negligibly small.*

All deduced relationships, Eqs. 18, 19, and 20, are valid for invariability of the magnetic moment of *MKSE* in magnetic fields changing slowly either with time, or in the space.

The magnetic dipole moment  $m$  as well as the magnetization  $M$  manifests themselves as a result of the anisotropy of *MKSE*. The elementary magnetic dipole moments, the action of which is summed up, manifest themselves at the atomic level (orbital precession diamagnetism), and for them the adiabatic invariability of the magnetic moment is valid even to a greater extent. This comes to explain the reasons for the a priori assumed invariability of  $m$  and  $M$  in magnetic fields changing slowly with time and in the space.

The analysis carried out helps making one more step forward: the magnetic torque  $T = T_0$  in real devices with slowly changing magnetic fields follows the change in the magnetic field, in accordance with Eqs. 10 and 11, or

the principle of invariability of the magnetic action is in force.

### Simplified magnetic treatment devices

#### Mathematical models

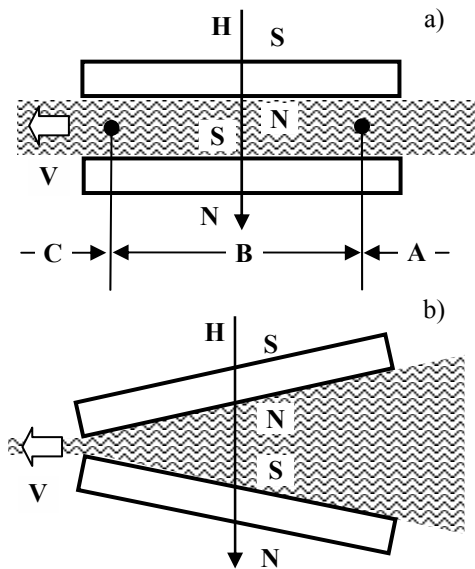


Fig. 7. Layout of the simplified magnetic devices – practically uniform (a) and non-uniform (b) magnetic fields.

The magnetic technological devices with permanent magnets are designed by constituting a structure of a design module repeated along the direction of motion of the material treated, Fig. 4.

The design nodule, or the so-called simplified magnetic treatment (SMT-) device, consists of two permanent magnets, situated at a determined distance –  $d = 15$  mm, which form together one polar group and create a practically uniform field, Fig. 7a; or a non-uniform, monotonously increasing magnetic field, the distance  $d$  being reduced in such a way that its average values remains  $d_{av} = 15$  mm, Fig. 7b.

SMTD is built of permanent strontium magnets (Cf 24) with dimensions  $50 \times 12 \times 32$  mm. They are characterized by coercive force  $H_c \geq 224$  kA/m; residual flux density  $B_r = 0.37$  T; and energy product  $(BH)_{max} \geq 24$  kJ/m<sup>3</sup>.

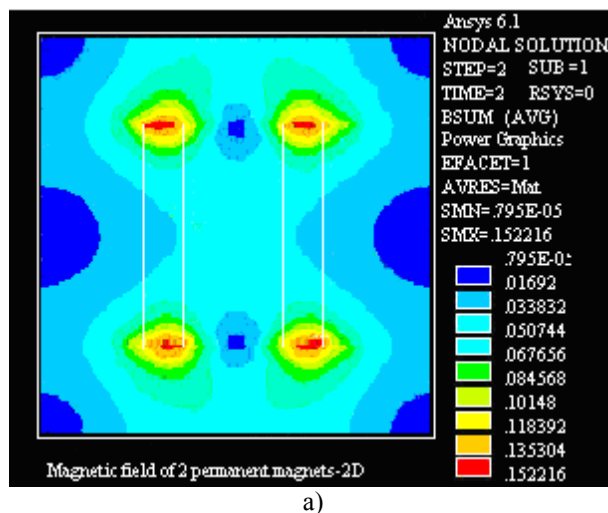
#### Calculation results

Analysis of the electromagnetic field for the two types of SMT-devices can be accomplished using a two-dimensional (2D-) model.

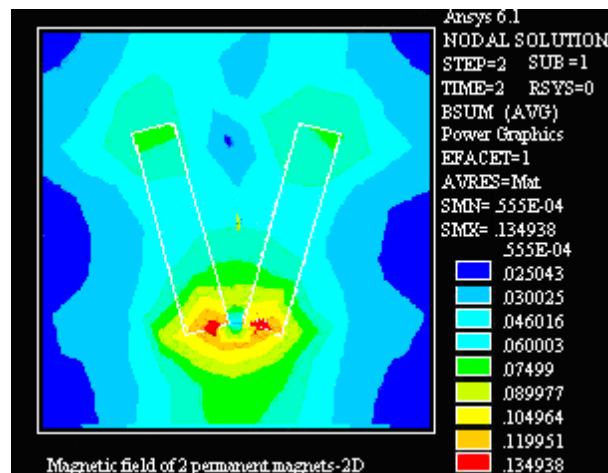
The distribution picture of the field  $B$  along the  $x - x$  axis of the SMT-device reveals a peculiarity – one polar group of two permanent magnets produces a picture corresponding to three polarity-alternating effective polar groups that correspond to the input part A, the subpolar space B and the output part C of the gap, Figs. 7 and 8.

Under each effective pole the magnetic flux density  $B$  increases, attains its maximal value of about  $B_{max} = 50$  mT ( $H_{max} = 39.8$  kA/m), maintains it, and then decreases. The sequencing of magnetic poles follows alternatively with the change in the direction of the flux density, Fig. 8a.

The SMT-device with a non-uniform field keeps the observed structure of the magnetic field, but the maximal value of the magnetic flux density goes up to  $B_{max} = 120$  mT ( $H_{max} = 95.5$  kA/m), or 2.4 times.



a)



b)

Fig. 8. Numerical models of the simple magnetic devices: practically uniform (a) and non-uniform (b) magnetic fields.

The distribution picture of the flux density along the  $x - x$  axis of SMT-device reveals even more clearly the changes emerging in all zones of the device - A, B, and C. There are no sectors with relatively uniform magnetic field, i. e. in each region the field  $H$  increases or decreases, Figs. 8a and 8b.

The magnetic torque  $T_0$  depends on the square of the field intensity  $H$ , in accordance with Eqs. 10 and 11, or the maximal torque increases 5.76 times for the SMT-device with a non-uniform field.

## Conclusion

The investigation carried out allows proposing the following major conclusions:

The magnetic dipole moment of *magnetic kinetic structural element* does not depend on the degree of non-uniformity of magnetic fields weakly changing in space and with time, i. e. for magnetic dipole moments at atomic level (orbital precession diamagnetism), as well as for *magnetic kinetic structural element* on molecular and over molecular levels, it is valid the known principle of adiabatic invariability of the magnetic dipole moment in a non-uniform field;

The magnetic force action or the magnetic torque does not depend on the degree of non-uniformity of magnetic fields weakly changing in space and with time, i. e. for *MKSE* it is valid the principle of adiabatic invariability of the magnetic force action in a non-uniform field;

The non-uniformity of the magnetic field does not affect substantially the process of orientational magnetic polarization (or magnetization), i. e. the force action upon *magnetic kinetic structural element* remains unchanged – the higher effectiveness of the magnetization modification technologies in non-uniform magnetic fields can be only explained with the increased maximal intensity of the magnetic field, and as a result – of the basic magnetic torque  $T_0$ ;

However, the physical model proposed in such a way for the magnetic modification of materials cannot explain adequately the observed experimental strong impact of the speed of motion of the material treated on the modification result;

The impact of the speed of motion of the material treated on the result of the magnetic modification should be sought outside the magnetic force interaction;

The magnetization modification in uniform and non-uniform magnetic fields has the character of an orientational polarization as the magnetic torque  $T_0$  depends on the square of the magnetic field intensity  $H$ .

## References

[1] Dineff, P. Diamagnetic Polarization Conditions. - International Conference on Magnetic-Abrasive Machining "AMO'89", Botevgrad, Bulgaria. Proceedings, Vol. 2, 1989, pp. 258-267.

[2] Dineff, P. Magnetic Polarization in a Non-Uniform Magnetic Field. Forces and Moments. International Conference on Magnetic-Abrasive Machining "AMO'89", Botevgrad, Bulgaria. Proceedings, Vol. 2, 1989, pp. 248-257.

[3] Dorfman, J. Diamagnetism and Chemical Bond. Moscow, Mir, 1961.

[4] Dineff, P., R. Tzeneva. Technological Device with Permanent Magnets for Treatment of Concrete Mixes. VI. International Conference on Applied Electromagnetics "PES 2003". Nish, Serbia and Montenegro, June 01.-03, 2003. Proceedings of Full Papers, pp. 95-98.

[5] Tzeneva, R., P. Dineff, A. Andonov. Analysis of Technological Devices with Permanent Magnets. X. International Conference on Electrical Machines, Drives and Power Systems "ELMA'02". Sofia, Bulgaria, September 13.-14, 2002. Proceedings, vol. I, pp. 311-318.

[6] Dineff, P., R. Tzeneva, A. Andonov. Magnetic Technological Devices with Non-Uniform Magnetic Field. X. International Conference on Electrical Machines, Drives and Power Systems "ELMA'02". Sofia, Bulgaria, September 13.-14, 2002. Proceedings, vol. I, pp. 319-324.

[7] Kraus, J. Electromagnetics. McGraw-Hill Book Company, London - Tokyo - Sydney, 1984.

## Acknowledgement

National Science Fund, Ministry of Education and Science, Bulgaria is gratefully acknowledged for the financial support of research project No **VUF 09/2005** "Plasma assisted technologies and devices for fire protection of polymeric and wood materials".

---

**Peter Dineff** – Associate Professor, Dr., Faculty of Electrical Engineering, Technical University of Sofia, 8 Kliment Ohridski Str., 1000 Sofia, BULGARIA. e-mail: dineff\_pd@abv.bg.

**Raina Tzeneva** – Associate Professor, Dr., Faculty of Electrical Engineering, Technical University of Sofia, 8 Kliment Ohridski Str., 1000 Sofia, BULGARIA. e-mail: tzeneva@tu-sofia.bg.



# Electrolysis as Electromagnetic Phenomenon: Effect of Self-Magnetic Influence on Anodic Dissolution and Cathodic Corrosion of Aluminium in Solution of Sodium Chloride

Peter Dineff

**Abstract:** *In a series of publications the electrolysis is considered an electromagnetic phenomenon, which requires studying the effect of the influence of its own magnetic field on such processes as the anodic dissolution, cathodic corrosion, cathodic mass deposition, and electrolytic mass transport phenomenon.*

*Two characteristic regions of influence are revealed experimentally – a region of weak influence, characterized by a strong Non-Faraday anodic dissolution of aluminium, and a region of strong influence expressed in a spatial magnetic pinch of the electric current and reduced effectiveness regarding the current.*

**Keywords:** *anodic dissolution phenomena, collinear electric-magnetic field's effect, electrical field geometric structure, magnetically assisted (aided, enhanced) electrolysis, magneto-electrolysis or M-electrolysis.*

## Introduction

For many years there has been an increased interest in a phenomenon called magneto-electrolysis, magnetically enhanced electrolysis, or M-electrolysis (*T. Fahidy and A. Olivier, 1973*). In fact, this means an electrolysis which includes the effect of (externally) imposed magnetic fields on electrolytic mass transport phenomena [1, 2], anodic mass dissolution and cathodic mass deposition phenomena [3, 4].

It is known an approach to studying the anodic mass dissolution of aluminium in aqueous electrolytes containing chloride ions, *P. Dineff at al. (1994)* that permits revealing the influence of the geometric structure (topology) of the electric field upon the aluminium anodic dissolution. Two characteristic quantities are introduced - degree of non-uniformity of electrical field  $\beta$  and relative average length of  $\mathbf{J}$  vector tube  $\alpha$ , through which it can be followed quantitatively the change in the geometric structure of the field of the electric current density  $\mathbf{J}$  for different conditions of electrolysis [6].

These tools have been used later by *P. Dineff at al. (2004)* for proving the existence of a pinch-effect in the electrolysis in relatively weak proper magnetic fields – above about  $9 \mu\text{T}$  ( $7 \text{ A/m}$ ), and its influence upon the anodic mass dissolution of aluminium in aqueous electrolytes [6].

The results from studies on the cathodic corrosion of technical grade aluminium electrodes in solution of sodium chloride were reported in an earlier paper [6]. In

these investigations it was experimentally established that the ratio between the amounts of aluminium received from the anode and cathode varied from 1.3:1 at low current densities up to 15:1 at high current densities [9].

The electrolysis, such as we know it, includes in itself two electromagnetic phenomena based on the applied force action of its own magnetic field of the electric current on the flow of positive and negative ions and on the modification of the geometric structure (topology) of the electric field [7, 8, 9]:

- **the effect of magnetic pinch** that can be also called “pinch-effect”, which is well for the electronic conductors;

- **the effect of magnetic pressing** as a result of modifying the geometry of the electric field, and particularly that of the cross-section along the path of the current, which acts analogously to the effect of *DeWitt* in electronic conductors, i. e. It acts with force on the ions and “presses” them to the surface of electrodes [5].

The electromagnetic action is explained on one hand with the effect of magnetic pinch, and on the other hand – with the effect of magnetic pressing of aluminium ions to the anode. At high currents this defines a relatively constant effectiveness regarding the current ( $\eta_a = 1.25$ ) and its corresponding effective degree of oxidation ( $N_e = 2.4$ ).

For “weak” magnetic fields it is observed an underlined domination of the chemical processes of oxidation of aluminium ions of lower degree of oxidation (below three) that determines the high effectiveness regarding the current and the effective degree of oxidation between 1 and 2.

THE PURPOSE of the present paper is to submit more evidences in benefit of the effect of self-magnetic influence on the anodic dissolution and cathodic corrosion of aluminium in a solution of sodium chloride.

The electrolysis is considered an Electromagnetic Phenomenon and it is sought an explanation of a number of deviations from Faraday's laws through the electromagnetic influence of its own magnetic field on the anodic and cathodic processes.

Aluminium has a specific electrochemical behavior that enables observing multiple deviations from Faraday's law both in the anodic and cathodic regions.

The anodic dissolution and corrosion of aluminium in solutions of sodium chloride goes along with active

destruction and dissolution of formed passivating oxide films on the anode [6].

### EXPERIMENTAL DETAILS

This investigation may be considered as a new look at the phenomenon of electrolysis from the position of the influence of the collinear electric-magnetic fields effect on anodic dissolution and cathodic corrosion of aluminium in 0.017 M solution of sodium chloride.

The experimental variants involve the following experiments carried out in an electrolysis cell of volume 0.800 dm<sup>3</sup>, in which there are placed flat-parallelly at a distance up to 15 mm two identical plane electrodes of aluminium with dimensions 40 x 40 mm (1600 mm<sup>2</sup>), electrically insulated from the back and lateral sides [6]:

- **Experiment 1**, or studying the influence of agitation on anodic and cathodic processes. The probability of meeting and interacting for metal Al<sup>1+</sup>, Al<sup>2+</sup> ions with OH<sup>-</sup> cathions should be increased with the agitation of the electrolyte.

- **Experiment 2**, or the influence of the type of electric current - direct (DC), one- (HPC) and two-halfperiod (OPC) rectified current on anodic and cathodic processes. The experimental investigation is conducted for the same quantity of transferred electricity through the electrolyte, which allows manifesting the electromagnetic nature of the electrolysis.

- **Experiment 3**, or the influence of an external magnetic field directed axially or transversally to the passing electric current (M-electrolysis) on anodic and cathodic processes.

The experiment methodology itself is presented in [6]. The experimental investigation is carried out in a galvanostatic regime of electrolysis ( $I, J = \text{const}$ ), for which the rate of cathodic corrosion (or anodic dissolution)  $V$  and the cathodic (or anodic) current efficiency  $\eta$  are connected to each other as follows:

$$(1) \eta = \frac{Z F}{A J} V : V = \frac{M}{t_e S}, \text{ g/(s.m}^2\text{)}; \eta = \frac{M}{M_F} 100, \%$$

where  $A$  is the atomic mass of aluminium, g/mol;  $F$  – Faraday’s number;  $Z$  – the normal oxidation level of aluminium;  $M$  – the cathodic corroded or the anodic dissolved mass of aluminium, g;  $M_F$  – the anode dissolved mass of aluminium (in accordance with Faraday’s law), g;  $t_e = 900 \text{ s} = \text{const}$  – the electrolysis time duration.

The cathodic corrosion is examined by comparing the cathodic corroded mass  $M_c$  with the anodic dissolved mass of aluminium  $M_a$ . The total parameters of the electrolysis are determined from the whole mass corroded and dissolved from the anode and corroded from the cathode:

$$(2) \eta = \frac{M_c + M_a}{M_F} 100, \%$$

### EXPERIMENTAL RESULTS AND DISCUSSION

The gravimetrically determined anodic dissolved and cathodic corroded masses of aluminium  $M_a$  and  $M_c$  permit determining the main parameters of the anodic and cathodic processes: the rate of anodic  $V_a$  and cathodic corrosion  $V_c$ , taken per unit active area of the anode or cathode; the anodic  $\eta_a$ , cathodic  $\eta_c$  and total current efficiency  $\eta$  in accordance with Eqns. 1 and 2; and the specific consumption of energy  $w$ . Especially informative are the corresponding relative quantities  $V_c^*$ ,  $\eta_c^*$ , and  $w^*$ , determined with respect to the normal condition of electrolysis.

#### Experiment 1

In Fig. 1 it is presented the main characteristics of the anodic and cathodic processes in relative units with respect to the case of agitation of the electrolyte.

The fact that is established immediately is the considerable influence of agitation on both the anodic dissolution of aluminium and the cathodic corrosion of metal.

In almost the whole region of “small” current densities or weak influence of the own magnetic field (absence of magnetic pinch), the agitation raises the rate of anodic dissolution at the expense of the increased probability of chemical oxidation of ions with low degree of oxidation - Al<sup>1+</sup> and Al<sup>2+</sup>.

However, if tracing the relative rate of cathodic corrosion, this agitation turns out to be a factor that suppresses the process of aluminium corrosion. It is known that the cathodic corrosion of aluminium is caused first of all by the alkalization of the space around the electrode. The agitation opposes the increase of pH, which also explains the growing difference between corresponding rates of corrosion with increasing the current density. This tendency is preserved and ensures a considerably larger difference in the region of “large” densities of the current.

In the region of “large” densities of the current the agitation affects weakly the anodic process as the electromagnetic action of the current has pinched the current lines and increased the probability of a contact between the ions and the electrode, or in the conditions of magnetic pinch the agitation contribution to the anodic dissolution becomes small. Total current efficiency is established at about 6 %, irrespective of the increase of current density, the specific consumption of electrical energy in agitation remaining higher.

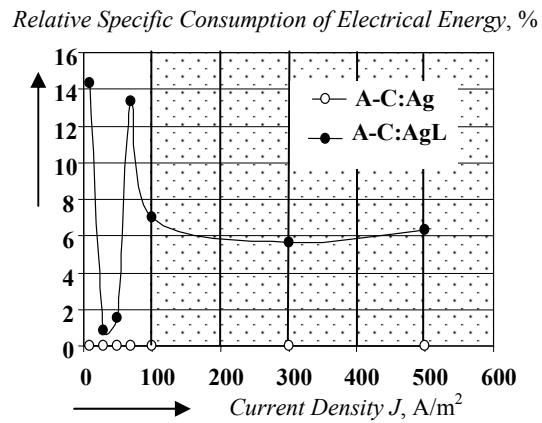
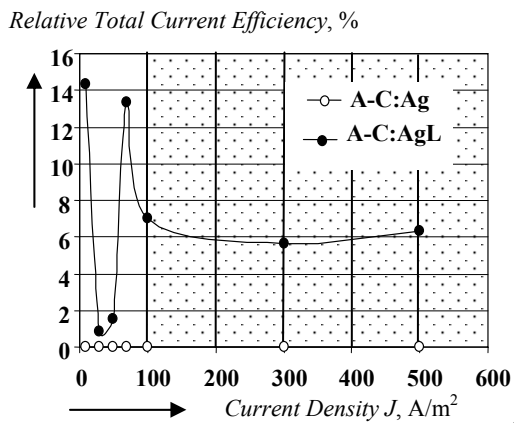
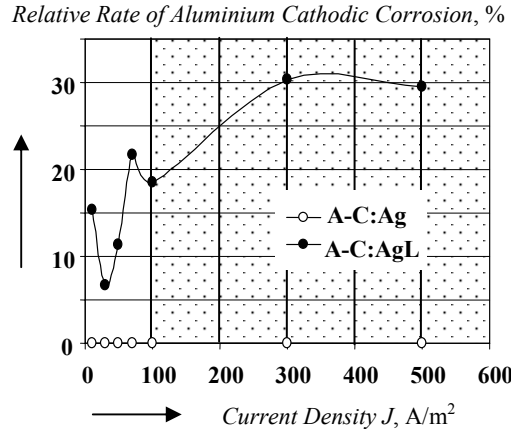
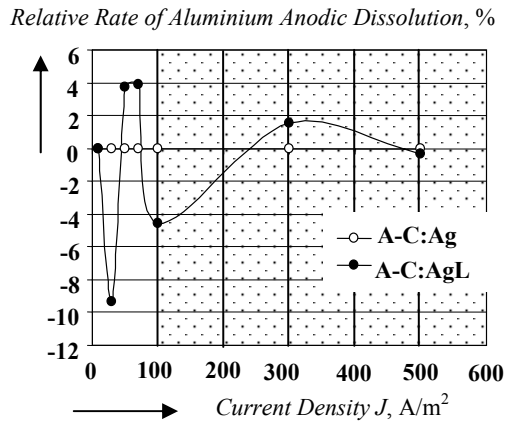


Fig. 1. Electrolysis at two-halfperiod rectified current with agitation (A-C:Ag) and without agitation (A-C:AgL): **a, b** – relative rates of dissolution and corrosion; **c** – relative total current efficiency of electrolysis; **d** – relative specific consumption of electrical energy (per unit weight).

The hatched field shows the region of “large” currents, or the region characterized by the presence of a magnetic Z-pinch, or a pinch of the current lines by the own magnetic field. The change in current density  $J$  does not exert substantial influence upon the change in the total current efficiency and specific consumption of electrical energy.

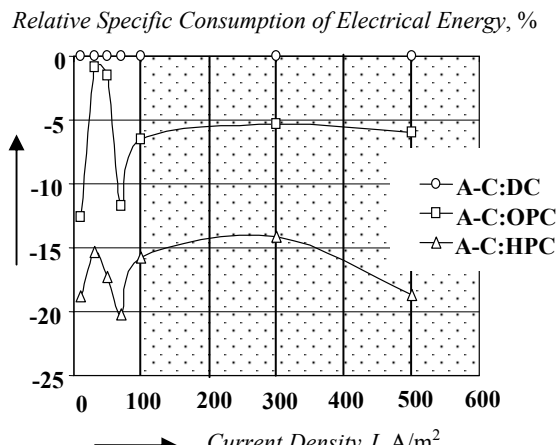
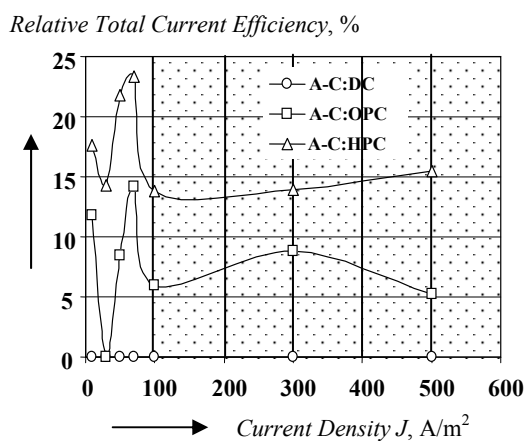
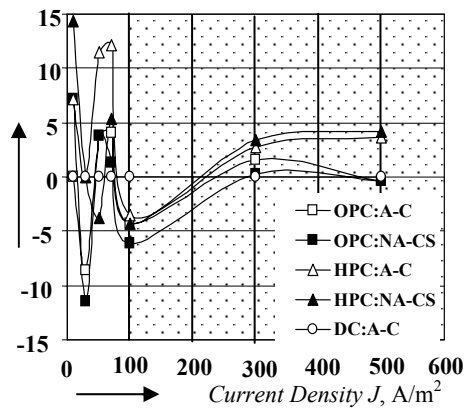


Fig. 2. Electrolysis at a different type of current – direct current (A-C:DC), two-halfperiod rectified current (A-C:OPC) and one-halfperiod rectified current (A-C:HPC): **a** – relative total current efficiency; **b** – relative specific consumption of electrical energy (per unit weight).

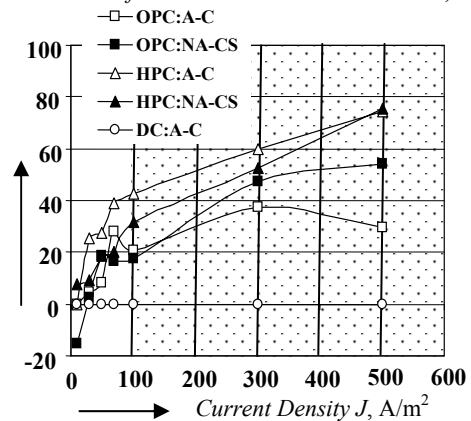
The hatched field shows the region of “large” currents, or the region of strong electromagnetic influence with manifestation of a magnetic Z-pinch.

Relative Rate of Aluminium Anodic Dissolution, %



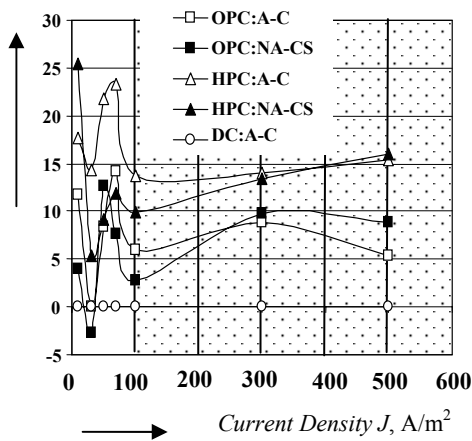
a)

Relative Rate of Aluminium Cathodic Corrosion, %

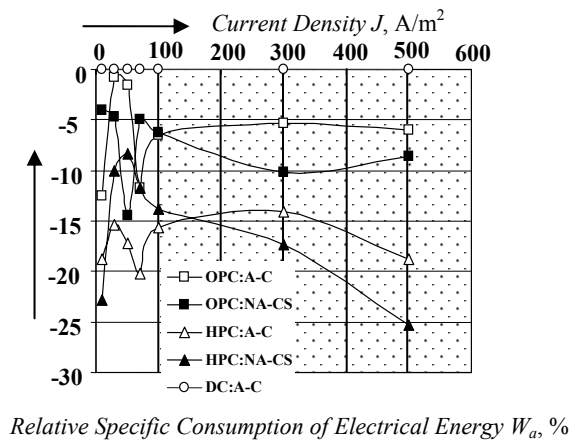


b)

Relative Total Current Efficiency  $\eta$ , %



c)



d)

Fig. 3. Electrolysis at direct current (DC:A-C), one-halfperiod rectified current (HPC:A-C) and two-halfperiod rectified current (OPC:A-C). *M*-electrolysis with longitudinal application of the external magnetic field with polarity (NA-CS): **a**, **b** – relative rates of dissolution and corrosion; **c** – relative total current efficiency of electrolysis; **d** – relative specific consumption of electrical energy (per unit weight).

The hatched field shows the region of “large” currents – the region characterized by the presence of a magnetic Z-pinch, or a pinch of the current lines by the own magnetic field.

## Experiment 2

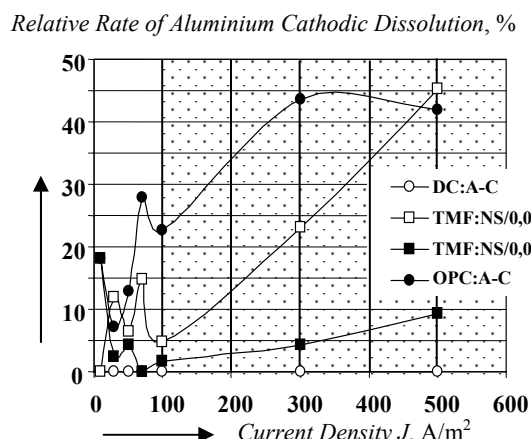
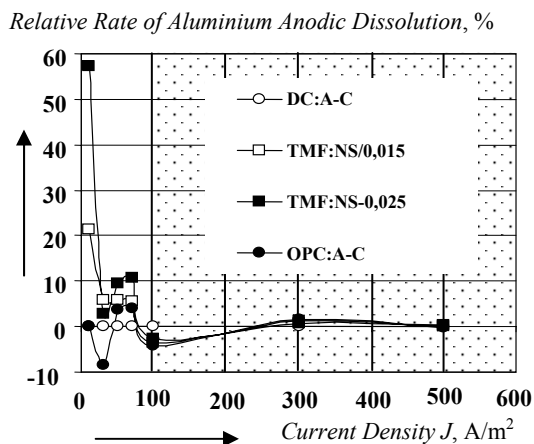
The experimental investigation relates to three cases of electrolysis, in which three different types of direct and rectified electric current are used. It is the same quantity of electricity that is conducted through the electrolyte, to which, according to Faraday’s laws, it corresponds to the same quantity of anodically solved aluminium, Fig. 2.

However, the electromagnetic forced action of the own magnetic field is different as the maximal value of the current is different, in spite of the identical average value satisfying the laws of electrolysis. The electromagnetic nature of the electrolysis is manifested most strongly at one-halfperiod rectified current: the total current effectiveness that takes into account the anodic

dissolution and cathodic corrosion is the highest, the specific consumption of electrical energy – the lowest. The great electromagnetic forces are combined with a continuous pause that permits free Non-Faraday interaction of aluminium ions with a low degree of oxidation.

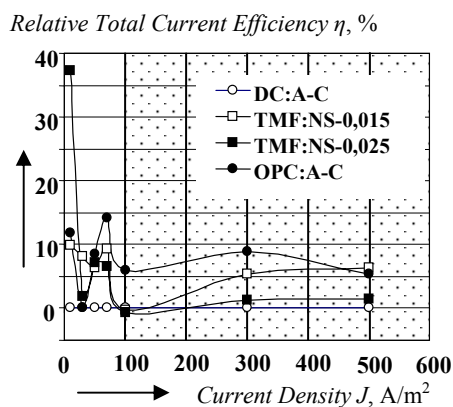
The DeWitt’s pressing of ions to the cathode is maximally strong, although for a short time, which determines the higher degree of corrosion of the aluminium cathode.

Irrespective of the type of the current, it can clearly distinguish the two intervals with different influence on the electrolysis characteristics – the region of „weak” influence of the own magnetic field and the region of “strong” influence of the magnetic pinch, Fig. 2.



a)

b)



c)

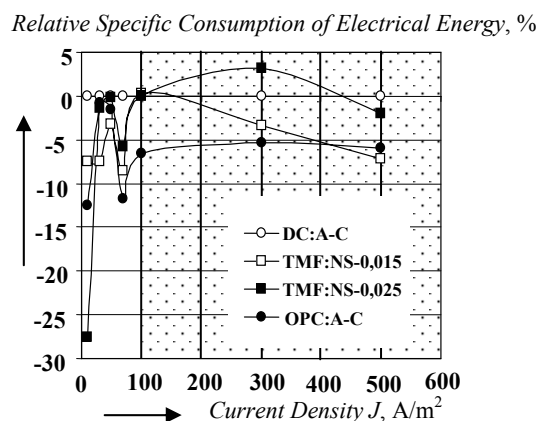


Fig. 4. Electrolysis at direct current (DC:A-C) and two-halfperiod rectified current (OPC:A-C). M-electrolysis with transversal application of the external magnetic field with polarity (NS), maximal value of the magnetic flux density 15 and 25 mT: a, b – relative rates of dissolution and corrosion; c - relative total current efficiency of electrolysis; d – relative specific consumption of electrical energy (per unit weight).

The hatched field shows the region of “large” currents – the region characterized by the presence of a magnetic Z-pinch, or the pinch of the current lines by the own magnetic field.

### Experiment 3

The experimental investigation is accomplished for different direction of the applied permanent external magnetic field: M-electrolysis at collinear electric and magnetic fields (CMF), Fig. 3, and M-electrolysis at transversal electric and magnetic fields (TMF), Fig. 3.

Irrespective of the way of applying and the intensity of the external magnetic field, again it can be observed the two characteristic regions of the electromagnetic manifestation of the electrolysis – the region of weak electromagnetic influence up to about 100 A/m<sup>2</sup>, and the region of manifestation of the magnetic pinch above 100 A/m<sup>2</sup>, Figs. 1 and 2.

The external magnetic field influences strongly the anodic dissolution of aluminium in the region of small values of the current density. Above 100 A/m<sup>2</sup> the Faraday’s behavior of the anode dominates. At high

current densities - 400, 500 A/m<sup>2</sup> – it is solely the one-halfperiod rectified current that insures growing of the yield with about 5 % for CMF, Fig. 3a.

The cathodic corrosion of aluminium is stimulated to a greater extent by CMF in electrolysis with one-halfperiod rectified current and high current densities, Figs. 3b and 4b. In that case the external magnetic field helps pinching the current lines and keeping the ions in the space around the electrode.

The total current effectiveness in using the two types of rectified electric current, which is simultaneously due to the anodic and cathodic processes, is increased from 5 to 25 %, Fig. 3c. Depending on the type of current OPC or HPC and the magnitude of current density J, the influence of the external magnetic field has a different direction – it increases or decreases the total current effectiveness, Figs. 3c and 4c.

The specific consumption electrical energy diminishes to a considerable extent for electrolysis with one-halfperiod electric current and applied external magnetic field  $CMF$  – from 10 to 25 %.

The transversal magnetic field  $TMF$  exerts a positive influence in the region of small current densities, Figs. 4c and 4d. In the region of high currents and action of the magnetic pinch, the external magnetic field  $TMF$  exerts a negative influence on the electrolysis with two-halfperiod rectified current with respect to both the yield of solved aluminium and the consumption of electrical energy.

### Conclusion

The experimental investigations carried out demonstrate the broader importance of the phenomenon studied.

The electromagnetic nature of electrolysis as a phenomenon remains hidden as its application to the practice is based on Faraday's laws reflecting its electrochemical nature. The influence of its own magnetic field through the manifestation of a magnetic pinch at high current densities is recorded with the help of deviations from the generalized Faraday's law.

The experimental investigations performed in a practically uniform electric field ( $\beta = 1$ ,  $\alpha \neq 1$ ) on various realizations of electrolysis with aluminium electrodes in solutions (0.017 M) of sodium chloride demonstrate the general validity of the conclusions made in [7, 8, and 9].

The facts observed can be explained by starting from:

- the difference effect and the behavior of aluminium in electrolysis in solutions of sodium chloride;
- the model of gradual oxidation of aluminium in anodic dissolution;
- the cathodic corrosion of aluminium in electrolysis that is caused by alkalization of the region around the electrode.

The electromagnetic character of electrolysis manifests itself in the change in the geometry (topology) of the electric field under the action of the own (pinch effect) or the own and external magnetic field (magneto-electrolysis).

“Pinching” the bundle of current lines increases the probability of contact between ions and anode and determines a more Faraday-type anodic behavior of aluminium.

The large Dewitt's forces (at higher values of current density) determine the holding of ions in the region of cathode and its alkalization, which defines the intensity of cathodic corrosion.

In these conditions the experimental results observed permit making the following conclusions:

1. The agitation of the electrolyte during electrolysis influences substantially the anodic dissolution and cathodic corrosion;

2. The electrolysis carried out for a different law of current variation creates different conditions for manifesting electromagnetic nature recorded through the deviation from Faraday's laws;

3. The results obtained are stimulating as regards the search for more effective electrolysis processes through influencing its electromagnetic nature.

### References

- [1] Mohanta, S. and T. Fahidy. The hydrodynamics of magneto-electrolytic cell. Journal of Applied Electrochemistry, No. 6, 1976, pp. 211-220.
- [2] Fahidy, T. and T. Rutherford. Retardation of electrolytic mass transport in collinear electric-magnetic fields. Journal of applied electrochemistry, No. 10, 1980, pp. 481-488.
- [3] Gu, Z., A. Olivier, and T. Fahidy. The effect of magnetic fields on the anodic dissolution of copper in NaCl-KSCN electrolytes. Electrochimica Acta, Vol. 35, No. 6, 1990, pp. 933-943.
- [4] Chopart, J., J. Douglade, P. Fricoteaux, and A. Olivier. Electrodeposition and electro-dissolution of copper with a magnetic field: dynamic and stationary investigations. Electrochimica Acta, Vol. 36, No. 3/4, 1991, pp. 459-463.
- [5] Taev, I., B. Bull, A. Godjelo at all. Theoretical Base of Electrical Apparatus. McGraw-Hill Book Company, London - Tokyo - Sydney, 1984 (in Russian).
- [6] Dineff, P. and E. Sabeva. Effect of some electric factors on the effective oxidation level and assessment of the effect of geometric structure of the electrical field upon dissolving aluminium electrodes. Indian Journal of Chemical Technology, Vol. 11, July, 2004, pp. 486-494.
- [7] P. Dineff and S. Ivanov. Magneto-electrolysis I: the collinear electric - magnetic fields effect on anodic dissolution phenomena. XIV-th International Symposium on Electrical Apparatus and Technologies SIELA'2005, 02 - 03 June 2005, Plovdiv, Bulgaria. Proceedings of Papers, vol. 2, 2005, pp. 34-39
- [8] Dineff, P. Magneto-electrolysis II: the collinear electric - magnetic fields effect on cathodic corrosion phenomena. XIV-th International Symposium on Electrical Apparatus and Technologies SIELA'2005, 02 - 03 June 2005, Plovdiv, Bulgaria. Proceedings of Papers, vol. 2, 2005, pp. 40-44
- [9] Dineff, P. and R. Tzeneva. An Approach to the Investigation and Assessment of Electric Field Non-Uniformity. XL-th International Conference on Information, Communication and Energy Systems and Technologies ICES'T'2005, 29 June-01 July 2005, Nish, Serbia and Montenegro. Proceedings of Papers, vol. 1, 2005, pp. 52-55.

---

**Peter Dineff** – Associate Professor, Dr., Faculty of Electrical Engineering, Technical University of Sofia, 8 Kliment Ohridski St., 1000 Sofia, BULGARIA.  
e-mail: dineff\_pd@abv.bg.

# Influence of High Frequency Welding Machines on Voltage Quality

Vasil Gospodinov, Borislav Bojchev and Magdalena Kushleva

**Abstract:** The development of the welding machines through the time and the most up-to-date high frequency constructions are surveyed. The results from the research of the voltage quality - asymmetry and nonsinusoidality caused by alternative current with normal frequency of the supplying voltage set, direct current sets and high frequency sets are shown. The advantages and disadvantages of the machines are compared according to the accepted requirements.

**Keywords:** welding set, nonsinusoidality, voltage quality

## Introduction

The sources of welding current are designed to transform the supplying network voltage to the needed safe low voltage, thus specific characteristics, required for the welding process, are provided.

The technological process is the basic one, but it influences the quality indices of the electronic power and above all the quality indices of voltage – deviation, fluctuation and THD of voltage. Different sources of welding current electric sets, shown on fig. 1 are applied in order to provide better technological technoeconomic indices for the welding processes.

With the improvement of the electric welding sets and technologies their weight is sharply reduced and they become easily portable and suitable for low power electric networks. Thus a corresponding influence on the voltage quality indices are expected, which must be taken into consideration in selecting of welding set. The purposes of the present paper are:

1. To investigate experimentally welding sets for: alternative current with normal frequency of the supplying voltage set; direct current set and high frequency set.

2. To evaluate the structure and the level of generated high harmonics in the curves of the current and voltage formed by the welding sets. For the investigations QualiStart C.A.8334 three phase power quality analyzer is used.

A single phase welding transformer KRAKRA E01Y, three phase direct current set KRAKRA E500 and inverter welding set KEMPOMIG G400 are investigated.

The experimental data for the currents, voltages and power (active, reactive and apparent) during the welding process are changed insignificantly, on the grounds of which it is considered that the process is stationary and the obtained integral evaluations of the current and voltage harmonics are reliable information of their structure and level.

The results for the harmonics of current and voltage, obtained by examining KRAKRA E 01Y are shown in tabl. 1. The current harmonics over twelfth are not shown. The are of insignificant magnitude (< 0,2 % of the first harmonic).

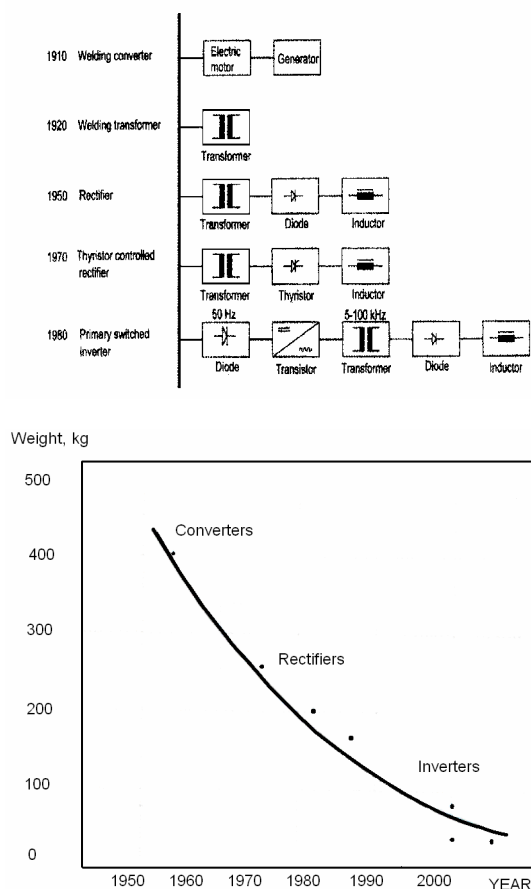


Fig.1

**Tabl.1**  
Single phase welding transformer KRAKRA E01Y

Technical data of the supplying current sources	Number of the harmonic, $\nu$	Relative value, %	
		$U_{\nu}$	$I_{\nu}$
KRAKRA E01Y 220 V 50 Hz $I_H=125A$ (46-160 A) $U_{20} = 56V$	0	0,1	3,68
	1	100	100
	2	0,05	7,46
	3	0,82	14
	4	0	3,28
	5	1,22	3,46
	6	0	2,13
	7	0,68	1,51
	8	0	0,93
	9	0,2	1,20
	10	0	0,48
	11	0,23	0,4
	12	0	0,2
	13	0	0,13
	14	0	0,11
15	0	0,05	
THD:		1.63	17.35

The harmonics generated by the welding set KRAKRA E01Y have quite high values in the range of the working frequency (low frequency) to 150 Hz and after that the values are significantly reduced to drop under 1%. (Over 500 Hz)

The harmonics of the voltage curve define allowed THD = 1,63% and the most salient harmonic is fifth with magnitude of 1,22% which is defined by the volt-ampere characteristic of the alternate current arc.

The three phase direct current set KRAKRA E500 generates higher harmonics in the wide frequency range with relatively low values. (tabl.2). Characteristic current harmonics are the following: even number – second, fourth, eight and number third, fifth (with the highest values), seventh and eleventh. The highest values of the voltage harmonics are that of the fifth one (for all the three phases) while the other harmonics have low values. The coefficient of THD of the voltage doesn't rise above 1,53%.

**Tabl.2**  
Three phase direct current set KRAKRA E500

Technical data of the supplying current sources	Number of the harmonic, $\nu$	Relative value, %					
		$U_{\nu}$			$I_{\nu}$		
		Phase 1	Phase 2	Phase 3	Phase 1	Phase 2	Phase 3
KRAKRA E5001 380 V 50 Hz $I_H=500 A$ (500-560 A) $U_{20} = 56V$	0	-	-	-	0,53	2,64	0,82
	1	100	100	100	100	100	100
	2	0,28	0,27	0,3	30,23	28,9	28,62
	3	0,53	0,59	0,19	1,78	2,64	1,6
	4	-	-	-	4,74	5,5	5,5
	5	1,26	1,36	1,28	7,46	6,1	6,03
	6	-	-	-	0,8	0,8	0,24
	7	0,49	0,41	0,61	2,71	3,21	2,61
	8	-	-	-	2,47	1,88	2,1
	9	-	-	-	0,31	0,37	0,1
	10	-	-	-	0,71	1,15	0,92
	11	0,22	0,34	0,27	1,54	1,15	1,28
	12	-	-	-	0,31	0,29	0,11
	13	0,06	0,11	0,1	0,35	0,64	0,5
	14	-	-	-	0,71	0,59	0,62
	15	-	-	-	0,14	0,17	0,04
	16	-	-	-	0,06	0,23	0,2
	17	-	-	-	0,4	0,23	0,25
	18	-	-	-	0,04	0,05	0,02
19	-	-	-	0,06	0,14	0,18	
THD:		1,48	1,52	1,53	38,9	30,5	30,1

The inverter welding set KEMPOMIG 4000 (a high frequency welding set) generates high harmonics of voltage of insignificant values (tabl.3). The prevailing fifth harmonic is up to 1,38% of the first harmonic.

The other harmonics (odd) to twenty fifth have low values (0,07-0,33). The (THD) of voltage is in the range of 1,51 to 1,67%. In the current curve there is a wide range of high harmonics. The odd harmonics have high values – The fifth harmonic rises up to 60 % of the first, seventh – 49 %, eleventh – 26%, thirteen – 20%. The values of the next odd voltage harmonics decrease with the increase of their number till they reach less than 1% for the forty ninth.

The even number harmonics take part in the current curve with the insignificant values. The value of the second harmonic is the highest and reaches 1,1% (phase 1). Similar values are obtained for the twelfth harmonic, after which the values are between 0,2 to 0,3%. At the end of investigated frequencies (after 44 harmonic) they increase up to 1%.



**Tabl.3**  
High frequency welding set KEMPOMIG 4000

Technical data of the supplying current sources	Number of the harmonic, v	Relative value, %					
		Uv			Iv		
		Phase 1	Phase 2	Phase 3	Phase 1	Phase 2	Phase 3
KRAKRA E5001 380 V 50 Hz I <sub>n</sub> =500 A (500-560 A) U <sub>20</sub> = 56V	0	-	-	-	4,4	6,1	1,5
	1	100	100	100	100,0	100,0	100,0
	2	-	-	-	1,1	0,7	0,7
	3	0,52	0,56	0,19	1,6	3,3	3,0
	4	-	-	-	0,7	0,5	0,5
	5	1,38	0,48	1,35	58,2	59,9	56,9
	6	-	-	-	0,8	0,6	0,6
	7	0,23	0,31	0,43	39,9	38,4	39,0
	8	-	-	-	0,8	0,7	0,8
	9	0,07	0	0	3,0	0,7	2,4
	10	-	-	-	0,9	0,8	0,8
	11	0,33	0,43	0,35	23,9	26,1	25,4
	12	-	-	-	1,0	0,9	0,9
	13	0,30	0,31	0,36	20,1	17,0	17,9
	14	-	-	-	1,0	0,9	0,9
	15	-	-	-	1,9	1,2	1,9
	16	-	-	-	0,8	0,6	0,7
	17	-	-	-	3,6	2,4	3,2
	18	-	-	-	0,7	0,6	0,6
	19	-	-	-	3,8	2,2	4,4
	20	-	-	-	0,6	0,5	0,5
	21	-	-	-	1,1	2,0	1,2
	22	-	-	-	0,4	0,4	0,4
	23	0,11	0,15	0,09	6,6	7,9	0,4
	24	-	-	-	0,3	0,2	0,3
25	0,15	0,13	0,17	6,6	4,6	5,8	
THD:		1,51	1,67	1,64	83,35	82,34	82,00

### Conclusion:

The results of the study of the disturbances, which the welding current sources produce, are presented in the paper. One- phase transformer type KRAKRA E O1Y, three phase direct current set KRAKRA E500 and three-phase inverter set KEMPOMIG 4000.

The current and voltage curves of the supplying network of the welding current sources are studied in order to evaluate its harmonic content (composition).

The results show the ranges of high relative values of the current and voltage harmonics, which depend on the type of the supplying source.

With all the studied welding sets the fifth voltage harmonic has the highest values.

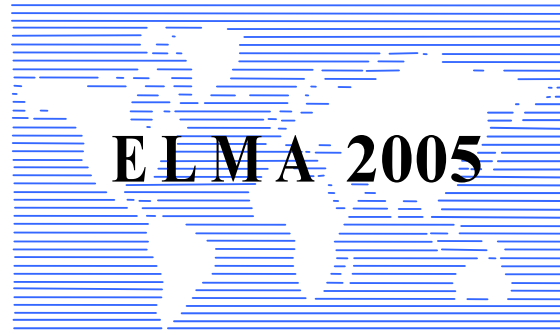
### References

- [1] Василев, Н., С.Сидеров Електроснабдяване на промишлени предприятия София Техника 1991г.
- [2] Arrilaga, J., N. Watson Power System Harmonics John Wiley and Sons Ltd (2003) ISBN 0-470-85129-5.
- [3] <http://www.kemppi.com>
- [4] <http://www.redcobg.com>

**Vasil Gospodinov** – Associate Professor, DSc., Faculty of Electrical Engineering, Technical University of Sofia, 8 Kl. Ohridski Str., 1000 Sofia, BULGARIA. e-mail: vgos@tu-sofia.bg.

**Borislav Bojchev** – Assistant Professor, Faculty of Electrical Engineering, Technical University of Sofia, 8 Kl. Ohridski Str., 1000 Sofia, BULGARIA. e-mail: bojchev@tu-sofia.bg.

**Magdalena Kushleva** – Ph.D. Student, Faculty of Electrical Engineering, Technical University of Sofia, 8 Kl. Ohridski Str., 1000 Sofia, BULGARIA e-mail: kushleva@tu-sofia.bg.



---

---

**ENERGY GENERATION  
AND DISTRIBUTION**

---

---



# Variable Speed Induction Generators Connected to the Grid or in Island Mode Operation

**Sorin Deaconu, Gabriel Nicolae Popa, Iosif Popa**

**Abstract:** This paper concludes a study on variable speed induction generators operating connected to the grid or in island mode, with constant output voltage and frequency, regardless of load and speed values.

**Keywords:** Induction generator, variable speed, frequency converter, national grid, island mode

### Introduction

Hydro turbines built for low head are generally provided with stator control drive and adjustable rotor blades in order to achieve constant generator speed over wide flow variations [4].

Turbine mechanical control system is complicated and implies high costs and a long investment pay off period.

Wind turbines which must continuously adjust their vanes orientation, depending on winds direction and speed are facing the same situation [9].

When operating a generator with variable drive frequency under voltage and frequency restrains imposed by the national grid, the turbines are simpler and the costs lower.

### Proposed method basics

In our study we assumed an induction generator with rings, driven by a hydro turbine or wind turbine with variable angular speed  $\Omega$  [6].

The slip formula is:

$$(1) \quad s = \frac{\Omega_1 - \Omega}{\Omega_1},$$

where  $\Omega_1$  is the stator rotating magnetic field angular speed.

The relation between the frequency of the stator induced voltage  $f_1$  and the frequency of rotor induced voltage  $f_2$  is:

$$(2) \quad f_1 \cdot s = \pm f_2,$$

In formula (2) above, signs “+” or “-” stand for different successions of rotor supply voltage.

The generator is an electric machine with double supply. Based on relations (1) and (2), the formula below can be deduced:

$$(3) \quad f_1 = \pm f_2 \cdot \frac{\Omega_1}{\Omega_1 - \Omega},$$

To keep a constant output voltage frequency  $f_1$  during angular speed  $\Omega$  variations, modifying the rotor supply voltage frequency  $f_2$  is required.

Relation (3) can be expressed as follows:

$$(4) \quad f_1 = \pm f_2 + \frac{p\Omega}{2\pi},$$

where  $p$  is the number of generator pole pairs. The latter relation (4) leads us to an automation concept for this system operation.

### Automation concept

Figure 1 shows the concept configuration of the induction generator operation, with the supply voltage connected to the rotor windings and driven with variable speed [5].

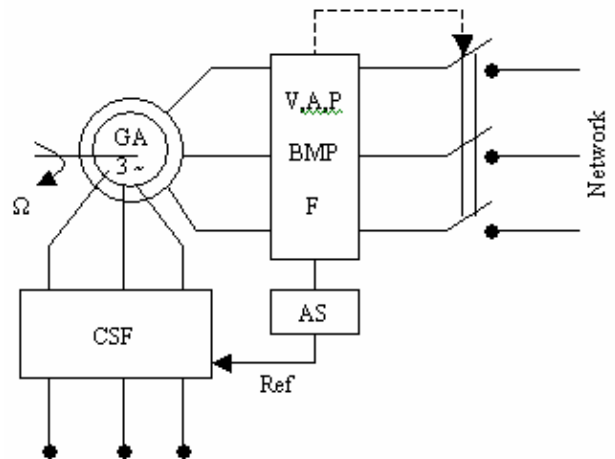


Fig.1. Automation concept

Abbreviations:

GA - induction generator

CSF - static frequency converter

BMP - measurement & protection unit (voltage, current, active power and frequency measurements and protection functions at grid interface)

K - grid circuit breaker

AS - generator voltage and frequency measurements signal transmitter

Ref - CSF set point

$\Omega$  - generator driven speed

The turbine is driving the generator with angular speed  $\Omega$ . The induced voltage frequency depends on  $\Omega$  value. To achieve a frequency  $f_1$  value that would match the grid frequency value, according with relation (4), the rotor winding is supplied via CSF with voltage frequency  $f_2$ .

The measurement & protection unit BMP provides the voltage, current, active power and frequency measurements. When the synchronizing conditions are fulfilled (phase succession, matching voltage and  $f_1$  frequency values) the grid circuit breaker is closed.

The signal transmitter AS generates the set point Ref for the frequency converter CSF, based on the frequency  $f_1$  measured value.

BMP also provides generator protection function.

### Experimental results

For laboratory experiments we have used an induction generator with rings, with the technical data below:

$P_N = 3 \text{ kW}$   
 $U_N = 380/220 \text{ V}$   
 $I_N = 12.3/7 \text{ A}$   
 $n_N = 925 \text{ rot/min}$   
 $\cos\varphi_N = 0.755$   
 $I_{2N} = 26 \text{ A}$   
 $U_{2N} = 81 \text{ V}$

The d.c. driving motor has the technical data specified below:

$P_N = 4 \text{ kW}$   
 $U_N = 220 \text{ V}$   
 $I_N = 18 \text{ A}$   
 $n_N = 1250 \text{ rot/min}$

The frequency converter CSF is ALTIVAR type, ATV-18U41M2, single-three phase [1,2,3].

The generator was tested both in idle mode and loaded mode, connected to laboratory electrical network and to normal grid (380 V, 50 Hz), for variable angular speed values within  $0.5 \Omega_1 \dots 1.2 \Omega_1$  range.

For the test with generator connected to the laboratory experimental network we applied a condenser battery,  $C = 10 \mu\text{F}$  for 400 V.

The measurements results are listed in the table below.

**Table 1**

n [rot/min]	$\Omega$ [rad/s]	$f_2$ [Hz]	$U_1$ [V]	$f_1$ [Hz]	Connected to:
500	48.4	26.8	400	50	grid
			382.5	49.9	lab network
600	62.8	20	400	50	grid
			383.7	50	lab network
700	73.26	15	400	50	grid
			384.4	49.99	lab network
800	83.73	10	400	50	grid
			385.1	49.99	lab network
900	94.2	5	400	50	grid
			385.8	50	lab network
1000	104.66	0.01	400	50	grid
			387.2	50	lab network
1100	115.13	- 5	400	50	grid
			383.3	50	lab network
1200	125.6	- 10	400	50	grid
			389.6	50	lab network

Negative  $f_2$  frequency values within the above table 1 signify the alteration of supply voltage phase's succession.

### Conclusions

With propose method and automation diagram was experimentally determine a r.m.s. voltage by 400V with frequency by 50Hz when the turbine speed has wide variation [7].

This application may be use to microhydroelectric power station, where the water flow has wide variation into a year [8]. To keep constantly the water level in the lake or in the catch may be made through the turbine speed. Thus, the quantity of delivered electric energy rising.

### References

- [1] ABB, ACS 800, Hardware Manual
- [2] ABB, ACS 800, Software Manual
- [3] ABB, ACS 800, Catalogue. Related tools and accessories.
- [4] Deaconu, S., Popa, I., Popa G.N., Gherman, L. Automatizarea funcționării stațiilor de pompare a apei potabile și a stațiilor de clorinare, Revista de Automatizări și Instrumentație, an XI, nr. 5-6/2002, pag. 24-25.
- [5] Deaconu, S., Gherman, L. Automatic speed control system for electropumps with 6 kV voltage in powerplants, DEMI 2003, Banja Luka, pag. 623-628.
- [6] Deaconu, S., Babău, R. The automation of hydroelectric plants, witch runs at variable flow capacity, SEBEȘ, 2003, pag. 393-398.
- [7] Deaconu, S., ș.a. Computer simulation of the minihydroelectric plants witch runs with variable speed to the electric network, EPE 2004, Iași, pag. 219-222.
- [8] Deaconu, S., Babău, R. Automatizarea funcționării microhidrocentralelor, Revista de Automatizări și Instrumentație, nr. 5/2004, pag. 15-17
- [9] Scherim, J., Schmitt, A. Turbines with variable speed control for the Hydropowerplant, Wasser-wistshaft 82 Jahrgang 5/1992, pag. 246-249

**Sorin Deaconu** – Associate Professor, PhD., Faculty of Engineering Hunedoara, „Politehnica” University of Timisoara, Revolutiei str. no 5, Hunedoara, ROMANIA, e-mail: sorind@fih.utt.ro.

**Gabriel Nicoale Popa** – Lecturer, PhD., Faculty of Engineering Hunedoara, „Politehnica” University of Timisoara, Revolutiei str. no 5, Hunedoara, ROMANIA, e-mail: gnpopa@fih.utt.ro.

**Iosif Popa** – Associate Professor, PhD., Faculty of Engineering Hunedoara, „Politehnica” University of Timisoara, Revolutiei str. no 5, Hunedoara, ROMANIA, e-mail: ipopa@fih.utt.ro.

# The Situation of Electricity Generation in Corsica Towards 40% Renewable Energy Sources Supply

Gilles Notton, Philippe Poggi and Christian Cristofari

**Abstract:** Corsica, a Mediterranean island, is not connected to the French mainland electrical grid. The French utility EDF has commitments as a public utility for the electricity supply but also for the price of the kilowatt-hour sold.. The various energy actors emphasize the reduction of electricity consumption and the development of alternative electricity sources such as hydraulic or wind energy. The Corsican Territorial Community wishes to reach 40% of the total electric production in 2010 provided by renewable energies.

**Keywords:** Electricity supply; Renewable energy; Islands

## Introduction

Chapter 17 of Agenda 21 [1] points out that islands are a special case both for the environment and development, and that they have very specific problems in planning sustainable development, as they are extremely fragile and vulnerable. In the context of sustainable development, energy is the cornerstone of their planning strategies.

Marin [2] said about islands that “The traditional limitations in the energy field like distance from the major grids, small scale, distribution difficulties and the lack of large conventional markets, are more than off-set by the extreme abundance of renewable energy sources, and the incredible adaptability and capacity of integration of renewable energy technologies; factors that are in sharp contrast with the progressive inefficiency and high cost of conventional energy systems in island regions. In fact, we would go as far as to say that islands have become genuine laboratories of the future of energy sustainability”.

Corsica is concerned by these problems. The particular 1982 statute – reinforced in 1991 and recently – gives the Territorial Assembly wide responsibilities in the energy and development fields. The guarantee of a permanent and quality energy supply needs a specific reply in islands. Moreover, the setting-up of equipments and the use of local resources must take into account the fact that the ecosystem is reduced and vulnerable.

## Presentation of the island of Corsica

With its 8680 km<sup>2</sup> and an average altitude of 568 meters, Corsica is the smallest, but the most mountainous of the three big occidental Mediterranean islands. The island is 183 km long from 41°19' to 43° North, and 83.5 km large from 6°31' to 7°13 East.

Mediterranean by its situation, Corsica is alpine by its structure. The central fold, of North-Northeast direction, South-Southeast direction which splits Corsica into 2

parts, forms an important barrier which can be crossed over by passes often situated at a height of more than 1,000 m and, with snow in winter. As 10 mountains exceed 2,000 m, the most important is Monte Cinto with 2,710 m. Moreover, Corsica is remarkable for the diversity and the complexity of its geological nature (Fig.1). Corsica has more than 1,000 km of coastal area (14% of the total French coasts).

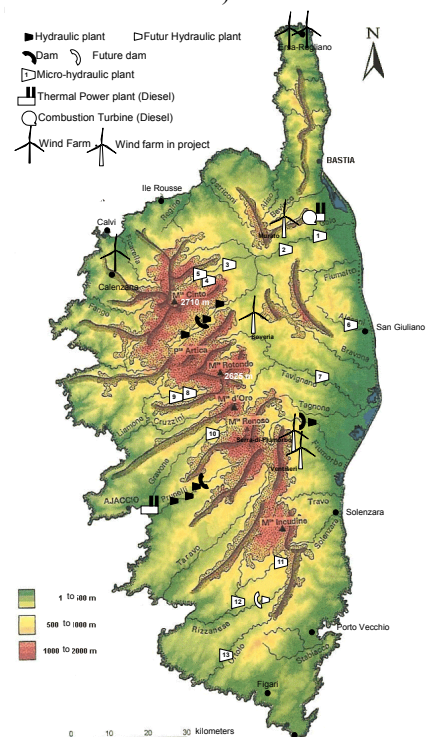


Fig. 1. Corsica map with energy facilities.

With about 260,000 inhabitants in 1999, up by some 10,000 in 40 years, the island of Corsica has an average population density equal to 30.1 inhabitants/km<sup>2</sup>, the lowest of France (compared with 107 inhab/km<sup>2</sup> in France). But in rural areas, this density falls down to 7-10 inhabitants/km<sup>2</sup>. 44% of the population live in district of less than 100 inhab/km<sup>2</sup>. The island is three times less populated than Balearics, six time less than Sardinia and twenty times less than Sicily. The increase of the population is moderated (+4% between 1990 and 1999) and mainly due to migrations. Two-thirds of the population live in coastal areas as and this is expected to rise up three-quarters by 2030.

During the summer, the island has more than 1 million inhabitants (60% of the tourism is in July-August), there are about 2 million tourists per year for 24 million occupied beds.

## The electrical energy situation

Electricity production is the result of thermal and hydraulic installations located on the island, of an electric contribution limited in power from the Italian mainland (DC cable between Italia to Sardinia) and of some wind turbines. More than the half of the 524 MW working installed capacity (Table 1 and Fig. 2.) and production (Fig. 3.) is handled by diesel thermal installations [3]. The hydraulic and wind power plants make up 33% of the total capacity of electric production in Corsica (in power).

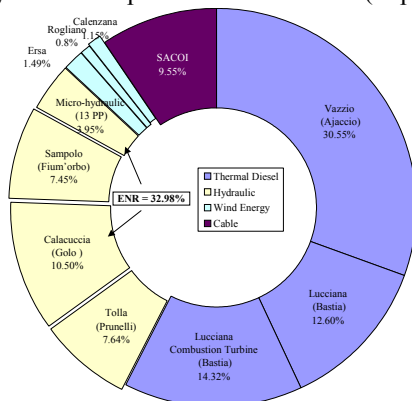


Fig. 2. Repartition of the installed power.

One of the characteristics of the energy production (Fig. 3.) is a first peak in the winter and a second one during the summer (June, July, August and September) due to an important tourist flow during this period (1,770,000 tourists in 1997 for a local population of 258,000 inhabitants). Concerning the electric energy production, the beginning of the wind turbine production appears in September 2000.

Table 1

Installed power in Corsica in 2004

Type		Power (MW)
Thermal	3	301
Vazzio	Fuel	8 x 20
Lucciana	Fuel	6 x 11
Lucciana	TAC	3x25
Hydraulic	3Dam + 7 PP	134
Prunelli (67,400 m <sup>3</sup> )	1Dam + 3 PP	20+15+5
Golo (79,500 m <sup>3</sup> )	1Dam + 3 PP	13+28+14
Fium'orbo (45,000 m <sup>3</sup> )	1Dam + 1 PP	39
Micro-Hydraulic	13	20.7
SACOI	Cable	50
Wind farms	3	18
Ersà	(11/2000)	13x 0.6
Rogliano	(09/2000)	7 x 0.6
Calenzana	(12/2003)	10 x 0.6
<b>Total guarantee power</b>		<b>485</b>
Total installed Power		523.7

Moreover, according to the month, the contribution of thermal or hydraulic generation is not the same: during the summer, the hydraulic part is very poor and almost the total electricity production is provided by thermal plants as seen in Table 2. Each type of source has specific

constraints (function of the seasons and electricity request).

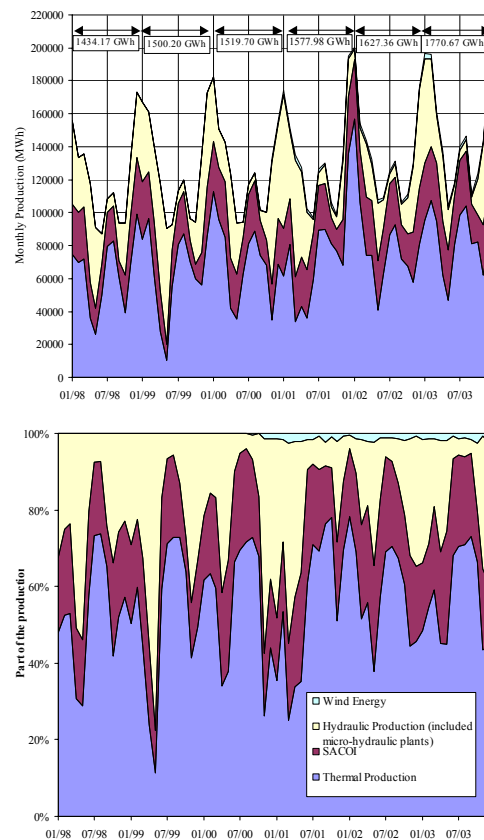


Fig. 3. Electrical production (absolute/ relative values)

The consumption in Corsica is the least important of all the departments of the metropolitan France. The domestic use is the most important part of the utilization of the electricity in 2003 [4], this being the characteristic of a region without a large industrialisation. In the tertiary sector, a large part of the consumption comes from the tourist activities which is marked by a strong seasonality. In the winter, the half of the electrical power is used for the heating and in the summer, this power depends on the tourist crowds.

Table 2

Part of production (on the period 1998-2003).

	On the year (from June to September)	
Thermal	55.25%	69.31%
Hydraulic	23.46%	8.78%
SACOI	20.44%	21.47%
Wind	0.86%	0.44%

### Hydroelectric installations

There are two types of hydroelectric installations: EDF power stations with a high nominal power (from 5 to 40 MW) and a dam, and private micro-hydroelectric power stations. The production of these installations depends on the water resource and thus on hydraulic variations. This production can therefore vary very strongly (Fig. 4.). The part of the hydraulic production in the total electricity production reached 61% in 1980 then

decreased in percentage because the total production increased without an increase of the hydraulic facilities. If hydroelectricity represents 285 GWh (27%) in 1995, it reaches 576 GWh (50%) in 1996.

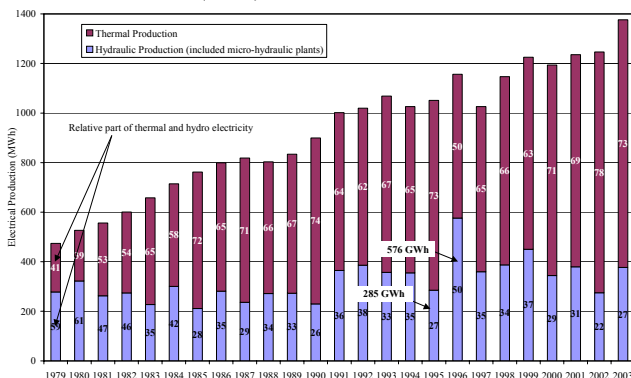


Fig. 4. Hydraulic and thermal production.

These installations thus provide a partially guaranteed energy, insofar as energy is not always available when that is necessary. The part of the renewable energy (hydraulic) in electric production varies greatly from a month to another, the maximum was reached in May 1999 with a renewable energies contribution of more than 77%. The production cost of EDF installations thus varies in the same way, but it is also related to the ratio of initial investment if we compare it to the expected production: between 0.030 and 0.061 €/kWh for the Prunelli installations, between 0.055 and 0.11 €/kWh for the Golo and Fiumorbu installations [5].

### Italy-Corsican-Sardinia electric connection

An electric cable SACOI (Sardinia-Corsica-Italy) made by the Italian government connects Tuscany, Elba island and Sardinia via Corsica. In return of the passage of this cable in Corsica, EDF signed a convention with ENEL authorizing EDF to have 20 MW guaranteed and 50 MW not guaranteed (but always available according to a low enquiry from Sardinia).

The SACOI HVDC link consists in a mono-polar link with sea return, with a rated voltage of 200 kV, a rated current of 1500 A and a rated power of 300 MW, which can flow both from Suvereto (Italy) to Condogainus (Sardinia) and vice-versa. This HVDC link is based on a conventional grid commuted twelve pulse thyristor bridge and has a third terminal tap station (50 MW) in Lucciana (Corsica) (the station began to work in 1987) [6]. The Lucciana conversion station thus allows to get guaranteed energy, and this at a weak cost (0.029 €/kWh).

### Thermal installations [7]

The production cost of electricity from the thermal equipment depends indirectly on hydraulic electricity. Indeed, the production of hydraulic electricity varying according to the years, the thermal installations mitigate these variations in comparison with the request.

In addition to the cost of fuel used, the production cost also includes maintenance, staff expense and equipment replacement, all this being independent from

consumption. In this context, diesel power stations provide a production cost varying from 0.091 to 0.14 €/kWh and constitute the principal revolving electricity reserve and are used under basic operation.

From the beginning of 2001, EDF use a heavy fuel with very low sulfur content. The over-cost induced by the utilization of the new fuel has been estimated at 3,776 k€ per year. A new "environmental" fuel (Straight Run) has been used at the Vazzio plant since December 2003 with an over-cost estimated at 3,000 k€ per year. A new fuel has also been tested since May 2004 in Lucciana and allows to respect environmental regulations with an over-cost estimated at 100 k€ per year.

Since August 2002, a denitrification experiment based on the HAM (Humid Air Motor) process has been in progress on a diesel engine (investment 6.3 M€) at the Lucciana plant. It consists in injecting water in the combustion chamber in view to decrease the temperature and the production of NO<sub>x</sub>. At the Vazzio plant, a process called SCR (Selective Catalytic Reduction), which involves processing exhaust fumes in order to substantially reduce their nitrogen oxide content, in process since May 30<sup>th</sup> 2004. The investment concerning four SCRs is about 5.5 M€ and the operation cost is about 550 k€ per engine only for the reagent (liquid urea).

On the other hand, the gas turbines located at Lucciana have a very high cost of operation (1.03 to 2.40 €/kWh), due to the use of an expensive combustible (domestic oil) and reduced operation (high investment and operation costs for a small production of energy). These two turbines are only used in case of high electricity demand.

### Wind turbines [8]

The technical potential of wind energy in Corsica has been identified at 433 MW for an annual average wind speed higher than 7m/s. On this basis, the economic potential is estimated at a level of 100 MW. In the frame of the Eole 2005 programme, 11 projects have been approved (52 MW): 3 projects in the Corsican Cape (extreme North of the island) for 14.4 MW, 2 projects in Balagne (Region of Ile Rousse) for 6 MW and 6 projects in the extreme South of Corsica for 32 MW. Between all these projects, only two are in operation :

- since September 2000, a wind farm at Ersa-Rogliano with 20 Wind Turbines (WT) of 600 kW (12 MW) which should produce 30 GWh per year; in fact, its yearly production varied between 22.6 and 26.8 GWh between 2001 and 2003.

- since December 2003, a wind farm at Calenzana with 10 WT of 600 kW (6 MW) which should produce 15 GWh per year; it produced 12.9 GWh in 2004.

To help the development of wind energy in France, new conditions of purchase of the wind kWh were announced by the French government in December 2000: 0.084 €/kWh during the first five years and between 0.03 and 0.084 €/kWh during the following 10 years according to the quality of the production [9]. Favourable conditions are present to develop the wind energy in Corsica.



## Energy management

The part of the electrical energy used for a thermal utilization is important (moreover 53% of the electricity is used for a domestic utilization), thus the replacement of electrical heating by other means may contribute greatly to the energy management. Moreover, an environmental advantage appears: an electrical kWh for heating produces 894 g CO<sub>2</sub> against only 200 g for a gas heating. Various actions have been developed for the substitution of the electricity in the frame of a partnership between ADEME and the Corsican Territorial Community. 1900 solar systems are used in Corsica today : 1300 solar home systems, 450 collective solar installations for water heating, 60 combined solar systems (home heating) and 50 solar air collectors. With 48 m<sup>2</sup> of solar collectors for 1000 inhabitants, Corsica has a good place in Europe (36 m<sup>2</sup> in Europe and 11 m<sup>2</sup> in France) and this market is growing.

The utilization of the biomass, after some problems, seems today to be able to contribute to reduce the electricity demand. 8 installations have been made for a heating power equal to 12 MW and a wood consumption of 10000 tons.

Several studies and diagnoses have been launched so as to manage the energy demand and several actions are in progress to replace electrical heating by gas heating.

## Problems occurring in the electrical production [3]

The size of the electrical network implies some difficulties to keep control of voltage and frequency. In such an isolated system, we noted numerous network failures : more than 200 failures per year on the transmission network with voltage dips; Several generation failures each year with less than 46 Hz. The quality of the electricity provided to the consumers is very bad. A way to ensure the inertia of the Corsican system consists in the interconnection with more powerful systems, as the Sardinian system which is eight times more important than the Corsican one.

According to EDF, constraints due to the small size of the electrical grid require to limit the unit power of each production system at 25% of the average power on the grid because the total electric system must not be weakened if a unit is down. The same constraint also lead to limit at each moment the wind turbine power on the grid at 30% of the total power produced. The connection of wind turbines in such a grid must take into account :

- a simultaneous decrease of wind speed over the island can rapidly decrease the wind turbines production.
- synchronic machines are very sensitive to voltage dips due to a problem on a production plant for example
- the wind turbines don't participate to the voltage regulation which must be continuously supervised.

For these three reasons, the production system must have an available power margin rapidly usable and the other production means must be sufficient.

In no-interconnected areas [10], the production over-costs are explained by physical and technical specific configurations. The energy sources for electricity production are reduced to renewable energies, coal (sometimes bagasse) and principally fuel. It is the small size of the plants in non-interconnected areas which explains a production cost of about 100 € per MWh i.e. about two times higher than on the mainland and largely superior to the kWh price for the user [11]. Thus, the deficit in Corsica has reached 70 M€ in 1999 (for a turnover of 105 M€) i.e. a same losses per kWh than in the French overseas departments.

These production units have a much smaller size than in the French mainland (about 20 MW en average, i.e. 70 times smaller than nuclear units) and they use fossil energies. In the French overseas departments, 75 % of the electricity comes from fuel and in mainland France, more than 75% is provided by nuclear energy. Other technical factors contribute to increasing the production cost: corrosion of the material, more modulated production peak, a more expensive maintenance, this being due to the problem of distance. Another specificity of non interconnected areas is the unusually high gap between the produced energy and the sold one (technical and non-technical losses). These gaps between interconnected and non-connected areas were in 2003, 7% in France, 10% in Guadeloupe, Martinique and Reunion, 12% in Guyana and remains close to 15% in Corsica [10-11].

In 2004, the distribution of electricity has been perturbed : some problems occurred with a fuel engine and the power required by the electric grid being not satisfied, the voltage fell below 198 V [12]. Thus the current system does not lay out an important power margin. In February 2005, the worst happened : the ambient temperature falls down under zero and the electrical consumption raised. EDF preferred to use its water resources rather than using the combustion turbines (for cost reasons). The cold went on and the dams were empties moreover the temperature did not allow to transform the snow into water. The island stayed far two weeks with numerous power cuts (30 minutes every three hours). Some engine generators were brought by plane from continental France, Canada and Ireland and a 20 MW TAC was brought from Athens.

## Current electricity needs and evolution.

In 2003, the maximum power required in Corsica was 390 MW for a guaranteed power available of 485 MW (thermal + SACOI + hydraulic with dam) as seen in Fig.4.

The load curve is characterized by [3]: in winter, from 200 up to 350 MW; in autumn and spring, from 80 up to 150 MW; in summer, from 120 up to 230 MW. Contrary to what happens in France [13], the consumption is higher in Summer than in Autumn-Spring in Corsica due to the presence of an important tourist population. Thus, the load curve of Corsica is very different to the distribution of the power in the French continent.

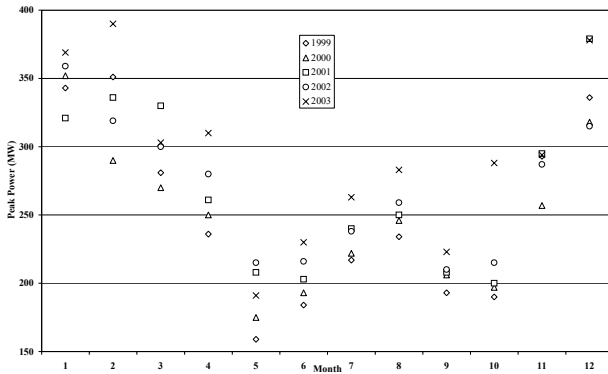


Fig. 4. Evolution of the peak power.

The evolution of the past and expected peak power is presented on Fig. 5. [14]. While referring to the power requested during the year 1991 (284 MW), an average evolution of 8 MW per year can be seen. EDF estimates an increase by about 3% per year [3]. From 1999 to 2003, the annual average of increasing was 2.7%. Forecasts [15] have been made on the basis of a sector-based analysis covering the industrial, residential and tertiary sectors. These forecasts take into account the Demand Side Management efforts made by various partners, as well as specific actions to promote gas heating in towns and oil heating in rural areas, as a substitute for electric heating. The conclusion is that in 2005 and 2010 the peak power will be respectively equal to 406 and 494 MW and thus, new equipments will be necessary to satisfy the load. In this context, considering the opening of the European market of electricity since 1999, EDF already seems to have adopted its choices in terms of new energy supplies, for the next 10 and 15 years and to adapt quickly to the evolutions of electricity demand actually seen.

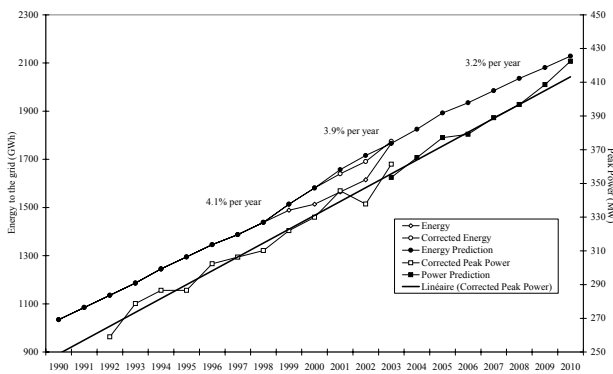


Fig. 5. Prevision for energy and peak power.

In 1993, 806 GWh were consumed in Corsica, 73% for domestic use and 27% for industrial use, inducing a total production of 1063 GWh (including the losses of the electrical supply network). In 1998, the production went up to 1433 GWh, that is to say an annual average growth of about 12.2 % per year over the 1993-1998 period. In 2015, INESTENE [16] expects an increase in consumption by 2% per year, that is to say a need for production of 1920 GWh per year. For its part, EDF envisages a growth ranging between 3.2% per year between 1999 and 2010 (against 7% per years in the

eighties) (see Fig.6.). According to RTE [15], the energy production in 2005 and 2010 should be equal to 1887 and 2129 GWh.

The means of electrical production are getting old : the thermal plants were set up between 1981 and 1988 for Vazzio and 1973 and 1978 for Lucciana. The latter was to be stopped between 1993 and 1995 but it is still operating. A new dam with 1.3 million m<sup>3</sup> on the Rizzanese river and a turbine of 50 MW for a yearly production equal to about 80.6 GWh should be set up by 2009 and would increase the hydraulic power to about 37%. Some new private hydro-power plants (about 10 MW) should be developed.

The two fuel thermal plants would operate until 2012 and no decision has been taken about their replacement. One solution consists in their redeployment in gas combined cycle. In fact, an of Algerian gas pipeline project is now studied to connect Algeria to Italy via Sardinia (1550 km) and it could pass by Corsica located only 14 km away from Sardinian coasts.

An alternative connection with Sardinia (limited at 50 MW) will be carried out soon (end 2005) and should allow to improve the quality of the electricity provided to the user : the interconnected network will be then of about 2000 MW, allowing a best response to the perturbations; an improvement of the quality with a more stable frequency and voltage; a reduction of power cuts: the potential of wind turbines on the electric grid could be increased.

The power of this connection should be increased and by this means, the electrical problem of Corsica should be partially solved but Corsica will become dependent on Italy and this choice would have negative consequences on the economic activities and on employment.

The wind turbine development in Corsica is linked to a technical limit of the electric grid. The wind electricity is unforeseeable and in small electric systems particularly reactive to perturbations and with a low inertia, such as the Corsican one, it is necessary to limit the wind farm integration at 30% of the electric power [17] keeping in mind that the load curve in Corsica is very variable. In these conditions, only 50 MW of wind turbine power is possible because the maximum power on the electrical grid is only 150 MW during autumn-spring. This limit could rapidly be increased to 100 MW after the setting up of the alternative cable with Sardinia. 55.7 MW could be installed at the end of 2005. The total of the other studied projects is higher than the 50 other possible MW after the interconnection with Sardinia. These wind farms (installed and in project) will be well spread over the territory with two advantages: an electric one because these farms will be submitted to different wind patterns leading to a better regularity of the production and an environmental one with a low visual impact.

All these previous considerations lead to predict for 2010 a repartition of the production in installed power and energy presented on Fig. 6 [16]. The renewable energies in the energy balance would reach 40% of the electric production in 2010. But today no decision has

really been taken, particularly concerning the future of the thermal plants. If new problems occur on the electrical grid before, which it is highly probable, the decisions would be taken very rapidly and we wish this fact had no negative impact on the development of renewable energies in Corsica.

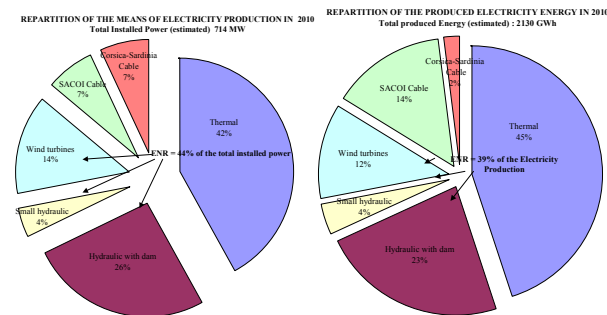


Fig. 6. Perspectives for 2010.

## Conclusion

The energy situation of the electrical production is very specific in Corsica. If the part of renewable energies in the electricity production is already high, the planning expects 40% for 2010.

The energy question is linked to other problems : sustainable development, water and transports, dependence of economy on tourism, sustainable tourism, environment, security and lesser dependence of the energy supplying.

Today, the energy policies are at the centre of all the talks and conflicts between the different actors : Corsican Territorial Community, EDF, ecologists (not always favourable to renewable energies). In the following months, numerous decisions will have to be taken and it is difficult to predict the future but the development of renewable energies in the island only seems to be established if a real dialogue with the population is developed. The concern about the environment is very important in Corsica but the debate about energy began in a certain confusion. The actors of energy development will have to inform and convince the population and the population often affected by the NIMBY syndrome “not in my backyard” will have to understand the links between the stakes in the lesser energy dependence and the economic development of the island.

This problem is not limited to Corsica, it concerns all insular territories around the world and must be apprehended specifically. Only in Europe, there are 300 islands that represent 13 millions inhabitants, i.e. a population higher than the population of some European countries.

## References

[1]. Action 21. Déclaration de Rio sur l'Environnement et le développement, Conférence des nations unies sur l'environnement et le développement (CNUED). United Nation Publications, ISBN 92-1-200147-5, 1992, pp. 140-141.  
 [2]. Marin, C. Towards 100% RES supply. An objective for the islands., 2004.

[3]. Barlier, Y. The situation of electricity generation in Corsica. Book of Proceedings : Dissemination of the advanced control technologies and SCADA systems for the isolated power networks with increased use of renewable energies, Ajaccio, France, 2000, pp. 27-35.

[4]. RTE. Statistiques de l'énergie électrique en France 2003, September 2004.

[5]. EDF-GDF, 2001. Private communication.

[6]. Corsi, S., Danelli, A., Pozzi, M. Emergency-stability control through HVDC links. *Proc. IEEE/PES 2000 Summer Meeting*, 2000.

[7]. Corsican Energy Committee (Conseil Energétique de la Corse), 2004. Third Meeting. October 2004.

[8]. Lynge Jensen, T. Renewable energy on small islands. Forum of Energy and Development, 2000, Second Edition, ISBN 87-90502-03-5.

[9]. ADEME. Eolien: un développement programme, the ADEME lettre n°75, 2001, ISSN 1165-5550.

[10]. Levratto, N. Fonctionnement et impact du mécanisme de compensation des charges de service public de l'électricité sur l'offre d'énergie dans les zones non-interconnectées" in L. Vidal, *Droit de l'énergie et des réseaux*, avril 2005, in press.

[11]. Syrota, J. Evaluation des missions de service public de l'électricité. Commission de régulation de l'électricité, 2000, La Documentation Française, Paris.

[12]. Grandju, P. Personal communication, EDF-GDF, January 2004.

[13]. RTE, 2005. French electrical consumption review, 2005.

[14]. Souchard, T. Personal communication, 2003, Corsican Economical Development Agency (ADEC).

[15]. RTE. Generation Adequacy Report 2006-2015, RTE Report, (08/2003).

[16]. INESTENE. Potentiels de maîtrise de la demande d'électricité en Corse à l'horizon 2015, Report of the Corsican Territorial Community, 1996.

[17]. Monlobou, P. Colloque « Energie éolienne dans les Iles », 18 January 2002, Ajaccio.

**Gilles Notton** – Assistant Professor, DSc., University of Corsica, Renewable energy team, Laboratory SPE (Physical Science for Environment), Scientific Center of Vignola, Route des Sanguinaires, F-20000 Ajaccio, FRANCE.

e-mail : gilles.notton@univ-corse.fr.

**Philippe Poggi**– Assistant Professor, DSc., University of Corsica, Renewable energy team, Laboratory SPE (Physical Science for Environment), Scientific Center of Vignola, Route des Sanguinaires, F-20000 Ajaccio, FRANCE.

e-mail : philippe.poggi@univ-corse.fr.

**Christian Cristofari** – Assistant Professor, DSc., University of Corsica, Renewable energy team, Laboratory SPE (Physical Science for Environment), Scientific Center of Vignola, Route des Sanguinaires, F-20000 Ajaccio, France

e-mail : christian.cristofari@iut.univ-corse.fr.

# The data handler of weather wind observations, calculation wind power potential and efficiency the use of wind power generators

Petr Kountsevich, Michail Kostyrev, Pavel Grachev

**Abstract.** *The report contains the design technique and program of calculation wind energy potential and efficiency the use of wind power generators for points bound to particular meteorological station is placed.*

**Keywords:** *wind power generator, wind speed, relief of terrain, wind power potential.*

## Introduction

Now for definition of a wind power potential many different design techniques will be used. Thus, as a rule, there is a subjective factor [1]. For example, the use of Weibull distribution the subjective factor introduces essential errors. In a well-known design technique « on gradation » the subjective factor is shown to a minimum, but the techniques allow only the past distribution of a wind speed.

There are offered the design technique and program of calculation technical wind energy potential and efficiency the use of wind power generators, in which one the subjective factor practically is eliminated, and are mirrored an outlook a distribution of a wind speed.

## Resources of a wind energy

In the majority of locales the considerable seasonal behaviors of wind flows are watched, and per winter months the wind speed usually is higher, than summer. The daytime alteration of velocities of a wind is watched, as a rule, near to the seas and large lakes. On wind velocity render considerable influencing geographic conditions and nature of a surface, including different natural and synthetic encumbrances, such, as hills, trees and buildings. For this reason wind power generator dispose, whenever possible, on raised and removed from high trees, apartment houses and other facilities places, since such encumbrances decelerate of a wind and result in flow swirling handicapping transformation of a wind power.

Average wind velocities ( $V_c$ ) characterize a wind potential of territory. It is wind velocity, which one is determined as mean arithmetic value of all observed wind velocities within one year. Average velocities of a wind can be computed and for other periods, for example: monthly, daytime and hour. Energy concluded in a wind, is in cubical relation to value of wind speed. The doubling of wind speed gives increase of energy in 8 times. Thus, average speed of a wind of 5 m/s can give approximately twice more to energy, than wind with a half speed of 4 m/s. To establish those locales of country, where are available sufficient ветроэнергетические

resources, it is possible with the help of the wind atlases [2]. Having learned(found out) среднегодовую the wind speed in locale, is possible to define(determine) a volume of electrical energy, which one can work out wind power generator within one year. More precise computational methods require(demand) a considerable volume of the padding information and should be made by the specialists.

## Techniques of definition of a wind energy potential

For efficiency *the use of* wind flow energy the installation of an elevation profile of wind velocities is necessary. The analytical investigation for wind stream on a flat equal surface by a fixed gas current gives following relation of speed in a flow at an altitude  $h$  from a surface [3]:

$$(1) \quad v(h) = a(\ln h - \ln h_0)$$

Where a - constant, determining general intensity of a flow;  $h_0$  - value scaling a surface roughness, and this formula is suitable under condition of  $h \gg h_0$ . On the other hand, the aiming  $v(h)$  of perpetuity at  $h$  seek to perpetuity is a consequent of an allowance, utilized in the theory, of the infinite size of a streamlined surface. The ratio for velocities at altitudes  $h_1$  and  $h_2$ .

$$(2) \quad v(h_1) = v(h_2) \frac{\ln h_1 - \ln h_0}{\ln h_2 - \ln h_0}$$

From which one in particular follows, that at decreasing a surface roughness the velocity profile becomes less sharp. Another frequently used expression for an elevation profile of speeds is represented by an empirical-formula dependence of a power mode kind [4]:

$$(3) \quad v(h_1) = v(h_2) \left( \frac{h_1}{h_2} \right)^m$$

The presence of idealized relation (2) with quite physically clear parameter of a scale of a roughness of a surface  $h_0$  allows to explain a seasonal behavior of trial-and-error parameter  $\tau$ , and also it's decreasing for coasts of the seas and lakes. The influencing of a roughness of a surface on an elevation profile of speeds was in detail studied in foreign activities, including with use of expression (2), and the rather full tables of profiles are created depending on the characteristics of a surface and its resistance to a wind. In the domestic literature about parameter  $m$  of a wind with a roughness of a surface is investigated a little. At the same time was clarified, that

the parameter  $m$  is not only function of time, geographic and climatic conditions of terrain, but also function of the velocity.

The expression (3), being simple under the form, actually introduces rather composite and implicit relation of velocities to an altitude. Besides for an inhomogeneous relief the parameter  $m$  appears different for different directions, so for realization there are enough of precise calculations the definition of trial-and-error values  $m$  as velocity values on separate directions is required. On a technique [4] it is possible to calculate wind speed for particular territory. For this purpose it is necessary to know, at what altitude there is a proximate meteorological station (in radius of 5-10 km) and at what altitude guess to set wind power generator. It is known [4], that the statistical data under the wind characteristics in the given terrain for last 10 years indispensable for the feasibility wind power generator. The computer card of terrain is indispensable for the precise registration of the local factors, which one mirrors a constitution of a relief, nature of a underlying surface, precise arrangement of a meteorological station, presence of neighboring constructions. The data processing can be made with the help of a specialized programmatic complex [5].

The essence of the design technique consists in following: the observational dates of wind speed for definite period are processed by mathematical methods. A function of smoothing on a least squares process at first is reshaped. The obtained function will be used for mathematical smoothing of outcomes of observations. It allows recording a system of algebraic equations, which one has the alone solution.

For recovery of a velocity-distribution law of a wind the following function will be used

$$(4) \quad y = ax^p e^{-qx^k},$$

where the factors  $a$ ,  $p$ ,  $q$ ,  $k$  are determined from the solution of a set of equations on given points of a function of smoothing.

The program allows to calculate an energy potential of a wind in a point bound to a particular meteorological station, effective operating time and annual production rate wind power generator, volume of the electric power developed for term of payback and service life wind power generator, cost price of the electric power, annual average profit during term of payback and annual profit after term of payback. In calculation all costs are allowed practically, including the costs of maintenance and repair, which one are calculated outgoing from parameters of reliability of autonomous wind power plants.

## References

- [1] 1] Методика ГУП МКБ «Радуга».
- [2] Атлас ветров России/ Старков А.Н., Ландберг Н., Безруких П.П., Борисенко М.М. М: РДИЭЭ-РИСО, 2000.
- [3] Ландау Л.Д., Лифшиц Е.М. Теоретическая физика. Т.6. Гидродинамика. М.: Наука, 1988.
- [4] Безруких П.П. и др. Ресурсы и эффективность использования возобновляемых источников энергии в России. С.П.: Наука, 2002.
- [5] Wind Atlas Analysis and application Program/ Mortensen N.G. and others/ Riso National Laboratory, Denmark, 2000.

---

***Petr A. Kountsevich** - candidate of Technical sciences., carrying on scientific employee of corporation « a Unified electrical power complex », 2, Vorontsovsky, building 1, 109044, Moscow, RUSSIA.*

*e-mail: pem@vniie.ru*

***Michail L. Kostyrev** - doctor of Technical sciences, professor, Samara state technical university, 244, Molodogvardeiskaja street, Samara, 443100, RUSSIA.*

*e-mail: eipo@samgtu.ru*

***Pavel Y. Grachev** - professor, Samara state technical university, 244, Molodogvardeiskaja street, Samara, 443100, RUSSIA.*

*e-mail: pgrachov@mail.ru*

# Modelisation and Performance of a Photovoltaic System connected to the electrical grid

Philippe Poggi, Marc Muselli, Gilles Notton, Nicolas Heraud, Stefka Nedeltcheva

**Abstract:** This paper summarises 4 years of monitoring of a 850 Wp roof-mounted grid-connected system in our laboratory in Ajaccio. The system has been in operation since December 2000. The PV array consists of 10 BP585F modules and a SMA Sunny Boy 700 inverter. Climatic and solar radiation conditions at the site are reviewed, each component is modelled and the monthly performance of the system is assessed from a component point of view and from a global perspective.

**Keywords:** PV Array, Small Grid-connected PV systems, Performance, modelisation

## Presentation of the system

We present the performance of a 850 Wp photovoltaic roof-mounted grid-connected system in our laboratory in Ajaccio. The system has been in operation since December 2000. The PV array consists of 10 BP585F modules and a SMA Sunny Boy 700 inverter. Climatic and solar radiation conditions at the site are reviewed, each component is modelled and the monthly performance of the system is assessed from a component point of view and from a global perspective (AC power delivered to the grid, system efficiency, system reliability, utilisation factor).

The PV modules are arranged in one string of 10 series modules and facing south and tilted at 45° (maximisation of the yearly energy production). The area of the array is 5.625 m<sup>2</sup>. The inverter is tied to the public grid EDF via a single-phase connection.

The PV system is fully monitored to asses the potential of PV technology in Mediterranean climate and the performance of the system with the local power grid. It consists on a meteorological station (on the laboratory roof) and an internal acquisition of the PV system parameters. The monitoring system measured each minute the following parameters:

- Electrical parameters (DC and AC voltages; DC and AC currents; AC power; utility grid impedance; utility grid frequency; errors and warnings reported by the inverter, ...);
- Meteorological parameters (Irradiance on plane of PV array; wind velocity, ambient temperature and PV module temperature).

## Modelling and performance of PV modules.

The first part of this study was to model the PV array.

From a PV I/V curve analyser (PV KLA 4.3 from Mencke and Tegtrneyer), we have recorded I/V curves for various irradiances during days (Figure 1).

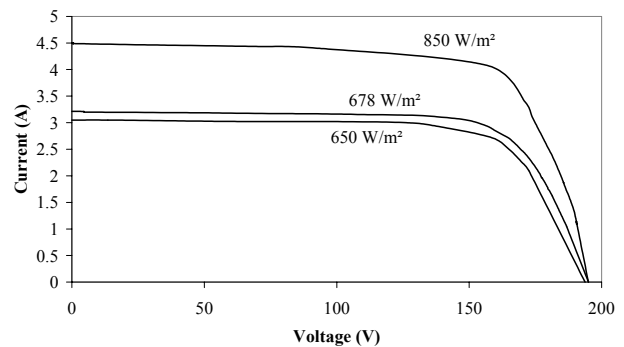


Fig.1. I-V curves of the PV array for 3 irradiances

From I/V curves and from a thermal model developed in the laboratory (which compute the cells temperature - Figure 2), we have modelled the PV array using single-diode (eq.1) or double-diode models (eq.2) [1].

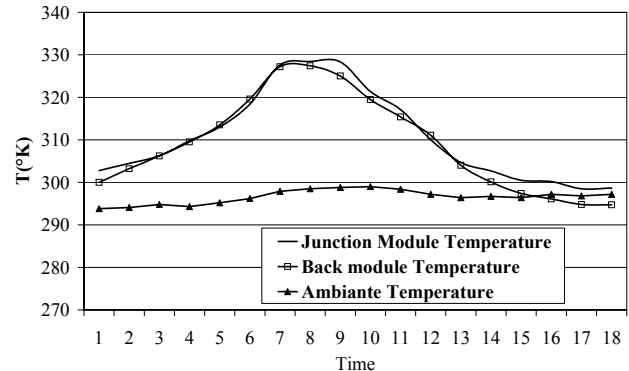


Fig.2. Evolution of the temperatures (back of the module, ambient) during one day

$$(1) \quad I = I_{ph} - I_0 \left[ \exp\left(\frac{V + R_s I}{nkT}\right) - 1 \right] - \frac{V + R_s I}{R_{sh}}$$

$$(2) \quad I = I_{ph} - I_0 \left[ \exp\left(\frac{V + R_s I}{nkT}\right) - 1 \right]$$

$$- I_{02} \left[ \exp\left(\frac{V + R_s I}{n_2 kT}\right) - 1 \right] - \frac{V + R_s I}{R_{sh}}$$

where  $I_{ph}$  is the photocurrent,  $I_0$ ,  $I_{o1}$ ,  $I_{o2}$  the saturation current,  $R_s$  the serial resistance,  $R_{sh}$  the shunt resistance,  $n$  the ideal factor,  $k$  the Boltzman constant,  $T$  the module junction temperature,  $I_{o2}$  the current saturation of the second diode, and  $n_2$  the ideal factor of the second diode.

We have computed the parameters of these 2 models from the I-V curves measured and the various errors between the single-diode model or the double-diode model versus experimental data are presented on Table 1, and on Figure 3.

**Table 1**

*Statistical coefficients between experimental data and single-diode and double-diode models*

	RMSE (%)	RRMSE	Coefficient Correlation
Single Diode	9.51	1.96	0.997
Double Diode	4.46	0.95	0.998

The double-diode model is the more accurate. From this model, it is possible to estimate the power curve, in order to compute the array efficiency.

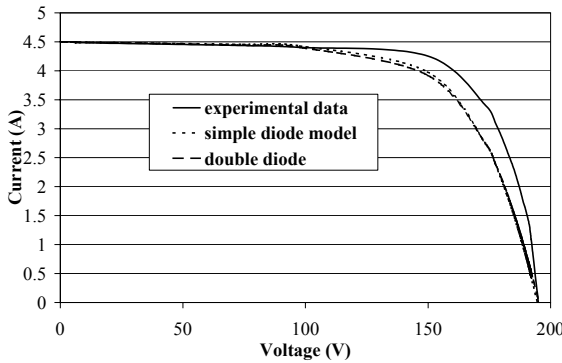


*Fig.3. Comparison simple diode and double diode model*

In a second part, we have studied the array efficiency. During the day it was observed a variation of the efficiency due to the variation of the temperature cells  $T_j$ . We have developed a model which verifies this variation, the relation (3) is the following:

$$(3) \quad \eta_{labo} = A\Phi^\alpha \times [1 - B\Phi^\beta \times (T_j - 298)]$$

where  $\Phi$  is the irradiance in the plane of the array.

The parameters  $A$ ,  $B$ ,  $\alpha$  and  $\beta$  are determined for the whole period of the study, and the values are:

$$A = 0.001803 \quad B = 0.03364$$

$$\alpha = 0.694 \quad \beta = 0.074$$

In Figure 4, the evolutions of the experimental and modelled efficiency for a given day are plotted. We can observe a good accordance between the two curves.

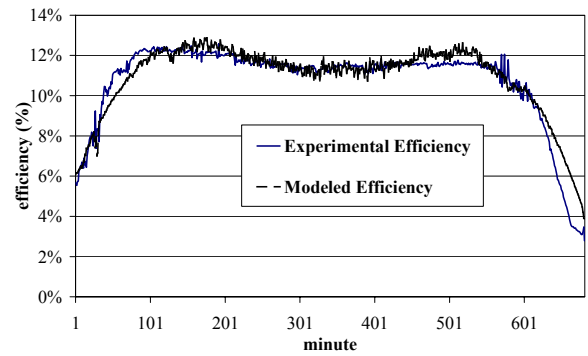


*Fig.4. Comparison between the experimental and modelled efficiency during a given day*

At the beginning of the day, there is no DC power generation by the PV modules until irradiances reaches about  $50 \text{ W/m}^2$ . During this time, the inverter performs an MPP search. During the day, when the modules generate the largest power, they became hot. Therefore, the efficiency of the PV modules decreases (Figure 4). When the irradiance decreases at the end of the day, a lower DC power is generated with the same irradiance (Figure 5a and 5b).

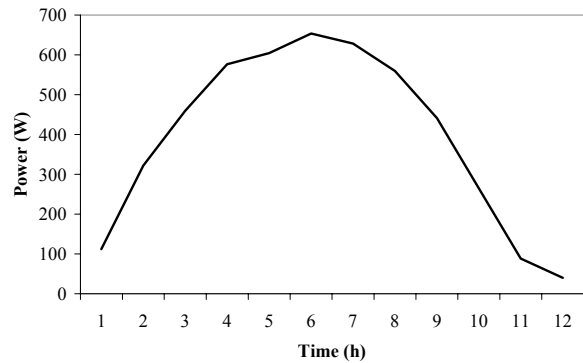


*Fig.5a. DC Power during a given day*

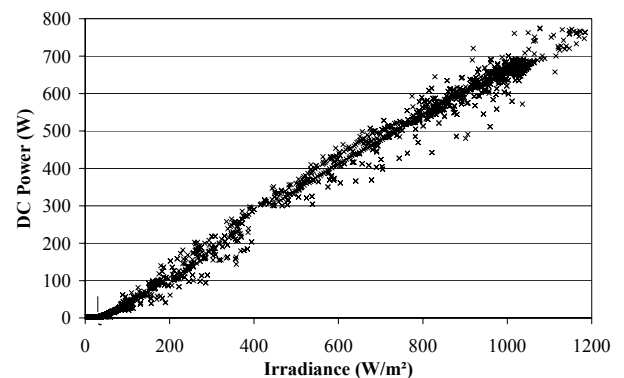


*Fig.5b. DC Power versus irradiance*

### Modelling, Optimisation and Performance of the inverter

The Sunny Boy SMA 700 is equipped with a MPP tracking system. The inverter starts supplying energy to the grid when the irradiance is about  $70 \text{ W/m}^2$  (i.e. the

DC power generated by the modules is about 7 W) and stops supplying when the irradiance goes down to about 50 W/m<sup>2</sup> (i.e. the DC power generated by the modules is about 3.5 W).

The efficiency of the inverter for values higher than about 150 W lm' is in a range from 92 to 96 %, but for the lower irradiance, the efficiency is strongly dependant on irradiation. The efficiency curve of the inverter is shown in Figure 6. We have also modelled this efficiency (Fig.6) and we have studied the optimal energetic configuration between PV Power installed and the nominal inverter power [2][3]. We do not present in this paper the method developed previously [4].

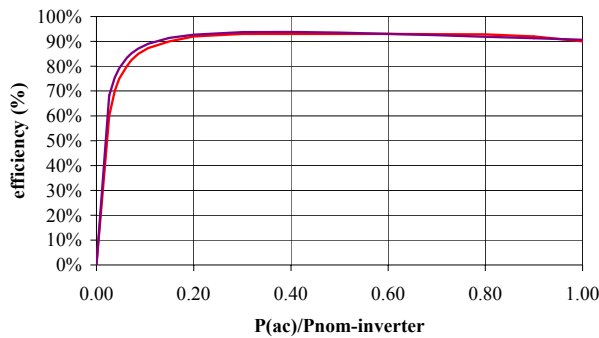


Fig6. Inverter efficiency

The result of the optimisation computation is shown in Figure 7. So, it could be seen that the present configuration is closed to the energetic optimal configuration. The difference between these 2 configurations is due to technical consideration (Input and Output Voltage).

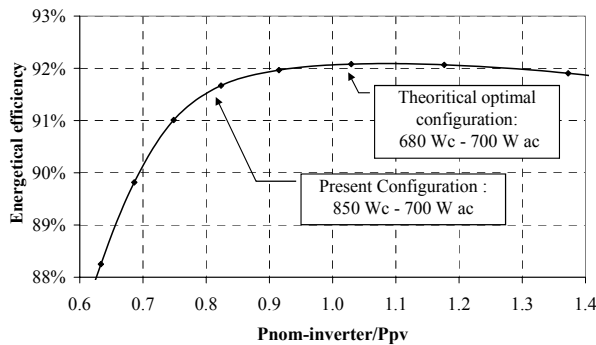


Fig. 7. Optimal configuration: PV Power installed -- Nominal Inverter Power

### Analysis of the PV system performance

To compare the production of energy and the performance of the various PV systems with different capacity and in various locations, the three following parameters have to be computed :

- normalised energy from the PV array

$$(4) \quad Y_a = \frac{E_{PV}(dc)}{P_{PV,peak}} \quad [\text{Wh/Wp}]$$

It represents the monthly or annually energy from the PV

array by unit of peak power installed

- normalised energy from the PV system:

$$(5) \quad Y_f = \frac{E_{PV}(ac)}{P_{PV,peak}} \quad [\text{Wh/Wp}]$$

It represents the monthly or annually energy from the PV system by unit of peak power installed

- Performance ratio:

$$(6) \quad PR = \frac{E_{PV}(ac)}{\Phi S \eta_{STC}}$$

where  $E_{PV}(dc)$  is the dc energy from the PV array,  $E_{PV}(ac)$  is the ac energy from the PV system,  $P_{peak}$ , the PV peak power installed,  $\Phi$  the total solar radiation in the plane of the PV array,  $S$  the surface of the PV array and  $\eta_{STC}$  the efficiency of the PV array for the standard condition.

We also use 3 other parameters, which are used to evaluate the performance of the PV system. The reference energy  $Y_r$  based on the solar radiation and represent the theoretical available solar radiation for the period (day, month annual, ...) and by watt peak:

$$(7) \quad Y_r = \frac{\Phi}{G_{STC}} \quad [\text{Wh/Wp}]$$

the losses by capture  $L_c$  :

$$(8) \quad L_c = Y_r - Y_a \quad [\text{Wh/Wp}]$$

and the system losses  $L_s$  :

$$(9) \quad L_s = Y_a - Y_f \quad [\text{Wh/Wp}]$$

The system is running since December 2000, so we can make a synthesis of the first four years of running.

During the 3 years of operation, the PV system generated in average about 800 kWh each year, and in 2004 the production was about 1030 kWh. The Table 2 summarises the annual performances of the PV System. We can observe a similar behaviour for each parameter during the years [5] [6] [7]. The parameters describe previously are presented in Table 2, for the 4 years.

On table 2, we can note that the availability of the system is varying between 0.80 and 0.85 for the 3 first years, and is exceed 0.9 in 2004 and the utilisation factor is varying 0.24 and 0.29.

Table 2

Annual performances of the PV system.

	2001	2002	2003	2004
<b>Yr</b>	2641.89	2626.08	1956.96	2504.56
<b>Ya</b>	1027.65	1001.47	965.69	1225.88
<b>Yf</b>	996.82	955.29	952.12	1210.08
<b>Lc</b>	1614.24	1624.61	991.27	1278.67
<b>Ls</b>	30.83	46.18	13.57	15.88
<b>PR</b>	48.7%	52.8 %	35.8 %	66.6 %
<b>AV</b>	83.5 %	84.8 %	80.2 %	96.2 %
<b>UF</b>	25.8 %	24.7%	24.7 %	29.5 %



The two last parameters are the Utilisation Factor (UF) and the availability (AV). The utilisation factor is defined as the ratio between the energy (ac) produce over the period and the maximal power the system multiplied by the number of hours. The availability allows to normalise the time during the PV system produce energy. It is defined like the ratio between the hours of running and the hours of sufficient solar radiation during the period.

On figure 8 we plotted the utilisation factor versus performance ratio. We can note a linear relation between these 2 parameters. More the system use the solar potential more the PR is high. However, if it is not the case, we can deduce that the system has some problems and that the losses are too high. When the system has not any running problem, the UF and PR are proportional, this is the case for our system.

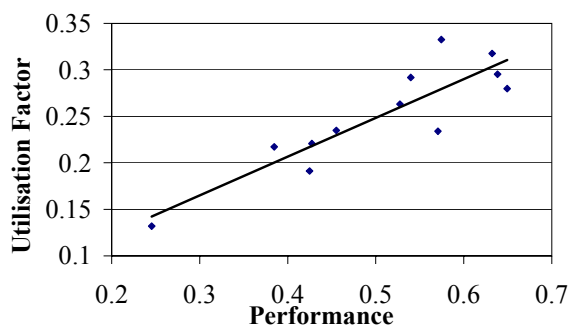


Fig.8. Utilisation Factor versus Performance.

In table 3, we give the annual production of energy and the overall efficiency of the system.

Table 3

Annual energy and efficiency of the PV system.

	Energy (kWh)	Efficiency
2001	847.3	6.7 %
2002	812.2	6.5 %
2003	809.3	6.35 %
2003	1028.5	7.30 %

The monthly study can allow to observe various transitions. The efficiency of the PV system has ranged from 6 to 10 % and decreased during the summer. The Monthly Normalised Parameters  $Y_f$ ,  $L_c$  and  $L_s$  are shown for 2 years (2001 and 2002) in Figure 9. The capture losses are due to the efficiency of the PV array and the system losses are due to losses in DC-AC energy conversion. The monthly final yield is about 90 %. Like the global efficiency of the PV array, the performance ratio (PR) is lower in summer time due to the module temperature of module: the efficiency of the PV array is then lower.

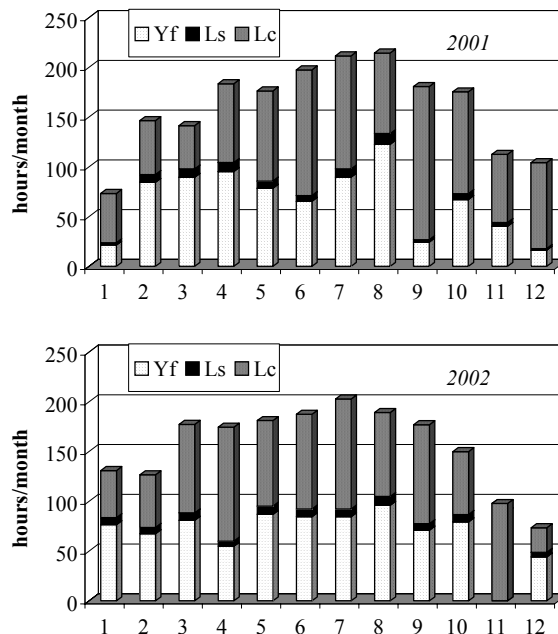


Fig.9. Monthly performances of the PV system.

The reasons for differences in energy production were only due to defects on the grid : high frequency and impedance variation. Since May 2004 we have modified the sensibility of the inverter and we hope this problems do not occur now. The detection of errors is about 33% over the 3 years (3% of the days do not have any switch). The energy loss due to these switches is important: about 30 % of the total production. Moreover, the augmentation of modules temperature during summer, and a tilted of 45° reduced the power output the PV array.

### Conclusion

The first PV system in Corsica, installed on the roof of our laboratory and totally monitoring since December 2000 has shown a good reliability of the system. Like a lot of PV grid systems the annual energy yields is about 950 kWh/kWp. We have related to the grid influence on the inverter performance, and consequently on the system performance. So, since the inverter sensibilities are modified, we have, for the first year, obtained a value greater than the 'magic limit' of 1000 kWh/kWp (1200 kWh/kWp). A such This energetic system have proved its high availability, and its great interest in grid connected application. In the future, we will modify the PV module support in the aim to set-up a tracker system in view to study the benefits we can obtain.

### Acknowledgements

The authors are thankful to the students Marenela MARKOVA and Krasimir Yordanov from the Technical University of Sofia, Faculty of Sliven, for participating to the project in the frame of SOCRA TES - ERASMUS program.

## References

- [1] Van Kerschaur E., Einhaus R., Szlufcik I., Nijts I., Mertens R. Simple and fast Extraction Technique for the Parameters in the Double Exponential Model for the I-V Characteristic of Solar Cells. 14th European PV solar energy conference, 1997, :p.2438-2441.
- [2] Peippo K., Lund P., Optimal Sizing of Solar Array and inverter in Grid-Connected PV Systems, Solar Energy Materials and Solar Cells, 1994, N°3, p.445-451.
- [3] Macagnan M.C., Lorenzo E. On the Optimal Size of Inverter for Grid Connected P V Systems, 11th European Conference on Photovoltaic Solar Energy Conversion, 1992, p.1167-1170.
- [4] Louche A., Notton G., Poggi P. Global Approach of an optimal grid connected PV systems sizing Systems, 12th European photovoltaic solar energy conference, 1994, p. 1638-1641.
- [5] Siegel M.D., Klein A., Beckman W.A. A Simplified Method for Estimating the Montly Average Performance of PV Systems, Solar Energy, 1981, Vol.26: p 413-415.
- [6] Wilk H. 200 kW PV Rooflop Program in Austria. 12th European photovoltaic solar energy conference, 1994, p. 923-926.
- [7] Haeberhn H., Beutler Ch. NormaLised Representation of Energy and Power for Analysis of Performance and on-line Error' Detection in PV Systems, 13th European Conference on Photovoltaic Solar Energy Conversion, 1995, p.15601563.
- 
- Philippe POGGI** - Associate Professor, Dr, University of Corsica, Laboratoire SPE UMR CNRS 6134, Route des Sanguinaires, Vignola, F-20000 Ajaccio, France.  
e-mail: philippe.poggi@univ-corse.fr
- Marc MUSELLI** - Associate Professor, Dr, University of Corsica, Laboratoire SPE UMR CNRS 6134, Route des Sanguinaires, Vignola, F-20000 Ajaccio, France.  
e-mail: marc.muselli@univ-corse.fr
- Gilles NOTTON** - Associate Professor, Dr-HDR, University of Corsica, Laboratoire SPE UMR CNRS 6134, Route des Sanguinaires, Vignola, F-20000 Ajaccio, France.  
e-mail: gilles.notton@univ-corse.fr
- Nicolas HERAUD** - Associate Professor, Dr-HDR, University of Corsica, Laboratoire SPE UMR CNRS 6134, Quartier Grosseti" F-20250 Corté, France.  
e-mail: heraud@univ-corse.fr.
- Stefka NEDELTCHEVA** - Professor, Dr, Technical University of Sofia, Faculty of Sliven, Sliven, Bulgaria.  
e-mail: stefned@abv.bg

# Solar Energy Resource Estimation for the Area of Rouse

Nicolay Mihailov and Ivaylo Stoyanov

**Abstract:** When we design photovoltaic systems it is necessary to have data base for solar radiation in the specific geographic area. For the area of Rouse this has been done by means of a specialized device for solar radiation measurement – piranometer. The main values for the intensity of solar radiation have been determined and the possibility for application of a photovoltaic system for agriculture has been estimated.

**Key words:** solar radiation, statistical analysis, photovoltaic systems

## Introduction

Nowadays industry development is going hand in hand with a non-stop increase of energy consumption. The main energy sources up to now are water power stations, heat power stations and nuclear power stations. The traditional energy source materials, such as gas, petrol and coals, are becoming less and less year after year and in only a few years we will have a serious energy problem. That is why the interest for using renewable energy sources (RES) is so big. The most famous RES is the sun, because it has the biggest energy potential. For one year we receive energy from the sun for about 100 000 000 000 MWh [1]. One little part of this energy has been transformed into movement of the air (wind). In order to estimate the optimal solar energy falling on a defined surface, many investigations have been done [2, 3]. It has been discovered that the intensity of solar radiation is related to the angle of falling of the rays through the atmosphere, as well as the angle of the slope of the radiated surface and so on. For example, the less height of the sun and the longer way of sun rays through the atmosphere, will lead to a decrease of the solar radiation during winter, and the opposite during summer. Based on these facts specialized atlases for solar radiation spreading all over the earth surface for different geographic areas during different seasons have been created [4, 5]. For direct design of a photovoltaic system it is necessary to have information about all year solar heating, total solar radiation for this area, possibility for sun heating, as well as the objects which can shadow the solar installation. [1]. The biggest part of this information is either missing or very limited for most areas of the country. This is the reason for bad design and bad exploitation of solar systems.

The aim of this paper is to analyze the solar energy resources of solar radiation in a horizontal surface for the area of the town of Rouse and after that to estimate the possibility for transforming this energy into electrical energy.

## Data base

The analysis of the solar energy resources for Rouse has been done based on direct measurements and integrated values for solar radiation in Rouse, in the area of Rouse University, which is situated at 43°49'22" northern longitude and 26°1'19" eastern longitude. The so measured values for solar radiation during the last spring season of 2005 have been compared to the theoretically obtained results for the same period.

## Investigation approach

The measurements for the solar radiation have been done by specialized measuring system [6], which consists of pyranometer CM 11, integrating block (SOLRAD Integrator) and personal computer (Fig. 1).

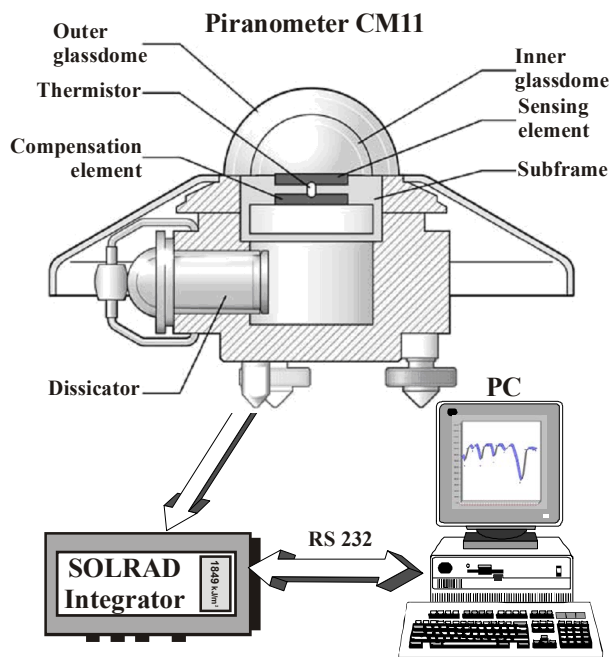


Fig.1. Construction of the CM 11 pyranometer [7] and connection of readout integrator SOLRAD with PC.

The sensitive element of the pyranometer CM 11 is a black disc of  $\text{Al}_2\text{O}_3$ . When the wavelength of the falling light is between 335 and 2200 nm, then the sensitive element temperature increases. The potential, which refers to the moment value of the solar radiation, has been generated by means of the thermistor and compensation element. For example, when the solar radiation has intensity  $1000 \text{ W/m}^2$ , then the temperature at the center of the  $\text{Al}_2\text{O}_3$  disc increases with  $3 \text{ }^\circ\text{C}$ , and from there on the value of out-going potential increases too. This potential goes to the integrator, which, depending on the mounting and construction, has the ability to show and

store the values of direct, reflected and spread solar radiation. The integrator can also integrate the so measured values and to store them for 31 days. The so registered moment and integrated values for solar radiation are transferred to PC by standard communication interface PC 232. By means of specialized software INTEGRATOR, all registered values for solar radiation intensity from the integrator, could be visualized and saved in real time, as well as after their pre-memorizing (Fig.2).

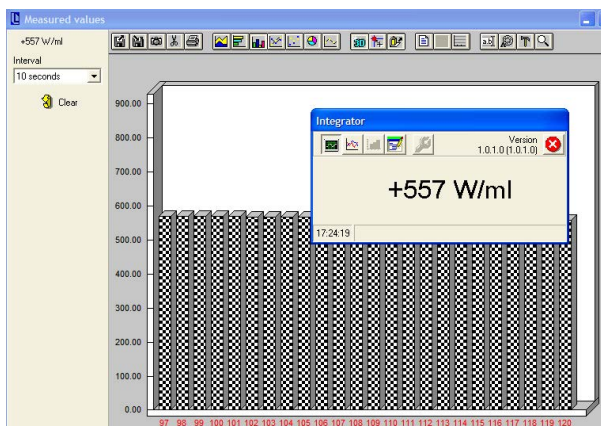


Fig.2. Main windows of the PC software program SOLRAD.

The measuring process accuracy for solar radiation is guaranteed by the unique certificate of the pyranometer and by following all the requirements for mounting of the company which has produced the device.

Following the above-described method we have measured the intensity of direct solar radiation (with interval of 10 s) in  $W/m^2$ , and integrated solar radiation (with interval 1 day) in  $kJ/m^2$ , for a flat surface during the period March 2005 – June 2005.

### Algorithm

The final results for solar radiation have been organized in three groups, for sunny days, for cloudy days, and for mixed days, respectively.

The moment value of the solar radiation for a specific geographic area depends on different factors, some of them not predictable. That is why in a specific moment of time this value is a random variable. Therefore the change of solar radiation in time is a stochastic process. This process has to be analyzed so that we will receive the main statistical parameters. The classical procedure for defining of the main probability characteristics for solar radiation as a stochastic process has been used – expected value, variance, normalized autocorrelation function and histogram of the distribution (probability density of the random variable due to residual sum of squares) [8].

### Results

During a bright sunny day the direct solar radiation change as a function of astronomic time (Fig. 3), looks like parabolic relation, following the azimuth of the sun  $\Phi$ , which could be defined by [5].

$$(1) \quad \Phi = \arcsin \left( \frac{\cos \delta \cdot \sinh}{\cos \alpha} \right),$$

where  $\delta$  is deviation,  $\alpha$  - the height of the Sun,  $h = \pm 15^0$  - number of hours from/to solar noon.

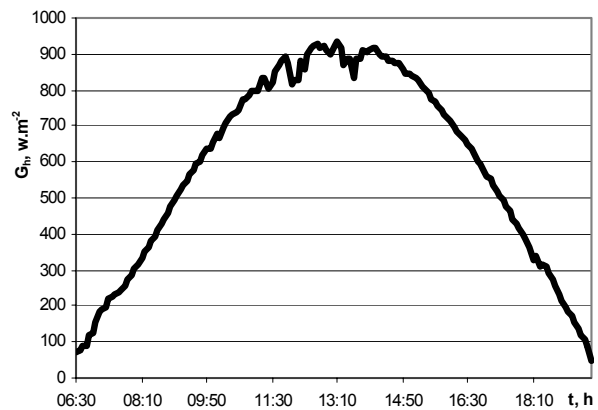


Fig.3. Deviation of direct solar radiation during a sunny day (17.06.2005).

On Fig. 4 is shown the deviation of the normalized autocorrelation function of the direct solar radiation during a bright sunny day. This deviation decreases slowly and there are no negative values. This fact shows

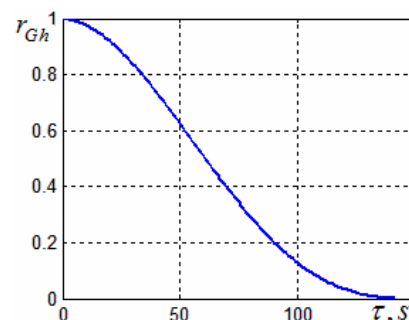


Fig.4. Normalized autocorrelation function of the total solar radiation during sunny day (17.06.2005).

that the stochastic process goes relatively smoothly and there is no periodicity, in other words, the process changes more or less in the same way in time, and has small deviations around expected value  $\bar{G}_h \approx 635, W/m^2$  with more or less constant dispersion  $S_{Gh} \approx 243, W/m^2$ .

During cloudy days the solar radiation change has a completely random character (Fig. 5). It is visible that the change of the accidental process is completely chaotic and has nothing in common with any known function, as in bright sunny days. When we have a fully cloudy sky, all registered values for directly measured solar radiation during different parts of the day are about two times lower than during sunny days. All the picks we can find could be described with short periods of clear sky.

During cloudy days the normalized autocorrelation function is slowly decreasing. This shows that in these cases the process changes very slightly in time. We have

received the following values for the expected value and for mean square deviation, respectively:  
 $\overline{G_h} \approx 241, \text{ W/m}^2$  and  $s_{Gh} \approx 154, \text{ W/m}^2$ .

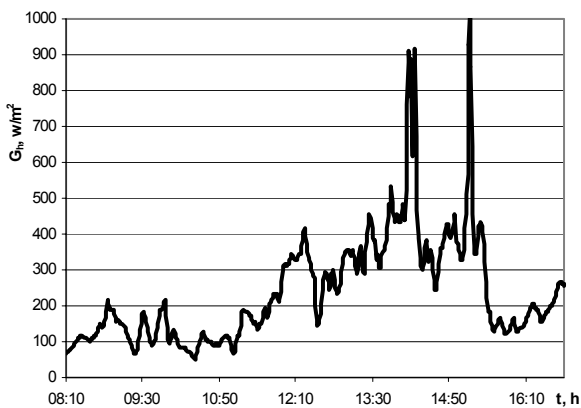


Fig.5. Change of total radiation during a cloudy day (17.06.2005).

During mixed days the results are the same and change slightly depending on whether the day is sunny or cloudy.

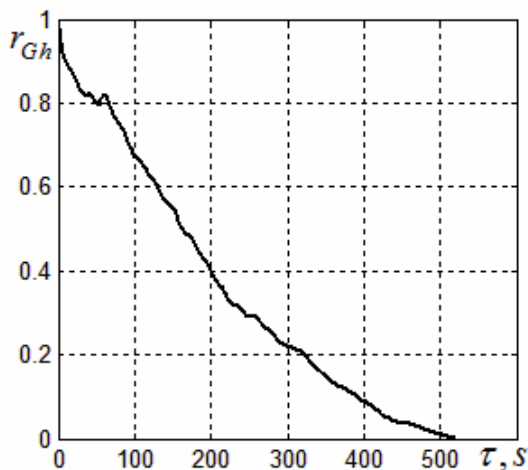


Fig.6. Standardized auto correlative function of direct radiation during a cloudy day (17.06.2005)

The results that are obtained for integrated values for solar radiation are shown on Fig. 7. There is a tendency generated mainly by the sharply increased average daylight in spring. In June the increase is almost double that in March. The total solar energy received in spring time is: 32% in June, 28% in May, 23 % in April and 17% in March, respectively, and it is 17811 MJ/m<sup>2</sup> average for the period.

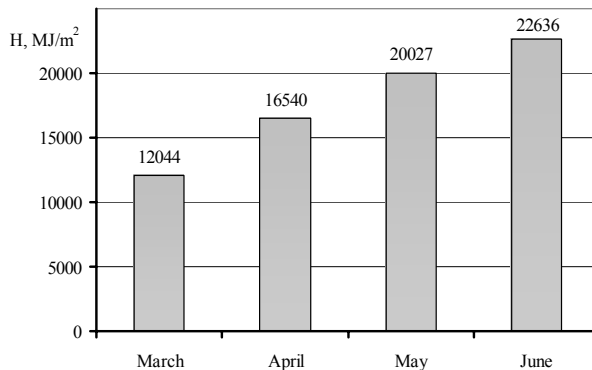


Fig.7. Averaged monthly integrated solar radiation for the area of Rousee.

The change of integrated values of solar radiation during the specific period is shown on Fig. 8. Here we can see specific cyclic recurrence about  $(11 \pm 3)$  days in the solar radiation intensity. It is good to estimate this cyclic recurrence during the remaining periods of the year too. If the values are proved then it is good to find out average weighted values for the specific periods, which will help the engineers in the design and operation of photovoltaic modules for generating of electric and heat energy. After analyzing the registered solar radiation it has been found that the value 1000 W/m<sup>2</sup> is registered on 23<sup>rd</sup> April, and the biggest value is 1336 W/m<sup>2</sup> – 25.05.2005 at 01.15 pm. The total solar radiation is about 1000 W/m<sup>2</sup> from the beginning of the June. In order to estimate the possibility for more optimal use of solar energy source, especially for supplying far located agricultural farms, it is nice to analyze the possibility

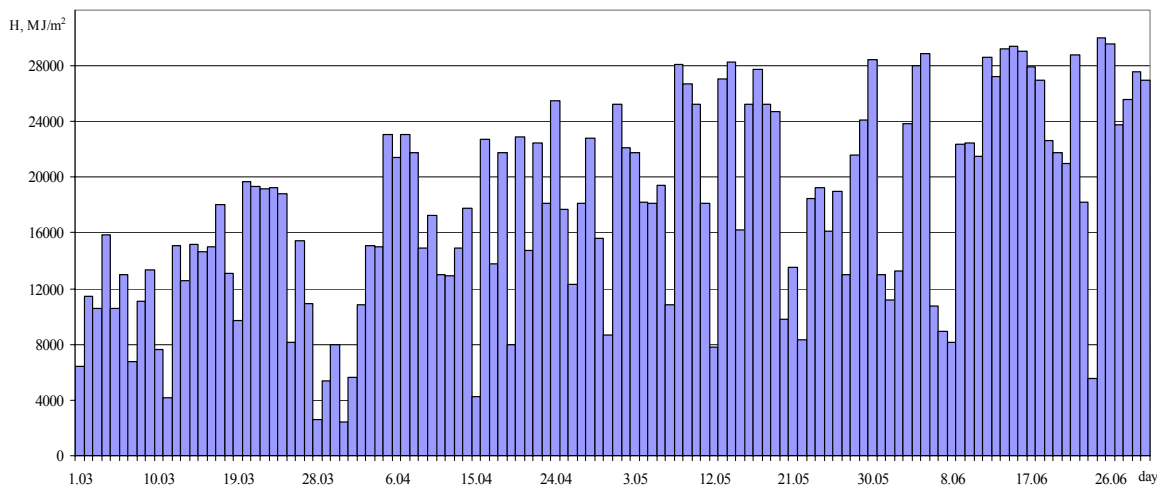


Fig.8. Daily integrated values for total solar radiation (Time integrated radiation).

character of the solar radiation and it is nice to estimate the main statistical parameters.

The comparison of the total, diffused and reflected solar radiation for the region of Rouse, received by means of known methods [8, 9] via a satellite, is of interest. For example, on Fig. 9 is shown the comparison between theoretical and real values of the direct solar radiation. The correlation coefficient between both relations is  $k = 0,894$ . This shows that there is a strong positive correlation between both values. Therefore, from theoretically obtained data we can get an objective idea about the level of the solar radiation in a specific area during a specific period. The observed deviation of the maximum in time rather than in value, can be explained with the use of summer time.

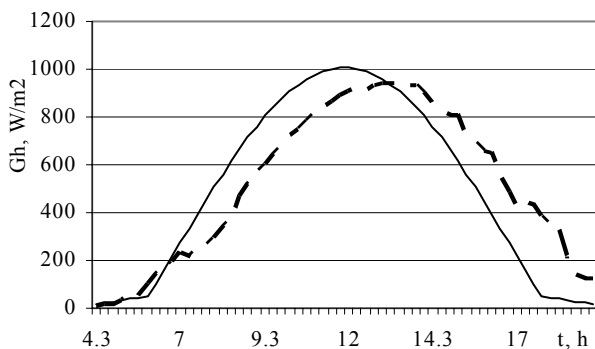


Fig.9. Comparison between theoretical (—) and current (---) values of solar radiation in a clear day for the area of Rouse in June.

### Conclusions

We have obtained data for direct solar radiation during the period between March and June 2005 for the area of Rouse, and this could be a base for creating a national database for different areas. The statistical analysis shows that solar radiation is an accidental process, which changes slowly in time. The cyclic recurrence of the sunny days has been estimated for springtime. The comparison between theoretical and real values of direct solar radiation has been done and the deviations have been analyzed.

### Reference

- [1] Дечев, Д. Слънчеви колектори и системи. Топлотехника за бита, бр. 5, 2005, стр. 31 – 36.
- [2] The Availability of Irradiation Data, International Energy Agency Photovoltaic Power Systems Programme. Report IEA-PVPS T2-04, April, 2004.
- [3] Минчев, М., Киряков, Ек. Колева, З. Велчев. Изследване интензивността на слънчевата радиация в град Пловдив. Топлотехника за бита, бр. 11, 2004, стр. 4 – 8.
- [4] The European Solar Radiation Atlas, Presses de l'Ecole des Mines. Paris, France, 2000.
- [5] PV Resources. [www.pvresources.com](http://www.pvresources.com).
- [6] Mihailov N., K. Gabrovska. A Computer System For Measurement Of Solar Radiation For The Region Of Rouse. 33rd International Symposium Actual Tasks On Agricultural Engineering, University of Zagreb, Croatia, 2005.
- [7] Pyranometer CM 11. Manual, Kipp & Zonen.
- [8] Remund, J., St. Kunz, Meteororm Handbook. A Tool for Solar Energy Applications Building Design, Heating & Cooling Renewable Energy System Design Agriculture and Forestry, Environmental Research Meteorological Reference. METEOTEST, November, 2004.
- [9] PV Potential Estimation Utility. <http://sunbird.jrc.it/pvgis>.
- [10] PV-GIS: Map-based Assessment of Solar Energy. European Commission, DG - Joint Research Centre Institute for Environment and Sustainability, Renewable Energies Unit.

---

**Nicolay Mihailov** – Assoc. Prof. PhD, Faculty of Electrical and Electronic Engineering, “Angel Kunchev” University of Rouse, 8, Studentska street, 7017 Rouse, BULGARIA.  
e-mail: [mihailov@ru.acad.bg](mailto:mihailov@ru.acad.bg).

**Ivaylo Stoyanov** – Assist. Prof. PhD, Faculty of Electrical and Electronic Engineering, “Angel Kunchev” University of Rouse, 8, Studentska street, 7017 Rouse, BULGARIA.  
e-mail: [stoyanov@ru.acad.bg](mailto:stoyanov@ru.acad.bg).

# Impact of the Deregulation of the Electric Power System on Its Optimal Operation

Lazar Petkanchin, Maria Kaneva

**Abstract:** *The technological process in the electric power system is unique both for physical laws that run it and for its importance for the civilization. Its organization, control and goals are unique and in this field the principles from other branches of industry can not be applied mechanically. Nevertheless such approach is a fact – it is so called deregulation. Together with the competition in electric power market it made the problems of operational optimization in EPS more complex and difficult than ever before. In this process the role of technical specialists increases considerably.*

**Keywords:** *electric power system, operational optimization, deregulation.*

## Introduction

There is no analogy in the industry with the technological process in the electric power system (EPS). The latter is unique from the point of view of the physical laws that run it as well as of its importance for the civilization. This means that the organization, control and the goals are unique and in this field the principles from other branches of industry can not be applied mechanically.

Nevertheless such approach is a fact – so called deregulation takes place all over the world. Deregulation is a process of removing regulations and restrictions with a purpose to introduce competition and participation of private agents on a free electric power market. As a result wholesale prices are formed. Deregulation is related with restructuring of the system.

## Deregulation

In DIRECTIVE 2003/54/EC OF THE EUROPEAN PARLIAMENT AND OF THE COUNCIL of 26 June 2003 concerning common rules for the internal market in electricity these European authorities conclude:

“(2) Experience in implementing this Directive 96/92/EC shows the benefits that may result from the internal market in electricity, in terms of efficiency gains, price reductions, higher standards of service and increased competitiveness.”

In the same point of the document some concerns are expressed: “However, important shortcomings and possibilities for improving the functioning of the market remain, notably concrete provisions are needed to ensure a level playing field in generation and to reduce the risks

of market dominance and predatory behaviour, ensuring non-discriminatory transmission and distribution tariffs, through access to the network on the basis of tariffs published prior to their entry into force, and ensuring that the rights of small and vulnerable customers are protected and that information on energy sources for electricity generation is disclosed, as well as reference to sources, where available, giving information on their environmental impact.”

In the same time it is mentioned in point (8) in the Directive:

“It is important however to distinguish between such legal separation and ownership unbundling. Legal separation does not imply a change of ownership of assets and nothing prevents similar or identical employment conditions applying throughout the whole of the vertically integrated undertakings.”

Obviously in every different country it is the Government that decided on the forms of restructuring and privatization. The latter is not compulsory requirement of EU.

At its meeting in Lisbon on 23 and 24 March 2000, the European Council called for rapid work to be undertaken to complete the internal market in both electricity and gas sectors and to speed up liberalisation in these sectors with a view to achieving a fully operational internal market, to adopt a detailed timetable for the achievement of accurately defined objectives with a view to gradually but completely liberalising the energy market.

In order to ensure efficient and non-discriminatory network access it is appropriate that the distribution and transmission systems are operated through legally separate entities where vertically integrated undertakings exist. However, a non-discriminatory decision-making process should be ensured through organisational measures regarding the independence of the decision-makers responsible.

With the constitution of interconnected EPS of different countries new possibilities are created to enhance security and economy of electric energy generation and supply for every one of them (UCTE). In the future every separate system, part of interconnected systems (generation, transmission, distribution and consumption) has to be consentient with competition conditions of the whole interconnected system.

### **Bulgarian power system and deregulation**

This Directive is important for Bulgaria as well. Desirable or not for the specialists deregulation and privatization took place in Bulgarian power system. All one can do is to find the right answers to the questions like: “What particularities of the operation of a deregulated power system are and how they influence the principles of its functioning?” (more detailed questions can be found in [1]).

In this paper these answers are searched for from a point of view of operational optimization.

The main characteristics of EPS are: (i) operation on vast territories (states, continents); (ii) wide ranges of time for process development – from parts of second (relay protection, emergency control, primary regulation) to dozens of years (EPS development); (iii) reliability of EPS operation is ensured by combined and coordinated actions in power plants, transmission and distribution systems; (iv) a strong mutual dependency exists between the processes on the whole territory of the system; (v) every consumer must be supplied whenever it shows; (vi) a significant losses occur as a result of supply interruption. Such kind of characteristics can not be fined in other systems (may be only Defense has similar ones).

These characteristics makes obvious that EPSs are not only the biggest systems and the most complex but the most responsible control systems too. The impact of their operation on the human lives increases continuously because of the increasing share of the electricity in the common quantity of used energy. The informational society of the future is not possible without electric energy usage. This shows the importance of such structures that ensure optimal technical and economical functioning of EPS correspondingly to the development and changes in EPS’ technical means. Historically the EPS development has pass through some stages: local (deregulated), national (vertically integrated), “single buyer”, free access to the transmission, free access to the network. Each of them has its advantages and shortcomings. The choice strongly depends upon historical, political, economical and personal factors.

One of the announced ambitions of deregulation is to make the expensive and labor-consuming technological process in EPS more effective economically – prime materials and personnel to be used in more efficient way. This is praiseworthy aim but its implementation is achieved sometimes by questionable means. That is why every change must relay on grounded conclusions made by well-motivated specialists knowing well the character and particularities of EPS.

In “open access” deregulated EPS an Independent System Operator (ISO) is responsible for the scheduling of the generation and load and for maintaining the system security. An ISO faces many complex tasks.

In most cases, the restructuring process has replaced traditional expansion and operation planning procedures of centralized optimization by market-oriented

procedures. The operational efficiency of free market for electricity is based upon a priority list of all units participating to the power production. The creation of the priority list is a critical task for ISO and relies on both, objective criteria and the experience of the operators in charge. The criteria are the following: operational cost, safety requirements, operation conditions in the past, maintenance scheduling, alternative supply availability, environmental impacts.

From the point of view of independent power producers issues that are important are: benefits, competitors’ bids, profit. These goals pursued by the market participants sometimes are contrary to the ones of the ISO. If only utilities’ benefits, competition and profit are driving forces in EPS operation and development then it is difficult to expect the quality and security of supply to be ensured.

There is another concern – the market efficiency is based on the assumption that no generating unit has the ability to make bids that all alone will increase the electricity price. This may not be the case in real life [3]. The more competitive the market is (with a large number of agents) the closer to the least cost dispatch the total output produced is.

Coordination in the environment of shared responsibilities requires efficient computational tools and methods. Current practice in reliability and security of operation in newly restructured EPS needs engineering tools to overcome unintended consequences, e.g., market power, capacity withholding, etc., that are detrimental to economic efficiency of the market forces. Secure and efficient operation in deregulated EPS requires fast and sure optimization tools. Deregulation is causing fundamental changes in the rules of the game for the electric power industry and is changing utterly the way of decision making.

In Directive 2003/54/EC is previewed: “In order to ensure efficient and non-discriminatory network access it is appropriate that the distribution and transmission systems are operated through legally separate entities where vertically integrated undertakings exist. However, a non-discriminatory decision-making process should be ensured through organizational measures regarding the independence of the decision-makers responsible.”

The operational decisions can be grouped in two categories. First is the decisions taken by the players on the market and second – the ones taken by the central authority such like ISO. The second group of decisions are supported by so called Energy Management System (EMS).

There are two considerations to be taken into account for EMS [2]:

- (i) EMS must ensure functionality of EPS – scheduling of the generation, state estimation and congestion management. Power grid control problems need to be continuously studied both in normal and in emergency conditions. Deregulation pushes the transmission system to operate closer than before to its security limits. The scarcity of



transmission capacity lead to transmission system congestions. The introduction of competition in electric power market has made operation control problems more complex and difficult than ever before.

(ii) The second issue concerns the sheared control of interconnected transmission systems where each utility can have its specific EMS and criterion. In the big interconnected systems (like UCTE) there are special rules and criteria for management and automatic control obligatory for all the members. The ISO's EMS is supposed to supervise the overall operation. Obviously there is a need to coordinate different solutions and to provide for overall optimal solution and hence operation. This report does not consider these issues.

For Bulgarian EPS there are some specific concerns. In the market we can see some power plant that participate independently one from another. These plant have been constructed for common operation thus overcome the shortcomings of different types of plant – they have been treated like an unity and now they are competitors! The only competitor to win in such circumstances is not in the country.

Another feature is that a low price energy from NPP “Kozloduy” goes for big consumers, while the expensive energy will go to the small end-users. It is interesting problem to be studied - how these plants of different types can work together in optimal way and be a competitive participant in the “open access” electricity market in our region provided that the owners want this.

### Operational optimization in EPS

What objective function is to be implemented for the complex problems of optimal operation in deregulated EPS by the ISO.

The main difficulties of automatic control in EPS are: (i) changes of the load in one day, week, season, year, etc.; (ii) big velocity and strong dependency of processes in EPS' elements (all they work in synchronism); (iii) there is no possibility for economic storage of electric energy of sufficient quantity.

Normally the EPS operates under following conditions: normal, before failure, emergency, recovering. The objective function for efficient operation changes depending upon the operating conditions of the moment.

Thus in normal operating conditions this function is the most economic production of electricity, parameters maintaining of EPS in given limits and environmental requirements' adherence.

The most economic production implies the minimization of the following objective function:

$$(1) F = \sum_i C_i(P_i) + \sum_j C_j(K_j) + \sum_{m,n} C_{mn}(P_{mn}) + \sum_p C_p(P_p)$$

where

- i – is generating unit number;
- j – tariffs in use;
- m,n – transmission lines with violation;
- p - unserved load.

The constraints of the problem are to ensure:

- 1) energy balance;
- 2) generating units limits;
- 3) phase shifter control constraints;
- 4) other security constraints.

There can be applied another constraints as well, depending on the aims and precision of the calculation – here is an example of how the objective is in most simple form.

In a deregulated EPS economical and technical interests of different generating and distributing utilities are conflicting. For everyone of them the aim is to maximize its profit and this is a natural result from the privatization of majority of power utilities in Bulgaria (and in many counties in the world). Electric power is not an obligatory service provided by the EPS any more. It is a commodity like every merchandise.

ISO is the unit that carries out a co-ordinated functioning in every moment of all participants in the multistage technological process of the unity – EPS – with maximal security and economy of supply. These two goals (economy and security) are contrary in many cases. Then the common goal pursued is to ensure security of supply.

The tasks for scheduling of the generation is accompanied by the ones for state estimation and congestion management. In an “open access” electricity market users can be supplied from anywhere in the interconnected system provided that the system security is assured. One very important function of ISO is to manage the use of transmission subsystem - available transmission capacity is studied, transmission rights are established both transmission congestion contracts and financial transmission rights. For a EPS with congestion, under the locational marginal prices scheme, loads in congestion area holding the transmission rights can import less expensive electric energy without paying for more expensive local energy. This creates some shortcomings that influence the transmission subsystem development [4].

It is well known that the optimal distribution of the active power in the EPS is not a simple sum of the optimal loading of different generators. Neither the optimal functioning of all elements lead to the optimal operation of the EPS as a whole. The problems of optimization of operation of EPS is complex, labor-consuming and require goals and objective functions by compromise.

Before emergency when abnormal (difficult to control) operating conditions exist the main goal is to maintain the integrity of the EPS and to return to normal operation (congestion management). The deregulation

and the competition in electric power market made power flow control more difficult than ever before. The scarcity of transmission capacity and the common and big demand for less expensive power purchase, and specific requirements of trade lead to transmission system congestion. The difficult to control operating conditions do not allow ISO to interfere with generators schedule unless congestion occurs. The congestion can threaten system security, increase system operating costs, raise the price for the users or hinder fair competition between generating utilities.

In emergency conditions the task is to protect the elements of the EPS, to minimize the power non supplied. It is accomplished by generation re-scheduling and interruptible load curtailment.

In recovery period of operation of EPS the purpose is to restore the system as quickly as possible. There are specifics of the problems here that are very appealing but go beyond the purposes of this report.

### **Conclusion**

Electric power is a very particular good regarding the particularities and main characteristics of EPS – existence of two components – active and reactive power, several types of stability in its operation (steady-state, transient and thermal stability), others.

To address many of tough issues mentioned above, it is crucial to apply objective optimization approach.

In times of deep and total changes in this complex, huge and important system it is of tremendous importance to realize these changes with the leading participation of technically qualified persons, having

enough experience in EPS of Bulgaria. Only doing so it is possible to embrace both economic and engineering aspects of big number of unsolved and difficult problems of EPS operation.

### **References**

- [1] Xiaoming F., Zh.Wang, others, ABB Inc., An Integrated Electrical Power System and Market Analysis Tool for Asset Utilization Assessment, Power Systems and Communication Infrastructures for the Future, Beijing, September 2002;
- [2] Javier Contreas, Ar. Losi, others, Simulation and Evaluation of Optimization Problem Solution in Distributed Energy Management Systems, IEEE Trans. On Power Systems, vol.17, No.1, February 2002
- [3] Rafael Kelman, L.A.N Barroso, M.V.F. Pereira, Market Power Assessment and Mitigation in Hydrothermal Systems, INTERNET
- [4] Applied Mathematics for deregulated Electric Power Systems: Optimization, Control, and Computational Intelligence. NSF Workshop, November, 2003, Arlington, USA

---

**Lazar Petkanchin** – Professor, DSc., Faculty of Electrical Engineering, Technical University of Sofia, 8 Kl. Ohridski Str., 1000 Sofia, BULGARIA.  
e-mail: lpetkanc@tu-sofia.bg.

**Maria Kaneva** – Associate Professor, Dr., Faculty of Electrical Engineering, Technical University of Sofia, 8 Kl. Ohridski Str., 1000 Sofia, BULGARIA.  
e-mail: mkaneva@tu-sofia.bg.

## Simulation Study of DG Effect on Fault Location Methods in Distribution Networks

D.Penkov, B. Raison, C. Andrieu, L. Stoyanov, J.-P. Rognon

**Abstract:** In this paper the results of simulation study for the estimation of Distributed Generation (DG) impact are presented. These are carried out in order to quantify the precision of a fault locating method in the worst case when these generators have a large penetration in the distribution network. Results are compared with those without DG and for different distributions in the network.

**Keywords:** Distributed Generation, Fault location

### Introduction

Distribution networks are often subject to faults as a result of phase to ground, phase to phase or three phase short-circuits. These faults are dangerous, and provoke the circuit breaker's opening in order to be cleared. The clearing time depends on the fault nature, and on the fault persistence. A steady fault can not be cleared by the breaker's action and needs to be reviewed by the maintenance crew. In order to reduce the operation time, the fault should be located in advance by analytical means. These are based on voltage and current measurements on the substation, made in the meantime before the breaker's opening. Some methods for fault location could be found in [1]. These methods work well in the case of a one-source network. The Kyoto's protocol, (1997) [2], establishes new conditions in the networks for a 'green' energy. It means that all the countries which have signed it should have a green energy production also called Distributed Generation. That could be wind turbines, hydro turbines, photovoltaic panels for the solar energy and others [3]. These sources are good for the ecology, but their introduction in the networks requires changing lots of the guiding principles related to their exploitation and maintenance. Such a problem is the fault location in distribution networks. DG impact the locating precision through the fault currents they supply. As known these currents depend mainly on the short-circuit power of the generators, and the conductor's impedance. The short-circuit power is defined as the power that a generator is able to supply when a three phase fault is next to its output. Since this power is calculated for the nominal voltage of the machine, it is proportional directly to the current supplied during the fault. When it is to

locate faults by measurements on the substation feeder only, the DG fault currents are going to modify those at the feeder. A higher short-circuit power of a DG source means a higher fault current supplied when a fault is and a possible greater impact on the fault signals. This effect has been studied for the fault location of three or two phase faults, taking place in a given distribution network when at least one 'green' generator is present. According to the position related to the fault location, one can distinguish two main situations:

- The feeder (main source) and the DG are both on the same side of the fault
- They are on the two sides of the fault location

This study can be extended to consider the short-circuit power ratio of the generators and the case of some generators dispersed over the network.

These three different criteria are studied in order to estimate the precision of a given fault-locating method. In the next four sections the method, the DG model, the network and program supply are presented respectively. Theory for DG impact is included in section 6. Results obtained for different situations described generally above are pointed out, and the appropriate conclusions made in section 7 and 8. Section 9 gives the main conclusions that could be tied out from this study.

### Fault locating method

The method used for fault distance computation is based on the impedance measured on one faulted phase on the power transformer's secondary coil [4]. On the next figure a simplified scheme shows the fault situation:

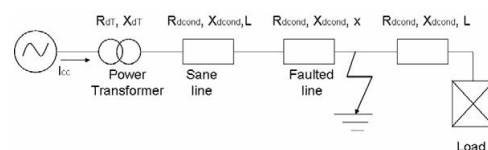


Fig.1. Simplified fault network scheme

The main equation for fault distance computation is:

$$(1) \quad (Rd_T + L.Rd_{cond} + x.Rd_{cond})^2 + (Xd_T + L.Xd_{cond} + x.Xd_{cond})^2 = k \left( \frac{U}{\sqrt{3}I_{cc}} \right)^2$$

Where:

- $k$  –coefficient, depending on the type of fault,  $k=1$ , for a three phase fault,  $k=0.75$  for a phase to phase fault.

Such a one-end method is sufficiently precise since the considered currents are very high, compared to the load ones. A passive distribution ‘RL’ load can be considered as an open circuit for the three and double phase fault currents. The contact impedance between phases is considered to be zero. The method needs no additional changes to work properly for distribution networks with many taps. It is suitable for permanent faults, since the variables are complex values for the fundamental frequency.

### The distribution network

The network is a 7MVA feeder, which has a total length of 55km, lines or cables. All the conductors have a length of 5 km, and the loads are 450MVA, power factor of 0.9 each. The network is developed for location purposes; the software that has been used is ARENE [5]. It has been developed and commercialized by the French utility EDF. The next figure shows the network topology and load distribution:

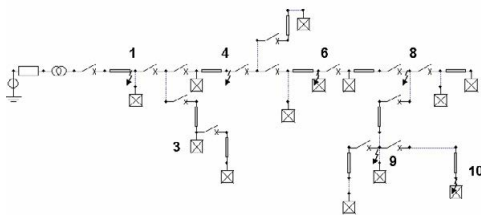


Fig.2. Studied distribution network

As it could be seen the load is equally distributed along the network. A brief description of the grid is given in the next table:

TABLE 1

Network parameters

Network part	Direct Resistance	Direct Reactance
Up Network	$R_{up} = 0.0266 \Omega$	$X_{up} = 0.3989 \Omega$
Transformer, 36MVA, 63kV/20kV	$R_{tr} = 0.0463 \Omega$	$X_{tr} = 1.664 \Omega$
Lines	$R_{li} = 0.2 \Omega / km$	$X_{li} = 0.299 \Omega / km$
Cables	$R_{ca} = 0.203 \Omega / km$	$X_{ca} = 0.1256 \Omega / km$
Load	$R_{ca} = 2400 \Omega$	$L_{ca} = 3.8207 F$

The short-circuit power of the main source is 180MVA. Faults are distributed on the points were an arrow is shown.

### Distributed Generation model

A 0.4MVA Diesel Generator has been simulated. As this is not a real “green” energy generator it is necessary to explain why this generator has been chosen for the study. Normally there are two possible connections for a generator to the network grid: one is its “direct” connection – if the generated voltage and frequency match with those of the grid, and the second possible connection is by power electronics devices, when they do not match directly. The power electronic devices are “smart” devices – they have a control loop that is very fast and does not allow high currents. When a direct connection is used the high fault currents are allowed. That is the case when induction or synchronous generators are considered. The first ones are rapidly demagnetized by the voltage drop and not really able to provide a really high contribution to the permanent fault. Synchronous generators are more independent since they have their own excitation like permanent magnets or excitation circuit. That makes this type of generators the most “dangerous” in terms of fault current contribution and so the most suitable if one wants to study the DG effect on the fault location. Synchronous generators directly connected to the distribution grid are mostly hydro turbines. Their behaviour is similar to that of a diesel generator, but the last is more rapid in terms of reaction. So that kind of generator is chosen for the representation of the worst case of reaction to a fault. Here next is shown a simplified scheme of the used generator:

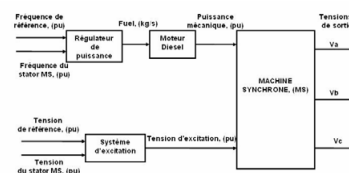


Fig.3. Diesel Generator

The excitation block is an IEEE standard Type 1 excitation, which description can be found in [6]. The Diesel engine model is developed and validated according to [6, 7, and 8]. The machine has 10% speed droop, and 400V out. The grid connection power transformer is Wye-Delta coupled.

### Program supply

The program supply is important since the fault location is found by consecutive sum of the conductor's active and reactive impedance. The program supply has been developed in our laboratory for various distribution network studies [9]. It has three main blocks that react mutually. These are:

- Network description extraction – the topology of the grid and the parameters of the different conductors are read and stored in a dedicated data base
- Network course block – used for the fault locating algorithms test or for generation of useful data needed by other applications
- Visualization block – used for the network representation and fault location shift on a map.

The whole algorithm has been developed on MATLAB, [10], and a part of it translated in C-code for the purposes of the European project CRISP [11].

Here next the studied network is presented as rebuilt by the program:

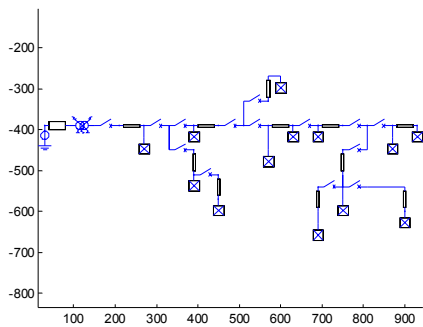


Fig.4. Studied network as seen in Matlab environment

During the network course the elements seen to be safe are coloured in cyan and those supposed to be faulted in red.

### DG impact on fault location

In this section the simulation study is described. As mentioned before there are some study cases that represent the most usual situations. In order to achieve a better explanation the theoretical basis for this study are going to be presented bellow. On the next figure a three phase fault for a simplified network with DG is shown:

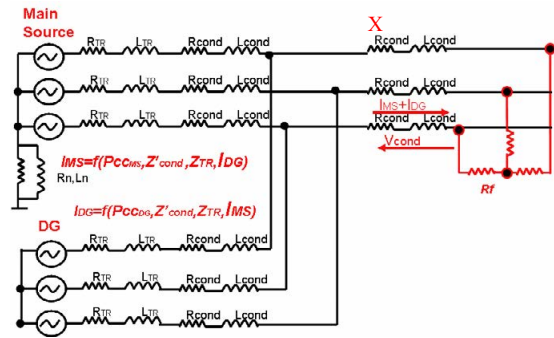


Fig.5. Theoretical situation for a three phase fault on network with DG

The length X of the common part for the main generator and the DG network is variable with the fault distance. For a three phase fault the KVL equations are:

$$(2) \begin{cases} V_{MS} = (Zd\_tr_{MS} + Zd_{MS} \cdot L_{MS}) \cdot I_{MS} + (I_{DG} + I_{MS}) \cdot Zd_{comm} X \\ V_{DG} = (Zd\_tr_{DG} + Zd_{DG} \cdot L_{DG}) \cdot I_{DG} + (I_{DG} + I_{MS}) \cdot Zd_{comm} X \\ Rf = 0 \end{cases}$$

Rearranging the equation with respect to X yields:

$$(3) X = \frac{1}{Zd_{comm}} \frac{(Zd\_tr_{DG} + Zd_{DG} \cdot L_{DG})(Zd\_tr_{MS} + Zd_{MS} \cdot L_{MS}) I_{MS} - V_{MS}}{V_{MS} - V_{DG} - (Zd\_tr_{MS} + Zd_{MS} \cdot L_{MS} + Zd\_tr_{DG} + Zd_{DG} \cdot L_{DG}) I_{MS}}$$

meaning that a measurement of the fault current on the substation should be sufficient to find the fault location. However for the purposes of this study the formula is to be used as is (1), without taking into account the DG contribution.

For a double phase to phase fault, considering the phase to phase voltages, the fault distance is the following:

$$(4) X = \frac{1}{Zd_{comm}} \frac{(Zd\_tr_{DG} + Zd_{DG} \cdot L_{DG})(U_{MS} - 2(Zd\_tr_{MS} + Zd_{MS} \cdot L_{MS}) I_{MS})}{U_{DG} + 2(Zd\_tr_{MS} + Zd_{MS} \cdot L_{MS} + Zd\_tr_{DG} + Zd_{DG} \cdot L_{DG}) I_{MS} - U_{MS}}$$

Since for phase-to-phase faults the fault currents are not totally identical, a mean absolute value has been taken for the fault distance calculation. Once again it should be noticed that the fault location is going to be found by applying the original formula in order to evaluate the DG's impact.

### Fault simulations and locating results

As it was said the simulation study is to be carried on following three main criteria:

- The fault position in respect to the generators
- The short circuit power of the DG
- The DG distribution over the network

Practically the simulations were performed in the following manners:

1. Fixed generator - various fault positions, (DG on p.6)
2. Fixed generator – various fault positions and DG powers
3. Two generators fixed –p.6 and p.3 - (sum power equal to maximal simulated) - various fault positions

Let us recall that the inserted generator has an apparent power of 0.4MVA and the total load on the feeder is 7MVA.

### Three phase faults

Table 2 presents the results obtained for the first case study:

TABLE 2

Fault location results with 1DG

Fault point	Real distance, km	Fault current for urban, A	Calculated Distance, km	Fault current for rural, A	Calculated Distance, km
1	5	3974,7	5,0121	3101,4	5,0062
4	10	2940,5	9,9874	2114,8	9,9692
6	15	2305,4	14,903	1605,8	14,842
8	20	1886,7	19,8	1303,4	19,512
9	25	1589,4	24,761	1088,1	24,404
10	30	1378	29,546	940,06	29,06

On the next figure the computational error is shown:

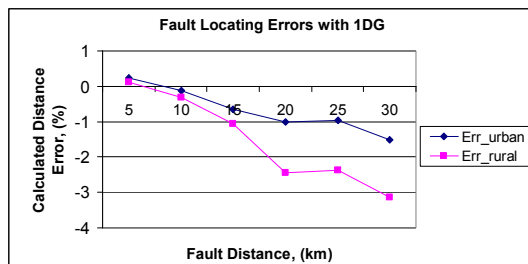


Fig.6. Fault Location Error

where the error is calculated as:

$$(5) \quad \varepsilon = \frac{D_{calculated} - D_{real}}{D_{real}} \cdot 100$$

As it could be seen the error in fault location is relatively small. The error is increased after the 15-th km, when the DG has a common path with the main source. The DG provides some fault current that decreases that of the main source. The computed fault distance is thus increased. For a better illustration the errors when there is no DG in the network being rural or urban, are shown on the next figure:

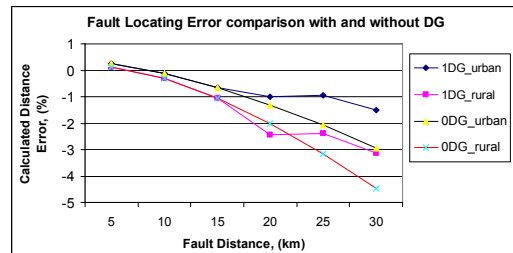


Fig.7. Fault location error comparison

The computed distance error is reduced due to the DG. Its influence is stronger with the shared network path. The “correction” is in the range of 2%. However this situation changes when the DG short-circuit power is bigger. On the next figure the results for different DG powers are shown. The DG power was increased by connecting other DG of the same size to the same connection point 6. For this type of connection is more realistic than a greater source, the “green” generators are not supposed to be small units [12]:

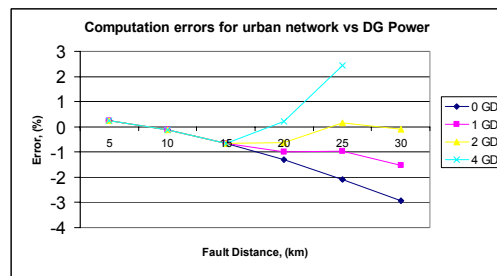


Fig.8. DG Power influence for urban network

Each added DG increases the calculated fault distance after the 15-th km. The locating error is smaller when 2DG are connected but when they double the error is increased to positive and for the 30km the obtained distance is greater than that of the network and no solution is found. Four DGs is the worst situation for the presented fault locating results, which remain however acceptable, with the

error of 3-5% maximum. Such a DG connection is very rare, to say not realistic at the moment, the generated power is too much for the network. On the next figure the results for a rural type of network are shown:

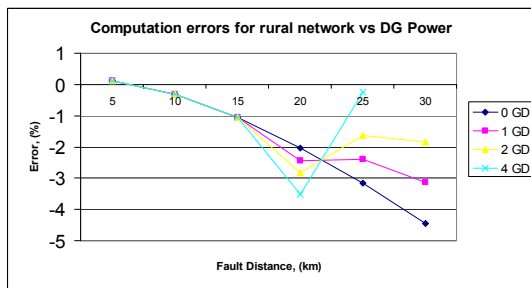


Fig.9. Error for a rural type of network

The results here are more pessimistic. The maximum error without DG is 4.3% while it is about 3% for the urban grid. The difference is result of the smaller cable reactance which increases the fault current and so the load effect of the bifurcations upstream to the fault position is thus reduced in urban network. The DG decrease the error, however on the 20km fault point that is next to the DG the influence is negative.

The case of two generators connected on two different points shows the influence of their distribution over the network for the same fault. The next figure illustrates this phenomenon:

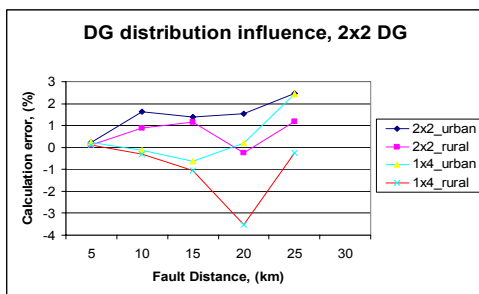


Fig.10. DG dispersion influence

Obviously the error is depending on the network type urban or rural. As it could be seen the DG dispersion on the network increases the error, due to the fact that they stand on the two ends of the network and deliver fault current for nearly all fault positions. But downstream the second DG group the error is greater than it is for one DG group of equal power connected on the same place. That is due to

the longer path shared by the first DG group and the main source which induces a smaller fault current from the last. So the worst place for fault location remains the 30km where the two DG groups deliver both fault currents.

### Double phase-to-phase faults

The same studies were performed for double faults. On the next figure results for the first case study are shown:

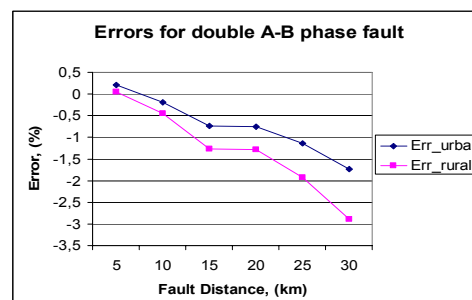


Fig.11. Errors in fault distance computation for double fault

The computed distance decreases with the fault distance. The range is the same as previously for the three phase faults. The point of 15 km is special for there is a DG connected. As previously, the DG fault current maintains the error in proximity of the fault but its influence is limited 10 km downstream. The DG power increase has an influence on fault location in urban network as follows:

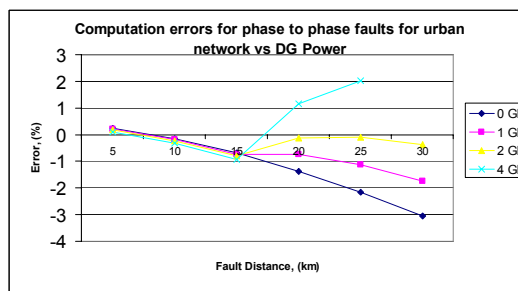


Fig.12. Results for urban network

The effect is greater for a double phase fault. It modifies the results even before the connection point, where DG and main source have no shared path. That is because they remain “connected” by the third safe phase. Its current induces some voltage on the two faulted phases. The DG insertion increases this voltage. Next are the results for a rural network:

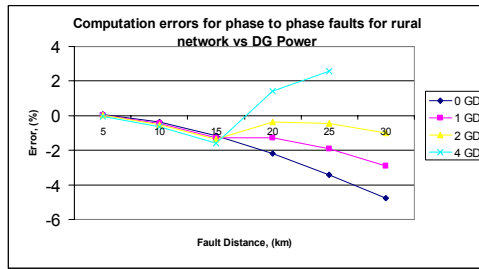


Fig.13. Results for rural network

As previously mentioned the error is greater but the tendencies remain the same.

The influence of the DG distribution on the fault location is visualized on the next figure:

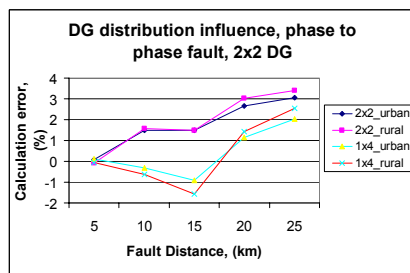


Fig.14. DG dispersion influence

The fault location results are similar to those obtained for three phase faults. The DG distribution increases the error. This effect is reduced when the fault is too far from the DG but their influence remains important.

## Conclusion

In this paper results for fault location of phase to phase or three phase faults in distribution network containing Distributed Generators are presented. A method based on one end data has been applied. The DG influence is depicted and commented. It is relatively small but not negligible. The DG distribution over the network increases the fault location error, since this implements a greater network path to be shared with the main source. Reducing their effect seems to be possible by connecting them on one point, which is preferably to be at the feeder, or they should have a dedicated feeder. The network type, urban or rural, impact is also studied and shows better results for smaller cable impedances which induce a greater fault current and so reduce the load effect.

## References

- [1] M. Saha, R. Das, P. Verho, D. Novosel, Review of Fault Location Techniques for Distribution Systems. Power Systems and Communications Infrastructures for the future, Beijing, September 2002
  - [2] Entrée en vigueur du protocole de Kyoto – Que laissera la date de 16 février 2005 dans nos mémoires ? , ACTU Environnement, 17.02.2005
  - [3] B. Multon, Production d'énergie électrique par sources renouvelables, Techniques de l'ingénieur, Traité Genie Electrique, D4005, 2001
  - [4] B. de Metz-Noblat, F. Dumas, G. Thomasset, Calcul des Courants de court-circuit. Cahier Technique No.158, Schneider Electric, [www.schneider-electric.com](http://www.schneider-electric.com)
  - [5] [www.rdsoft.edf.fr/ARENE.html](http://www.rdsoft.edf.fr/ARENE.html)
  - [6] G.S. Stavrakakis, G.N. Kariniotakis, A General Simulation Algorithm for the Accurate Assessment of Isolated Diesel-Wind Turbines Systems Interaction Part I: A General Multimachine Power System Model and Part II: Implementation of the Algorithm and Case-studies with Induction Generators, IEEE Transactions on Energy Conversion, Vol.10, No.3, September 1995
  - [7] G. Claeys, Modélisation de la production indépendante dans les réseaux de distribution, Phd Thesis, LEG, 2001
  - [8] D. Penkov, Simulation d'un centre de production adapté aux réseaux isolés pour les pays en voie de développement électrique, DEA, LEG, 2003
  - [9] D. Penkov, Le parcours et la visualisation de réseaux électriques pour la localisation de défauts, JCGE Montpellier, 2005
  - [10] [www.mathworks.com](http://www.mathworks.com)
  - [11] C. Andrieu, B. Raison, D. Penkov, M. Fontela, S. Bacha, N. HadjSaid, Fault Detection, Analysis and Diagnostics in High-DG Distribution Systems. EESD Project ENK8-CT-2002-00673 CRISP, 2002
  - [12] J.-F. Canard, Impact de la génération dispersée dans les réseaux de distribution, Phd Thesis, LEG, 2000
- D. Penkov** – PhD student in the Laboratoire d'Electrotechnique de Grenoble (LEG), INPG, France  
e-mail: [penkov@leg.ensieg.inpg.fr](mailto:penkov@leg.ensieg.inpg.fr)
- B.Raison** – Associate professor in the Ecole Nationale Supérieure d'Ingénieurs Electriciens de Grenoble,  
e-mail: [Bertrand.Raison@leg.ensieg.inpg.fr](mailto:Bertrand.Raison@leg.ensieg.inpg.fr)
- C.Andrieu**– Research Engineer in Schneider Electric  
e-mail: [christophe.andrieu@leg.ensieg.inpg.fr](mailto:christophe.andrieu@leg.ensieg.inpg.fr)
- L.Stoyanov** – student master degree in LEG,  
e-mail: [stoyanov@leg.ensieg.inpg.fr](mailto:stoyanov@leg.ensieg.inpg.fr)
- J.-P. Rognon** – professor in in the Ecole Nationale Supérieure d'Ingénieurs Electriciens de Grenoble  
e-mail : [rognon@leg.ensieg.inpg.fr](mailto:rognon@leg.ensieg.inpg.fr)



# Models of Transient Processes during Operation and Faults in Autonomous Energy Systems

Lyubomir V.Dimitrov and Stefka G. Kanturska

**Abstract:** *The present paper discusses some possibilities of simulating transient processes in vessel electric energy systems.. The results allow choice and adjustment of commutation system and protection circuits of such equipment. Cases related to system parameters change are also presented. Further, capabilities to detect and classify vessel electric energy systems failures using adequately suited models and digital fault recorders are given. (DFR)*

**Keywords:** *Transient Processes, Models, Fault*

## Introduction

The transient processes (TP) in an electric system are related to sudden changes in either its topology or parameters.

The reasons causing transient processes can be various: short circuits in a section, various switchings, like that of powerful consumers, etc. All these phenomena can be viewed as faults and disturbances appearing in system operation and are subjected to detection and classification. The failure should not only be identified, but also located as well as disturbance influence evaluated. Hence the question whether the existing methods of fault detection and diagnose in electric devices machines in particular [ 2] are applicable in this case as well. The present study deals with fault detection and diagnose by means of models. This method establishes actual state of devices by comparing real basic parameter values to corresponding computational model ones. An energy system is a complex structure and its wholesome model creation is a complex task on its own. On the other hand, contemporary devices exist [3], capable of recording (DFR) and analyzing transient processes. This allows in the event of fault, its type and location to be identified, with suitable protection and its actuation inclusive. Diagnostic reliability depends therefore, on the accuracy of transient process simulation in model.

The aim of this work is to present a method for automated fault and/or disturbance detection and classification in an independent electric energy system of limited power and simplified structure.

## Algorithms

Fig.1 shows a Among the most important units in the system are the following: system model elements used; protection equipment (circuit breakers, relays) transient processes simulation and analysis tools.

These processes can be recorded using different recorders [3]. In this case, the use of a digital fault

recorder is considered, with transient processes digitally filed, whereupon they will be further processed and compared to the basic simulation data parameters.

The methods used for data processing are: modern digital signal processing, expert systems, fuzzy logic, neural networks) Analysis results can be used for:

- Equipment operation assessment;
- Real device and model device testing;
- Model system elements check up, single events and system operation testing;
- Protection relays choice parameter tests and evaluation in real fault events.

## Experimental Results

A ship electric energy system supplied by 3 diesel generators of 630 kVA each,  $U = 400V$ ,  $f = 50$  Hz was used for the aims of the present study. The transient processes were simulated using MATLAB.

The model studied is diagrammatically presented in Fig. 2 Transient processes occurring in a short circuit fault section located near the main switchboard and consecutive disturbances of grid voltage following a powerful induction motor connection were studied.

Two possible arrangements were studied: with one generator operating single, and with two generators operating in parallel. Notwithstanding the causes generating the short circuit, these faults are always related to voltage and current variations in the system. These

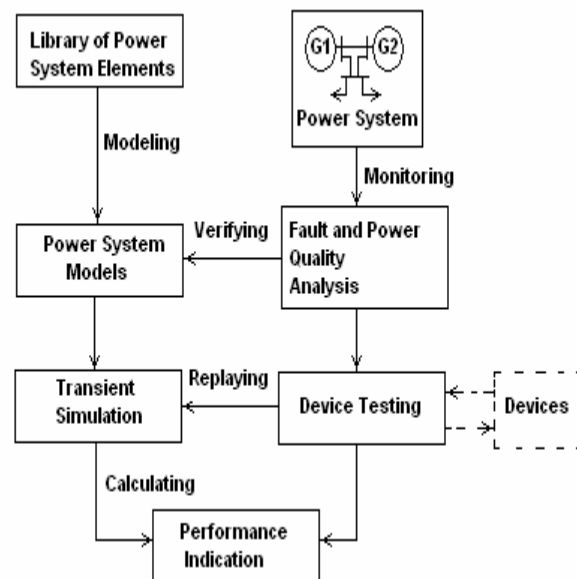


Fig.1. Block Diagram of the Fault Identification System

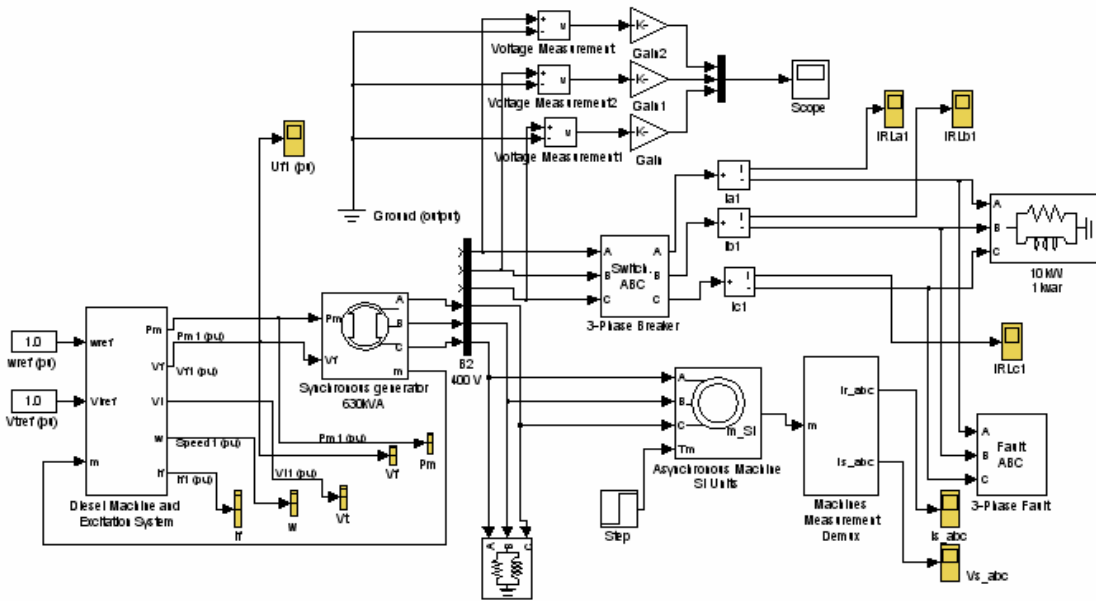


Fig.2. The Simulation Model of Autonomous Energy Systems

value variations can be analyzed and the results obtained can be used in fault detection, its location and identification. Fig.3 illustrates the short circuit oscillogram of a single operating synchronous generator and Fig. 4- Transient voltage drop. Fig. 5 - shows voltage grid disturbances due to Induction motor (rated

350kW) starting. The excessive voltage drop necessitates the input of another synchronous generator of the same rating. The voltage changes in result are illustrated in Fig.6 . The values above can be directly digitally filed for future reference and comparison with the corresponding DFR recorded values. During the transient process (100ms) current peak value is 14.kA, while grid voltage change in above cases is 20 % and 10 % respectively.

Figs. 7 and 8 shows transient process development in the system with two synchronous generators operating in parallel and an incoming induction generator with a resulting short circuit fault due to the new consumer entering the system. The short circuit tripping is within the 50 ms time limits.

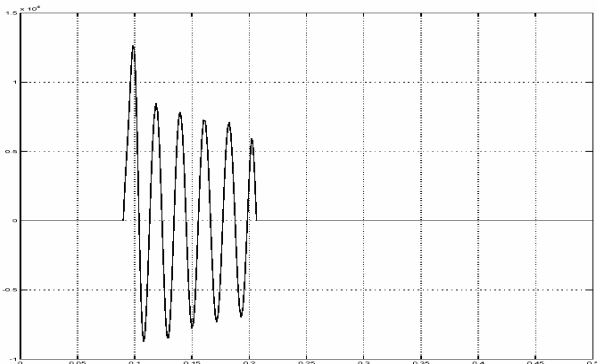


Fig.3 Short circuit current

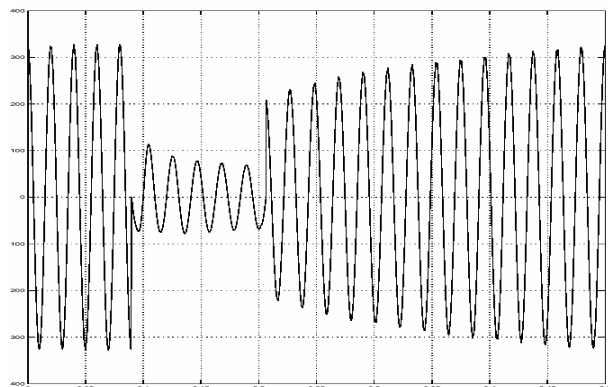


Fig.4. Transient voltage drop

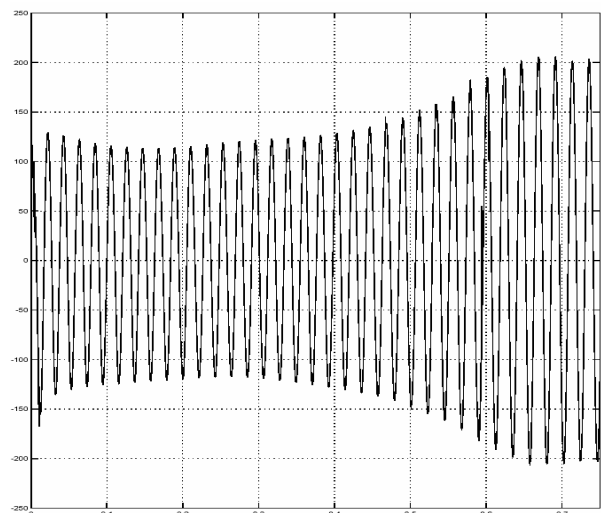


Fig.5.Voltage sag with one Generator

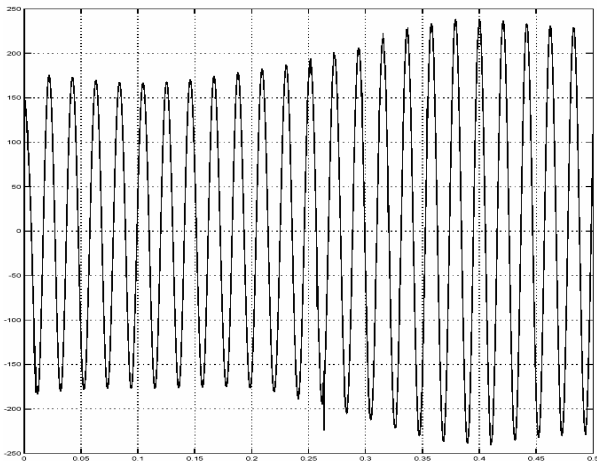


Fig.6.Voltage sag with two Generators

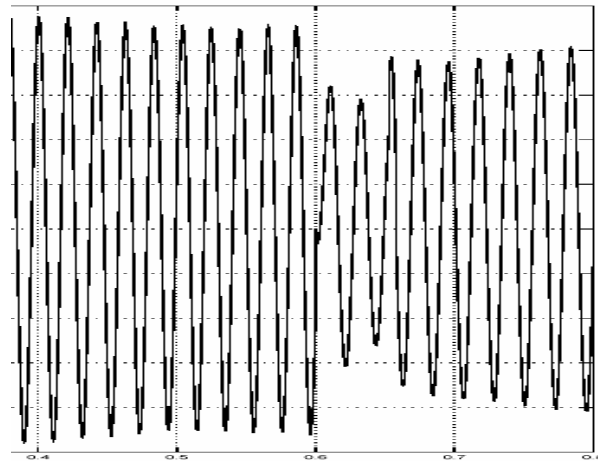


Fig.7.Switching transient disturbance

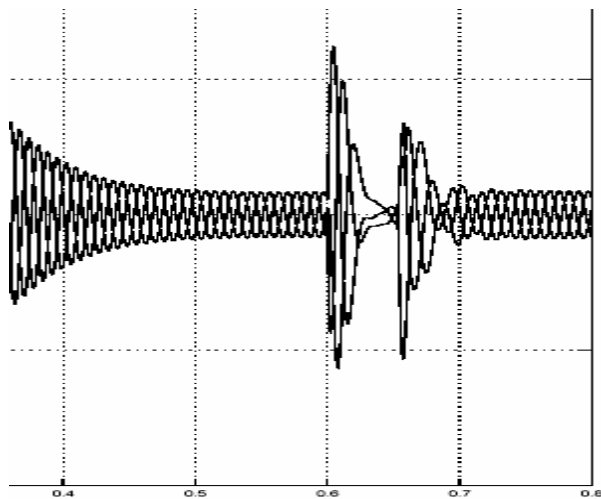


Fig.8.Induction Motor Stator Current

## Conclusion

Transient processes are still manually analyzed, which requires expertise and experience. The method offered eliminates human touch and transient processes can be automatically analyzed with greater efficiency. The cases studied use a basic and simplified ship electric power station. However, the obtained results show that this

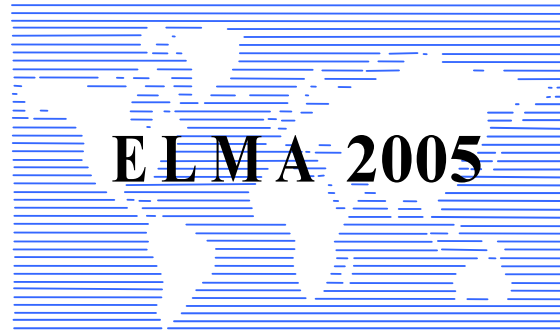
model is applicable with complex systems as well. This method will undoubtedly simplify problem assessment and assist protective equipment timely adjustment and system maintenance and servicing.

## References

- [1] [1].M.Kezunovic et al. "Design, implementation and validation of a real-time digital simulator for protection relay testing" IEEE Transaction on Power Delivery,vol.11,April 1996,pp.158-164.
- [2] [2]. Benbouzid M.H,Kliman G."What stator current processing -based technique to use?" IEEE Trans on Energy Conversion,vol.18, № 2,June 2003,p.238 A
- [3] [3].UTILITY SYSTEMS INC.-"Model 2002 Digital Fault Recorder sequence of event Recorder and Disturbance Recorder"-Users Guide.

**Lyubomir Dimitrov** – Assoc.Professor, Dr., Faculty of Electrical Engineering, Technical University of Varna Studentska Str1 ., 9000 Varna BULGARIA.  
e-mail: [lubo.dimitrov@mail.bg](mailto:lubo.dimitrov@mail.bg).

**Stefka Kanturska**-Dr.Ing  
Varna  
e-mail: [sgkanturska@abv.bg](mailto:sgkanturska@abv.bg)



---

---

**ELECTRONICS**

---

---



# Development of micro heat spreaders integrated in 3-dimensional stacked electronic packages

Nataliya Popova, Christian Schaeffer, Claude Sarno, Serge Parbaud, Georges Kapelski

**Abstract:** The continuing demand for smaller and lighter electronic devices requires minimum size, volume and weight. Today the concept of stacking up packages seems to be gaining popularity as an alternative for the electronic packaging. The 3-dimensional (3D) assembly methods bring along several challenges in the assembly process. The encapsulation approaches authorize broad applications thanks to more flexible vertical interconnections between the layers. The goal of this work is to develop and validate a design of a multilayer 3D package, able to dissipate 50 W, and to integrate heat exchangers (heat pipes) in each layer in order to evacuate the required total power. The potential applications are envisioned in avionics, space and radar sectors.

**Keywords:** Thermal management, heat pipes, 3D packaging

## Introduction

The concept of three-dimensional electronics (3D) is very attractive for the packaging technologies, in particular for high-performance and high-density packages. The XY plane contains most circuitry and the Z plane has the routing. Surface mounting technology allows more space for the routing and possibilities to preserve the high-density circuitry. The 3D packages, obtained by stacking of electronic substrates, ensure better performances of all the system. The main constraint generated by these developments is the thermal management of the entire module. An adequate cooling technique has to be added. We proposed to use integrated passive cooling systems (micro heat pipes) to cool the stacked substrates and to transfer the heat to an external cold source.

## Methodology

### A. Spécifications du système

The studied system, part of the European project Microcooling, is a 3D module developed from the stacking of three electronic layers. Figure 1 depicts a sketch of such structure. The module contains a metallic frame, a clamping system (to apply compressive efforts

on the interconnection systems), a metallic casing and electronic layers. Two sides of each layer are used as heat spreaders, the other two sides being reserved for the interconnection systems between the layers (Figure 2) and from the casing to the supporting PCB (printed circuit board). The stacked assembly must be able to dissipate 50 W. The dimensions of the total package are 55 x 55 x 12 mm<sup>3</sup>.

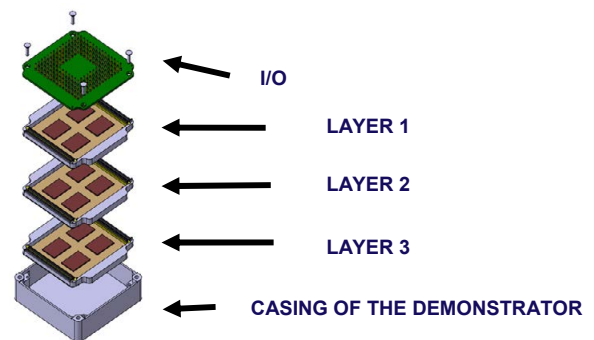


Figure 1: Three layered stacked module

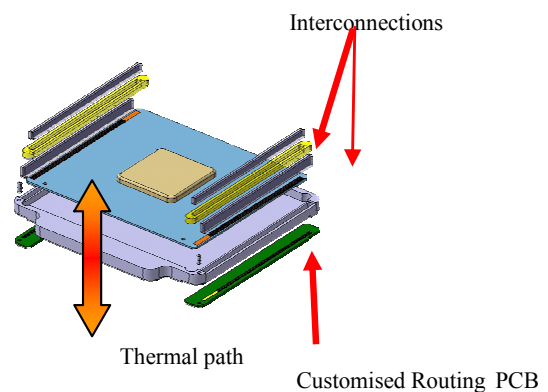


Figure 2: Interconnections representation between the layers

### B. Results and works in progress

A first thermal study, based on simulations and validated experimentally was undertaken. The objective of this work was to study the influence and the relative

contributions of the thermal resistances on the thermal performances of the module. Experimentally we have tested two prototypes with different sources of heat dissipation - one aluminium mock-up and one copper mock-up (Figure 3).

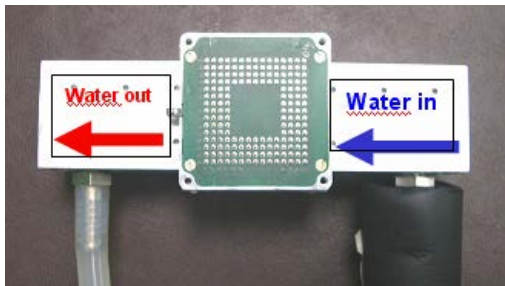


Figure 3: Test bench

The objective of the testing of the both prototypes was to measure various points of temperature of the architecture, to be able to evaluate the thermal contact and substrate resistances, the convective exchanges and with these data to model the thermal behaviour of the module. The first results showed that the contact thermal resistances affect significantly the thermal response of the stacked 3D module. Several layers of additional interfaces (thermal dissipative materials, silicone thermal grease) were used to improve the thermal behaviour of the prototypes and to reduce the contact thermal resistances. We have found experimentally using various thermocouples the values of the thermal contact resistances between the different interfaces.

We have modelled the 3D module with the software Flotherm specialized for thermal simulations. The studied package is presented on Figure 4. Each layer contains 6 components.

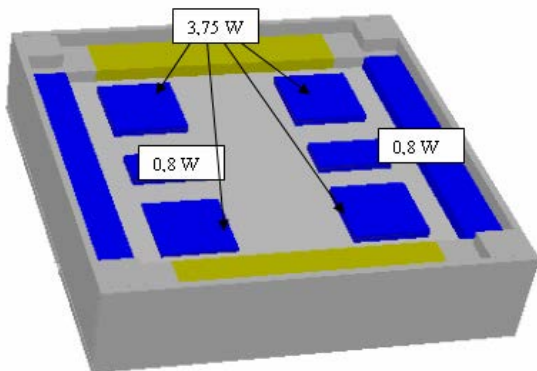
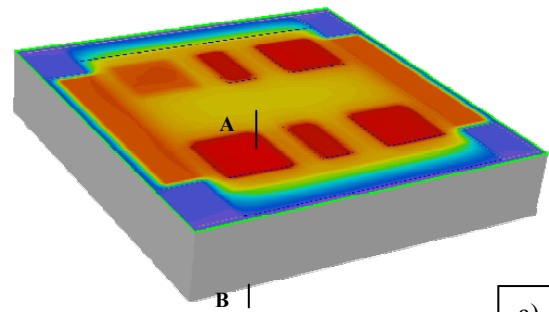


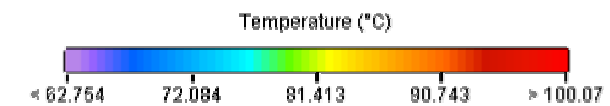
Figure 4: Design of the simulated 3D modular package

At the lower face of the module we apply a convective exchange coefficient equal to  $400 \text{ W/m}^2\text{K}$  which corresponds to forced water cold source (values taken from the experimental bench). The power input is of 50 W for the whole module (17 W per layer).

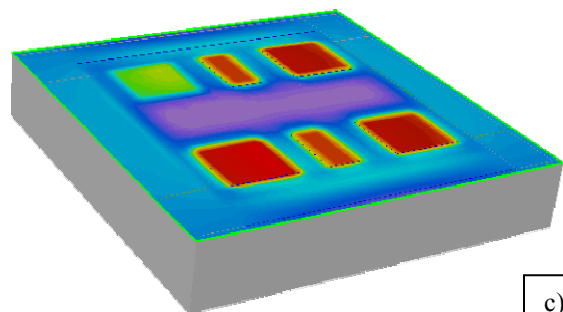
On the Figure 5 we present the temperature distribution inside the studied module. We have modelled the system at the beginning without taking into account the contact thermal resistances. We have considered that the thermal interfaces were perfect – Figure 5a). We made a section along the height of the electronic package to observe the temperature profile through all the layers Figure 5b). For the next simulations we have added the values of the thermal contact resistances measured experimentally between all the interfaces – Figures 5c) and 5d).



a).



b).



c).

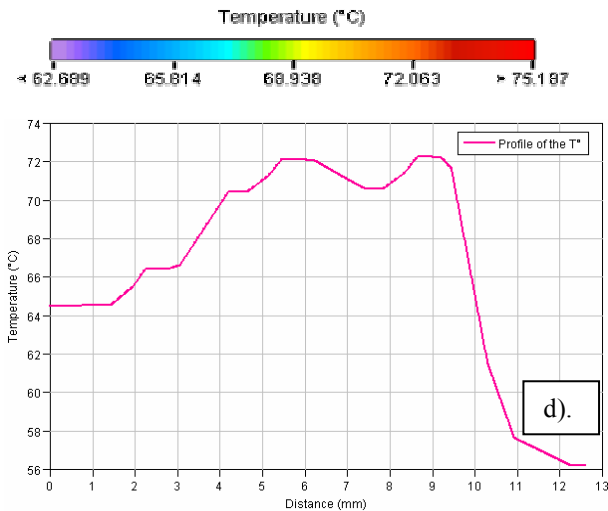


Figure 5: a). Temperature distribution inside the module - perfect interactions between the interfaces b). Temperature profile (without contact resistances) c). Temperature distribution inside the module – real thermal interactions between the interfaces d). Temperature profile (with contact resistances)

For the same injected power we have more than 20 °C of temperature difference when the thermal contact resistances are taken into account. The test and simulation results showed that the interlayer thermal interactions affect significantly the thermal behaviour of the system.

We proposed a better adapted configuration which can allow removing some of the contact resistances and in the same time to improve the effective thermal conductivity of the substrate (by integrating micro heat pipes). It consists to combine two electronic layers and to make only one of them (Figure 6). It will allow us also to have double thickness substrate where it will be easier to integrate a micro heat pipe. The principle of the heat pipes is presented on Figure 7. The heat pipes are heat exchangers allowing the passive circulation of the coolant thanks to a phase shift and capillary wick. They consist of an evacuated hermetically sealed enclosure with three distinct regions: an evaporator, a condenser, and an adiabatic region separating these two regions. The heat is transported from one place to another without using of pump or another mechanical device in both radial and axial directions. [1] [2] [3]

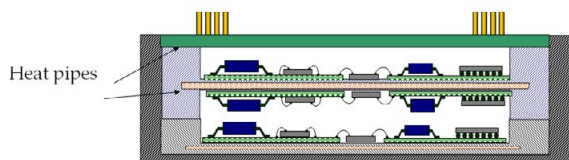


Figure 6: Alternative configuration

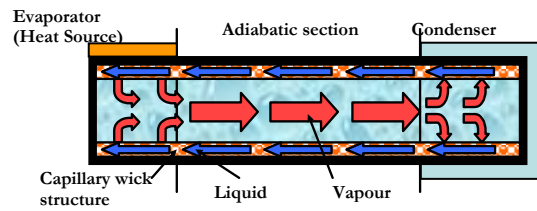


Figure 7: Heat pipe principle

Thermal simulations were undertaken to validate the benefit of the alternative configuration. They showed that the total thermal resistance could be decreased with about 34 % using the double sided configuration with integrated heat pipes against passive aluminium substrates.

#### D. Experimental part

A first prototype (double sided H-structure with integrated  $\mu$ heat pipe) was manufactured to study the principle heat pipe and to validate the simulations results. The realization of a prototype includes several stages:

- Manufacturing of the frame of the heat pipe;
- Deposition of the wick structure (in our case – sintered copper powder);
- Oxidation of the wick;
- Assembling;
- Making vacuum inside the prototype;
- Injecting of a precise quantity of working fluid;
- Testing;

The studied prototype consists of two copper parts which form the whole frame of the prototype. The wick structure, which is the driving force of the heat pipe, consists of a copper sintered powder with diameter of 80 - 100  $\mu$ m. Three layers of copper spheres were sintered under 1000 °C on the interior walls of the prototype (Figure 8). The porosity of the used copper powder is about 35 %. It enables large capillary pumping pressure but large pressure drops can occur in the liquid-flow passage.

The wetting of the copper is not very good, so in order to improve it and to increase the damping of the fluid on the spheres, the wick structure was oxidized (Figure 9). The prototype was being degreased under rather severe conditions and afterwards a thin layer of CuO was deposited (2-3  $\mu$ m).



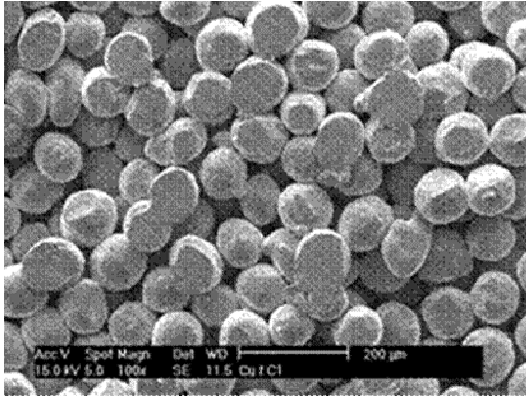


Figure 8: Copper spheres after sintering

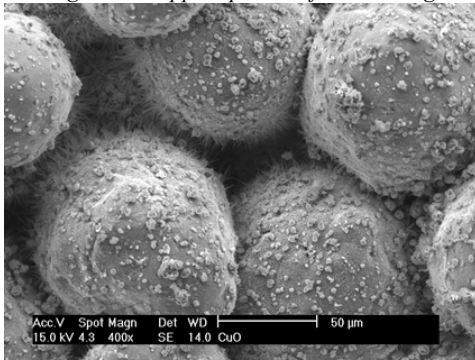


Figure 9: Oxidized sintered copper powder

Once the prototype was oxidized, it was hermetically assembled. The next stages to be made before testing the prototype were to make vacuum inside the heat pipe (vacuum pump) and to inject into it a precise quantity of the purest possible water. The water was chosen as a working fluid because it is appropriate when the working temperatures are between 30 and 100 °C and it is compatible with the copper. [4] [5] [6]

The experimental setup is represented below (Figure 10). Heat source consists of a thermal silicone resistance glued on the substrate. Different powers were applied to study the variation of the thermal resistances. A thermocouple was fixed into a groove under the heat source to show the temperature of the chip without taking into account the thermal contact resistance of the glue. The prototype is cooled by a cold plate with forced circulation of water at a given temperature. [7]

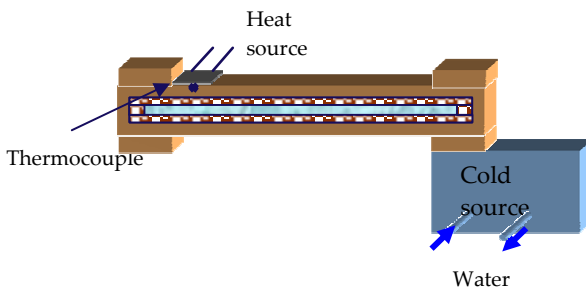


Figure 10: Experimental setup

A first test was the study of an empty heat pipe. In this case the heat transfer between the heat source and the cold source consists of only conduction through the prototype's walls. Infrared thermal images give the temperature distribution on the heat pipe. An equivalent thermal resistance was calculated for this first test equal to 1,65 °C/W.

The same test was made with a copper substrate with the same dimensions. It allows comparing later the plane copper substrate and the functioning heat pipe. The thermal resistance in this case is 0,95 °C.

Then the same test was made with the heat pipe filled with 500 μl of pure water. The temperature decreases with about 15 °C for the same injected power. The temperature distribution from the heat source to the cold source for the both cases (functioning heat pipe and copper) is presented on Figure 11.

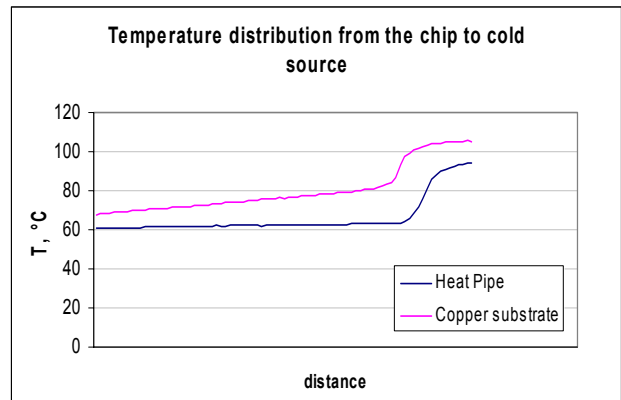


Figure 11: Comparison between a plane copper substrate and a functioning heat pipe for the same injected power (15 W)

The first results were encouraging and new prototypes are currently developed. Our objective is to study the wick structure influence on the effective work of the heat pipes, keeping the same external dimensions. The new prototypes are conceived with slightly different dimensions of the capillary wick structure, with different diameters of the copper spheres and with different oxidation processes.

New tests are envisaged which will take into account the angle of inclination of the heat pipes, in the objective to study their operation against gravity, as well as the different positions of the heat sources on the prototypes.

## Conclusions

First results of experimental and modelling studies of stacked 3D module with integrated micro heat pipe were presented. A copper heat pipe with sintered powder wick structure was tested and compared with plane copper substrate. The experimentations showed an improvement of the thermal performance of the system using heat pipe

against simple metallic substrates. This first work proves the interest of using heat pipes in the domain of power electronics.

## Acknowledgements

The authors would like to thank Bruno Mallet for his help and support in making this work possible. His participation and ideas in the elaboration of the test setup were much appreciated.

## References

- [1] Faghri Amir – “Heat pipe science and technology”, 1995.
- [2] Chi S.W. – “Heat Pipe Theory and Practice”, 1976.
- [3] Dunn P.D., Reay D.A. – “Heat Pipes”, 1994.
- [4] Alexander E.G.Jr. – “Structure property relationships in heat pipe wicking materials”, 1972.
- [5] Avenas Yvan – “Etude et realisation de caloducs plats miniatures pour l’intégration en électronique de puissance”, 2002.
- [6] M. Ivanova, Y. Avenas, O. Karim, G. Kapelski, C. Schaeffer, “Application of sintered metal powder in power electronics cooling”, 8<sup>th</sup> THERMINIC Workshop, 1-4 October 2002, Madrid.
- [7] Y. Avenas, M. Ivanova, N. Popova, C. Schaeffer, “Thermal analysis of thermal spreaders used in power electronics cooling”.

---

**Nataliya Popova** – Ph D student, Laboratoire d'Electrotechnique de Grenoble, ENSIEG, Institut National Polytechnique de Grenoble – BP46 – 38402 SMH Cedex, France

e-mail: nataliya.popova@leg.ensieg.inpg.fr

**Christian Schaeffer** – Professor, Laboratoire d'Electrotechnique de Grenoble, ENSIEG Institut National Polytechnique de Grenoble – BP46 – 38402 SMH Cedex, France

**Claude Sarno** – Project coordinator, Thales Avionics 25, Rue Jules Védrières 26027 VALENCE CEDEX – France

**Serge Parbaud** – Packaging ingenier, Thales Avionics 25, Rue Jules Védrières 26027 VALENCE CEDEX – France

**Georges Kapelski** – Professor, Laboratoire de Génie Physique et Mécanique des Matériaux INPG, ENSPG, BP 46 38402 SMH France

# Modelling and analysis of three-phase boost rectifier bidirectional converters in open loop

Jenica Ileana CORCĂU\*

**Abstract:** In this paper is presents modelling and analysis of three-phase boost rectifier bidirectional converters switch based PWM converters, which include three-phase ac/dc boost rectifiers and a dc/ac voltage source inverters. Both boost rectifier and voltage source inverter are usually classified as bidirectional current converter s because they share the same switching cells that are current bidirectional. In this paper the small-signal models of the three-phase boost rectifier bidirectional converters are developed. In this paper, the average large-signal model and the small-signal models of three-phase bidirectional current converter s are developed. The average model for a three-phase bidirectional current converter is based on phase-to-phase (or line-to-line) averaging, which intentionally neglects common-mode components. After the phase-leg averaging, the average model of a three-phase bidirectional current converter can be easily obtained by connecting three averaged phases' legs. The plots of the transfer functions were obtained using software Matlab/Simulink.

## 1. Three-phase boost rectifier modelling

The boost rectifier provides three-phase-to-dc power conversion from the synchronous generator to the dc distribution bus. The rectifier operates with unity power factor and draws sinusoidal current from the three-phase source. When the output current reverses its direction the boost rectifier reverses the power flow through it and operates as a voltage source inverter.

Both boost rectifier and voltage source inverter are classified as bidirectional current converters because they share the same switching cells that are current bidirectional. The switching cells either inherent have anti-parallel diodes, for example, MOSFETs and IGBTs, or have external anti-parallel diodes, for example, GTOs with anti-parallel diodes.

The symbolic representation and its voltage and current operational states are shown in figure 1 [3].

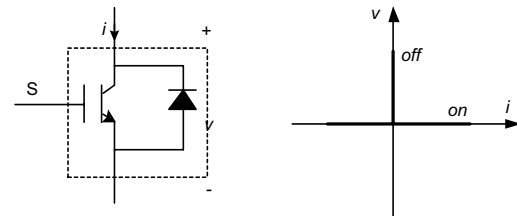


Figure 1. a. Symbolic representation; b. Voltage and current operational states

A three-phase boost rectifier is shown in figure 2. To simplify the discussions, the load for rectifier is resistive.

In this paper, the average large-signal model and the small-signal models of three-phase bidirectional current converters are developed.

The average model for a three-phase bidirectional current converter is based on phase-to-phase (or line-to-line) averaging, which intentionally neglects common-mode components. After the phase-leg averaging, the average model of a three-phase bidirectional current converter can be easily obtained by connecting three averaged phases' legs.

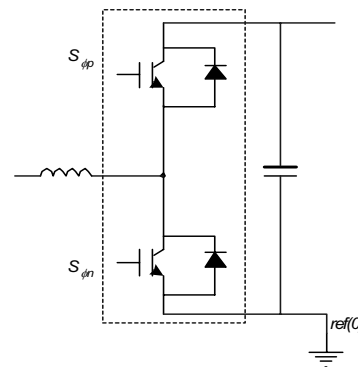


Fig.3. Generic phase leg in bidirectional current converter s

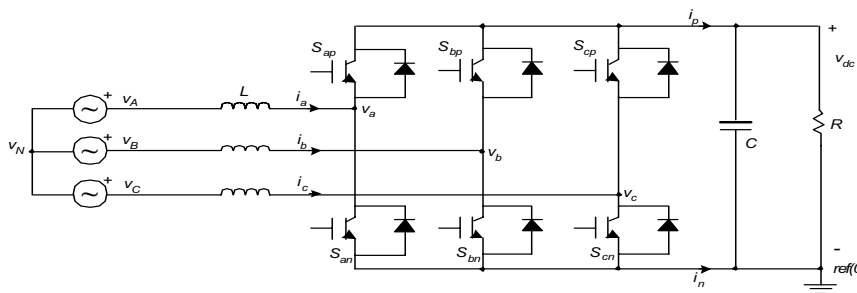


Figure 2. Three-phase boost rectifier

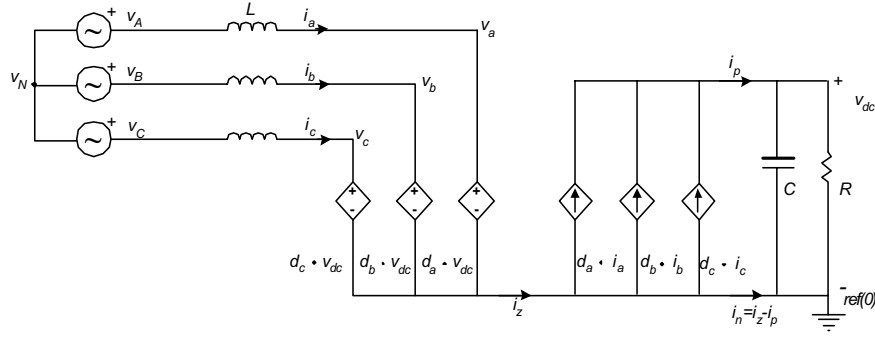


Figure 4. Average model of the boost rectifier

In the current-bidirectional switch based converters, a generic switching unit, called a phase leg, is presented in figure 3. The phase leg is composed of two switching cells, and has a voltage source (or a capacitor) on one side and a current source (or an inductor) on the other. These features make the phase leg a generic switching unit.

## 2. Average model of a boost rectifier

After averaging the phase leg, the average model of a three-phase boost rectifier can be readily obtained by connecting three averaged phase legs, as shown figure 4.

The state-space equations of the boost rectifier are [2]:

$$(1) \quad \frac{d}{dt} \begin{bmatrix} i_a \\ i_b \\ i_c \end{bmatrix} = \frac{1}{L} \begin{bmatrix} v_{AN} \\ v_{BN} \\ v_{CN} \end{bmatrix} + \frac{1}{L} \begin{bmatrix} v_N \\ v_N \\ v_N \end{bmatrix} - \frac{1}{L} \begin{bmatrix} d_a \\ d_b \\ d_c \end{bmatrix} \cdot v_{dc}$$

where  $i_a$ ,  $i_b$ ,  $i_c$  the phase currents,  $d_a$ ,  $d_b$ ,  $d_c$  duty cycle of the switch,  $v_{AN}$ ,  $v_{BN}$  and  $v_{CN}$  which are normally given, for example:

$$(2) \quad \begin{bmatrix} v_{AN} \\ v_{BN} \\ v_{CN} \end{bmatrix} = \begin{bmatrix} v_m \cdot \cos(\omega t) \\ v_m \cdot \cos(\omega t - 2\pi/3) \\ v_m \cdot \cos(\omega t + 2\pi/3) \end{bmatrix},$$

$$(4) \quad \frac{dv_{dc}}{dt} = \frac{1}{C} [d_a \quad d_b \quad d_c] \cdot \begin{bmatrix} i_a \\ i_b \\ i_c \end{bmatrix} - \frac{v_{dc}}{R \cdot C},$$

In order to obtain a dc steady-state operating point so, as to linearize the system to design controllers, the model in the stationary coordinates is usually transformed into rotating coordinates.

The transformation matrix is

$$(3) \quad T_1 = \sqrt{\frac{3}{2}} \cdot \begin{bmatrix} \cos(\omega t) & \cos(\omega t - 2\pi/3) & \cos(\omega t + 2\pi/3) \\ \sin(\omega t) & \sin(\omega t - 2\pi/3) & \sin(\omega t + 2\pi/3) \\ 1/\sqrt{2} & 1/\sqrt{2} & 1/\sqrt{2} \end{bmatrix}$$

where  $\omega$  is chosen as same frequency as the ac line frequency in (3).

The variables in the stationary coordinates  $X_{abc}$  can be transformed into the rotating coordinates  $X_{dqz}$  using

$$(5) \quad \frac{d}{dt} \begin{bmatrix} i_d \\ i_q \\ i_z \end{bmatrix} = \frac{1}{L} \begin{bmatrix} v_d \\ v_q \\ v_z \end{bmatrix} + \frac{1}{L} \begin{bmatrix} 0 \\ 0 \\ 3 \cdot v_N \end{bmatrix} - \begin{bmatrix} 0 & -\omega & 0 \\ \omega & 0 & 0 \\ 0 & 0 & 0 \end{bmatrix} \cdot \begin{bmatrix} i_d \\ i_q \\ i_z \end{bmatrix} - \frac{1}{L} \begin{bmatrix} d_d \\ d_q \\ d_z \end{bmatrix} \cdot v_{dc}$$

where

$$(6) \quad \begin{bmatrix} i_d \\ i_q \\ i_z/\sqrt{3} \end{bmatrix} = T_1 \cdot \begin{bmatrix} i_a \\ i_b \\ i_c \end{bmatrix},$$

$$(7) \quad \begin{bmatrix} v_d \\ v_q \\ v_z/\sqrt{3} \end{bmatrix} = T_1 \cdot \begin{bmatrix} v_{AN} \\ v_{BN} \\ v_{CN} \end{bmatrix},$$

$$(8) \quad X_{dqz} = T_1 \cdot X_{abc}.$$

Applying (5) to (1) and (2), can be obtain the average model of a boost rectifier in the rotating coordinates:

$$(9) \quad \frac{dv_{dc}}{dt} = \frac{1}{C} [d_d \quad d_q \quad d_z] \cdot \begin{bmatrix} i_d \\ i_q \\ i_z \end{bmatrix} - \frac{v_{dc}}{R \cdot C}$$

$$(10) \quad \begin{bmatrix} d_d \\ d_q \\ d_z/\sqrt{3} \end{bmatrix} = T_1 \cdot \begin{bmatrix} d_a \\ d_b \\ d_c \end{bmatrix}$$

Because

$$v_z = v_{AN} + v_{BN} + v_{CN}, d_z = d_a + d_b + d_c,$$

$$i_z = i_a + i_b + i_c = i_p + i_n, i_z \equiv 0$$

for the single converter operation, the z channel equations dropped from the model.

The average model of the boost rectifier in the state-space becomes

$$(11) \quad \frac{d}{dt} \begin{bmatrix} i_d \\ i_q \end{bmatrix} = \frac{1}{L} \begin{bmatrix} v_d \\ v_q \end{bmatrix} + \frac{1}{L} \begin{bmatrix} 0 & -\omega \\ \omega & 0 \end{bmatrix} \cdot \begin{bmatrix} i_d \\ i_q \end{bmatrix} - \frac{1}{L} \begin{bmatrix} d_d \\ d_q \end{bmatrix} \cdot v_{dc}$$

The average model of the boost rectifier in dq coordinates is presents in figure 5.

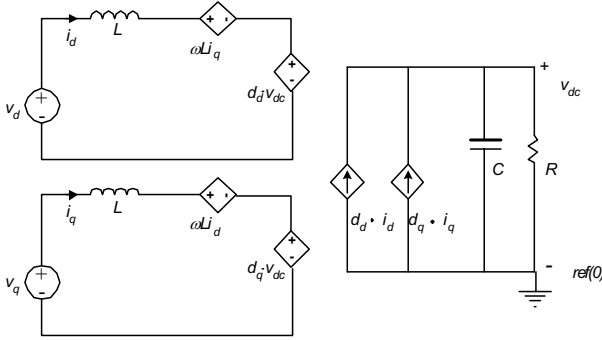


Fig.5. Average model of the boost rectifier in coordinates dq

### 3. Small-signal model of the boost rectifier.

Transfer functions of boost rectifier

To obtain the small-signal model of the three-phase boost rectifier, a steady state operating point is obtained first:

$$(12) \quad \begin{cases} i_d = \frac{v_{dc}}{R \cdot D_d} \\ i_q = 0 \\ D_d = \frac{v_d}{v_{dc}} \\ D_q = \frac{-\omega \cdot L \cdot i_d}{v_{dc}} \end{cases}$$

$$(13) \quad \frac{dv_{dc}}{dt} = \frac{1}{C} [d_d \quad d_q] \cdot \begin{bmatrix} i_d \\ i_q \end{bmatrix} - \frac{v_{dc}}{R \cdot C}$$

where  $R, L$  and  $V_m$  (given as in (3)) are given,  $V_{dc}, I_q$  are controlled to their reference values.  $I_d, D_q, D_d$  are calculated based on the given values and the control objectives. The reference signal for the q channel is set to zero since the input currents should be in phase with the input voltages.

Assuming that the input voltage source are ideal, then

$$(14) \quad \tilde{v}_d = \tilde{v}_q = 0$$

The small-signal model of boost rectifier is

$$(15) \quad \frac{d}{dt} \begin{bmatrix} \tilde{v}_{dc} \\ \tilde{i}_d \\ \tilde{i}_q \end{bmatrix} = \begin{bmatrix} -1/RC & D_d/C & D_q/C \\ -D_d/L & 0 & \omega \\ -D_q/L & -\omega & 0 \end{bmatrix} \cdot \begin{bmatrix} \tilde{v}_{dc} \\ \tilde{i}_d \\ \tilde{i}_q \end{bmatrix} + \begin{bmatrix} i_d/C & i_q/C \\ -v_d/C & 0 \\ 0 & -v_{dc}/L \end{bmatrix}$$

The parameters of boost rectifier are:  $V_m = 120\sqrt{2}$  V,  $\omega = 2\pi \cdot 400$  rad/sec,  $V_{dc} = 400$  V,  $P_0 = 15$  kW,  $R = V_{dc}^2 / P_0$ ,  $L = 200$   $\mu$ H,  $C = 100$   $\mu$ F.

The plots of the following transfer functions were obtained using software Matlab.

Figures 6 and 7 shows transfer functions of the open-loop controls to output currents.

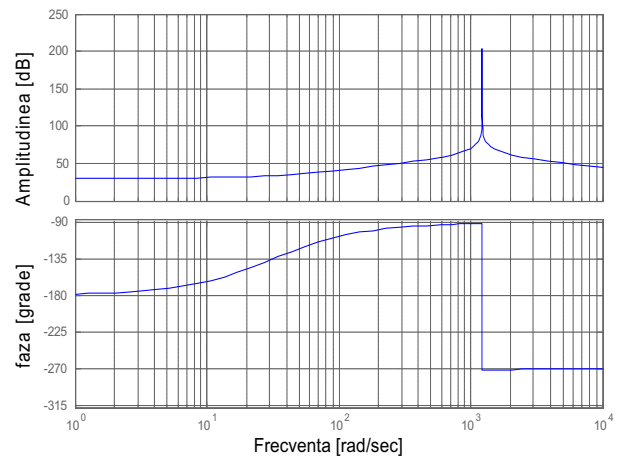


Fig.6. Bode diagram of function  $\frac{\tilde{i}_d}{\tilde{d}_d}$

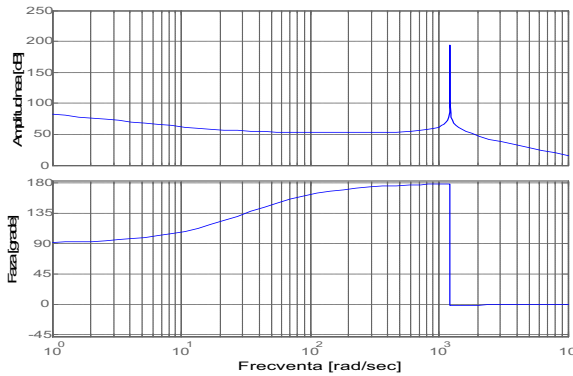


Fig.7. Bode diagram of function  $\tilde{i}_q/\tilde{d}_q$

Figure 8 and figure 9 shown that the z- channel is decoupled from d and q channels

Using software Matlab can be obtained transfer functions. The symbolic expressions for the transfer functions  $\tilde{i}_q/\tilde{d}_q$  have general form:

$$(16) \quad \frac{\tilde{i}_d}{\tilde{d}_d} = k \frac{(s/z+1)}{(s/p+1)(s/p^*+1)},$$

where \* denotes a complex conjugate.

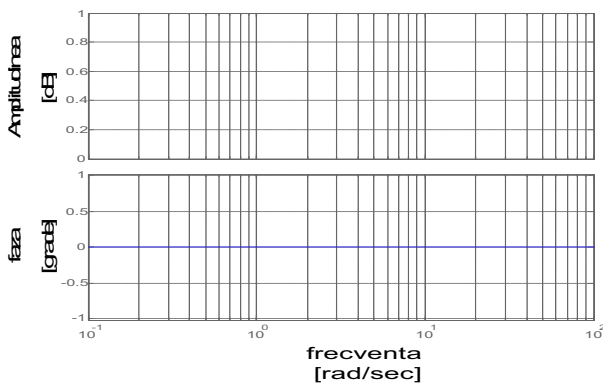


Fig.8. Bode diagram of function  $\frac{\tilde{i}_d}{\Delta_{dz}}$

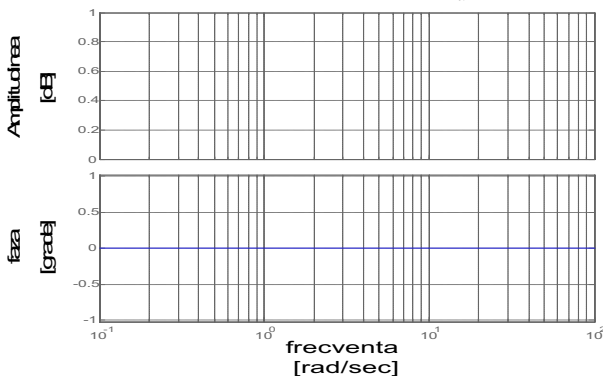


Fig.9. Bode diagram of function of  $\frac{\tilde{i}_q}{\Delta_{dz}}$

The resonant frequency of the double pole  $p_p$  and  $p_p^*$  is exactly the same as the rotating frequency in transformation (3). To design a compensator, one has to examine the open-loop control output transfer functions.

### Conclusions

This paper presents modelling and analysis of three-phase boost rectifier bidirectional converters using software Matlab/Simulink. The small-signal model of a three-phase boost rectifier is developed. The transfer functions of the open-loop controls to output currents are presented. To design a compensator, one has to examine the open-loop control-to-output transfer functions.

### References

- [1]. Corc au J. Three-phase synchronous generator modelling as subsystem of a PDS (Power Distribution System). 7th International Conference of Applied and Theoretical Electricity ICATE 2004, B ile Herculane, October 14-15, 2004, pag. 543-547.
- [2]. Lounganski K.P. Modeling and Analysis of power distribution system in 21st century air lifters. Thesis of Master of Science in Electrical Engineering, 1999.
- [3]. Zhihong Ye. Modeling and control of parallel three-phase PWM converters. Dissertation submitted to the Faculty of the Virginia Polytechnic Institute. September 15, 2000, Blacksburg, Virginia.

---

\* **Jenica Ileana CORC AU** - Assist. drd. eng., University of Craiova, Faculty of Electrotechnics, Avionics Division, Blv. Decebal, nr.5, Craiova, Dolj, [jcorcau@elth.ucv.ro](mailto:jcorcau@elth.ucv.ro)

## A Study About Power Transfer In Buck PWM AC Regulators

**Liliana Miron, Mihai Miron, Ioan Matlac and Cristian Constantinescu**

**Abstract:** This paper is focused on predicting the power transfer in Buck PWM AC regulators. The commutation process is studied and the article presents a method to establish the mathematical model of the power transfer. The circuit simulation and results prediction were carried out using specific computational tools such Mathcad. It is wanted that  $\eta$ , is the ratio between apparent voltamps of load and supplying source, will become an unity ratio.

**Keywords:** buck pwm ac-ac regulator, steady-state values, power transfer

### Introduction

AC regulators (AC-AC converters) are used to obtain variable ac voltage from a fixed ac source. Thyristor power controllers are commonly used in industrial practice. Thyristor phase control has major disadvantages like: generation of high harmonics in the source current, generation of sub harmonics at integral control and a displacement power at phase angle. One methods to eliminate these unfavorable properties are a PWM or APWM AC line power control. The power circuit [1] of PWM Buck regulator is shown in fig.1.

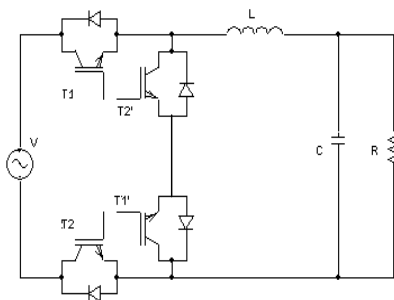


Fig.1. PWM Buck regulator.

### Control modes of load current and voltage

When control signal is applied to the AC converter switches, a PWM output voltage appears. To determine the power transfer in AC-AC converters we use the Mathcad functions for a number of harmonics that rehabilitate the load and source waveforms. The power regulation can be made with phase angle control for one constant duty factor [2], fig. 2.

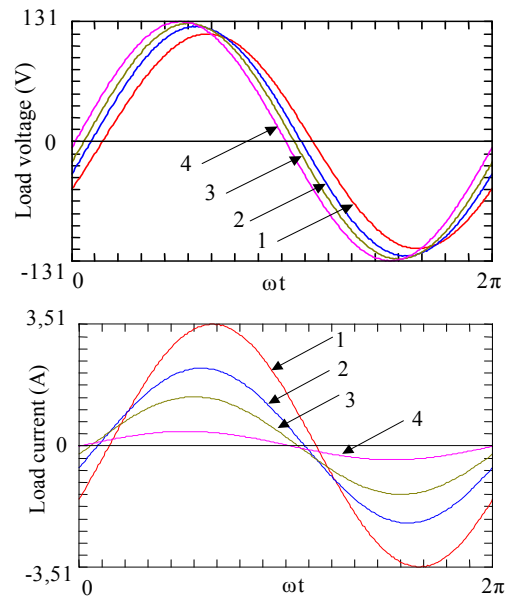


Fig. 2. The load waveforms for duty factor  $\Gamma=0.4$  and different phase angles:  
1)  $\Phi = 6^\circ$ ; 2)  $\Phi = 10^\circ$ ; 3)  $\Phi = 16^\circ$ ; 4)  $\Phi = 40^\circ$ .

Besides, the load power can be control with duty factor variation for constant phase angle, fig.3.

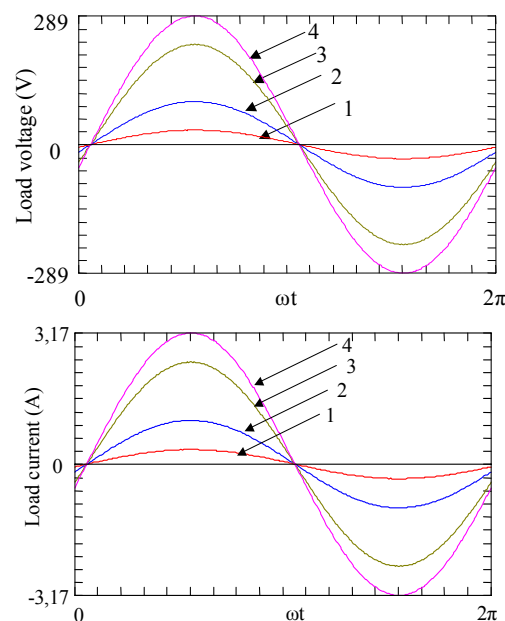


Fig. 2. The load waveforms for duty factor  $\Phi = 16^\circ$  and different phase angles:  
1)  $\Gamma = 0.1$ ; 2)  $\Gamma = 0.3$ ; 3)  $\Gamma = 0.7$ ; 4)  $\Gamma = 0.9$ .

For load it is necessary sinusoidal waveforms. To obtain sinusoidal load current waveforms it assumed 50 pulses in one half period. The switching frequency is 5kHz. This value performs the relationship between R, C from fig.1. and  $f_{switching}$ .

$$(1) \quad RC > \frac{1}{f_{switching}}$$

### Mathematical determination

Because the load current and the load voltage are not sinusoidal, to estimate the power transfer it's necessary to determine the load current and voltage Fourier coefficients for 100 harmonics. The steady state for power transfer and the Fourier coefficients are studied. The *MathCad* functions for wave forms and power transfer is made with a data base of phase angles and duty factor values.

Data base contains: L=0.05H; C=10<sup>-5</sup>F and

$$\Phi = \begin{pmatrix} 6 \\ 8 \\ 10 \\ 12 \\ 14 \\ 16 \\ 30 \\ 35 \end{pmatrix} \text{deg} \quad \Gamma = \begin{pmatrix} 0,1 \\ 0,2 \\ 0,3 \\ 0,4 \\ 0,5 \\ 0,6 \\ 0,7 \\ 0,8 \\ 0,9 \end{pmatrix}$$

The load resistance values are calculated with

$$(2) \quad R = \frac{tg\Phi}{\omega C}$$

Fourier coefficients are:

$$(3) \quad u(t) = U_0 + \sum_1^{\infty} U_k \cos(k\omega t + \varphi_{uk})$$

$$(4) \quad i(t) = I_0 + \sum_1^{\infty} I_k \cos(k\omega t + \varphi_{ik})$$

$$(5) \quad U_{ef} = \sum_{NrArm} U_k^2$$

$$(6) \quad I_{ef} = \sum_{NrArm} I_k^2$$

$$(7) \quad \begin{cases} U_k = \sqrt{S_{uk}^2 + C_{uk}^2} \\ \varphi_{uk} = -arctg \frac{S_{uk}}{C_{uk}} \end{cases}$$

$$(8) \quad \begin{cases} I_k = \sqrt{S_{ik}^2 + C_{ik}^2} \\ \varphi_{ik} = -arctg \frac{S_{ik}}{C_{ik}} \end{cases}$$

MathCad relationship for Fourier coefficients are[3]:

$$C := \left[ \sum_{k=0}^{last(Uc)-1} 2f \left[ \frac{U_{c,k+1}}{\omega} \int_{U_{c,k}}^{U_{c,k+1}} fct1 \cdot \cos(n \cdot \omega t) \cdot (1 - \text{mod}(k,2)) dt + \frac{U_{c,k}}{\omega} \int_{U_{c,k}}^{U_{c,k+1}} fct2 \cdot \cos(n \cdot \omega t) \cdot \text{mod}(k,2) dt \right] \right] \text{ if } n > 0$$

$$S := \left[ \sum_{k=0}^{last(Uc)-1} f \left[ \frac{U_{c,k+1}}{\omega} \int_{U_{c,k}}^{U_{c,k+1}} fct1 \cdot (1 - \text{mod}(k,2)) dt + \frac{U_{c,k}}{\omega} \int_{U_{c,k}}^{U_{c,k+1}} fct2 \cdot \text{mod}(k,2) dt \right] \right] \text{ otherwise}$$

$$S := \left[ \sum_{k=0}^{last(Uc)-1} 2f \left[ \frac{U_{c,k+1}}{\omega} \int_{U_{c,k}}^{U_{c,k+1}} fct1 \cdot \sin(n \cdot \omega t) \cdot (1 - \text{mod}(k,2)) dt + \frac{U_{c,k}}{\omega} \int_{U_{c,k}}^{U_{c,k+1}} fct2 \cdot \sin(n \cdot \omega t) \cdot \text{mod}(k,2) dt \right] \right]$$

where "Uc" are the turn on and turn off angles values. Function "fct1" can be the load current expression, the source current or load and source voltage expressions in turn on time. Function "fct2" is the turn off expression of current and voltage of different electrical quantities.

The rehabilitated load wave forms, with (9), denotes the uprightness of Fourier coefficients calculus.

$$(9) \quad Sr = \sqrt{2} \sum_{k=1}^{lastM} M_k^i \sin(k\omega t + M_k^{i+1}) + M_0^i$$

where "M" is coefficients Fourier matrix and M<sub>0</sub> is continuous component:

Table 1

The coefficients Fourier matrix

	0	1	2	3	4	5	6	7	8	9	10	11	12
0	0	1.571	1.766·10 <sup>-6</sup>	1.571	0	1.571	0	1.571	-0.077	1.571	0	1.571	0
1	20.725	-0.459	0.619	-0.459	0.063	1.083	0.624	-0.358	39.033	0.041	0.175	-0.466	21.685
2	0	1.7	2.567·10 <sup>-6</sup>	1.7	0	-1.441	0	-1.441	0.112	-1.441	0.001	-1.441	0
3	0	1.701	2.567·10 <sup>-6</sup>	1.701	0	-1.441	0	-1.441	0.112	-1.441	0.001	-1.441	0
4	0	1.701	2.569·10 <sup>-6</sup>	1.701	0	-1.441	0	-1.441	0.112	-1.441	0.001	-1.441	0
5	0	1.7	2.57·10 <sup>-6</sup>	1.7	0	-1.441	0	-1.441	0.112	-1.441	0.001	-1.441	0
6	0	1.697	2.566·10 <sup>-6</sup>	1.697	0	-1.441	0	-1.441	0.112	-1.441	0.001	-1.441	0
7	0	1.701	2.57·10 <sup>-6</sup>	1.701	0	-1.441	0	-1.441	0.112	-1.441	0.001	-1.441	0
8	0	1.702	2.572·10 <sup>-6</sup>	1.702	0	-1.442	0	-1.442	0.112	-1.441	0.001	-1.441	0
9	0	1.7	2.568·10 <sup>-6</sup>	1.7	0	-1.441	0	-1.441	0.112	-1.441	0.001	-1.441	0

The matrix have submatrixes with :

- Column i = harmonics amplitudes corresponding to each signal;
- Column i+1 = phase angle corresponding to each signal;

It wants to achieve the power balance. It must calculate the active power, P, reactive power, Q, apparent power, S. Between these, relation (10) is verified.

$$(10) \quad D = \sqrt{S^2 - P^2 - Q^2}$$



Table 2

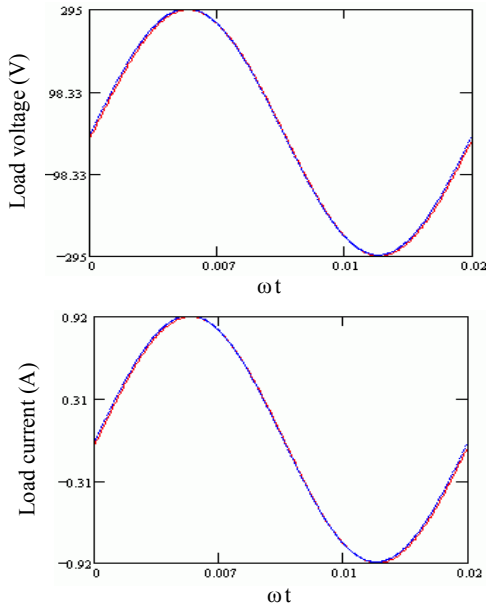


Fig. 3. The load waveforms for duty factor  $\Phi = 30^\circ$  and the phase angles  $\Gamma = 0.8$ .

The ratio (11)

$$(11) \quad \eta = \frac{\text{load power}}{\text{source power}}$$

is calculated with:

```

PowerTransfer := | c ← 0
                  | for i ∈ 0..rows(T) - 1
                  |   | A<c> - [ <T<0>>_i
                  |   |   | <T<1>>_i
                  |   |   | <T<2>>_i
                  |   |   | <T<14>>_i ]
                  | c ← c + 1
                  | A^T
    
```

Part of matrix with power transfer values in table 2 is presented. "T" is matrix with power values for all phase angle and all duty factor.

The power values are obtained for 220V a.c. input voltage.

Matrix columns in Table 2 are representing:

1. column1-duty factors;
2. column2-phase angles;
3. column 3-ratio  $\eta$ .

It perceives that the ratio  $\eta$  is nearly 1.

In fig. 4. power transfer surface is presented.

To achieve the equivalent circuit, it necessary to determine one function, being a polynomial regression.

The power transfer matrix

	0	1	2
41	0.6	0.14	0.874
42	0.6	0.175	0.881
43	0.6	0.209	0.879
44	0.6	0.244	0.872
45	0.6	0.279	0.862
46	0.6	0.524	0.753
47	0.6	0.785	0.604
48	0.7	0.105	0.868
49	0.7	0.14	0.901
50	0.7	0.175	0.913
51	0.7	0.209	0.916
52	0.7	0.244	0.913

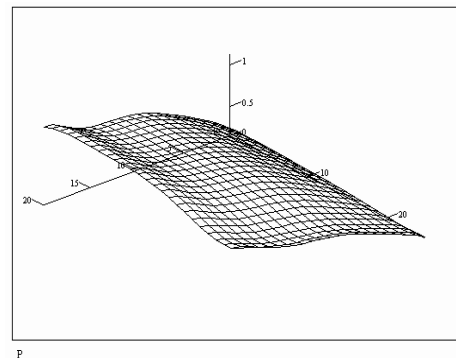


Fig. 4. Power surface for all duty factor and phase angles  $\Phi = ct$ .

Duty factor and phase angle are the variables of this function. The relation (12) is the expression of function.

$$(12) \quad p(\Gamma, \Phi) = \sum_{i=1}^n \left( \Gamma^i \cdot \sum_{j=1}^m b_j \Phi^j \right)$$

Fig. 5. shows the approximation of power transfer with the function deriving from (12).

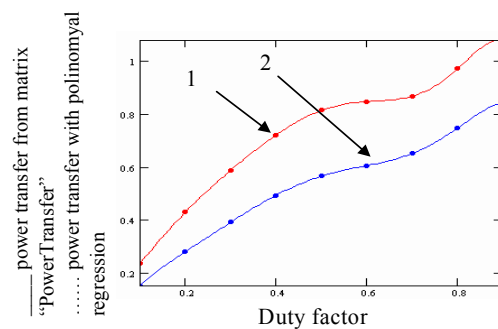


Fig. 5. Power transfer values: (1)  $\Phi = 6^\circ$ ; (2)  $\Phi = 35^\circ$

The errors between power from matrix of table 2 and polynomial regression are smaller from 1%, like it sees in fig.6.

It wants to establish an approximation for power consumption with multiple polynomial regression.

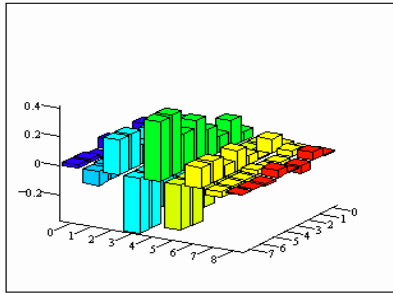
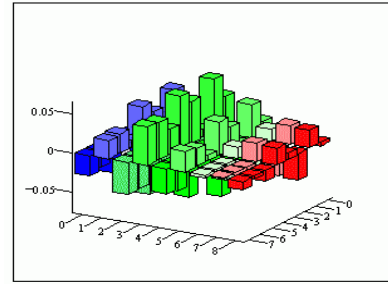


Fig. 6. Power transfer error values.



ErrPBuck  
Fig. 9. Power transfer error values.

In fig.7. apparent power diagram is presented.

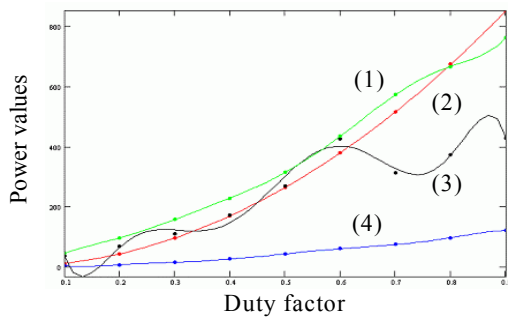


Fig. 7. Apparent power.

(1) source apparent power; (2) load apparent power;  
(3) inductance apparent power; (4) capacitive apparent power.

In fig.8. power surface is presented.

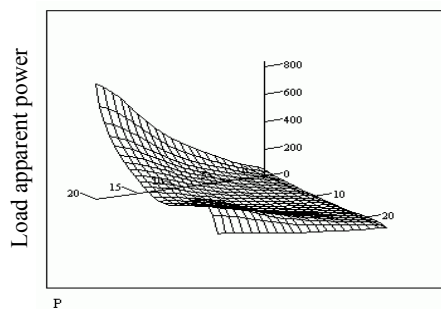
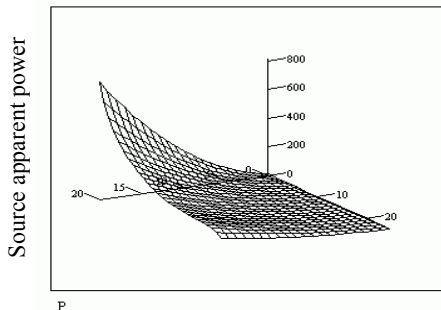


Fig. 8. Power surface

The error between power values and power polynomial regression is in fig.9. To determine power transfer in Buck AC PWM regulator the steady-state switching process must be studied.

Power transfer can be controlled with variable phase angle values, like in fig. 2 and 3, or with variable duty factor, like in fig.4.

Power transfer polynomial regression is a function of phase angle and duty factor. The error values are small, so the approximation is useful in regulator modeling.

**List of used symbols:**

$\Phi$  - phase angle

$\Gamma$  - duty factor

$\eta$  - ratio between load power and source power.

**References**

[1] Divan, D. M. – “Simple topologies for single phase ac line conditioning”, IEEE -IAS, 1991  
 [2] Miron, L., Miron, M. – “A study about commutation and power transfer of direct AC-AC converter”, AI XXXV –lea Simpozion de comunicări științifice cu participare internațională, București, 2004  
 [3] Miron, L., Constantinescu C.G. : Power transfer in direct AC-AC converter to a resistive-inductive load . The 30<sup>th</sup> Internationally Attended Scientific Conference of the Military Technical Academy “ Modern Tehnologies in the 21<sup>st</sup> Century ”, 2003 .

**Liliana Miron** – engineer, “Henri Coanda” Air Force Academy, Brasov, 160 Mihai Viteazul street, 500183, ROMANIA,

email: [miron\\_liliana@yahoo.com](mailto:miron_liliana@yahoo.com)

**Mihai Miron** – engineer, “Henri Coanda” Air Force Academy, Brasov, 160 Mihai Viteazul street, 500183, ROMANIA,

email: [mihaimiron@hotmail.com](mailto:mihaimiron@hotmail.com)

**Ioan Matlac** – Professor, Dr., “Transilvania” University of Brasov, Faculty of Electrical Engineering, ROMANIA  
 email: [matlac@leda.unitbv.ro](mailto:matlac@leda.unitbv.ro)

**Cristian Constantinescu** – engineer, Dr., “Henri Coanda” Air Force Academy, Brasov, 160 Mihai Viteazul street, 500183, ROMANIA,  
 email: [cgc\\_cristi@yahoo.com](mailto:cgc_cristi@yahoo.com)

# Active Power Sharing and Frequency Restoration in Parallel Operated Inverters

Koray Şener Parlak, Mehmet Timur Aydemir, Mehmet Özdemir

**Abstract:** The network structure of parallel operating inverters has been investigated in this paper. The active power demand of the whole structure is shared between the units in the network proportionally with their rated power values. As there is no communication between the units, problems that may arise due to disturbances, constraints related to the placement of the load and inverters have to be solved by the individual units. Parallel operation increases the established power value of the system. It also increases the reliability of the power system as the rest of the system keeps operating and providing power even when one of the units has a fault.

**Key Words:** Parallel operation, inverters, load-sharing, load-frequency droop, frequency restoration.

## Introduction

Power quality and uninterrupted power flow have become one of the most important issues of today, especially for critical loads. Uninterrupted Power Supplies (UPS) have been in use for a long time for this purpose. Increasing the capacity of the power system and providing a continuous power by connecting several UPSs in parallel has attracted a lot of interest in recent years. Increased capacity allows the connection of more loads to a system. Also, in the case of a fault in one or more units, the rest of the system may keep providing power. This results in increased system reliability. Operating UPSs with different ratings in parallel, adding or removing a unit or a load provide flexibility [1, 2, 3]. Figure.1 shows the system structure that can support these operations.

An important challenge arises from the fact that the units are not under one roof, but distributed. The control of the system under at this condition is difficult. Application of different control techniques becomes necessary if there is no communication between the units.

Each parallel operating unit needs to be controlled to share the load of the system. There are various control methods that are suggested for this purpose.

In the "Concentrated Control" method, an independent control unit sends synchronization signals to each inverter unit. Each unit, then, operates on its own output voltage error to regulate its output [4]. In the "Master-Slave Control" method, one of the units is designated to be "master" and the others become "slaves". The status of the units may be changed by a switch. The master unit controls the voltage, while the slaves control the current [5]. In the "Distributed Logic Control" method, a synchronization signal is synthesized

by using current and frequency data of each unit. This signal is then sent to the UPSs by an independent controller to provide synchronization and current control [6, 7]. There are other control methods that measure the load current, divide this value by the number of the units to calculate an average current value, calculate the current error by taking the difference between the real unit current and the average value, and regulate the output by operating on this error.

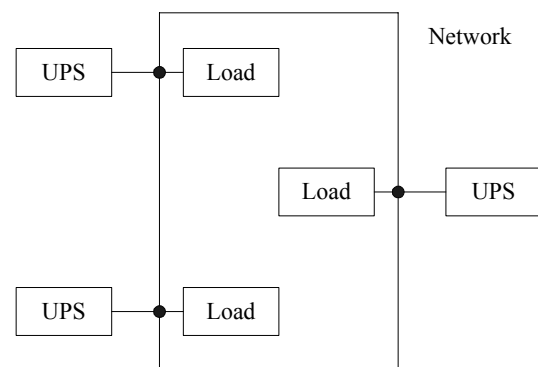


Figure.1. Structure of parallel operating UPSs

The biggest problem of these methods is the requirement of a communication line between the units. Noise related problems on the communication lines cause unreliable operation and create constraints on the placement locations of the units. Also, the power ratings of the units must be the same.

Different control methods have been suggested in the literature to overcome these problems. System information may be distributed to the units over the power line at a different frequency at the systems which do not have tie-lines between the units [8]. For the systems including tie-lines, active power-frequency and reactive power-voltage droop characteristics are utilized to sense the changes in power demands [9, 10, 11]. In this system which is also utilized in synchronous generators each unit has its own controller. Each controller uses only the output information of the unit it is designated to control. This eliminates the necessity of using a communication line between the units. Using droop characteristics also allows the parallel connection of UPSs with different power ratings. This makes it possible to share the total load among the units in proportion with their rated values.

Parallel operation of UPSs also means parallel operation of inverters. In this paper, Space Vector PWM (SVPWM) method is used to share the load to individual inverters according to their power ratings. The control system brings the inverter output frequency which deviates during load sharing, back to its nominal value.

### Load-Frequency Droop Characteristic

The load-frequency droop characteristic technique that is used in the automatic control of generators connected to a power grid can also be used in parallel operation of inverters. By using this technique, total load of the system is shared between each unit in proportion with their rated values. This characteristic naturally exists in synchronous generators. As the power drawn from the generator increases, the speed decreases; and as the drawn power decreases the speed increases. The same concept can be applied to the inverters.

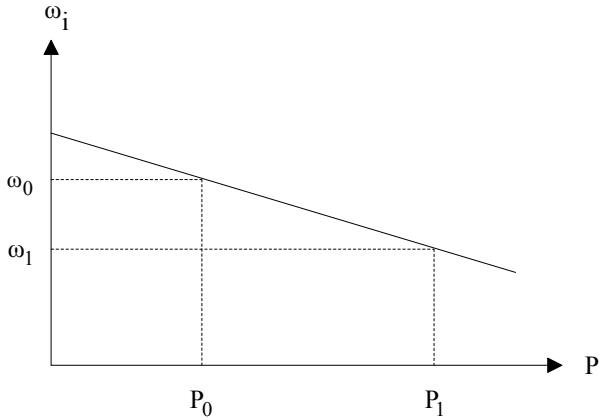


Figure.2. Load-frequency droop characteristic

Figure.2 shows the frequency deviation in response to power variation of the inverter. The variation is defined as

$$(1) \quad \omega_1 = \omega_0 - b(P_0 - P_1)$$

Where “-b” is the slope of the line,  $P_0$  is the power at the speed  $\omega_0$ , and  $P_1$  is the power at the speed  $\omega_1$ . In order to share the total load proportionally, following selection of the slopes becomes necessary:

$$(2) \quad b_1 P_{01} = b_2 P_{02} = \dots b_n P_{0n}$$

Where  $P_{01}, P_{02}, \dots, P_{0n}$  represent the powers of the unit 1, unit 2, ... unit n.

### Distributed Parallel Connection

Figure.3 shows one phase of two three-phase inverters operating in parallel. There are low-pass LC filters at the outputs of each inverter, and the line connecting the two outputs has an inductance of “L”.  $V_1$  and  $V_2$  represent the filter output voltages. Depending on the inverter ratings and load values, there may be a power flow through the tie-line between the inverters.

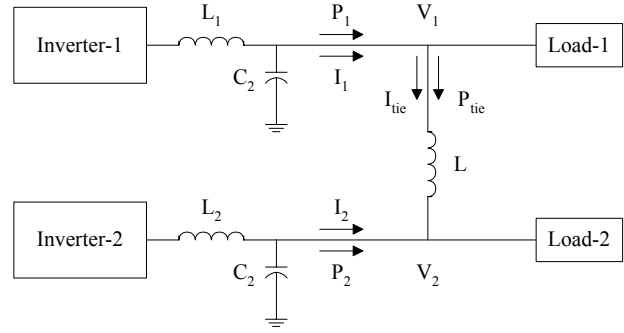


Figure.3. Connection diagram of distributed inverters operating in parallel.

The current of the tie-line is expressed as follows:

$$(3) \quad P = \frac{3V_1V_2}{2\omega L} \sin \delta$$

$$(4) \quad Q = \frac{3V_1}{2\omega L} (V_1 - V_2 \cos \delta)$$

Equation (3) shows that the active power is proportional with  $\sin(\delta)$ .  $\delta$  is the angle between the phasors  $V_1$  and  $V_2$  seen in Figure.4.

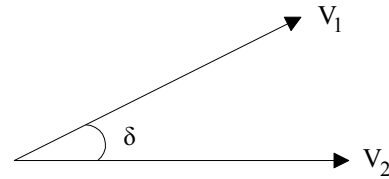


Figure.4.  $V_1$  and  $V_2$  voltage phasors

In order to better understand the parallel operation of the inverters let us consider the following special case: Assume that the rated power of the inverter 1 in Figure.3 is twice that of the inverter 2. In this case, inverter 1 takes over 2/3 of the total load, while 1/3 is taken over by inverter 2. If at any moment the load that is near by inverter increases, inverter 2 meets this increase with a corresponding frequency variation determined by its load-frequency droop characteristic. This frequency change results in an increase in the phase angle between the voltage phasors of the inverters, and a power flow from inverter 1 to inverter 2. Since the power inverter 1 supply to the system also increases, its frequency drops too. Consequently, inverter 2 starts decreasing the power it supplies and its frequency starts increasing again. One thing that has to be mentioned here is that the frequency does not increase or decrease by itself like it is in generators, but has to be controlled. The frequencies of the inverters have to be equal eventually. At that moment, the phase difference between the  $V_1$  and  $V_2$  voltage phasors and the power flow through the tie-line will reach a constant value and the system reaches to steady-state.

## Frequency Restoration

Frequency restoration with correct power sharing can be achieved by shifting the droop characteristic in the vertical direction. The shift should be proportional to the inverter power rating. The process is depicted in Figure.5. The desired frequency restoration is maintained during the load sharing process.

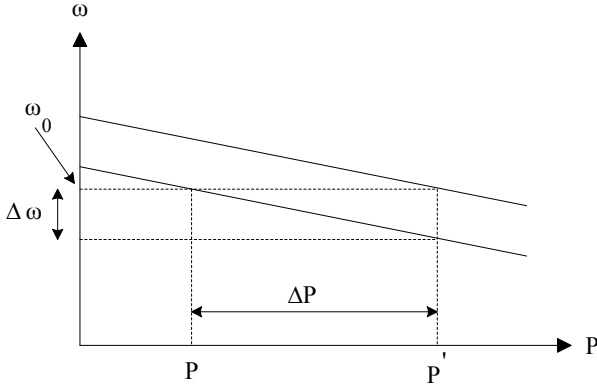


Figure.5. Frequency Restoration

If the locally measured frequency deviation is;

$$(5) \quad \Delta\omega = \omega_0 - \omega_1$$

then the active power  $P$  changes at the following rates for each inverter;

$$(6) \quad \frac{d}{dt} P = kres * \Delta\omega$$

The load-frequency droop and frequency restoration methods are shown schematically in control diagram in Figure.6.

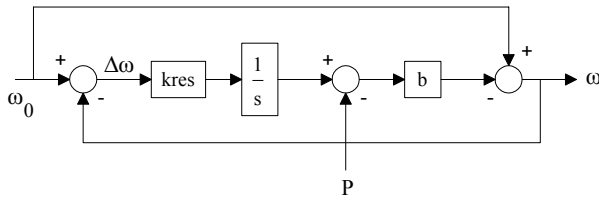


Figure.6. Load-frequency droop and frequency restoration

## Simulations

Figure.7 shows the block diagram of the system simulated in MATLAB-SIMULINK: The variable with (\*) represents the frequency command.

Following parameters are used in the simulations:

- $L_{f1} = L_{f2} = 1.3\text{mH}$
- $C_{f1} = C_{f2} = 100\ \mu\text{F}$
- $L = 0.01\ \text{H}$
- $b_1 = -0.001\ \text{Watt} / (\text{rad}/\text{sn})$
- $b_2 = -0.002\ \text{Watt} / (\text{rad}/\text{sn})$
- $kres_1 = 500\ \text{W} / \text{rad}$
- $kres_2 = 250\ \text{W} / \text{rad}$
- $f(\text{rated}) = 50\ \text{Hz}$
- $V_{\text{rms}} = 220\ \text{V}$
- Switching frequency = 5 kHz

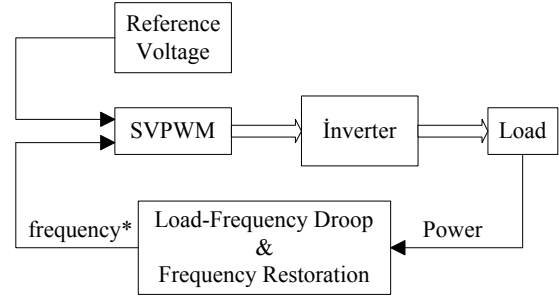


Figure.7. Block diagram of the system used in the simulations

A  $64.5\ \Omega$  resistor has been used as load for both inverters. As can be understand from the droop slopes, the rated power of inverter 1 is twice that of inverter 2.

Initially, both loads draw  $220^2/64.5 = 750\ \text{W}$ , and the total load is  $1500\ \text{W}$ . Inverter 1 supplies  $1000\ \text{W}$ , and inverter 2 supplies the remaining  $500\ \text{W}$ . This requires  $250\ \text{W}$  power flows through the tie-line from inverter 1 towards inverter 2. At this situation,  $V_1$  phasor leads  $V_2$ .

At the  $400\ \text{ms}$  instant, the load nearby inverter 1 is increased to  $1500\ \text{W}$ , changing the total load to  $2250\ \text{W}$ . As the load is increased, the frequency of inverter 1 is reduced, and this results in a smaller phase angle between phasors  $V_1$  and  $V_2$ . This, in turn, reduces the power flow through the tie-line. As expected, at the steady state inverter 1 should supply  $1500\ \text{W}$ , and inverter 2 should supply the remaining  $750\ \text{W}$ . These values are equal to the loads nearby each inverter, and no power flow occurs through the tie-line.

As mentioned earlier, frequency restoration and load sharing are carried out at the same time.

Figures 8-15 show the, voltage line current, power, frequency, tie-line power and tie-line current values of the phase "a" of each inverter as well as the power through the tie-line

Figures 8-15 are plotted in 0-6 sec. time tange, additionally zoomed in 0-0.8 msec. time range.

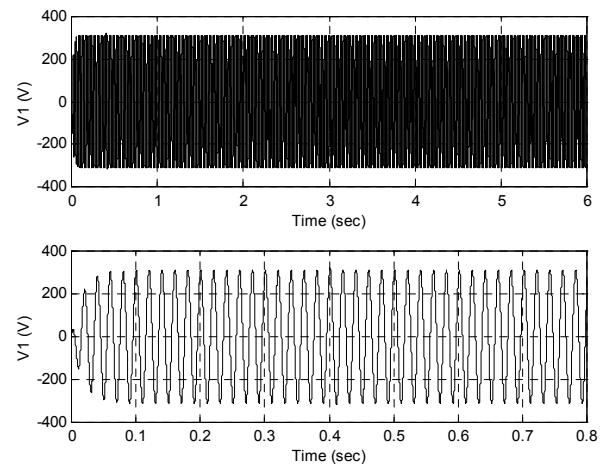


Figure.8. Voltage of inverter-1 ( $V_1$ ).

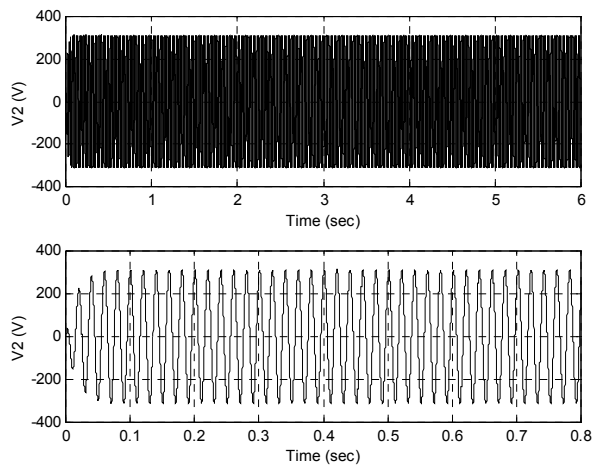


Figure.9. Voltage of inverter-2 ( $V_2$ ).

Figure.8 and Figure.9 show the filter output voltages of the inverters. It is clear from the figures that the load change does not affect the inverter output voltages.

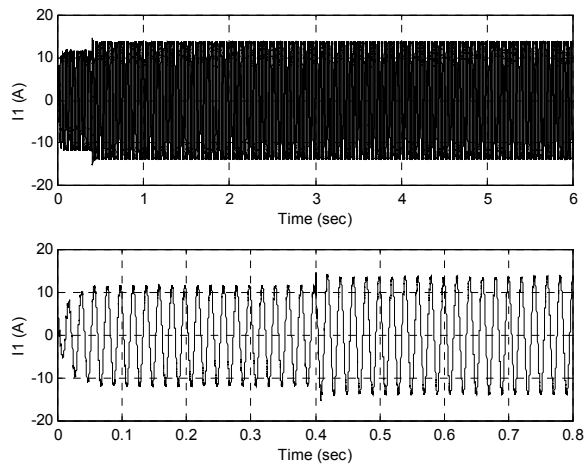


Figure.10. Output current of inverter-1 ( $I_1$ ).

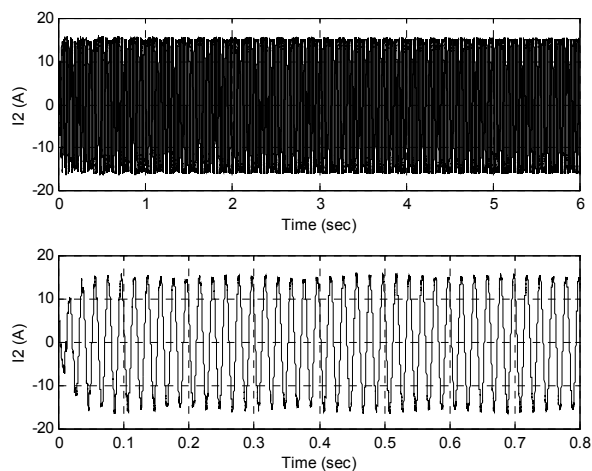


Figure.11. Output current of inverter-2 ( $I_2$ ).

Increased power demand from the load increase the power and current drawn from the inverters. Figure.10-11 shows that increase in the load of any inverter causes increase current in both inverters.

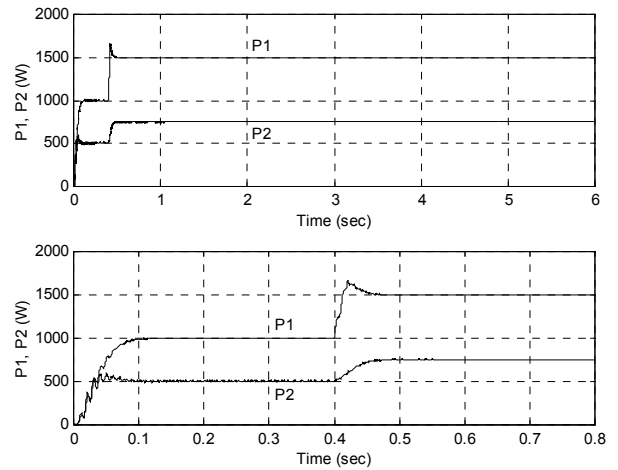


Figure.12. Power supplied by each inverter ( $P_1, P_2$ )

Figure.12 shows the power supplied by each inverter. Load sharing between the inverters is as expected proportional to the power ratings.

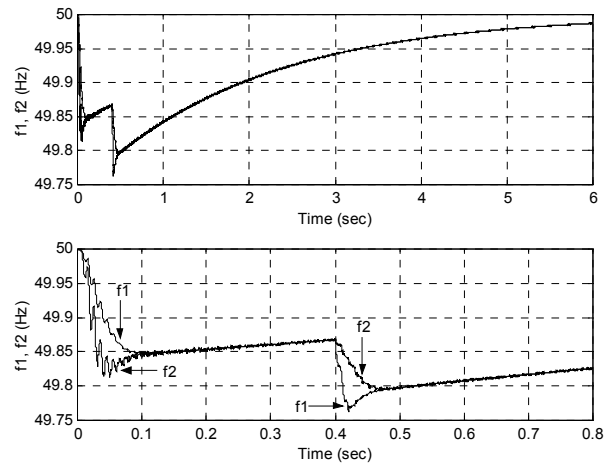


Figure.13. Output frequency of each inverter ( $f_1, f_2$ )

Figure.13 shows the inverter frequency variations. The loads are initially the same for each inverter. As the rated power of inverter 2 is lower, the frequency deviation for this inverter is higher. Frequencies of the two inverters are brought to an equal value by the effect of load-frequency characteristic. As the load increase at 400 ms occurs near inverter 1, this inverter responds first and its frequency drop is higher. Then, the second inverter starts to support the load and its frequency also drops. After the load sharing transient is over, inverter frequencies are restored to the original value.

Frequency restoration continues along with the load sharing period. As seen from Figure.13, it approaches the rated value during the transient.

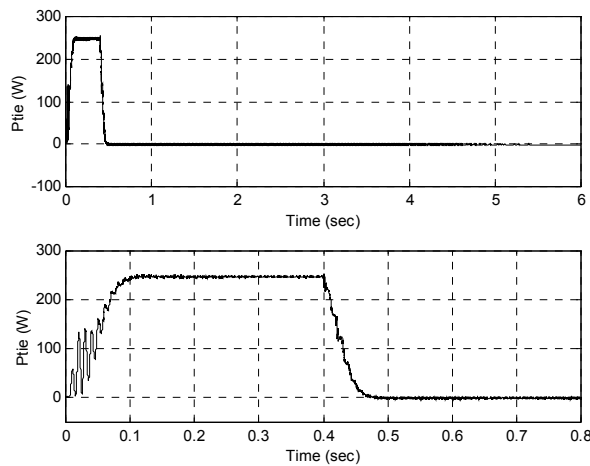


Figure.14. Power flow through the tie-line following the load increase nearby inverter-2 ( $P_{tie}$ ).

Figure.14 shows the power flow through the tie-line. As mentioned before, initial value of the power flowing in this line is 250 W. Following the load increase, power flow through the line diminishes as both inverters have loads equal to their rated values.

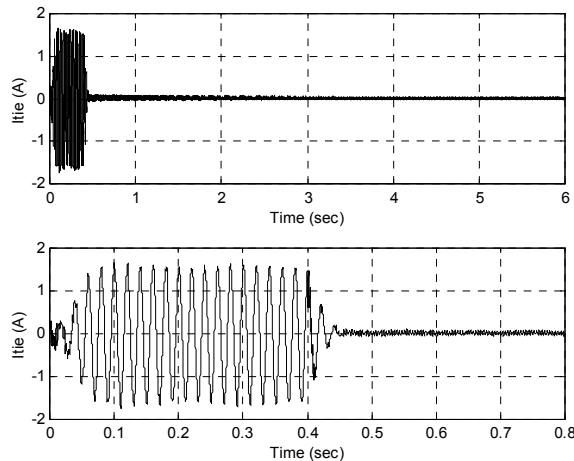


Figure.15. Current through the tie-line following the load increase nearby inverter-2 ( $I_{tie}$ ).

As seen from Figure.15, while some current flows through the tie-line prior to load increase, after the demand increase, due to the load and inverter power rating values, the current diminishes at the steady state.

### Conclusion

Load sharing of the distributed inverters operating in parallel has been demonstrated for the case where no communication exists between the inverters. Inverters share the load in proportion with their rated powers and deviated frequency is brought back to its nominal value. This provides flexibility for the units or loads to be added to or removed from the network. Moreover, this structure makes it possible to use inverters with different ratings together, without overloading them.

In a network consisting of several UPS units controlled properly, it is possible to obtain quality and reliable, continuous power independently from the main power grid.

### References

- [1] Lasseter, R.H (2002). *Microgrids*. Power Engineering Society Winter Meeting. IEEE, vol: 1, Jan. 305-308.
- [2] Mamay, C., F.J. Rubio, A.S. Siddiqui (2001). *Shape of the Microgrid*. Power Engineering Society Winter Meeting. IEEE, Vol: 1 Feb. 150 - 153.
- [3] Venkataramanan, G., M. Illindala (2002). *Microgrids and sensitive loads*. Power Engineering Society Winter Meeting. IEEE, vol: 1, 27-31 Jan, 315-322
- [4] Shanxu, D., M.X. Yu, J.K. Yong, C. Jian (1999). *Parallel operation control technique of voltage source inverters in UPS*. IEEE-PEDS'99, July, 883-887.
- [5] Broeck, H., U. Boeke (1998). *A simple method for parallel operation of inverters*. Intelec, San Francisco, CA.
- [6] Kawabata, T., S. Higashino (1998). *Parallel operation of voltage source inverters*. IEEE Trans. on Industry Applications, 281-287, March/April.
- [7] Lee, C. S., S. Kim, C. B. Kim, S. C. Hong, J. S. Yoo, S. W. Kim, C. H. Kim, S. H. Woo, S. Y. Sun (1998). *Parallel UPS with a instantaneous current sharing control*. IECON, 568-573.
- [8] Tuladhar, A., H. Jin, T. Unger, K. Mauch (1997). *Parallel operation of single phase inverters with no control interconnections*. Proc. IEEE. APEC'97, vol: 1, 94-100.
- [9] Chandorkar, M.C., D.M. Divan, R. Adapa (1993). *Control of parallel connected inverters in stand-alone ac supply systems*. IEEE Trans. on Industry Applications, January/February.
- [10] Chandorkar, M.C., D.M. Divan, Y. Hu, B. Banerjee (1994a). *Novel architectures and control of distributed UPS systems*. In Applied Power Electronics Conf. (APEC), 683-689, Orlando, USA.
- [11] Chandorkar, M.C., D.M. Divan, B. Banerjee (1994b). *Control of distributed UPS systems*. In IEEE Power Electronics Specialists Conf. (PESC), 197-204, Taiwan.

**Koray Şener Parlak** – Ph.D. Student, Faculty of Electrical Engineering, Firat University, Firat University, Teknik Bilimler MYO., Elazığ, TURKEY. e-mail: kparlak@firat.edu.tr

**Mehmet Timur Aydemir** – Associate Professor, Dr., Faculty of Electrical Engineering, Gazi University, Gazi University, Faculty of Electrical Engineering., Maltepe, Ankara, TURKEY. e-mail: aydemirmt@gazi.edu.tr

**Mehmet Özdemir** – Associate Professor, Dr., Faculty of Electrical Engineering, Firat University, Firat University, Faculty of Electrical Engineering., Elazığ TURKEY. e-mail: mozdemir@firat.edu.tr.

## Uniform approach for analysis of resonant inverters with reversed diodes

Nikola Gradinarov, Nikolay Hinov, Tsvetan Marinov

**Abstract:** This paper obtains an analysis of resonant inverters with reversed diodes at R and RL load. The basic characteristics of the two possible modes (sub- and over resonant) are built. There is also a comparison at equal power dissipation between the operating conditions of the semiconductors at both modes, and the advantages and disadvantages are evaluated.

**Keywords:** resonant inverter, reversed diodes, induction technologies

### Introduction

There are known analysis of resonant inverters with reversed diodes (RIRD), operating at continuous current mode and control frequency respectively greater (overresonant) [3, 5, 6, 8] or lower (subresonant) than the serial resonant circuit natural frequency [1, 2, 4, 7]. Due to the fact, that the full-bridge circuit of RIRD (shown at fig.1) has one and the same equivalent circuit in both modes, an uniform approach for analysis of the electrical processes could be used and proposed. The differences between the common expressions for the inverter current and the voltage over the commutating capacitor, which originate all the other quantities, are due to the opposite signs of the initial value of the inverter current.

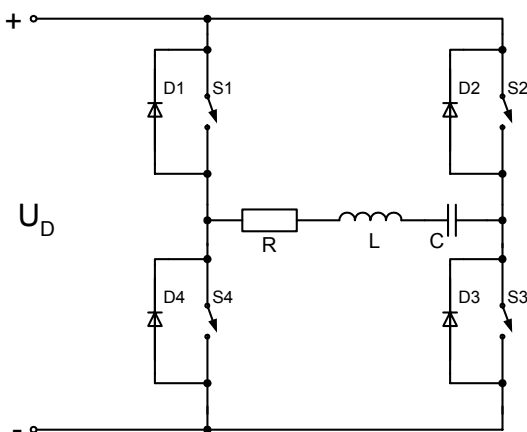


fig.1

The established mode analysis of the processes in subresonant frequency operation [1, 2] and expressions for the inverter current and commutating capacitor voltage, which are obtained from the analysis are:

$$(1) \quad i(\vartheta) = \frac{2k_{od}U_d}{\omega_0 L} \sqrt{\left(1 - a \frac{\delta}{\omega_0}\right)^2 + a^2 e^{-\frac{\delta\vartheta}{\omega_0}} \sin \frac{\pi}{\lambda} (\vartheta + \psi)},$$

$$(2) \quad u_c(\vartheta) = U_d - 2k_{od}U_d \sqrt{1 + \left(\frac{\delta}{\omega_0} - a - a \left(\frac{\delta}{\omega_0}\right)^2\right)^2} \times e^{-\frac{\delta\vartheta}{\omega_0}} \sin \frac{\pi}{\lambda} (\vartheta + \varphi)$$

where  $\theta = \omega t$ ,  $\omega$  - control frequency,  $R=R_{(1)}$  is the equal load resistance,  $L$  and  $C$  are the equal commutating inductance and capacitance,  $U_d$  is the DC power supply voltage,  $\omega_0 = \sqrt{\frac{1}{LC} - \delta^2}$  is the resonant frequency of

the serial resonant circuit, and  $\delta = \frac{R}{2L}$  is its attenuation,

$v = \frac{\omega}{\omega_0}$  is frequency coefficient,  $\lambda = \frac{\pi\omega}{\omega_0}$  - conduction

angle, which is normalized to the control frequency,  $h$  and  $a$  represent:

$$h = \frac{\frac{1}{\pi} \ln \left(\frac{k}{k-1}\right) \sin \frac{\pi}{v} + \cos \frac{\pi}{v} + \left(\frac{k-1}{k}\right)^{\frac{1}{v}}}{\left(\frac{k-1}{k}\right)^{\frac{1}{v}} \left(\frac{1}{\pi} \ln \left(\frac{k}{k-1}\right) \sin \frac{\pi}{v} - \cos \frac{\pi}{v}\right) - 1}$$

$$a = \frac{\sin \frac{\pi}{v}}{\frac{1}{\pi} \ln \left(\frac{k}{k-1}\right) \sin \frac{\pi}{v} - \cos \frac{\pi}{v} - \left(\frac{k}{k-1}\right)^{\frac{1}{v}}}$$

The hesitation coefficient  $k$  has the description

$$k = \frac{1}{1 - e^{-\frac{\delta\pi}{\omega_0}}}, \text{ and } \psi' = \text{arctg} \frac{a}{1 - a \frac{\delta}{\omega_0}}$$

$\varphi' = \text{arctg} \frac{1}{\frac{\delta}{\omega_0} - a - a \left(\frac{\delta}{\omega_0}\right)^2}$  are the initial phase

angles of the inverter current and the commutating capacitor voltage, and  $\psi = \frac{\lambda}{\pi} \psi'$ ,  $\varphi = \frac{\lambda}{\pi} \varphi'$ . The

coefficient 
$$k_{od} = \frac{1}{1 - h e^{-\frac{\delta\pi}{\omega_0}}} = \frac{1}{1 - h \left(\frac{k-1}{k}\right)^{\frac{1}{v}}}$$

characterizes the serial RLC circuit, and it is called RIRD hesitation coefficient, operating at subresonant mode.



The average consumed from the power supply current  $I_d$  is determined from:

$$I_d = \frac{1}{\pi} \int_0^{\pi} i(\vartheta) d\vartheta = \frac{1}{\pi} \int_0^{\pi} \frac{2k_{od}U_d}{\omega_0 L} \sqrt{\left(1 - a \frac{\delta}{\omega_0}\right)^2 + a^2} e^{-\frac{\delta}{\omega} \vartheta} \sin \frac{\pi}{\lambda} (\vartheta + \psi) d\vartheta$$

and it is

$$(3) \quad I_d = - \frac{\frac{2k_{od}\delta U_d}{\omega_0 R} \sqrt{\left(1 - a \frac{\delta}{\omega_0}\right)^2 + a^2}}{\pi F} \times \left( e^{-\frac{\delta\pi}{\omega}} \sin \left( \frac{\pi}{\lambda} (\pi + \psi) + \alpha \right) - \sin \left( \frac{\pi}{\lambda} \psi + \alpha \right) \right)$$

where  $F = \sqrt{\left(\frac{\delta}{\omega}\right)^2 + \left(\frac{\pi}{\lambda}\right)^2}$  and  $\alpha = \arctg \frac{\lambda}{\delta} \frac{\pi}{\omega}$ .

The average current through the switch  $I_{av}$  is:

$$I_{av} = \frac{1}{2\pi} \int_0^{\lambda-\psi} i(\vartheta) d\vartheta = \frac{1}{2\pi} \int_0^{\lambda-\psi} \frac{2k_{od}U_d}{\omega_0 L} \sqrt{\left(1 - a \frac{\delta}{\omega_0}\right)^2 + a^2} e^{-\frac{\delta}{\omega} \vartheta} \sin \frac{\pi}{\lambda} (\vartheta + \psi) d\vartheta$$

$$(4) \quad I_{av} = \frac{\frac{2k_{od}U_d}{\omega_0 L} \sqrt{\left(1 - a \frac{\delta}{\omega_0}\right)^2 + a^2}}{2\pi F} \times \left( e^{-\frac{\delta}{\omega}(\lambda-\psi)} \sin \alpha + \sin \left( \frac{\pi}{\lambda} \psi + \alpha \right) \right)$$

The average current through the diodes  $I_{dav}$  is determined from:

$$(5) \quad I_{dav} = I_{av} - \frac{I_d}{2}$$

For determination of the load voltage RMS value  $U$  the input and output active power balance equation for the inverter must be used, which has the following appearances at different loads:

$$P_d = U_d I_d = UI = \frac{U^2}{R} \text{ - at active load,}$$

$$(6) \quad P_d = U_d I_d = UI \cos \varphi_T = \frac{U^2}{R} \cos^2 \varphi_T \text{ - at RL load,}$$

where  $I$  is the RMS value of the inverter current,  $\varphi_T$  is power factor of the RL load.

Finally the RMS value of the load voltage is:

$$U = \sqrt{U_d R I_d} \text{ - at active load,}$$

$$(7) \quad U = \frac{1}{\cos \varphi_T} \sqrt{U_d R I_d} \text{ - at RL load,}$$

where the  $I_d R$  quantity is substituted by the determined from expression (3), which is function of the coefficients  $k$  and  $v$ .

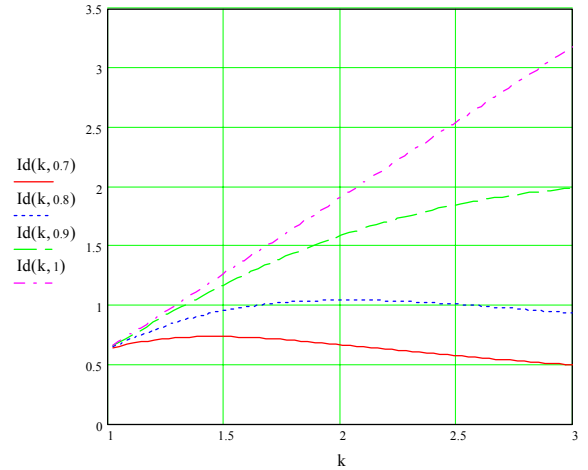


fig.2a Input characteristics of RIRD, operating at subresonant mode

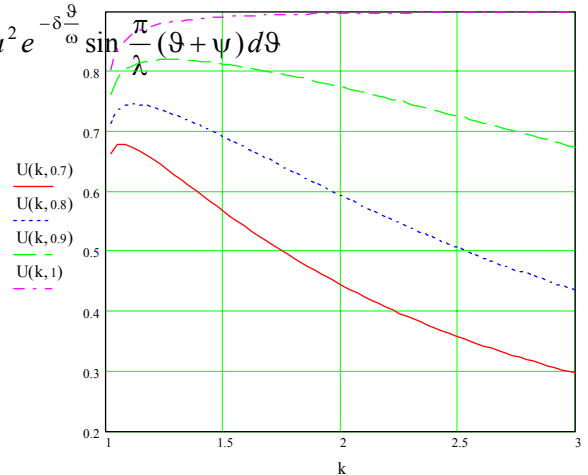


fig.2b Output characteristics of RIRD, operating at subresonant mode

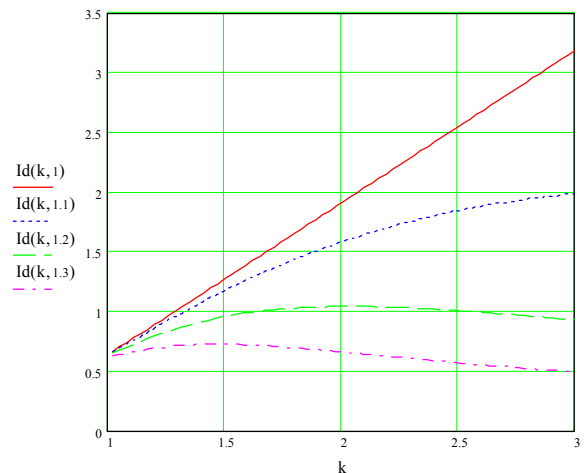


fig. 3a Input characteristics of RIRD, operating at overresonant mode

It could be proven, that the analysis of RIRD, operating at subresonant mode, whose basic expressions (1) to (7) could be used for overresonant mode by using

values of the frequency coefficient  $\gamma$  peculiar to the overresonant mode ( $\nu > 1$ ) [10].

Figures 2a, 2b, 3a and 3b show the input and output characteristics at both modes, when the subresonant expressions (3) and (7) are used.

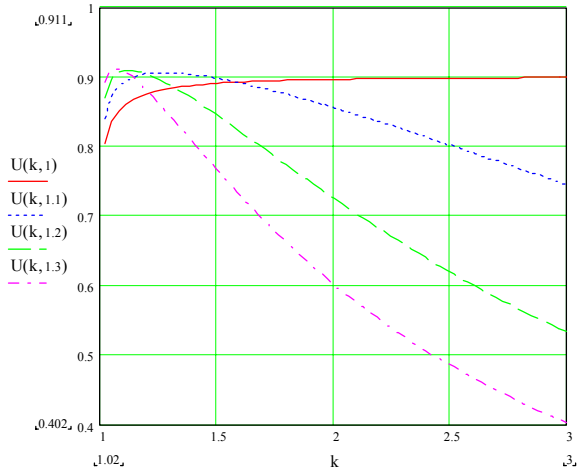


fig.3b Output characteristics of RIRD, operating at overresonant mode

At the next two figures fig.4a and fig.4b these characteristics are built, using the overresonant expressions [5, 6].

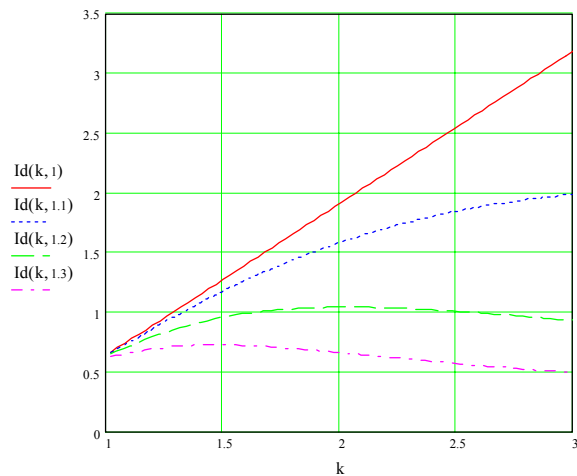


fig. 4a Input characteristics of RIRD, operating at overresonant mode

The comparison between the progresses of the characteristics proves the rightness of the assertion, that the known analysis of RIRD, operating at subresonant mode could be used for both operation modes [8, 9, 10].

Fig. 5 shows the correspondence between the frequency coefficients of both operation modes of RIRD, at equal output power. The graph fig. 6 shows the dependence of the output voltage of RIRD, when the load is purely active, which allows the chosen coefficients  $k$  and  $\nu$  to be enough for load voltage determination hence the harmonizing method between the inverter and the load.

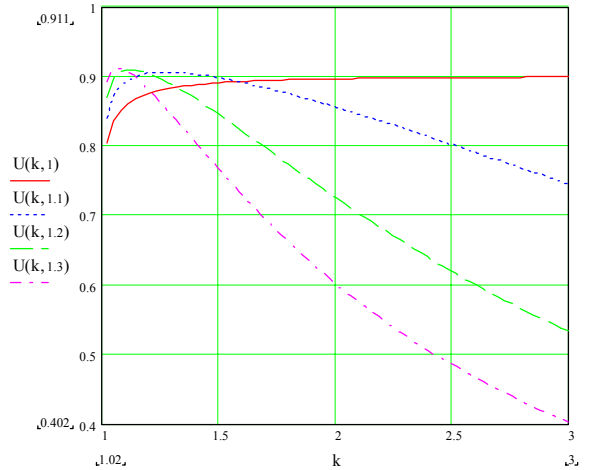


fig. 4b Output characteristics of RIRD, operating at overresonant mode

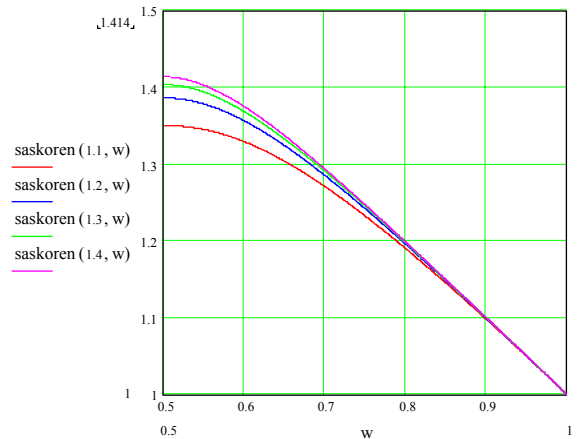


fig.5 Correspondence between the frequency coefficients of both operation modes of RIRD

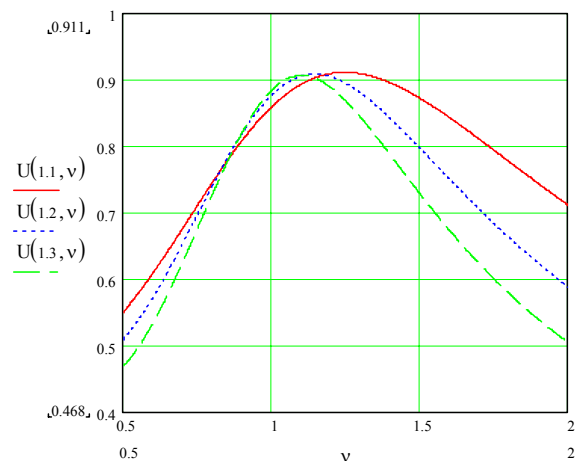


fig. 6 Dependence of the RMS value of the load voltage by the frequency coefficient

## Conclusion

The expressions, which were presented and the correspondences between the characteristics between both operation modes of RIRD, allow when the recommended values of  $k$  and  $v$  are chosen to be determined the necessary design quantities independently from the operation mode.

## Reference

- [1] Gradinarov N., N. Hinov "Analysis and design of resonant inverter with reverse diodes", Proceeding at fifth national scientific-practical conference with international participation "Electronics '96". Symposium of scientific works, book 3, pp.185-190, 27-29 September, 1996, Sozopol.
- [2] Gradinarov N., N. Hinov, "Analysis of resonant inverter with reverse diodes operating at complex load". Symposium of scientific proceedings at sixth national scientific-practical conference with international participation "Electronic engineering – ET'97" 24-27 September 1997, Sozopol, pp.74-79.
- [3] Gradinarov N., N. Hinov, "Analysis of serial resonant RLC inverters with reverse diodes, operating at over resonant frequency mode", Proceedings of The seventh international conference "ELECTRONICS '98", pp.177-182, 23-25 September, 1998, Sozopol.
- [4] Karov R. D., "Theoretical generalization, dual correlation and schematic improvements of power inverter circuits and sections", Dissertation for Doctor of Sciences, Sofia, 2004.
- [5] Hinov N., "Design of resonant inverters with reverse diodes, operating at over resonant frequency mode – part I", Symposium of scientific proceedings of the National conference with international participation "Electronics'2002", 17 - 18 October 2002, Sofia, 2002, pp.78-84.
- [6] Hinov N., "Design of resonant inverters with reverse diodes, operating at over resonant frequency mode – part II", Symposium of scientific proceedings of the National conference with international participation "Electronics'2002", 17 - 18 October 2002, Sofia, 2002, pp.85-90.
- [7] Bobtcheva M., N. Gradinarov and Co. Power electronics. TU-Sofia, 2001.
- [8] Mohan N., Undeland T. E., Robbins W. Power electronics - Converters, Applications and Design. Second edition, John Wiley&Sons Inc, New York, 1995.
- [9] Gradinarov N. P., "Research elaboration and development of resonant inverters with technical application" Doctorate Thesis. Technical University – Sofia, 2002.
- [10] Marinov Tsvetan, "Design of resonant inverters with reversed diodes, operating at sub- and over- resonance mode at constant power", "Bulgarian International Session of young engineers, interested about science and application", Sofia, 2005, in Bulgarian.
- 

*Nikola Gradinarov – professor, Dr. Sc., dept. Power Electronics, Faculty of electronic engineering and technologies, Technical University of Sofia, "8, Kliment Ohridski blvd.", 1000 Sofia, BULGARIA.*  
e-mail: [n\\_gradinarov@tu-sofia.bg](mailto:n_gradinarov@tu-sofia.bg)

*Nikolay Hinov – assistant, Ph.D., dept. Power Electronics, Faculty of electronic engineering and technologies, Technical University of Sofia, "8, Kliment Ohridski blvd.", 1000 Sofia, BULGARIA.*  
e-mail: [hinov@tu-sofia.bg](mailto:hinov@tu-sofia.bg)

*Tsvetan Marinov – engineer, Ph.D. Student, dept. Power Electronics, Faculty of electronic engineering and technologies, Technical University of Sofia, "8, Kliment Ohridski blvd.", 1000 Sofia, BULGARIA.*  
e-mail: [cmarinov@abv.bg](mailto:cmarinov@abv.bg)

## Analysis of Parallel Resonant Inverter, Operating at Active Load

Nikolay Hinov, Nikola Gradinarov, Tsvetan Marinov, Vasil Trenkov

**Abstract:** The paper presents analysis of parallel resonant inverter, operating at active load. There is an examination of the operating modes of resonant inverters, operating at forced commutation mode of the switching devices (overresonant mode). The input current and load voltage expressions are worked out, which generate all the other quantities, which are required for the inverter design. Analogical to the serial compensated resonant inverters here is suggestion of hesitation coefficient of parallel-compensated resonant inverter –  $k_p$  and frequency coefficient  $\nu$

**Keywords:** current source inverter, parallel load, induction technologies.

### Introduction

The autonomous resonant inverter (ARI), are widely used in the industry and home use for realization of power supplies with various form and frequency of the voltage and current. They are examined by lots of Bulgarian and foreign authors [1, 2, 3, 5, 7, 9, 10, 11, 12]. There is known an uniform approach for analysis and design of serial resonant inverter (serial compensated resonant inverter) with and without reversed diodes, operating at natural and forced commutation (current source inverter mode) of the switching devices [4, 7, 8]. The goal of the present work is the development of such approach for analysis and design of parallel resonant inverters, operating at active load. The reference presents analysis of parallel current source inverters (highly forced commutation resonant inverter with parallel-compensated load) [1, 2, 3, 6], but it is developed assuming unlimited value of the input inductance, which is not realized in all practical cases.

### Fundamental expressions and circuits

The paper utilizes the presentation of the current sources inverter as resonant inverter, operating at forced commutation mode. The full-bridge parallel resonant inverter circuit, operating at active load is shown at fig. 1. Fig. 2 shows its equivalent Laplace representation.

The following references are used: S1 ÷ S4 – controlled one-way semiconductor switches (thyristors and transistors), L – commutating (input) inductance, C – commutating (compensation, parallel, load) capacitor, R – load (parallel) resistance,  $U_d$  – power supply DC voltage,  $I(0)$  and  $U_c(0)$  – initial values of the inverter current and commutating capacitor voltage.

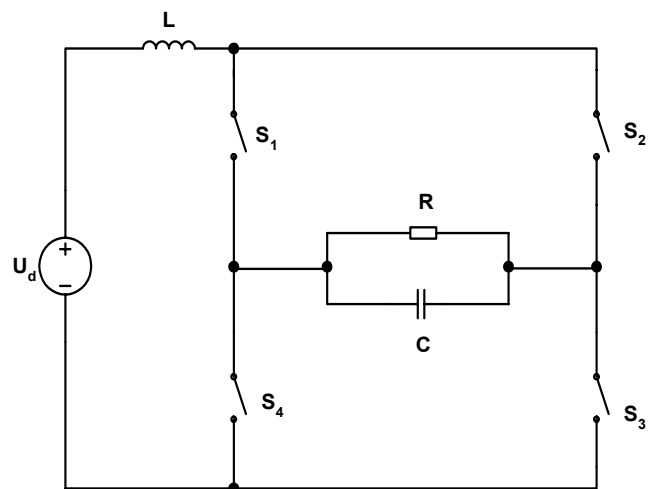


Fig.1 Full-bridge parallel resonant inverter circuit

The analysis is performed assuming, that the power supply is ideal (zero-equalled self resistance), ideal switches and instant current commutation.

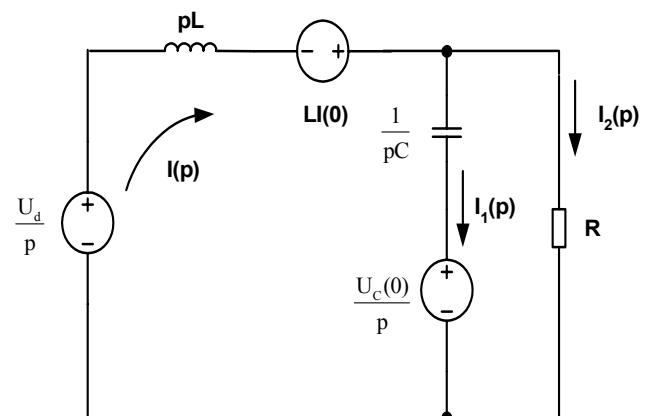


Fig.2 Equivalent Laplace circuit

This circuit could be described by the system of these Laplace equations:

$$\frac{U_d}{p} + LI(0) + \frac{U_c(0)}{p} = pLI(p) + \frac{1}{pC} I_1(p)$$

$$\frac{1}{pC} I_1(p) - \frac{U_c(0)}{p} = RI_2(p)$$

$$I_2(p) = I(p) - I_1(p).$$

Its solution generates the following inverter current and commutating capacitor voltage expressions:

$$I(p) = \frac{\frac{U_d}{pCRL} + \left[ \frac{U_d}{L} + \frac{U_c(0)}{L} + \frac{I(0)}{CR} \right] + pI(0)}{p^2 + \frac{1}{CR}p + \frac{1}{CL}},$$

$$U_c(p) = \frac{\frac{U_c(0)}{p} + R \frac{\frac{U_d}{pCRL} + \left[ \frac{U_d}{L} + \frac{U_c(0)}{L} + \frac{I(0)}{CR} \right] + pI(0)}{p^2 + \frac{1}{CR}p + \frac{1}{CL}}}{1 + pCR}$$

For the particular LCR circuit the resonant conditions could be present or not. As the goal of this work is the examination of the resonant inverters, we will assume that the resonant condition is present in the further analysis.

When the forced commutation of the switches is present, the equivalent circuit, shown at fig. 2 is valid i.e. the inverter current initial conditions are not zero.

After performing inverse Laplace transformation and introduction of the references:  $\omega_0 = \sqrt{\frac{1}{CL} - \delta^2}$  - resonant circuit of the serial resonant circuit, consisted of C, L and R and  $\delta = \frac{1}{2RC}$  - resonant circuit fading, the results for the desired current and voltage are:

$$i(t) = \frac{U_d}{R} + \left[ \frac{U_d + U_c(0)}{\omega_0 L} - \frac{\delta}{\omega_0} \frac{U_d}{R} + \frac{\delta}{\omega_0} I(0) \right] e^{-\delta t} \sin \omega_0 t +$$

$$+ \left[ I(0) - \frac{U_d}{R} \right] e^{-\delta t} \cos \omega_0 t,$$

$$u_c(t) = U_d - 2 \frac{\delta}{\omega_0} U_d e^{-\delta t} \sin \omega_0 t +$$

$$+ [U_d + U_c(0)] e^{-\delta t} \left[ \frac{\delta}{\omega_0} \sin \omega_0 t - \cos \omega_0 t \right] + \frac{I(0)}{\omega_0 C} e^{-\delta t} \sin \omega_0 t$$

For resonance condition accomplishment for LCR circuit it is necessary  $R > \frac{1}{2} \sqrt{\frac{L}{C}}$ .

The initial values of the inverter current and commutating capacitor voltage at continuous current mode (corresponding to forced commutation mode  $\omega_0 < \omega$ ) are determined according to the periodical conditions of the output voltage  $u_c(0) = -u_c(\frac{\pi}{\omega})$  and input

current  $i(0) = i(\frac{\pi}{\omega})$  and they are:

$$U_c(0) = (2k_{III} - 1)U_d,$$

$$I(0) = \frac{U_d}{R} + \frac{2U_d}{\omega_0 L} \frac{\sin \left[ \frac{\pi}{v} \right]}{e^{\frac{\delta \pi}{\omega}} - 2 \frac{\delta}{\omega_0} \sin \left[ \frac{\pi}{v} \right] - e^{-\frac{\delta \pi}{\omega}}},$$

where  $k_{III} = \frac{1}{1 - h_{III} e^{-\frac{\delta \pi}{\omega}}}$  is quantity, which

characterizes the resonant process in the hesitating circuit and it is analogical to the hesitation coefficient k, which is introduced at the serial resonant inverters and it is called hesitation coefficient of parallel compensated resonant inverters, operating at forced commutation

mode, but  $k_{II} = \frac{1}{1 - e^{-\frac{\delta \pi}{\omega_0}}}$  is parameter, which is called

hesitation coefficient of parallel resonant inverters, operating at natural commutation mode,  $v = \frac{\omega}{\omega_0}$  is the

frequency coefficient, but  $h_{III}$  means:

$$h_{III} = \frac{\frac{\delta}{\omega_0} \sin \frac{\pi}{v} - \cos \frac{\pi}{v} + e^{-\frac{\delta \pi}{\omega}}}{1 - \left( \frac{\delta}{\omega_0} \sin \frac{\pi}{v} + \cos \frac{\pi}{v} \right) e^{-\frac{\delta \pi}{\omega}}}$$

The condensed expressions for the inverter current and output voltage are:

$$i(t) = \frac{U_d}{R} + \frac{2U_d}{\omega_0 L} T_I e^{-\delta t} \sin(\omega_0 t + \psi'_{III}) \text{ are}$$

$$u_c(t) = U_d - 2U_d T_I \sqrt{1 + \left( \frac{\delta}{\omega_0} \right)^2} e^{-\delta t} \sin(\omega_0 t - \varphi'_{III}),$$

where

$$T_I = \frac{\sqrt{e^{2\frac{\delta \pi}{\omega}} - 2e^{\frac{\delta \pi}{\omega}} \cos \frac{\pi}{v} + 1}}{e^{\frac{\delta \pi}{\omega}} - 2 \frac{\delta}{\omega_0} \sin \frac{\pi}{v} - e^{-\frac{\delta \pi}{\omega}}},$$

$\psi'_{III} = \text{arctg} \frac{\sin \frac{\pi}{v}}{e^{\frac{\delta \pi}{\omega}} - \cos \frac{\pi}{v}}$  - represents the initial phase

angle of the inverter current,

and  $\varphi'_{III} = \text{arctg} \frac{e^{\frac{\delta \pi}{\omega}} - \frac{\delta}{\omega_0} \sin \frac{\pi}{v} - \cos \frac{\pi}{v}}{\frac{\delta}{\omega_0} e^{\frac{\delta \pi}{\omega}} + \sin \frac{\pi}{v} - \frac{\delta}{\omega_0} \cos \frac{\pi}{v}}$  is the

initial phase angle of the inverter (load) voltage.

In order to be obtained generalized expressions it is more comfortable to be presented as functional dependent by the control frequency  $\omega$ :

$$i(\vartheta) = \frac{U_d}{R} + \frac{2U_d}{\omega_0 L} T_I e^{-\frac{\delta \vartheta}{\omega}} \sin \frac{\pi}{\lambda} (\vartheta + \psi_{III}) \quad \text{and} \quad (1)$$

$$u_C(\vartheta) = U_d - 2U_d T_I \sqrt{1 + \left(\frac{\delta}{\omega_0}\right)^2} e^{-\frac{\delta \vartheta}{\omega}} \sin \frac{\pi}{\lambda} (\vartheta - \varphi_{III}),$$

where  $\vartheta = \omega t$ ,  $\lambda = \pi v$  is conduction angle of the semiconductor devices, normalized to the control frequency  $\omega$ , and the normalized values of the angles  $\psi$  and  $\varphi$  are respectively:

$$\psi_{III} = \frac{\lambda}{\pi} \psi'_{III} \quad \text{and} \quad \varphi_I = \frac{\lambda}{\pi} \varphi'_{III}.$$

The average value of the consumed current, according to expression (1) is determined by the integral:

$$I_d = \frac{1}{\pi} \int_0^{\pi} i(\vartheta) d\vartheta = \frac{1}{\pi} \int_0^{\pi} \left( \frac{U_d}{R} + \frac{2U_d}{\omega_0 L} T_I e^{-\frac{\delta \vartheta}{\omega}} \sin \frac{\pi}{\lambda} (\vartheta + \psi_{III}) \right) d(\vartheta)$$

which has this solution :

$$I_d = \frac{U_d}{R} - \frac{2U_d T_I}{\omega_0 L \pi F} \left( e^{-\frac{\delta \pi}{\omega}} \sin \left( \frac{\pi^2}{\lambda} + \psi'_{III} + \alpha \right) - \sin(\psi'_{III} + \alpha) \right), \quad (2)$$

$$\text{where } F = \sqrt{\left(\frac{\delta}{\omega}\right)^2 + \left(\frac{\pi}{\lambda}\right)^2} \quad \text{и} \quad \alpha = \text{arctg} \frac{\frac{\pi}{\lambda}}{\frac{\delta}{\omega}}.$$

The average value of the switch current is  $I_{av} = \frac{I_d}{2}$ .

The maximum value of the switch current is determined by the expression for the current (1), at

$$\vartheta = \frac{\lambda}{\pi} \alpha - \psi_{III} :$$

$$I_{\max} = i \left( \frac{\lambda}{\pi} \alpha - \psi_{III} \right) = \frac{U_d}{R} + \frac{2U_d}{\omega_0 L} T_I e^{-\frac{\delta}{\omega} \left( \frac{\lambda}{\pi} \alpha - \psi_{III} \right)} \sin \alpha \quad (3)$$

The maximum value of the parallel capacitor voltage is:

$$U_{C\max} = (2k_{III} - 1)U_d. \quad (4)$$

The expression for the commutating inductance voltage is:

$$u_L = \omega L \frac{di(\vartheta)}{d\vartheta} = \omega L \frac{2U_d}{\omega_0 L} T_I F e^{-\frac{\delta \vartheta}{\omega}} \sin \left( \alpha - \frac{\pi}{\lambda} (\vartheta + \psi_{III}) \right)$$

The maximum value of the reverse voltage across the switches is at the moment  $\vartheta = 0$  and it is:

$$U_{RRM} = U_d - \omega L \frac{2U_d}{\omega_0 L} T_I F \sin \left( \alpha - \frac{\pi}{\lambda} \psi_{III} \right). \quad (5)$$

The maximum value of the forward voltage across the

switches is at the moment  $\vartheta = 2\frac{\lambda}{\pi} \alpha - \psi_{III}$  and it is :

$$U_{DRM} = U_d + \omega L \frac{2T_I U_d}{\omega_0 L} F e^{-\frac{\delta}{\omega} \left( 2\frac{\lambda}{\pi} \alpha - \psi_{III} \right)} \sin \alpha. \quad (6)$$

The value of the forward voltage across the switch at the end of the pause is nearly equal to the maximum and it is:

$$U_{D(\vartheta=\pi)} = U_d + \omega L \frac{2T_I U_d}{\omega_0 L} F e^{-\frac{\delta \pi}{\omega}} \sin \left( \alpha - \frac{\pi}{\lambda} (\pi + \psi_{III}) \right).$$

In order to be developed a method for design in this mode, which is analogical to the complex mode method it is necessary to know the relative to the power supply

inverter voltage characteristics  $U' = \frac{U}{U_d}$  functionally

dependent from the hesitation coefficient of the parallel compensated resonant inverters  $k_{\Pi}$  and the frequency coefficient  $v$ . This purpose could be accomplished, using the equality between the inverter's input and output

active power:  $P_d = U_d I_d = UI = \frac{U^2}{R}$ , where I is the RMS value of the inverter current, and for determination of consumed current value it could be used expression (2).

Finally the RMS value of the load voltage is:

$$U' = \sqrt{R I_d}. \quad (7)$$

These characteristics are illustrated at fig. 3

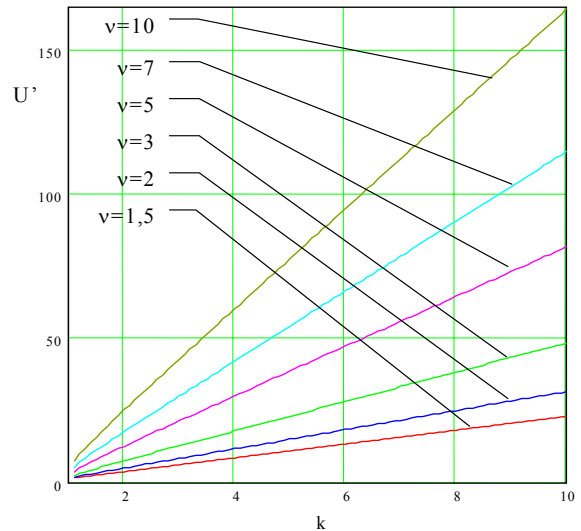


Fig.3 Output characteristics of parallel compensated resonant inverter, operating at active load

The recovery time of the devices is determined by the outstrip phase angle of the inverter current towards the load voltage  $\beta$  ( $tg\beta = \omega CR = \frac{v}{2} \frac{\omega_0}{\delta}$ ) and it is:

$$(8) \quad t_{qc} = \frac{\beta}{\omega}.$$

Using the expressions from (1) to (8) the parallel compensated resonant inverter could be designed both in active and complex load, because the tuned out parallel load circuit could be represented as parallel connected active resistance and capacitance. Besides this in the most cases when complex load is present, the energetically considerations for reactive power network relief, the parallel load circuit operates near the resonance, which simplifies significantly the analysis when the load is purely active [5].

### Conclusion

This analysis obtains the general expressions, which are necessary for the design of parallel-compensated resonant inverters, operating at active load. Particularly from the output characteristics, which are built at given values of the hesitation coefficients of the parallel compensated load  $k_p$  and frequency coefficient  $v$  it could be determined the range of the possible load voltage values, which are in the base of the analogical design method for complex load resonant inverters, proposed in [1, 8, 9].

This analysis could be used for other versions of parallel resonant inverters and active load (half-bridge resonant inverter and push-pull schematic), by using the known coefficients [1, 8, 9], relating their currents and voltages with the full-bridge ones.

### Reference:

- [1]. Bercovich E. I., G. V. Ivenskii, Y.S. Yoffe, A. T. Matchak, V. V. Morgun, *High-frequency thyristor converters for electrical networks*. Energoatomizdat, Leningrad, 1983 (in Russian).
- [2]. Bobtcheva M., St. Tabakov, P. Goranov, *Energy Converters*, TU-Sofia, 1997 (in Bulgarian).
- [3]. Bobtcheva M., N. Gradinarov and Co. *Power electronics*, TU-Sofia, 2001, (in Bulgarian).
- [4]. Gradinarov N., N. Hinov, "Analysis of autonomous resonant inverters, operating at complex load". Proceedings of the Sixth international conference for science and application "Electronics - ET'97" 24-27 September 1997, Sozopol, p.p. 68-73, (in Bulgarian).

[5]. Karov R., "Comparison between the conditions for periodical and aperiodical mode of serial and parallel current source inverter", Proceedings of the Ninth international conference for science and application "Electronics ET'2000" 20-22 September 2000, Sozopol, p.p. 231-218, (in Bulgarian).

[6]. Angelov, Kiril, "Reengineering", textbook, Sofia, TU-Sofia, 2004, (in Bulgarian).

[7]. Todorov T. S., *Autonomous Thyristor Inverters in the frequency converters for the electrical installations*. Dissertation, Gabrovo, 1987, (in Bulgarian).

[8]. Hinov N., N. Gradinarov, "Analysis of autonomous resonant inverters with forced commutation", Proceedings of the Sixth international conference for science and application "Electronics - ET'97" 24-27 September 1997, Sozopol, 61-67, (in Bulgarian).

[9]. Brichant F., L'ondistor, Dunod, Paris, 1974.

[10]. Dede E. J., J. Gonzalez, J. Jordan, V. Esteve, "On the design and experimental results of a high power, very frequency inverter for contour induction heating applications", Proc. of the PCIM'96 Conf. Nuremberg, Alemania, 1996, 263-269.

[11]. Dede E. J., J. Gonzalez, V. Esteve, J. Jordan, L. Lapiedra, E. Maset, "High frequency generator for induction heating", PCIM Europe Vol.3, No3 R.F.A., 1991, 160-165.

[12]. Angelov, Kiril, "Reengineering", manual, Sofia, ISBN 954-438-354-9, TU-Sofia, 2003, (in Bulgarian).

---

**Nikolay Hinov** – assistant, Ph.D., dept. Power Electronics, Faculty of electronic engineering and technologies, Technical University of Sofia, "8, Kliment Ohridski blvd.", 1000 Sofia, BULGARIA.

e-mail: [hinov@tu-sofia.bg](mailto:hinov@tu-sofia.bg).

**Nikola Gradinarov** – professor, Dr. Sc., dept. Power Electronics, Faculty of electronic engineering and technologies, Technical University of Sofia, "8, Kliment Ohridski blvd.", 1000 Sofia, BULGARIA.

e-mail: [n\\_gradinarov@tu-sofia.bg](mailto:n_gradinarov@tu-sofia.bg).

**Tsvetan Marinov** – engineer, Ph.D. Student, dept. Power Electronics, Faculty of electronic engineering and technologies, Technical University of Sofia, "8, Kliment Ohridski blvd.", 1000 Sofia, BULGARIA.

e-mail: [cmarinov@abv.bg](mailto:cmarinov@abv.bg).

**Vasil Trenkov** – engineer, dept. Power Electronics, Faculty of electronic engineering and technologies, Technical University of Sofia, "8, Kliment Ohridski blvd.", 1000 Sofia, BULGARIA.

e-mail: [trenkov@abv.bg](mailto:trenkov@abv.bg).

# Design of a modular DC/DC converter for Fuel cell application

DANG Bang Viet, Yves LEMBEYE, Jean BARBAROUX, Jean Paul FERRIEUX

**Abstract:** this paper presents a complete approach for the design of a DC/DC converter associated with a fuel cell. This design is carried out to find the best couple converter/fuel cell in regard with efficiency, cost, volume and reliability. The study starts with the presentation of all possible converter configurations. Interlacing effect is applied to solve the problem of high current - low voltage. The converter working and all components dimensioning is analysed analytically. Models for active and passive components losses determination are, then, presented. Losses, cost and volume are taken into account to compare all solutions. After, a global synthesis permits to conclude on the optimized association. Finally, the chosen converter is realized to valid our choice.

**Keywords:** modular converter, high current - low voltage, fuel cell interface, interlacing effect, losses model.

## 1. Introduction :

The Fuel cell (FC) is currently known as an effective electric generator using hydrogen which is considered as an interesting energy vector for the future [1], [2] and [3]. In order to be usable, it is necessary to have a power electronic (PE) interface system to adapt it to the load. Thus, the objective of this paper is to provide a new design of a PE converter for the FC based on the possibility of modularity so as to solve the problem of efficiency, cost, volume and reliability. The design will begin with an analysis on a unitary structure and the possibilities to associate several of this unitary structure in series or in parallel (modular aspect) in order to answer to the given project specifications. In this part, variables  $m$  (number of interlaced branches in a unitary converter),  $n$  (number of FC in series per group),  $g$  (number of FC - converters groups connected in series or in parallel) are introduced to vary the system configuration. Then, the analysis of the dimensioning of each structure is necessary to choose components. After, to compare the various structures, the evaluation of losses in active and passive components is presented. Finally, the analysis of results will conclude on the interests of the selected structures and on the modularity.

## 2. Project specifications:

This paper will present the study and the dimensioning of converters using one or several modules of FC of 2.5kW to produce a 2.5kW to 10kW generator aiming at telecommunication applications. Each module of FC consists of 100 cells of 80cm<sup>2</sup> surface which gives a nominal output voltage of 60V corresponding to a nominal current of 42A and with a voltage of 100V at off load. The output voltage of the converter is 48V DC. By looking at the specifications, we can notice that this application requires a step-down converter. The constraints in current and in voltage lead us to the high current - low voltage domain. In addition, we have to care about the other specific characteristics of FC like: low ripple output current and variation of voltage and current in function of the output power.

## 3. Analysis on the unitary structures and their associations.

### 3.1. Unitary structures:

The step-down converter power varies from 2.5 kW to 10 kW and the voltage level doesn't require an isolated structure. In this range of power and voltage, the interlaced BUCK (fig. 1) takes absolute superiority. In fact, the effect of interlacing allows a reduced dimensioning in current, FC current ripple and the possibility to cancel output current ripple. In addition, the behaviour of this converter is robust, well known and the conversion remains possible even with a default in a branch. But the interest of the current reduction thanks to the increase in number of branches is limited by the complexity of the system. A variable  $m$ , number of branches, is thus introduced to find the optimal number of branches.

### 3.2. Analysis on structures association:

#### \* Association of the converter inputs:

For a power corresponding to a given number of modules of FC, we can connect several FC in series and then connect the unit to a converter or each FC connected with a converter. The connection in parallel of FC is impossible because of impossibility to control the output power distribution in each FC.

#### \* Association of converter outputs:

The output of a converter can be connected in parallel for a low output voltage or in series for a high output voltage.

The configuration of a system FC - converter is, thus, determined by:

- $n$ : number of FC in series in each group.
- $m$ : number of branches interlacing.
- $g$ : number of groups FC - converter.

By varying the values of  $n$ ,  $m$ ,  $g$ , we obtain all the possible configurations of the system. They are presented fig.1, fig. 2 and fig. 3.

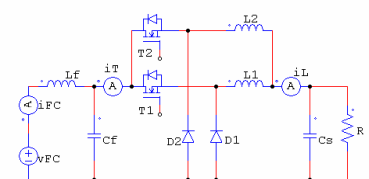


Fig. 1. BUCK interlaced (m branches T-D-L)

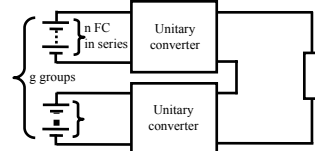


Fig. 2. Output connected in series

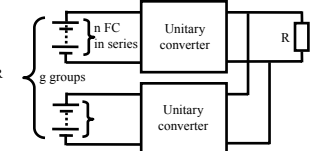


Fig. 3. Output connected in parallel

## 4. Analysis of the structure behaviour:

### 4.1. Interlacing effect:

Interlacing allows a dimensioning reduced in current not only in average value but still a less ripple. The relation between the ripple of the total current and that in each branch is given by:



$$\frac{\Delta I_{Lk}}{\Delta I_L} = \frac{1}{m - \frac{m_1(m_1 - 1)}{am} - \frac{m_2(m_2 - 1)}{(1 - \alpha)m}}$$

and is presented in figure 4.

with  $m_1 = [\alpha m] + 1$ ;  $m_2 = [(1 - \alpha)m] + 1$

where  $\alpha$  is duty cycle

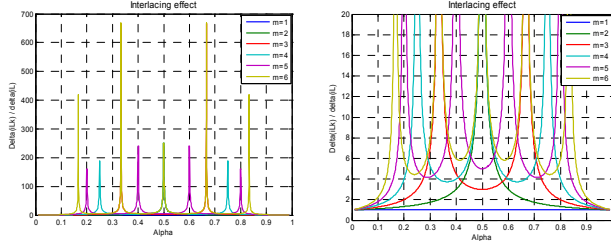


Fig. 4. Interlacing effect

Zoom of the figure 4.

With a fixed ripple of output current  $\Delta I_L$ , we can easily calculate the ripple in each branch and determine the current in each component (transistor, diode, and inductor).

We can notice that with a high ripple of current in each branch ( $i_{Lk}$ ), a low ripple (even ripple zero if  $\alpha m$  is entity) can be obtained in the output ( $i_L$ ). But this favour is limited by various conditions such as: continuous conduction of inductor current, losses in inductors. These disadvantages and favours will be presented in the next paragraphs.

#### 4.2. Input filter capacitor $C_f$ :

In an interlaced BUCK, this capacitor is the passive component the most difficult to dimension due to the variety of current waveforms (in function of number of branches and duty cycle) to filter. It essentially influences the converter volume, especially in high voltage domain.

The value of this capacitor is determined by:  $C_f = A / \Delta V_s$  where  $A$  is the area limited by the positive (or negative) part of the current and the Ox axis. This area varies in function of the duty cycle and the number of branches. We will calculate this value for the case  $m = 3$ . This result is applicable with others values of  $m$ .

- When  $\alpha m < 1$ ,  $i_T$  will be discontinuous (fig. 5):

$$A = \left(1 - \frac{\alpha m}{2}\right)^2 \frac{\alpha T \cdot I_{Tmax}}{2}$$

- When  $\alpha m$  is integer, two transistors commutate at the same time (fig. 6):

$$A = \frac{1}{4} \cdot \frac{\Delta i_{Lk}}{2 \cdot m \cdot F}$$

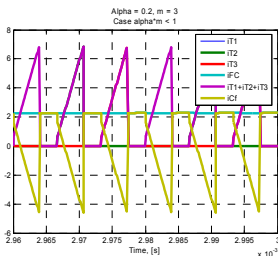


Fig. 5. Total current discontinuous

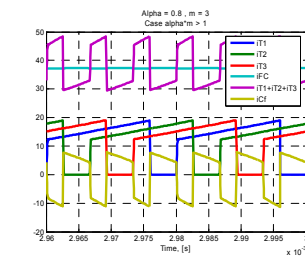


Fig. 7. Total current continuous – Only one transistor commutate at one moment

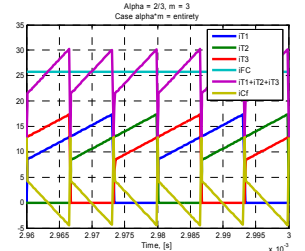


Fig. 6. Two transistors commutate at the same time

- When  $\alpha m > 1$  and different to integer (fig. 7):

This case is more complex. By introducing the variables  $a_p$ ,  $a_n$ ,  $\alpha'$ ,  $T'$ ,  $x$ , we can calculate the current in  $C_f$  in 3 sub-cases where the current in  $C_f$  is in intersection with Ox axis in the middle of  $I_{min}$  (fig. 7a), in the slope  $a_p$  (fig. 7b) or in the slope  $a_n$  (fig. 7c).

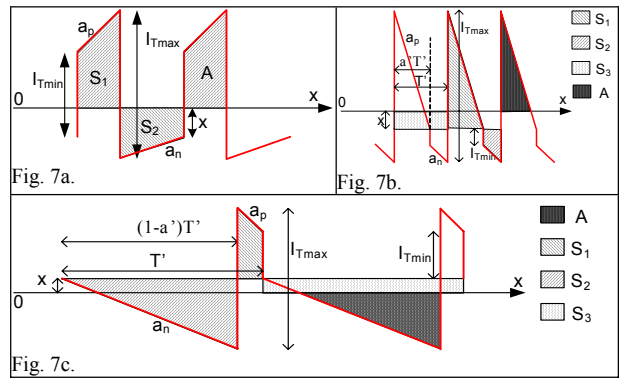
Case a:

$$A = S_2 = (\Delta I_p + \Delta I_n + 2 \cdot I_{T\_min}) \cdot \alpha' (1 - \alpha') T'$$

$$\text{Case b: } A = S_1 - \frac{1}{2} \left(2\alpha' T' - \frac{x}{a_p}\right) x$$

Thanks to the interlacing effect, input current ripple is lower. Capacitor's size is, thus, reduced. This dimensioning method is applicable for the output filter capacitor in the interlaced BOOST due to the same characteristics.

$$\text{Case c: } A = S_2 - \frac{1}{2} \left(2(1 - \alpha') T' - \frac{x}{a_n}\right) x$$



#### 4.3. Input filter inductor $L_f$ :

This inductor is calculated by the first harmonic method:

$$L_f = \frac{\Delta V_{Cf}}{\Delta i_{FC} \cdot \omega_f} = \frac{10\% V_{FC}}{10\% I_{FC} \cdot \omega_f} = \frac{V_{FC}}{I_{FC} \cdot \omega_f}$$

where:  $\omega_f = m \cdot 2 \cdot \pi \cdot F$

#### 4.4. Output filter capacitor $C_s$ : $C_s = \frac{\Delta I_s}{8 \cdot m \cdot F \cdot \Delta V_s}$

#### 4.5. Losses prediction in components:

The component losses prediction contributes for a significant part in the comparison and the choice of structures.

##### 4.5.1. Inductors:

The dimensioning of inductors is based on the area product (windows area and cross section). In a switching-mode power supply (SMPS), losses in inductors are composed by copper losses and core losses. The first are caused by skin effect and proximity effect. The second are due to the hysteretic phenomena and eddy currents. When the current ripple isn't very high, the copper losses are essential.

The prediction of these losses is achieved by the Dowell method [5]. The figure 8 shows the computation result of the serial resistance of an inductor versus the frequency corresponding to 2 types of wire: AWG wire and Litz wire. At the working frequency of SMPS (until about 100 kHz), skin effect

is predominant causing a higher resistance in AWG wire than in Litz wire. But, at high frequencies, it is the proximity effect that causes essentially losses.

Core losses (in the case of non saturation of the core) are determined by the Steinmetz method:

$$P_{\text{core}} = k \cdot f^a \cdot (B_{\text{ac}})^d$$

Where  $k$ ,  $a$ ,  $d$  are constants

depending on the material of the core used and  $B_{\text{ac}}$  the AC maximal induction in Tesla. It can be noticed that core losses and copper losses in the AWG wire are considerable when the current ripple is high. This will unbalance interlacing benefit.

#### 4.5.2. Semi conductor:

- Transistor MOS:

The model for conduction losses is represented by a resistance  $R_{\text{DS(on)}}$ :

$$P_{\text{MOS}} = R_{\text{DS(on)}} I_{\text{RMS}}^2$$

Switching losses and additional losses due to capacitive effects are calculated as presented after:  $P_{\text{off}} = \frac{1}{2} E \cdot I_{\text{off}} \cdot t_{\text{off}} \cdot F$  and  $P_{\text{on}} = \frac{1}{2} E \cdot (I_{\text{on}} + R_{\text{RRM}}) \cdot t_{\text{on}} \cdot F$ ,  $P_{\text{capa}} = \frac{1}{2} C_{\text{oss}} \cdot E^2 \cdot F$

Using several MOS in parallel allows a reduction of conduction losses in these components but increase losses due to capacitive effects.

- Diode: Conduction losses in a diode are given by  $P_{\text{diode}} = V_0 I_{\text{dav}} + R_{\text{DS(on)}} I_{\text{RMS}}^2$ . The turn-off switching losses during the reverse recovery period are given by:

$$P_{\text{off}} = F \int_0^{t_{rr}} i_{\text{diode}} \cdot E dt = \frac{1}{2} t_{rr} \cdot I_{\text{RRM}} \cdot E \cdot F$$

Due to the relatively low frequency working of the converter, diode and MOS switching losses are negligible compared to conduction losses.

- IGBT: the conduction loss in an IGBT is due to the voltage drop  $P_{\text{con}} = V_0 \cdot I_{\text{av}} + R_0 I_{\text{RMS}}^2$ . The IGBT switching losses are not negligible due to the tail current. Manufacturers usually give in datasheets the switching losses  $E_{\text{on}}$  and  $E_{\text{off}}$ .

+ Turn-off switching loss:  $P_{\text{com\_off}} = E_{\text{off}} \cdot F$

+ Turn-on switching loss:  $P_{\text{com\_on}} = E_{\text{on}} \cdot F$

#### 4.5.3. Capacitor:

Losses in the capacitor are determined using the equivalent series resistor (ESR). In our case these losses are low and negligible. Nevertheless, the capacitor influences essentially the converter volume.

### 5. Synthesis :

The systematic study of all possible configurations

	2.5kW	5kW	7.5kW	10kW
1	4	8	12	16
2	4	8	12	16
3	6	12	12	18
4	4	8	12	16
5	5	10	15	20
6	6	12	12	18

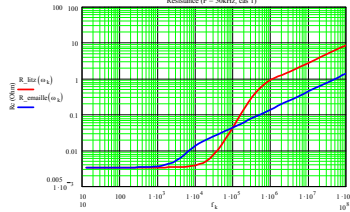


Fig. 8. Serie resistance prediction in the inductor with Litz wire and AWG

permits us to determine, for each of them, losses in components and volume of inductances as well as their cost. These are the various criteria which will permit us to compare the various configurations.

In this paper, we have also presented the interests and the limits of interlacing effect. It offers the possibility to reduce the size of all passive components while maintaining constant ripple of input or output current and voltage. Figure 13 shows that it is not, therefore, interesting to increase the number of branches. In fact, to assure a correct working of the system, we can't tolerate a too important ripple in each branch (in this study, rate of ripple forced to a maximal value of 160% to ensure the continuous conduction). On the other hand, the reduction of inductance is limited by its loss. Indeed, when  $L$  decreases, current ripple in each branch increases causing high losses in this one. Figure 13 shows the relation between maximal ripple current and the value corresponding to optimal losses. In fact, optimal ripple is about of 20% - 60% of average value. Figure 9 shows the limit of the interest of interlacing according to the number of branches with various powers. We can, for

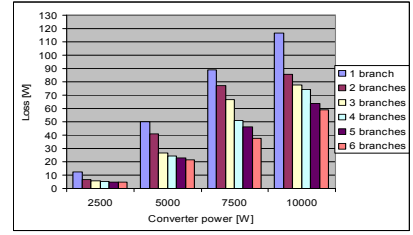


Fig. 9. Total losses in the inductors

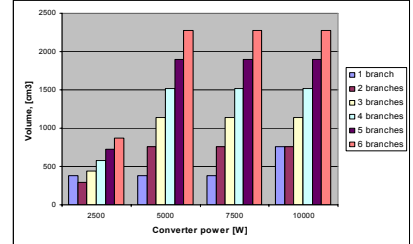


Fig. 10. Volume of inductors

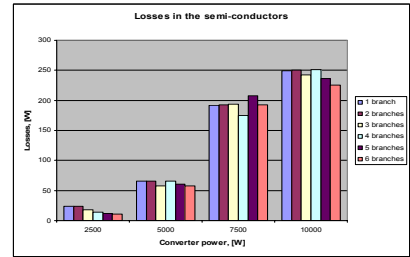


Fig. 11. Losses in the SC

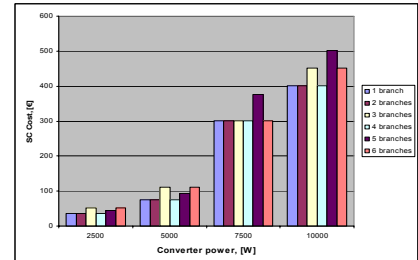


Fig. 12. Cost of SC

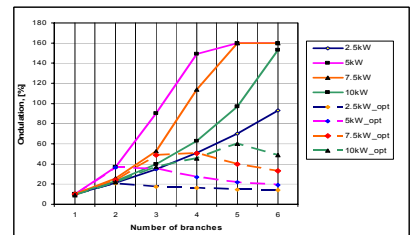


Fig. 13. Interlacing effect on current ripple

to a maximal value of 160% to ensure the continuous conduction). On the other hand, the reduction of inductance is limited by its loss. Indeed, when  $L$  decreases, current ripple in each branch increases causing high losses in this one. Figure 13 shows the relation between maximal ripple current and the value corresponding to optimal losses. In fact, optimal ripple is about of 20% - 60% of average value. Figure 9 shows the limit of the interest of interlacing according to the number of branches with various powers. We can, for

example, stop with 2 branches for a 2.5kW converter or 3 for the a 5kW, 4 or 5 for the a 7.5kW... Beyond that, there is no more profit on the losses. On the other hand, volume continues to increase (fig. 10).

Figure 11 and 12 show the interest to use low voltage SC ( $V_{SC} < 200V$ ) as they present less losses and are cheapest. We can notice that losses in SC are higher than losses in inductance, especially with high voltage SC. Because of the important influence on losses, the number of SC used is given in table 1. With the same number of SC and at the same power, losses in SC are constant and are independent of number of branches.

All these results tend to show that it is more interesting, in this application, to use several modules of 2.5kW in parallel to produce a higher power converter (for example 10kW) than to use only one high power converter. Moreover, the use of several modular converters makes possible to operate in default modes (default of 1 module). The realization of a 2 branches BUCK of 2.5kW is presented in the following paragraph.

## 6. Experimental results:

A 2 branches BUCK of 2.5 kW is realized.

Inductance parameters: core 58438A2 of MAGNETICS with 14 turns.  $L_0$  (non load) = 63  $\mu H$ ,  $L_{nom}$ (nominal load) = 36  $\mu H$ .

MOS: IRFP90N20D, 2 MOS per branch.

Diode: 30EPH02, 1 diode per branch.

Input filter: 5 capacitors of 2.2  $\mu F$ , 100V MKS4 of WIMA in parallel. Input filter inductor: core 58324A2 of MAGNETICS with 6 turns,  $L = 2.5\mu H$  at nominal load.

Output filter: 2 capacitors of 2.2  $\mu F$ , 100V MKS4 of WIMA in parallel.

Waveforms of the ripple current and of the output voltage of the converter realized is represented in figures 14 to 16.

At nominal load, efficiency is of 97.4%. Current ripple in each branch is of 5A corresponding to 20% of  $I_{Lk\_av}$ . Output current ripple is of 3.5A = 7% of  $I_{load\_av}$ . Fuel cell current ripple is of 2A = 5% of  $I_{FC\_av}$ . Output voltage (fig. 16) is controlled at 48V with a low residual ripple (4%).

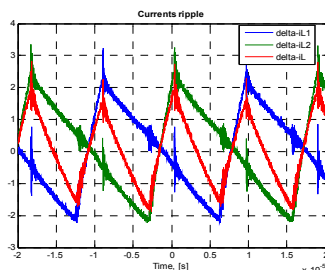


Fig. 14. Current ripple in each branch and output current ripple – nominal load

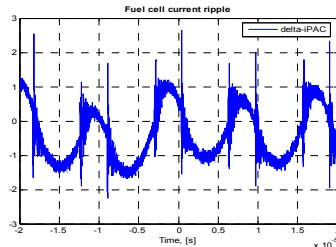


Fig. 15. Fuel cell's current ripple – nominal load

The current and voltage quality is better than analytical prediction thanks to a higher value of filter inductance.

Figure 17 shows the special case when  $\alpha_m = 1$ . It is the case of low load where fuel cell's voltage increases to 98V corresponding to the duty cycle of 0.5. Although a high current ripple is present in each branch and the output current ripple is zero.

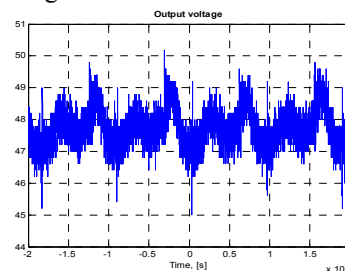


Fig. 16. Output voltage - nominal load

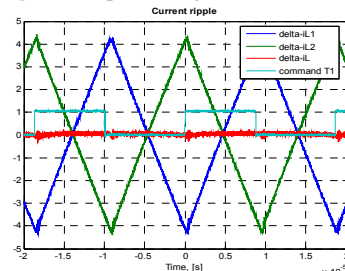


Fig. 17. Current ripple in case of low load

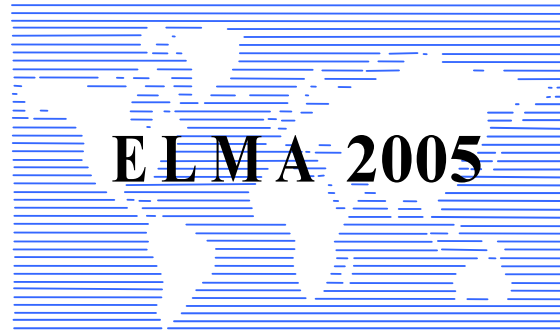
## 7. Conclusions:

In this paper, we have presented an analysis on choice of a unitary structure and the association of several of this unitary structure to solve the problem of high current - low voltage applications. Then, the behaviour of the converter is studied and favours and drawbacks of interlacing effect is presented. The dimensioning of passive and active components is analyzed versus the number of branches and of the duty cycle. Losses models for active and passive components are, then, constructed. This represents an important point of this work. The systematic study of all possible configurations offers us a global view of all aspects, efficiency, volume, cost and reliability. It enables us to conclude on the possibility to manufacture modular converters. In the studied case, the 2 branches BUCK of 2,5kW have to be chosen. Finally, a prototype is realized to valid these results.

## References:

- [1] Clé CEA No 44, Hiver 2000 – 2001
- [2] National Fuel cell research center, Power electronics for Fuel Cell Workshop, August 8 – 9, 2002
- [3] Future energy challenge, August 31, 2001
- [4] J.P. FERRIEUX – François FOREST « Alimentation à découpage – Convertisseurs à résonance »
- [5] G. LEFEVRE « Conception de convertisseur statiques pour l'utilisation de pile à combustible » - Thèse INPG 2004
- [6] Magnetic powder core data 2002 – [www.mag-inc.com](http://www.mag-inc.com)
- [7] Website <http://fr.farnell.com/>

**DANG Bang Viet** Ph.D. student: [dang@leg.ensieg.inpg.fr](mailto:dang@leg.ensieg.inpg.fr)  
**Y. LEMBEYE** Pr. assistant: [Yves.Lembeve@inpg.fr](mailto:Yves.Lembeve@inpg.fr)  
**J. BARBAROUX** Engineer: [Jean.barbaroux@inpg.fr](mailto:Jean.barbaroux@inpg.fr)  
**J.P. FERRIEUX** Professor: [Jean-Paul.Ferrieux@inpg.fr](mailto:Jean-Paul.Ferrieux@inpg.fr)  
 Laboratory Electro-technique of Grenoble  
 ENSIEG, BP46, 38402 St Martin d'Hères Cedex – FRANCE



---

---

# **ELECTRICAL MACHINES IV**

---

---



## Experimental determination of non-linear parameters of a single-phase commutator motor

Gancho Bojilov, Adrian Ivanov, Nezabravka Ivanova

**Abstract:** In this paper is proposed an approach for determination of non-linear parameters of a single-phase commutator motor by an experimental way that is necessary for investigation of transients and sensorless control of motors. By means of non-linear character of the inductance of coils, they are not constants and they are functions of the current of the motor. For their experimental determination some electrical values of the field and armature circuits are measured. There are used some equations for calculation of inductances, which follows from the phasor diagram of the motor, constructed with appropriately arranged vectors.

**Keywords:** single-phase commutator motor, non-linear parameters, experimental determination, transient

### Introduction

Single-phase commutator motors with series excitation (SPCM) have an extremely high practical use, when they are used for operating of electrical tools and appliances [12]. Very often in modern electrical tools sensor less control of the speed is applied. For this reason it is necessary to know the equations of magnetic fluxes and inductances of coils from the current of the motor.

Well-known is the fact that these motors operate generally in transients, connected with frequent starts, stops, reversals and changes of the load and because of that reason investigation of the transients is of great importance. Their investigation consists in formulation of differential system equations, which describe their electromagnetic and electromechanical condition. The currents are unknown in these systems, and the coefficients before them are the parameters of the motor – resistances and inductances of the coils. SPCM are non-linear devices, and for an accurate description of the processes, running in them, it is necessary to make a non-linear mathematical model of the motor. The currents are unknown in this model, and the coefficients before them are a function of the currents themselves.

The non-linear character of the inductances can be an electromagnetic, electro mechanic or electro thermal one that complicates the mathematical description for analysis of the processes. The solution of the mathematical problem is divided into two parts:

1 - Task of the magnetic field theory which gives the nonlinearity of electromagnetic character. The nonlinearity of electromagnetic character is a result of the magnetic saturation of the magnetic circuits, the inductances of the coils are a function of the currents which flow through them;

2 - Task of the circuits theory, which also gives the

nonlinearity of the electromechanic character. The nonlinearity of the electro mechanic character expresses itself in that the self-inductances and the mutual inductances of the coils are functions of the currents and of the rotating angle of the rotor.

It is very often that by investigation of the processes into the electrical machines by mathematical models arises the question about an estimate of their accuracy. For this purpose it is necessary to specify the results to compare with the experimental ones. The accuracy of the model depends on the accuracy of the solution of these two tasks, coupled with each other by means of approximating analytic functions of the fluxes and of the inductances from the currents into the coils. For this reason an “intermediate” check of the results, obtained from the determination of the task of the magnetic field theory has to be made.

### Determination of the nonlinear parameters by an experimental way

The calculations are made for a single-phase commutator motor with series excitation having catalogue data:  $P_n=80\text{W}$ ,  $U_n=220\text{V}$ ,  $I_n=0,75\text{A}$ ,  $n_n=5000\text{min}^{-1}$ ,  $\eta_n=0,56$ ,  $\cos\phi_n=0,77$ , which are the rated values.

One of the typical features of making a mathematical model for solving the magnetic field for these kinds of motors [1,4,9,10] is the determination of the correct points for measurement of the respective magnetic fluxes. These points are directly dependent on the geometrical location of the brushes in relation to the geometrical neutral line (g.n.l.) as it is shown on Figure 1a and Figure 1b. The parts of the magnetic flux vectors are represented in co-ordinate systems: dq-connected with geometrical neutral line and d'q'-connected with the line of the brush position.

For the calculation of the experimental results equations are used, got by means of analysis of the phasor diagram of SPCM, as that is shown on Figure 2. The phasor diagram of the voltages is constructed according to the classic theory of SPCM [11], but with rearranged vectors. This originates from the vectors of the measured voltage in excitation and armature circuits.

$M$ -total torque,  $P_I$ -input power,  $U$ - supplied voltage,  $I$ -current,  $U_a$ -voltage in the armature circuit,  $U_f$ -voltage in the field circuit,  $R_a$  and  $R_f$  – resistances of the armature and field coils are measured. The phase angles between vectors of specific values are shown on Figure 2. From the phasor diagram originate following equations

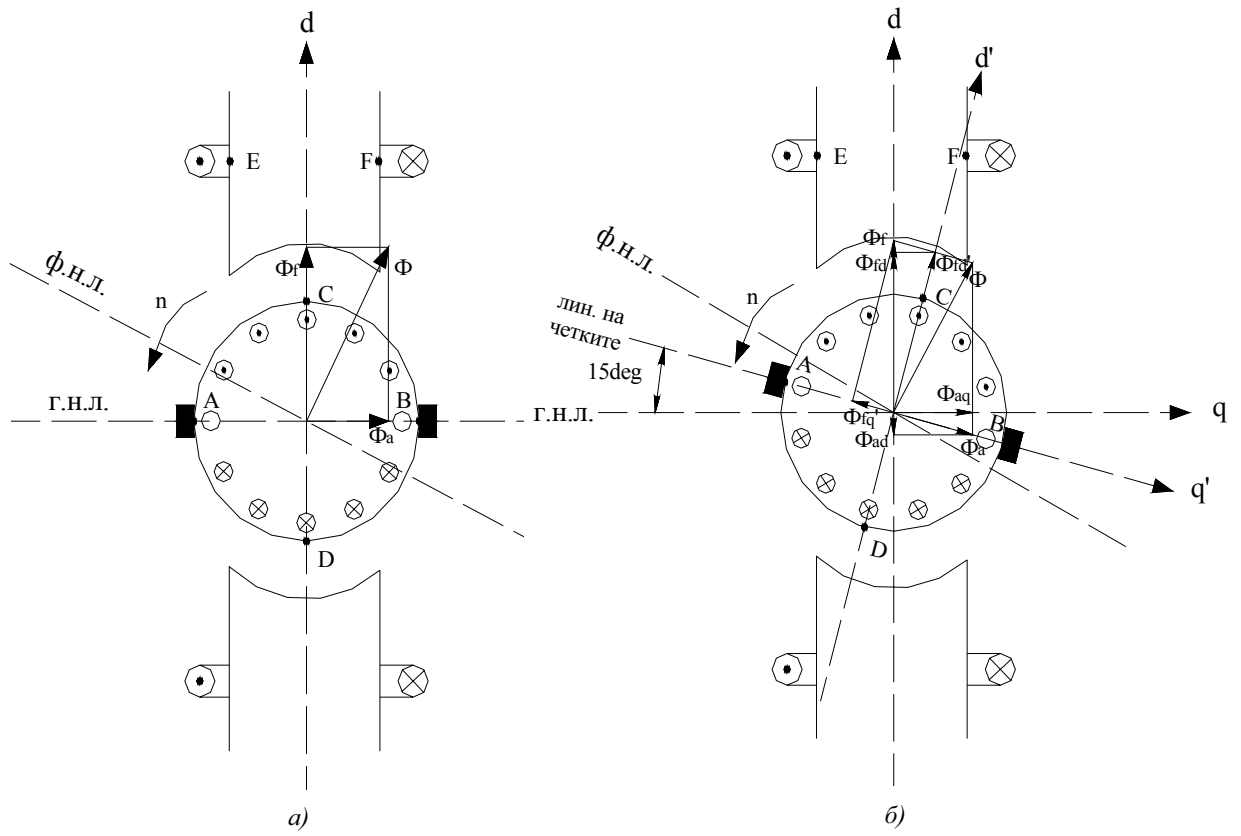


Fig.1. Two dimensional representation of magnetic field in vector mode of SPCM:

a) brushes situated in geometrical neutral line

б) brushes moved to  $15^\circ$  from geometrical neutral line

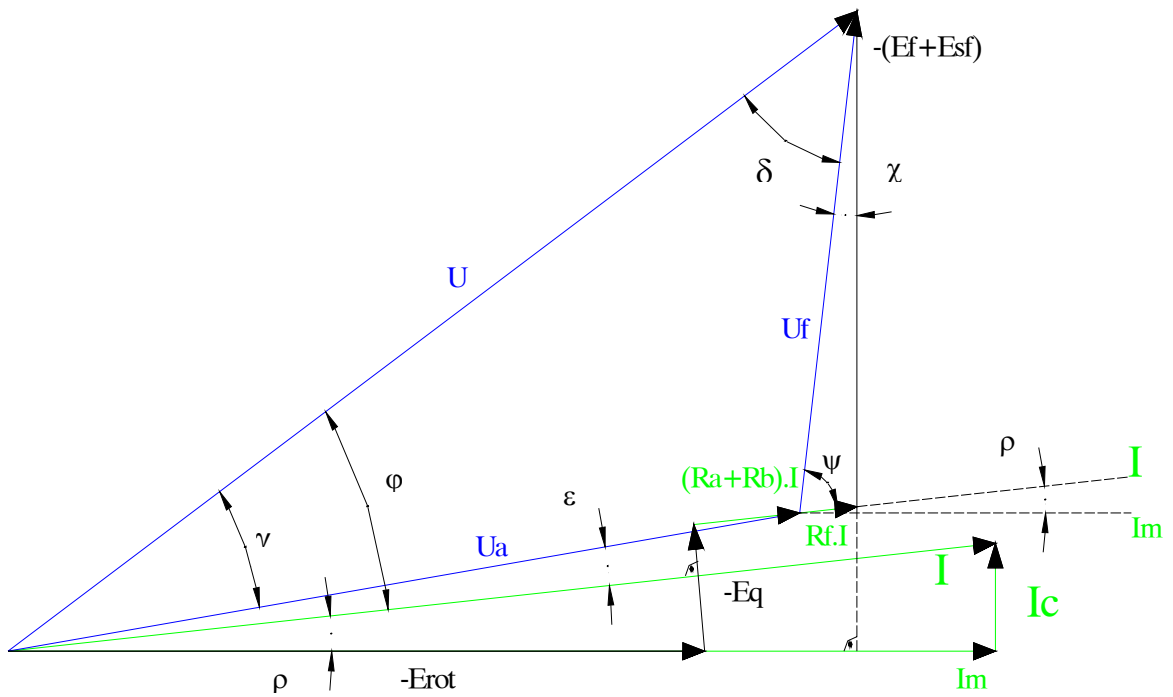


Fig.2. Phasor diagram of SPCM

$$(1) \quad \gamma + \delta = \arccos \frac{U^2 - U_a^2 - U_f^2}{2U_a U_f}$$

$$(2) \quad \gamma = \arctg \frac{U_f \sin(\gamma + \delta)}{U_a + U_f \cos(\gamma + \delta)}$$

$$(3) \quad \varepsilon = \varphi - \gamma$$

$$(4) \quad \psi = \gamma + \delta + \varepsilon$$

$$(5) \quad E_f + E_{\sigma f} = \sqrt{(U_f \sin \psi)^2 + (U_f \cos \psi - R_f I)^2}$$

where  $E_f$  is the e.m.f. of the self-inductance of the excitation circuit produced from general magnetic flux;  $E_{\sigma f}$  – the e.m.f. of the self-inductance of the excitation circuit produced from magnetic leakage flux;  $\sigma$  – factor of leakage from data got by investigation of magnetic field by the program FEMM [2,5].

$$(6) \quad E_f = \frac{E_f + E_{\sigma f}}{\sigma}$$

$$(7) \quad \chi = \arccos \frac{U_f^2 + (\sigma E_f)^2 - (R_f I)^2}{2U_f \sigma E_f}$$

$$(8) \quad \rho = \arccos \frac{U_f \sin \chi}{R_f I}$$

where  $\rho$  is the phase angle between vectors of the magnetized current and of the total current, grounded of magnetic loss in armature and excitation because in these coils runs an alternative current.

$$(9) \quad E_{rot} = \frac{U_a \cos \varepsilon - R_a I}{\cos \rho}$$

where  $E_{rot}$  is the rotating e.m.f.

$$(10) \quad E_q = \frac{U_a \sin(\varepsilon + \rho)}{\cos \rho} - R_a I \operatorname{tg} \rho$$

where  $E_q$  is the total e.m.f. of self-inductance of the armature coil produced from the magnetic flux of armature reaction in the direction of the q-axis and through mutual inductivity from e.m.f. of transformation (when the brushes are moved).

The magnetic flux produced from the current of the excitation coil in direction of axes d

$$(11) \quad \Phi_f = \frac{E_f}{2\pi f w_f}$$

The magnetic flux of leakage of the excitation coil

$$(12) \quad \Phi_{\sigma} = \frac{E_{\sigma f}}{2\pi f w_f}$$

The resultant magnetic flux into the air gap

$$(13) \quad \Phi_{\delta} = \frac{E_{rot}}{\Omega w_a'}$$

The magnetic flux of the armature reaction in direction of the q-axes produced from the current of the armature coil

$$(14) \quad \Phi_q = \frac{E_q}{2\pi f w_a'}$$

Mutual inductance of the resultant magnetic flux into the air gap

$$(15) \quad L_m = \frac{\Psi_{\delta}}{I \cos \rho} = \frac{w_a' \Phi_{\delta}}{I \cos \rho}$$

Self-inductance of the excitation coil

$$(16) \quad L_f = \frac{\Psi_f}{I} = \frac{w_f \Phi_f}{I}$$

Self-inductance of leakage of the excitation coil

$$(17) \quad L_{\sigma f} = \frac{\Psi_{\sigma f}}{I} = \frac{w_f \Phi_{\sigma f}}{I}$$

Self-inductance of the armature coil produced from the magnetic field of armature reaction

$$(18) \quad L_q = \frac{\Psi_q}{I} = \frac{w_a' \Phi_q}{I}$$

where  $w_f$  is the number of windings of the excitation coil,  $w_a'$  – the effective number of windings of the armature coil [7,8].

The magnetic fluxes are approximated with the following fractional-rational functions determined by the program SigmaPlot 8.02 [3].

$$(19) \quad \Phi_f = \frac{a_1 I}{b_1 + I}$$

$$(20) \quad \Phi_{\delta} = \frac{a_2 I}{b_2 + I}$$

$$(21) \quad \Phi_q = \frac{a_3 I}{b_3 + I} + c_3 I$$

Dynamic inductance of the excitation coil

$$(22) \quad L_{fd} = \frac{d\Psi_f}{dI} = w_f \frac{d\Phi_f}{dI} = w_f \frac{a_1 b_1}{(b_1 + I)^2}$$

Dynamic inductance of the armature coil produced from the magnetic field of armature reaction



$$(23) \quad L_{qd} = \frac{d\Psi_q}{dI} = w_a' \frac{d\Phi_q}{dI} = w_a' \left[ \frac{a_3 b_3}{(b_3 + I)^2} + c_3 \right]$$

### Graphical performance of the experimental results and the results obtained from the calculation

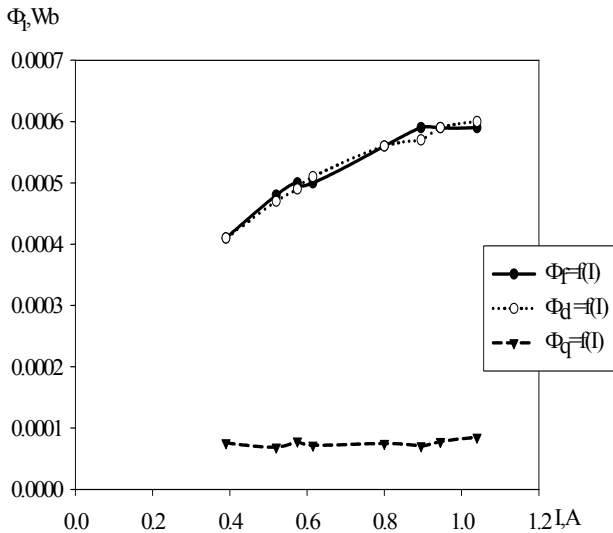


Fig.3. Dependence of the magnetic fluxes from the current of the investigated SPCM

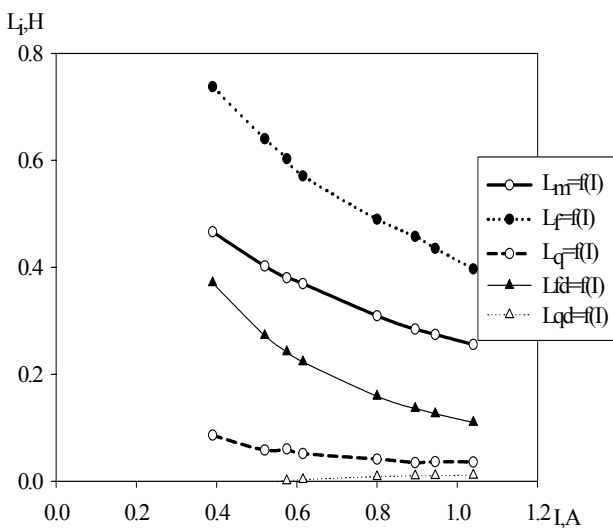


Fig.4. Dependence of the inductances from the current of the investigated SPCM

### Conclusion

The mathematical method developed in this article can be effectively used for determining the accuracy of the results obtained for the non-linear parameters of SPCM, which are received from the solution of the task

for the magnetic field. A typical feature of this method is the small number of necessary input values as they can be determined easily by experimental way. The mathematical method used for the determination is simple for use.

### References

- [1] MATLAB R12, High performance numeric computation and visualization software – reference guide, The Math works, 1992.
- [2] Meeker, D., Finite Element Method Magnetics, FEMM 4.0, Ver. 3.3, User's Manual, 2002.
- [3] SigmaPlot 8.02 Demo, User's Guide, SPSS Inc. 2003.
- [4] Mathcad 11 Trial version, Mathsoft Engineering & Education Inc. 2001.
- [5] Брандиски, К., И. Ячева, САД системи в електромагнетизма, С., Сиела, 2002.
- [6] Божилов, Г., Заместваща схема на еднофазен колекторен двигател, Е+Е, 2003, No 7-9.
- [7] Божилов, Г., А. Иванов, Нелинейна заместваща схема на еднофазен колекторен двигател, свързана с метода на крайните елементи, Е+Е, 2004, No7-8
- [8] Божилов, Г., М. Михов, А. Иванов, Нелинеен математичен модел на електромеханичните преходни процеси в еднофазен колекторен двигател, базиран на метода на крайните елементи – I част – постоянен ток. Годишник на ТУ – София, т. 52, 2003.
- [9] Божилов, Г., Е. Рац, М. Михов, А. Иванов, Нелинеен математичен модел на електромеханичните преходни процеси в еднофазен колекторен двигател с отчитане на загубите в стоманата – II част – променлив ток. Годишник на ТУ – София, т. 53, 2004.
- [10] Божилов, Г., Е. Рац, М. Михов, А. Иванов, Симулационен модел на еднофазен колекторен двигател с отчитане на нелинейната магнитна характеристика на магнитопровода. Годишник на ТУ – Варна, 2004.
- [11] Попадиин, Ст., Електрически микромашини ч. II. С., Техника, 1970.
- [12] Catalogues and business materials of Bosch, Huskvarna, Sparky and Black & Decker.

**Gancho Bojilov** – Professor, DSc., Faculty of Electrical Engineering, Technical University of Sofia, 8 Kl. Ohridski Str., 1000 Sofia, BULGARIA.

e-mail: [gboj@tu-sofia.bg](mailto:gboj@tu-sofia.bg)

**Adrian Ivanov** – Assistant Professor, Faculty of Electrical Engineering, Technical University of Sofia, 8 Kl. Ohridski Str., 1000 Sofia, BULGARIA.

e-mail: [api@tu-sofia.bg](mailto:api@tu-sofia.bg)

**Nezabravka Ivanova** – Ph.D. Student, Faculty of Electrical Engineering, Technical University of Sofia, 8 Kl. Ohridski Str., 1000 Sofia, BULGARIA.

e-mail: [nezi\\_ivanova@tu-sofia.bg](mailto:nezi_ivanova@tu-sofia.bg)

# Replacement of the standard graphic concept of synchronous machines Potier's diagram with analytic calculation

Miho Mihov and Gancho Bojilov

**Abstract:** It's well known that Potier diagram consists of two parts: phasor voltage diagram and spatial current diagram. Their connection is based on no-load test characteristic of the machine  $U_0 = E_0 = f(i_f)$ , which application gives the possibility to be calculated the magnetic circuit saturation. In this material the no-load characteristic is presented analytically, which eliminates the necessity of graphical operations. By this way arises the opportunity to use proper software products for defining the parameters.

**Keywords:** synchronous machines, Potier diagram, no-load characteristic

## Introduction

To develop and exploit the synchronous machines (SM) it's necessary to define the following quantities: electromotive force (e.m.f.)  $E_0$ , excitation current  $i_f$ , loading angle  $\theta$ , direct-axis armature reactance  $x_{ad}$  and saturation factor  $K_\mu$ , for the corresponding work opperation according to the real magnetic conditions – magnetic circuit saturation. In the specialized bibliography [1,2,3] is described a graphical approach for problem determination with Potier diagram – fig. 1. It consists of two parts - *phasor voltage diagram* and *spatial current diagram*.

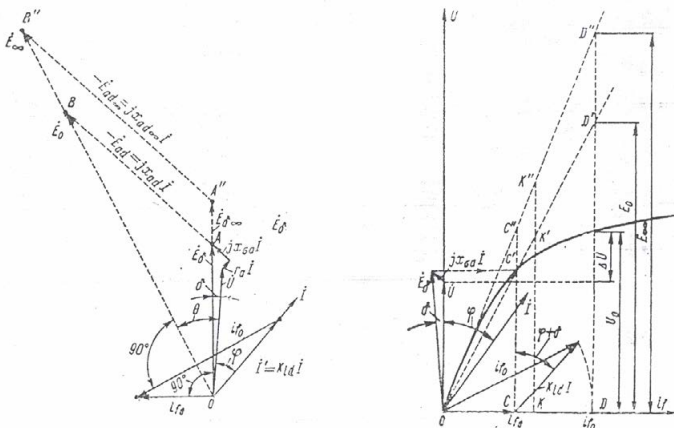


Fig. 1 Potier diagram and combination with its no-load characteristic

The saturation influence of magnetic circuit of SM is defined through graphical determination the necessary value couples for drawing the above mentioned phasor diagram - electromotive force and excitation current from the no-load characteristic  $U_0 = E_0 = f(i_f)$ .

Naturally, the graphical approach has few disadvantages with its subjective determination and accuracy, as well with the impossibility to automate the calculation process.

The saturation influence of magnetic circuit of SM is defined through graphical determination the necessary value couples for drawing the above mentioned phasor diagram - electromotive force and excitation current from the no-load characteristic .

Naturally, the graphical approach has few disadvantages with its subjective determination and accuracy, as well with the impossibility to automate the calculation process.

In the current paper is presented an analytical approach, which excludes the necessity of graphical readings. By this way we use specialized software as Matlab, Mathcad [5], where the calculation are done with complex numbers and if there is an appropriate organization - even with EXCEL.

## Method essence

With the help of this approach can be resolved direct and opposite tasks, for every concrete problem. The direct task follows the consequence for defining the values. It is  $U \rightarrow E_s \rightarrow i_{fs} \rightarrow i_{f0} \rightarrow E_0$ . In this case, the current in the excitation winding  $i_{f0}$  is an argument or function in the examined characteristic of the SM. These are the load characteristic  $U = f(i_{f0})$ , excitation characteristic  $i_{f0} = f(U)$ , short-circuit characteristic  $I_\kappa = f(i_{f0})$  and V – curves. In the opposite tasks the current in the excitation winding is a given parameter, just as it is in the external characteristics  $U = f(I)$ . In any case, the task resolving goes through defining the second co-ordinate of the no-load characteristic of the machine, which traditionally known is non-linear. In the present practice, this is made by graphical determination.

The graphical determination is substituted by application of analytical interpolation relationship for the curve, which should perform the following requirements:

- It should have minimal deviation from the input curve – machine's no-load characteristic  $U_0 = E_0 = f(i_f)$

- It should have, if it is possible, an analytical resolution for  $i_f$  with preliminary given  $E$ .

In the current paper is suggested an analytical relationship, which performs the requirements. It is a solution of the so called normal characteristic of the SM -  $E^* = f(i_f^*)$  i.e. the no-load characteristic in per-units [1,2,3]. The interpolation is made with the help of software product Sigma Plot [4]. Naturally, such an interpolation could be done for every numerical relationship with physical values. The suggested relationship is

$$(1) \quad E^* = \frac{ai_f^*}{b+i_f^*} + ci_f^*$$

with preliminary give is defined through

$$(2) \quad i_{fX}^* = \frac{-Y + \sqrt{Y^2 + 4cZ}}{2c}$$

where

$$(3) \quad Y = a + bc + E_X^*; \quad Z = bE_X^*$$

The interpolation relationship coefficients have the following values

$$(4) \quad a = 3.209850 \quad b = 1.78268 \quad c = -0.181924$$

With the physical values are taken into consideration the equation (1) is

$$(5) \quad E(i_f) = U_n i_f \left( \frac{a}{bi_{fn} + i_f} + \frac{c}{i_{fn}} \right)$$

The direct task is resolved as a non-salient pole synchronous machine in the following input data: SM no-load characteristic, SM supply voltage  $U$ , current in the armature winding  $I$  and phase angle according the voltage  $\varphi$  in a voltage oriented frame of reference  $/\varphi_U = 0/$ , the phasor  $\dot{I}$  of armature current is known. It's generally accepted that the following values are already known - the resistance of armature winding  $r_a$ , the inductive leakage reactance  $x_{\sigma a}$ , windings data of armature and field windings. In case of working with per-units, it is necessary to define and the rated voltage  $U_n$ , rated current  $I_n$ , rated excitation current  $i_{fn}$ , the parameters  $r_a^*$ ,  $x_{\sigma a}^*$ .

As a final result we receive the underwritten values, defined through determination of the magnetic core saturation - the load voltage phasor  $\dot{E}_0$  therefore and the loading angle  $\theta$ , which is only conditionally generated from the flux in the excitation winding; the current in the excitation winding  $i_{f0}$ , creating this flux; the inductive

reactance of the current armature reaction  $x_{ad}$ , saturation coefficient  $K_\mu$ , the differences between the no-load voltage  $U_0 / I = 0$  / recorded with the same excitation current and during the operation with the present load.

The analytical determination of the Potier's diagram phasors is not a problem, if they are calculated with complex numbers, appropriately chosen frame of reference in a complex plane.

$$(6) \quad \dot{E}_\delta = \dot{U} + \dot{I}r_a + j\dot{I}x_{\sigma a}, \quad \varphi_{E_\delta} = \arctg \frac{\text{Im}[\dot{E}_\delta]}{\text{Re}[\dot{E}_\delta]}$$

as

$$(7) \quad \dot{U} = Ue^{j\varphi_U}, \varphi_U = 0; \quad \dot{I} = Ie^{j\varphi}; \quad \pm j = e^{\pm j\frac{\pi}{2}}$$

By the chosen frame of reference - when R-L load,  $\varphi < 0$ ; when R load,  $\varphi = 0$ ; when R-C load,  $\varphi > 0$ . Since in this case we work with no-load characteristics

in relative units is defined and  $E_\delta^* = \frac{|E_\delta|}{U_H}$ .

From equation (2) analytically are  $i_{f\delta}^*$  and

$i_{f\delta} = i_{f\delta}^* i_{fH}$ , when  $\varphi_{i_{f\delta}} = \varphi_{E_\delta} + \frac{\pi}{2}$ .. From this

equation, in accordance to [1,2,3] the current  $i_{f0}$  is

$$(8) \quad \vec{i}_{f0} = \vec{i}_{f\delta} + (-\vec{I}'), \quad \varphi_{i_{f0}} = \arctg \frac{\text{Im}[i_{f0}]}{\text{Re}[i_{f0}]}$$

The phasor  $\vec{I}' = k_{id} \vec{I}$  defined from excitation winding armature current and the coefficient descends from the basic SM theory relationships, shown in [1,2,3].

In this way, we have all the necessary quantities for defining

- the phasor  $\dot{E}_0 = E_0 e^{j\varphi_{E_0}} = E_0 e^{j\theta}$

$$(9) \quad |E_0| = |E_\delta| \frac{|i_{f0}|}{|i_{f\delta}|}, \quad \varphi_{E_0} = \varphi_{i_{f0}} - \frac{\pi}{2} = \theta$$

- the inductive reactance  $x_{ad}$

$$(10) \quad x_{ad} = \frac{|\dot{E}_0 - \dot{E}_\delta|}{|jI|}$$

- the coefficient  $K_\mu = \frac{E_{\delta\infty}}{|E_\delta|}$

The "unsaturated" value  $E_{\delta\infty}$  of loading voltage is determined through the linear characteristic in no-load mode with preliminary defined current value, corresponding to. The linearization is realized through drawing a tangent from the beginning of the no-load characteristic. The analytical interpretation of this equation is line, which goes through the specified point

and has an angle coefficient, equal to the derivative of the interpolating function

$$(11) \quad y' = \frac{ab}{(b+i_f^*)^2} + c; \quad K^* = y'(0) = \frac{a}{b} + c \Rightarrow K^* = 1.6187$$

from where is defined and:

$$(12) \quad E_{\delta\infty}^* = K^* i_{f\delta}^*$$

Taking into consideration (1), (12) and the relationships for the relative quantities, becomes equal to

$$(13) \quad K_\mu = \frac{K'}{i_{fn} \left( \frac{a}{b i_{fn} + i_{f\delta}} + \frac{c}{i_{fn}} \right)}$$

- the differences  $\Delta U = U_0(i_{f0}) - U$

$$(14) \quad \Delta U = U_n i_{f0} \left( \frac{a}{b i_{fn} + i_{f0}} + \frac{c}{i_{fn}} \right) - U$$

With the help of the software application Mathcad [5] are calculated and computer drawn the characteristics of the supposed SM, with rated data  $U_n = 6000V, I_n = 500A, r_a^* = 0.008, x_{\sigma a}^* = 0.15$

In the work are performed three cases - resistive (R), resistive-capacitive (R-C) and resistive-inductive (R-L) load.

### A. Load characteristics – fig. 2, 3, 4

$$U = f(i_f), \quad I = I_n = const, \quad \cos\varphi = const$$

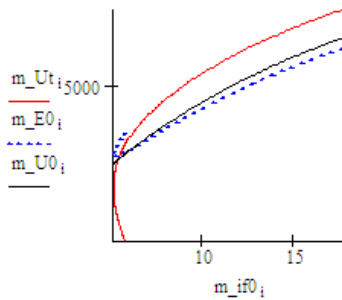


Fig. 2 Load characteristic  $I=I_n, \cos\varphi = 0.8, R-C$  load

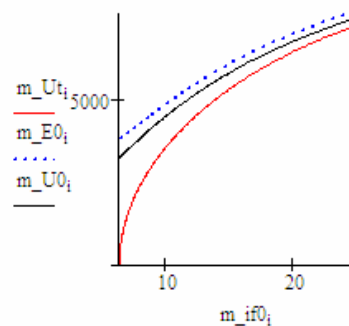


Fig. 3 Load characteristic  $I=I_n, \cos\varphi = 0, R$  load

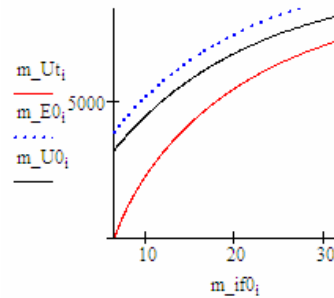


Fig. 4 Load characteristic  $I=I_n, \cos\varphi = 0.8, R-L$  load

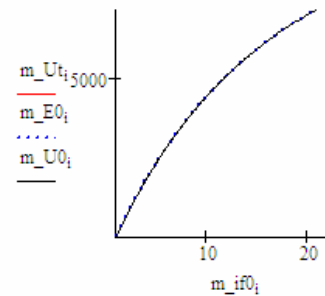


Fig. 5 No-load characteristic  $I=0$

From the graphics above it can be clearly seen the reaction influence of the armature current in different load – magnetizing when the load is R-C and demagnetizing when R-L load. Fig. 5 shows the test quality of no-load characteristic, i.e.  $I = 0$ .

### B. Excitation characteristics – fig. 6

$$i_f = f(I), \quad U = const, \quad \cos\varphi = const$$

Calculation approach:

- With constant value of the voltage phasor  $\dot{U} = U e^{j\varphi_U}, / \varphi_U = 0 /$  are assigned armature current  $\dot{I} = I e^{j\varphi}, / \varphi = const /$  from  $I = 0$  till the necessary border.

- The direct task is resolved for every value of  $\dot{I}$ .

- The result is an array of values of excitation currents  $i_{f0}$

Calculation approach:

- With constant value of the armature current  $\dot{I} = I e^{j\varphi}, / \varphi = const /$  are assigned

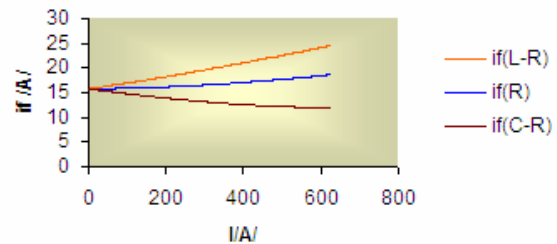


Fig. 6 Excitation characteristics with reactive load (R-L, R-C)  $/ \cos\varphi = 0.8 /$  and resistive load  $/ \cos\varphi = 1 /$ ,  $U=U_n$

$\dot{U} = U e^{j\varphi_U}$ ,  $\varphi_U = 0$  / varying from  $U = 0$  till the necessary border.

- The result is an array of values of excitation current

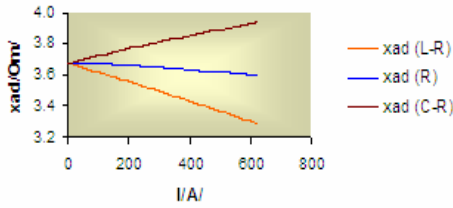


Fig. 7 Deviation of  $x_{ad}$  when calculating the controlling characteristics with reactive load (R-L, R-C) with  $\cos \varphi = 0.8$  and resistive load  $\cos \varphi = 1$ ,  $U = U_n$

### C. V-curves – fig. 8, 9

Calculation approach:

$$i_f = f(I), P_\delta = mU_n I \cos \varphi \pm mI^2 r_a = const, (U_n = const)$$

- With constant value of the electromagnetic power  $P_\delta$  and voltage phasor  $\dot{U} = U e^{j\varphi_U}$ ,  $\varphi_U = 0$  are given values to the phase angle  $\varphi$  of armature current  $\varphi_{min} \leq \varphi \leq \varphi_{max}$ .

- For every value of the angle  $\varphi$  is defined the module of the armature current  $I$ , as a square root of the equation  $P_\delta = mU_n I \cos \varphi \pm (mI^2 r_a + p_{Fe}) = const$ . In the equation above the sign “+” is for generator mode of SM and the sign “-” for motor mode  $\dot{I} = I e^{j\varphi}$ ,  $\varphi = const$ ;

- The right task is resolved for every value of  $\dot{I}$   
 - The result is an array of values of excitation current  $i_{f0}$

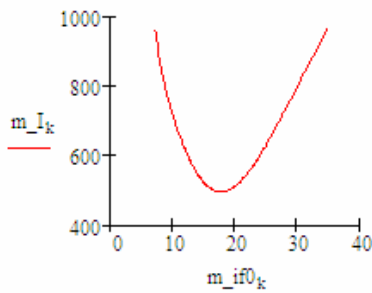


Fig. 8 V-curve when  $P=P_n$

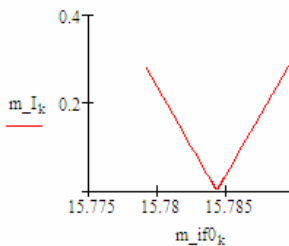


Fig. 9 V-curve when  $P=P_n / 100000$

The curve on fig. 8 is calculated and computer drawn for generator mode and at fig. 9 – actually corresponds to the compensator mode of SM.

### D. Short-circuit characteristic – fig. 10,11

$$I = f(i_f), U = 0$$

When calculating this characteristic, it can be applied the already performed algorithm for computing the exciting characteristics with current angle

$$\varphi = \arctg\left(\frac{x_{\sigma a}}{r_a}\right) \text{ read according to } E_\delta \text{ because}$$

$\dot{U} = 0$  /First approach/, but it should be taken into consideration the concrete features of the short-circuit. Defining current can be done with the help of (5), as a solution of the equation (15).

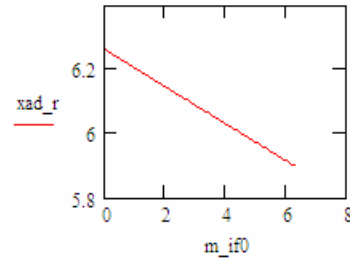
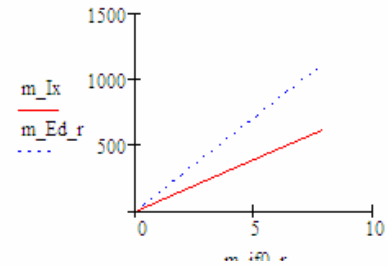


Fig. 11 Deviation of the inductive reactance from the armature reaction in short-circuit with recognizing the saturation

$$(15) \quad \begin{aligned} E_\delta(i_{f\delta}) &= I \sqrt{r_a^2 + x_{\sigma a}^2} \\ U_n i_{f\delta} \left( \frac{a}{b i_{fn} + i_{f\delta}} + \frac{c}{i_{fn}} \right) &= I \sqrt{r_a^2 + x_{\sigma a}^2} \end{aligned}$$

Second calculation approach:

- Armature current module values are assigned

$$\dot{I} = I e^{j\varphi}, \varphi = \arctg\left(\frac{x_{\sigma a}}{r_a}\right) / \text{varying from } I = 0$$

till the necessary border.

- The direct task is resolved for every value of  $\delta$ , when is defined with (15)

- The result is an array of values of excitation current

### E. External characteristics - fig. 12

$$U = f(I), \quad i_{f0} = const, \quad \cos\varphi = const$$

The development of the external characteristics of the SM is mainly done with resolution of the so called opposite task – the value of the current  $i_{f0}$  in the excitation winding is given in advance and after that is defined the value of the voltage in armature winding  $U$ . A formal application of the graphical solution requires long graphical iteration process, which disadvantages are well-known.

The possibilities of the general modern software products Mathcad, Matlab, Maple, allow a numerical resolution of the problem with precise accuracy.

The algebraic equation conditions are:

- The triangle similarity, formed of the phasors  $\dot{E}_\delta, j\dot{I}x_{ad}, \dot{E}_0$  and current phasors  $i_{f\delta}, I', i_{f0}$ ;

$$(16) \quad \frac{i_{f0}}{E_0} = \frac{i_{f\delta}}{E_\delta}$$

$$\frac{I'}{Ix_{ad}} = \frac{i_{f\delta}}{E_\delta}$$

or in developed mode

$$(17) \quad \frac{i_{f0}}{E_0} = \frac{1}{U_n \left( \frac{a}{bi_{fn} + i_{f\delta}} + \frac{c}{i_{fn}} \right)}$$

$$\frac{k_{id}}{x_{ad}} = \frac{1}{U_n \left( \frac{a}{bi_{fn} + i_{f\delta}} + \frac{c}{i_{fn}} \right)}$$

- The connection of the triangle sides in the corresponding triangle. In consideration with the above equation is enough an equation from that kind:

$$(18) \quad i_{f0}^2 = i_{f\delta}^2 + I'^2 - 2i_{f\delta}I' \cos[\pi - (\varphi_{E_\delta} - \varphi)]$$

- A requirement for location of the vector groups in relation to the beginning of the frame of reference.

$$(19) \quad \varphi_U = 0 \rightarrow \text{Im}[\dot{U}] = 0 \rightarrow E_\delta(i_{f\delta}) \sin(\varphi_{E_\delta}) = Ix_{\sigma a} \cos\varphi + Ir_a \sin\varphi$$

or

$$(20) \quad U_n i_{f\delta} \left( \frac{a}{bi_{fn} + i_{f\delta}} + \frac{c}{i_{fn}} \right) = Ix_{\sigma a} \cos\varphi + Ir_a \sin\varphi$$

$\dot{E}_0, i_{f\delta}, x_{ad}, \varphi_{E_\delta}$  are unknown. The task is resolved with Mathcad, by using the build in construction for numerical resolution of non-linear algebraic equations

### Calculation approach:

- The direct task is resolved when  $U = U_n, I = I_n, \cos\varphi = const$  or depending of the necessity. The value of the received excitation current  $i_{f0}$  helps to calculate the external characteristic.

- With constant value of the excitation current  $i_{f0}$  are given the module values of the armature current  $\dot{I} = Ie^{j\varphi}, \varphi = const$  / varying from  $I = 0$  till the necessary border.

- The described above non-linear algebraic system is resolved.

- The result is an array of values of  $\dot{E}_0, i_{f\delta}, x_{ad}, \varphi_{E_\delta}$

-  $E_\delta = U_n i_{f\delta} \left( \frac{a}{bi_{fn} + i_{f\delta}} + \frac{c}{i_{fn}} \right)$  is calculated

- The array with the necessary values of the input voltages is defined through the relationship

$$(21) \quad |\dot{U}| = |\dot{E}_\delta - j\dot{I}x_{\sigma a} - Ir_a|, \varphi_U = 0$$

because of the saturation, provoked of the magnetizing action of the armature current reaction. The demagnetizing action of the armature current reaction in (R-L) load is the reason for growth of  $\delta$ .

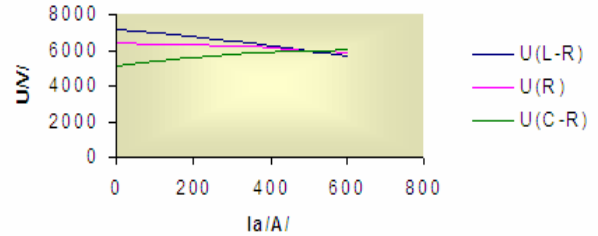


Fig. 12 External characteristics of reactive load (R-L, R-C) with  $\gamma\sigma\varphi = 0$  and resistive load (R) / with  $\cos\varphi = 1$

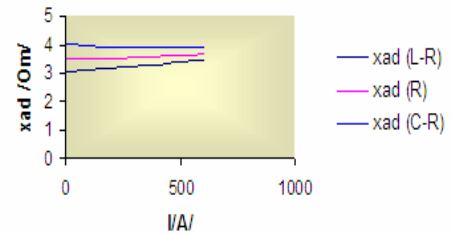


Fig. 13 Deviation of  $x_{ad}$  during calculation of external characteristics reactive load (R-L, R-C) with  $\cos\varphi = 0.8$  and resistive load (R) / with  $\cos\varphi = 1$

## Conclusion

In this work is presented an analytical approach with numerical solution, which excludes the necessity of graphical readings.

The graphical presenting of the no-load characteristic is replaced by interpolating curve with the corresponding quantities for after transformations and calculations.

With the help of the software application Mathcad are resolved the direct and opposite task when defining the performances of the synchronous machine. The main subject of this presented development is observing and determination of the saturation influence on the leakage inductive reactance .

## References

[1] Волдек, А. Электрически машини, С., Техника, 1971.

[2] Динов, В. Электрически машини, С., Техника, 1981.

[3] Ангелов, А., Д. Димитров. Электрически машини – ч. II, С., Техника, 1988.

[4] Sigma Plot 8.02 Demo, User's Guide. SPSS Inc 2003.

[5] Дьяконов, В. Mathcad 8/2000, Санкт-Петербург, Питер, 2001.

[6] Иванов-Смоленский, А. Электрические машины, М., Энергия, 1980.

[7] Bojilov, G., M. Mihov, V. Stipzov. Replacement of the graphical drawing of direct curent generator characteristics with analitical calculation. Proc. of 10-th Int. Conf. of El. Mach. ELMA'2002, Sofia, 2002, vol. 1.

[8] Божилов, Г., М. Михов, В. Стипцов. Замяна на графичното построение на характеристиките на постояннотокови двигатели с аналитично изчисление. Год. на ТУ – София, 2003, т. 52.

---

*Miho Mihov* – Associate Professor, DSc., Faculty of Electrical Engineering, Technical University of Sofia, 8 Kl. Ohridski Str., 1000 Sofia, BULGARIA.  
e-mail: [mpmi@tu-sofia.bg](mailto:mpmi@tu-sofia.bg).

*Gancho Bojilov* – Professor, Dr., Faculty of Electrical Engineering, Technical University of Sofia, 8 Kl. Ohridski Str., 1000 Sofia, BULGARIA.  
e-mail: [gb@tu-sofia.bg](mailto:gb@tu-sofia.bg).

# Diagnostic Laboratory Module for Coils of Electric Power Tools

Milko G. Dochev

**Abstract:** *The mass use of electric power tools (EPT) called for the demand of contemporary apparatuses for control and diagnostics of the coils in the built-in electric motors. A diagnostic portable module was developed and carried into effect which enables determining the diagnostic condition of coils in EPT and small electric tools (SET) – disconnection, inter-winding short circuit, rupture to mass, inter-lamella short circuit, faulty connections.*

**Keywords:** *electric power tools, diagnostics, control*

## 1. Introduction

The principles of market economy raised the requirements to companies dealing with production, maintenance and exploitation of electric motors with regard to their quality and exploitation reliability. This led to a significant interest and the necessity of applying diagnostic methods and systems. There is a rise in the number and variety of control-diagnostic apparatuses, including such for continuous control (monitoring). Many national companies and enterprises, especially ones related to power engineering, import apparatuses and complete systems which are rarely used efficiently, and sometimes their working principles, potentialities and application are unclear or lacking. In some cases there is neither any competent and trained personnel nor specialized diagnostic and analytic teams.

In the activities of service and repair of EPT and electric operative motions the problems are even more significant. The qualification of servicing and repairing personnel is on a low level, there is no possibility and desire for self-training and pre-qualification. Most often the available servicing equipment is elementary, on a low technical level, or amortized and obsolete. The activity is concentrated in small firms, with not numerous but variable members of the personnel. Those firms do not have the potential to allot financial resources for pre-qualification, and to afford buying modern equipment. The board of directors often lacks the desire for changes.

All this calls for developing and putting portable diagnostic modules on the market. Those modules possess a definite multifunction, they are easy to be exploited and maintained, they have very clear diagnostic procedures based on firm logic (of Yes-No type), and they are relatively cheap.

## 2. Introduction to the problem and choice of a method

The defects and flaws of coils in small electric tools and EPT might be generalized and classified into two basic groups:

a/ Exploitation:

1. In stator coils: disconnection, inter-winding and inter-lamella short circuits, rupture to mass, etc.

2. In rotor coils

2a. In cage rotors – bar disconnection, bar-ring disconnection, breaking the entity of cage bar, etc.

2b. In armature coils - inter-winding and inter-lamella short circuits, coil interruption, rupture to mass (shaft, package), interruption of collector-coil junction, etc.

b/ Constructive-technological

1. In stator coils – faulty connections, turnover sections, faulty markings, wrong coiling direction and groove resting, etc.

2. In rotor coils

2a. In cage rotors – bad pouring on the grooves, available pores in the cage, lamella penetration in groove zones, bars coming out of the plate package, etc.

2b. In armature coils – bad collector-coil welding, faulty connections, turnover sections, rupture to mass, etc.

The diagnostic condition “interruption” is discovered and diagnosed easily, and so is the condition of short circuits to mass (shaft, package).

The discovery of metal short circuit (inter-winding, inter-lamella and inter-phase s.c.) is more difficult to be determined, especially through trivial equipment – test lamp, current tester or multiset. Using a measuring bridge is an applicable method, but it is slower and not always diagnostically reliable (e.g. in case the coil has a great number of thin conductor windings).

Therefore, the diagnostic conditions of windings (coils) might be conventionally defined as: from condition “1” – in a totally good working order, to condition “0” – totally ineffective. Interstate conditions appear within the range between those 2 borderline conditions during exploitation, e.g. inter-winding short circuit, rupture to mass and interruption of borderline conditions.

It is obvious that the faults most frequently occurring in coils (e.g. in EPT) are: the inter-winding short circuits (i.s.c.), corpus short circuits (c.s.c.) and leading conductor disconnection (l.c.d.). Since failures due to those reasons occur suddenly, and each of them leads to tool damage,



then the probability for flawless operation is the following:

$$(1) P(t) = \exp \{ -(\lambda_{i.s.c.} + \lambda_{c.s.c.} + \lambda_{l.c.d.}) t \},$$

where  $\lambda_i$  stands for the intensity of failures in the three cases.

It was proven that the distribution of failures due to aging of the insulation system and the exploitation load of EPT and SET approaches the normal law.

The basic goal and task of coil diagnostics is identifying their diagnostic condition after being technologically completed in the factory, or their exploitation load after a certain period. The tested diagnostic parameters are: active and reactive resistance, number of windings in rotor and stator coils, insulation resistance, etc. Determining them through passive diagnostic procedures is not always accurate, that's why the use of active diagnostic methods is necessary, and in this case the most successful one turns to be the electric-impulse diagnostics. Its principle is based on the transmission of a specifically shaped impulse signal, generated by a high-frequency oscillator, towards the coils to be diagnosed. The signal passing through them, is deformed in a certain pattern due to their wave resistance, and might be indicated, for example on an oscilloscope screen, in the form of two waves – a falling one and a reflected one. The various defects and abnormalities in the coil deform the signal in a different way, and through a comparison on a basis and current form, the nature of the defects might be judged.

It is known that the inductive resistance is generally expressed in the following way:

$$(2.1) X_M = \omega \cdot L,$$

and if there are any short-circuit coils, then:

$$(2.2) X_M = \omega \cdot (W_k^2 / r_k),$$

where  $r_k$  is the active resistance in the contour with short-circuit coils.

Then the inducted e.d.v. in this contour is:

$$(3) E_k = 2\pi f \cdot W_k \cdot \Phi_{\delta m},$$

which might be used as a parameter for indication, comparison and visualization. For correctness of testing, the following requirements should be observed:

- linearity of the tested item – it is necessary that the exerted low-frequency voltage should be  $U < 0,5 U_{nom.}$ , so that there is no saturation of the magnetic system.

- repetitiveness of the working conditions – e.g. for armature sections the measuring shouldn't be interrupted unless the whole periphery of the collector is outflanked with the examining tester.

The idea is that a generator for frequencies up to 10-20 kHz is used, at a voltage of 10-50 V, the signal from which is transmitted to the tested section / coil / winding, and through a proper contour (e.g. inductive), the signal progress and alteration are observed. It is obvious that the period of oscillations in the contour will depend on the circuit parameters. In general, it is a serial RLC group. The visualization of different defects in stator and rotor coils are shown in [1] and [2], respectively.

If the coil is defective, the resistance and induction in the contour modulate, depending on the flaw. For example, in inter-winding and inter-section s.c. the dependences are:

$$(4) R_d = k \cdot R; \quad L_d = k^2 \cdot L; \quad k = (W_d / W) < 1$$

which are: the active resistance, inductiveness, and the effective remaining number of operating windings of the defective coil, respectively, and  $R, L, W$  are the active and inductive resistance, and the whole number of windings in a standard coil (in a good working order).

### 3. Implementation

Analyzing the nature of the problem and on the basis of conclusions made so far, a device for coil diagnostics in EPT and SET was synthesized. The device (module) executes the following functions:

1. Testing for a loop, including a “low” and “high-resistance” loops with the specific light and sound indication;

2. Testing of coils and windings for a possible interruption or for a inter-winding s.c.

3. Testing of armatures – for a possible inter-winding and inter-lamella s.c., as well as for a winding disconnection and the presence of corpus s.c.

The device was built as a portable module /pic.1/, with the possibility to plug in auxiliary measuring apparatuses, including a programmable multi-measurer with a standard PC interface.

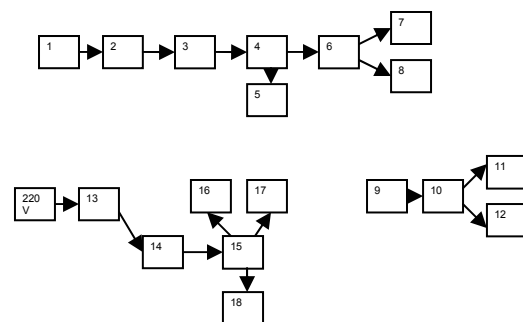


Fig.1

The block-scheme of the module is shown in fig.1. The main centers of the diagnostic module are the following: 1 – low-frequency generator; 2 – inductor (coil) – emitter of the generator; 3 – receiver (coil) of the amplifier; 4 – mode switcher; 5 – outlet to a multi-measurer; 6 – amplifier; 7 – light indicator; 8 – sound indicator; 9 – line-in for a universal tester; 10 – universal tester (circuit controller); 11 – light diode; 12 – sound indicator of the tester; 13 – power-supplying block 220V AC / 3V DC; 5V DC; 14 – generator of stabilized current; 15 – measuring bridge; 16 – standard impedance /coil/; 17 – measured impedance /coil L<sub>x</sub>/; 18 – measuring device /mili-ammeter/.

The separate assemblies of the module are the following:

Power-supplying block /fig.2/ - devised for two power-supplying voltages: 3V DC and 5V DC obtained

through a reducing transformer rectified after Gretz's scheme, with capacitor filters, an integral stabilizer "7805" for 5V DC, and a regulated stabilizer "317" for 3V CD. At the outlet, "C" groups for filtering and pulsation reduction were mounted.

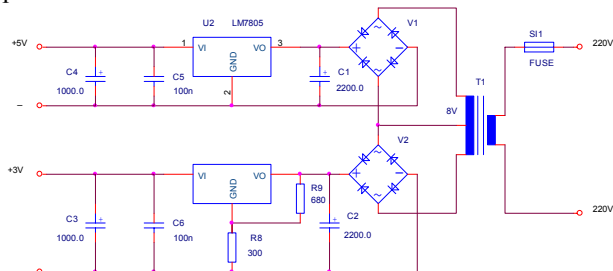


fig.2

**Bridge and electric current generator /fig.3/** - implemented as a Winston bridge supplied through stabilized current built with integral stabilizer "7805". The goal is that the current doesn't exceed a certain value when low-resistance impedance is turned on. The bridge is balanced through the potential-meter  $R_5$ , and the potential-meter  $R_6$  is used for fine adjustment of bridge sensitiveness, so it is possible that the bridge arms are made equal without a load or a standard measure. This assembly serves for measuring coils and stator windings, and for discovering defects in them /inter-winding s.c., interruption, etc./

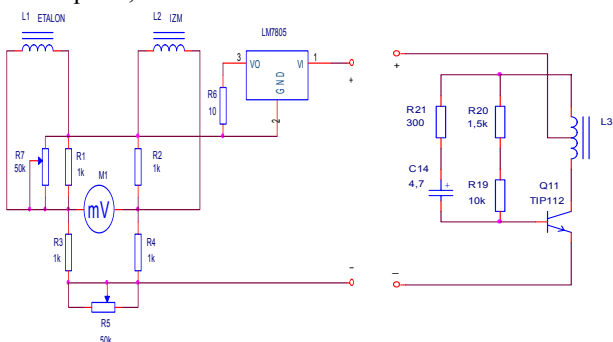


fig.3

**Generator of low-frequency impulses /fig.4/** - it generates impulses with frequencies about 10 kHz. It is a blocking-generator built after "Darlington" scheme (or with transistor T12 only), and its amplitude is up to 50 which is induced as an e.d. voltage in the coils of the tested block /in case there are short-circuit or inter-lamella s.c. coils/.

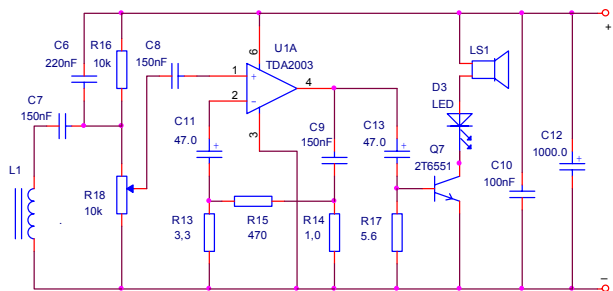


fig.4

This e.d.v. is received by the inductor  $L_1$  and is amplified after the scheme built with an amplifier with

power "TDA 2003", as the sensitiveness is adjusted through the potential-meter  $R_{18}$ . The amplified signal is transmitted to the sound indicator /loud-speaker LS1/ and to the light indicator LED. A level indicator built of light-diode scale, implemented through LI type KA 2281, is used for a light indicator.

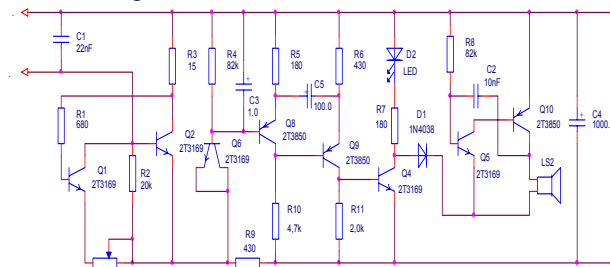


fig.5

**Universal tester /fig.5/** - it serves for testing coils, electric circuits and stator coils of SET and MPT. It is composed of a generator built of transistors  $Q_1$  and  $Q_2$ , and the amplitude of the generated signal is regulated through the potential-meter  $R_{12}$ . The amplitude and frequency of the generated signal depends on the ingoing impedance created by the tested coil plugged in the tester inlet through proper terminals. The generator signal passes through the detector  $D_3$  and is filtrated by the condenser  $C_3$ . The obtained continuous level, depending on the ingoing impedance, sets in operation the light indicator  $D_2$  and the sound indicator built by the generator of sonic frequency  $Q_7$  and  $Q_8$  and transmitting a sound signal through the loud speaker  $LS_2$ . Depending on the signal level, the sound might be continuous, interrupted, or there might be no sound. At a low impedance /0/, the signal is continuous, at other fixed (adjusted) value, e.g. 1000  $\Omega$ , it has an interrupted sound generation, and at a discontinuation the sound or light signal is missing, that is, a "disconnection", an "inter-winding" and a "normal condition" of the tested coil are present, respectively.

#### 4. Experimental research

50 measurements were conducted, 25 on stator and 25 on rotor assemblies for EPT, respectively. The defects were simulated, and the flaws – described in section3 in constructed testing samples. The defects and flaws were identified and indicated through the light and sound indicators installed in the module. The conclusion is that the developed diagnostic module is reliable, it is easy to be serviced, and it enables making a quick and qualitative assessment of different types of diagnostic conditions of rotor and stator coils in EPT.

The developed sample is shown in pic.1.



pic.1.

## 5. Conclusion

In conclusion, the following inferences might be made:

1. A universal measuring stagecraft for determining the diagnostic condition of rotor and stator coils in EPT was synthesized and implemented.

2. The constructed diagnostic module enables discovering the defects and flaws in rotor and stator coils in EPT and SET.

3. The received diagnostic information, through the use of auxiliary measuring apparatuses, might be assembled and stored, and a database for coils of different size might be built.

4. The constructed device is portable, comparatively cheap, with good diagnostic characteristics, and it can

serve as a basis for a testing sample for the production of small-batch diagnostic equipment.

## 6. References

- [1] G.Bojilov – Methods and devices for technical diagnostics of electric tools, Dissertation, 1995;
- [2] M.Dochev – Technical diagnostics of electric power tools, Sofia, TU, Post-graduate qualification;
- [3] S.Popadiin – Electric micro-tools, pt.1, Sofia, Tehnika, 1976;
- [4] Ermolin – Electric low-power tools, L., Energia, 1972;
- [5] Materials and prospects of the firms: Sparky-Eltos, AEG, Bosch, etc.

---

**Milko Dochev-Sen.** *Assistant, TK-Lovech*  
*Tel: 0887 294 990; E-mail: dochev@mail.bg*

# Computer System for Research and Control of Electromechanical Objects

Emil Marinov and Nikolai Nikolov

**Abstract:** A graphic program medium has been worked out by means of which on the basis of specialized functional units a wide range of systems for the model and experimental studies purposes as well as the real control purposes can be set up. The connection with the power converters and the taking down of signals from the objects is carried out by the a hardware interface, which has been worked out exactly for that purpose. By virtue of the developed computer system, adaptive control of the speed of the direct-current motor is realized. Results of experimental studies of the system are shown.

**Keywords:** computer control system, adaptive control

## Introduction

Computer systems, based on specialized graphic media and relevant mathematical provision [1,2] afford great opportunities in designing, studying and controlling of technological processes. In this regard, the development of analog systems orientated towards the specific requirements of such objects and processes as the electromechanical ones and distinguished for their fast action, simplicity and lower cost price is of great interest.

## Description of the Program Medium

A graphic program medium has been worked out by means of which on the basis of specialized functional units a wide range of systems for the model and experimental studies purposes as well as the real control purposes can be set up. The blocks are classified into libraries according to their function:

- **generators** (sine-wave, square-wave, constant value, noise);
- **linear blocks** (elementary type dynamical blocks);
- **non-linear blocks** (multipliers, dividers, type non-linearity);
- **controllers** (P, PI, PID, D);
- **logical** (AND, OR, Schmitt trigger);
- **graphic** (oscilloscope, visualization by means of pointer instruments or text value, lamp);
- **steering visual controllers** (buttons, check boxes, scrollers);
- **connection with real objects** (analogue inputs and outputs);
- **auxiliary** (reading and recording of signals from/in a file and others).

Each block possesses a certain number of inputs and/or outputs according to its function. Incoming and outgoing signals type is fixed and can be analogue, digital or other type like integral, stringer and others. The

graphic medium prevents from construction of outlines of heterogeneous signals as well as the connection in one outline of more than one unit.

It is possible the completing of several systems, independent from one another, which function simultaneously within an experiment and their signals are observed on one and the same time diagram.

There is an opportunity for connection with other program media (Matlab, Mathcad) through recording of experiments results in a suitable format. This makes possible the high qualities of the shown products for result processing to be used in off-line regime.

The integration is completed through the rectangle method.

The program product is worked out on the basis of Microsoft Visual C ++ 6.00 [3].

## Configuration and Computer System Operation

In general the computer system consists of a personal computer with the operating system Windows 98 being installed or a more recent version, hardware interface which makes the connection with the real world and object possible and which in this case includes a power converter and a DC motor (figure 1). The power converters control and the taking down of signals from the objects is carried out by the hardware interface, which has been worked out exactly for that purpose. The latter is connected to the computer through the standard LPT port.

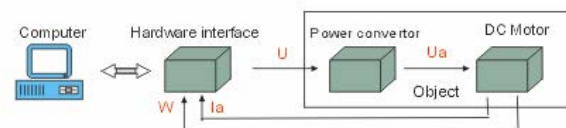


Fig.1. Configuration computer system

The system allows operation in the following regimes: simulating investigations (without connection with the real object); test and adjustment; study and control in real time.

The start of the process includes the following actions, executed automatically – the composed block diagram and its parameters are saved in a file in text format (this standard output can be used for connection with other graphic media or for configuration of steering controllers). Next step is the saved information to be interpreted by a program module for synthesise of the mathematical model of the process in computer memory.

Thus the connections between the blocks in the memory guarantee great quick action of the effective model.

The system allows operation with a specified simple time, as well as determination in test and adjustment regime of the minimum simple time by measuring the speed of the synthesized model – number of calculations for a time unit. Thus the minimum simple time of a certain system is appointed on the basis of the necessary time for servicing the program which is different for one and the same computer depending on the composed block diagram. After holding the test – all gathered values in the blocks of the system are nullified. The next step is initialization of the hardware module – specification of initial values of the incoming and outgoing signals including a signal to the power converter. If the above mentioned steps are successfully fulfilled, the real process begins.

The consequence of actions, carried out by the computer system is shown on figure 2.

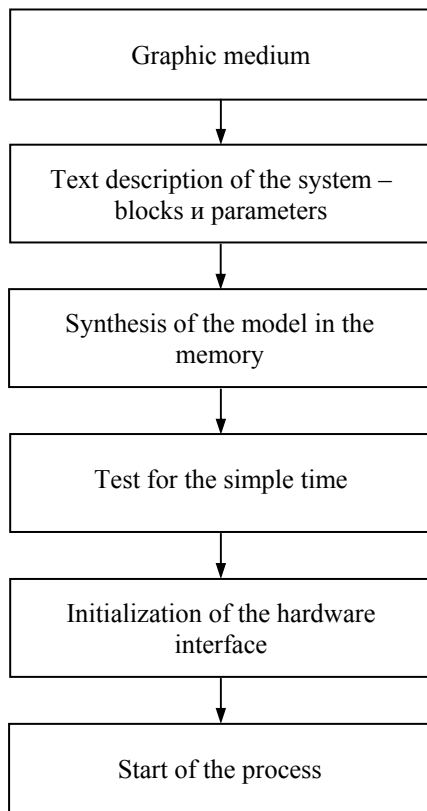


Fig. 2. Computer system operation

### Adaptive Control of DC Motor Speed

Adaptive system with reference model is realized on the basis of the developed interface modules and program medium. The adaptive system is synthesized through the theory of hyperstability [4,5,6]. The structural diagram of the system is shown in figure 3, where the following symbols are used:  $\omega_r$  – reference speed;  $\omega_m$  – output of a reference model;  $\omega$  – motor speed;  $u$  – control signal;  $e$  – error;  $M_c$  – resistance (load) moment;  $W_m(p)$  – transfer

function of the reference model;  $W_{ou}(p)$ ,  $W_{oi}(p)$  – transfer functions of objects of control and interference. The object includes a power converter (uncontrollable rectifier and symmetric transistor commutator) and a direct-current motor

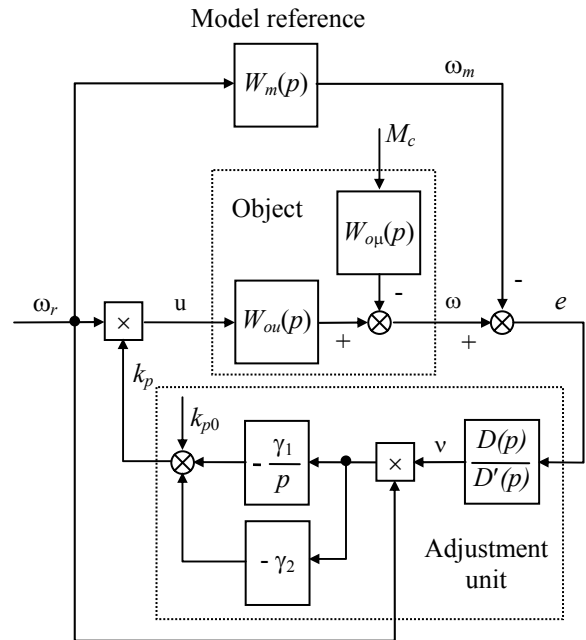


Fig. 3. Structural diagram of the adaptive system

The following mathematical description of the object and reference model is used in the synthesis:

$$(1) \quad W_{ou}(p) = \frac{K_{pc}K_d}{T_{em}p^2 + T_e p + 1},$$

$$(2) \quad W_{oi}(p) = \frac{K_\mu(T_e p + 1)}{T_{em}p^2 + T_e p + 1},$$

$$(3) \quad W_m(p) = \frac{1}{T_m p + 1},$$

where  $K_{pc}$ ,  $K_d$  – transmission coefficients of the power converter and DC motor,  $K_\mu$  – transmission load coefficient,  $T_{em}$ ,  $T_e$  – electromechanical and electromagnetic time constants,  $T_m$  – time constant of the reference model.

The control signal is formed as follows:

$$(4) \quad u = k_p \omega_r.$$

The coefficient of the controller  $k_p$ , which is changing during work process is obtained according to:

$$(5) \quad k_p = -\int_0^t \gamma_1 v \omega_r dt - \gamma_2 v \omega_r + k_{p0},$$

where  $\gamma_1$ ,  $\gamma_2$  are adjustment coefficients and  $v$  – output of polynomial  $D(p)$ .

The polynomial  $D(p)$  is to find in the form:

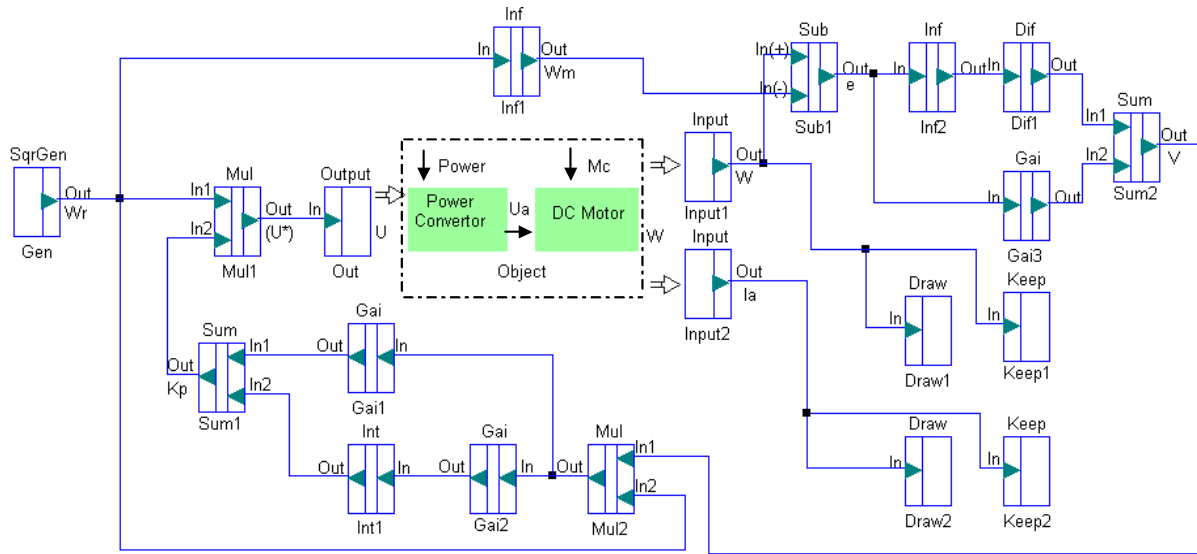


Fig.4. Block diagram of the adaptive system.

$$(6) \quad D(p) = d_0 p + d_1,$$

and the coefficients  $d_0, d_1$  are defined from the condition:

$$(7) \quad \text{Re}[D(j\omega)W(j\omega)] > 0.$$

The polynomial  $D'(p) = d'_1 p + d'_2$  is added with the purpose of physical implementation.

The block diagram of the system, realized by means of the developed program medium is shown in figure 4.

### Experimental Studies and Results

The experimental studies of the adaptive system are carried out for a motor PIVT 6/25A whose rated data are: voltage  $U_{an}=30V$ , current  $I_{an}=1.6A$ ; torque moment  $M_n=0.11Nm$ ; speed  $\omega_n=314.16rad/s$ ; inertia moment  $J_d=2.5 \cdot 10^{-5}kgm^2$ . The simple time is 0.5ms.

The results of the experimental studies are shown in figures 5÷8 considering different reference speed and changes in the parameters of the reference model and the mechanical part. Figures 5a÷8a present the motor speed variation, compared to the reference speed  $\omega_r$  and the output of a reference model  $\omega_m$  (dashed line), while figures 5b÷8b present the variation of current  $I_a$  in relevant processes.

The results being produced show that the curves  $\omega(t)$  and  $\omega_m(t)$  practically coincide. Especially in steady-state regime a considerable strengthening of the noise from the signals is observed, and for its elimination an additional filtration block is necessary.

### Conclusion

The proposed computer system that is distinguished for its fast action and simplicity afford great opportunities in designing, studying and control of real electromechanical objects and processes. This system is used in the teaching process of the Technical University of Varna, Department of Production Automation.

Adaptive system with reference model is realized and its serviceability and high qualities are proved in the operation process.

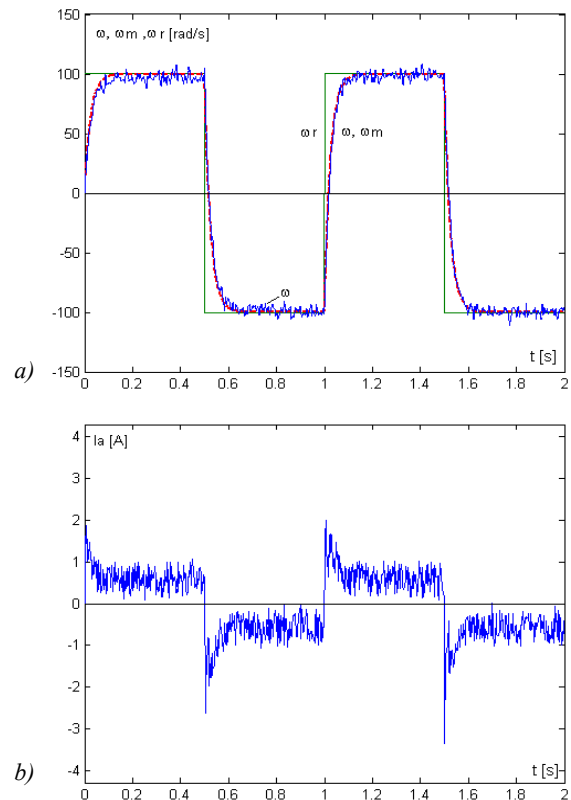


Fig. 5. Adaptive system operation in case  $J=J_d, T_m=25ms$ .

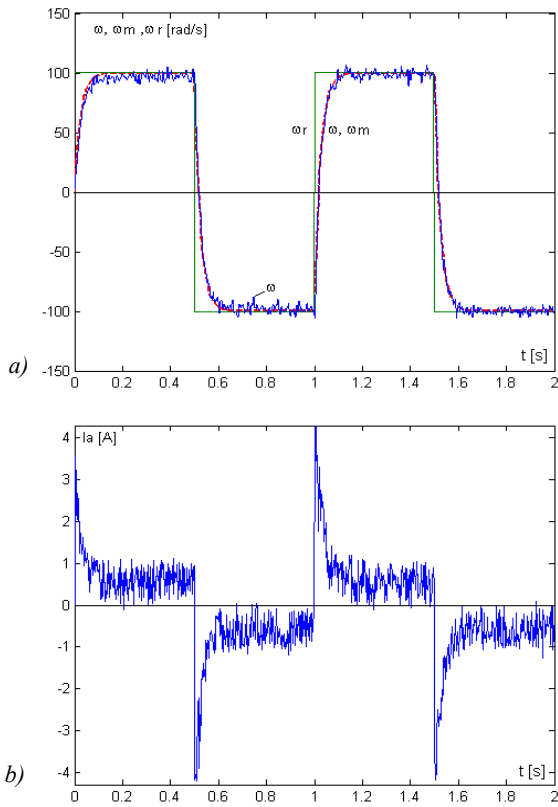


Fig. 6. Adaptive system operation in case  $J=2J_d$ ,  $T_m=25ms$ .

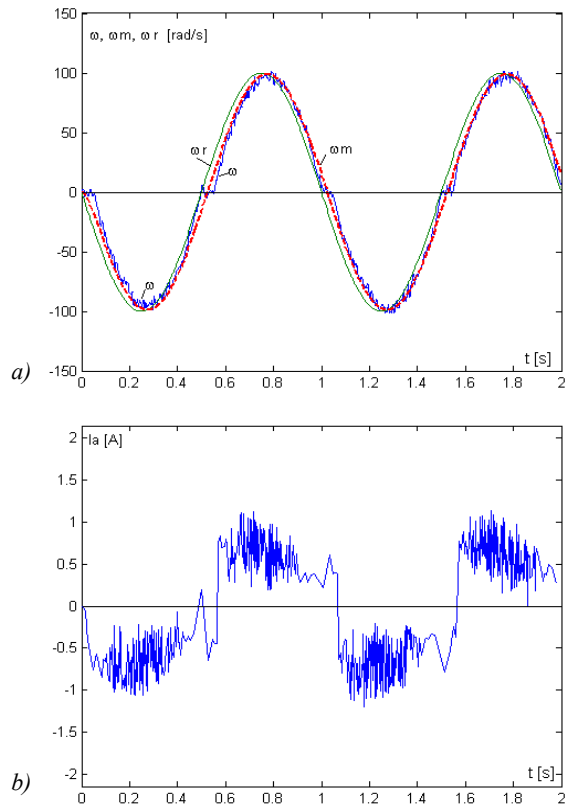


Fig. 8. Adaptive system operation in case there is a sinusoid reference signal,  $J=J_d$ ,  $T_m=25ms$ .

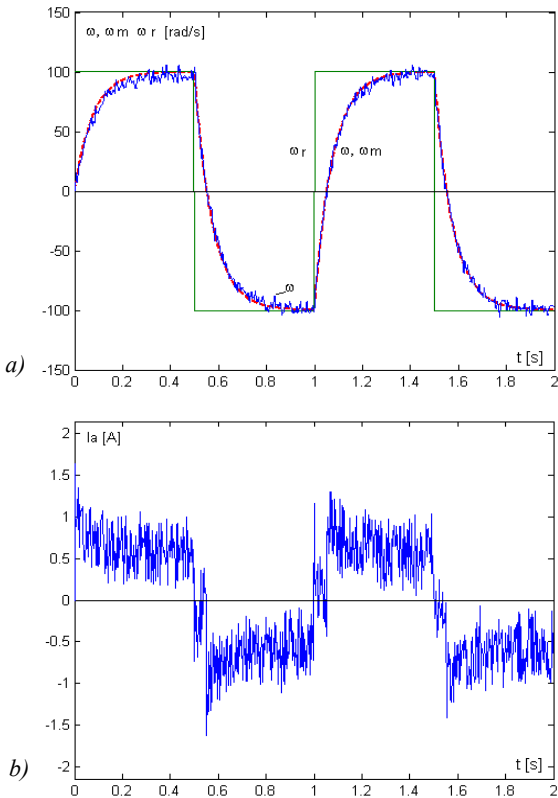


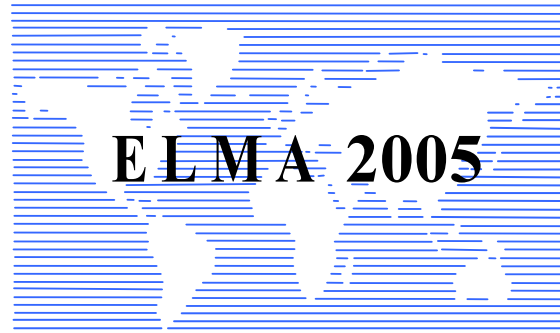
Fig. 7. Adaptive system operation in case  $J=J_d$ ,  $T_m=75ms$ .

## References

- [1] LabVIEW. Graphical Programming for Instrumentation. National Instruments, 1998.
- [2] Matlab Reference Guide. June 2002 by the Math Works, Inc.
- [3] Prosiše, J. Programming Windows with MFC, Second Edition. Copyright 1999 by Microsoft Corporation.
- [4] Åström K.J., B. Wittenmark. Adaptive Control. Addison Wesley, Mass. 1989.
- [5] Велев, К.В. Адаптивни системи. София, 1995.
- [6] Marinov, E., Y. Batanova. Possibilities for Adaptive Control of Electromechanical Systems, International Seminar on Advanced Control Theory. Varna, Bulgaria, 1995, pp. 82÷85.

**Emil Marinov** – Assistant Pprofessor, PhD.Eng., Department of Production Automation, Technical University of Varna, 1, “Studentska” Str., 9010 Varna, BULGARIA.  
e-mail: marinov52@mail.bg.

**Nikolai Nikolov** – Master Engineer, “C&C Technology” LTD Engineering, 6, “A. Glavchev” Str., 9000 Varna, BULGARIA.  
e-mail: nikolov99@yahoo.com.



---

---

**POWER SYSTEMS AND  
DISTRIBUTION SYSTEMS II**

---

---





# On the topological observability of an electrical system

Nicolas Héraud, Olivier Wailly, Ouadie Bennouna, Philippe Poggi

**Abstract:** The aim of this article is to extract the totality of determinable parameters (measured or deduced) of an electrical power network in stationary state, in order to estimate their true values. These systems are described by linear and bilinear equations which involve the complex intensities  $I_r$  and  $I_c$ , the impedances  $Z_r$  and  $Z_c$ , and voltages  $U_r$  and  $U_c$ . The study of observability is presented. The methodology presented allows to extract the observable part of the instrumentation, by using symbolic calculus software. Finally, this algorithm will be applied to an electrical system.

**Keywords:** Observability, State Estimation, Diagnosis, Instrumentation, Redundancy

## Introduction

Electrical networks are used in all industries; it is sometimes necessary to know the state of the different branches of a such network, to control (study of the system's control) or to insure the correct working order of the piloted process (analysis and/or supervision of the power network). We are going therefore to, on the one hand, determine all of the observable variables (measured or deduced) of a given network, then on the other hand, estimate true values of these variables from stemming collector values of measure. Quote the authors [1], [2], [3], [4], [5] and [6] which have worked in this field. Two ways exist: algebraic one [7] and more recently [8] or using graph's theory [9] and [10]. In this paper, we present an algebraic method, applied to systems with polynomial model. The work presented here concerns the structural observability. It is anyhow possible that some variable values make impossible to use the deductions' relation. The method that we present is particularly attractive because we can use it whatever the linearity degree and the complexity of the model's relations. It is especially innovative for electric systems, which are at once polynomial and multi-linear. An electrical variable is described by, either the knowledge of its modulus and phase, or the knowledge of its reactive and active parameters.

## System's equations

An electrical system comprising  $n$  nodes,  $v$  branches and  $m$  meshes is described by parameters of tension  $U_i$  (tension to terminals of a branch),  $E_i = U_i / I_i$  (voltage generator), component impedance  $Z_i$  and current  $I_i$ ; these variables are governed by next general equations: Kirchhoff laws

$$(1) \quad \sum_{\text{node}} I_i^* = 0 \quad \text{node statement}$$

where the indication \* represents the true value of the parameter. This statement provides 2 linear equations:

$$(2) (3) \quad \sum_{\text{node}} I_{ri}^* = 0 \quad \sum_{\text{node}} I_{ci}^* = 0$$

$$(4) \quad \sum_{\text{mesh}} \begin{pmatrix} U_i^* \\ E_i^* \end{pmatrix} = 0 \quad \text{mesh statement}$$

This statement provides 2 linear equations :

$$(5) (6) \quad \sum_{\text{mesh}} \begin{pmatrix} U_{ri}^* \\ E_{ri}^* \end{pmatrix} = 0 \quad \sum_{\text{mesh}} \begin{pmatrix} U_{ci}^* \\ E_{ci}^* \end{pmatrix} = 0$$

Ohm law:

The relationship between tension and current is:

$$(7) \quad U = Z I$$

This relationship provides 2 bilinear equations:

$$(8) \quad U_{ri} = Z_{ri} I_{ri} - Z_{ci} I_{ci}$$

$$(9) \quad U_{ci} = Z_{ci} I_{ri} + Z_{ri} I_{ci}$$

Matrix writing:

These equations can be built with matrix with the help of connection matrixes as follows:

$$(10) \quad M_r I_r^* = 0 \quad \text{from relation (2)}$$

$$(11) \quad M_c I_c^* = 0 \quad \text{from relation (3)}$$

$$(12) \quad L_r \begin{pmatrix} U_r^* \\ E_r^* \end{pmatrix} = 0 \quad \text{from relation (5)}$$

$$(13) \quad L_c \begin{pmatrix} U_c^* \\ E_c^* \end{pmatrix} = 0 \quad \text{from relation (6)}$$

$$(14) N_r \begin{pmatrix} (Z_r^* \cdot I_r^*) - (Z_c^* \cdot I_c^*) \\ E_r^* \end{pmatrix} = 0 \quad \text{from relation (8)}$$

$$(15) N_c \begin{pmatrix} (Z_c^* \cdot I_r^*) + (Z_r^* \cdot I_c^*) \\ E_c^* \end{pmatrix} = 0 \quad \text{from relation (9)}$$

where  $\cdot$  represents the component-wise multiplication of two vectors.

$I_r$  and  $I_c$  are vectors representing currents crossing components, dimension (v.1).

$Z_r$  and  $Z_c$  are vectors representing the components impedance, dimension (v.1).

$U_r$  and  $U_c$  are vectors representing tensions to terminals of components, dimension (v.1).

$E_r$  and  $E_c$  are vectors representing voltage generators, dimension ((u-v).1) where u corresponds to the number of tensions and voltage generators.

$(M_r, M_c)$ ,  $(N_r, N_c)$  and  $(L_r, L_c)$  group together the node equations and mesh equations, respective dimensions (n.v), (m.u) and (m.u).

An connection matrix characterizes the structure of the system. Terms  $m_{ij}$  making up  $M_r$  and  $M_c$  have for value: -1 if the branch j comes from the node i, 0 if the branch j is not connected to the node i, +1 if the branch j comes into the node i.

Terms  $n_{ij}$  (respectively  $l_{ij}$ ) making up  $N_r$  and  $N_c$  (respectively  $L_r$  and  $L_c$ ) have for value: -1 if the tension j is in the mesh direction, 0 if the tension j is not present in the mesh, +1 if the tension j is opposite from the mesh direction.

Matrixes N and L are initially identical but we will allow thereafter to differentiate the branches according to the electrical parameter measured in those branches.

### Methodology

Groëbner bases give a rewritten system's relation in order to eliminate variables in the priority order indicated in the command.

Groëbner bases are searched from a set of polynomials. They are obtained by dividing leading monomials. Groëbner bases algorithms are an extension of Euclid algorithm when degree are above one and multi unknown polynomials. Their definition gives the insurance that the division stays in a determined ideal, the ideal generated by the initial system. So, the algorithm can find all the possible dividers, for every monomial. The search for the divider is not made in any direction. The order is determined. A good order is an order that does not generate a strictly decreasing suite in the successive divisions. So, the division algorithm is sure to stop. It is a good order, in the sense defined by [11] and [12].

Note:

F: set of system equations ; v: number of equations

Var: set of the system variable ;  $k=\text{card}(\text{Var})$ : number of variables.

Var\_mesure: set of measured variables ( $\text{Var\_mesure} \subset \text{Var}$ ).

Var\_nonmesure: set of unmeasured variables ( $\text{Var\_nonmesure} = \text{Var} - \text{Var\_mesure}$ ).

I: ideal generated by F.

Each Groëbner base will be calculated in  $K[\text{Var\_mesure}]$  (ring of polynomial containing the measured variables).

#### Algorithm:

begin

1.  $F' = F - \{\text{relation with measured variables}\}$
2. find R a Groëbner base of  $F'$  with the

lexicographical order of Var\_nonmesure

3. isolate the resolved variables in R and place them in the set: Var\_dedit
4. the observable variables are in the set:  $\text{Var\_mesure} \cup \text{Var\_deduite}$
5. if  $\text{Var\_deduite} = \text{Var\_nonmesure}$ , then the system is globally observable

end

We will call "observability bases" a variable set included in the whole variable set and that has the minimum number of elements allowing the system to be observable. These observability bases are the possible combination number of necessary variables from the variable set. Let us notice that it is not so easy to know the exact number of them. [13] and [14] have tried to do it, introducing a numbering tree and looking at the dimensions of the different sets. But even without knowing the exact number of them, we can observe the every base union form the whole system variable set. From their intersection, we can deduce system redundancy. We will do now an important remark on the nature of system's relation. When some variables are measured, they are considered as known. From that, some relations take a particular sense. Three different kinds exist:

- redundancy relations: they are relations where there are measured variables only.
- deduction relations: they are relations that permit to deduce a unmeasured variable value from measured variables values.
- relations where they are a few unmeasured variables: there are relations with unmeasured relations.

### Example

Let us consider the simple electrical network following:

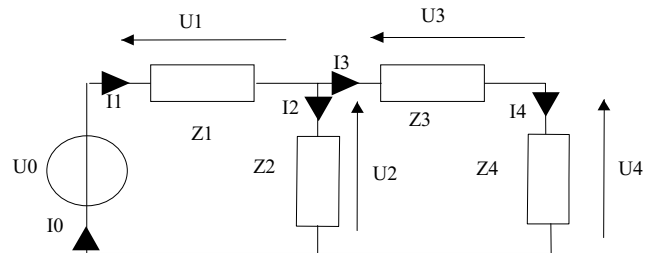


Fig. 1. Electrical network

This method concern multi-linear systems. If some relations are linear and others are multi-linear, the method is even more interesting. We take as example the electric circuit shown on figure 1. We have the equations resumed in the system F:

$$(16a) \quad M I = 0$$

$$(16b) \quad L U = 0$$

$$(16c) \quad U_Z - Z I_Z = 0$$

We have the vectors  $I_Z = [i_1 \ i_2 \ i_3 \ i_4]^T$ ,  $I = [I_Z^T \ i_0]^T$ ,  $U_Z = [u_1 \ u_2 \ u_3 \ u_4]^T$ ,  $U = [U_Z^T \ u_0]^T$ ,  $Z = [z_1 \ z_2 \ z_3 \ z_4]^T$ .

Note:  $F = [-i_1 + i_0, i_1 - i_2 - i_3, i_3 - i_4, -u_1 - u_2 + u_0, u_2 - u_3 - u_4, u_1 - z_1 * i_1, u_2 - z_2 * i_2, u_3 - z_3 * i_3, u_4 - z_4 * i_4]$ ;  $\text{var\_mesure} = \{i_1, i_3, u_1, u_2, u_3\}$ ;  $\text{var} = \{i_1, i_0, i_2, i_3, i_4, u_1, u_2, u_0, u_3, u_4, z_1, z_2, z_3, z_4\}$ ;  $\text{var\_nonmesure} = \{i_0, i_2, i_4, u_0, u_4, z_1, z_2, z_3, z_4\}$

A Groëbner base of F with the lexicographical order of Var\_nonmesure is given by:

$$R = [z_4 * i_1 - z_4 * i_2 - u_2 + u_3, -u_3 + z_3 * i_1 - z_3 * i_2, -u_2 + z_2 * i_2, -u_1 + z_1 * i_1, -u_2 + u_3 + u_4, -u_1 - u_2 + u_0, i_4 - i_1 + i_2, -i_1 + i_2 + i_3, -i_1 + i_0]$$

R is an observability base of F; The unmeasured variables (underlined) can be deduced from the measured variables. So, the system is observable.

If you take a new list:  $\text{var\_mesure} = \{i_1, i_2, i_3, i_4, z_2, z_3\}$ ; The system is no more observable. If we want obtain an observable sub-system, we must have more measurements.

### Using cost'S algorithm

We can find diverse algorithms of cost optimisation in the literature [15], [16] and [17]. Their biggest disadvantage is there increasing complexity when the system becomes multi-linear. This is not the case here. We present a method that does not care about the linearity degree of the system. This algorithm has the minimum number possible of iterations: the number of sensors that must be added to make the system observable.

Thus, we will propose the algorithm below. The equation system is F. The whole variable vector is Var. The cost of variables is indicated in the vector C.

#### Algorithm:

begin

1. rank the variables according to cost from the lowest to the highest in a list called Var\_cost
2. remove the first variable in Var\_cost and add this to Var\_measured; to search for the GB in the Var\_measured direction and remove the solved variables from the Var\_cost list.
3. if the system is globally observable the optimal end list is Var\_measured else go back to step 2.

end

Notice that in the example presented below, we can obtain the configurations giving the lowest cost with this algorithm directly. We take again the circuit of the figure 1. The equation system has not changed. We take the cost vector:  $C = [4, 4, 4, 4, 4, 2, 2, 2, 2, 1, 2, 2, 2, 10]$ . Once aranged in growing order, we have the list:  $\text{var\_cost} = [u_0, u_1, u_2, u_3, u_4, z_1, z_2, z_3, i_1, i_2, i_3, i_4, i_0, z_4]$ . We obtain the sensor list to implement:  $\text{Var\_measured} = [i_1, i_2, z_1, z_2, z_3]$ . It could be interesting to see in every possible case in the same figure and verify that the solution we found is the optimal one. We can notice the obvious simplification of our algorithm compared to the previous works.

### Conclusion

The presented study allows to classify the different variables of the process according to their observability. An efficient algorithm has been developed for cost and

observability optimal sensor design. Moreover, it can be directly implemented for multi-linear systems This classification (observable-unobservable variables) appears very interesting since it allows the estimate of the true values on the observable sub-system. We can obtain the redundancy equations and analyze the signature of the default. If the number of redundant equations is sufficient, it is possible to detect where is the default. The analysis of the residues can allow us to plan a diagnosis of the system, in view to detect possible defects of the instrumentation.

### References

- [1] K.A. Clement, G.R.Krumpholtz, P.W. Davis, "Power System State Estimation with Measurement Deficiency: An algorithm that determines the maximal observable subnetwork" IEEE Transactions on Power Apparatus and systems, Vol. PAS-101, n°9, September 1982.
- [2] T.E. Dy Liacco, "Security functions in power system control systems - The state-of-art in Control Center Design", 6<sup>th</sup> IFAC Symposium on Computer Applications in large-scale power systems, New Dehli, Août 1983.
- [3] R.L. Lugtu, D.F.Hackett, K.C.Liu, D.D.Might, "Power system state estimation: detection of topological errors", IEEE Transactions on Power Apparatus and systems, vol. PAS-99, n°6, pp. 2406-2412, novembre-décembre 1980.
- [4] K.Richert, A.C.Sullivan, "A systematic Study of State Estimation in Electrical Power System", Proceedings of the IFAC Symposium, Melbourne, pp. 434-440, 1977.
- [5] G.R. Krumpholz, K.A.Clements, P.W.Davis, "Power System Observability: A practical Algorithm using Network Topology", IEEE Transactions on Power Apparatus and systems, Vol. PAS-99, N°4, July/August 1980.
- [6] P. Tréhin, N. Héraud, "Observability and state estimation of an electrical network", International Congress IMACS, IMACS'97, Berlin, pp. 263-268, august 1997.
- [7] J. Ragot, D. Maquin, G. Bloch, W. Gomolka, « Observability and variables classification in bilinear processes, » Journal A, vol. 31, n° 4, 1991, pp. 17-24.
- [8] O. Wailly, N. Héraud, E. H. Mazzour. Optimal sensor design in polynomial system using symbolic calculus software, IEEE, International Conference on Computational Cybernetics, ICC3, Siofok, Hungary, august 29-31, 2003.
- [9] Kretsovalis A., R.S.H. Mah, "Observability and redundancy classification in generalized process networks - II Algorithms," Computer Chemical Engineering, vol. 12, n° 1, 1988, p. 689-704.
- [10] Luong M., Maquin D., Huynh C.T., Ragot J., "Observability, redundancy, reliability and integrated design of measurement system," in proceeding of the 2nd IFAC Symposium on

- Intelligent Components and Instruments for Control Applications, SICICA'94, Budapest, Hungary, June 8-10, 1994.
- [11] Saux Picart P., Cours de calcul formel Ellipses, Paris, 1999.
- [12] Cox D., Little J., O'Shean D., Ideals, varieties and algorithms, Springer Verlag, 1991.
- [13] Héraud N., Battesti M., Mazzour E.H.. Observability and redundancy on generalized bilinear systems. Second International Conference on Industrial Automation, Nancy, France, June 7-9, 1995.
- [14] Héraud N., Mazzour E.H., Alfonsi M., "Architecture d'instrumentation d'une installation sous contrainte de coût," in proceeding of the 2<sup>ème</sup> conférence, Automatique Génie informatique Image, Poitiers, 2-3 juin, 1994.
- [15] Mazzour E.H, Héraud N., Alfonsi M., "Observabilité des systèmes n-linéaires sous contrainte de coût" in proceeding of Mediterranean conference on electronics and automatic control, Grenoble, 13-15 septembre, tome II, 1995.
- [16] Héraud N., Mazzour E.H.. Sensor network design for processes described by linear-bilinear equations. Journal of systems and control engineering, vol. n° 213, Part I, p. 321-329, 1999.
- 
- Nicolas Héraud** – Assistant Professor,.CNRS UMR 6134, University of Corsica, quartier Grossetti 20250 Corte, FRANCE.  
e-mail: [heraud@univ-corse.fr](mailto:heraud@univ-corse.fr).
- Olivier Wailly**– Ph.D. Student,.CNRS UMR 6134, University of Corsica, quartier Grossetti 20250 Corte, FRANCE.  
e-mail: [wailly@univ-corse.fr](mailto:wailly@univ-corse.fr)
- Ouadie Bennouna** – Ph.D. Student, CNRS UMR 6134, University of Corsica, quartier Grossetti 20250 Corte, FRANCE.  
e-mail: [bennouna@univ-corse.fr](mailto:bennouna@univ-corse.fr)
- Philippe Poggi** – Assistant Professor,.CNRS UMR 6134, University of Corsica, Vignola, Route des Sanguinaires, 20000 Ajaccio FRANCE.  
e-mail: [poggi@univ-corse.fr](mailto:poggi@univ-corse.fr).

## Mathematical Description of Complicated Power Supply Systems

Soloviov Vyacheslav, Kupov Alexandr, Khandoshko Konstantin  
and Kupova Anastasia

**Abstract:** In submitted article the results of modeling program of electro technical system in Matlab 6.5 environment are shown. Modeling was carried out on system of the differential equations received for the simplified electric circuit of power supply system. Results of model calculations are submitted together with diagrams.

**Keywords:** reactive capacity, modeling compensative system.

### Introduction

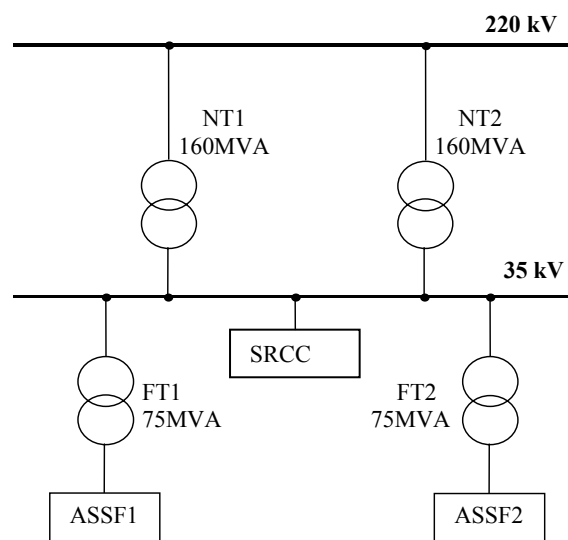
It is well-known, that the complex loading connected on a sine wave voltage always causes phase shift between a consumed current and the enclosed voltage. In consequence of it reactive capacity is consumed. The listed problems can be solved in the certain extent if you provide the capacity coefficient close to unit. It is possible in case of the intentional reduction of phase shift between a current and voltage.

The consumption of reactive capacity falls under compensation if you know beforehand character of loading change. However there are technological processes in which it is not obviously possible to predict the specified changes. On account of it the compensation of phase shifts between current and voltage is impeded that has an effect for quality parameters of electric power receivers. A deviation and fluctuations of voltage and frequency; no sinuous forms of voltage; displacement of zero and voltage asymmetry of the base frequency refer to number of such parameters.

Electro steel smelting industry is a standard technological process, where sharp unpredictable character changes of complex loading are inevitable with the appropriate jumps of consumed reactive capacity. The system of reactive capacity compensations (SRCC) is used for performing the requirements on quality of electric power.

### Electric circuit.

The circuit of analyzing power supply system is given on fig.1. A feeding of 35 kV furnace bus-bar is carried out from two transformers by 160 MVA capacity (the network transformer) and 75 MVA (furnace). The system of reactive capacity compensations is connected to 35 kV general bus-bar to which transformers of two furnaces (ASSF1, ASSF2) are connected.



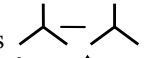
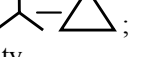
NT1, NT2 – network transformers ;  
FT1, FT2 – furnace transformers ;  
SRCC – system of reactive capacity compensations;  
ASSF1, ASSF2 – arc steel-smelting furnaces.

Fig. 1 – Functional scheme of power supply ASSF

Supposing, that mutual influence of furnaces is not considerably and distortion (which is characterized by coefficient of distortion) brought by the network transformer is insignificantly, further we shall examine the connection circuit only of one furnace. The equivalent power circuit is submitted on fig.2 (the network transformer is not shown).

The compensative system of reactive capacity represents by filter compensative circuits (FCC) which consist from capacitive (C) and inductive (L) elements.

To the designations given in figure 2 correspond:

$\Phi_A, \Phi_B, \Phi_C$  – fluxes in the phases of the transformer;

$i_0$  – a current of a zero wire between network and furnace transformers;

$U_A, U_B, U_C$  – a voltage of a power line;

$I_A, I_B, I_C$  – primary currents of the furnace transformer;

$i'_A, i'_B, i'_C$  – currents of secondary windings of the furnace transformer;

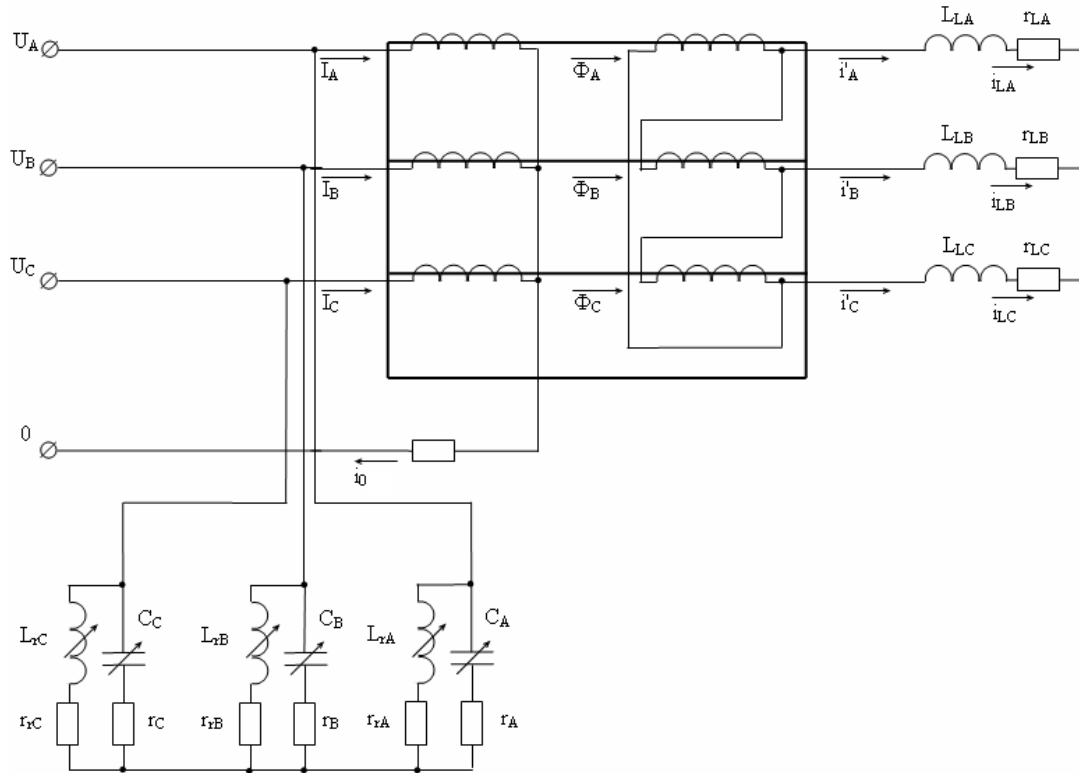


Fig. 2 – The equivalent power circuit of furnace feeding

$r_A, r_B, r_C$  – active resistance FCC;  
 $C_A, C_B, C_C$  – values of capacitive elements FCC  
 $i_{LA}, i_{LB}, i_{LC}$  – currents of loading;  
 $r_{LA}, r_{LB}, r_{LC}$  – active resistance of loading;  
 $L_{LA}, L_{LB}, L_{LC}$  – reactance of loading;

### Preconditions to the mathematical description

The mathematical model of all power system is necessary for development and research of a modern effective control system. Modeling the greatest complexity is represented with the description of three-phase power transformer.

In the given circuit the transformer with the armored core uses. In this transformer it is necessary to take into account the additional fluxes closed through the walls of an oil tank, therefore three rods of the core are submitted as four rods, distinguished by the presence of artificial entered fictitious rod which resistance aspires to infinity.

The transformer work is based on a principle of electromagnetic interaction of circuits, motionless to each other. The analysis of system work is based on laws Kirchhoff.

At the analysis of the examined circuit (fig. 2) we assume, that flux  $\Phi$  is distributed to regular intervals on the transformer profile of the core and linked to all coils both primary and secondary windings  $w$ . This flux

creates in windings of transformer Electromotive force (EMF).

$$(1) \quad e = w \frac{d\Phi}{dt}.$$

Besides magnetized multipliers create primary and secondary fluxes of dispersion. Under the primary flux of dispersion we shall understand a flux created by current  $i_A$  and linked with the primary winding only, and as the secondary flux of dispersion - a flux created by current  $i'_A$  and linked with the secondary winding only. As fluxes of dispersion are distributed mainly to the non magnetic environment having constant magnetic permeability it is possible to count, that inductance of dispersion  $L_{\sigma 1}$  and  $L_{\sigma 2}$  are constant. In accordance with EMF of the dispersion, created by fluxes of dispersion in primary and secondary windings of the transformer, will be:

$$(2) \quad \begin{cases} e_{\sigma 1} = L_{\sigma 1} \frac{di_A}{dt}; \\ e_{\sigma 2} = L_{\sigma 2} \frac{di'_A}{dt}. \end{cases}$$

According to the second law of Kirchhoff, we have equation EMF of the primary winding:

$$(3) \quad U_A = i_A r_{\sigma 1} + e + e_{\sigma 1}$$

where:

$r_{\sigma 1}$  – active resistance of primary winding of the transformer

The equation written in such form is the equation of EMF balance under which voltage  $U_A$  is examined as action of a network in relation to the primary winding of the transformer. EMF ( $i_A r_{\sigma 1}$ ) determines counteraction which meets a current  $i_A$ , proceeding on a conductor with resistance  $r_{\sigma 1}$ .

As the transformer works in an asymmetrical mode and can enter a mode of saturation at its description it is necessary to take into account nonlinearity of magnetization current  $f(i_0)$ .

Besides character of loading has the big value under the development of mathematical model of object. At the mathematical description of the loading block it was taken into account that the secondary winding of the furnace transformer is connected into a triangle, and furnace electrodes connect resistance of loading into a star. Resistance of loading was represented in actively inductive form.

### The mathematical description

Using Kirchhoff laws for the analysis of power system work the circuit is broken into several parts: the primary winding, the secondary winding of the transformer, filter compensative device.

The primary winding of the transformer is characterized by the following equations:

$$(4) \quad \begin{cases} U_A = W_1 \frac{d\Phi_A}{dt} + L_{\sigma 1} \frac{dI_A}{dt} + r_{\sigma 1} I_A + r_0 i_0; \\ U_B = W_1 \frac{d\Phi_B}{dt} + L_{\sigma 1} \frac{dI_B}{dt} + r_{\sigma 1} I_B + r_0 i_0; \\ U_C = W_1 \frac{d\Phi_C}{dt} + L_{\sigma 1} \frac{dI_C}{dt} + r_{\sigma 1} I_C + r_0 i_0; \\ i_A + i_B + i_C = i_0. \end{cases}$$

where:

$r_0$  – active resistance of a zero wire between network and furnace transformers;

$W_1$  – coils amount of primary winding of the furnace transformer;

$L_{\sigma 1}$  – leakage inductance of primary winding of the furnace transformer;

Magnetic system of the transformer:

$$(5) \quad \begin{cases} \Phi_A + \Phi_B + \Phi_C = \Phi_0; \\ W_1 i_A + W_2 i'_A = W_1 i_{0m} + r_m \Phi_0; \\ W_1 i_B + W_2 i'_B = W_1 i_{0m} + r_m \Phi_0; \\ W_1 i_C + W_2 i'_C = W_1 i_{0m} + r_m \Phi_0; \end{cases}$$

where:

$i_{0m}$  – magnetic current of the furnace transformer;

$r_m$  – magnetic resistance;

$\Phi_0$  – a fictitious zero flux of the transformer.

The secondary winding of the transformer is characterized by the following equations:

$$(6) \quad \begin{cases} i'_A - i'_B = i_{LB}; \\ i'_B - i'_C = i_{LC}; \\ i'_C - i'_A = i_{LA}; \end{cases}$$

$$(7) \quad \begin{cases} W_2 \frac{d\Phi_A}{dt} + L_{\sigma 2} \frac{di'_A}{dt} + r_{\sigma 2} i'_A + L_{LB} \frac{di_{LB}}{dt} + \\ + r_{LB} i_{LB} - L_{LA} \frac{di_{LA}}{dt} - r_{LA} i_{LA} = 0; \\ W_2 \frac{d\Phi_B}{dt} + L_{\sigma 2} \frac{di'_B}{dt} + r_{\sigma 2} i'_B + L_{LC} \frac{di_{LC}}{dt} + \\ + r_{LC} i_{LC} - L_{LB} \frac{di_{LB}}{dt} - r_{LB} i_{LB} = 0; \\ W_2 \frac{d\Phi_C}{dt} + L_{\sigma 2} \frac{di'_C}{dt} + r_{\sigma 2} i'_C + L_{LA} \frac{di_{LA}}{dt} + \\ + r_{LA} i_{LA} - L_{LC} \frac{di_{LC}}{dt} - r_{LC} i_{LC} = 0; \end{cases}$$

where:

$W_2$  – coils amount of secondary winding of the furnace transformer;

$L_{\sigma 2}$  – leakage inductance of secondary winding of the furnace transformer;

$r_{\sigma 2}$  – active resistance of secondary winding of the furnace transformer;

Filter compensative device is characterized by the following equations:

$$(8) \quad \begin{cases} W_1 \frac{d\Phi_A}{dt} + L_{\sigma 1} \frac{dI_A}{dt} + r_{\sigma 1} I_A - W_1 \frac{d\Phi_B}{dt} - \\ - L_{\sigma 1} \frac{dI_B}{dt} - r_{\sigma 1} I_B + U_{CB} + r_B i_{CB} - U_{CA} - r_A i_{CA} = 0; \\ W_1 \frac{d\Phi_B}{dt} + L_{\sigma 1} \frac{dI_B}{dt} + r_{\sigma 1} I_B - W_1 \frac{d\Phi_C}{dt} - \\ - L_{\sigma 1} \frac{dI_C}{dt} - r_{\sigma 1} I_C + U_{CC} + r_C i_{CC} - U_{CB} - r_B i_{CB} = 0; \end{cases}$$

$$(9) \quad \begin{cases} r i_C + U_C = L_r \frac{di_r}{dt} + r_r i_r; \\ i_C = C \frac{dU_c}{dt}; \\ i_S = i_C + i_r; \\ i_S = i'_1 + i'_2; \\ i_{SA} + i_{SB} + i_{SC} = 0; \end{cases}$$

where:

$U_{CA}$ ,  $U_{CB}$ ,  $U_{CC}$  – voltage drop in capacitive elements FCC;

$U_C$  – voltage vector in capacitive elements FCC;

$i_{CA}$ ,  $i_{CB}$ ,  $i_{CC}$  – currents on active element FCC;



$i_{rA}, i_{rB}, i_{rC}$  – currents on active - reactive elements FCC;

$L_r, r_r$  – value vectors of inductive and active elements FCC;

$i_C$  – a current vector in active elements FCC;

$r$  – a vector of active resistance FCC;

$C$  – a value vector of capacitive elements FCC;

### Results of modeling

Modeling of system was carried out in MatLab environment. The equations wrote in relative numbers, recognizing that  $R_{RL} = 1$  и  $L_{RL} = 1,5 \cdot R_{RL}$ . All other parameters of system among which are resistance of windings, their inductance, amount of transformer coils, transformer currents, a submitted voltage are considered proportional to  $R_{RL}$  and  $L_{RL}$ .

Diagrams of voltage and current transients of the transformer primary winding, the system designed on model are represented on fig.3, and on fig.4 the data received in the real system (bus-bar 35 kV). Apparently diagrams are identical; therefore it is possible to speak about adequacy of model to real system.

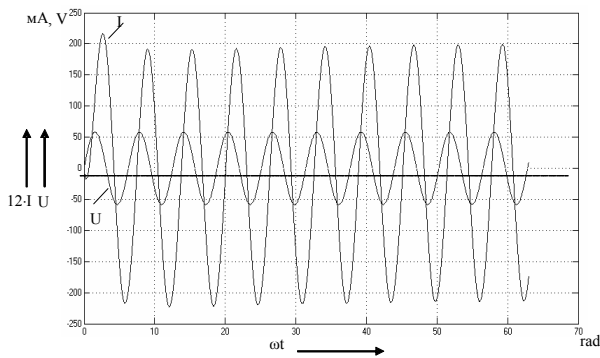


Fig.4 – Melting of charge

The equalizer of reactive component of current is carried out by a principle of step regulation of

compensating capacity and smooth readjustment of inductance. The device compensating once given size and loading character was created under modeling system. The diagrams of voltage and compensated current are given on fig.5. As we can see from figure diagrams inphase that speaks about correct adjustment of the equalizer.

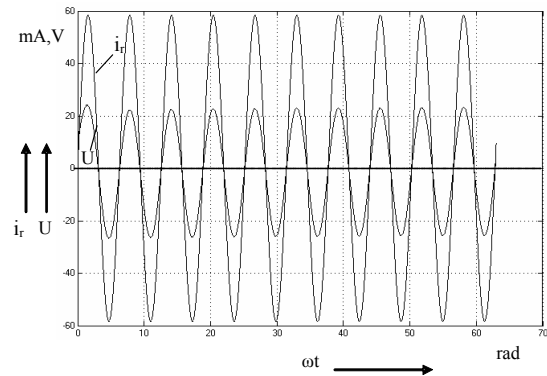


Fig.5. – Transients of current and voltage got from the model system under reactive multiplier

### Conclusion

Presence of the developed mathematical description of electro supply system allows carrying out the automated calculation of parameters of electric power quality, such as: asymmetry of phase-to-phase voltage, factor of distortion in system etc. Except for that a number of control systems, parameter stabilization of power supply system by enterprise, providing for comparatively high parameters of electric power quality is developed on the basis of the received model.

**Vyacheslav Soloviov** – Professor, DSc., Faculty of Electrical Engineering, Technical University of Komsomolsk-on-Amur, 27 Lenins Str., Komsomolsk-on-Amur, Russia, [kepapu@knastu.ru](mailto:kepapu@knastu.ru).

**Aleksandr Kupov** –assistant professor, Dr., Faculty of Electrical Engineering, Technical University of Komsomolsk-on-Amur, 27 Lenins Str., Komsomolsk-on-Amur, Russia, [alek-epapu@rambler.ru](mailto:alek-epapu@rambler.ru).

**Konstantin Khandoshko** – Ph.D. Student, Faculty of Electrical Engineering, Technical University of Komsomolsk-on-Amur, 27 Lenins Str., Komsomolsk-on-Amur, Russia.

**Anastasia Kupova** – Ph.D. Student, Faculty of Electrical Engineering, Technical University of Komsomolsk-on-Amur, 27 Lenins Str., Komsomolsk-on-Amur, Russia, [k\\_asya@rambler.ru](mailto:k_asya@rambler.ru).

# Computer program for setting of earth protection in electric power networks of average voltage

Mediha Mehmed-Hamza and Anton Filipov

**Abstract** When computing the settings of the earth protection problems usually arise in connection with the precise determination of their selectivity and sensitivity, namely with computation of the own capacitive currents of the terminals and of the current of zero sequence in ground circuit. The created computer program allows in a dialog mode to introduce data for the terminals that feed the power transformer, the loads and others, of a concrete electric network. Also, to determine the capacitive currents of the terminals, the currents at the beginning of the terminal in a three-phase short and ground circuit at the end nodes of the terminal. On the basis of thus obtained data the settings of the earth protection can be determined.

**Keywords:** earth protections, power networks of average voltage

## Computer program for setting of earth protection

When designing earth protections, filters for zero sequence currents and voltages are used. A three transformer filter is used in overhead lines, and a current transformer of Ferranti type is used in cable lines. When computing the settings of earth protections, the usual problems refer to determining the own capacitive currents of the terminals and computing the zero sequence current in earth connection of the terminal.

When setting earth protections which use a current transformer of Ferranti type, the value of the shock coefficient ( $\text{Coef}_{\text{shock}}$ ) is decisive. The sensitivity and velocity of the protection will change depending on the value assigned to the shock coefficient.

The current for triggering the earth protection is determined by [1]:

$$(1) \quad I_{\text{ep}} = \text{Coef}_{\text{saf}} \cdot \text{Coef}_{\text{shock}} \cdot 3 \cdot \omega \cdot C_{0i} \cdot U_{\text{phase}}$$

where  $\text{Coef}_{\text{saf}}=1.1-1.2$ - coefficient of safety,  $C_{0i}$  – capacity of the phase wire of power distribution line  $i$  in relation to the earth,  $U_{\text{phase}}$  – phase voltage before occurrence of the earth connection.

The coefficient of sensitivity is determined by the expression [1]:

$$(2) \quad \text{Coef}_{\text{sens}} = \frac{3I_{\text{min}}}{I_{\text{ep}}}$$

For the shock coefficient and the time of triggering the earth protections ( $t_{\text{ep}}$ ) the following values are used [2]:

-  $\text{Coef}_{\text{shock}}=1$ , at which the time of protection triggering must be as follows:

$$t_{\text{ep}} \geq 0.1 \text{ s for overhead (mixed) terminals;}$$

$$t_{\text{ep}} \geq 0.05 \text{ s for cable terminals;}$$

-  $\text{Coef}_{\text{shock}}=5$ , at which the time of protection triggering must be as follows:

$$t_{\text{ep}} \geq 0.05 \text{ for overhead (mixed) terminals ;}$$

$$t_{\text{ep}} \geq 0.03 \text{ for cable terminals.}$$

In earth protections which use a three transformer filter, the setting of the earth protection is done by the following algorithm [1]:

$$(3) \quad I_{\text{min,ep}} = \text{Coef}_{\text{saf}} \cdot \text{Coef}_{\text{non-b}} \cdot I_{\text{nom}}$$

where  $\text{Coef}_{\text{saf}}=1.3$  to  $1.5$ - coefficient of safety,  $I_{\text{nom}}$  – nominal primary current of the current measuring transformer;  $\text{Coef}_{\text{non-b}} = 0.05$  to  $0.1$  – it reads the error of the current measuring transformer, the influence of the aperiodic component in the current and the inequality of the current measuring transformers.

By help of the minimum setting-up current computed in this manner ( $I_{\text{min,ep}}$ ), the maximum coefficient of sensitivity can be determined ( $\text{Coef}_{\text{sens,max}}$ ):

$$(4) \quad \text{Coef}_{\text{sens,max}} = \frac{3I_{\text{min}}}{I_{\text{min,ep}}}$$

where  $3I_{\text{min}}$  – the triple minimum current of zero sequence.

By taking into account the coefficient of sensitivity ( $\text{Coef}_{\text{sens}}$ ), which is to read the influence of the transient resistance too, we can also determine the maximum value of the triggering current for earth protections ( $I_{\text{max,ep}}$ ) using a three transformer filter. This is done by the formula

$$(5) \quad I_{\text{max,ep}} = \frac{3I_{\text{min}}}{\text{Coef}_{\text{sens}}}$$

With an active resistance of  $40\Omega$  at the star center and transient resistance of  $100\Omega$ , the coefficient of sensitivity is 4. The maximum setting-up current of the earth protection is determined by  $\text{Coef}_{\text{sens}}=4$ .

By the minimum triggering current of the earth protection computed in this manner, a check is made for unsetting from the own capacitive current (1) and from the zero sequence current as a result of asymmetry (6). 10% asymmetry is assumed in the elements of the power network (distribution lines and loads).

$$(6) \quad I_{\min, ep} > 3I_{0_{as}}$$

The created computer program offers the possibility, for a concrete power network, to determine the capacitive currents of the terminals, the currents at the beginning of the terminal in three phase and one phase short circuit at the end nodes of the terminal and the setting of the earth protection by the algorithms given above.

The main program menu is shown in Fig.1.

The algorithm of the program is built of 5 independent modules.

Module 1 "Review and correction of catalogs" presents catalog data about the used wires and transformers in networks of average voltage. Block 1.1 "Wires" stores catalog data about the types of wires, Block 1.2 "Transformers AV/LV" stores data about the decreasing power transformers of average/low voltage in use at present, and Block 1.3 "Transformers HV/AV" stores data about the supplying power transformers. Each of Blocks 1.1, 1.2 and 1.3 offers the possibility to record (1.1.1 "Record") and update (1.1.2 "Update"), to receive instructions on the operation steps of a block (1.1.3 "Help") and to exit (1.1.4 "Exit").

Module 2 "Review and correction for a minimum and maximum loading mode of the network" is made up of three blocks. Block 2.1 "Review" is where the data about the power network are entered – about the supplying power transformer, power distribution lines, loads, nominal primary and secondary current of the measuring current transformers in use at present and also the names of the terminals.

Block 2.1 offers the possibility to review and correct existing files with data (2.1.1 "Loading of a file with data") and to record these data (2.1.2 "Recording of a file with data").

Block 2.2 "Correction for minimum" is where files with data can be selected (2.2.1 "Selecting a file with data") and the loading of the terminals can be altered for a minimum mode (2.2.2 "Correction").

Block 2.3 "Correction for maximum" functions similarly to Block 2.1 for maximum loading mode of the network. For both the blocks, by default, a correction is offered which is 0.2 of the power capacity of the supplying power transformer in minimum mode, and 0.8 in maximum mode respectively.

Module 3 "Preparation of the data for transient and established mode" allows the possibility to select the exit file with data in which the data are recorded in the necessary format so that the program could be used for computing currents and voltages with earth protections in transient mode - "PZS" (Block 3.10) and in established mode - "Analysis" (Block 3.2)

Module 4 "General characteristic of the power network" is where the parameters of the power network

can be computed and visualized. By help of Block 4.1 "Computing" the following can be computed: the summary power of the loads, the summary length of the terminals, the summary length of the overhead and cable part of the terminals, the summary capacity of the network, the capacity of zero and straight sequence of the individual terminals and so on. Block 4.2 is where the computed data can be visualized.

Module 5 "Setting of earth protections" consists of three blocks.

By help of Block 5.1 "Computing", after selecting a file with data (5.1.1 "Selecting a file with data") and entering the data about the star center of the supplying power transformer (5.1.2 "Data about the star center"), Y – matrix of the network is formed and the currents at the earth connection ( $k^{(1)}$ ) are computed, at the three phase short circuit ( $k^{(3)}$ ) and at 10% asymmetry. Computation is made for all end nodes of the reviewed terminal. The obtained results are used in 5.1.4 "Computing the settings of earth protections". For each terminal a check is made for the beginning of a terminal – overhead or cable one. Depending on this, the setting-up current is computed and the coefficient of sensitivity and the time of setting-up the earth protection are determined. When computing the coefficient of sensitivity, the minimum value of the current at earth connection in the end nodes of the reviewed terminal is taken. Here a check is made whether the computed setting-up current is larger than 3I0 at 10 % asymmetry.

Block 5.2 "Visualization" is where a file with data can be chosen and the results from Block 5.1 can be visualized for all terminals in the reviewed power network.

Block 5.3 "Ikc/Terminal" is used to select a concrete terminal in the reviewed network, to visualize the currents at three phase and earth connection in the end nodes of the terminal and to set the earth protection .

Fig.2 shows the window of Module 4.

The visualization of the obtained results from the computations in Module 5 "Setting of earth protections" is shown in Fig. 3, where besides the parameters for setting by current ( $I_{ep}$ ) and time ( $t_{ep}$ ) information is also given about the provided coefficient of sensitivity  $Coef_{sens}$  at the respective settings.

Fig. 4 shows the visualization of the data about the currents at earth connection and three phase short circuit in the end nodes of a given terminal as well as the setting of the earth protection with a provided coefficient of sensitivity (Block 5.3).

Fig. 5 shows the block schematic diagram of the algorithm for setting the earth protections in power networks of average voltage .

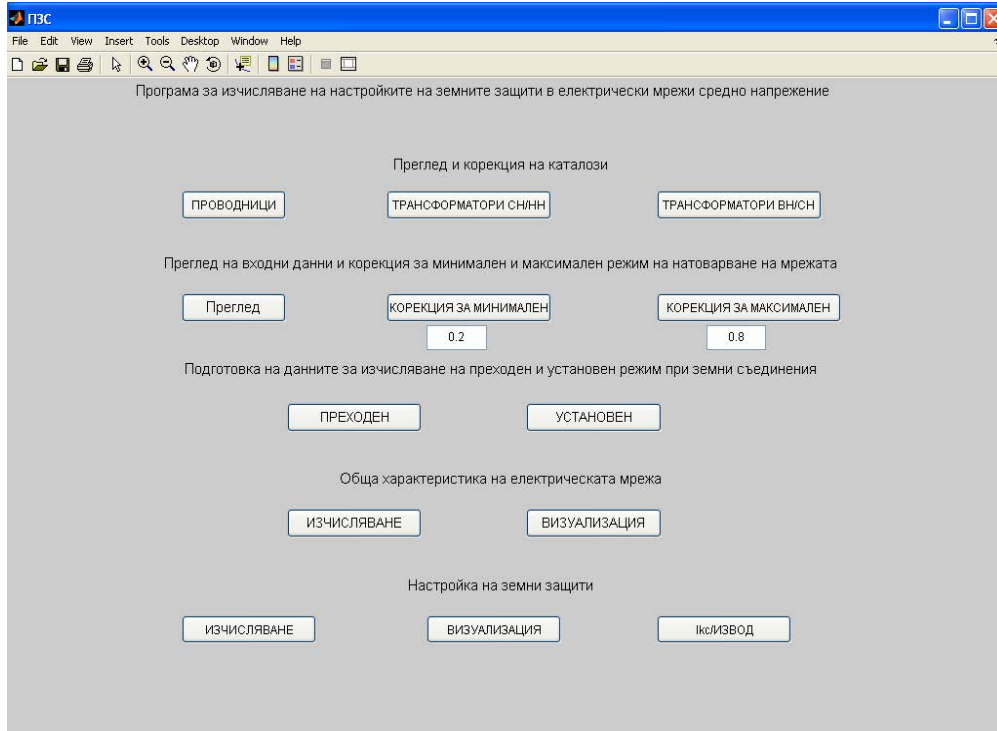


Fig.1. Main menu of the program for computing the settings of earth protections in power networks of 20 kV.

Обща характеристика на електрическата мрежа

ОБЩА ХАРАКТЕРИСТИКА НА ЕЛЕКТРИЧЕСКАТА МРЕЖА

Име на файла с данни - Kazanlak1o\_ID.mat

Брой изводи - 17

Брой товари - 132

N на шини средно напрежение - 2

Сумарна мощност на товарите - 20000

Сумарна дължина на изводите, [km] - 156.761

Сумарна дължина на въздушната част на изводите, [km] - 136.615

Сумарна дължина на кабелната част на изводите, [km] - 20.146

Сумарен капацитет на мрежата C1, [mF] - 6.8711

Сумарен капацитет на мрежата C0, [mF] - 6.5353

Сумарен капацитивен ток на мрежата 3Ic0, [A]- 74.6405

Име Извод	N Извод	Лъвца, [km]	L кабел, [km]	L, [km]	S, [kVA]	Co, [mF]	Ic, [A]	
1	Cherapanovk	1	32.11	0	32.11	2327	0.154	1.758
2	Kabakchiew	2	0	1.148	1.148	481	0.335	3.829
3	Chinar	3	0	1.228	1.228	1146	0.359	4.095
4	Zornica	4	0	1.922	1.922	1387	0.561	6.41
5	St.dom	5	0	1.812	1.812	695	0.529	6.043
6	Boadjew	6	0	1.688	1.688	1028	0.493	5.629
7	Izlok	7	0	3.104	3.104	1486	0.906	10.352
8	Saedinenie	8	0	1.642	1.642	1387	0.479	5.476
9	Sewer	9	0	1.672	1.672	1387	0.488	5.576
10	Shkolata	10	4.71	0.2	4.91	466	0.081	0.92
11	Serwiza	11	6.509	0	6.509	451	0.031	0.354
12	Magji	12	14.246	0	14.246	798	0.067	0.77
13	Cheshmite	13	26.523	1.2	27.723	2174	0.477	5.453
14	Prechistwaki	14	14.517	0.8	15.317	1650	0.303	3.46
15	Shanow	15	3.24	2.4	5.64	818	0.716	8.182
16	Hidrawlika	16	1.51	0	1.51	241	0.007	0.083
17	Derlika	17	33.25	1.33	34.58	2078	0.547	6.251
18								
19								

Fig.2. General characteristic of the power network.

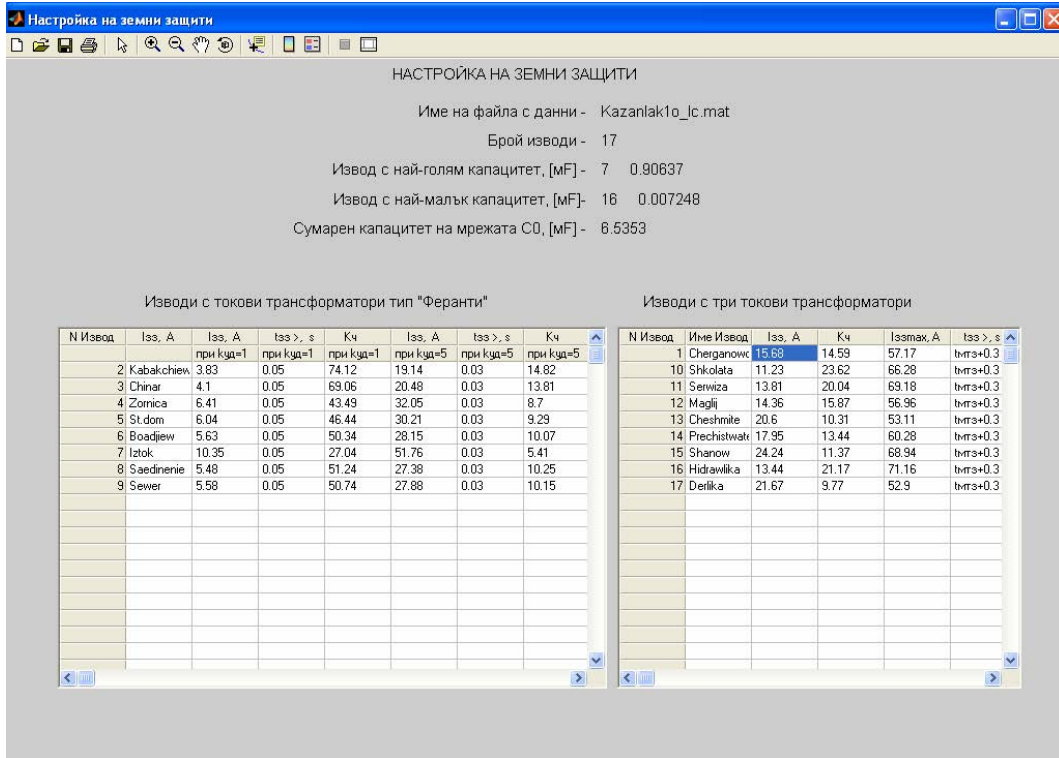


Fig.3. Visualization of the "Adjustment of the earth protections".

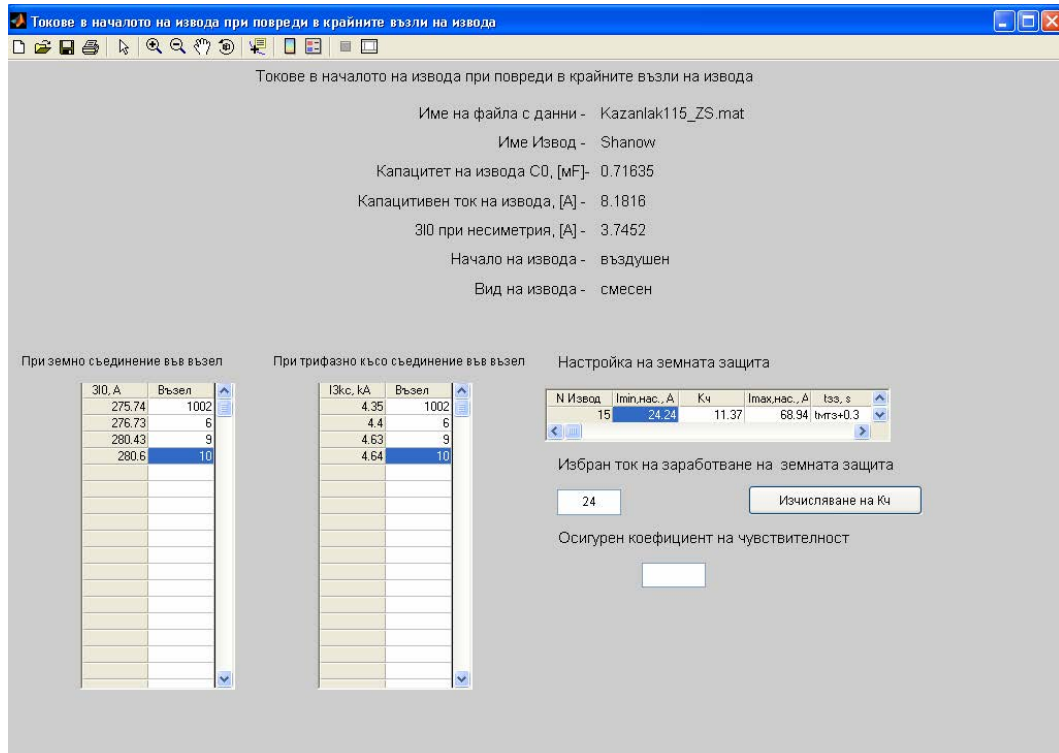


Fig.4. Visualization of the currents in failures at the end nodes

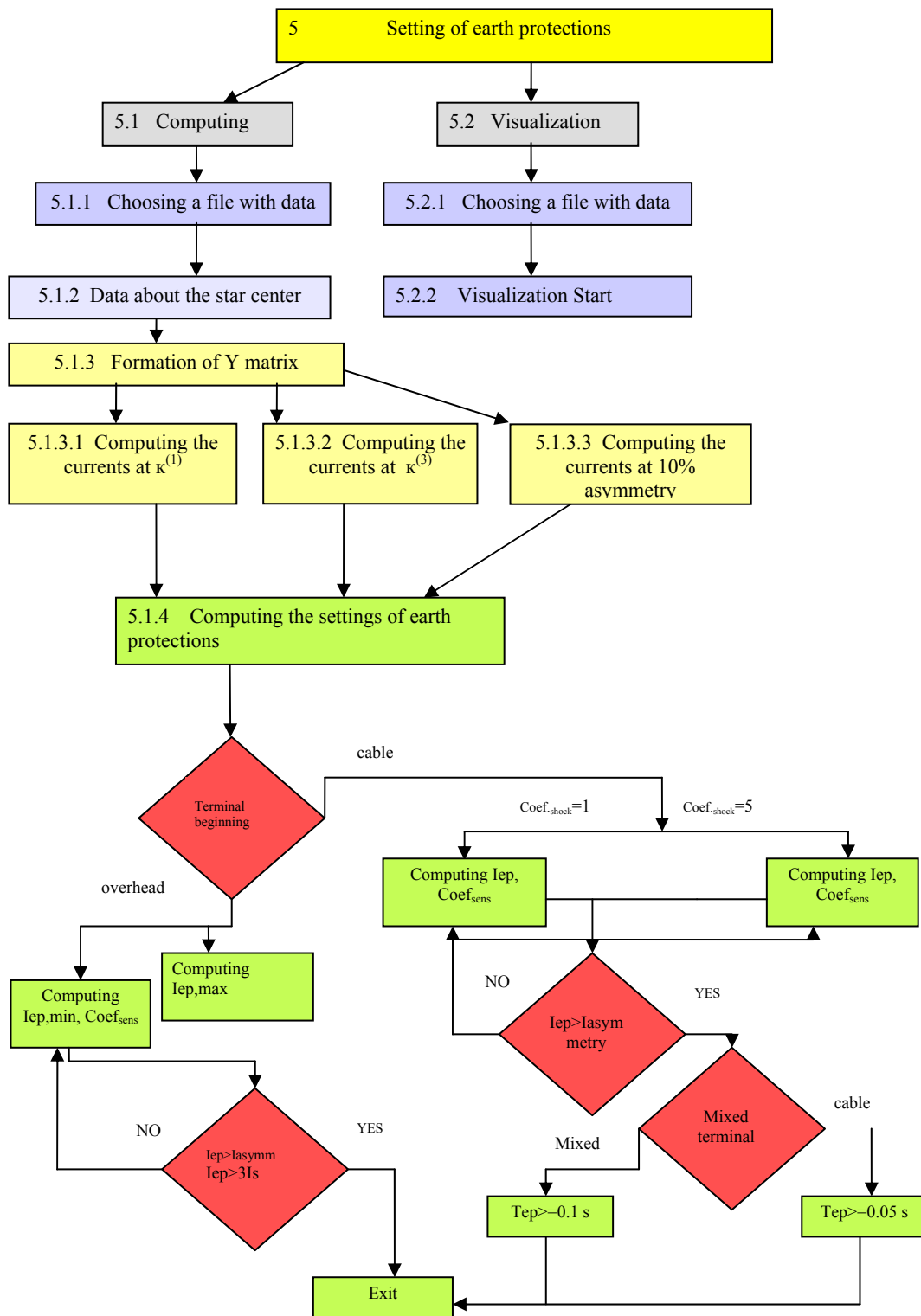


Fig.5. Block schematic diagram of the algorithm for setting earth protections in power networks

### Conclusion

By the values of the shock coefficient proposed here, which is bound to the decrease of the time of triggering

of earth protections, the sensitivity and velocity of the earth protections are increased.

The lower values of the times of triggering are not a problem taking into account that digital relay protections

and fast breakers have massively been introduced into our electric power system over the past years.

1. The proposed methodology of setting the earth protections takes into account the configuration of the power network, the type of the terminal and the current measuring transformers in use.

2. The developed computer program, through assigning input data, can automatically compute the settings of the earth protections by the triggering current and by the time of delay which are necessary to provide its selective function, and it also evaluates the level of sensitivity with these settings.

3. The computer program for setting the earth protections in power networks of average voltage considerably shortens the time for determining the settings of the earth protections and does not require any specialized knowledge on the part of the user.

### References

[1] Федосеев, А. М. Релейная защита электрических систем. Москва, Энергия, 1976. М

[2] E. Mehmed-Hamza, K. K. Gerasimov, St. A. Georgiev, A. B. Filipov. On the adjustment of earth protections in power networks of average voltage. *Acta universitatias pontica Euxinus*, 2005, N 1, vol. 4, pp. 76-79.

[3] Герасимов, К. К., Й. Л. Каменов. Моделиране на земни съединения в разпределителни електрически мрежи за средно напрежение.- Юбилейна научна сесия-ТУ-Варна, 1997, с. 266-274.

---

*M. Mehmed-Hamza* — Head Assistant in Electrical Power Engineering Department, Technical University of Varna, BULGARIA. e-mail: [mediha.hamza@tu-varna.acad.bg](mailto:mediha.hamza@tu-varna.acad.bg).

*Anton Filipov* — Assistant in Electrical Power Engineering department, Technical University of Varna, BULGARIA. e-mail: [filipov\\_a@yahoo.com](mailto:filipov_a@yahoo.com).

# Computer Graphic Processing of Discretely Registered Electrical Quantities in Electric Power Objects

A. Filipov, M. Mehmed-Hamza, St. Andreev

**Abstract:** *The registration of processes in electric power industry is possible by using analog and digital oscilloscopes and spectroanalyzers. The selection of measuring or registering equipment is done depending on the concrete signals, their form and duration. The modern digital equipment gives the possibility to obtain discrete values of the measured signal and to transmit them from the measuring device to the personal computer in binary or textual form. For the subsequent research and computation it is possible to use suitable mathematical and graphic software of Matlab, Mathcad and other types.*

*This publication presents a program which allows graphic processing of discretely registered signals. We have applied an approach of incorporated usage of expansion by Fourier and mono-dimensional decomposition combined with the possibility to determine the level and the coefficients of the polynomial of the investigated signal.*

*The program allows fast and convenient processing of large arrays of digital data. The feasibility of this methodology is in research and analysis of concrete discretely registered processes.*

**Keywords:** *Experimental Results Processing*

## Computer Graphic Processing

In electric power industry, the measured electric quantities are usually current, voltage, power and energy. Of particular interest are the moment, maximum (minimum) and effective values of these quantities. There is a wide range of measurement and registering devices – conventional ones, mostly of arrow-type, as well as digital. The selection of measurement or registering equipment depends on the concrete signals, their form and continuance. As regards the devices, measurement of slowly changing quantities is a comparatively easy task. Registering of fast changing processes, such as transitional processes in electric power industry is possible by using analog and digital oscilloscopes and spectrum analyzers. The modern digital equipment gives the opportunity to obtain discrete values of the measured signal and to transmit them from the measuring device to a PC in a binary or text form. Some of measurement equipment manufacturers also offer multi-feature software but its capacities are still limited. When registering certain processes a high level of signal

discretization is desirable or necessary but there are cases when this advantage is undesirable.

It is possible to use suitable mathematical and graphic software, such as Matlab, Mathcad and others to investigate and compute.

To achieve a higher level of a detailed investigation in the program packages listed above, several approaches are possible. Matlab offers the opportunity for the signal under investigation to be drawn as a graph identical to that of an oscilloscope. The Basic Fitting function allows for finding an equation of polynomial up to tenth power and overlapping it over the basic signal. In most cases, the order of this polynomial is sufficient, and the coefficients and the equation can be written in a very convenient form. The opportunity to compute the function  $Y=f(X)$  by an assigned value of  $X$  is exceptionally felicitous.

Regardless of the listed opportunities and advantages, the limitation in the order of the polynomial and the necessity to manually enter scale coefficients, necessitated the development of the program “Graph\_processing” whose general layout is presented in Figure 1.

The requirements on the program are: the input value is to be recorded in mat file, and the variable “v” is to be a matrix of  $N$  rows and one column. In case the values of time “t” are known, the matrix is the same as the preceding one, in the contrary case  $v=f(t)$  is drawn with a time unit of one  $t=1:1:N$ .

The functional opportunities of the program are:

- correction of the signal in relation to a conditional zero axis (chosen by mouse or key board);
- assigning of scale coefficients along two axes;
- assigning of limits to the start and end time;
- assigning of the number of repetition cycles of the creeping integration method;
- “Filtering” of the signal by breaking it into its componential, more elementary wavelets (denoising using wavelets);
- assigning of a polynomial up to 160 row and comparing of the mean quadratic error between the signal and polynomial;
- comparing of the input signal with the obtained images;
- determining of the frequency spectrum of the signal through expanding in a Fourier series in relative units in relation to the basic component (50 Hz);



- computing of the maximum and the effective value of the signal;
- recording of the obtained results in mat files;

The program has two main windows. Fig. 1 shows a block schematic diagram of the developed

program; the blocks which refer to the first window, performing the first seven functional opportunities, are marked in yellow, as shown in Fig. 2, and the blocks referring to the second window are marked in green.

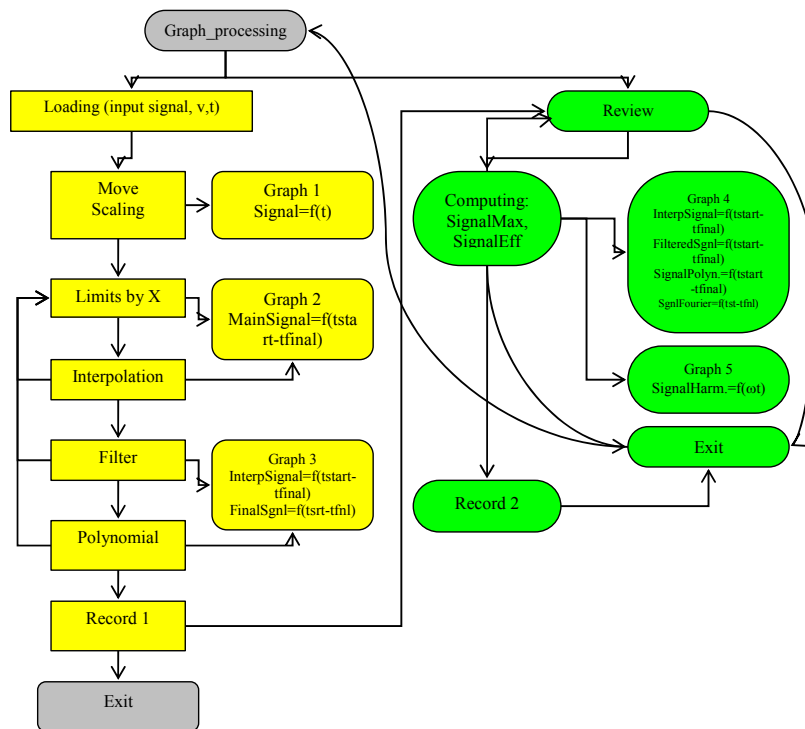


Fig.1. Block schematic diagram of the developed program

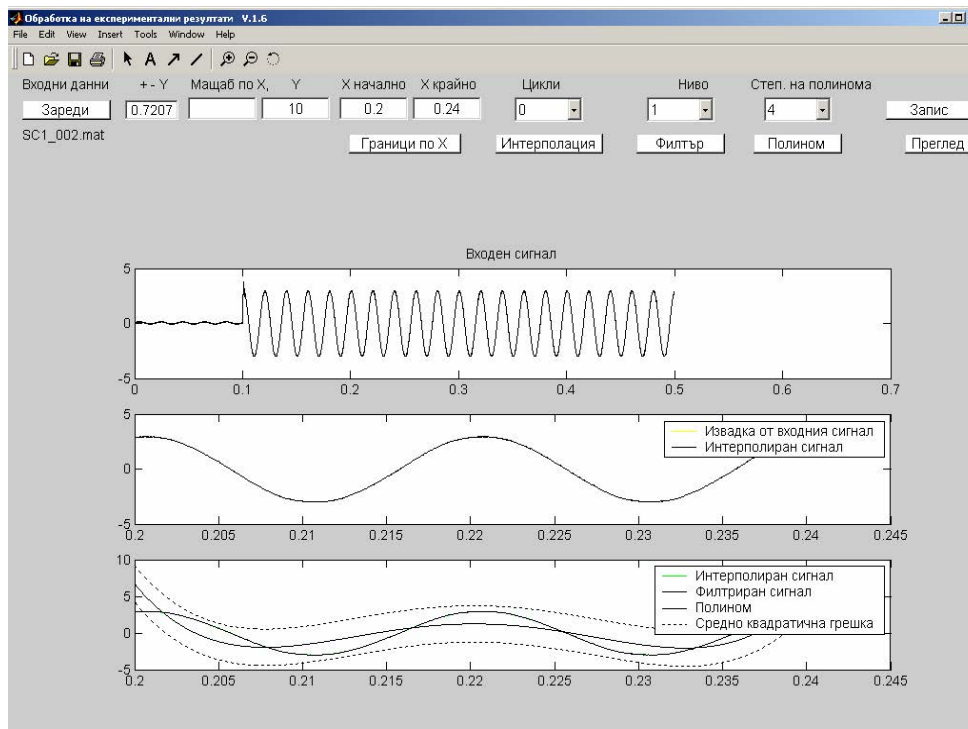


Fig.2. Window program

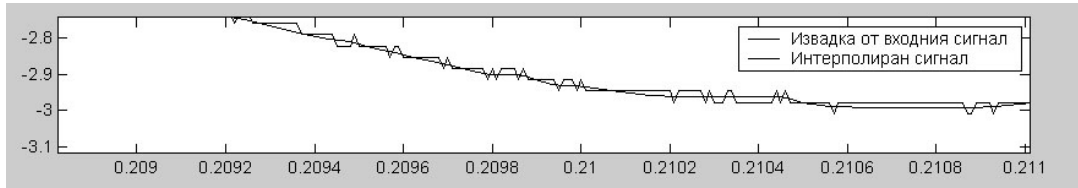


Fig.3. Signals

Fig. 3 shows part of the input signal and the alternative signal is overlapping after creeping averaging has been done (interpolation button). The number of loaded points describing the signal, is considerably decreased, and the curve is smooth. The input signal is discretized at  $L$  even intervals  $\Delta t$  in which approximation by a straight line is possible. The number of data on discretization by time -  $L$  is determined by the number of input data, and by using the button “Cycles” the number of cyclic computing of equation 1[1] can be determined.

$$(1) \quad y'_{i+\frac{L}{2}} = \frac{1}{L+1} \sum_{j=0}^L y_{i+j}; \quad i = 1, 2, \dots, n-1,$$

A suitable wave function can be chosen by “Level” button, and the result from the third graph in Fig. 1 is compared with the interpolated signal. Type functions of Wavelet Toolbox are used and the

coefficients and their lengths are obtained by means of the inbuilt function `wden` [4]. For functions which can be determined by a suitable polynomial, the power of the polynomial is assigned and the polynomial and mean quadratic error are overlapped in the same figure.

By means of the second window of the program the effective and maximum values of the signal can be determined, a discrete Fourier transformation is done [2, 3] in equations 2 and the values of 1, 2, 3, 5, 7, 9, 11 harmonics are computed in named and relative units in relation to the first one. Frequency 50 Hz is assumed as the first. The amplitude-temporal and amplitude-frequency characteristics are graphically represented in Fig. 4.

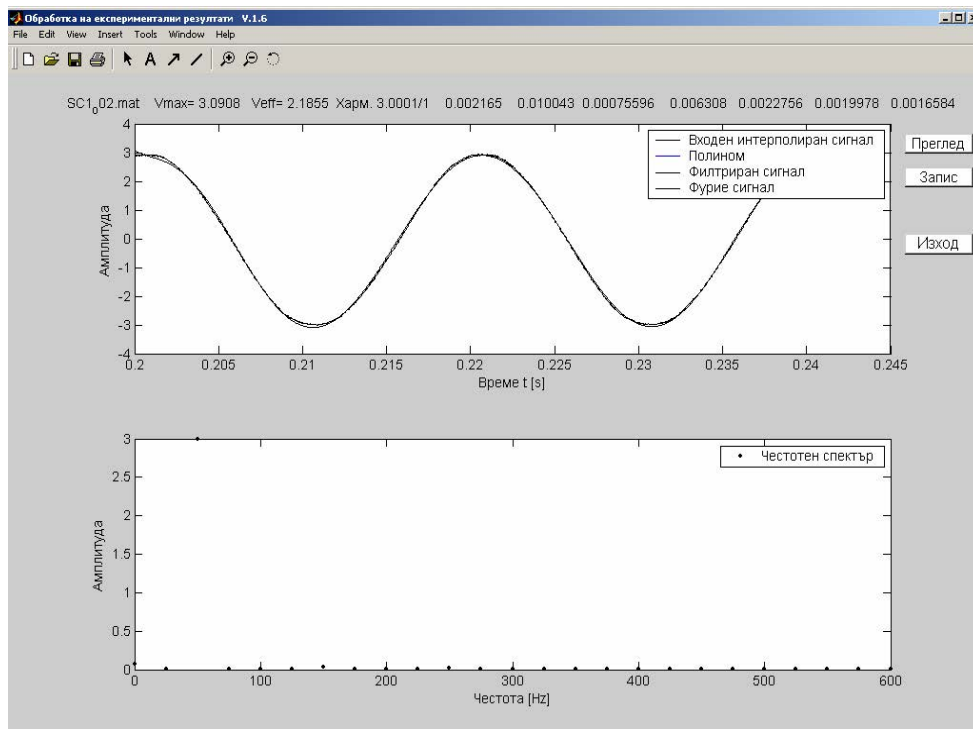


Fig.4. Signals

$$y_{(k)} = \sum_{j=1}^n y_{(j)} \omega_n^{(j-1)(k-1)}$$

$$(2) \quad y_{(j)} = \left( \frac{1}{n} \right) \sum_{k=1}^n y_{(k)} \omega_n^{-(j-1)(k-1)},$$

$$\omega_n = e^{\frac{(-2\pi)}{n}}$$

Measures have been taken that the program does not allow error while performing the succession of operations; for example, it is impossible to repeat operations which will change the parameters of the input signal in the course of processing. The program can also be used for processing of other discretely registered quantities, such as temperature, pressure and others.

### References

[1] Prof. I. N. Vuchkov, PhD, Identification, Yurapel, 1996 (in Bulgarian)

[2] <http://www.mathworks.com/>

[3] <http://www.fftw.org>

[4] <http://www.walet.org>

---

**Anton Filipov** – Assistant in Electrical Power Engineering department, Technical University of Varna, BULGARIA. e-mail: [filipov\\_a@yahoo.com](mailto:filipov_a@yahoo.com).

**M.Mehmed-Hamza** – Head Assistant in Electrical Power Engineering department, Technical University of Varna, BULGARIA. e-mail: [mediha.hamza@tu-varna.acad.bg](mailto:mediha.hamza@tu-varna.acad.bg).

**St. Andreev** – Assoc. Professor in Electrical Power Engineering department, Technical University of Varna, BULGARIA. e-mail: [st.andreev@tu-varna.acad.bg](mailto:st.andreev@tu-varna.acad.bg)

# Fuzzy Logic PWM Current Controller based Shunt Active Power Filter for Power Quality Compensation

K. Cagatay Bayindir, Mehmet Tumay, M. Ugras Cuma

**Abstract:** In this paper a fuzzy logic PWM current controller is presented for a shunt active power filter. The advantage of the proposed controller over conventional hysteresis controller is fixed switching frequency, less switching loss and improved ripple content. Due to flexibility of fuzzy logic, the controller can be tuned according to required filtering performance. The proposed controller is presented in detail and performance of the proposed system is validated through simulation studies.

**Keywords:** fuzzy logic, current control, switching converters, active power filters

## Introduction

In recent years, shunt active power filters have appeared as an effective method to solve the problem of harmonics and reactive power compensation. Since load harmonics to be compensated may be very complex and changing rapidly and randomly, active power filter has to respond quickly and work with high control accuracy in current tracking. It is clear that active power filter current control technique is the key issue of its performance [1]. For active power filter applications, the hysteresis-band current control shows a superiority with respect to other techniques due to its quick response, good accuracy, simple implementation and inherent peak current limiting capability. However this technique presents variable switching frequency, which makes difficult the inverter input passive filter design and can provoke undesirable resonance situations [2]. For this reason the emphasis is on developing fixed frequency current controllers for active power filters.

Recently, fuzzy logic controllers have generated a good deal of interest in certain applications. The advantages of fuzzy logic controllers over conventional controllers are that they do not need an accurate mathematical model, they can work with imprecise inputs, can handle non-linearity and they are more robust than conventional nonlinear controllers.

In this paper a fuzzy logic PWM current controller based shunt active power filter is presented. Instantaneous reactive power theory is used to generate reference currents and a fuzzy logic PWM current controller in combination with a PI controller for DC link voltage regulation enables tracking the reference current. To provide the switching actions of active power filter the rules of the fuzzy logic controller with their membership functions are defined. The use of fuzzy logic controller in the control loop will reduce the cost of the active

power filter because there is no need to use so accurate devices for measuring load current and obtaining reference current. It also enables fixed switching frequency and lower switching losses compared to conventional hysteresis controller. Besides it has much flexibility than other controllers and parameters can be tuned according to desired performance. Current controllers based on fuzzy logic are mentioned in [3] and [4]. However, it is difficult to understand the operation of whole system and no detailed simulation results are given. The models also are not presented in detail and only results are emphasized. In this paper fuzzy logic PWM current controller based shunt active power filter model is presented clearly and in a detailed manner so that the reader can easily understand and use the model for his further studies. Performance of the modeled shunt active power filter is illustrated by considering a six pulse fully controlled bridge rectifier supplied from a typical distribution system. The performance of the current control achieved with fuzzy logic is also compared to hysteresis current control. The proposed system not only cancels harmonic currents but also compensates reactive power to unity pf. The proposed fuzzy logic PWM current controller can also be used in other converter control applications.

## System Description

The active power filter uses power electronic switching to generate harmonic currents that cancel the harmonic currents from a nonlinear load. The approach is based on the principle of injecting harmonic current into the AC system, of the same amplitude and reverse phase to that of the load current harmonics.

The main components of the active power filter system are as follows.

- Mains supply
- Nonlinear load
- Active Power Filter
  - Voltage source inverter and interface reactor (Power circuit)
  - Reference current generator and fuzzy logic PWM current controller

Fig.1 shows the Matlab / Simulink model of the designed system including main components of a typical active power filter system and their interconnections.

## Mains Supply and Nonlinear Load

Mains supply is a three phase 380V 50 Hz wye connected power supply with a grounded neutral. The nonlinear load is a 400 kVA three phase fully controlled

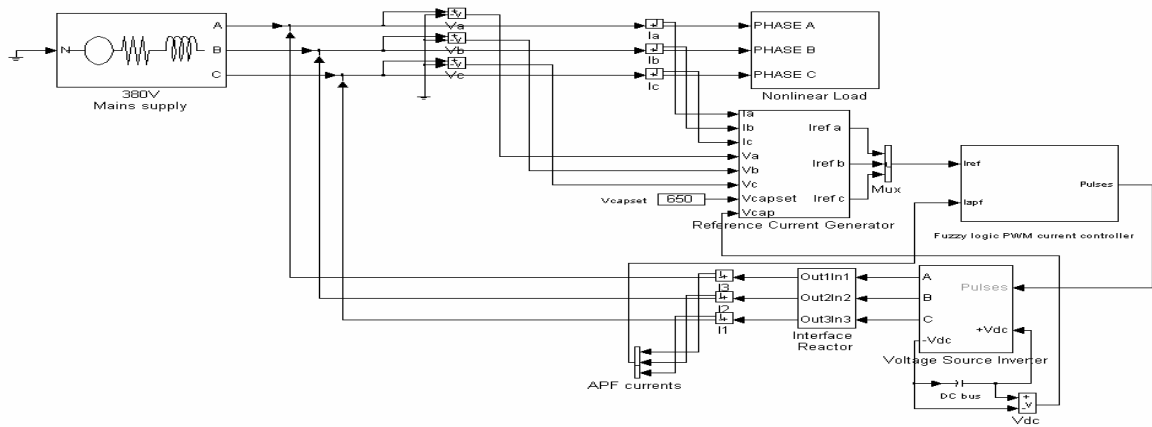


Fig.1. Matlab/Simulink model of the designed system.

six-pulse bridge rectifier feeding a DC motor. Firing pulse of the rectifier is selected as  $10^\circ$  for the simulations.

### Voltage Source Inverter and Interface Reactor

The voltage source inverter used in the active filter makes the harmonic control possible. This inverter uses a dc capacitor as the supply and can switch at a high frequency to generate a signal that will cancel the harmonics from the nonlinear load.

The current waveform for canceling harmonics is achieved with the voltage source inverter and an interface reactor. The interface reactor converts the voltage signal created by the inverter to a current signal. The desired waveform is obtained by accurately controlling the switches in the inverter. Control of the current wave shape is limited by the switching frequency of the inverter and by the available driving voltage across the interface reactor. The driving voltage across the interface reactor determines the maximum  $di/dt$  that can be achieved by the filter. Sizing of the inductor value must take into account control of the inverter switching frequencies and the characteristics of the nonlinear load to be compensated.

Nominal d.c. bus voltage must be at least  $\sqrt{2} V_{rms}$  in order to assure control over the shape of the active power filter current at all times. To charge and maintain adequate charge on the d.c. side capacitor, a PI regulator is used to control the flow of real power from a.c. side towards the d.c. side of the converter. Since the converter is designed only to compensate harmonics and reactive power, this real power transfer merely compensates the losses in the voltage source inverter. The choice of capacitance value and capacitor type depends on both the minimum necessary d.c. bus voltage that it must support and also the rms and harmonic components of the current that pass through it. The capacitor must be capable of handling the required rms current without overheating and the harmonic components should not cause excessive ripple on the d.c. bus voltage. This knowledge is utilized in rating the converter switches [5].

### Reference Current Generator and Fuzzy Logic PWM Current Controller

The control circuit is composed of reference current generator and current controller. In this shunt active power filter, control is accomplished by monitoring the three phase line currents to the nonlinear load and the three phase line-to-neutral voltages at the load bus, and then generating the three phase reference currents that should be supplied by the voltage source inverter using the Instantaneous Reactive Power Theory based method. In [6] and [7] the general definitions of Instantaneous Reactive Power Theory is presented. By using the Instantaneous Reactive Power Theory, the transformation of the three-phase bus voltages  $v_a$ ,  $v_b$  and  $v_c$  and the three-phase nonlinear load currents  $i_{La}$ ,  $i_{Lb}$  and  $i_{Lc}$  into the  $\alpha$ - $\beta$  orthogonal coordinates gives the following expressions:

$$(1) \quad \begin{bmatrix} e_\alpha \\ e_\beta \end{bmatrix} = \frac{\sqrt{2}}{\sqrt{3}} \begin{bmatrix} 1 & -1/2 & -1/2 \\ 0 & \sqrt{3}/2 & -\sqrt{3}/2 \end{bmatrix} \begin{bmatrix} v_a \\ v_b \\ v_c \end{bmatrix}$$

$$(2) \quad \begin{bmatrix} i_{L\alpha} \\ i_{L\beta} \end{bmatrix} = \frac{\sqrt{2}}{\sqrt{3}} \begin{bmatrix} 1 & -1/2 & -1/2 \\ 0 & \sqrt{3}/2 & -\sqrt{3}/2 \end{bmatrix} \begin{bmatrix} i_{La} \\ i_{Lb} \\ i_{Lc} \end{bmatrix}$$

The instantaneous real power  $p_L$  and the instantaneous reactive power  $q_L$  on the load side can be defined as:

$$(3) \quad \begin{bmatrix} p_L \\ q_L \end{bmatrix} = \begin{bmatrix} e_\alpha & e_\beta \\ -e_\beta & e_\alpha \end{bmatrix} \begin{bmatrix} i_{L\alpha} \\ i_{L\beta} \end{bmatrix}$$

$$(4) \quad p_L = \bar{p}_L + \tilde{p}_L$$

$$(5) \quad q_L = \bar{q}_L + \tilde{q}_L$$

$\bar{p}_L$  and  $\tilde{p}_L$  are the dc and ac components of  $p_L$ . Likewise,  $\bar{q}_L$  and  $\tilde{q}_L$  are the dc and ac components of  $q_L$ , respectively.

In the calculation circuit of the compensating reference currents, the following expression results:

$$(6) \quad M = \begin{bmatrix} 1 & 0 \\ -1/2 & \sqrt{3}/2 \\ -1/2 & -\sqrt{3}/2 \end{bmatrix}$$

$$(7) \quad \begin{bmatrix} i_{refa} \\ i_{refb} \\ i_{refc} \end{bmatrix} = \sqrt{\frac{2}{3}} M \begin{bmatrix} e_\alpha & e_\beta \\ -e_\beta & e_\alpha \end{bmatrix}^{-1} \begin{bmatrix} p^* + p_{loss} \\ q^* \end{bmatrix}$$

where  $p_{loss}$  is the instantaneous real power corresponding to the loss of the active filter which is necessary for DC capacitor voltage control and  $p^*$  and  $q^*$  are given by

$$(8) \quad p^* = -\tilde{p}_L \text{ and } q^* = -q_L$$

The DC bus voltage  $V_{DC}$  of the voltage source inverter cannot be kept constant; owing to the power loss of the inverter circuit as no suitable DC voltage control circuit is used. This problem can be solved by controlling the magnitude of mains current. A PI controller is used to control the DC capacitor voltage.

Once the compensating currents are detected, they are used as a reference signal in the inverter current control loop and thus compared with the real voltage source inverter currents to generate the switching pulses. Fuzzy logic PWM current controller generates the necessary switching pulses for the voltage source inverter to track the reference current. These filtering actions result in harmonic cancellation and reactive power compensation at the source side.

The Matlab / Simulink model of the fuzzy logic PWM current controller is shown in Fig.2. In Fig.2  $I_{ref}$  is a vector of the desired compensation current reference signals.  $I_{apf}$  is a vector of the fed back actual voltage source inverter output currents. Memory block is a requirement of the simulation program.  $I_{ref}$  and  $I_{apf}$  signals are each demultiplexed to 3 signals phase A, B

and C reference current signals and phase A, B, and C actual fed back current signals. Reference and actual signals are compared and error is obtained. Error signal is discretized using a hold and sample function. By using a unit delay, error rate is also obtained. Error and error rate being multiplied by gains and passing through saturation blocks are inputs to the fuzzy logic controller through a multiplexer. The output of the fuzzy logic controller is compared by a PWM carrier signal to obtain the firing pulses through a relay. The PWM signal is obtained by the comparison of the fuzzy logic controller crisp output with the sawtooth carrier signal and the result of the comparison will denote how fast the active power filter current must be increased or decreased respectively. The constant switching frequency will cause reduction in high frequency harmonics of inverter output current and lower stresses on the semiconductor devices. The self controlled DC link is used with PI controller to stabilize the capacitor voltage having zero steady state error. Current compensation is done in time domain leading fast time response [4].

The outputs of the relay blocks are directly fed as the firing pulse of upper bridge device of each leg of the inverter and NOT of that signal is fed as the firing pulse of lower bridge device of each leg. This is necessary for operation and avoiding the conduction of same leg switches simultaneously.

### Proposed Fuzzy Logic Controller

In a fuzzy logic controller, the control action is determined from the evaluation of a set of simple linguistic rules. The development of the rules requires a thorough understanding of the process to be controlled, but it does not require a mathematical model of the system [8]. In fuzzy logic, the linguistic variables are expressed by fuzzy sets defined on their respective universes of discourse. Fig.3 shows the structure of the fuzzy logic controller. The input variables for the necessary control action of active power filter are the error between active filter output current and the reference current and the rate of change of error. The output of the fuzzy logic controller is a reference signal to be compared with the sawtooth PWM carrier signal to generate the necessary switching actions.

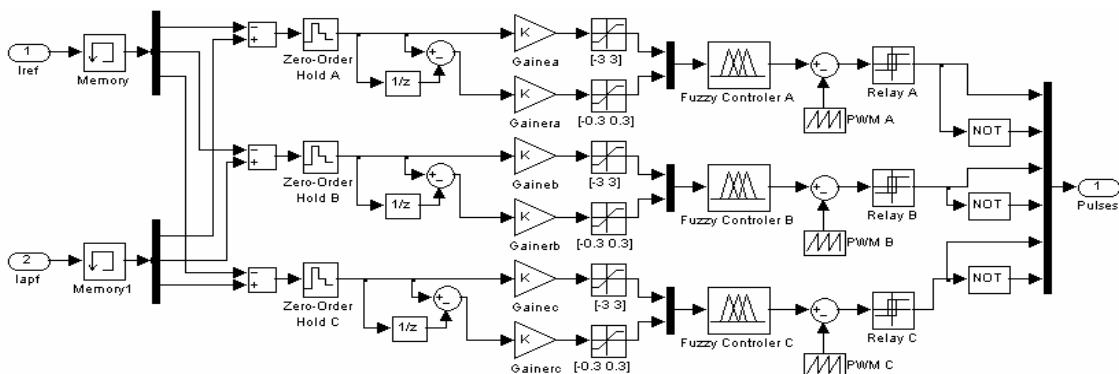


Fig.2. Matlab/Simulink model of fuzzy logic PWM current controller.

The fuzzy logic controller is characterized as follows:

- three fuzzy sets for each of the two inputs;
- three fuzzy sets for the output;
- triangular and trapezoidal membership functions;
- fuzzification using continuous universe of discourse;
- implication using the "min" operator;
- Mamdani fuzzy inference mechanism based on fuzzy implication;
- Defuzzification using the "centroid" method;

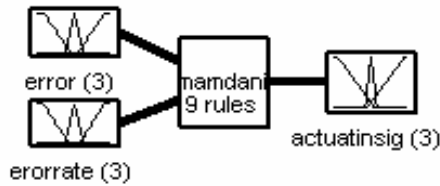
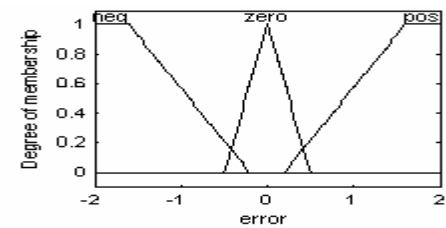
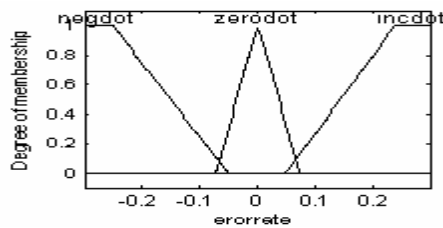


Fig. 3. Structure of fuzzy logic controller

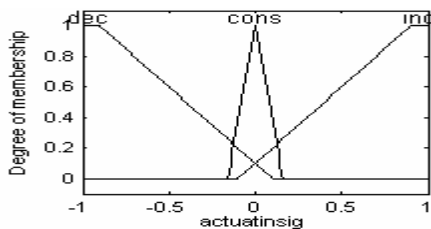
The decision making by the use of the data about the error between the actual current and the reference current and the error rate is done by the inference about corresponding rules to make the actual active power filter current to track the reference signal. The membership functions for inputs and output are shown in Fig.4.



a) Membership function for error



b) Membership function for errorrate



c) Membership function for actuatsinsig

Fig.4. Membership functions used in fuzzification.

The linguistic rules for the fuzzy logic controller are tabulated as follows.

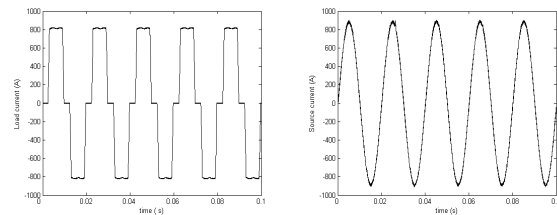
Table 1

Rule table for the fuzzy controller

errorrate	error		
	NEG	ZERO	POS
NEGDOT	INC	INC	DEC
ZERODOT	INC	CONS	DEC
INCDOT	INC	DEC	DEC

### Simulation Results

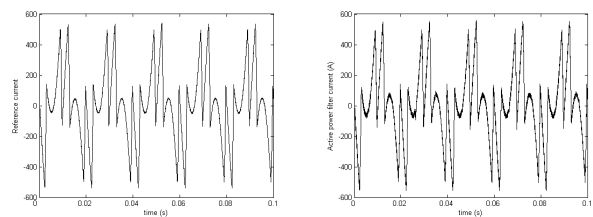
In this part simulation results for the system shown in Fig.1 is presented. The nonlinear load current and the compensated source current by the fuzzy logic PWM current controlled active power filter is shown in Fig.5



a) Nonlinear load current b) Source current

Fig.5. Load current and compensated source current.

Nonlinear load is a three-phase six-pulse fully controlled rectifier driving a dc motor. The line-line voltage, the value of interface reactor, dc bus voltage set value and dc bus capacitance is 380 V, 90  $\mu$ H, 650 V and 10 mF respectively. As seen from the figures harmonic and reactive power compensation is performed. The THD of load current is 25.05 while that of source current is 0.61. Fig.6 shows the reference current for the fuzzy logic PWM current controller and the actual active power filter current. As seen from the figure the current tracking capability of the fuzzy logic PWM current controller is very good.



a) Reference current

b) Active power filter current

Fig.6. Reference current for the fuzzy logic PWM current controller and active power filter

Among the various current control techniques, hysteresis control is the simplest and most extensively used technique. However, a fixed-band hysteresis current control has drawbacks on various switching frequencies and has large ripple current [8]. Results for a conventional hysteresis controller and the proposed fuzzy logic PWM current controller are also compared. With all other parameters and the maximum switching frequency

the same, results for the same active power filter with a hysteresis current controller is obtained.

Fig.7 and Fig.8 show one cycle and magnitudes of harmonics in % of fundamental component of nonlinear load current, source current for hysteresis current control and source current for fuzzy logic PWM current control. Magnitude of the fundamental component of load current is 890 A. THD of the nonlinear load current is 25.05, while the THD of source current for the hysteresis current control and proposed fuzzy logic PWM current control are 0.83 and 0.61 respectively.

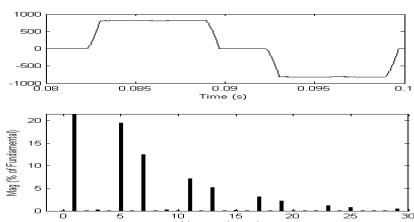


Fig.7. One cycle and magnitudes of harmonics in % of fundamental component of nonlinear load current

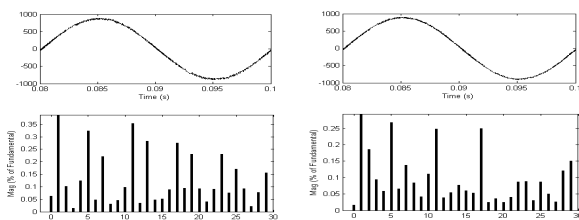


Fig.8. One cycle and magnitudes of harmonics in % of fundamental component of source current for a) hysteresis control b) fuzzy logic PWM current control

Fig.9 shows the error between reference and actual active power filter current for hysteresis current control and fuzzy logic PWM current control. As seen from the figures error is nearly constant for all times of operation for hysteresis control that causes a variable switching frequency and large current ripples. For the fuzzy logic PWM current control error is variable. This is necessary for obtaining optimum conduction times and this is like a variable hysteresis band control but much more flexible than a variable hysteresis band control. During one operation cycle, the difference between the dc bus voltage and the line voltage is changing and this causes variable di/dt filtering capability of the active power filter.

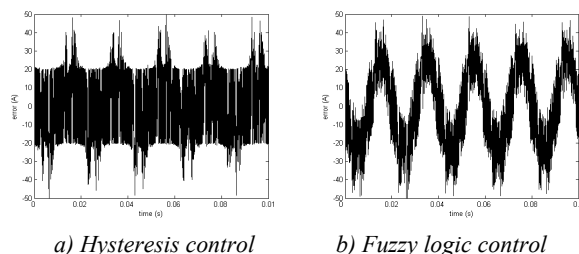


Fig.9. The error between reference and actual active power filter current

This causes a variable switching frequency for hysteresis control and this problem is compensated in fuzzy logic PWM current control. Besides these, fuzzy logic PWM current controller performance can be tuned according to desired criteria.

The dynamic performance of the proposed fuzzy logic PWM current controller is also evaluated by changing the firing angle of the three-phase six-pulse fully controlled rectifier. At time 0.06 second firing angle is increased from  $10^\circ$  to  $40^\circ$ . Fig.10 shows the changing load current. Fig.11 shows the dynamic responses of hysteresis current control and fuzzy logic PWM current control. As seen from the figures also the dynamic response of the proposed controller is better. The spikes on the source current are due to the di/dt filtering capability of active power filter that is affected from the value of interface reactor and dc bus voltage.

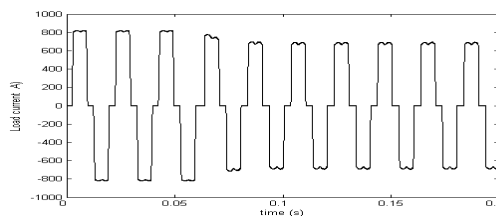


Fig.10. Load current change for a changing firing angle of  $10^\circ$  to  $40^\circ$  for the nonlinear load at time 0.06 s

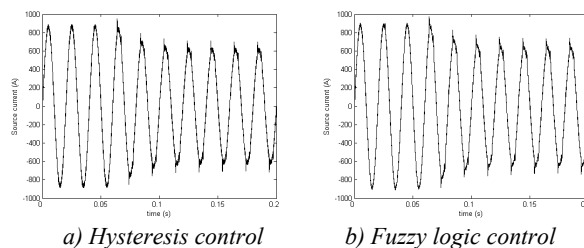


Fig.11. Dynamic response of active power filter

## Conclusion

In this paper a fuzzy logic PWM current controller is presented for a shunt active power filter. The fuzzy logic controller has two inputs: the error that is the difference between actual active power filter current and compensation reference current and the rate of change of error. Optimum conduction times and quick response is obtained by employing this approach. Performance of the proposed system is evaluated through a case study employing a three-phase six-pulse fully controlled rectifier driving a dc motor. The advantage of the proposed controller over conventional hysteresis current controller is fixed switching frequency, less switching loss and less switching ripple. The dynamic performance of the proposed current control is also better than hysteresis control. Due to flexibility of fuzzy logic, the controller can be tuned according to required filtering performance. Because high precision data is not required for the fuzzy logic current controller, low cost measuring devices can be used to implement the system. The



proposed current controller can also be used for similar converter applications.

### References

- [1] Zeng, J., Yu, C., Qi, Q., Yan, Z., Ni, Y., Zhang, B.L., Chen, F., Wu, F. A Novel Hysteresis Current Control for Active Power Filter with Constant Frequency. *Electric Power Systems Research*, ELSEVIER, 2003, Vol.68, Iss.1, pp.75-88.
- [2] Rodriguez, P., Pindado, R., Bergas, J. Alternative Topology for Three-Phase Four-Wire PWM Converters Applied to a Shunt Active Power Filter. *IEEE 28<sup>th</sup> Annual Conference of the Industrial Electronics Society, IECON'02*, 2002, Vol.4, pp.2939-2944.
- [3] Dell'Aquila, A., Lecci, A., Monopoli, V.G. Fuzzy Controlled Active Filter Driven by an Innovative Current Reference for Cost Reduction. *Int. Symp. ISIE*, 2002, Vol.3, pp.948-952.
- [4] Palandoken, M., Aksoy, M., Tumay, M. Application of Fuzzy Logic Control to Active Power Filters. *Electrical Engineering* 86, 2004, Vol.4, pp.191-198.
- [5] Madtharad, C., Premrudeepreechacharn, S. Active Power Filter for Three-Phase Four Wire Electric Systems Using Neural Networks. *Electric Power Systems Research*, ELSEVIER, 2002, Vol.60, Iss.3, pp.179-192.
- [6] Akagi, H., Kanazawa, Y., Nabae, A., Instantaneous Reactive Power Compensators Comprising Switching Devices without Energy Storage Components. *IEEE Transactions on Industry Applications*, 1984, Vol. IA-20, No:3, pp.625-630.

[7] Akagi, H., Nabae, A., Atoh, S. Control Strategy of Active Power Filters Using Multiple Voltage Source PWM Inverters. *IEEE Transactions on Industry Applications*, 1986, Vol. IA-22, No: 3, pp.460 – 465.

[8] Jain, S.K., Agrawal, P., Gupta, H.O. Fuzzy Logic Controlled Shunt Active Power for Power Quality Improvement, *IEE Proc. Electr. Power Appl.*, 2002, Vol. 149, No:3, pp.317-328.

---

**Mehmet Tumay** – Associate Professor, Faculty of Engineering and Architecture, Department of Electrical and Electronics Engineering, University of Cukurova, 01330, Balcali, Yuregir, Adana, TURKEY. e-mail: mtumay@cu.edu.tr.

**K. Cagatay Bayindir** – Ph.D. Student, Faculty of Engineering and Architecture, Department of Electrical and Electronics Engineering, University of Cukurova, 01330, Balcali, Yuregir, Adana, TURKEY. e-mail: cbayindir@isdemir.com.tr.

**M. Ugras Cuma** – MS.c. Student, Faculty of Engineering and Architecture, Department of Electrical and Electronics Engineering, University of Cukurova, 01330, Balcali, Yuregir, Adana, TURKEY. e-mail: mehmet@eemb.cu.edu.tr.

## Assessment of the influence of the tower grounding resistance on the lightning overvoltages in the substation

Danail Dachev, Valentin Kolev

**Abstract:** The paper describes experimental studies of the influence of the tower grounding resistance, tower surge impedance and soil resistivity. Results obtained from a simulation process using the Sigma SPX software package are presented. Typical Bulgarian's high voltage substation was studied and was made assessment of the influence of the tower grounding resistance on the lightning overvoltages.

**Keywords:** insulation co-ordination, overvoltages, back-flashovers, lightning, grounding.

### Introduction

The actual mechanisms by which lightning overvoltages can be impressed on the conductors of an overhead power line can be of three forms – induced voltage; shielding failure and backflash. The induced voltages occur when the lightning strikes the earth vicinity of the line. Most often, lightning strikes the overhead power lines, which are usually shielded by one or several earth wires. In that case the lightning overvoltages are caused by strokes to a phase conductor, shield wires or to a tower. Shielding failures occur when lightning bypasses the shield wire and strikes a phase conductor directly. Overvoltages caused by this mechanism are more dangerous, but their probability is low, mainly determined by the shielding angle. The vast majority of the strokes are to a tower or to a shield wire. The lightning current reaching the shield wire at a tower will divide between each section of the wire and the tower. The tower's voltage is generated by multiple reflections at the tower footing and at the tower top, thus raising the voltages across the insulator strings. If these voltages equal or exceed its withstand level, flashover occurs. This event is called a backflash. Obviously, backflashovers are mainly determined by the insulation level of the power line, tower grounding resistance, coupling factors between shield wire and phase conductors, span and the current waveshape. Soil resistivity is the factor that determines what the tower grounding resistance will be. The soil resistivity may vary from less than  $10 \Omega\text{m}$  for cinders or brine to more than  $10\,000 \Omega\text{m}$  [1] for dry sand or gravel. The resistivity of the soil is also influenced by temperature. In temperature range from  $-15^\circ$  to  $20^\circ \text{C}$  the resistivity of sandy loam, containing 15.2% moisture, can vary from  $72 \Omega\text{m}$  to  $3\,300 \Omega\text{m}$ . It is obvious that soil resistivity and thus tower footing resistance depends largely on the water content of the soil and temperature.

The purpose of this paper is to assess the influence of the tower footing resistance on the lightning overvoltages

and to discuss some results obtained by simulation process using the SIGMA SPX digital simulation program designed for insulation coordination in high voltage substations.

### Modeling

The lightning overvoltages have duration between 1 and  $100 \mu\text{s}$  and front wave lasts between 1 and  $5 \mu\text{s}$  [2]. Therefore the equipments located in substation – potential transformers, current transformers, breakers are presented by lumped capacitance. The bus and leads are presented by propagation elements with distributed parameters and limited distance. Lines connected to the substation are illustrated as an infinity line and resistance equal to the line surge impedance.

The equivalent substation diagram generally has many points and it is advisable to be simplified. The values of the lumped capacitances which are removed can be allocated according to the moment rule described in [3].

The study process is related to the IEC 71-2 procedure, which is described in [4]. This is a statistical method, which requires several electromagnetic transient computations to the back flashovers and shielding failures.

### Back flashovers

Fig. 1 illustrates the backflash mechanism.

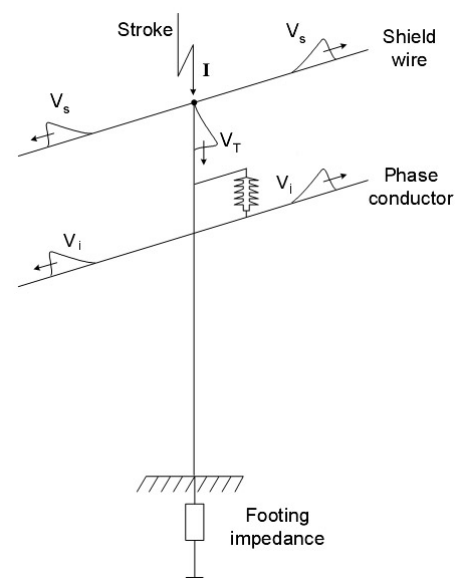


Fig. 1 Lightning stroke to the tower.

The amplitude the impinging surge is given as a function of lightning current and tower grounding impulse resistance:

$$(1) U_i = (1 - C_f) R_{hc} I$$

where

$U_i$  is impinging surge amplitude (kV);

$C_f$  is coupling factor of voltage between earth wire and phase conductor (p.u.);

$R_{hc}$  is high current value of the tower footing resistance ( $\Omega$ );

$I$  is lightning current amplitude (kA).

The lightning current, which is used for the design of impinging surge, is determined as a function of considered overvoltage return rate  $R_t$  and number of strokes to ground wires and in the line limit distance  $N_x$ :

$$(2) F(I) = \frac{R_t}{N_x}$$

where

$F$  is function describing cumulative distribution of the current amplitude.

For high current, representative of lightning, when the gradient exceeds a critical gradient  $E_0$ , breakdown of soil occurs. The process is illustrated in Fig. 2.

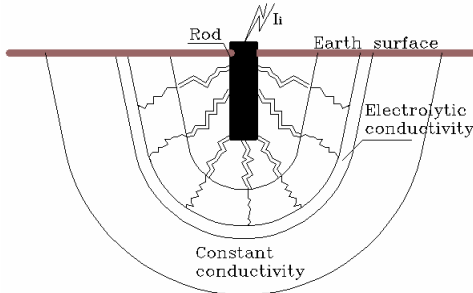


Fig. 2 Impulse breakdown of soil.

As the current increases, streamers are generated that evaporate the soil moisture, which produces arcs. Thus within the streamer and arc zones, the resistivity decreases from its original value. This soil breakdown can be viewed as increasing the diameter and length of the rod. The ionization zone is described by the critical field strength  $E_0$  at which the radius is equal to  $r$ . As the ionization increases, the shape of the zone becomes more spherical. Thus at high current, the ground rod can be simply modeled as a hemisphere electrode. Therefore the hemisphere electrode is studied. For the hemisphere electrode having a radius  $r_0$  low frequency resistance is given by equation (3):

$$(3) R_{lc} = \frac{\rho}{2\pi r_0}$$

where

$\rho$  is the soil resistivity ( $\Omega \cdot m$ );

$r_0$  is radius of the hemisphere (m).

The current density  $J$  at a distance  $r$  from the rod and the voltage gradient  $E$  for an injected current  $I$  are:

$$(4) J = \frac{I}{2\pi r^2}$$

where

$J$  is current density ( $kA/m^2$ );

$r$  is distance from the rod (m).

$$(5) E = \rho J = \frac{\rho I}{2\pi r^2}$$

Assuming the soil resistivity is zero within the ionization zone means that the perfectly conducting hemisphere radius has expanded to a radius  $r$  i.e.  $E = E_0$ ,  $E_0$  is the soil ionization gradient with recommended value 400 kV/m. Replacing  $r_0$  with this new radius and we receive the equation (6):

$$(6) R_{hc} = \sqrt{\frac{E_0 \cdot \rho}{2\pi I}}$$

where

$R_{hc}$  is the high current value of the tower footing resistance.

The impulse resistance is proportional to the reciprocal of the square root of the current, or on log-to-log scale as in Fig.3 [5].

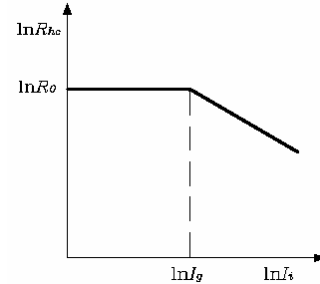


Fig. 3 Impulse resistance of hemisphere.

However, the relationship does not exist until there is sufficient current to produce the critical gradient  $E_0$  at the surface of the sphere. To determine this current  $I_g$ , set  $r=r_0$ ,  $E=E_0$  and  $I=I_g$  in Eq.5, we obtain:

$$(7) I_g = \frac{2\pi r_0^2 E_0}{\rho} = \frac{1}{2\pi} \frac{\rho E_0}{R_{lc}^2}$$

Then substituting Eq.7 into Eq.6, we obtain:

$$(8) R_{hc} = \frac{R_{lc}}{\sqrt{\frac{I}{I_g}}}$$

For the rod electrodes the Eq.8 is applicable for currents above  $I_g$ . The desire is to remake this equation for ground rods noting that for high currents, rods act as spheres. Therefore it is only the initial portion of the function that needs modification:

$$(9) R_{hc} = \frac{R_{lc}}{\sqrt{1 + \frac{I}{I_g}}}$$

where  
 $I_g$  is the limit current represents the soil ionization and is given by Eq.7.

### Shielding penetration

Fig. 4 illustrates the shielding failure mechanism.

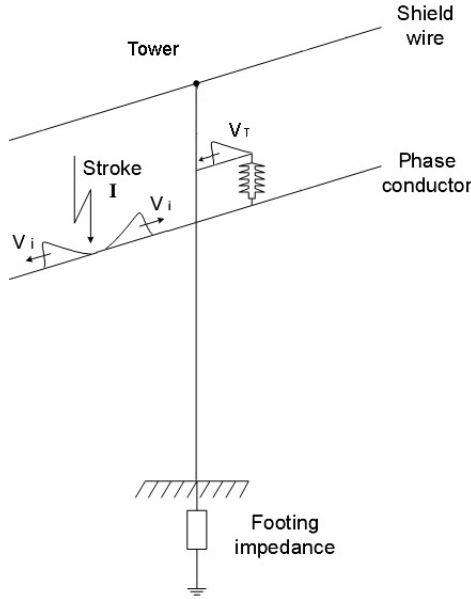


Fig. 4 Lightning stroke to the phase conductor.

The lightning current injected into phase conductor will tend to flow in the both directions along the conductor and traveling waves will be initiated in each direction of peak amplitude  $U$  given by equation (10):

$$(10) U = \frac{1}{2} I Z_0$$

where  
 $Z_0$  is the surge impedance of the conductor ( $\Omega$ ), which is function of the conductor radius  $r$  and height  $h$  above ground:

$$(11) Z = 60 \ln \frac{2h}{r}$$

The surge impedance of the single conductor can be varying in a narrow band between 400 and 500 ohms.

The lightning current  $I$  determining the impinging surge is determined using equation (12):

$$(12) F(I) = F(I_m) + \left( \frac{R_t}{N_p} \right)$$

where

$F(I_m)$  is the lightning current probability corresponding to the maximum shielding current;  
 $R_t$  is the considered return rate;  
 $N_p$  is the shielding penetration rate within the limit distance.

In the determination of the impinging surge amplitude, several iterations are performed for the correct determination of the phase conductor corona radius. In the termination of the impinging surge steepness, steepness related to the stroke current is also taken into account. Overvoltage generated by the lightning stroke to a phase conductor is compared with line insulation volt-time curve. For the cases without flashovers, the impinging surge with liner tail is taken. When flashover happens, it normally occurs across an insulator string at a tower, impinging surge chopped at wave tail is taken.

The steepness of the impinging overvoltage may be assumed to correspond to equation (13):

$$(13) S_i = \frac{1}{K_{co} X_s}$$

where  
 $S_i$  is the impinging surge steepness ( $kV/\mu s$ );  
 $K_{co}$  is the corona damping constant ( $\mu s/(kV.m)$ );  
 $X_s$  is the surge travel distance (m).

## Results and discussion

In this section we will describe the results of a calculation of lightning overvoltages with the SIGMA SPX digital simulation program, using the example of a 110 kV.

The limit distance of the incoming line is accepted 1000 m. The surge impedance of line is about 480  $\Omega$ . The distance between towers, the span is about 250 m. The selected distance from, which strokes will be injected in the IEC procedure is 250 m. In this procedure the software generate a sufficient number of lightning strokes. The keraunic level in a region is 39 thunderstorm days per year  $T_d$ . The maximum current in the back flashover BFO simulations is selected about 250 kA. The low frequency, low current grounding resistance of the towers  $R_{lc}$  is changed from 5  $\Omega$  to 30  $\Omega$ , the soil resistivity  $\rho$  is changed also from 25  $\Omega.m$  to 1200  $\Omega.m$ . Permissible values of the low current tower grounding resistance  $R_{lc}$  are depending on soil resistivity  $\rho$  and they are listed in Table 1 [6].

**Table 1**  
Maximum permissible values of the low current tower grounding resistance  $R_{lc}$

Soil resistivity $\rho$ , $\Omega.m$	Low current tower grounding resistance $R_{lc}$ , $\Omega$
up to 100	10
from 100 to 500	15
from 500 to 1000	20
over 1000	30

Fig. 5 and 6 gives the results of overvoltages by back flashover as a function of the soil resistivity and respectively of the low current value of the tower grounding resistance  $R_{lc}$ . The curve 1 is obtained for the node, in which is connected the power transformer. The power transformer is protected by surge arrester and for that reason the values are approximately equal to the residual voltage  $U_{res}$  at the surge arrester. The curve 2 gives the overvoltages obtained in the substation entrance node at the line disconnector.

When the obtained amplitudes are higher than 1,6 times the negative flashover of the line insulation, an impinging surge with this amplitude is used. For that reason the curves have approximately straight part after  $\rho = 250 \Omega \cdot m$ , when for some case the amplitude is higher than 1,6  $U_{-50\%}$  of the line insulation.

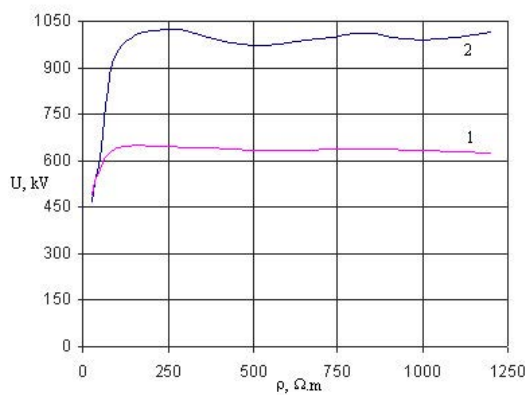


Fig. 5 Overvoltages as a function of soil resistivity  $\rho$ .

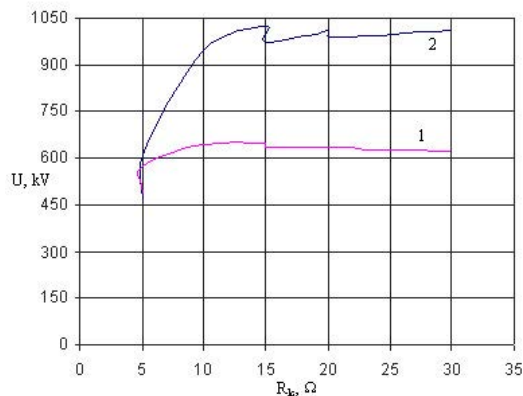


Fig. 6 Overvoltages as a function of grounding resistance.

Fig. 5 and 6 shows the comparison between probability curves of overvoltages at different values of the soil resistivity. It is obviously, that at higher soil resistivity the probability an overvoltage to reach the critical voltage value is greater than to the less values of soil resistivity.

Typical of overvoltages oscillation in the substation entrance node at the line disconnector, obtained by digital simulations of back flashovers are given in Fig. 9.

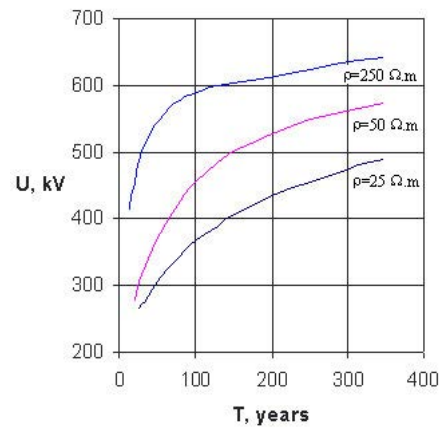


Fig. 7 Probability curves of overvoltages in cases of soil resistivity  $\rho$  25, 50, 250  $\Omega \cdot m$ .

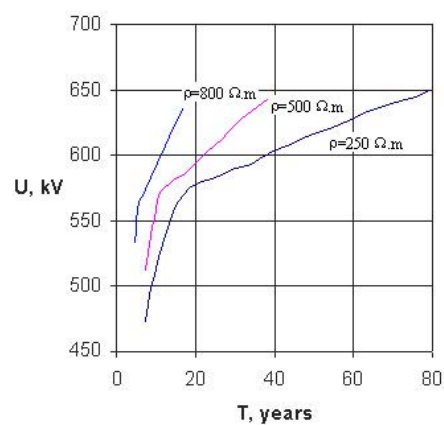


Fig. 8 Probability curves of overvoltages in cases of soil resistivity  $\rho$  250, 500, 800  $\Omega \cdot m$ .

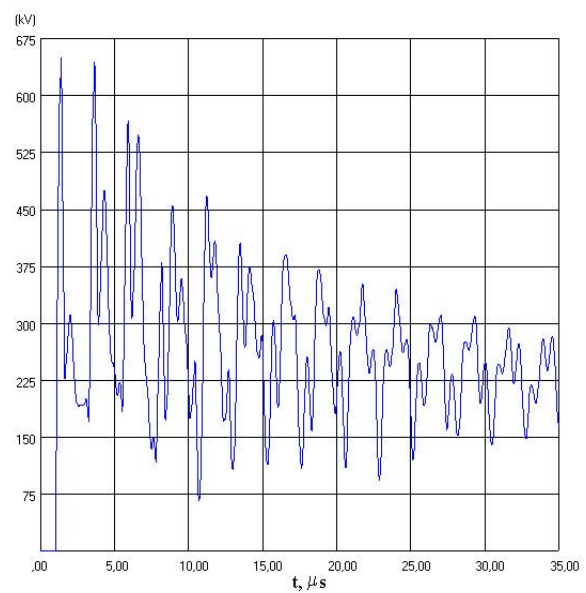


Fig. 9 Overvoltage at the substation entrance node,  $\rho = 250 \Omega \cdot m$ ,  $R_{lc} = 15 \Omega$ .

## Conclusion

Calculation of lightning overvoltages requires simulation of the electrical equipment, such as for example overhead transmission lines, cables, towers and substations as travelling wave model. Simulation of remote strikes reproduces lightning strike voltages corresponding to the standardized 1.2/50  $\mu$ s impulse voltage, while lightning strike currents in the case of strikes to towers or direct strikes to the overhead line conductor possess a concave wave shape. The peak values of the lightning strike currents in the case of direct strikes to the overhead line conductor are determined essentially by the tower geometry and the shielding effect of the overhead earth wires, and are determined individually for each substation. The peak values of the overvoltages obtained in the case of back flashovers depends on a variety factors, among which the most important are the tower earthing, the soil resistivity, the insulation strength, the height of the overhead line.

The use of the SIGMA SPX simulation program enables quick and easy calculations of lightning overvoltages. The software presents the representative overvoltage distribution as a function of mean time between voltage return, which enables risk of failure determination obtained directly.

From the above results it may be concluded that the variation of the tower grounding resistance and soil resistivity must be taken into account at assessment of the lightning overvoltages in the substation.

In the cases when the impinging surge amplitude is higher than 1,6 times the negative flashover of the line insulation, it is recommended more carefully studies.

## References

- [1] H. Seljeseth, A. Campling, M. Kuussaari. Station earthing. Safety and interference aspects. *Electra* # 71 – July 1980.
- [2] A. J. Eriksson. Lightning overvoltages on high voltage transmission lines. Investigation of wave-shape characteristics. *Electra* # 47 – July 1976.
- [3] Тиходеева, Н. Н. Руководство по электрических сетей 6-1150 кВ от грозных и внутренних перенапряжений, ПЭИПК Минтопэнерго РФ, Санкт-Петербург 1999.
- [4] IEC 71-2/1996 Insulation co-ordination Part 2: Application guide.
- [5] Hileman, A.R. Insulation Coordination for Power Systems, Marcel Dekker Inc, 1999.
- [6] Генов, Л. Г. Техника на високите напрежения в електроенергийните системи, Техника, София 1979.

## Possibilities and application of LOVATO Electric's multimeter DMK32

Vasil – Mario Piperov, Valery Assev and Georgie Stanchev

**Abstract:** The purpose of the following article is to present the possibilities of the multimeter DMK32, as well as to present the optimal design, production of highest quality, distribution and consumption of electric energy in energy systems.

### Introduction

An important quality requirement for production and consumption of the electric energy and for optimal perspective design is accumulation of much variable information, i.e. much information about many parameters. The advantages of the macro processed calculating apparatuses are:

- Possibility of value calculation and registration for numerous and various quantities with great precision and speed.
- the parameters are measured and registered in parallel through independent channels.
- Small amount of consumption which allows high sensitivity.
- Peripheral devices can be connected, which allows huge amount of data to be saved, presented in understandable form; processing of the results and duly making of decisions.; possibility of apparatus control when an operation is to be done.

The multimeters DMK32 are constructed to match to the highest degree the mentioned earlier advantages. The department of Electric Apparatuses at Technical University of Sofia has the DMK32 multimeter, made by LOVATO Electric's company, used in scientific researches and for educational purpose

### I. The DMK32 multimeter is able to read various quantities.

The DMK32 has the possibility to read in parallel up to 32 different quantities, which can be grouped in the following order:

1. Line and phase voltages
  - 1.1. Each phase voltage separately from each line voltage
    - 1.1.1. Continuous reading  $v_{1t}; v_{2t}; v_{3t}$
    - 1.1.2. Indication of maximal and minimal value of a defined interval of time.

- 1.1.3. Average effective value (TRMS) of the phase voltages :

$$v_{pN} = \sqrt{\frac{1}{n} * \sum_{1}^n v_{pt}^2}, \text{ where } p=1, 2, 3.$$

- 1.1.4. Average effective value of the line voltages::

$$v_{12} = \sqrt{\frac{1}{n} * \sum_{1}^n (v_{1t} - v_{2t})^2};$$

$$v_{23} = \sqrt{\frac{1}{n} * \sum_{1}^n (v_{2t} - v_{3t})^2}$$

$$v_{31} = \sqrt{\frac{1}{n} * \sum_{1}^n (v_{3t} - v_{1t})^2}$$

- 1.2. Equivalent phase voltage:

$$\sum V_f = \frac{v_{1N} + v_{2N} + v_{3N}}{3}$$

- 1.3. Phase voltage and reading of the nonsine (the presence of high harmonics) TND

- 1.3.1. Harmonic structure

$$v_{pTND} = \sqrt{\frac{\sum_{2}^n (v_{pn})^2}{(v_{pN})^2 + \sum_{2}^n (v_{pn})^2}}, \quad p=1, 2, 3.$$

- 1.3.2. Relative harmonic structure

$$v_{pTND} = \sqrt{\frac{\sum_{2}^n (v_{pn})^2}{(v_{pN})^2}}, \quad p=1, 2, 3.$$

2. Phase current of the separate phases:

- 2.1. Continuous reading of phase currents :  $A_{1t};$

$$A_{2t}; A_{3t}$$

- 2.2. Indication of the maximal and the minimal value for a defined interval of time.

- 2.3. Average effective value of the phase currents (TRMS)

$$A_p = \sqrt{\frac{1}{n} * \sum_{pt} A_{pt}^2}, \quad p=1, 2, 3.$$

2.4. Equivalent current of the three phases together

$$\sum A_f = \frac{A_1 + A_2 + A_3}{3}$$

2.5. Phase currents with indication of the non-sine (presence of high harmonics) TND:

2.5.1. Harmonic structure :

$$A_{pTND} = \sqrt{\frac{\sum_{pn}^n (A_{pn})^2}{A_1^2 + \sum_{pn}^n (A_{pn})^2}}, \quad p=1, 2, 3.$$

2.5.2. Relative harmonic structure:

$$A_{pTND} = \sqrt{\frac{\sum_{pn}^n (A_{pn})^2}{A_p^2}}, \quad p=1, 2, 3.$$

3. Active, reactive and full powers (W, Q, S);
  - 3.1. Present values for each phase
  - 3.2. Minimal and maximal values
  - 3.3. Average values of each phase
  - 3.4. Average value of the three phases together
4.  $\cos \varphi$  and the power factor (if non-sine is indicated).
  - 4.1. Present values for each phase
  - 4.2. Minimal and maximal value for each phase
  - 4.3. Average value of the three phases together
5. Average frequency
6. Phase and line overcompensation
7. Admissible maximal active and full power
8. Admissible maximal phase current
9. The values of the harmonics from the second to the twenty-second for phase voltage and for phase currents

## II. Influence of the different quantities read about the electric supply and electric consumption.

A. Power factor

1. General information

It is known that  $\cos \varphi = \frac{\sum W}{\sum S}$  – or in the presence of high harmonics  $\sum P_f = \frac{\sum W'}{\sum S'} < \cos \varphi$  (because if

$\sum W = \sum W'$  then  $\sum S' = \sum S$ ). In that case  $\varphi$  is the angle between the current and the voltage. Because the losses in transport and transformation of electric energy (or electric energy production) in other ways are proportional; to the full current square ( $I^2 R$ ), therefore the reactive power  $Q = \sqrt{S^2 - P^2}$  must be compensated. Besides, because of the higher current, higher voltage occurs  $\Delta V = I.Z$ , then low voltage reaches the consumer. And because the spinning moment

of the unsynchronized engine  $M \equiv U^2$ , when the mechanical load is too big, the engine can stop, which is almost equivalent to short connection.

In practice improvement of  $\cos \varphi$  to  $\cos \varphi = 1$  is not attempted for two reasons:

- frequent changes of the active loads, which can lead to overcompensation  $\cos \varphi$ ;
- when  $\cos \varphi = 0,95$  the increase of 1% is possible when the capacity is increased by 10%, which raise the cost of the capacitor.

## III. Ways for compensation

2.1. Individual compensation. To each capacitor, a capacitor battery is connected in parallel, controlled by an automatic system for regulation..

2.2. Group compensation. The capacitor battery improve  $\cos \varphi$  of a group of consumers.

2.3. Centralized compensation. Except with the capacitor battery, a centralized compensation can be accomplished with synchronous engine, i.e. by regulation of the direct current stimulation.

In that case, there's an objective possibility of automated regulation by a computer, connected with multimeter.

When the electrical wiring is measured off the average  $\cos \varphi = 0,7$ . For compensation of the power factor up to 0,9 at individual compensation, reactive power of  $Q_C = \omega.C.U^2 \approx 0,5.P$  is necessary. The necessary power  $Q_C$  in [kVAr] is precisely shown *table 1*.

The practical recommendation is that  $Q_C$  should not surpass 90% from the reactive power, consumed by the engine when it floats. If that's not the case, when the engine stops, the voltage of the electric network would rise over the rated level, because of the self-excitation of the system engine-capacitor.

For compensation of the reactive power of the floating transformers, the capacitor the capacitor is selected with the formula  $Q_C \approx S_0 \frac{i_0 S_{nom}}{100}$ , where  $Q_C$  and  $S_0$  are respectively the reactive power and the full power when the transformer floats;  $i_0$  is the current when floating in percents of the nominal current. More precise value of  $Q_C$ , as function of  $S_{nom}$  for pressure transformers and transformers GEAFOL, are shown according to DIN in *table 2*.



Table 1.

текущ cosφ	капацитивна мощност, в kvar за всеки kW от активната мощност, за достигане на cosφ				
	0,8	0,85	0,9	0,95	1
0,4	1,54	1,67	1,81	1,96	2,29
0,42	1,41	1,54	1,68	1,83	2,16
0,44	1,29	1,42	1,56	1,71	20,4
0,46	1,18	1,31	1,45	1,6	1,93
0,48	1,08	1,21	1,34	1,5	1,83
0,5	0,98	1,11	1,25	0,14	1,73
0,52	0,89	1,02	1,16	1,31	1,64
0,54	0,81	0,94	1,08	1,23	1,56
0,56	0,73	0,86	1	1,15	1,48
0,58	0,66	0,78	0,92	1,08	1,41
0,6	0,58	0,71	0,85	1	1,33
0,62	0,52	0,65	0,78	0,94	1,27
0,64	0,45	0,58	0,72	0,78	1,2
0,66	0,39	0,52	0,66	0,81	1,14
0,68	0,33	0,46	0,59	0,75	1,08
0,7	0,27	0,4	0,54	0,69	1,02
0,72	0,21	0,34	0,48	0,64	0,96
0,74	0,16	0,29	0,43	0,58	0,91
0,76	0,11	0,24	0,37	0,53	0,86
0,78	0,05	0,18	0,32	0,47	0,8

Table 2

Пълна мощност S <sub>п</sub>	маслени и GEAFOЛ по DIN		с редуцирани загуби	
	маслени	GEAFOЛ	маслени	GEAFOЛ
kVA	kVA	kvar	kVA	kvar
250	4,5	5	2,8	3
315	7,8	7,5	3,6	4
400	8,2	7,5	4,4	4
500	10,6	10	4,7	5
630	13,2	12,5	5,7	5
800	15,5	15	6,5	7,5
1000	19	20	7,5	7,5
1250	20,6	20	10,1	10
1600	23,2	25	10,6	10
2000	27	25	-	-

## B. High harmonics

### I. General information

High harmonics of voltage appear in synchronous generators (because of the presence of magnetic system or because of the pulsations in the active layer) or along the grid (because of the presence of non-line elements). The influence of the high harmonics in the voltage leads to few detrimental consequences:

- possibility of voltage resonance (with unacceptable increase of the voltage) for some of the high harmonics;
- the harmonics with numbers  $n=3k$  ( $k=1, 2, 3, \dots$ ) do not pass to the three phase systems, connected in the shape of a star, which leads to big potential difference between the neutral of the generator and the neutral of the consumer;
- the harmonics with numbers  $n=3k-1$  ( $k=1, 2, 3, \dots$ ) form indirect systems, which create resistance moments in the asynchronous machines;
- cause additional ferromagnetic losses (from currents of Foucault and hysteresis) and so on.

Sources of high harmonics of currents can be grouped in three:

- powerful semi-conductor devices – rectifiers, inverters, thyristor regulators in electric drives etc.
- arc equipment for welding or for lighting (mercurial or fluorescent lamps) I so on;
- saturating devices – transformers, engines, generators, non-line capacitors and so on.

The amplitude of the  $n$ th line harmonic equals

$$A_n = \frac{A_1}{n},$$

while in three phase systems the non-line harmonics keep the ratio of the currents  $I_5 = 0,25.I_1$ ;

$I_7 = 0,13.I_1$ ;  $I_{11} = 0,09.I_1$ ;  $I_{13} = 0,07.I_1$  и т.н.

### 2. The effect when capacitors for improvement of the power factor are used

When capacitors are connected in parallel to improve  $\cos \varphi$  current resonance could appear. Most dangerous is the case when there is a resonance with the basic harmonic. Appropriately connected filters or inductive resistances should be connected consequently for fading to occur.

Considering to the data of the multimeter, the computer can calculate what values of the additional elements should be included to suppress the resonant harmonic.

## Conclusion

My The DMK32 multimeter has the following advantages:

- Compact size;
- Easily used;
- Five channels for consecutive display, plus light emitting diodes for additional information;
- The multimeter has relay outputs, which can perform warning or control functions;
- Easy configuration of the system computer-multimeter, which allows receiving and keeping of a great amount of data;
- Possibility for system elements control, which improve the quality of the production, carrying and consumption if electric energy.

*Vasil-Mario Piperov – engineer., PhD, associate professor in Faculty of Electrotechnics, Technical University – Sofia, Boulevard “Kliment Ohridski” 8, 1000 Sofia, BULGARIA. E-mail pipi@tu-sofia.bg*

*Valery Assev – master-engineer, one working for a doctor’s degree, Faculty of Electrotechnics, Technical University – Sofia, Boulevard “Kliment Ohridski” 8, 1000 Sofia, BULGARIA. E-mail: valery666@mail.bg*

*Georgy Stanchev – Faculty of Electrotechnics, Technical University – Sofia, Boulevard “Kliment Ohridski” 8, 1000 Sofia, BULGARIA.*

# Hybrid Power Systems with Renewable Energy Sources – Types, Structures, Trends for Research and Development

Vladimir Lazarov, Gilles Notton, Zahari Zarkov, Ivan Bochev

**Abstract:** *The article deals with the state of the art of a hybrid power systems with renewable energy sources (HSRES). These systems are classified according to different criteria. It has been made a short review of the current state of their design, modelling, simulation and optimisation. The respective analysis has been made also. In conclusion, it has been made a summary of the future trends for research and development.*

**Keywords:** *renewable energy, hybrid power systems*

## Introduction

Variability and random behaviour mark the main characteristics of renewable energy sources (RES). Nevertheless, there is certain regularity and cyclic recurrence in their behaviour. The intensity of the different energy sources into time is not the same. In general, when one of the sources is intensive, the other tends to be extensive, i.e. the sources complement one another. The distribution into time and the intensity of the energy sources depend on the meteorological conditions of the chosen area, on the season, on the relief, etc.

The following definition of a hybrid system with renewable energy sources can be suggested. *This is a power system, using one renewable and one conventional energy source or more than one renewable with or without conventional energy sources, that works in "stand alone" or "grid connected" mode* [1], [2], [3], [4]. The National electrical energy system is a hybrid system.

HSRES are used for energy production for distant, not connected to the common electrical distribution system objects, e.g. distribution systems for small islands [5], villages [6], hotels, houses [7], as well as the supply of telecommunication, meteorological and other stations, research laboratories, etc. In connection with the distributed generation these systems are being more widely used as grid connected systems. Their undisputed advantage is the more efficient way of use of the disposable renewable energy.

## Classification of HSRES

*According to the presence of conventional energy sources:*

- Hybrid systems with conventional sources – mostly the systems, using conventional sources are more powerful and responsible;
- Hybrid systems without conventional sources – as a general, that kind of systems are relatively low-power and/or tend to be more irresponsible. If the

systems are correctly designed and if energy storage is provided, they would be able to generate sustainable energy. These systems are independent of energy sources, which make them especially preferred. Hence comes the need to develop reliable optimisation models.

*According to the number of the sources* – The number of the energy sources is one of the factors that define the complexity of the HSRES as well as its sustainability and efficiency. The large number of sources makes the system more complicated, but at the same time leads to an increase in the sustainability and energy efficiency.

*According to the type of the produced energy:*

- Mechanical – each turbine, regardless of its kind generates mechanical energy, which later is converted to electrical. That mechanical energy can be also consumed directly, e.g. for pumping water;
- Electrical – the electrical energy can be easy distributed and converted to another type. It can be stored and consumed, when is needed. All these features rouse a deep interest for the electrical HSRES;
- Thermal – it is used for heating and warming up water. Here can be assigned both the systems with solar thermal collectors and the ones, using geothermal energy;
- Light – providing daylight in buildings through the medium of a concentric collector and optic cable [8];
- Fuel production – a case in point can be hydrogen production by means of electrolysis [9];
- Mixed – a typical example is a power system with solar thermal collector, combined with wind turbine and photovoltaics [1], [2], [3], [4].

*According to the rated power:*

- Low power (less than 1 kW) – they are used for telecommunication, meteorological and other stations, etc;
- Middle power (more than 1 and less than 10 kW) – used for the supply of houses, hotels, etc;
- High power (more than 10 kW) – used for the supply of isles, towns and villages, which are remote from the electricity distribution system, etc.

*According to the energy storage:*

- Without storage – they are not profitable, because the needs do not coincide with the energy availability. Thus, certain amount of the available energy remains unused and also the load can easily remain without supply;
- With storage – the surplus of the generated electric power is stored and used when needed. In this way,

the fluctuating nature of the RES is buffered which enables the hybrid system to work more effectively. The stored energy can be electrical (batteries, superconductive magnetic energy storage (SMES)), thermal (boiler), mechanical (flywheel), fuel conversion (hydrogen) and potential (water tower). The fuel cells (FC) provide a clean technology that uses hydrogen (from a fuel source) and oxygen (from the air) to generate electricity and heat, the only basic emission being water vapour. FCs suitable for DG operate between 80 and 1 000 °C and in CHP mode can deliver efficiencies of over 80%. Small (1-10 kW) FCs could be developed for residential power generation.

According to the connection to the distribution grid:

- Grid connected – they must be synchronised with the distribution system;
- Stand alone – used for the supply of remote objects.

### Electrical HSRES

According to the type and configuration of power buses, hybrid systems can be defined as AC, DC and mixed. They also can be classified as serial and parallel.

Figure 1 is up to show the serial structure of a hybrid system. It is typical for this case that the energy flows are unidirectional and passes through the structure of the system (from DC to AC bus in the given example).

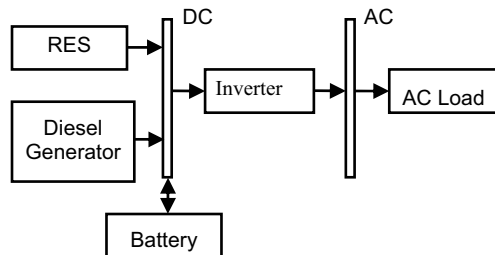


Fig.1. Serial structure of a hybrid system.

Figure 2 represents the parallel structure of a hybrid power system. The energy flows in both directions.

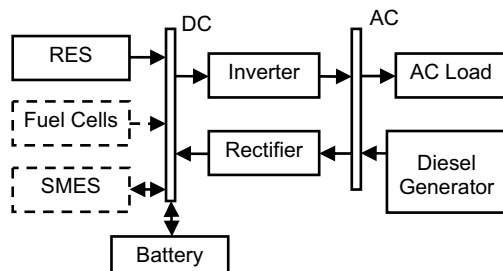


Fig.2. Parallel structure of a hybrid system.

HSRES face many difficulties due to the characteristics of the renewable energy sources and especially their variability. On the other hand, hybrid systems should meet the same requirements as the conventional power systems.

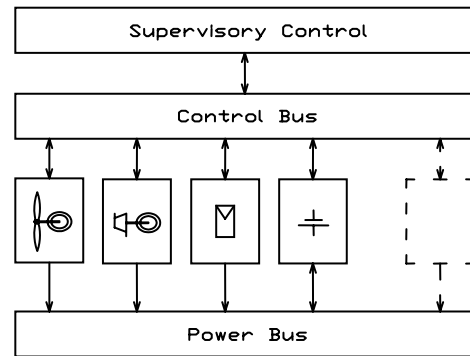


Fig.3. Modular structure of a hybrid system.

With the purpose of unification have the modular HSRES been created [5]. They possess standard power (for example ~230V/50Hz) and information bus and are subject to uniform supervisory control. The units are connected parallel.

The modular systems have a high level of modularity and flexibility. They should be sustainable and are supposed to show stable parameters of produced energy (according to the relevant standards). Figure 3 shows the general structure of a modular hybrid system. Local mini- and microgrids with distributed generation can be created using modular technology.

In the modern systems more widely used are the Flexible AC Transmission Systems (FACTS) of a different type (SVC, STATCOM, SPS, TCSC, UPFC), which increase the flexibility and stability of the system. In the future can be expected integration of inverter and FACTS functions [17].

### Common Types of Hybrid Systems

The Wind – Diesel System is a typical representative of a powerful hybrid system (figure 4). It is commonly used to supply objects beyond the scope of the electricity distribution system (buildings, villages, etc)[6], [11].

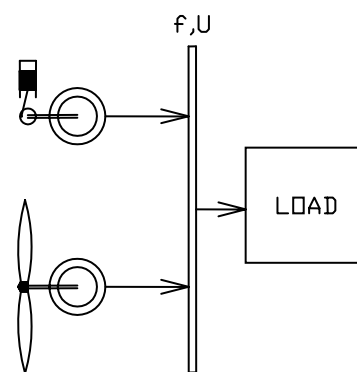


Fig.4. Wind – Diesel system.

The Wind – Photovoltaic (PV) – Diesel System [7], [10] is suitable for terrains where both solar and wind energy have balanced potential (figure 5). It possesses high-energy effectiveness, but at the same time, this type of system appears to be more complex.

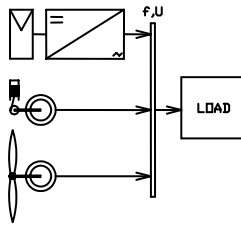


Fig.5. Wind – PV – Diesel system.

As to the Wind – PV System, its resources have predominantly favourable distribution into time (figure 6). When the wind gets stronger, the solar radiation is usually lower, and vice versa. This trend has been observed likewise during the earth's yearly round. If the system is situated on appropriate place, designed correctly and energy storage supplied, it can work in a highly effective and steady way.

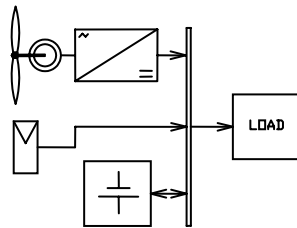


Fig.6. Wind – PV system.

Another profitable system providing complex supply is the Wind – Photovoltaic System combined with a solar thermal collector. The electric power generated by the RES is consumed on the one hand by the loads, and on the other – by the solar circulating pumps. The surplus electric power generated by the wind turbines can be used to heat up the water additionally, instead of the alternative to lose it in the dump load. This system is especially suitable for mountain chalets, villas and hotels [2], [3].

The configurations described above do not reveal all the possibilities for HSRES structure. The option which structure to choose depends on a large number of factors – renewable energy potential, purpose of the system, energy needs, price, etc.

### Design of Hybrid Systems

The first step in the design of hybrid systems is the analysis of the renewable energy potential, which is external to the system. Based on both the received meteorological measurements and some internal to the system factors the most suitable configuration of a HSRES is being sought after. Such a configuration should assure the sustainable work of the system, knockdown price, top return on investment, maximum efficiency, etc.

Among the internal factors are:

*Energy consumption* – not only the consumption quantity should be examined, but also its distribution into time.

*Energy storage* – this storage is usually carried out by batteries. When the consumption is intensive and the batteries capacity is not picked out correctly, an

interruption in the power supply may appear. Also if the capacity is too high, the battery cannot be fully used. When choosing a battery, the stored energy should vary between 30% and 85% of its rated capacity [12].

*Units selection* – this selection is carried out according to the specific methodology of the unit type (turbine, photovoltaic panel, etc.).

Based on the above-mentioned, one general conclusion could be drawn: the design of HSRES is a difficult, multifactor task, whose main goal is to achieve an optimum. This task is done according to some technical, technological and economical criteria. Creating a computer model of the system and using computing machinery makes the design process easier and more effective.

### Control

When controlling the energy systems with RES, it should be taken into account that part of the input indicators cannot be controlled. This makes the limited and determines the introduction of feedbacks in order to increase the system stability. The control can be centralised, scattered on the units or combined.

Batteries, generator with conventional fuel and their joint work are more often subject to control. However, the control system can be even more complicated.

According to their course of action, control systems are determined as passive or active.

Passive systems are used with the simple HSRES. Most of the existing systems are passive; they work on the “on/off” principle.

Active systems are used with HSRES consisting of a large number of components. They measure and calculate the input data (meteorological, energy flows). These systems are flexible and can work in different modes.

The information is transmitted by cable, wireless or optically. Cables can be different types – coaxial, phone, twisted pair or the power cables (power line communication). Wireless connection is established by radio modems and wireless controllers. As to the optical lines, they are built up by optical cables, amplifiers and media converters. The way of transmission of the information depends on the data amount, distances, unit interfaces, and the cost of the lines.

Actually, control systems work by means of controllers, programmable controllers, software, etc. The control algorithm is periodically executed – this is a sequence of activities that keep the system in a certain mode of work. Its complexity depends on the structure of the system and on the tasks set before it. Figure 7 represents an example of a control algorithm for Wind – Photovoltaic – Diesel system. The control system protects the battery from overcharging. It switches the exceeded energy to a dump load. If the stored energy drops below 30% of the battery capacity, the diesel generator switches on.

Examples for working control systems are: Schneider Electric DC Panel – Square D QO [7], Mechron's Cycle Charge [11], products of Xantrex [13], etc.

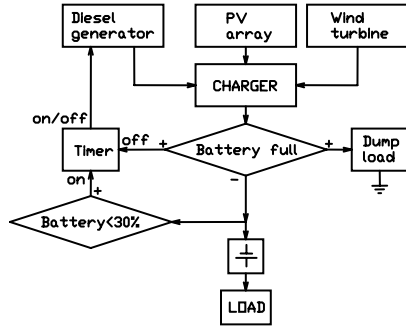


Fig.7. Example of a control algorithm.

### Optimising and Modelling

To find an optimal configuration and control of HSRES an analysis of the multifactor target functions should be conducted. Some of those functions are:

*Cost of energy*

$$(1) \quad COE = f(L, CU_i, n_i, COF_i, QF_i, RE, T_i, P_i, \dots),$$

$L$  – Energy consumption,  $CU_i$  – Overall cost of each unit,  $n_i$  – Number of the units of the same type,  $COF_i$  – Cost of the fuel,  $QF_i$  – Fuel consumption of the units €/kWh,  $RE$  – Available renewable energy,  $T_i$  – Life of the unit,  $P_i$  – Rated power of the units.

The return on investment is inversely proportional to the cost of energy, i.e. minimizing the energy cost leads to maximizing the yield upon investment.

*System sustainability*

The objective is to find a configuration with maximum stability, i.e. minimum number of supply interruptions.

$$(2) \quad Err = f(L_i, RE, P_i, SE_{min}, SE_{max}, \dots),$$

$Err$  – Number of supply interruptions,  $L_i$  – Load with its own priority,  $RE$  – Renewable energy,  $P_i$  – Power of the unit,  $SE_{min}, SE_{max}$  – Minimum/ maximum stored energy.

*Fuel consumption / Use of RES*

The objective is to find a configuration with maximum use of renewable energy and minimum fuel consumption.

$$(3) \quad \max(REU = f(L, RE, P_i, SE_{min}, SE_{max}, \dots)),$$

$$(4) \quad \min(FC = f(L, RE, P_i, SE_{min}, SE_{max}, \dots)).$$

Optimisation done according to this criterion increases the ecological conformity of the system, but at the same time reduces its stability and leads to a rise of the overall cost.

It is possible to combine different optimisation criteria – for example (1) and (2). In this case the target function is:

$$(5) \quad opt(\min(COE), \min(Err))$$

It is also possible to charge different importance to every criterion, which will lend variety to the operation modes of the hybrid systems.

The above-mentioned arguments considering target functions are the most important factors, which those functions depend on.

An optimized sizing method has been developed and it is based on an energy behaviour simulation coupled with a cost optimization. The simulation uses a numerical method based on an energy balance and a storage continuity equations conducing to various possible configurations for the HSRES system. The production cost is calculated taking into account the inflation rate and the configuration producing the kWh with the lowest cost is chosen [15].

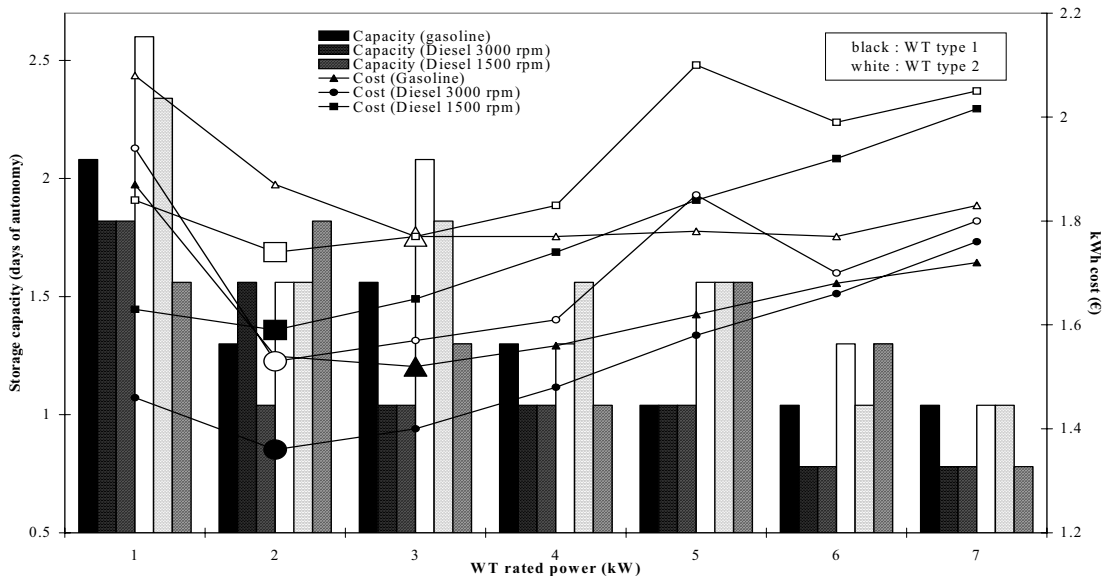


Fig.8. Optimal configurations for a hybrid wind/diesel/storage system and kWh cost

Various parameters are optimized, not only the size of the components but also the threshold of engine generator run on or off, the strategy of energy flows control, ... as an example, we show on figure 8 the results of this method applied to a wind-diesel-storage hybrid system for two types of wind turbines; the optimal rated power of the wind turbine and storage capacities with corresponding kWh cost are plotted. [16]

Modelling of a hybrid system means creating a computer model of its components, as well as of the factors that influence it [14]. The modelling and simulation of an already designed or still being designed system allow its behaviour to be examined for a short period time under different circumstances.

Some simulations are performed by specialized software. Several products that simulate and optimize hybrid systems are shown below:

#### Hybrid2

Hybrid2 [14] is designed to study a variety of hybrid power systems with different components. The program also includes economic analysis tool. The results are provided in two levels of output, a summary and a detailed time step by time step description of power flows.

#### HOMER (Hybrid Optimization Model for Electric Renewables)

It is a computer modelling software, that models the work of both off-grid and grid-connected power systems for remote, stand-alone, and distributed generation. The package models both conventional and renewable energy technologies. It performs optimisation and sensitivity algorithms, that allow choosing a better configuration of the designed system.

#### RAPSIM (Remote Area Power Supply Simulator)

A computer modelling product, designed to simulate alternative power supply options. The program helps sizing PV, wind, diesel stand-alone and hybrid systems.

For development of new models can be used programming languages, as well as Matlab and other environments for computer modelling.

## Flexible Hybrid Systems

Hybrid systems, which can change their structure, mode (stand-alone or grid-connected) and control, can be defined as flexible.

The Laboratory for Renewable Energy Sources by the Technical University of Sofia, Bulgaria, was created within the framework of Project TEMPUS 09704-94. Its main purpose is education and research. It disposes of an experimental flexible hybrid power system (Figure 9), that comprises the following elements: digital meteorological station, wind generator, photovoltaics, lead-acid battery, inverter-rectifier, solar thermal collector with vacuum tubes, monitoring system based on hardware from National Instruments.

The system is flexible, because the disposal units can work in a different combination. Moreover, monitoring system has been developed [2]; it allows monitoring the operation of the system, as well as the meteorological conditions for a long period of time. The measured indicators (current, voltage, power, meteorological data, etc.) are kept in a database [4]. The collected information allows analyzing the system work under different weather conditions and operation modes, as well as choosing suitable control strategy.

A lot of experiments with the described hybrid system have been conducted. As examples, the results for a period of 24 hours are presented thereafter [4]. It has to be mentioned that in order to increase the possibilities of the hybrid system the wind generator is simulated by a motor-generator group with an asynchronous generator of the same rated power. In that way is used the capability to explore the system behaviour having preliminary defined wind energy potential [3]. To make it more comprehensible, it is assumed that the charging powers are taken for positive and the discharging – for negative.

Figure 10 shows the generated and consumed power, as well as the overall power of the DC bus. The results are summarized in Table 1. Under the existing conditions the produced energy is 2,061 kWh and the consumed is 3,305 kWh. This means that the battery has lost 1,244 kWh of its energy.

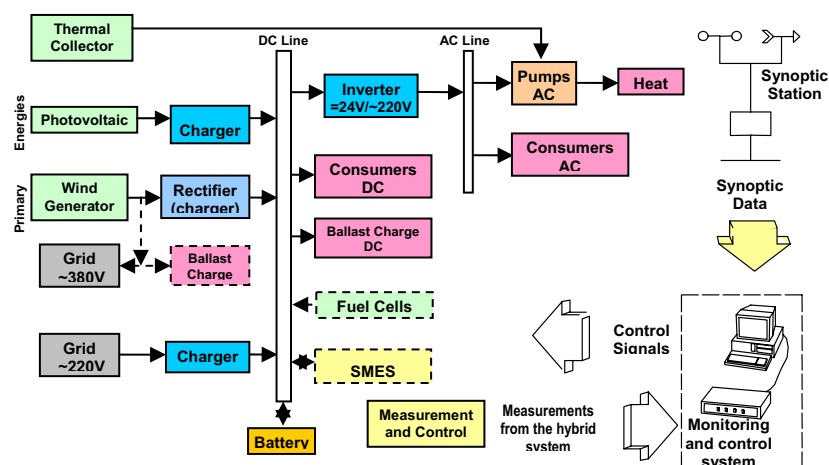


Fig.9. Flexible experimental hybrid system of a mixed type (the elements, marked by dashed line will be accomplished in the future).

**Table 1**  
Produced and consumed energy during the period

Sources	
Photovoltaics	1,273 [kWh]
Wind generator	0,788 [kWh]
Subtotal Ech	2,061 [kWh]
Consumers	
DC loads	- 0,0091 [kWh]
Inverter	-3,296 [kWh]
Subtotal Edisch	-3,305 [kWh]
Total Ebat	-1,244 [kWh]

The flexibility of the described hybrid system allows research of different unit combinations and development of methods for design and control under different conditions, as well as validation of the results.

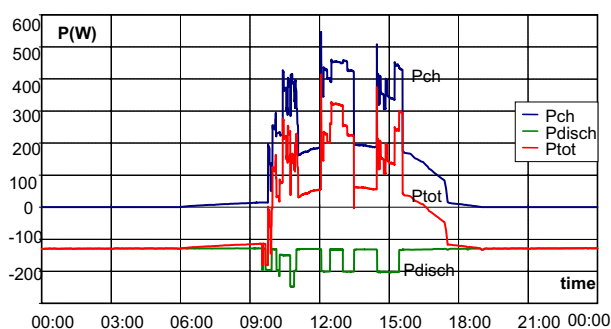


Fig.10. DC Power – produced, consumed, overall

## Conclusion

In the present article hybrid systems with renewable energy sources are considered. They are classified and some special features and problems on their design, management and simulation are reviewed.

In recent years, a trend to a decrease in the cost of renewable energy technologies has been observed, which comes together with the arisen tendency towards distributed generation of energy. Those two factors provide the opportunity many solutions to be reconsidered.

The state of the art shows that in the near future in the structures of the hybrid systems will appeared the fuel cells and the SMES. The FACTS technologies will interfered with the traditional power electronic converters.

Research work in this field shows that further studies should be conducted in the sphere of HSRES with different configuration comprising a great number of sources and producing both electricity and heat. Using an existing computer model of hybrid systems or creating a new ones allows an extensive research on their work under different conditions and configurations and facilitates their design. It is advisable to use flexible experimental systems in order to validate the obtained results.

## References

[1] Dimitrov D., Lazarov V. – sous la redaction, auteurs–equipe internationale: Sources d’énergie renouvelables. UTS, Sofia, 1999.  
[2] Lazarov, V., Z. Zarkov. Monitoring of Renewable Energy Sources Hybrid System. Proc. of Int. Conf. ICATE’2002, Craiova/Baile Herculane, Romania, pp.224-229.

[3] Driviere, J., F. Massouh, A. Laborie, D. Dimitrov, V. Lazarov, E. Sokolov, Z. Zarkov, K. Varsamov, I. Dobrev. Renewable Energy Sources Hybrid System. Proc. of Int. Conf. ELMA’99, Varna, Bulgaria, 1999, pp.226-236.  
[4] Zarkov, Z., V. Lazarov. Energy Balance of a Hybrid Renewable Energy Sources System. Proc. of Int. Conf. ICATE’2004, Baile Herculane, Romania, pp.291-296.  
[5] Landau M., Geipel R. Modulare PV-Hybridssysteme für netzferne Gebiete - Pilotanlagen Kythnos und Starkenburger Hütte, Kasseler Symposium Energie-Systemtechnik, Germany, 2004  
[6] Drouilhet S., M. Shirazi. Wales, Alaska High-Penetration Wind-Diesel Hybrid Power System. Technical Report, NREL, 05.2002.  
[7] Back to the Past – Wind and Sun Replace the Energy Grid. [www.schneider-electric.ca/www/en/cms/copeland.pdf](http://www.schneider-electric.ca/www/en/cms/copeland.pdf).  
[8] Muhs J. ORNL’s Hybrid Solar Lighting Program: Bringing sunlight inside, NCPV and Solar Program Review Meeting 2003.  
[9] Ulleberg Ø, Pryor TL. Optimization of integrated renewable energy hydrogen systems in diesel engine mini-grids. WHEC 2002 - 14th World Hydrogen Energy Conference, Montreal, 9-14 June 2002.  
[10] Strauss, Ph., A. Engler. AC Coupled PV Hybrid Systems and Microgrids – State of the Art and Future Trends. 3-rd World Conference on Photovoltaic Energy Conversion, Osaka, Japan, May 2003.  
[11] Cycle Charge™ DC Power System for Stand-Alone and Hybrid Applications. [www.mechron.com](http://www.mechron.com).  
[12] Notton G. Systèmes de production à sources renouvelables d’énergie: application aux sites isolés. HDR, Université de Corse, 2002.  
[13] Xantrex website – [www.xantrex.com/products.asp](http://www.xantrex.com/products.asp).  
[14] Manwell J., A.Rogers et al. Hybrid 2 – A Hybrid System Simulation Model. Theory Manual, NREL, 1998.  
[15] G. Notton, M. Muselli, P. Poggi, A. Louche. Optimization of stand-alone hybrid photovoltaic/engine generator/battery system for small energy load – Case study in Corsica. *Actes du PV Hybrid power systems 2000 Conference*, Aix en Provence, France, 7-8 Septembre 2000.  
[16] G.Notton, C.Cristofari, P.Poggi, M.Muselli. Wind electrical supply system : behaviour simulation and sizing optimization. *Wind Energy*, 4-2, 43-59, (2001).  
[17] Lazarov V., A. Krusteva, Z. Zarkov, D. Apostolov. Electrical aspects of the research of renewable energy sources. Reports of the Third Conference on Renewable Energy Sources, Sofia, Bulgaria, October 2003, pp.36-41 (in Bulgarian)

**Vladimir Lazarov** – Associate Professor, Dr., Responsible for the “Laboratory on Renewable Energy Sources,” Faculty of Electrical Engineering, Technical University of Sofia, 8, Kl. Ochridski Blvd., 1000 Sofia, BULGARIA. e-mail: vl\_lazarov@tu-sofia.bg.

**Gilles Notton** – Associate Professor, Dr., Université de Corse, BP 52 – 20250 Corte, France. e-mail: gilles.notton@univ-corse.fr.

**Zahari Zarkov** – Assistant Professor, Dr., Faculty of Electrical Engineering, Technical University of Sofia, 8, Kl. Ochridski Blvd., 1000 Sofia, BULGARIA. e-mail: zzza@tu-sofia.bg.

**Ivan Bochev** – Ph.D. Student, Faculty of Electrical Engineering, Technical University of Sofia, 8, Kl. Ochridski Blvd., 1000 Sofia, BULGARIA e-mail: ivan.bochev@gmail.com.

# Commutation of capacitor circuits at compensation of power factor

Vasil-Mario Piperov and Galia Georgieva

**Abstract:** This article presents in brief a theoretical basement of processes in alternating current circuits and some contactors for commutation of capacitor circuits. They guarantee efficient and stabile action during the exploitation of main contacts of contactors of capacitors. The pointed figure – Investigation of circuit parameters at RLC-load – is used for developing a stand for laboratory work. This type of laboratory work gives the students visual idea of processes taking place in capacitor circuits.

## Introduction

The contactors for capacitors present an essential part of the modern industry of electrical apparatuses. This article aims to present the investigation of the processes that take place during the processes of commutation of capacitor circuits.

The article presents the theory of transient processes during the processes of commutation in capacitor circuits, the principle of acting and the construction of the capacitor.

It is useful for the students to be presented the point of the processes (at commutation in capacitor circuits when compensated the power factor). Electrical circuit diagram is developed and by the means of this diagram the parameters are investigated at RLC-load.

This stand gives the possibility to present the contactors for commutation of capacitors and to investigate the circuit parameters at real conditions.

## Processes in alternating current circuits

### Process of recharging at circuits with alternating current source

In general, the ohmic resistance  $R$  of the wires in power-transmission lines and distributing nets for alternating current and with great capacity  $C$  (see fig.1), is small. This means that the voltage drop is significantly less then the capacity.

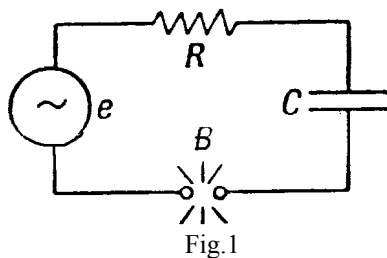


Fig.1

In the circuit diagram in fig.1 the distance between the contacts  $B$  is adjusted in such a way that to be break through by the alternating voltage of the source  $E$ . Each

time when the current value of the source voltage reaches the value for creating an electric arc  $E_z$ , an electric sparking jumps between the contacts and the condenser charges for a short time up to the voltage of the electric sparking  $E_b$ . After a short period of time  $\pi T$  the electric sparking dies out and the capacitor keeps the voltage with that meanwhile it has charged. The voltage of the source changes and after a certain time it accepts the opposite sign. Therefore, the voltage between the contacts gradually grows up and finally it reaches a value that is enough for a new break through voltage and electric arc. Meanwhile the capacitor quickly charges up to a voltage that is almost equal to the new current value of the voltage of the source. Its value retains after dieing out the electric arc till the next recharging that will follow as a result of the following change of the voltage of the source.

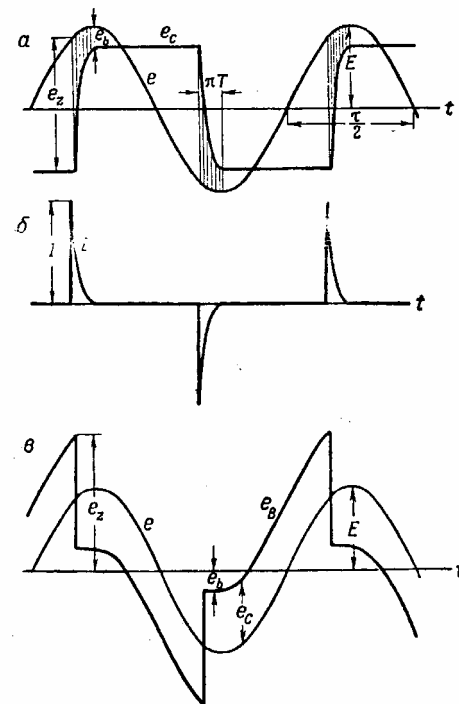


Fig.2

The process above described is graphically presented in fig.2. As soon as the difference between the alternating network voltage  $E$  and the capacitor voltage  $E_c$  reaches the value of the firing voltage, the capacitor recharges and keeps this new voltage till the next appearance of the electric arc. The current flows in the circuit during the time intervals hatched in fig.2. Obviously this current is not like a sinusoid alternating current. It consists of separate picked pulses. Due to the small value of the resistance  $R$  these pulses begin with jump like short



circuit current in circuits without inductivity. The form of pulses is shown in fig.2b; their fast fading is due to the short time.

The voltage of the electric arc is equal to:

$$(1) e_b = e - e_c - e_R$$

When there is no electric arc the voltage between the contacts is equal to the value of the difference between the voltage of source and the voltage of the capacitor. During the process of arc firing its voltage is  $E_b$ .

Fig.2 shows how the voltage between the contacts varies in the course of time. At each arc firing the voltage charges with jump to the value of  $e_z - e_b$ . It is seen in fig.2 that the form of the curve of capacitor voltage, the curve of distance between the contacts and the curve of the resistance  $R$  ?? has changed despite of the sinusoid characteristic of the voltage of the source. The capacitor voltage seems to be almost rectangular; the voltage between the contacts consists of shifted sinusoids; the resistance voltage has the form of pulses of current.

The relative position of the curves of capacitor voltage and the source voltage depends on the value of the arc firing voltage. It is accepted in fig.2 that the arc firing voltage  $E_z$  is approximately  $2E$ . At this value of  $E_z$  the firing may take place when there is an initial charge in the capacitor. Otherwise the value of the voltage is insufficient for breakdown. Nevertheless the process of recharging has started, it will continuously repeat after each half-period. The largest value of the firing voltage at which it is possible the breakdown to take place, is defined by the following formula:

$$(2) E_z = 2E - e_b$$

where  $E$  means the magnitude of the network voltage.

If the distance between the contacts is adjusted then the capacitor will always recharge at the moment of maximum value of the network voltage. Therefore the rectangular wave of the capacitor voltage will be shifted to a quarter period relative to the sine curve of the network voltage. Along with at such adjustment the pulses of current will immediately occur with the magnitude of network current. In this way the general ideas for shifting of the phase of the charge currents appears to be out of place for circuits with possible electric arches. Other characteristic feature of these circuits is the overvoltage that may reach almost twice the value of the network voltage – see (2). This overvoltage arises between the contacts at the moment of time that precedes the firing. This overvoltage is transferred by pulses of current to the other parts of the circuit.

If the duration of the breaking up the contacts is for example a half-period (see fig.3) then the voltage jumps will be significantly less than  $2E$ . The shortening of the time of the braking up the contacts only in small degree influences the residual charge of the capacitor and therefore the voltage that undergoes the switcher after

turning off. The overvoltage is equal to the double magnitude of the network voltage. It would take place in the switcher in case of instantly opening of the contacts and without repeated firings.

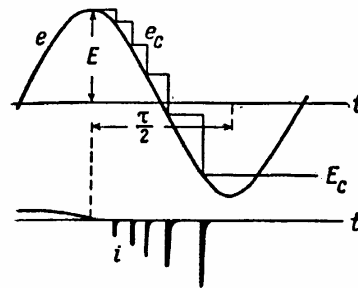


Fig.3

In case of switching on a circuit with high voltage a spark arises between the moving towards each other contacts if the value of the firing voltage has dropped to such a degree that the working voltage may break out the distance between the contacts. If the circuit is slowly turned on and there is no initial charge in the capacitor, the first firing arises at the moment of the maximum value of the sine voltage. The jumps arising at repeated firings became smaller and smaller due to the decreasing distance between the contacts. This process is shown in fig.4. The switching on the non-charged capacitor is not as dangerous as its slowly switching off.

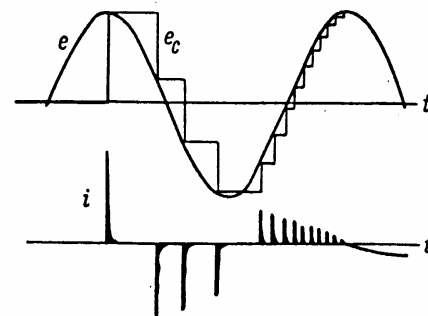


Fig.4

The strong peaks of the current and voltage that arise as the arc occurs are due to the keeping of residual charge in the capacitor after breaking the current. This happens only in case of absence of paths of leakage of the charge. If there is a resistance in the circuit that is parallel to the capacitor (see fig.5) or to the switcher (see fig.6) then the capacitor voltage significantly drops for a half-period. Consequently the voltage that causes repeated firing may drop to such a small value that the distance between the contacts may become unbreakable. The capacitor recharges through a by-pass resistance  $r$  exponentially:

$$(3) e_c = E_c e^{-t/rC}$$

After finishing the half-period the capacitor voltage changes several times:

$$(4) \left( \frac{e_c}{E_c} \right)_{\tau/2} = e^{-\pi/\omega r C}$$

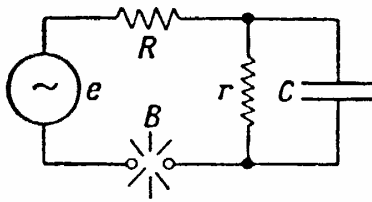


Fig.5

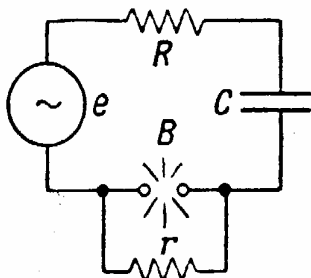


Fig.6

If the by-pass resistance is equal to the reactance of the capacitor reactance:

$$(5) r = \frac{1}{\omega C}$$

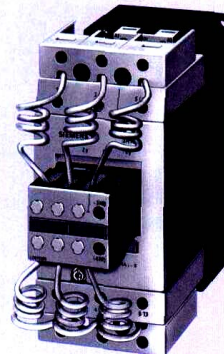
then the capacitor voltage drops for a half-period to its initial value. In this way the recharge almost completes before a possible dangerous repeating firing. If the value of the bypass resistance is twice the value in (3) then the capacitor voltage will decrease only with 20% of its output value and the voltage between the contacts will be higher. The protective resistance with value defined in (3) makes easier the process of switching off. Furthermore this resistance causes appearance of active current with the same magnitude as the magnitude of the normal capacitor current. Besides the phase shifting of the summary current relative to the capacitor decreases from 90 to 45° that also makes easier the switching off. Each active load acts the same way as the bypass resistance acts (see fig.5). It follows from this fact that the dangerous repeated firings will appear only in the case of significant capacity in the circuit.

There is another way to ease the conditions of switching – the consecutive switching on of the resistance which value is defined in (3).

## Capacitor contactors

### Heavy duty series

For switching capacitors only devices should be used that are specially designed. Contactors for capacitors should be designed to avoid hits between the contacts and



high instability caused by hits. Currents should be limited to smaller values than the values of the rated current of the contactor.

Consider the modern capacitors the high power and reducing of losses lead to low inductivity and small resistance.

Consider the contactors with recharge resistors they are switched by the means of the auxiliary contacts made of lead. These auxiliary contacts close before the main ones and recharge the capacitor. In this way the high currents of the capacitor weak at a considerable degree.

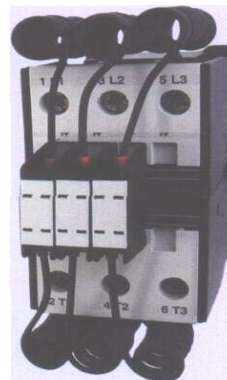
Some characteristic features of the capacitor contactors:

- excellent decreasing of the current
- improving the power factor
- longer useful life of the main contacts
- soft switching off the capacitors
- improving the average life cycle of the system
- decreasing the ohmic losses
- stability at high temperatures

### Regular series

This type of capacitor contactors are used for switching the delay capacitors and conventional three-phase capacitors.

When switched on the capacity in the alternating current



circuit the result is a resonance diagram delayed at a certain degree. In addition to the rated current the capacitor takes some transient current which value is equal to several times of the rated current (about 200 times). Fast-switching contactors should be used. Due to the main contacts the peaks of the input current are limited or delayed by the connected resistance. These current peaks may cause fusing of the main contacts of the

contactor and failure of the capacitors. Decreasing of the input currents leads to avoiding transient and voltage curvatures. The capacitor contactors are suitable for direct switching of low inductive capacitors and capacitors with low losses that are with or without delaying reactors.

### Laboratory stand for investigation

The electrical diagram shown in fig.7 is used for investigation of circuit parameters at different loads. Based on this circuit a laboratory stand is developed. The diagram consists of two contactors, device for measuring

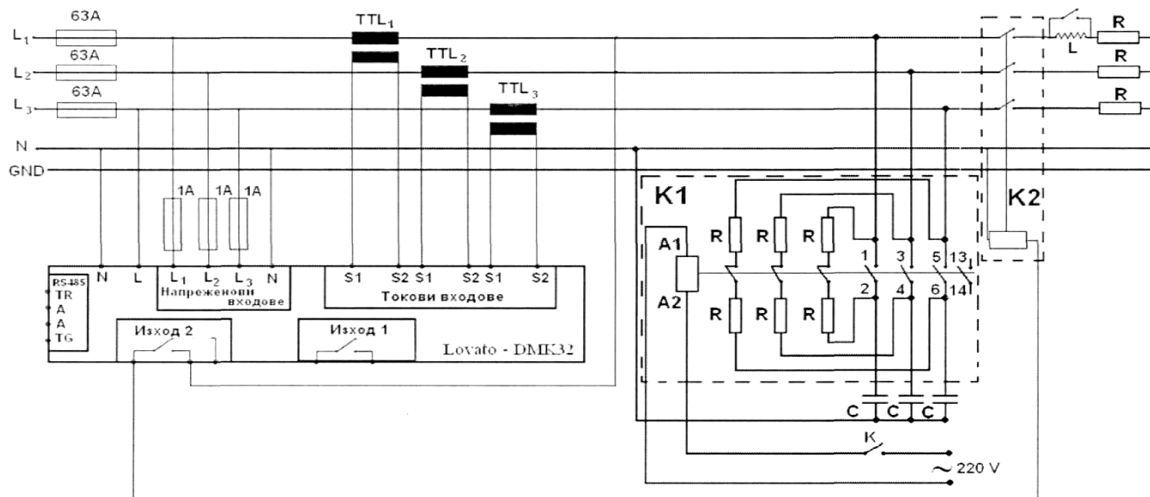


Fig.7. Investigation of parameters in circuits with RLC - loads

of the circuit parameters, active load – an electric heater, linear inductive circuit that is connected only to one phase and a capacitor group, connected in spider with outside spider center.

In order to protect the commutating and measuring devices and the load, three automatic fuses - each one for 63A are used. They switch off the circuits in the case of short circuit. The circuit is switched off for several milliseconds in order to protect the devices from the large current in case of short circuit. The values of the current in the circuit are not large – they are in the range of 1-4A. For protecting the measuring device Lovato-DMK32 three fuses of 1A are used, one for each phase.

The circuit is controlled by two contactors. The contactor K1 is for 16A, 220V, with two contact systems – main and auxiliary. The auxiliary contact system is predicting one in order to recharge the capacitor group. The resistors R that are in the auxiliary contact system are called blow-out resistors. They recharge the capacitors after each charging.

The contactor K2 is for 80A, 220V. It commutates L and R loads and is controlled by the auxiliary contact system of the measuring device that is switched on depending on the set time delay. The inductance L may be by-passed that means the load may change and may be purely active.

After supplying with voltage the contactor K1 is switched on; it switches on the capacitor group. The necessary measurements are done at C-load by a measuring device and by a personal computer connected to it.

In order to have active load the circuit supply is switched off at first by the switch K. Again the supply is delivered and the measurements are done.

In order to have an inductive load the procedure must repeat; instead of the active load the inductivity I is with RLC-loads included.

The load resistance is not controlled. Due to the nature of the resistance (electrical heating) after heating the heating wires it is possible to change the resistance at several

ohms. Bad connections in the circuit should be avoided as there is a danger of short circuits and measurement errors.

### Conclusion

The compensation of power factor is of great importance for the industry and for the power supply. Capacitors are widely used for correction of the power factor.

Therefore, this area of capacitor application has been continuously developed aiming to improve the quality of the electrical power and decreasing of energy losses.

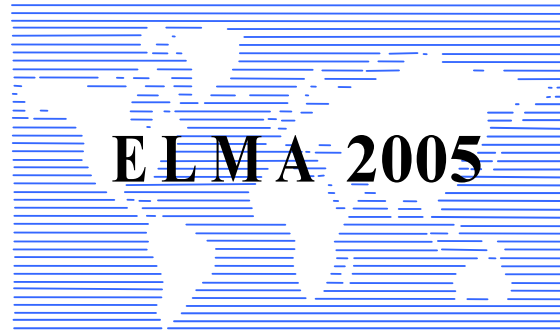
This is the reason for developing a stand that may be used by the students at their laboratory works. They got an idea about the processes taking place in the capacitor circuits when compensated the power factor. This will harden their knowledge.

### References

- [1] Capacitor, de-tuned capacitor and filter bank products; ABB Control Inc.
- [2] Denis Coch, Control equipment for MV capacitor banks-142; Merlin Gerin
- [3] F-2856E I-96 Reprinted 6-01; What is the capacitor?
- [4] Low voltage expert guides №6, Schneider Electric
- [5] Р.Рюденберг, Переходные процессы в электроэнергетической системах
- [6] <http://www.grossautomation.com>  
<http://www.kemet.com>  
<http://www.schneider.co.uk>

**Vasil-Mario Piperov** – associate professor, doctor, Faculty of electricity, department “Electrical apparatus”, Technical university, Sofia, 8 “Kliment Ohridsky” Bul., 1000, Sofia, Bulgaria  
e-mail: pipi@tu-sofia.bg

**Galia Georgieva** – post-graduate student, Faculty of electricity, Technical university, Sofia, 8 “Kliment Ohridsky” Bul., 1000, Sofia, Bulgaria



---

---

**TECHNOLOGIES, NEW MATERIALS  
AND COMPONENTS III**

---

---



# Geometric nonlinear control of the induction motor

Stanislav Enev

**Abstract:** An overview of the differential-geometric methods for nonlinear control of the induction motor is presented in the paper. Some of the existing approaches to input-to-state and input-output feedback linearization of the induction motor, along with some simulations results are given.

**Keywords:** induction motor, differential-geometric methods, dynamic feedback linearization, input-output linearization.

## Introduction

The induction motor is probably the most widely used electric machine in industrial applications due to its reliability, ruggedness and relatively low cost. Its control however presents an extreme challenge because of the highly complicated nonlinear dynamics of the machine. These two reasons make it very attractive for control researchers and practitioners. A lot of approaches to this problem can be found in the literature. The first solutions gave the so-called field-oriented control, which consists of rewriting the equations of the motor through a nonlinear transformation in order to decouple the rotor flux and the rotor speed. The disadvantage is that this decoupling is valid after the flux is constant. Thus when a high dynamic performance is needed their dynamics remain nonlinearly coupled. A presentation of two other approaches to the control of the induction motor, the passivity-based and the flatness-based approaches can be found in [2].

The goal of this paper is to present a brief overview of the differential-geometric methods for control, especially the input-output and input-state feedback linearization, and the nonlinear control of the induction motor from this perspective. A thorough overview of the differential-geometric control techniques for nonlinear control of electric machines can be found in [1].

In Section 2, both  $\alpha$ - $\beta$  and d-q dynamic models of the motor are derived. In Section 3, 4 and 5 dynamic feedback linearizing transformations and an input-output linearizing controller are presented. In Section 6 are given some simulation results.

## Dynamic modeling of the induction motor

The induction motor considered here is a three-phase stator, three-phase short circuited rotor machine. Since a squirrel-cage rotor can be represented as a three-phase short-circuited one by means of a simple transformation, the following considerations are valid for this case too. The common assumptions are adopted i.e. symmetrical construction, linearity of the magnetic circuits, sinusoidal distribution of the field in the air-gap.

The fundamental equations of the motor are:

$$(1) \quad \begin{aligned} \Psi_{S123} &= L_S I_{S123} + M_{SR}(\theta) I_{R123} \\ \Psi_{R123} &= M_{RS}(\theta) I_{S123} + L_R I_{R123} \end{aligned}$$

for the fluxes and the currents,

$$(2) \quad \begin{aligned} V_{S123} &= R_S I_{S123} + \dot{\Psi}_{S123} \\ V_{R123} = 0 &= R_R I_{R123} + \dot{\Psi}_{R123} \end{aligned}$$

for the voltages and

$$(3) \quad \tau = I_{S123}^T \partial M_{SR}(\theta) / \partial \phi I_{R123},$$

for the torque, where:

$$L_S = \begin{bmatrix} l_S & m_S & m_S \\ m_S & l_S & m_S \\ m_S & m_S & l_S \end{bmatrix}, \quad L_R = \begin{bmatrix} l_R & m_R & m_R \\ m_R & l_R & m_R \\ m_R & m_R & l_R \end{bmatrix}$$

$$R_S = r_S I_{3 \times 3}, \quad R_R = r_R I_{3 \times 3},$$

$$M_{SR}(\theta) = M_{RS}^T(\theta) = m_0 \begin{bmatrix} \cos(\theta) & \delta & \phi \\ \phi & \cos(\theta) & \delta \\ \delta & \phi & \cos(\theta) \end{bmatrix},$$

with  $l_{S(R)}$  - the stator(rotor) windings inductances,  $r_{S(R)}$  - the stator(rotor) windings resistances,  $m_{S(R)}$  - mutual inductances between the stator (rotor) windings,  $I_{3 \times 3}$  - unity matrix,  $m_0$  - mutual inductance between stator and rotor windings,  $\theta = n_p \phi$  - the electrical angular displacement of the rotor,  $\phi$  - the rotor angular position,  $\phi = \cos(\theta - 2\pi/3)$ ,  $\delta = \cos(\theta + 2\pi/3)$ .

Applying a transformation given by the Concordia matrix for the stator variables:

$$X_{S123} = T X_{S\alpha\beta}, \quad \text{where } T = \sqrt{2/3} \begin{bmatrix} 1 & 0 \\ -1/2 & \sqrt{3}/2 \\ -1/2 & -\sqrt{3}/2 \end{bmatrix},$$

and the same transformation followed by a rotation for the rotor variables (expressing the rotor variables in the fixed  $\alpha$ - $\beta$  stator frame),

$$X_{R123} = TR(-\theta)X_{R\alpha\beta}, \quad R(\theta) = \begin{bmatrix} \cos(\theta) & -\sin(\theta) \\ \sin(\theta) & \cos(\theta) \end{bmatrix}$$

the following equations are obtained:

$$(4) \quad \begin{aligned} \Psi_{S\alpha\beta} &= \bar{l}_S I_{S123} + m I_{R\alpha\beta} \\ \Psi_{R\alpha\beta} &= m I_{S\alpha\beta} + \bar{l}_R I_{R\alpha\beta} \\ V_{S\alpha\beta} &= r_S I_{S\alpha\beta} + \dot{\Psi}_{S\alpha\beta}, \quad \text{where} \\ 0 &= r_R I_{R\alpha\beta} + n_p \omega \begin{bmatrix} 0 & 1 \\ -1 & 0 \end{bmatrix} \Psi_{R\alpha\beta} + \dot{\Psi}_{R\alpha\beta} \\ \tau &= n_p m / \bar{l}_R I_{S\alpha\beta}^T \begin{bmatrix} 0 & -1 \\ 1 & 0 \end{bmatrix} \Psi_{R\alpha\beta} \end{aligned}$$

$$\omega = \dot{\phi}, \quad m = 3/2m_0, \quad \bar{l}_S = l_S - m_S, \quad \bar{l}_R = l_R - m_R.$$

The zero axes equations are neglected since it can be shown [8] that they are independent of the other axes variables and do not participate in the energy conversion.

The mechanical equation of the rotor is given by:

$$(5) \quad J\dot{\omega} = \tau - \tau_L - c\omega, \quad \text{where}$$

$J$  - the rotor moment of inertia,  $\tau_L$  - a load torque,  $c$  - friction coefficient.

Excluding the stator fluxes and the rotor currents from these equations and adopting a common notation for the parameters [1],[3],[7], the following dynamic model of the induction motor is obtained:

$$(6) \quad \begin{aligned} \dot{\omega} &= \mu(\Psi_{R\alpha} I_{S\beta} - \Psi_{R\beta} I_{S\alpha}) - c/J\omega - \tau_L/J \\ \dot{I}_{S\alpha} &= -\gamma I_{S\alpha} + \eta \zeta \Psi_{R\alpha} + \zeta n_p \omega \Psi_{R\beta} + V_{S\alpha} / (\sigma \bar{l}_S) \\ \dot{I}_{S\beta} &= -\gamma I_{S\beta} + \eta \zeta \Psi_{R\beta} - \zeta n_p \omega \Psi_{R\alpha} + V_{S\beta} / (\sigma \bar{l}_S) \\ \dot{\Psi}_{R\alpha} &= -\eta \Psi_{R\alpha} - n_p \omega \Psi_{R\beta} + \eta m I_{S\alpha} \\ \dot{\Psi}_{R\beta} &= -\eta \Psi_{R\beta} + n_p \omega \Psi_{R\alpha} + \eta m I_{S\beta} \end{aligned}$$

where the parameters are defined as follows:

$$\begin{aligned} \mu &= n_p m / (\bar{l}_R J), \quad \eta = r_R / \bar{l}_R, \quad \zeta = m / (\sigma \bar{l}_R \bar{l}_S), \\ \sigma &= (\bar{l}_R \bar{l}_S - m^2) / \bar{l}_R \bar{l}_S, \quad \gamma = (\bar{l}_R^2 r_S + m^2 r_R) / (\sigma \bar{l}_R^2 \bar{l}_S). \end{aligned}$$

In [7] high-gain PI controllers are used in order to force the currents to follow a reference trajectory. Thus, if the tracking is fast enough, the current dynamics equations can be neglected and one can achieve current command of the motor, with  $I_{S\alpha}$  and  $I_{S\beta}$  the new inputs, which simplifies the design.

Another transformation leads to the model which serves as a basis for the so-called field-oriented control. It consists of defining a new reference-frame, the so-called d-q - frame by the following transformation matrix:

$$T = R(\rho), \quad \text{where } \rho = \arctan(\Psi_{R\beta} / \Psi_{R\alpha}), \quad \text{i.e.}$$

aligning the  $\alpha$  - axis with the rotor flux vector. Thus by applying:

$X_{*\alpha\beta} = R(\rho)X_{*dq}$  one has:

$$(7) \quad \begin{aligned} \dot{\omega} &= \mu \Psi_d I_q - c/J\omega - \tau_L/J \\ \dot{\Psi}_d &= -\eta \Psi_d + \eta m I_d \\ \dot{I}_d &= -\gamma I_d + \eta m \Psi_d / (\sigma \bar{l}_R \bar{l}_S) + n_p \omega I_q + \\ &+ \eta m I_q^2 / \Psi_d + V_d / (\sigma \bar{l}_S) \\ \dot{I}_q &= -\gamma I_q - n_p m \omega \Psi_d / (\sigma \bar{l}_R \bar{l}_S) - n_p \omega I_d - \\ &- \eta m I_d I_q / \Psi_d + V_q / (\sigma \bar{l}_S) \\ \dot{\rho} &= n_p \omega + \eta m I_q / \Psi_d \end{aligned}$$

Again a current command can be achieved by the use of PI current control loops, with  $I_d$  and  $I_q$  the new inputs. All of the derived models can be put in the following general form:

$$(8) \quad \dot{x} = f(x) + g_1(x)u_1 + g_2(x)u_2, \quad \text{where}$$

$x$ ,  $f(x)$ ,  $g_1(x)$ ,  $g_2(x)$ ,  $u_1$ ,  $u_2$  are given by the corresponding model.

### Feedback linearization of the induction motor

First, the used notations and some basic theory lying behind the input-output and input-state linearization are introduced. Let  $f(x)$  and  $g(x): R^n \rightarrow R^n$  be two vector functions. The Lie bracket of the vector fields  $f$  and  $g$  is given by:  $[f, g] = \partial g / \partial x f - \partial f / \partial x g \in R^n$ .

Pose  $ad_f g = [f, g]$  and  $ad_f^j g = [f, ad_f^{j-1} g]$ .

Let  $h(x): R^n \rightarrow R$  be a scalar function. The Lie derivative of  $h$  with respect to the vector field  $f$  is given by:  $L_f h = \partial h \cdot f$ ,  $\partial h = [\partial h / \partial x_1, \dots, \partial h / \partial x_n]$ .

Given the system (8) and  $y_1 = h_1(x)$ ,  $y_2 = h_2(x)$ . The system is said to have vector relative degree [4]  $(\gamma_1, \gamma_2)$  at  $x_0$  if  $L_{g_j} L_f^k h_i(x) \equiv 0$ , for  $0 \leq k \leq \gamma_i - 2$ ,  $i=1,2$ ,  $j=1,2$  and the matrix

$$(9) \quad A(x) = \begin{bmatrix} L_{g_1} L_f^{\gamma_1-1} h_1 & L_{g_2} L_f^{\gamma_1-1} h_1 \\ L_{g_1} L_f^{\gamma_2-1} h_2 & L_{g_2} L_f^{\gamma_2-1} h_2 \end{bmatrix}$$

is nonsingular at  $x_0$ . Thus, [4] if a system has well-defined vector relative degree  $(\gamma_1, \gamma_2)$  after differentiating  $y_1$ ,  $\gamma_1$  times and  $y_2$ ,  $\gamma_2$  times one has:

$$(10) \quad \begin{bmatrix} y_1^{(\gamma_1)} \\ y_2^{(\gamma_2)} \end{bmatrix} = \begin{bmatrix} L_f^{\gamma_1} h_1 \\ L_f^{\gamma_2} h_2 \end{bmatrix} + A(x) \begin{bmatrix} u_1 \\ u_2 \end{bmatrix}$$

A control law of the form:

$$(11) \quad \begin{bmatrix} u_1 \\ u_2 \end{bmatrix} = -A(x) \begin{bmatrix} v_1 - L_f^{\gamma_1} h_1 \\ v_2 - L_f^{\gamma_2} h_2 \end{bmatrix},$$

transforms the system into two decoupled differential equations representing two chains of integrators,  $v_1$  and  $v_2$  being the new inputs. The zero dynamics are given by [4]:

$$(12) \quad \dot{x} = f(x) - [g_1 \ g_2] A(x)^{-1} [L_f^{\gamma_1} h_1 \ L_f^{\gamma_2} h_2]^T.$$

The system (8) is full-state feedback linearized if  $\gamma_1 + \gamma_2 = n$  i.e. there is no zero dynamics. The necessary conditions are given by the following expressions.

Define the distributions:

$$\Delta_i = \text{span}\{ad_f^k g_1(x), ad_f^k g_2(x)\}, \\ 0 \leq k \leq i, i = 0, \dots, n-1.$$

The system is feedback linearizable in a neighborhood  $U$  around  $x_0$  if and only if [5]:

- for  $i = 0, \dots, n-1$   $\Delta_i$  has constant dimension in  $U$ ;
- $\Delta_{n-1}$  has dimension  $n$ ;
- for  $i = 0, \dots, n-2$   $\Delta_i$  is involutive i.e. for any  $i = 0, \dots, n-2, j = 0, \dots, n-2, k = 0, \dots, \max(i, j)$   $p = 1, 2$ , the Lie bracket:

$$[ad_f^i g_p, ad_f^j g_p] \in \text{span}\{ad_f^k g_1(x), ad_f^k g_2(x)\}$$

If the above stated conditions are satisfied, one is able to find scalar functions  $h_1(x)$  and  $h_2(x)$  in order to have

$$\gamma_1 + \gamma_2 = n \text{ and } A(x) \text{ nonsingular.}$$

The induction motor is not (static) input-state linearizable. By performing dynamic extension (adding an integrator) in one of the inputs the system is made full-state linearizable as long certain singularity conditions are met.

### Dynamic feedback linearizing transformations

Dynamic feedback linearizing transformations using (6), the  $\alpha$ - $\beta$  model, are found in [3] for the reduced model and in [6] for the full-order model.

By adding an integrator in the  $\alpha$  - axis, the following outputs are found:

$$(13) \quad h_1 = \Psi_{R\alpha}, \quad h_2 = \omega - \mu \Psi_{R\alpha} \Psi_{R\beta} / (\eta m)$$

By adding an integrator in the  $\beta$  - axis one has for the output maps:

$$(14) \quad h_1 = \Psi_{R\beta}, \quad h_2 = \omega + \mu \Psi_{R\alpha} \Psi_{R\beta} / (\eta m).$$

Following (9),(11) for the reduced model, two controllers are found with  $\gamma_1 = 2$  and  $\gamma_2 = 2$ . As shown in [3], if the motor torque is nonzero, one of these controllers is nonsingular. The use of this control scheme requires the switching between two controllers, and as given by the

singularity condition, doesn't provide control with zero torque. Another disadvantage of the proposed algorithm is that with these outputs and state variables  $(h_1, \dot{h}_1, h_2, \dot{h}_2)$  the control of the two generally targeted for control quantities, i.e. the rotor flux and speed, is not evidential.

A thorough mathematical considerations on the input-state linearizing transformations using the d-q model is given in [1] and [3]. Here the basic results are given and discussed.

Adding an integrator in the d-axis, for the reduced model the state equations become:

$$(15) \quad \begin{bmatrix} \dot{\omega} \\ \dot{\Psi}_d \\ \dot{\rho} \\ \dot{I}_d \end{bmatrix} = \begin{bmatrix} -c/J\omega - 1/J\tau_L \\ -\eta\Psi_d + \eta m I_d \\ n_p \omega \\ 0 \end{bmatrix} + \begin{bmatrix} 0 \\ 0 \\ 0 \\ 1 \end{bmatrix} I'_d + \begin{bmatrix} \mu\Psi_d \\ 0 \\ \eta m / \Psi_d \\ 0 \end{bmatrix} I_q$$

The output maps are found such that:

$$\partial h_{1,2} [g_1 \ g_2] = 0 \text{ i. e. } \gamma_1 = \gamma_2 = 2.$$

$$(16) \quad h_1 = \Psi_d, \quad h_2 = \omega - \mu \Psi_d^2 \rho / (\eta m).$$

The decoupling matrix from (9)  $A$  is nonsingular when:

$$(17) \quad 2\eta m \mu \dot{\Psi}_d + n_p \mu^2 \Psi_d^3 = 0.$$

In the case of the full-order model the addition of the integrator in the d-axis transforms the model into:

$$(18) \quad \begin{bmatrix} \dot{\omega} \\ \dot{\Psi}_d \\ \dot{\rho} \\ \dot{I}_d \\ \dot{I}_q \\ \dot{V}_d \end{bmatrix} = \begin{bmatrix} \mu\Psi_d I_q - c/J\omega - \tau_L/J \\ -\eta\Psi_d + \eta m I_d \\ n_p \omega + \eta m I_q / \Psi_d \\ -\gamma I_d + \eta m \Psi_d / (\sigma \bar{l}_R \bar{l}_S) + n_p \omega I_q + \\ + \eta m I_q^2 / \Psi_d + V_d / (\sigma \bar{l}_S) \\ -\gamma I_q - n_p m \omega \Psi_d / (\sigma \bar{l}_R \bar{l}_S) - n_p \omega I_d - \\ -\eta m I_d I_q / \Psi_d \\ 0 \end{bmatrix} +$$

$$+ \begin{bmatrix} 0 \\ 0 \\ 0 \\ 0 \\ 0 \\ 1 \end{bmatrix} V'_d + \begin{bmatrix} 0 \\ 0 \\ 0 \\ 0 \\ 1/(\sigma \bar{l}_S) \\ 0 \end{bmatrix} V_q$$

The same outputs as in the reduced model case are found, satisfying:  $\partial h_{1,2} [g_1 \ ad_f g_1 \ g_2 \ ad_f g_2] = 0$ ,



equivalent to  $L_{g_{1,2}} h_{1,2} = L_{g_{1,2}} L_f h_{1,2} = 0$  [5]. Thus, we have  $\gamma_1 = \gamma_2 = 3$ . Again following (9) and (11), the linearizing control law is constructed, with singularity condition given by (17), again as in the reduced model case.

Although that in this case the singularity condition is less restrictive, since it is common to maintain a non-zero flux, the speed control is not obvious and the addition of the angular position equation  $\dot{\phi} = \omega$  is not possible without losing linearity of the system.

The addition of an integrator in the q-axis yields, for the reduced model, the following output maps:

$$(19) \quad h_1 = \omega, \quad h_2 = \rho, \text{ satisfying:}$$

$$\partial h_{1,2} [g_1 \quad g_2] = 0 \text{ i. e. } \gamma_1 = \gamma_2 = 2.$$

The model equations are not given since they are transformed in a similar way (as in the d-axis dynamic extension). It is easily seen that in this case the position equation can be appended to the system, the system remaining feedback linearizable. For position control, we have the following:

$$(20) \quad h_1 = \varphi, \quad h_2 = \rho \text{ with,}$$

$$\partial h_1 [g_1 \quad ad_f g_1 \quad g_2 \quad ad_f g_2] = 0,$$

$$\partial h_2 [g_1 \quad g_2] = 0 \text{ i. e. } \gamma_1 = 3, \quad \gamma_2 = 2.$$

Constructing the feedback control law using (9),(11), the singularity condition is found to be:

$$(21) \quad 2\eta^2 m^2 \mu I_q / \Psi_d = 0,$$

equivalent to the condition of having a non-zero motor torque.

For the full-order model the same output maps for both cases (without and with the angular position equation in the system), and the same singularity condition are found. One has  $\gamma_1 = 3$ ,  $\gamma_2 = 3$ , and  $\gamma_1 = 4$ ,  $\gamma_2 = 3$  for both cases respectively.

In this case, the control scheme doesn't provide a way of controlling the flux. In order to obtain a position control, the load torque must be non-zero. This strategy presents another obstacle, due again to the singularity condition, when a change of the sign of the motor torque is needed.

A common disadvantage for all of the presented dynamic feedback linearizing transformations, especially for these using the full-order models, is that (11) yields a very complicated control laws, making them hard to implement from computational point of view.

### Input-output linearization

In the case, when a linearizing transformation is applied with  $\gamma_1 + \gamma_2 < n$ , the system is only input-output linearized i.e. the system is made linear between

the input(s) and the output(s). The issue in this case is to guarantee that the zero dynamics, the dynamics of the  $n - \gamma_1 - \gamma_2$  state variables made unobservable through the transformation [4], is stable. An input-output linearization of the induction motor which decouples the flux and the speed dynamics is found in [1],[7]. Here, another input-output linearizing control law is presented, again using the reduced model in the d-q frame.

The model of the system is given by:

$$(22) \quad \begin{bmatrix} \dot{\omega} \\ \dot{\Psi}_d \\ \dot{\rho} \\ \dot{\phi} \end{bmatrix} = \begin{bmatrix} -c/J\omega - \tau_L/J \\ -\eta\Psi_d \\ n_p\omega \\ \omega \end{bmatrix} + \begin{bmatrix} 0 \\ \eta m \\ 0 \\ 0 \end{bmatrix} I_d + \begin{bmatrix} \mu\Psi_d \\ 0 \\ \eta m/\Psi_d \\ 0 \end{bmatrix} I_q$$

$$h_1 = \varphi, \quad h_2 = \Psi_d$$

We have the following:

$$\begin{aligned} L_f h_1 &= \omega, & L_{g_1} h_1 &= 0, & L_{g_2} h_1 &= 0, \\ L_f^2 h_1 &= -c/J\omega - \tau_L/J, & L_{g_1} L_f h_1 &= 0, \\ L_{g_2} L_f h_1 &= \mu\Psi_d, & & \text{for the first output, and} \\ L_f h_2 &= -\eta\Psi_d, & L_{g_1} h_2 &= \eta m, & L_{g_2} h_2 &= 0, \end{aligned}$$

for the second output.

The decoupling matrix is given by:

$$(23) \quad A = \begin{bmatrix} 0 & \mu\Psi_d \\ \eta m & 0 \end{bmatrix}$$

and  $\det(A) = -1/(\eta m \mu \Psi_d)$ . Thus the matrix is nonsingular as long as the flux is not zero.

The feedback control law is given by (9),(11), yielding:

$$(24) \quad \begin{bmatrix} I_d \\ I_q \end{bmatrix} = \begin{bmatrix} v_q / (\eta m) + \Psi_d / m \\ v_d / (\mu \Psi_d) + c\omega / (\mu \Psi_d) + \tau_L / (\mu \Psi_d) \end{bmatrix}$$

where  $v_d$  and  $v_q$  are the new current inputs. The application of this feedback linearizing law yields the following system:

$$(25) \quad \begin{aligned} \ddot{\phi} &= v_d \\ \dot{\Psi}_d &= v_q \end{aligned}$$

which is linear and decoupled system as seen from the equations. The zero dynamics, given by (12) are:

$$(26) \quad \dot{\rho} = (n_p + \eta m c / (\mu \Psi_d^2)) \omega + \eta m \tau_L / (\mu \Psi_d^2).$$

The stability of (26)  $\rho$  is not an issue since  $\rho$  is an angle.

This approach provides control of the position(speed) and the flux of the motor and yields a much simpler controller than those constructed by the dynamic feedback linearization approach. The singularity

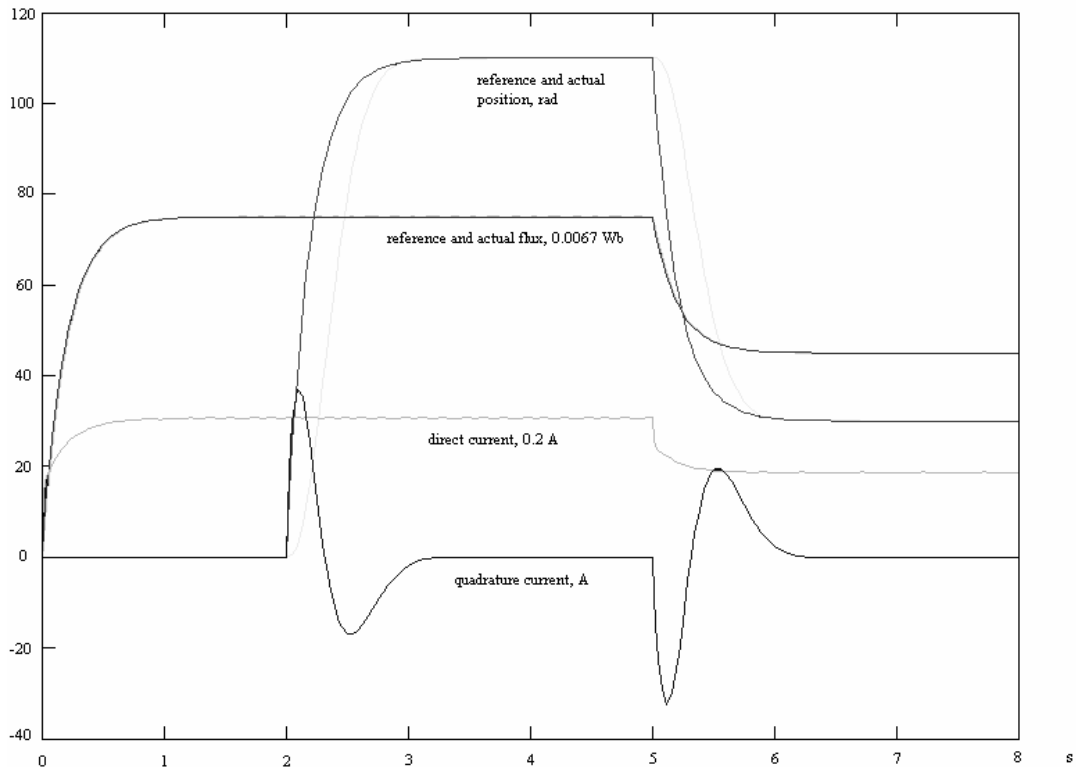


Fig.1. Some transient responses.

condition isn't an obstacle since it is common to maintain a non-zero flux.

### Simulations

As an example, here are presented some transient responses of the motor using the described input-output linearizing controller. Generally, the rotor flux and the load torque are not available for measurement but since the observers for electric machines are not the subject of this paper, in this simulation all of the state variables are supposed measured and the load torque zero. In [9] is shown that an observer with arbitrary exponential speed of convergence for the flux can be conceived. A lot of load torque observer realizations can be found in the literature. For the simulation the same motor as in [8] is selected. The motor parameters are as follows:

$$m = 0.0813H, \bar{l}_S = 0.084H, \bar{l}_R = 0.0852H, \\ r_R = 0.842\Omega, r_S = 0.687\Omega, J = 0.03kgm^2, n_p = 2 \\ c = 0.0014kgm^2s^{-1}.$$

In the outer control loops, P controller is used for the flux control subsystem and a lead transient controller for the position control subsystem. The results of the simulation are presented in Fig. 1.

### Conclusion

A brief presentation of the dynamic feedback linearization and the input-output linearization, as differential-geometric methods for the nonlinear control

of the induction motor is given in the paper. A common disadvantage of the dynamic feedback linearizing transformations is the complexity of the obtained controllers. Most of them do not provide control (present a singularity) when the motor torque is zero which is quite restrictive from application point of view. Not in the last place, the generally targeted for control variables, the rotor speed (position) and flux, are not part or are "hidden" in the transformed state variables, which reduces the benefits of having a linear system as a result of the transformation. Input-output linearizing controller presented here is much simpler, with an easily avoided singularity, providing a decoupled control of the rotor speed and flux. The stability of the zero dynamics is not relevant, because of the nature of the unobservable variable, an angle in this case. The simulation results show the good dynamic performance of the motor.

### References

- [1] Chiasson J. Differential-Geometric Methods for Control of Electric Motors. Int. J. Robust Nonlinear Control, pp. 923-954, 1998.
- [2] Delaleau E., Louis J.P., Ortega R. Modeling and Control of Induction Motors. Int. J. Appl. Math. Comput. Sci., 2001, Vol. 11, № 1, pp. 105-129.
- [3] Chiasson J. A New Approach to Dynamic Feedback Linearization Control of an Induction Motor. IEEE Trans. On Automatic Control, vol. 43, № 3, pp. 391 – 397, March 1998.

- [4] Sastry S., Bodson M. Adaptive Control: Stability, Convergence, and Robustness, Prentice-Hall Advanced Reference Series (Engineering), 1989.
- [5] Respondek W. Geometry of Static and Dynamic Feedback. Summer School on Mathematical Control Theory, Trieste, Italy, Sept. 2001.
- [6] Chiasson J. Dynamic Feedback Linearization of the induction motor. IEEE Trans. On Automatic Control, vol. 38, pp. 1588 – 1594, Oct. 1993.
- [7] Bodson M., Chiasson J. Novotnak R. High-Performance Induction Motor Control Via Input-Output Linearization. IEEE Control Systems, August 1994.
- [8] Hu J., Dawson D.M., Qu Z. Adaptive tracking control of an induction motor with robustness to parametric uncertainty. IEE Proc.-Electr. Power Appl, Vol. 141, No. 2, March 1994
- [9] Martin P., Rouchon P. Two remarks on induction motors, Internet site: [cas.ensmp.fr/~rouchon/publications](http://cas.ensmp.fr/~rouchon/publications).
- 

*Stanislav Enev* – Ph.D. Student, French Language  
Department of Electrical Engineering, Technical  
University of Sofia, 8 Kl. Ohridski Str., 1000 Sofia,  
BULGARIA  
e-mail: [sta\\_enev@yahoo.com](mailto:sta_enev@yahoo.com).

## Finite Element Analysis of Linear Actuator with Moving Permanent Magnet

Ivan YATCHEV, Krastio HINOV, Georgi DIKOV, Stoiko KRASSTEV, Dimitar ATANASOV

**Abstract:** Linear actuator with moving permanent magnet has been studied. The actuator consists of two ferromagnetic cores with coils placed in slots of the inner parts of the cores. A permanent magnet is moving between the cores. Finite element method has been used for magnetic field analysis and for obtaining the static force characteristics of the actuator. Results are obtained for two principle constructions of the actuator. The influence of different geometric parameters on the force characteristics is also estimated.

**Keywords:** Linear actuators, permanent magnets, electromagnetic force, finite element method.

### Introduction

Development of the technologies for production of rare-earth permanent magnets gives possibilities for combining the traditional features of the polarized electromagnetic systems with the new high-energy properties of the rare-earth magnets [1-7]. The main problems for their application are connected with the difficulties with magnetizing the magnets, in case of radial magnetizing of toroids. That is why significant interest can be seen in constructions that allow employment of permanent magnets of prismatic shape. One such a construction is with moving permanent magnet.

In the present paper, force characteristics of two constructions of linear actuators of different slot shapes and moving permanent magnet are obtained and compared.

### Studied Constructions

The principal construction of the actuator is two ferromagnetic cores and exciting coils placed on the cores – Fig. 1. The permanent magnet is located between the cores and moves in longitudinal direction. It is rare-earth NdFeB magnet. On the inner side of the cores there are slots, where the coils are located. The two studied constructions are of different shape of these slots. First one is with open slots of rectangular shape, as shown in Fig. 1. The second one is with closed slots, as shown in Fig. 2.

The displacement  $x$  of the mover is considered from its symmetry position. Some dimensions are fixed - the dimensions of the permanent magnet, the air gap  $\delta$ , the length and the height of the cores. The slot width  $a$ , slot height  $b$  and distance between slots  $c$  are varied.

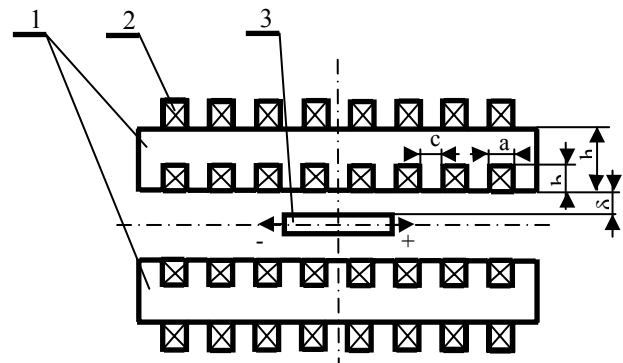


Fig. 1. Principal construction of the actuator

1 – cores, 2 – coils, 3 – permanent magnet

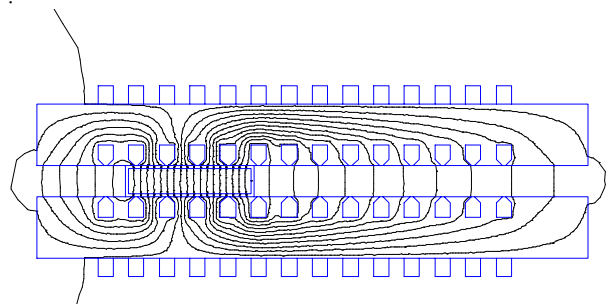


Fig. 2. Construction with closed slots with field map

### Finite Element Modelling

The finite element method has been employed for magnetic field analysis and force computation. Two-dimensional magnetic field problem is solved as non-linear, taking into account the properties of the core material and the permanent magnet. Homogeneous Dirichlet boundary conditions are imposed on the boundary of a buffer zone around the actuator. The electromagnetic force is obtained using Maxwell stress tensor approach.

For solving the problem the program FEMM [8] version 3.3 has been employed. For automating the computations a program in Lua Script<sup>®</sup> language is developed, which allows obtaining results for series of positions of the mover. For keeping accuracy level of the force computation, at each position of the mover a region of denser mesh around the mover is created and the force is computed by generating the integration contour within this region.

## Force-Stroke Characteristics

The force-stroke characteristics are obtained for dimensions of the permanent magnet 20x4 mm, air gap 0.5 mm, current density in the coils 12 A/mm<sup>2</sup> and stroke  $\pm 20$ mm from the symmetry position of the mover. The number of nodes of the finite element mesh was about 15 000.

The results for force-stroke characteristics of the two constructions under variation of some dimensions are shown in Fig. 3 to Fig. 15. The dimensions varied are slot width  $a$ , slot height  $b$  and tooth width  $c$ . The number of slots  $n$  is also given.

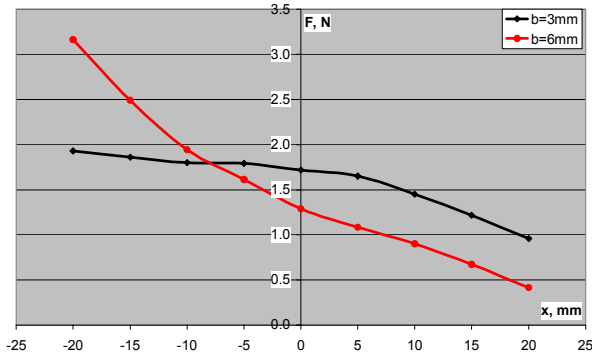


Fig. 3. Construction with closed slots,  $a=2.5$ ,  $c=2.5$ ,  $h=10$ ,  $n=13$ .

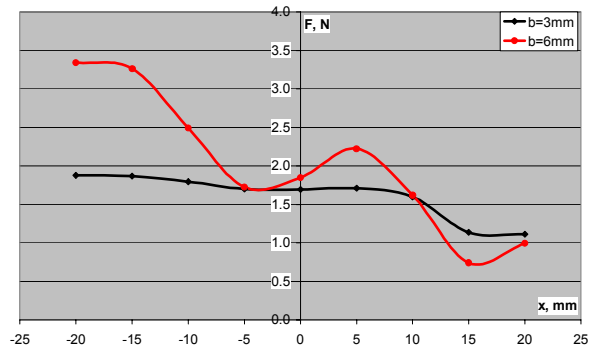


Fig. 4. Construction with closed slots,  $a=2$ ,  $c=2$ ,  $h=10$ ,  $n=16$ .

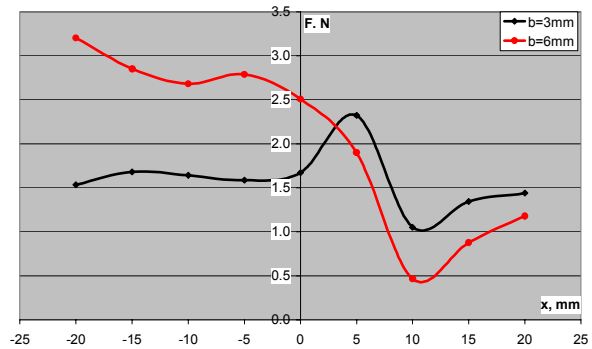


Fig. 5. Construction with closed slots,  $a=3$ ,  $c=3$ ,  $h=9$ ,  $n=11$

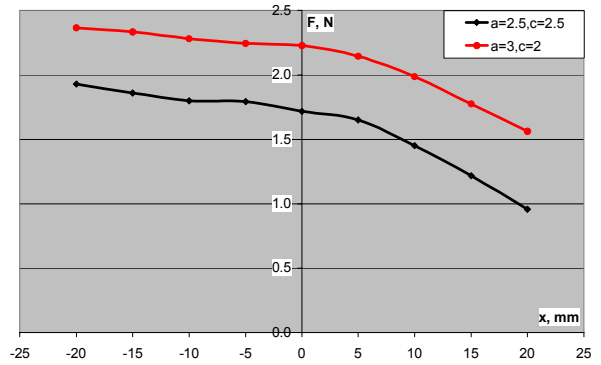


Fig. 6. Construction with closed slots,  $b=3$ ,  $h=10$ ,  $n=13$

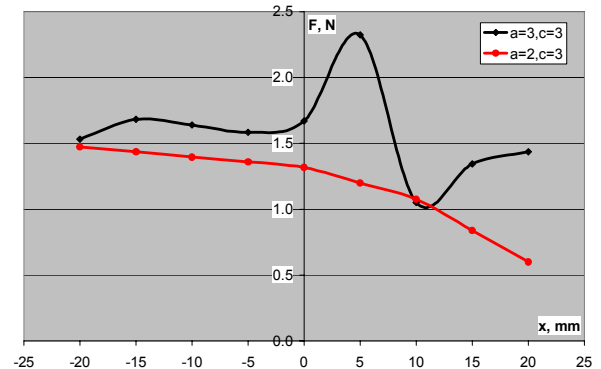


Fig. 7. Construction with closed slots,  $b=3$ ,  $h=9$ ,  $n=11$

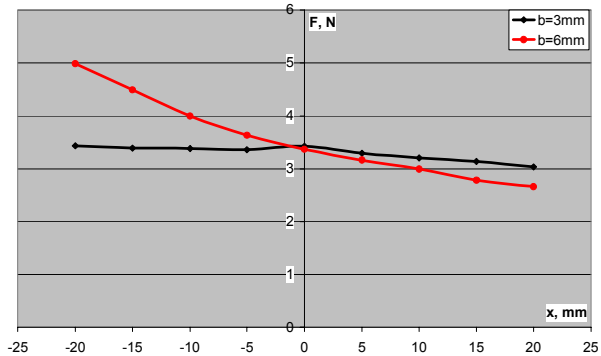


Fig. 8. Construction with open slots,  $a=2.5$ ,  $c=2.5$ ,  $h=10$ ,  $n=13$

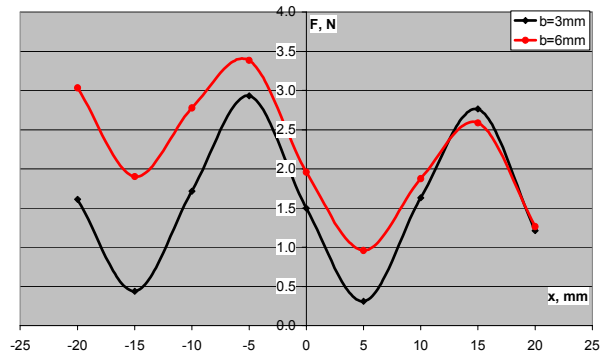


Fig. 9. Construction with open slots,  $a=2$ ,  $c=2$ ,  $h=10$ ,  $n=16$ .

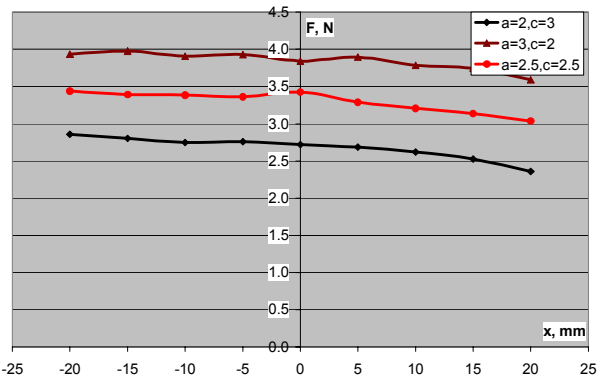


Fig.10. Construction with open slots,  $b=3, h=10, n=13$ .

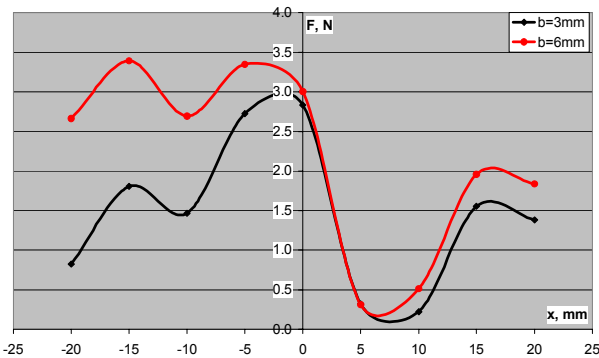


Fig.11. Construction with open slots,  $a=3, c=3, h=10, n=11$

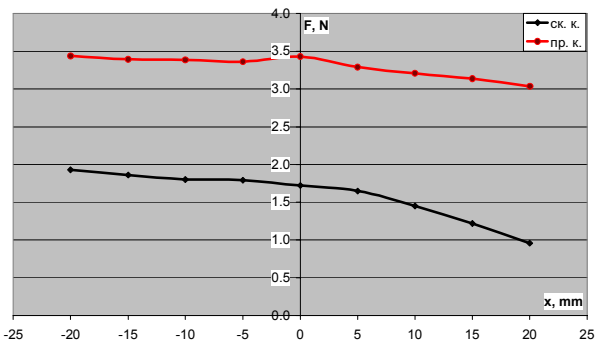


Fig.12. Constructions with closed(ck.k.) and open(np.k.) slots,  $a=2.5, c=2.5, b=3, h=10, n=13$

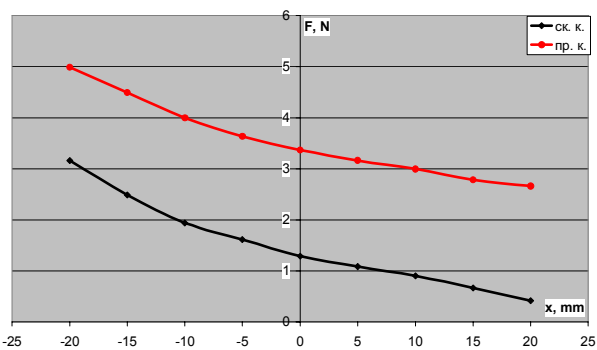


Fig.13. Constructions with closed(ck.k.) and open(np.k.) slots,  $a=2.5, c=2.5, b=6, h=10, n=13$ .

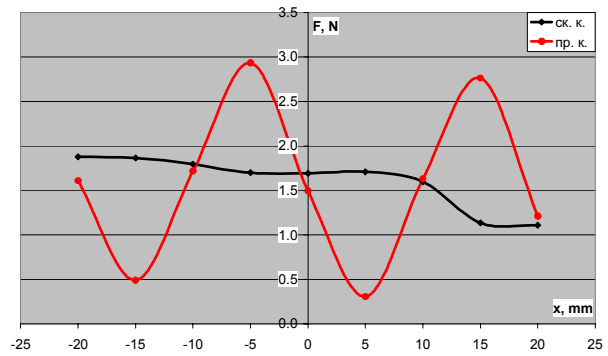


Fig.14. Constructions with closed(ck.k.) and open(np.k.) slots,  $a=2, c=2, b=3, h=10, n=16$ .

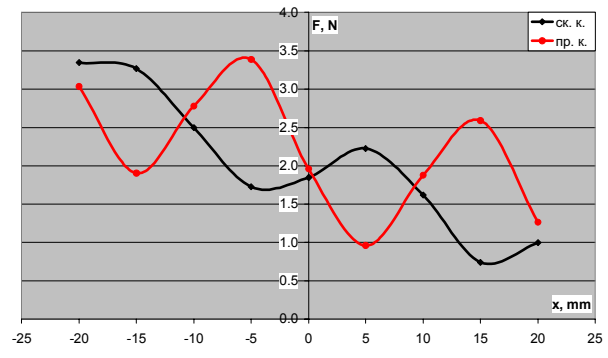


Fig.15. Constructions with closed(ck.k.) and open(np.k.) slots,  $a=2, c=2, b=6, h=10, n=16$ .

Increasing the slot height at equal other conditions leads increase in the force for both constructions. The force pulsations with the stroke are also grater.

Increasing the slot height at equal other conditions leads increase in the force for both constructions. The force pulsations with the stroke are also grater.

For both constructions increasing the slot width and decreasing the tooth width leads to greater force.

The construction with open slots gives about 2 times greater electromagnetic force.

## Conclusions

The computer modelling and the obtained results show that there is significant influence of the varied geometric dimensions on the force-stroke characteristics of the actuator. This allows obtaining different characteristics depending on the application.

The comparison between the two studied constructions shows definite advantage of the one with open slots in terms of greater electromagnetic force.

### References

- [1] Boldea, I., S. Nasar, *Linear Electric Actuators and Generators*, Cambridge University Press, 1997.
- [2] Campbell, P. *Permanent magnet materials and their application*. Cambridge University Press, 1994.
- [3] Zhu, Z. Q., Z. P. Xia, D. Howe, Reduction of Cogging Force In Slotless Linear Permanent Magnet Motors, IEE Proc.- Electr. Power Appl., Vol. 144, No. 4, July 1997.
- [4] Hanitsch, R. E., Design and Performance of Selected Permanent Magnet Devices: Brushless DC Motor And Linear Actuator, [magnet.ee.umist.ac.uk/reports/P12/p12.html](http://magnet.ee.umist.ac.uk/reports/P12/p12.html).
- [5] Hor, P. et al.: Minimisation of cogging force in a linear permanent magnet motor, IEEE Trans. Magn., vol. 34, No. 5, 1998, pp. 3544-3547.
- [6] International Journal of Applied Electromagnetics and Mechanics, Vol. 15, Nos. 1 – 4, 2001/2002, IOS Press.
- [7] Howe, D., Z. Q. Zhu, High-Speed Brushless Permanent Magnet Drives, Electrical Machines & Drives Group, [www.shef.ac.uk](http://www.shef.ac.uk).
- [8] Meeker, D. *Finite Element Method Magnetics* version 3.3. User's Manual, 2003.

## Influence of Some Constructive Parameters on the Electromagnetic Force of a Solenoid Actuator

Dimitar DIMITROV, Kamen YANEV, Ivan YATCHEV

**Abstract:** Two constructions of a solenoid actuator have been studied with different positions of the spring. The influence of different constructive parameters on the electromagnetic force acting on the plunger has been estimated. The magnetic field of the actuator has been studied using the finite element method. Maxwell stress tensor approach has been employed for force computation. The contribution to the total force of the different force components has been estimated. Force-stroke characteristics are also obtained..

**Keywords:** Solenoid actuators, electromagnetic force, finite element method.

### Introduction

Solenoid actuators are widespread electrical apparatus and have numerous applications in different areas [1-3]. Usually their force-stroke characteristics are of interest both for researchers and for manufacturers that embed such actuators in their production.

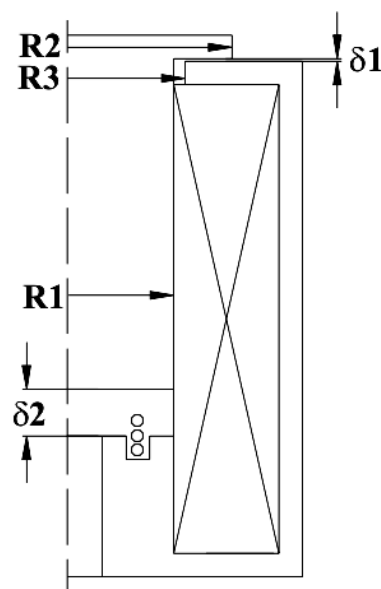
Finite element method has become the most popular one for modelling the magnetic field and computation of the electromagnetic force in actuators [4-7].

In the present paper, the finite element method has been employed for the force computation of a kind of solenoid actuators and the force components have been estimated with the variation of some constructive parameters.

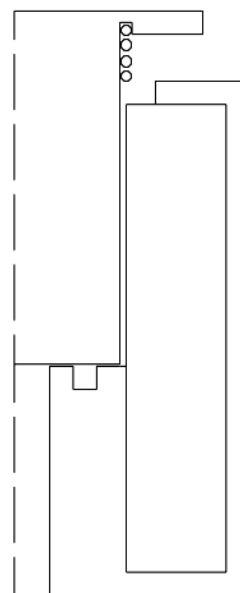
### Studied Actuator

The mover of the studied actuator consists of an armature and fixed to it non-magnetic lever system, which passes through the stopper. The return spring can be placed on at least two places – at the stopper (Fig. 1a) or outside – at the transverse part of the armature – Fig. 1b. Each of the above mentioned two variants has its advantages and drawbacks concerning control and adjustment of the spring, value of the initial and final electromagnetic force, different values of the air gaps, etc.

The study is carried out under DC voltage supply of the coil, the current density in the coil being  $j = 3.55 \text{ A/mm}^2$ . As the control circuits connected to the actuator are of short duty, the core could be made of solid material at AC supply. In this case shading ring can be mounted.



a)



b)

Fig.1. Two principle constructions of the solenoid actuator.



## Mathematical Model and Approach

The magnetic field of the actuator is assumed to be axisymmetric and pseudo-Poissonian equation is to be solved in cylindrical  $r, \varphi, z$  co-ordinate system in the form:

$$(1) \quad \frac{\partial}{\partial r} \left[ \frac{\nu}{r} \frac{\partial(rA)}{\partial r} \right] + \frac{\partial}{\partial z} \left[ \frac{\nu}{r} \frac{\partial(rA)}{\partial z} \right] = -J$$

where

$\nu$  is the reluctivity;

$A, J$  are the  $\varphi$ -components of the magnetic vector potential and the current density.

For the magnetic field modelling of the actuator the finite element method and the program FEMM [8,9] have been employed. Typical field map is shown in Fig. 2.

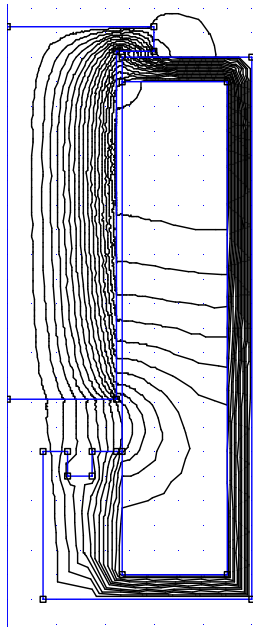


Fig.2. Typical field map.

Maxwell stress tensor approach is used for the computation of the electromagnetic force. The total force  $f_{tot}$  acting on the armature can be considered as composed of four components as shown in Fig. 3.

## Results

The study has been carried out by varying some of the constructive parameters. The values of the parameters for the different variants are shown in Table 1.

$R_{2opt}$  is the value of  $R_2$  for which maximal value of the total force on the armature is obtained.

The results are shown in Fig. 4 a, b and c.

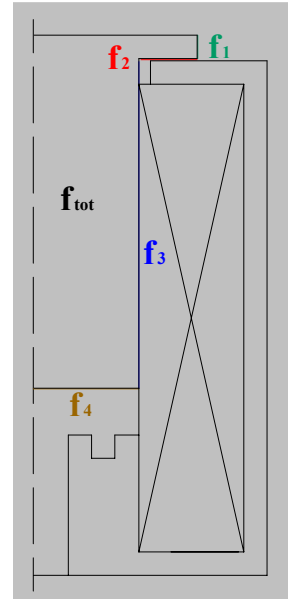


Fig.3. Force components.

Table 1

Variant No.	$R_3$ [mm]	$R_2$ [mm] range	opt. $R_2$ [mm]	$\delta_1$ [mm]	$\delta_2$ [mm]
1	4,75	5÷7	6	0,1	2
2	5,00	5÷7	6	0,1	2
3	5,25	5,5÷7	6,25	0,1	2
4	5,00	5,5÷7,5	7	0,2	2
5	5,25	5,5÷7,5	7,00	0,2	2
6	5,50	6÷7,5	7	0,2	2
7	6,00	6,5÷8	7,5	0,2	2
8	6,00	6÷8	8	0,5	1
9	6,00	6,5÷8	8	1	1
10	6,00	6,5÷8	8	0,5	0,5
11	4,75	5÷7	7	3	4,9
12	5,25	5,5÷7	7	3	4,9

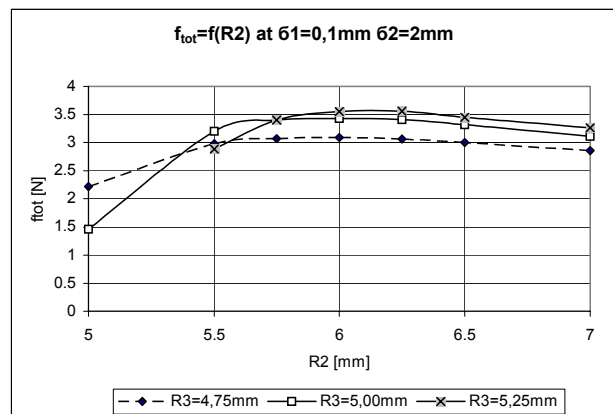


Fig 4a.

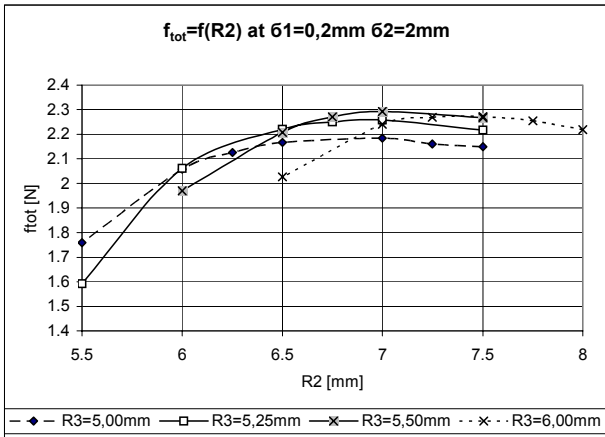


Fig 4b.

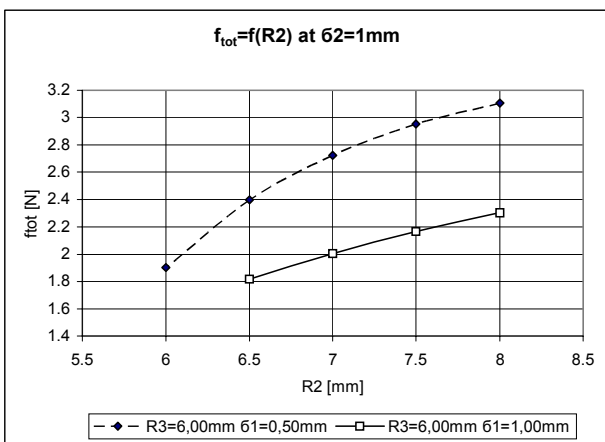


Fig 4c

The contributions of the force components to the total force for variants 1,3 and 10 are shown in Fig. 5 a, b, and c.

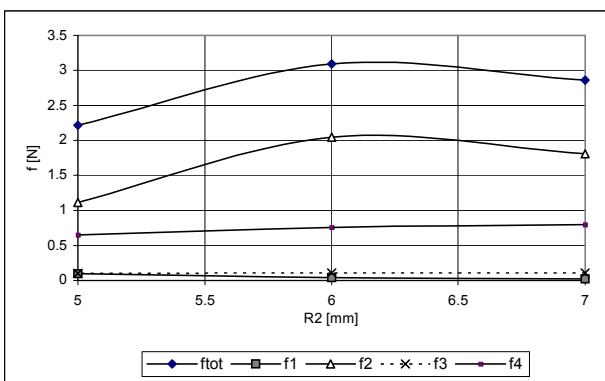


Fig 5a. Force and its components at  $R3=4,75 \text{ mm}$  ;  $\delta l=0,1 \text{ mm}$  ;  $\delta 2=2 \text{ mm}$  – Variant 1

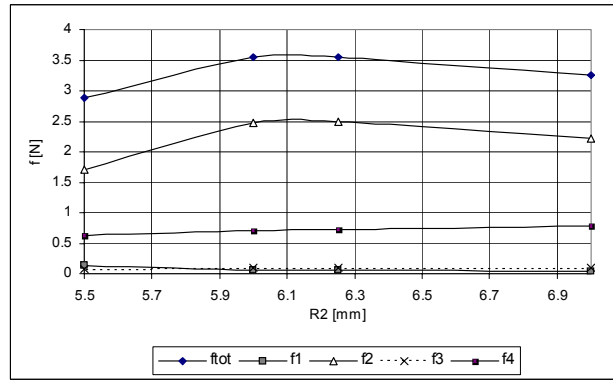


Fig 5b. Force and its components at  $R3=5,25 \text{ mm}$  ;  $\delta l=0,1 \text{ mm}$  ;  $\delta 2=2 \text{ mm}$  – Variant 3

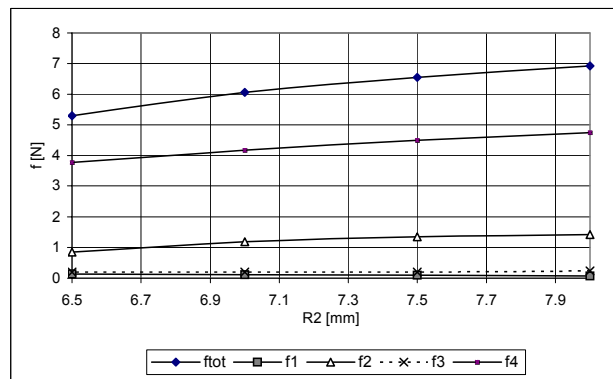


Fig 5c. Force and its components at  $R3=6,00 \text{ mm}$  ;  $\delta l=0,5 \text{ mm}$  ;  $\delta 2=0,5 \text{ mm}$  – Variant 10

For the rest of the variants at parameters, for which the force is maximal, the force components are shown in Table 2.

Table 2

Fig.	Variant №	$f_1$ [N]	$f_2$ [N]	$f_3$ [N]	$f_4$ [N]
1a	2	0,058	2,382	0,094	0,725
	4	0,035	1,188	0,102	0,732
	5	0,035	1,267	0,098	0,711
	6	0,045	1,304	0,099	0,702
	7	0,040	1,287	0,099	0,707
1b	8	0,058	0,883	0,140	1,837
	9	0,036	0,384	0,119	1,617
	11	0,001	0,006	0,032	0,179
	12	0,002	0,012	0,029	0,156

The force-stroke characteristics for variants 1, 2, and 3 are shown in Fig. 6 a), variants 4, 5, 6 ,7 – in Fig. 6 b), and for variants 8, 9 and 10 – in Fig. 6c).

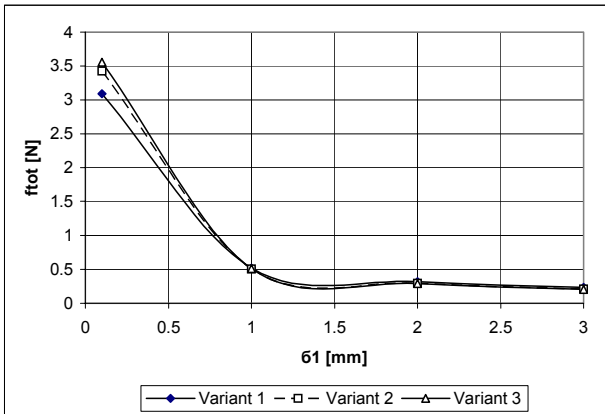


Fig 6a.

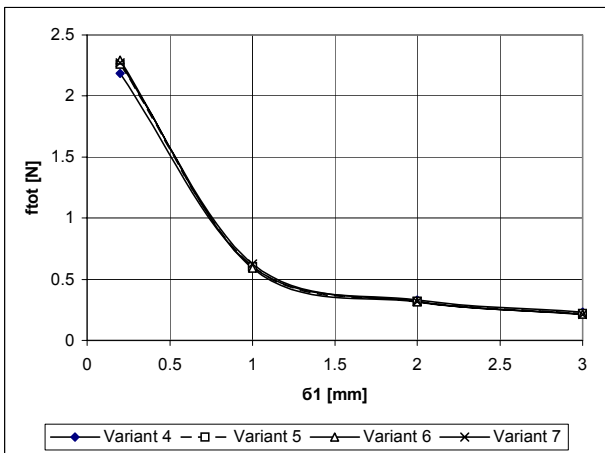


Fig 6b.

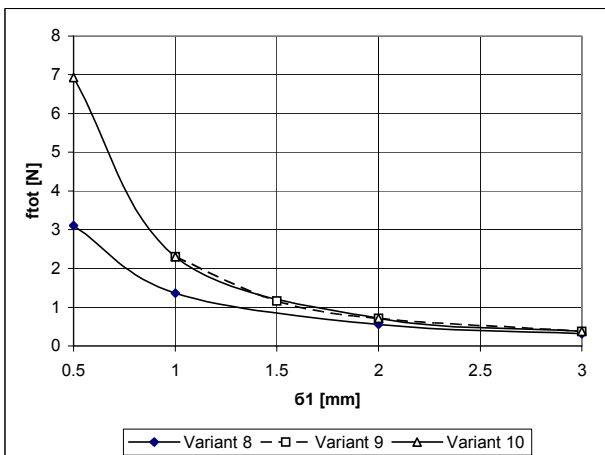


Fig 6c.

Experiments are also carried out to verify the computed results. The comparison shows good agreement between computed and measured forces.

### Conclusions

The main results obtained in the paper are:

- The values of the radius of the transverse part of the armature, for which the electromagnetic force is maximal, are obtained. They depend also on the other constructive parameters.
- The force components are obtained as well as their dependence on the constructive parameters.
- The force-stroke characteristics are obtained for all studied variants of the actuator.

These results could be of help when designing solenoid actuators for embedding in more complex systems.

### References

- [1] Boldea, I., S. Nasar, Linear Electric Actuators and Generators, Cambridge University Press, 1997.
- [2] Alexandrov A. Electrical Apparatus. Sofia, 1999. (In Bulgarian)
- [3] Goldberg O. et al. Transients in electrical machines and apparatus and points of their design. Moscow, 2001. (In Russian)
- [4] J. L. Coulomb and G. Meunier, "Finite element implementation of virtual work principle to magnetic or electric force and torque computation," IEEE Trans. Magn., vol. MAG-20, no. 5, pp. 1894–1896, Sep. 1984.
- [5] S. McFee, J. P. Webb, and D. A. Lowther, A tunable volume integration formulation for force calculation in finite-element based computational magneto-statics, IEEE Trans. Magn., vol. 24, no. 1, pp. 439–442, Jan. 1988.
- [6] F. Henrotte, H. V. Sande, G. Deliege, and K. Hameyer, "Electromagnetic force density in a ferromagnetic material," IEEE Trans. Magn., vol. 40, no. 2, pp. 553–556, Mar. 2004.
- [7] Hinov K. Study of polarized electromagnetic systems. PhD Thesis, TU-Sofia, 2004. (In Bulgarian)
- [8] Meeker D. Finite element method magnetics. Ver. 3.3. User's manual, 2003.
- [9] Brandiski K., I. Iatcheva. CAD systems in electromagnetism. CIELA, Sofia, 2002.

## AUTHOR INDEX

### A

ABRUDEAN Cristian 382  
ACEVSKI Nikolce 92  
ACKOVSKI Risto 92  
AGGARWAL Raj K. 84  
AKBILEK Nevra 237  
ALEKSIĆ Slavoljub R. 350, 361  
ALEXANDROV Anatolij 134  
ALLAB Farid 163  
ANDREEV St. 497  
ANDRIEU C. 426  
ANISIMOV Vladimir 314  
ARSENIEV Igor A. 49  
ASSEV Valery 512  
ATANASOV Dimitar 531  
AVENAS Yvan 169  
AVRAMOV Plamen 184  
AYAZ Murat 346  
AYDEMIR Mehmet Timur 448

### B

BARBAROUX Jean 461  
BAYINDIR K. Cagatay 98, 103, 501  
BEKIROGLU K. Nur 24  
BENNOUNA Oudie 483  
BESPALOV Victor 283  
BOCHEV Ivan 515  
BOJCHEV Borislav 400  
BOJLOV Gancho 465, 469  
BOTEANU Nicolae 317  
BULUCEA Aida Cornelia 18, 125, 317

### C

ÇANAKOGLU A. İhsan 24  
CENGİZ Abdulkadir 14, 346  
CHADEBEC Olivier 321  
CHAMROO Afzal 119  
CISMARU Daniel Cristian 18, 125, 317  
CIUFUDEAN Călin 195  
CONSTANTINESCU Cătălin 109  
CONSTANTINESCU Cristian 223, 227, 444  
CORCAU Jenica Ileana 440  
COULOMB Jean-Louis 321  
CRET Laura 327  
CRISTOFARI Christian 405  
CUMA M. Ugras 98, 103, 501  
CVETKOVIC Zlata Ž. 361  
CVETKOVSKI Goga 303

### D

DACHEV Danail 507  
DARIE Eleonora 1, 5, 131  
DARIE Emanuel 1, 5, 131  
DEACONU Sorin 53, 403  
DIKOV Georgi 531  
DIMITRIJEVIĆ Bojan 336  
DIMITROV Lyubormir 40, 248, 432

DIMITROV Vladislav 253  
DIMITROV Dimitar 535  
DIMITROVA Petya 233  
DINEFF Peter 174, 388, 394  
DINIŞ Corina 382  
DJERDIR Adesslem 257  
DOCHEV Milko 475  
DRAGANOV Nikola 134  
DRIGHICIU Mircea Adrian 138

### E

EJOVA Elena 314  
ENEV Stanislav 525  
EVSTAIEV Ivan 38

### F

FERRIEUX Jean Paul 461  
FILIPOV Anton 491, 497  
FODOREAN Daniel 257  
FOURNIER Jean Marc 163

### G

GADJEVA Elissaveta 207  
GENCHEV Lubomir 160  
GEORGIEV Pencho 243  
GEORGIEVA Galia 521  
GERASIMOV Krum 72, 76  
GETZOV Georgi 248  
GŁOWACZ Zygfryd 278  
GOLDSHTEIN Valery 69  
GOSPODINOV Dinko 243  
GOSPODINOV Vasil 400  
GRACHEV Pavel 314, 411  
GRADINAROV Nikola 453, 457

### H

HERAUD Nicolas 413, 483  
HINOV Krastyo 531  
HINOV Nikolay 453, 457

### I

IATCHEVA Ilona 293  
ILIEV Totyo 253  
IVANOV Chavdar 72, 76  
IVANOV Adrian 465  
IVANOVA Mariya 169  
IVANOVA Nezabravka 465

### J

JANET Fleur 321

### K

KALAPISH Anton 215  
KANEVA Maria 422  
KANTURSKA Stefka 432  
KAPELSKI Georges 335  
KARACOR Mevlut 8  
KEDOUS-LEBOUC Afef 163  
KHADER Sameer H. 263

KHANDOSHKO Konstantin 487  
KOLEV Valentin 507  
KOLONDZOVSKI Zlatko 298  
KOSTYREV Michail 411  
Koubarkov Youri 69  
KOUNTSEVICH Petr 411  
KRASTEV Stoiko 531  
KRÓMER István P-I  
KRUMOV Andrei 233  
KRUSTEVA Anastassia 184  
KUNOV Georgi 207  
KUPOV Alexandr 487  
KUPOVA Anastasia 487  
KUSHLEVA Magdalena 400  
KUYUMCU Feriha Erfan 8  
KUZMICHEV Vladimir 44

## L

LARIONESCU Alexandru Bogdan 195  
LAZAROV Vladimir 515  
LEMBEYE Yves 461

## M

MARINOV Tsvetan 184, 453, 457  
MARINOV Emil 479  
MARINOVA Iliana 330  
MARKOVA Deshka 31  
MATANOV Nikolay 189, 374  
MATEEV Valentin 330  
MATLAC Ioan 444  
MEHMED-HAMZA Mediha 491, 497  
MESE Erkan 346  
MEUNIER Gérard 321, 340  
MICU Dan Doru 327  
MIHAILOV Nicolay 38, 201, 418  
MIHOV Miho 233, 469  
MILOŠEVIĆ Nenad 336  
MIRAoui Abdellatif 257  
MIRON Liliana 444  
MIRON Mihai 223, 444  
MLADENOVIC Ana N. 350  
MOJSOSKA Natasa 286  
MOSHTAGH Jamal 289  
MUSELLI Marc 413

## N

NAUMOV Velko 40  
NEDELTCHEVA Stefka 413  
NICOLA Doru Adrian 18, 125, 317  
NICOLAE Petre-Marian 144  
NICOLAE Ileana-Diana 144  
NIKOLIC Zorica 336  
NIKOLIC Bojana Z. 361  
NIKOLOV Nikolai 367, 371  
NIKOLOV\* Nikolai 479  
NIKOLOVA Kamelia 189  
NOTOV Petko 59, 63  
NOTTON Gilles 405, 413, 515

## O

ÖZDEMIR Mehmet 448

## P

PACHAMANOV Angel 189, 374  
PANIKHIN Michail 283  
PARBAUD Serge 335  
PARLAK Koray Şener 448  
PAVLOV Bozhidar 72  
PEARSICA Marian 115, 180  
PENKOV D. 426  
PERIĆ Mirjana T. 361  
PETKANCHIN Lazar 422  
PETKOV Tsvetozar 160  
PETKOVSKA Lidija 298, 303  
PETRAKIEVA Simona 355  
PIPEROV Nikolay 378  
PIPEROV Vasil-Mario 378, 512, 521  
POGGI Philippe 405, 413, 483  
POPA Gabriel Nicolae 53, 382, 403  
POPA Iosif 53, 403  
POPA Valentin 195  
POPOV Victor V. 49  
POPOV Marian 207  
POPOVA Nataliya 335

## R

RAISON B. 426  
RANGELOV Yulian 72  
RATZ Neli 189, 374  
RATZ Emil 233, 374  
ROGNON J.-P. 426

## S

SAMUELSSON Olof 76  
SAPUNDJIEV Georgi 355  
SARAC Vasilija 303  
SARNO Claude 335  
SCHAEFFER Christian 169, 435  
SIMION Emil 327  
SÎRBU Ioana-Gabriela 144  
SLAVTCHEV Yanko 174  
SOKOLOV Emil 211  
SOLOVIOV Vyacheslav 487  
SOTIROV Dimitar 215  
SPASOV Radoslav 220  
SPIROV Dimitar 31, 149, 155  
SPIROVSKI Mile 92  
STANCHEV Georgie 512  
STANCHEVA Rumena 293  
STANEV Rad 59, 63  
STANEV Iliya 309  
STOYANOV Valentin 201  
STOYANOV Ivaylo 418  
STOYANOV L. 426  
STRÎMBU Constantin 223, 227

## T

TAHRILOV Hristofor 371

TEKE Ahmet 103  
TIRIAN Ovidiu 382  
TODOROV George 220  
TOKUNC Onur 98  
TRENKOV Vasil 457  
TSUKAMOTO Osami P-VI  
TUMAY Mehmet 98, 103, 501  
TZENEVA Raina 174, 388  
TZVETKOVA Svetlana 81

## **V**

VASSEUR Christian 119  
VIET Dang Bang 461  
VIOREL Ioan-Adrian 257  
VITAN Viorel-Dumitru 144  
VLADIMIROV Pencho 31, 149, 155

## **W**

WALLY Olivier 483  
WANG Haoping 119

## **Y**

YANEV Kamen 535  
YATCHEV Ivan 531, 535  
YETGIN A. Gökhan 24, 237  
YILMAZ Kadir 8, 14, 346  
YONNET Jean Paul 163

## **Z**

ZARKOV Zahari 272, 515  
ZDROJEWSKI Antoni 278  
ŽIVKOVIC Milan 336  
ZORLU Sibel 24



# TECHNICAL UNIVERSITY OF VARNA

The Technical University of Varna is the second largest state technical university in Bulgaria with its over 7.000 students.

The University is situated on an area of 189,000 sq.m. The University disposes of 11 buildings where the education and sport processes are conducted, 3 students' hostels and a canteen. The education process is conducted in 86 lecture halls and 176 laboratories, situated on 26,300 sq.m. Since its establishment in 1962 more than 31,000 undergraduates and postgraduates have completed their academic studies at the University, including 630 foreigners from 49 countries.



During its long history the Technical University of Varna won recognition as a prestigious research center with its own place in Bulgarian science and technology.

The structure of the University consists of 8 faculties with 31 departments, 2 colleges, Foreign Languages Department, University Center of Foreign Students, Center for Obtaining Professional Qualification, Francophone Center, Department for Qualification, Computing Center, University Library, Sport Hall and etc.

The training is provided by 454 lecturers, 199 of them are professors and associate professors. The majors offered by the University are as follows:

*Computer Systems and Technologies. The curriculum is developed in accordance with the one at Aberdeen University, Dundee, Scotland and there is an opportunity to obtain two diplomas;*

*Communication Engineering and Technologies;*

*Electronics;*

*Automation, Information and Control Technologies;*

*Navigation;*

*Fleet and Port Operation;*

*Marine Engineering;*

*Shipbuilding and Marine Technologies;*

*Mechanical Engineering Equipment and Technologies;*

*Mechanical and Tool Engineering;*

*Transport Machines and Technologies;*

*Heat Technologies;*

*Electrical Power Engineering and Equipment;*

*Electrical Engineering;*

*Engineering Design;*

*Industrial Management;*

*Ecology, Marine and Environmental Conservation;*





# SPARKY

PROFESSIONAL



[WWW.SPARKYGROUP.COM](http://WWW.SPARKYGROUP.COM)

**ЕЛМОТ АД**



**ELMOT JSC**

**Адрес:**

Велико Търново 5000  
ул. Никола Габровски 73  
тел./факс: 062/ 642845  
тел.: 062/ 641963, 641951  
факс: 062/ 644861  
e-mail: [elmot1@vt.bia-bg.com](mailto:elmot1@vt.bia-bg.com)  
<http://elmot.dir.bg>

**Ръководител:**

дипл.ик. Ел. Николова – Изп.  
директор

**За контакти:**

Инж.Бистра Петкова-Началник  
Отдел Продажби

**Година на основаване:**1967

**Брой служители:**600

**Дейност:**

Разработване, производство,  
продажба и сервиз на подежни  
съоръжения и резервни части за тях.

**Продукти:**

- Въжени телфери с товароподемност 1-32т
- Асинхронни електродвигатели с конусен кафезен ротор и вградена спирачка с мощност от 0.12 до 30 kW
- Взривозащитени ел.двигатели с мощност до 8 kW
  - редуктори, моторредуктори, съединители, кранови компоненти и въжени ограничители на товара
- Хаспели с товароподемност от 100 до 1000 кг
- Резервни части за ел.телфери и ел.двигатели

Изделията са маркирани със знака CE.

**Address:**

Veliko Tarnovo 5000  
73, Nikola Gabrovski St.  
tel./fax: 00359 62/ 642845  
tel.: 00359 62/ 641963, 641951  
fax: 00359 62/ 644861  
e-mail: [elmot1@vt.bia-bg.com](mailto:elmot1@vt.bia-bg.com)  
<http://elmot.dir.bg>

**Managing Director:**

Mrs.Elisaveta Nikolova

**For contacts:**

Bistra Petkova  
Chief of Sales Department

**Established:** 1967

**Number of Employees:** 600

**Business:**

Design, manufacturing, sale and service of hoisting machines and spare parts for them.

**Products:**

- Electric wire rope hoists with capacity from 1 up to 32 t
  - Asynchronous AC brake motors with conical rotor and power from 0.12 to 30 kW
  - Ex-proof motors with power up to 8 kW
  - Reduction gears, geared motors, couplings, overload limiters, crane cits and other components
  - Electric winches with capacity from 100 to 1000 kg
  - Spare parts for electric hoists and electric motors.
- All products are CE marked.

# **"Elprom – ILEP" Ltd.**

**For the purpose of Conformity Assessment and certification**

**For your technical file**

**For your Declaration of conformity**

## **CHOOSE, THRUST YOUR PREFERRED PARTNER**

- ⇒ **Safety of electrical equipment and machinery**
- ⇒ **Energy efficiency of household and similar electrical appliances**
- ⇒ **Electro-physical indexes of electro-insulation materials**
- ⇒ **Electro-static characteristics of materials and products**
- ⇒ **Reliability of electrical and electronic engineering**

---

  
**"Testing Laboratory for  
Electro-technical products"**

43 "Cherni Vrah" blvd., Sofia 1407,  
tel./fax: +359 /2/ 868 32 95  
e-mail: ilep@abv.bg

mobile: +359 88/ 865 25 34; +359 88/ 725 25 03

# **"Elprom – ILEP" Ltd.**



## **PREFERRED PARTNER OF MANUFACTURERS, MERCHANTS, IMPORTERS AND EXPORTERS**

### **Nikolay Popov – Manager of "Elprom – ILEP" Ltd.**

The area of activity of the company is: "Production testing, Conformity Assessment of production, activities related to quality management".

In essence "Elprom -ILEP" Ltd. is an actual and valid legal identification of "Testing laboratory for electro-technical production" ILEP. ILEP, as part of "Elprom - ILEP" Ltd. is the natural and only legal successor of ILEP as part of "Elprom - IEP" JSC (since 1995 ILEP is the public name by which the company is known domestic and abroad on the market of "production testing" service) and back in time with all the previous names of the laboratories of "Institute for electro-technical industry".

The major activity of "Elprom - IEP" JSC is development and production of electro-insulation materials, fill-in compounds, premixes and shaped details, electro-technical products, details and components, electro-magnetical brakes for asynchronous and customized electrical engines, commercial activities (including import), with customized electro-insulation materials, copper wires and specialized elements for clients in the electro industry, energetics, mining and other. Since year of 2000 for the purpose of the testing activities there had been created "Testing laboratory for electro-technical production" as part of the newly founded company "Elprom -ILEP" Ltd. In 2000 ILEP is registered under No 500021 in the Information department (TICQA Conformity Assessment Activity) of the European Organization for Conformity Assessment (EOTC) with headquarters in Brussels.

In its activities "Elprom -ILEP" Ltd. follows its stated policy for client satisfaction regarding to the planned, comprehensive and quality testing as long as the overall quality of the service offered by ILEP - all in accordance to the constantly changing requirements of the society and other

requirements regarding the environment etc. All those requirements are in the name of setting a competence standard in the sector, the successful adoption on the Bulgarian market as long as for better quality of its clients' products and their image not only on domestic market but abroad too.

ILEP as part of "Elprom - ILEP" Ltd. conducts testing for:

- Safety, for type tests, for the purpose of Conformity Assessment and certification of:
  - household and similar electrical appliances;
  - automatic electrical controls for household and similar use;
  - audio, video and similar electronic apparatus;
  - IT and office equipment;
  - amusement machines and personal service machines;
  - electrical equipment for measurement, control and laboratory use;
  - devices for electrical installations;
  - electrical medical devices;
  - machinery and devices for furniture, tailoring, textile, food, perfume, cosmetics and pharmaceutical industries;
  - electrical appliances for low voltage;
  - low-voltage switchgear and controlgear assemblies and other.
- Energy efficiency of household and similar electrical appliances for the purpose of Conformity Assessment, for acquisition of correct and competitive information regarding the energy consumption, in accordance to the directives for labeling of the household and similar electrical appliances (Global approach);
- Electro-static characteristics of materials, products and personal protective equipment;
- Electro-physical indexes of electro-insulation materials;
- Reliability of electrical and electronic engineering;

For the abovementioned activities ILEP is sub-contractor for "Bodies for conformity assessment" and "Bodies for certification of products".

The true assessment of our activities is the clients' satisfaction which, no doubt to the facts, is achieved. Some of the persistent clients of "Elprom - ILEP" Ltd. are leaders and major manufacturers of electrical equipment and household and similar electrical appliances in Bulgaria. Some are from Great Britain, Greece, Turkey and Macedonia. Some others are Bulgarian "Bodies for conformity assessment" and "Bodies for certification of products".

---

**Additional information:**

**"Elprom – ILEP" Ltd.**

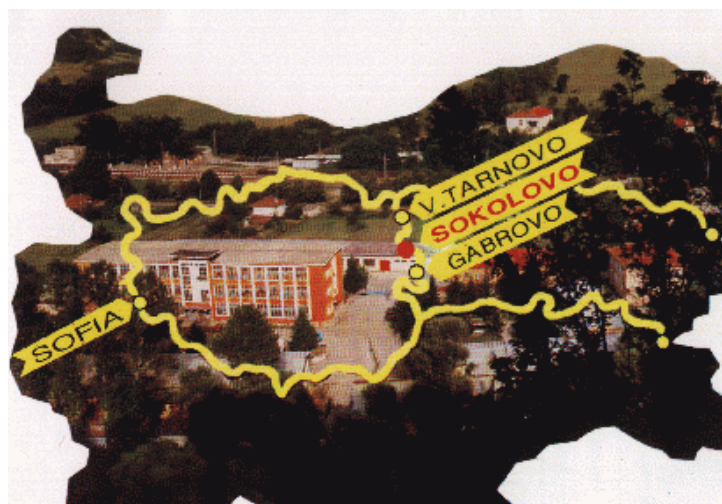
**43 "Cherni Vrah" blvd., Sofia 1407**

**tel./fax: +359 /2/ 868 32 95**

**e-mail: ilep@abv.bg**



България  
обл. Габрово  
общ. Дряново  
5392 Соколово  
Тел: (+359 6722) 290  
(+359 6722) 298  
GSM: (+359) 899/912705  
Факс: (+359 6722) 275  
E-mail: [unitraf@mail.bg](mailto:unitraf@mail.bg)  
[www.unitraf.com](http://www.unitraf.com)



офис София  
1606 София  
ул. "Феликс Каниц" 32  
Тел: (+359 2) 952 16 08  
Факс: (+359 2) 952 26 52

“Унитраф” АД Соколово е специализирана фирма за производство на трансформатори с малка мощност. Многогодишната история на фирмата (основана през 1962 г.) обуславя трайно наложилите се традиции в трансформаторостроенето. В комбинация с натрупания опит, те са достатъчна гаранция за авангарден производствен опит, осигуряващ производството на изделия с високо качество, функционалност и надежност.

Фирма “Унитраф” АД предлага на



DRYANOVO  
MONASTERY

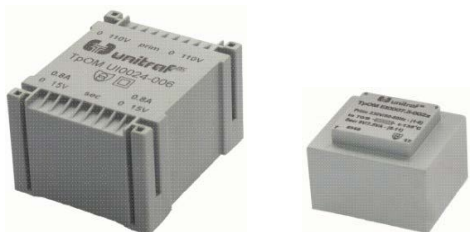
Изработването и внедряването на ISO 9001-2000 е крайна гаранция, че “Унитраф” АД Соколово ще задоволи изискванията и на най-критичните си клиенти в станата и в чужбина.



Трансформаторите се изработват съобразно конструкцията на изделията, в които се влагат. На следващата страница от брошурата е представена пълната гама на произвежданите трансформатори в “Унитраф” АД.



**SOKOLOVO**



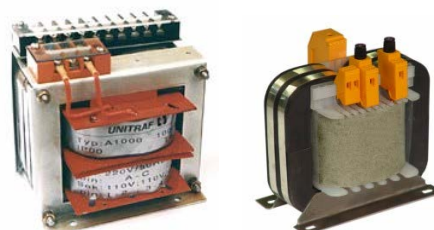
Трансформатори мрежови за печатен монтаж 1,5-24 VA



Трансформатори мрежови тороидални 20-1000 VA



Трансформатори мрежови с ламелен магнитопровод 1,5-660 VA



Трансформатори мрежови с вит магнитопровод 500-2500 VA



Трансформатори мрежови с вит магнитопровод 5-500 VA (тип А)



Трансформатори мрежови с общо предназначение 10-100 VA (тип В)



Трансформатори и дросели мрежови монофазни 2-12 kVA



Трансформатори и дросели мрежови трифазни 0,3-20 kVA



Заваръчни монофазни и трифазни трансформатори и дросели



# **DIT - M Ltd.**

**BULGARIA, 1124 Sofia, 9 Leonardo Da Vinci str**

**Tel/fax: ++359 2/943-47-16 ; 943-47-46**

**E-mail: [dit1@datacom.bg](mailto:dit1@datacom.bg)**

**Web - page: [www.ditm.visa.bg](http://www.ditm.visa.bg)**

---

## **✚ DIT – M Ltd. – DIAGNOSTICS, ENGINEERING, TECHNOLOGIES – MANAGEMENT**



The company was established in 1995, at first as a company for diagnostics and repairs of power transformers and autotransformers on the field.

At present DIT-M Ltd can guarantee high quality work and professional performance on modern technological level in the following activities:

- ✚ power transformers;
- ✚ high-voltage bushings for transformers;
- ✚ on load tap changers (OLTC);
- ✚ diagnostics of high-voltage engines, hydrogenerators and turbogenerators;
- ✚ reconstruction of electric power supply units of 0.4 kV; 6 kV; 20 kV;
- ✚ consulting services.



The company is an official representative for Bulgaria of next companies:

- ✚ Omicron electronics GmbH Austria;
- ✚ Imas Nuova – Italy;
- ✚ Diveco – Slovenia;
- ✚ Dalekovod – Croatia;
- ✚ TESMEC – Italy.

In this activity DIT-M Ltd has reliable foreign partners:

- ✚ Scientific Electric Institute of Moscow;
- ✚ Moscow plant Izolator JSC;
- ✚ Transformator JSC – Toliaty, Russia;
- ✚ Electrosila JSC – St. Petersburg, Russia;
- ✚ Energoservis JSC - St. Petersburg, Russia;
- ✚ Zaporijsky Transformer Plant – Zaporijie, Ukraine;
- ✚ THYSSEN GmbH – Germany;
- ✚ PASSONY & VILLA – Italy;
- ✚ Company IPDD – Minnesota, USA;



✚ On the base of our business contacts we are able to deliver:

- all equipment for power transformers;
- measurement devices;
- machines and devices for erection cable lines, air transmissions lines to 400kV and optic lines;
- spare parts for transformers and generators;
- switching equipment



✚ For these ten years we have performed many diagnostics and repair work in:



- ✚ NPP Kozloduj;
- ✚ TPP Maritza-iztok 2;
- ✚ TPP Maritza-iztok 3;
- ✚ PSHPP Chaira;
- ✚ National Electrical Company
- ✚ TPP Varna



✚ We have fulfilled a number of Contracts in Macedonia, Lebanon, Egypt and so on.

✚ More detailed information you can find on our web page: [www.ditm.visa.bg](http://www.ditm.visa.bg)





# ЕЛПРОМ ХАРМАНЛИ АД ELPROM HARMANLI JSCo



## Централен офис:

1592 София  
бул.: "Асен Йорданов" № 14  
тел.: 02 9651 220, 9651 235  
факс: 02 9651 234  
e-mail: [sales@elprommotors.com](mailto:sales@elprommotors.com)  
[info@elprommotors.com](mailto:info@elprommotors.com)  
[www.elprommotors.com](http://www.elprommotors.com)

## Ръководител:

Борис Бояджиев – Изпълнителен Директор  
За контакти:  
Любка Байова – Търговски Директор

Фирмата е основана през 1976

## Предмет на дейност:

Проектиране, разработване и производство на стандартни и със специално предназначение еднофазни и трифазни асинхронни електродвигатели

## Продукти:

- Еднофазни асинхронни електродвигатели от сериите:  
ASR /с пусков и работен кондензатор/,  
AS /с пусков кондензатор/ и  
AR /с работен кондензатор/.
- Трифазни асинхронни електродвигатели от серия АТ.
- Специални електродвигатели от серия А.

## Производствени бази:

6450 Харманли  
бул. "България" № 99  
тел.: 0373 3029, 2938  
факс: 0373 2150

4006 Пловдив  
ул. "Удроу Уилсън" № 18  
тел.: 032 682 737  
факс: 032 683 254

## Сертификати за качество: ISO 9001:2000

Стандарти: БДС EN, IEC, ГОСТ и др

## Headquarters:

1592 Sofia  
14 Asen Yordanov Blvd.  
tel.: +359 2 9651 220, 9651 235  
fax: +359 2 9651 234  
e-mail: [sales@elprommotors.com](mailto:sales@elprommotors.com)  
[info@elprommotors.com](mailto:info@elprommotors.com)  
[www.elprommotors.com](http://www.elprommotors.com)

## Executive:

Boris Boyadjiev – Executive Director  
Contact person:  
Lyubka Bayova – Sales Director

The company was established in 1976

## Scope of activity:

Design, development and production of standard and special-purpose single-phase and three-phase asynchronous electric motors

## Products:

- ASR /with starting and running capacitor/,  
AS /with starting capacitor/ and  
AR /with running capacitor/  
series of single-phase asynchronous electric motors.
- AT series of three-phase asynchronous electric motors.
- A series of special purpose electric motors.

## Production units:

6450 Harmanli  
99 Bulgaria Blvd.  
tel.: +359 373 3029, 2938  
fax: +359 373 2150

4006 Plovdiv  
18 Woodrow Wilson Str.  
tel.: +359 32 682 737  
fax: +359 32 683 254

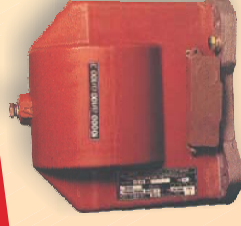
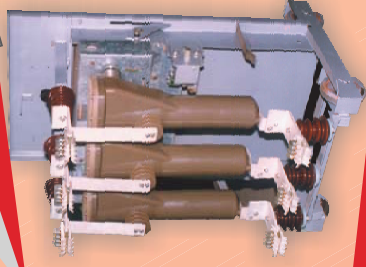
## Certificated: ISO 9001:2000

Standards: BDS EN, IEC, GOST etc.

# ЗАВН-ДОБРИЧ АД



40 ГОДИНИ



до 35 кВ  
енергетично оборудуване

Конструирани, производство и монтаж на електроенергетично оборудуване до 35 кВ

Комплетни разпределителни устройства с маломаслени, елегазови и вакуумни прекъсвачи 7.2, 12, 24 кВ  
Колички с елегазови и вакуумни прекъсвачи - ABB, Siemens, Schneider; Комплектни трансформаторни подстанции 7.2, 12 и 24 кV с апаратура на ABB, Siemens, Schneider; Маломаслени прекъсвачи тип А, АК - 7.2, 12 и 24 кV;  
Измервателни токови и напрежениви трансформатори 0.75, 7.2, 12, 24 и 40,5 кV; Високомощни предпазители тип ВПм 7.2, 12, 24 и 36 кV; Епоксидни изолатори 0.66, 7.2, 12 и 24 кV;  
Модулен типов ред електрически табла ниско напрежение.

Добрич, ул. Свещеник П. Атанасов 18, тел.: 058/ 600 647, 600 659, факс: 058/ 600 532  
e-mail: [zavndobrich@dobrich.net](mailto:zavndobrich@dobrich.net); [http:// www.zavnbhg.com](http://www.zavnbhg.com)

